



Cumhuriyet Science Journal  
Faculty of Science, Cumhuriyet University  
58140 - Sivas - Türkiye  
Phone: +90(346) 487 13 72  
Fax: +90(346) 219 11 86  
e-mail: [csj@cumhuriyet.edu.tr](mailto:csj@cumhuriyet.edu.tr)  
<http://csj.cumhuriyet.edu.tr/en>  
<http://dergipark.org.tr/en/pub/csaj>

Cumhuriyet Science Journal Vol: 43 No: 2 Year 2022



**Sivas Cumhuriyet University**

ISSN : 2680-2587

e-ISSN : 246-2587X

[dergipark.org.tr/tr/pub/csaj](http://dergipark.org.tr/tr/pub/csaj)  
e-mail: [csj@cumhuriyet.edu.tr](mailto:csj@cumhuriyet.edu.tr)



Cumhuriyet Science Journal (CSJ) is an official publication of Sivas Cumhuriyet University, Science Faculty. The high quality research papers related to the natural sciences are published as online four times a year. CSJ is an open access, free of charge journal and all articles in CSJ have undergone peer review and upon acceptance are immediately and permanently free for everyone to read and download.

Volume: 43

Number: 2

Year: 2022



ISSN:2587-2680  
e-ISSN:2587-246X  
Period:Quarterly  
Founded:2002  
Publisher:Sivas Cumhuriyet  
University

# Cumhuriyet Science Journal (CSJ)

**Journal Previous Name:** Cumhuriyet Üniversitesi Fen-Edebiyat Fakültesi Fen Bilimleri Dergisi

**Old ISSN:** 1300-1949

**Owner on behalf of the Sivas Cumhuriyet University, Faculty of Science**

Prof. Dr. İdris ZORLUTUNA (Sivas Cumhuriyet University)

**Editor in Chief**

Prof. Dr. İdris ZORLUTUNA (Sivas Cumhuriyet University)

**Managing Editor**

Assoc. Prof. Dr. Adil ELİK (Sivas Cumhuriyet University)

**Editors**

Prof. Dr. Baki KESKİN

[bkeskin@cumhuriyet.edu.tr](mailto:bkeskin@cumhuriyet.edu.tr)

*Subjects:* Mathematics and Statistics

Institution: Sivas Cumhuriyet University

Assoc. Prof. Dr. Adil ELİK

[elik@cumhuriyet.edu.tr](mailto:elik@cumhuriyet.edu.tr)

*Subjects:* Chemistry and Chemical Engineering,  
Environmental Sciences, Basic Sciences (General)

Institution: Sivas Cumhuriyet University

Prof. Dr. Nilüfer TOPSAKAL

[ntopsakal@cumhuriyet.edu.tr](mailto:ntopsakal@cumhuriyet.edu.tr)

*Subjects:* Applied Mathematics

Institution: Sivas Cumhuriyet University

Prof. Dr. Serkan AKKOYUN

[sakkoyun@cumhuriyet.edu.tr](mailto:sakkoyun@cumhuriyet.edu.tr)

*Subjects:* Physics and Physical Engineering

Institution: Sivas Cumhuriyet University

Prof. Dr. Halil İbrahim ULUSOY

[hiulusoy@cumhuriyet.edu.tr](mailto:hiulusoy@cumhuriyet.edu.tr)

*Subjects:* Chemistry, Analytical Chemistry, Drug Analysis, Pharmacy

Institution: Sivas Cumhuriyet University

Prof. Dr. Fatih UNGAN

[fungan@cumhuriyet.edu.tr](mailto:fungan@cumhuriyet.edu.tr)

*Subjects:* Optics, Phonotics and Fiber optics

Institution: Sivas Cumhuriyet University

Assoc. Prof. Dr. Nail ALTUNAY

[naltunay@cumhuriyet.edu.tr](mailto:naltunay@cumhuriyet.edu.tr)

*Subjects:* Bioanalytical Chemistry, Chemometric Analysis

Institution: Sivas Cumhuriyet University

#### **Section Editors**

Prof. Dr. Natalia BONDARENKO

[bondarenkonp@info.sgu.ru](mailto:bondarenkonp@info.sgu.ru)

*Subjects:* Applied Mathematics and Physics

Institution: Samara University

Prof. Dr. Marcello LOCATELLI

[marcello.locatelli@unich.it](mailto:marcello.locatelli@unich.it)

*Subjects:* Analytical Chemistry

Institution: University "G. d'Annunzio" of Chieti-Pescara

Prof. Dr. Konstantin P. KATIN

[kpkatin@yandex.ru](mailto:kpkatin@yandex.ru)

*Subjects:* Theoretical Chemistry, Computational design of nanostructures, nanodevices and nanotechnologies

Institution: National Research Nuclear University

Assoc. Prof. Dr. Duran KARAKAŞ

[dkarakas@cumhuriyet.edu.tr](mailto:dkarakas@cumhuriyet.edu.tr)

*Subjects:* Inorganic Chemistry, Theoretical Chemistry

Institution: Sivas Cumhuriyet University

Assoc. Prof. Dr. Yaşar ÇAKMAK

[ycakmak@cumhuriyet.edu.tr](mailto:ycakmak@cumhuriyet.edu.tr)

*Subjects:* Applied Mathematics

Institution: Sivas Cumhuriyet University

Assoc. Prof. Dr. Sevgi DURNA DAŞTAN

[sdurna@cumhuriyet.edu.tr](mailto:sdurna@cumhuriyet.edu.tr)

*Subjects:* Molecular Biology

Institution: Sivas Cumhuriyet University

Assist. Prof. Dr. Yener ÜNAL

[uyener@cumhuriyet.edu.tr](mailto:uyener@cumhuriyet.edu.tr)

*Subjects:* Statistics

Institution: Sivas Cumhuriyet University

### **Abstracted&Indexing**

ULAKBİM TR-Dizin

Index Copernicus (ICI Journals Master List)

Clarivate Analytics Zoological Record

Crossref

WorldCat

Akademik Dizin

Arastirmax Bilimsel Yayın İndeksi

Bielefeld Academic Search Engine (BASE)

Directory of Research Journal Indexing (DRJI)

Google Scholar

Research Gate

Idealonline

## **Editorial Board**

Prof. Dr. Sezai ELAGÖZ (ASELSAN)  
Prof. Dr. Mustafa SOYLAK (Erciyes University)  
Prof. Dr. Chuan Fu Yang (Nanjing University of Science and Technology)  
Prof. Dr. Münevver SÖKMEN (KGTU)  
Prof. Dr. Hüseyin MERDAN (TOBB ETU)  
Prof. Dr. Mehmet AKKURT (Erciyes University)  
Prof. Dr. Mustafa KAVUTÇU (Gazi University)  
Prof. Dr. Francois VOS (The University of Queensland)  
Prof. Dr. Abuzar KABIR (International Forensic Research Institute)  
Prof. Dr. Mustafa TÜZEN (GOP University)  
Prof. Dr. Songül KAYA MERDAN (METU)  
Prof. Dr. Jose Javier Valiente-Dobon (INFN-LNL, Padova University)  
Prof. Dr. Yeşim SAĞ AÇIKEL (Hacettepe University)  
Prof. Dr. Mehmet ŞİMŞİR (Sivas Cumhuriyet University)  
Prof. Dr. Atalay SÖKMEN (KGTU)  
Prof. Dr. Ricardo I. JELDRES (Universidad de Antofagasta)  
Prof. Dr. Mustafa YILDIRIM (Sivas Cumhuriyet University)  
Prof. Dr. Ali DELİCEOĞLU (Erciyes University)  
Prof. Dr. Tuncay BAYRAM (Karadeniz Technical University)  
Prof. Dr. Gökhan KOÇAK (Erciyes University)  
Prof. Dr. Nadjat Laouet (Freres Mentouri Constantine-1 University)  
Assoc. Prof. Dr. Savaş KAYA (Sivas Cumhuriyet University)

## **Layout Editors:**

Lecturer Aykut HASBEK

## **Copyeditors:**

Assist. Prof. Dr. Doğa Can SERTBAŞ  
Assist. Prof. Dr. Hacı Ahmet KARADAŞ  
Research Assistant Özgür İNCE

## **Proofreader:**

Assist. Prof. Dr. Yener ÜNAL  
Lecturer Aykut HASBEK

**Publication Type:** Peer Reviewed Journal

**Cite Type:** Cumhuriyet Sci. J.

## **Contact Information**

Faculty of Science Cumhuriyet University  
58140 Sivas- TURKEY  
Phone: +90 (346) 487 13 72  
Fax: +90 (346) 219 11 86  
e-mail: [csj@cumhuriyet.edu.tr](mailto:csj@cumhuriyet.edu.tr)  
<http://dergipark.gov.tr/csj>

CONTENTS			PAGES
1	<b>Hani ALOTAİBİ</b> <i>Crif1 is Required for Proper Mesenchymal to Epithelial Transition</i>	Research Article	165 - 170
2	<b>Hatice TANER SARAÇOĞLU, Mehtap AKIN, Ahmet ÜNVER</b> <i>Total Phenolic Content, Free Radical Scavenging Activity and Antibacterial Activity of Some Buplerum Species</i>	Research Article	171 - 175
3	<b>Emin Ufuk KARAKAŞ, Ayşe Nur PEKTAŞ, Şeyda BERK</b> <i>Selection and Validation of Potential Reference Genes for Quantitative Real-Time PCR Analysis in Blaptica Dubia (Serville, 1838) (Blattidae, Blaberidae)</i>	Research Article	176 - 182
4	<b>Tuğba KUMTEPE, Murat DOĞAN</b> <i>The Role of Cisplatin Loaded Biocompatible Nanoparticles in Cancer Treatment</i>	Research Article	183 - 187
5	<b>Bilal YILMAZ</b> <i>Analysis of Carvedilol in Pharmaceutical Preparations by Spectrofluorometric Method</i>	Research Article	188 - 192
6	<b>Arzu BİNİCİ</b> <i>Syntheses of Hexaminomonoferrrocenylo(N/O)cyclotetraphosphazenes: Spectral Properties and Antituberculosis Activities</i>	Research Article	193 - 200
7	<b>Gülşen TAŞKIN ÇAKICI, Ergün KASAKA, Nail ALTUNAY</b> <i>The Quality of Yıldız River Water and Determining Trace Elements by Liquid-Liquid Micro-Extraction Analytical Method</i>	Research Article	201 - 210
8	<b>Burak TÜZÜN, Koray SAYIN, Hilmi ATASEVEN,</b> <i>Could Momordica Charantia Be Effective In The Treatment of COVID19?</i>	Research Article	211 - 220
9	<b>Sümeyya SERİN, Öznur DOĞAN ULU</b> <i>Quantum Chemical Benchmark Study on Valdecoxib, a Potent and Selective Inhibitor of COX-2, and its Hydroxylated Derivative</i>	Research Article	221 - 231
10	<b>Dilara ÜLGER ÖZBEK , Deniz KURUÇAY</b> <i>Investigation of In Vitro Effect and Molecular Docking of Aluminum on Glucose-6-Phosphate Dehydrogenase Activity</i>	Research Article	232 - 237
11	<b>Samet KOCABAY, Mehmet Abdullah ALAGÖZ, Hıncal Gökhan BAKIR, Birnur AKKAYA</b> <i>In Silico Studies of Synthetic Sulfatide as a Potential Drug Candidate Against Covid-19</i>	Research Article	238 - 245
12	<b>Sultan ERKAN, Doğan Can DİKYOL</b> <i>Computational Structure Characterization of 1,2,3-Selendiazole Isomers, Investigation of Some Molecular Properties and Biological Activities</i>	Research Article	246 - 256
13	<b>Mehmet Akif HAFIZOĞLU, Tahsin BOYRAZ, Ahmet AKKUŞ</b> <i>The Effect of Mullite Addition on Wear Properties of SiO2 Doped ZrO2 Ceramics</i>	Research Article	257 - 265
14	<b>Özlem Pelin CAN, Ayşegül DEMİR</b> <i>The Effects of Cooking Temperatures and Times on the Formation of Aromatic Amines of Meatballs Derived from Sivas Province</i>	Research Article	266 - 272
15	<b>Esra ÇİÇEK ÇETİN, Mehmet BEKTAŞ, Münevver Yıldırım YILMAZ</b> <i>On the Associated Curves of a Frenet Curve in <math>R_1^4</math></i>	Research Article	273 - 276
16	<b>Nusret KARAASLAN</b> <i>On Gaussian Jacobsthal-Padovan Numbers</i>	Research Article	277 - 282
17	<b>Morufu Oyedunsi OLAYİWOLA, Kabiru KAREEM</b> <i>A New Decomposition Method for Integro-Differential Equations</i>	Research Article	283 - 288
18	<b>Demet BİNBAŞIOĞLU</b> <i>On Fixed Point Results for Generalized Contractions in Non-Newtonian Metric Spaces</i>	Research Article	289 - 293

<b>19</b>	<b>Canan SÜMBÜL, Cemal BELEN, Mustafa YILDIRIM</b> <i>Properties of <math>J_p</math>-Statistical Convergence</i>	<i>Research Article</i>	294 - 298
<b>20</b>	<b>Ümit Ziya SAVCI</b> <i>Kinematic Analysis in 3-Dimensional Generalized Space</i>	<i>Research Article</i>	299 - 307
<b>21</b>	<b>Emel KARACA</b> <i>Singularities of the Ruled Surfaces According to RM Frame and Natural Lift Curves</i>	<i>Research Article</i>	308 - 315
<b>22</b>	<b>Ahmet KARAKAŞ</b> <i>A Study on Generalized Absolute Matrix Summability</i>	<i>Research Article</i>	316 - 320
<b>23</b>	<b>Murat ARI, Bahar KARAMAN, Yılmaz DERELİ</b> <i>Solving the Generalized Rosenau-KdV Equation by the Meshless Kernel-Based Method of Lines</i>	<i>Research Article</i>	321 - 326
<b>24</b>	<b>Bakiye ÇAKIR</b> <i>Variation of Pinning Force Density Throughout the TSMG Y123 Superconductor with Location</i>	<i>Research Article</i>	327 - 332
<b>25</b>	<b>Özgür POLAT</b> <i>Altering Electrical Features of LuFeO<sub>3</sub> Compound Via Ir Doping into Fe Sites</i>	<i>Research Article</i>	333 - 341
<b>26</b>	<b>İbrahim ÇINAR</b> <i>Analysis of Magnetization Change with Temperature in an Artificial Spin Ice Network by Three Dimensional Finite Element Modeling</i>	<i>Research Article</i>	342 - 345
<b>27</b>	<b>Furkan KURUOĞLU</b> <i>Influence of the Core Pillar Height on the Bandgap Characteristics of Piezoelectric Phononic Crystals with Ring-Shaped Grooves</i>	<i>Research Article</i>	346 - 350
<b>28</b>	<b>Çiğdem TOPÇU GÜLÖKSÜZ, Nuri ÇELİK</b> <i>A New Extension Form for Continuous Probability Distributions: Uniform-X Distributions</i>	<i>Research Article</i>	351 - 357

## Crif1 is Required for Proper Mesenchymal to Epithelial Transition

Hani Alotaibi<sup>1,2,a,\*</sup>

<sup>1</sup> İzmir Biomedicine and Genome Center, İzmir, Türkiye

<sup>2</sup> İzmir International Biomedicine and Genome Institute, Dokuz Eylül University, İzmir, Türkiye

\*Corresponding author

### Research Article

#### History

Received: 24/01/2022

Accepted: 09/04/2022

#### Copyright



©2022 Faculty of Science,  
Sivas Cumhuriyet University

### ABSTRACT

The epithelial to mesenchymal and the mesenchymal to epithelial transitions (EMT and MET) are fundamental developmental processes required for shaping the embryo but are also hijacked by cancer cells during metastasis. The regulation of EMT is very well studied, and major regulators have been identified. A similar understanding of the regulation of MET is needed. Recently we and others have described essential factors for the initiation and progression of MET; among them is the ETS transcription factor E1f3. Recent reports showed that Crif1 is critical for the function of E1f3, yet the influence on MET has not been reported. Here, we studied the involvement of Crif1 in MET using a loss of function approach in NMuMG cells. We found that the depletion of *Crif1* resulted in an impaired MET. We have also noticed that *Cdh1* mRNA and protein expression was not affected; instead, E-cadherin, the protein product of *Cdh1*, was localized to the cytoplasm. These results are in agreement with our previous findings following the depletion of E1f3. In conclusion, *Crif1* was essential for the mesenchymal to epithelial transition, and it may exert its function in cooperation with E1f3.

**Keywords:** EMT, E1f3, Crif1,

[hani.alotaibi@deu.edu.tr](mailto:hani.alotaibi@deu.edu.tr)

<https://orcid.org/0000-0001-7423-9653>

### Introduction

The epithelial to mesenchymal transition (EMT) is a very well studied developmental process [1]. It is essential for proper gastrulation as well as many developmental stages, including organogenesis and embryo shaping [2, 3]. This process is also hijacked by tumor cells for dissemination into distant sites during metastasis [4-6]. The cells undergoing EMT establish a new non-polarized phenotype and motile capacity due to changes in gene expression of key EMT-related genes [7, 8]. The most notable changes include the downregulation of *Cdh1* and the upregulation of *Cdh2* (the cadherin switching) [9].

On the other hand, the mesenchymal to epithelial transition (MET) is also a developmental process; it is critical for cell fate determination and during organogenesis [2]. MET is the reversal of EMT because the cells will gain epithelial characteristics. Still, recent research suggested that MET is not simply the opposite of EMT, considering the differences in the regulatory cues controlling these transitions [10-12]. Despite the well-characterized EMT, a similar understanding of MET and its regulation is lagging.

The regulation of MET has gained attention in recent years, and novel mechanisms appear to impact its control. One of the earlier reports suggested that MET is required to reprogram induced pluripotent stem cells (iPSCs) [12]. MET activation is initiated by the activation of *Cdh1* in response to exogenous Klf4 leading to the activation of the core pluripotency network [12]. More recently, *Grhl2* and *Grhl3* have been shown to regulate MET by activating *Cdh1*

expression [10, 13]. Other factors such as *Ovo2* have also been attributed to safeguarding the epithelial state by sustaining MET [14, 15]. Finally, the Ets transcription factor *E1f3* was described as an essential requirement for proper MET, which may be due to its role in regulating the transcription of *Grhl3* [16]. The accumulated evidence on the regulation of MET is still limited to a few transcription factors and pathways, limiting the understanding of MET in general and negatively impacting the understanding of metastasis. A better knowledge of MET is of utmost importance for knowing the associated disease and understanding basic concepts in developmental biology.

Recently, the CR6-interacting factor 1 or *Crif1* was described as an essential factor for the proper function of E1f3 during intestinal development. Crif1 is better known as mitochondrial protein taking part in the large mitochondrial ribosomal subunit [17]. But other reports showed a nuclear expression of *Crif1* acting as a transcriptional repressor of the orphan nuclear receptor NR4A1 [18]. Despite the diverse roles of *Crif1* in controlling different aspects of cellular metabolism, the relationship with *E1f3* was of significant interest to us. We have recently shown a fundamental requirement of *E1f3* during MET [16], which makes it reasonable to ask whether *Crif1* is also assisting *E1f3* during its role on MET. To this end, we hypothesized that *Crif1* could be a component of the regulatory circuit of MET, and to test this hypothesis, we applied a loss of function approach using the well-known NMuMG cells.



## Materials and Methods

### Cell Line

NMuMG, normal murine mammary gland cell line, was obtained from ATCC. In general, cells were cultured at 37°C in an incubator supplied with 10% CO<sub>2</sub>. The culture medium was DMEM (Gibco) supplemented with 10% fetal bovine serum (FBS), 10 U ml<sup>-1</sup> Penicillin/Streptomycin, 0.1 mM non-essential amino acids, 2 mM L-glutamine (Gibco), and 10 µg ml<sup>-1</sup> insulin (Sigma). Culture media were replenished every couple of days. Cell passaging was performed at 80-90% confluence.

### Initiation of EMT and MET

NMuMG cells were treated with TGFβ3 (5 ng/ml, PeproTech) for 3 days. For the induction of MET, TGFβ withdrawal was applied by washing the cells two times with PBS and incubating for an additional 3 days in fresh DMEM.

### siRNA Transfection

For loss of function experiments, 100000 cells were seeded in 6-well plated and transfected with 50 nM siRNAs targeting *Elf3* (Qiagen), *Crif1* (Qiagen), or a non-targeting control siRNA (Ambion) using Lipofectamine RNAi Max (Invitrogen). After transfection, cells were incubated for 3 days and then collected for RNA isolation or immunofluorescence labeling.

### mRNA Expression Level Analysis

Total RNA was prepared from treated and control cells using the Nucleospin RNA II kit (Macherey-Nagel). Changes in mRNA levels were measured from isolated RNA by qPCR. Generally, 1 µg total RNA was used for cDNA synthesis using Maxima First Strand cDNA Synthesis Kit (Thermo). qPCR analysis and quantification were performed using the ΔΔCt method. Primer sequences are available upon request.

### Western Blot Analysis

For gene expression changes at the protein level, cultured cells were collected with the aid of a cell lifter (Corning). Cells were then lysed in cell lysis buffer (50 mM Tris-HCl, pH 8.0, 250 mM NaCl, 0.1% Nonidet P-40, and 1X protease inhibitor cocktail (Roche)). Protein quantification was performed with Bradford assay. 50 µg total lysate was loaded on a 10% acrylamide gel transferred onto PVDF membranes (Millipore). The membranes were blocked in Blotto containing 5% nonfat milk for 1 h at room temperature. The membranes were then incubated with mouse monoclonal anti-E-cad (1:1000, BD), anti-Vimentin (1:1000), or anti-Gapdh (1:1000, SantaCruz) for 1h at RT, washed three times with Blotto and incubated with peroxidase-conjugated secondary

antibodies for 1h. Detection of protein bands was done with ECL-plus (Amersham). The membranes were exposed to X-ray films (AGFA) for 1 min. The films were then developed using a hyper-processor developer (Amersham).

### Immunofluorescence Labeling and Confocal Microscopy

Cells on coverslips were washed two times with PBS and fixed with 4% formaldehyde for 10 min. The cells were then washed two times with PBS and permeabilized with 0.25% Triton X-100 for 5 min. After washing twice with PBS, the cells were incubated with anti-E-cadherin antibodies (BD Bioscience) in PBS (1:200) for 2 h at room temperature. Next, the cells were washed twice with PBS and incubated with Alexa594-conjugated secondary antibodies together with Phalloidin (Invitrogen) for 1 h. Nuclei were stained with DAPI (1:1000, Invitrogen), and the slides were mounted with CitiFluor antifadant solution. Immunostained cells were imaged with a Zeiss LSM780 confocal microscope powered by the ZEN software (Zeiss).

### Statistical Analysis

qPCR experiments were performed in triplicates. Statistical evaluation of the results was performed using the student's t-test; a 95 % confidence interval was applied. All experiments were performed at least three times. Error bars depict "standard error of the mean", \* p-value < 0.05; \*\* p-value < 0.01; \*\*\* p-value < 0.001.

## Results

### EMT and MET in NMuMG Cells

We used NMuMG cells to study the role of *Crif1* during MET. We first confirmed the transition to the mesenchymal and the epithelial states by monitoring the cellular morphology changes associated with each transition, followed by immunofluorescent staining with E-cadherin-specific antibodies. The results revealed, as expected, a successful EMT and MET (Figure 1A). The reduction of E-cadherin expression and its disappearance from the plasma membrane during EMT is accompanied by the rearrangement of actin filaments (visualized by phalloidin staining) as stress fibers (Figure 1A - middle). E-cadherin expression reappears at the plasma membrane after the completion of MET (Figure 1A - right). These changes are also associated with a typical cadherin switching, where *Cdh1* expression is lost in mesenchymal cells and restored during MET (Figure 1B).

In contrast, *Cdh2* expression is upregulated during EMT and then downregulated in MET (Figure 1C). The mesenchymal transition can also be confirmed by the elevated *Vim* and *Zeb1* expression (Figure 1C). The expression pattern of *Crif1* during EMT and MET resembled that of *Elf3* (Figure 1B).

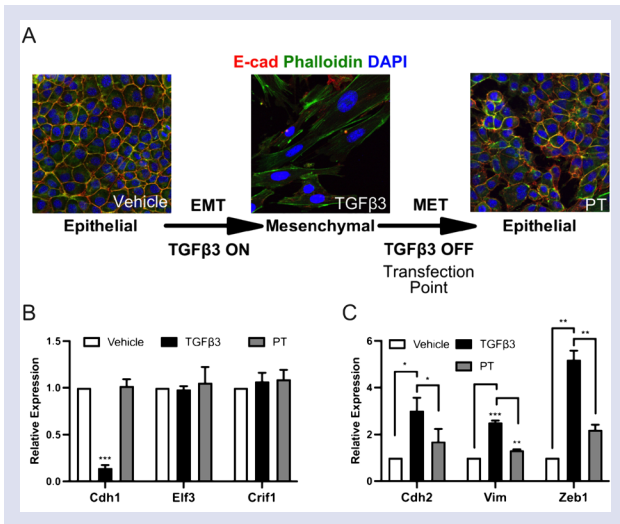


Figure 1. Cellular and gene expression changes in NMuMG cells in response to EMT and MET induction. A) Confocal images of NMuMG cells treated with vehicle (epithelial), TGFβ3 (mesenchymal), or PT (post-treatment). B) Gene expression changes of *Cdh1*, *Elf3*, and *Crif1* during EMT and MET. C) Changes in gene expression of the mesenchymal markers *Cdh2*, *Vim*, and *Zeb1*. qPCR results represent 3 independent experiments. \*:  $P < .05$ , \*\*:  $P < .001$ , \*\*\*:  $P < 0.0001$ .

### Depletion of *Crif1* Results in an Impaired MET

We extended the correlation of expression studies to loss of function experiments. For this purpose, we utilized siRNAs against *Crif1* and transfected NMuMG cells undergoing MET with either si*Crif1* or siCntrl siRNAs at the time of TGFβ withdrawal (i.e., at the onset of MET). The cells were monitored daily, and changes in morphological appearance were recorded and were discernible using phase-contrast microscopy (Figure 2A). After 72 hours of treatment, the cells were prepared for confocal microscopy imaging by immunofluorescent staining as described in the methods section. The morphological changes resulting from *Crif1* depletion were reminiscent of the changes previously described in response to *Elf3* depletion (Figure 2A, B). The absence of *Elf3* expression resulted in an impaired MET [16]. We also noticed that the E-cad expression was not reduced but rather present in the cytoplasm (Figure 2B), leading to rearrangement of actin filaments as stress fibers, similar to what was observed in the *Elf3* depleted cells (Figure 2B).

To confirm the observed morphological changes, we studied the expression of key markers of EMT and MET in response to si*Crif1* treatment. NMuMG cells were prepared and transfected as described in the previous section. 72 hours later, the RNA was isolated, and changes in *Crif1* and *Cdh1* mRNA levels were determined by qPCR and western blot analyses (Figure 3).

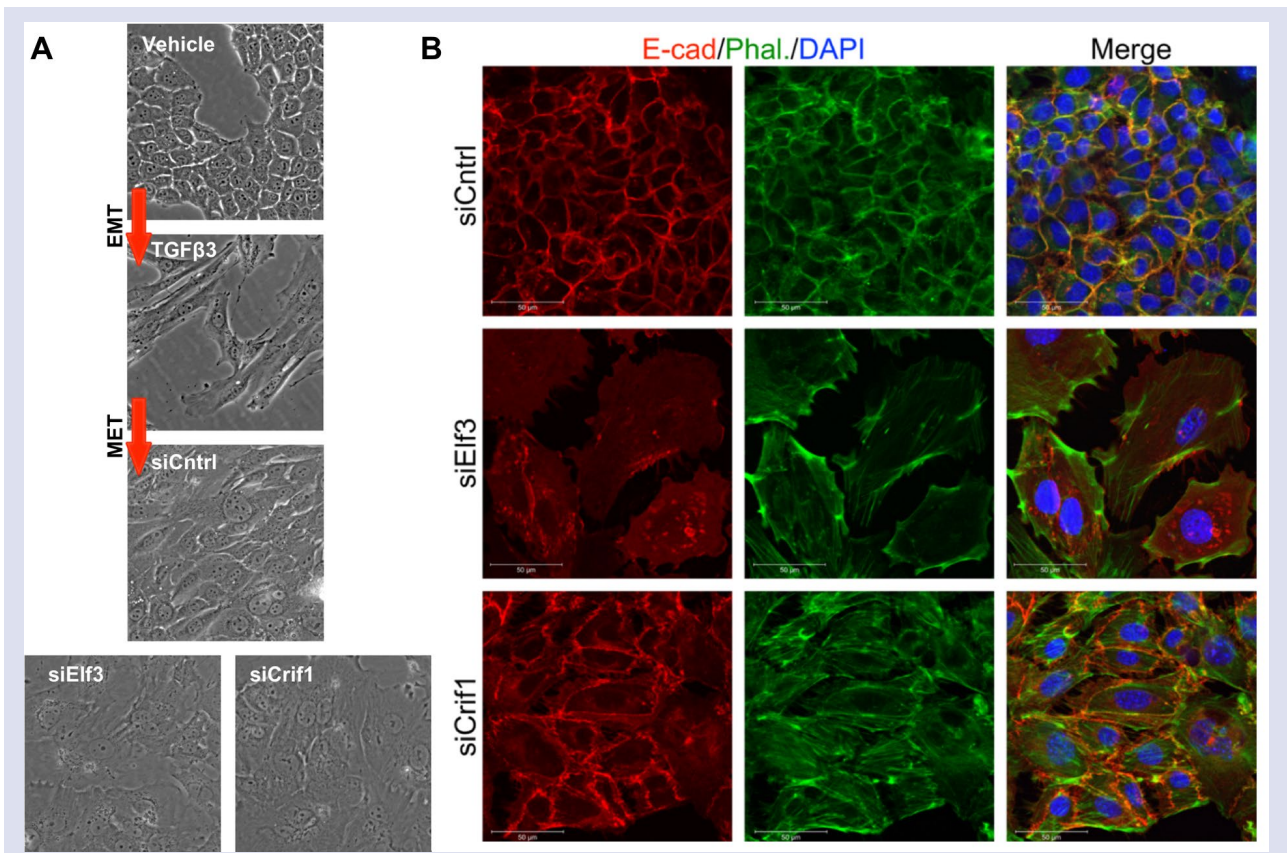


Figure 2. The effect of *Crif1* loss on MET. A) Phase-contrast images of NMuMG cells during EMT and MET, showing the morphological changes in control and siRNA treated cells. B) Confocal images of *Crif1* and *Elf3* depleted cells compared to the control.

First, we examined the knock-down efficiency by both siCrif1 and siElf3. Both genes were significantly downregulated upon siRNA treatment (Figure 3A, C). The downregulation of Crif1 did not impact the expression levels of Cdh1. Significant expression of Cdh1 was observed compared to the control-treated sample (Figure 3A). This result confirmed our confocal imaging results, in which E-cad expression was detected but not localized to the plasma membrane (Figure 2B).

The downregulation of Crif1 was also accompanied by elevated levels of key mesenchymal markers such as Snai1, Snai2, Zeb1, and Twist (Figure 3B). Finally, the levels of E-cad and Vimentin were studied by western blot. The results indicated the presence of E-cad protein and the increased Vim levels (Figure 3E, F).

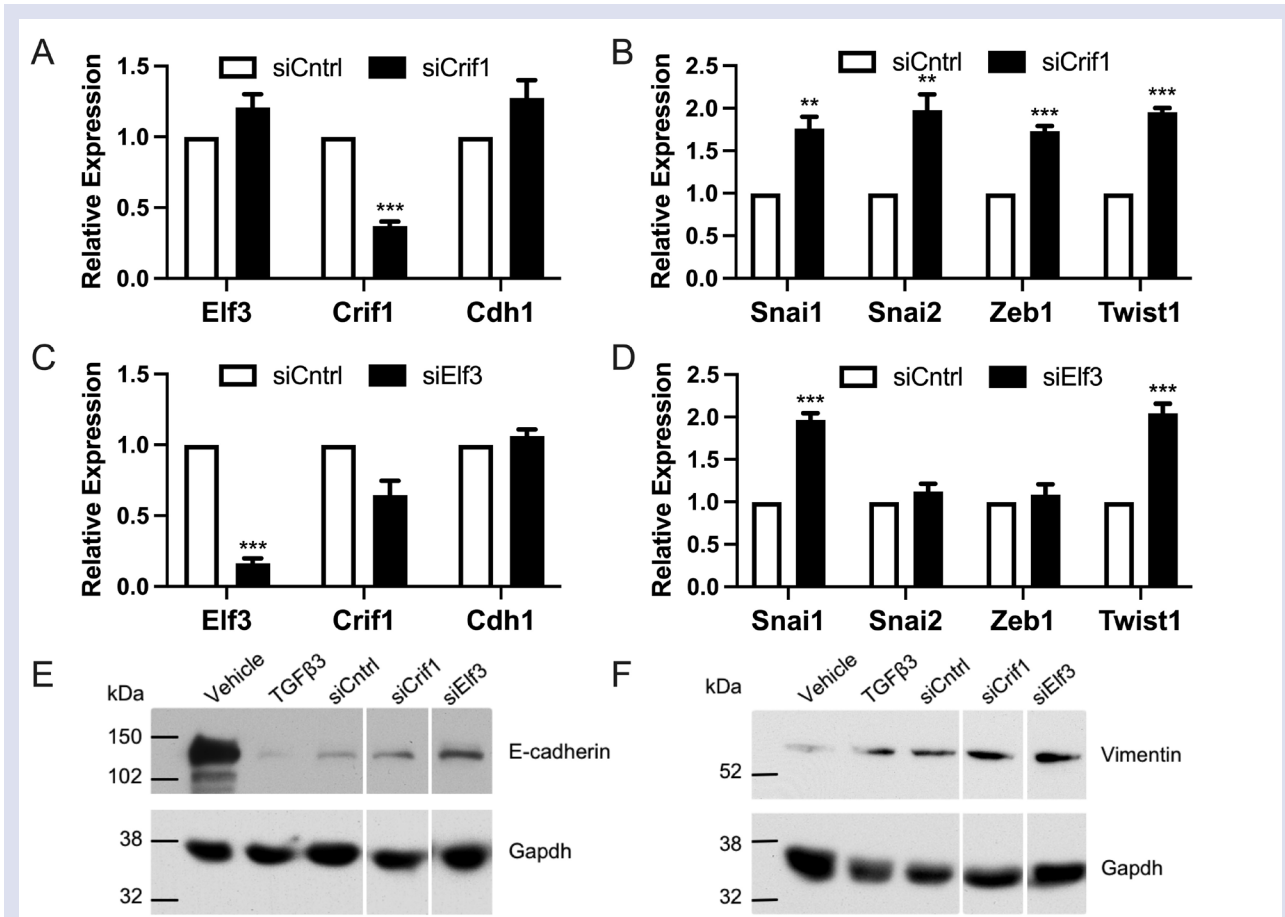


Figure 3. Gene expression changes in response to Crif1 depletion. A and C) qPCR results of Crif1 and Elf3 depleted cells showing the knock-down efficiency and the expression of Cdh1. B and D) the expression of key mesenchymal genes in response to Crif1 and Elf3 downregulation. qPCR results represent 3 independent experiments. \*\*:  $P < .01$ , \*\*\*:  $P < .001$ . E and F) Western blot analysis of E-cadherin and Vimentin in response to Crif1 and Elf3 depletion. Gapdh was used as an internal control

## Discussion

In this study, we examined the effects of Crif1 depletion on the progression of MET in NMuMG cells. Crif1 was selected for this study based on previous reports showing its importance for the function of Elf3 [19]. We have previously reported the importance of Elf3 for the progression of MET [16], so it was plausible to hypothesize a functional impact of Crif1 on MET.

We selected the normal murine mammary gland cell line NMuMG, which is well known for its ability to switch between epithelial and mesenchymal states in response to TGFβ treatment and withdrawal [10, 16]. Besides,

Besides, these cells are isolated from normal mammary tissue; thus, their lack of chromosomal abnormalities makes them a perfect cellular model for studying the biology of EMT and MET.

The successful EMT and MET transitions are visible through the changes in cellular morphology and the changes in the expression of key epithelial or mesenchymal markers. For example, the cadherin switch [9] is the hallmark for a bona fide EMT since E-cad and N-cad are expressed in a mutually exclusive manner, although they share about 70% homology [20]. Elf3 is a

known epithelial transcription factor [21], its expression was found essential for MET [16], yet its expression is not diminished in cells undergoing EMT. This may relate to a specific function of E1f3 in the mesenchymal cells. A similar expression pattern for Crif1 can also be observed during EMT and MET; its expression is not changed during the transitions, which provides evidence for the correlation of E1f3 and Crif1 expression. This correlation supports the possible dependency of E1f3 on Crif1; as suggested by published research, Crif1 was reported as an essential factor for the function of E1f3 during intestinal development [19].

Depleting Crif1 during MET resulted in an aberrant transition; cells could not progress to the epithelial state and retained the expression of mesenchymal markers. The reduction of E-cadherin expression and its disappearance from the plasma membrane is accompanied by the rearrangement of actin filaments (visualized by phalloidin staining) as stress fibers. These changes are also associated with cadherin switching [9]; epithelial cells lose Cdh1 expression and gain Cdh2 expression. These changes in morphology and gene expression were also visible in response to the loss of other key regulators of MET, such as Grhl3 and Hnf4a [10] and, more recently, E1f3 [16]. In fact, having a similar phenotype due to the depletion of several transcription factors can only suggest a common mechanism controlled by different factors in the form of a regulatory network. Growing evidence suggests the involvement of other transcription factors within this network, such as Ovol2 [15, 22, 23].

The disrupted localization of E-cadherin away from the plasma membrane is as critical to the cells as its reduced mRNA levels (during EMT, for example). The impact of E-cad loss has many outcomes, it is a key pluripotency marker [20], and its loss results in a disturbed epithelial state, with indications of EMT [24].

Crif1 was previously associated with functions in the mitochondria and the nucleus. It is a component of the mitochondrial large ribosomal subunit [17, 25]. The mitochondrial function is not limited to the ribosome since Crif1 has been reported to interact with key mitochondrial DNA replication components such as ATAD3A and ATAD3B [26]. In the nucleus, Crif1 was found to interact with DNA damage sensors such as GADD45A, GADD45B, and GADD45G [27] and also with the nuclear receptor NR4A1 via the NR4A1 AB domain [18]. Crif1 negatively impacts the progression of the cell cycle; its overexpression led to latency in the G1 phase, while its inhibition accelerated the cell cycle by interacting with CDK2 [28].

The regulation of MET and the mechanisms governing its initiation and progression are poorly understood compared to EMT. The impaired MET observed here suggests a cell cycle defect, marked by the enlarged cells and the presence of multinucleation. It is reasonable to assume that the function of Crif1 during MET is, in part, to regulate the cell cycle through its interaction with Cdk2. The increasing evidence elucidating the regulation of MET

will increase our knowledge about this vital process and widen our perspective for the search for novel therapeutics for the management of advanced cancer and metastasis.

## Conclusion

In this study, we examined the effects of Crif1 loss on MET. We used the well-known EMT/MET cellular model, NMuMG cells, for their well-documented cellular plasticity and responsiveness to TGF $\beta$ . The overall results obtained here are in agreement with the current literature and with our previous research; they also provide new insights into the functional requirement of Crif1 during the initiation of MET. We showed for the first time a novel function for Crif1 during MET; Crif1 played a critical role within the transcriptional regulatory network regulating MET. This is of particular importance not only for understanding the basics of EMT/MET from the regulatory point of view but also for translational implications, which would help design novel therapeutics for the management of metastasis.

## Acknowledgment

This work was supported by TÜBİTAK Grant 219Z034.

## Conflicts of interest

The author states no conflict of interests.

## References

- [1] Chen T., You Y., Jiang H., Wang Z.Z., Epithelial-mesenchymal transition (EMT): A biological process in the development, stem cell differentiation, and tumorigenesis, *J. Cell Physiol*, 232(12) (2017) 3261-3272.
- [2] Chen J., Han Q., Pei D., EMT and MET as paradigms for cell fate switching, *J. Mol. Cell Biol.*, 4(2) (2012) 66-69.
- [3] Kim D.H., Xing T., Yang Z., Dudek R., Lu Q., Chen Y.H., Epithelial Mesenchymal Transition in Embryonic Development, Tissue Repair and Cancer: A Comprehensive Overview, *J. Clin. Med.*, 7(1) (2017).
- [4] Banyard J., Bielenberg D.R., The role of EMT and MET in cancer dissemination, *Connect Tissue Res.*, 56(5) (2015) 403-413.
- [5] Brabletz T., Kalluri R., Nieto M.A., Weinberg R.A., EMT in cancer, *Nat Rev Cancer*, 18(2) (2018) 128-134.
- [6] Chaffer C.L., San Juan B.P., Lim E., Weinberg R.A., EMT, cell plasticity and metastasis, *Cancer Metastasis Rev.*, 35(4) (2016) 645-654.
- [7] Kalluri R., EMT: when epithelial cells decide to become mesenchymal-like cells, *J. Clin. Invest*, 119(6) (2009) 1417-1419.
- [8] Sayan A.E., Tumour-promoting role of EMT-inducing transcription factor ZEB1 in mantle cell lymphoma, *Cell Death Differ*, 21(2) (2014) 194-195.
- [9] Wheelock M.J., Shintani Y., Maeda M., Fukumoto Y., Johnson K.R., Cadherin switching, *J. Cell. Sci.*, 121 (Pt 6) (2008) 727-735.

- [10] Alotaibi H., Basilicata M.F., Shehwana H., Kosowan T., Schreck I., Braeutigam C., Konu O., Brabletz T., Stemmler M.P., Enhancer cooperativity as a novel mechanism underlying the transcriptional regulation of E-cadherin during mesenchymal to epithelial transition, *Biochimica Et Biophysica Acta-Gene Regulatory Mechanisms*, 1849(6) (2015) 731-742.
- [11] Li Q., Hutchins A.P., Chen Y., Li S., Shan Y., Liao B., Zheng D., Shi X., Li Y., Chan W.Y., Pan G., Wei S., Shu X., Pei D., A sequential EMT-MET mechanism drives the differentiation of human embryonic stem cells towards hepatocytes, *Nat. Commun.*, 8 (2017) 15166.
- [12] Li R., Liang J., Ni S., Zhou T., Qing X., Li H., He W., Chen J., Li F., Zhuang Q., Qin B., Xu J., Li W., Yang J., Gan Y., Qin D., Feng S., Song H., Yang D., Zhang B., Zeng L., Lai L., Esteban M.A., Pei D., A mesenchymal-to-epithelial transition initiates and is required for the nuclear reprogramming of mouse fibroblasts, *Cell Stem Cell*, 7(1) (2010) 51-63.
- [13] Werth M., Walentin K., Aue A., Schonheit J., Wuebken A., Pode-Shakked N., Vilianovitch L., Erdmann B., Dekel B., Bader M., Barasch J., Rosenbauer F., Luft F.C., Schmidt-Ott K.M., The transcription factor grainyhead-like 2 regulates the molecular composition of the epithelial apical junctional complex, *Development*, 137(22) (2010) 3835-3845.
- [14] Haensel D., Sun P., MacLean A.L., Ma X., Zhou Y., Stemmler M.P., Brabletz S., Berx G., Plikus M.V., Nie Q., Brabletz T., Dai X., An Ovov2-Zeb1 transcriptional circuit regulates epithelial directional migration and proliferation, *EMBO Rep.*, 20(1) (2019).
- [15] Watanabe K., Liu Y., Noguchi S., Murray M., Chang J.C., Kishima M., Nishimura H., Hashimoto K., Minoda A., Suzuki H., OVOL2 induces mesenchymal-to-epithelial transition in fibroblasts and enhances cell-state reprogramming towards epithelial lineages, *Sci. Rep.*, 9(1) (2019) 6490.
- [16] Sengez B., Aygun I., Shehwana H., Toyran N., Tercan Avci S., Konu O., Stemmler M.P., Alotaibi H., The Transcription Factor Elf3 Is Essential for a Successful Mesenchymal to Epithelial Transition, *Cells*, 8(8) (2019).
- [17] Brown A., Rathore S., Kimanius D., Aibara S., Bai X.C., Rorbach J., Amunts A., Ramakrishnan V., Structures of the human mitochondrial ribosome in native states of assembly, *Nat Struct Mol Biol.*, 24(10) (2017) 866-869.
- [18] Park K.C., Song K.H., Chung H.K., Kim H., Kim D.W., Song J.H., Hwang E.S., Jung H.S., Park S.H., Bae I., Lee I.K., Choi H.S., Shong M., CR6-interacting factor 1 interacts with orphan nuclear receptor Nur77 and inhibits its transactivation, *Mol. Endocrinol.*, 19(1) (2005) 12-24.
- [19] Kwon M.C., Koo B.K., Kim Y.Y., Lee S.H., Kim N.S., Kim J.H., Kong Y.Y., Essential role of CR6-interacting factor 1 (Crif1) in E74-like factor 3 (ELF3)-mediated intestinal development, *J Biol Chem.*, 284 (48) (2009) 33634-33641.
- [20] Bedzhov I., Alotaibi H., Basilicata M.F., Ahlborn K., Liszewska E., Brabletz T., Stemmler M.P., Adhesion, but not a specific cadherin code, is indispensable for ES cell and induced pluripotency, *Stem. Cell Res.*, 11(3) (2013) 1250-1263.
- [21] Brembeck F.H., Opitz O.G., Libermann T.A., Rustgi A.K., Dual function of the epithelial specific ets transcription factor, ELF3, in modulating differentiation, *Oncogene*, 19(15) (2000) 1941-1949.
- [22] Kitazawa K., Hikichi T., Nakamura T., Mitsunaga K., Tanaka A., Nakamura M., Yamakawa T., Furukawa S., Takasaka M., Goshima N., Watanabe A., Okita K., Kawasaki S., Ueno M., Kinoshita S., Masui S., OVOL2 Maintains the Transcriptional Program of Human Corneal Epithelium by Suppressing Epithelial-to-Mesenchymal Transition, *Cell Rep.*, 15(6) (2016) 1359-1368.
- [23] Roca H., Hernandez J., Weidner S., McEachin R.C., Fuller D., Sud S., Schumann T., Wilkinson J.E., Zaslavsky A., Li H., Maher C.A., Daignault-Newton S., Healy P.N., Pienta K.J., Transcription factors OVOL1 and OVOL2 induce the mesenchymal to epithelial transition in human cancer, *PLoS One*, 8(10) (2013) e76773.
- [24] Alotaibi H., Transcriptional Impact of E-cadherin Loss on Embryonic Stem Cells, *Jordan Journal of Biological Sciences*, 14(5) (2021) 1035-1043.
- [25] Amunts A., Brown A., Toots J., Scheres S.H.W., Ramakrishnan V., Ribosome. The structure of the human mitochondrial ribosome, *Science*, 348 (6230) (2015) 95-98.
- [26] He J., Cooper H.M., Reyes A., Di Re M., Sembongi H., Litwin T.R., Gao J., Neuman K.C., Fearnley I.M., Spinazzola A., Walker J.E., Holt I.J., Mitochondrial nucleoid interacting proteins support mitochondrial protein synthesis, *Nucleic Acids Res.*, 40(13) (2012) 6109-6121.
- [27] Chung H.K., Yi Y.W., Jung N.C., Kim D., Suh J.M., Kim H., Park K.C., Song J.H., Kim D.W., Hwang E.S., Yoon S.H., Bae Y.S., Kim J.M., Bae I., Shong M., CR6-interacting factor 1 interacts with Gadd45 family proteins and modulates the cell cycle, *J. Biol. Chem.*, 278(30) (2003) 28079-28088.
- [28] Ran Q., Hao P., Xiao Y., Xiang L., Ye X., Deng X., Zhao J., Li Z., CRIF1 interacting with CDK2 regulates bone marrow microenvironment-induced G0/G1 arrest of leukemia cells, *PLoS One*, 9(2) (2014) e85328.

## Total Phenolic Content, Free Radical Scavenging Activity and Antibacterial Activity of Some *Bupleurum* Species

Hatice Taner Saraçoğlu<sup>1,a,\*</sup>, Mehtap Akin<sup>1,b</sup>, Ahmet Ünver<sup>2,c</sup>

<sup>1</sup> Department of Biology, Faculty of Science, Selçuk University, 42075, Konya, Türkiye

<sup>2</sup> Department of Food Engineering, Faculty of Engineering and Architecture, Necmettin Erbakan University, Konya, Türkiye

\*Corresponding author

### Research Article

#### History

Received: 05.07.2021

Accepted: 21.05.2022

#### Copyright



©2022 Faculty of Science,  
Sivas Cumhuriyet University

### ABSTRACT

The aim of this research was to determine the total phenolic content, free radical scavenging activity and antibacterial activity of some *Bupleurum* species. In the study, twelve *Bupleurum* L. (Apiaceae) species were extracted using a mixture of methanol-water and tested for total phenolic content, free radical scavenging activity and antibacterial activity. Total phenolic content of *Bupleurum* species extracts ranged between 56.64 and 317.54 mg gallic acid equivalent (GAE)/g dry extract. The free radical scavenging activity of extracts was determined using the IC<sub>50</sub> method, and the results for the samples ranged from 0.39 to 3.41 mg/ml. The antibacterial properties of *Bupleurum* species extracts were tested using the microdilution method against a total of eleven bacterial strains in this study; no inhibition was observed in the range of the investigated extract concentrations. *Bupleurum* species were contained phenolic compounds and had some free radical scavenging potential, but they did not show inhibitory impact on bacteria in the investigated extract concentration range. All the analyses were made in three replications. Results were provided as a mean of the replicates. The methods for results were looked at by utilizing the single direction and multivariate investigation of difference (MANOVA) followed by Duncan's different reach tests. The contrasts between singular methods were considered to be critical at  $P < 0.05$ .

**Keywords:** Antibacterial activity, Antioxidant activity, *Bupleurum* species, Extract, Microdilution.

<sup>a</sup> [htaner@selcuk.edu.tr](mailto:htaner@selcuk.edu.tr)

<sup>c</sup> [unverae@erbakan.edu.tr](mailto:unverae@erbakan.edu.tr)

<sup>ib</sup> <https://orcid.org/0000-0001-9502-3739>

<sup>id</sup> <https://orcid.org/0000-0002-6310-809X>

<sup>b</sup> [makin@selcuk.edu.tr](mailto:makin@selcuk.edu.tr)

<sup>id</sup> <https://orcid.org/0000-0003-2554-236X>

### Introduction

The Apiaceae (Umbelliferae) family includes high economic and medicinal plants [1]. Extracts and essential oils of *Bupleurum* use in traditional medicine for their antiseptic and anti-inflammatory activity [2].

In Turkey, the genus *Bupleurum* of the Apiaceae (Umbelliferae) family has 49 taxa, 21 of which are endemic [3, 4]. Recent studies are generally focused on the hepatoprotective activity of the plant commonly used in China. *Bupleurum kaoi* Liu has been utilized as a main component in traditional Chinese herbal therapy to treat hepatitis. *B. kaoi* Liu (Chao et Chuang), one of numerous variants of this species, is native to Taiwan. Only the root is utilized in Chinese medicine. As aerial portions such as leaves and stems also contain bioactive components, using these tissues in the creation of health-promoting goods is both practicable and cost-effective. Leaf infusion is one of the most economically feasible leaf products [5]. *B. kaoi* Liu (Chao et Chuang) is a traditional Chinese plant that has been used as a herbal drink in the Far East for many decades [6]. *B. kaoi*, according to Lin et al. [6] and Ohtsu et al. [7] has a wide range of actions, including hepatoprotective and antioxidant properties.

Free radicals are hazardous wastes of cellular metabolism and transition-metal ions, and they appear to play a role in biomacromolecule destruction *in vivo* [8]. Antioxidants may protect our system from

oxidative damage linked to diabetes, cancer, cardiovascular disease, and neurological disorders such as Alzheimer's and Parkinson's disease [9]. Several naturally occurring antioxidative substances derived from plants have been found as active oxygen scavengers, free radical inhibitors, or reducing agents *in vitro* [10, 11].

*B. heldreichii*, *B. sulphureum*, *B. lycaonicum* and *B. pauciradiatum*, which are among our study materials, are known as "tavşan kulağı" in our country [12, 13, 14].

*B. rotundifolium* species is known by the names "değirmi yapraklı tavşan kulağı", "yuvarlak yapraklı tavşan kulağı", "sarıgayşek" and "gıcır" [15, 16, 17].

*B. croceum* species is known as "altuni tavşan kulağı" and "tavşan kulağı", while *B. lancifolium* is known as "sivri tavşan kulağı" and "tavşan kulağı" [18, 12, 17, 14].

*Bupleurum* species are not widely used in our country. There are limited studies on antimicrobial activity and antioxidant activity of *Bupleurum* species growing in Turkey.

The purpose of this research was to evaluate the antibacterial activity, total phenolic content and free radical scavenging activity of the methanol-water extract of some *Bupleurum* species.

## Materials and Methods

### Plant Materials

Twelve samples of *Bupleurum* taxa collected from Turkey (Table 1) between May and August 2009 during their blossoming period and identified by Tuna Uysal from Selcuk University in Turkey used Flora of Turkey and East Aegean Islands Book [3].

A voucher specimen was placed in the Herbarium of the Faculty of Science at Selcuk University in Turkey (HT1001 KNYA, 1011, 1008, 1006, 1005, 1010, 1007, 1003, 1004, 1002, 1014 and 1009). The aerial parts were air-dried and grinded.

Table 1. Sampled taxa of *Bupleurum*

Species	Location of the samples
<i>Bupleurum rotundifolium</i> L.	Konya: Bozkir, Cemetery of Bozkir, 1100 m, HT1001 KNYA
<i>Bupleurum falcatum</i> L. subsp. <i>cernuum</i> (Ten.) Arcang.	Konya: Between Altinapa and Basarakavak, Han position, 1280 m, HT1011 KNYA
<i>Bupleurum cappadocicum</i> Boiss.	Karaman: Nearby Sertavul Gateway, 1400 m, HT1008 KNYA
<i>Bupleurum heldreichii</i> Boiss.&Bal.*	Konya: Karapinar, Erosion area, 960 m, HT1006 KNYA
<i>Bupleurum turcicum</i> Snogerup*	Konya: Salt lake, Nearby Yavsan Memlehasi, 910 m, HT1005 KNYA
(Syn.) <i>Bupleurum intermedium</i> Poiret <i>Bupleurum subovatum</i> Link ex Spreng.	Karaman: Ermenek, Ermenek-Kazanci road intersection, 1450 m, HT1010 KNYA
<i>Bupleurum croceum</i> Fenzl	Konya: Altinapa, Nearby Degirmenkoy, 1200 m, HT1007 KNYA
<i>Bupleurum sulphureum</i> Boiss.&Bal.*	Konya: Konya-Beysehir road, Quarry position, 1250 m, HT1003 KNYA
<i>Bupleurum lycanicum</i> Snogerup*	Konya: Konya-Beysehir road, Quarry position, 1250 m, HT1004 KNYA
<i>Bupleurum pauciradiatum</i> Fenzl*	Karaman: Baskişla, Yaylapinar position, 1450 m, HT1002, KNYA
<i>Bupleurum zoharii</i> Snogerup*	Icel (Mersin): Mut-Ermenek roadside, 250 m, HT1014 KNYA
<i>Bupleurum lancifolium</i> Hornem.	Karaman: Ermenek, Ermenek-Kazanci road intersection, 1125 m, HT1009 KNYA

### The Preparation of Extracts

For the separation of non-polar compounds, mainly oils, the materials (20 g) were extracted with petroleum ether using a Soxhlet device at 40-60 °C. The petroleum ether was evaporated at 40 °C. The residue was mixed with 100 ml methanol-water mixture (70% methanol + 30% water), stirred for 30 min and filtrated. The filtrate was collected and this process was repeated for three times and the collected extracts were concentrated on a rotary evaporator in vacuum at 40 °C. Then the extracts were lyophilized and stored until the analysis [19].

### Antimicrobial Assay

The minimum inhibitory concentrations (MICs) of extracts, obtained by methods of microdilution identified by the National Committee for Clinical Laboratory Standards [20]. In microbiological tests, standard 11 bacterial strains that could be in humans, animals and foods as hazardous contaminants were used. These bacteria were *Escherichia coli* ATCC 25922, *Escherichia coli* ATCC 29988, *Escherichia coli* ATCC 25923, *Escherichia coli* ATCC 3166 09:K35:K99, *Streptococcus salivarius* RSHE 606, *Proteus mirabilis* ATCC 43071, *Bacillus cereus* ATCC 11778, *Staphylococcus aureus* ATCC 29213, *Staphylococcus aureus* ATCC 6538, *Pseudomonas aeruginosa*

ATCC 15442, *Pseudomonas aeruginosa* ATCC 29853. Bacterial strains were taken from the Biotechnology Laboratory in Selcuk University. Bacterial cultures were activated for 24 hours at 37 °C in Mueller Hinton Broth (MHB, Merck). The cultures grown in the liquid medium were standardized to 10<sup>8</sup>cfu/ml at the conclusion of the incubation period (McFarland No: 0.5). The extracts were dissolved in 25% dimethylsulfoxide (DMSO) and diluted to the maximum concentration of 4 mg/ml to be evaluated, followed by a two-fold serial of dilutions in concentrations ranging from 2 mg/ml to 1.95 g/ml. Antibacterial activity was determined using the microdilution technique. A pre-sterilized micro titration dish (Brand) with 96 "U" type wells was used for antibacterial tests. At a microtitration petri plates, serial solutions of the extracts were made. The wells were filled with 100 µL of each microbial solution. The negative control was the last well, which contained serial dilutions of antibacterial agents without microorganisms. The solvent DMSO was used as a negative control, and Chloramphenicol (Sigma) was used as a positive control.

### Total Phenolic Content

The results were expressed as mg GAE/g dry extract using the Folin-Ciocalteu colorimetric method. As a standard

phenolic compound, gallic acid was used. In a 25 ml volumetric flask containing 9 ml distilled water, 1 ml of standard solution of gallic acid or 1 ml of diluted samples were added. Also, blank was made with addition of 1 ml of distilled water. The mixture was stirred after adding 1 ml of Folin-Ciocalteu reagent. After 5 minutes, 10 ml solution of 7% Na<sub>2</sub>CO<sub>3</sub> was added, mixed thoroughly for 2 hours. At 760 nm, the absorbance was measured. Using an equation derived from a standard gallic acid graph, the content of total phenolic compounds in samples were determined as milligrams of gallic acid equivalent in gram dry extracts [21].

### Free Radical Scavenging Activity

Extracts were diluted to nine concentrations (0.1, 0.3, 0.6, 0.9, 1.0, 1.5, 2.0, 3.0 and 4.0 mg/ml) with 70% methanol mixture. To make, DPPH was weighted and dissolved in ethanol 0.004% (w/v) solution. A magnetic stirrer was used to make that the mixture dissolved equally. A solution of 0.004% DPPH (1 ml) was applied on each test tube containing 50 µL dilutes. The test tubes were then placed in the dark for 30 minutes. At the same time, the blank test tubes were treated with DPPH, which contained only 70% methanol. After 30 min, the absorbances of each test tube were measured by a UV spectrophotometer at 517 nm. IC<sub>50</sub> values were calculated from percent inhibition versus concentration graphs. IC<sub>50</sub> (mg/ml) value is the minimum extract required to inhibit the 50% of 1,1-diphenyl-2-picrylhydrazyl [22].

### Statistical Analyses

All experiments were performed in three replications. The mean of the data was recorded. The results of multivariate analysis of variance (MANOVA) and Duncan multiple range test were given in this part. Since p-values of these tests are less than 0.05, it can be concluded that the individual mean differences are statistically significant [23].

## Results and Discussion

The total phenolic content of the extracts of *Bupleurum* species ranged from 56.64 to 317.54 mg GAE/g dry extract. The detected total phenolic content of *Bupleurum cappadocicum* Boiss. was the highest while it was lowest for the *Bupleurum pauciradiatum* Fenzl. The IC<sub>50</sub> values of the samples have ranged between 0.39-3.41 mg/ml. The lowest free radical scavenging activity was detected for the *Bupleurum pauciradiatum* which was in correlation with total phenolic content. The total phenolic content of *B. cappadocicum*, *B. zoharii* Snogerup, and *B. lycaonicum* Snogerup was higher in comparison to other samples and their free radical scavenging activities was also higher. While the total phenolic content of *Bupleurum turcicum* Snogerup was three times of *Bupleurum intermedium* Poirret, their free radical scavenging activities were similar (Table 2).

It was seen that the mixture of methanol-water extracts of twelve *Bupleurum* species, studied surprisingly

did not present any antibacterial activity against the test microorganisms used in the study.

Sökmen et. al. [24, 25] studied on antimicrobial activity of *Bupleurum sulphureum* Boiss&Bal. They tested the activity of the methanol extracts of culture and methanol extract of aerial parts. They were examined through the method of Minimal Inhibitory Concentration (MIC) Test. They reported no antimicrobial activity against *B. cereus*, *E. coli*, *S. aureus* for both mentioned extracts.

Bazzaz and Haririzadeh [26] studied for the determination of antimicrobial activity of 306 plants representing 52 families. They examined the method of cylinder plate assay. According to their results the methanol extract of the total parts of *Bupleurum rotundifolium* L. had no antimicrobial activity towards to *E. coli* ATCC 10536 and *Pseudomonas aeruginosa* ATCC 4027. Their findings are in accordance with our findings for the aerial parts of the *Bupleurum rotundifolium*.

Shafaghat [27] prepared the methanol extract of *B. lancifolium* plant collected from Iran. The antimicrobial activities of the extracts were determined by the disc diffusion method. It has been reported that methanol extract has antimicrobial activity against *E. coli* ATCC 25922, which we also used in our study.

Jaradat et al. [28] obtained different extract of *B. lancifolium* plant collected from Palestine. In their study, they reported that methanol extract had antibacterial activity against *E. coli* ATCC 25922 strain, which we also used in our study.

Ertan [29] studied on antimicrobial activity and antioxidant activity of *B. lycaonicum*. According to researcher's results, the methanol extract of *B. lycaonicum* had antibacterial activity against *E. coli* ATCC 25922 and antioxidant activity. However, we did not detect antibacterial activity on the same bacteria.

Tseng et. al. [5] studied the infusion prepared from the leaves of *B. kaoi*. They reported the IC<sub>50</sub> of DPPH free radical scavenging activities of leaf infusion as 0.46 mg/ml. Also, they expressed as a conclusion that the leaf infusions possessed antioxidant activities and hepatoprotective capacity. Their results on free radical scavenging activity of the leaf extracts are higher than the *Bupleurum* species we studied except for *Bupleurum lycaonicum* and *Bupleurum zoharii*. The higher free radical scavenging activity may be due to the higher amounts of phenolic substances.

Wang et. al. [30] applied supercritical carbon dioxide extraction at four different pressures on ethanol extraction of roots of *B. kaoi*. They stated that the scavenging activity of 10 g/l fractions of supercritical carbon dioxide extracts on DPPH were ranged between 53%-76%. They also noticed that the phenolic content of the root extracts from 4.7 to 18.3 mg GAE/g dry extract. Their findings on scavenging activity of root extracts are lower than the results we obtained for extracts of aerial part. Besides, the total phenolic content they expressed for root extracts are lower than our findings on aerial parts of *Bupleurum* species.

There are limited studies on free radical scavenging activity and total phenolic content of *Bupleurum* species. Limited studies are generally focused on *Bupleurum kaoi*. Our results may be valuable data for the further studies.



Table 2. Total phenolic content and antioxidant activity of *Bupleurum* species

Sample	Total phenolic content (mg/g dw of extract)	DPPH (IC50)(mg/ml)
<i>Bupleurum rotundifolium</i>	202.39±2.57 e	1.31±0.02 e
<i>Bupleurum falcatum</i> subsp. <i>cernuum</i>	210.57±1.43 e	1.08±0.01 d
<i>Bupleurum cappadocicum</i>	317.54±2.52 h	0.71±0.03 b
<i>Bupleurum heldreichii</i>	157.54±2.06 d	1.27±0.02 e
<i>Bupleurum turcicum</i>	208.45±2.67 e	1.61±0.02 f
<i>Bupleurum intermedium</i>	73.00±0.82 b	1.61±0.03 f
<i>Bupleurum croceum</i>	74.82±0.57 b	2.97±0.02 h
<i>Bupleurum sulphureum</i>	109.66±1.47 c	2.66±0.06 g
<i>Bupleurum lycaonicum</i>	288.75±0.88 f	0.41±0.01 a
<i>Bupleurum pauciradiatum</i>	56.64±0.57 a	3.41±0.04 i
<i>Bupleurum zoharii</i>	301.18±1.40 g	0.39±0.02 a
<i>Bupleurum lancifolium</i>	151.18±2.39 d	0.94±0.01 c

## Acknowledgment

An earlier version of this study entitled by "Determination of total phenolic content, antibacterial activity and free radical scavenging activity of some *Bupleurum* species" was presented by the same authors at European Biotechnology Congress, 05-07 May, 2016, Riga, Latvia.

## Conflicts of interest

All authors declare that they have no conflict of interest.

## References

- [1] Kubeczka K.H., Aromatic plants, basic and applied aspects. The Hague, Boston, London: Martinus Nijhoff Publishers, (1982) 165.
- [2] Nose M., Amagaya S., Ogihara Y., Corticosterone secretion-inducing activity of saikosaponin metabolites formed in the alimentary tract., *Chemistry Pharmacy Bulletin*, 37 (1989) 2736-40.
- [3] Davis P.H., Turkey and the East Aegean Islands. University Press: Edinburgh, 4 (1982) 393-418.
- [4] Güner A., Özhatay N., Ekim T., Başer K.H.C., Flora of Turkey and the East Aegean Islands. University Press: Edinburgh, 11 (2000) 143-144.
- [5] Tseng C.Y., Liu C.T., Chen W.L., Weng Y.M., Antioxidative properties and in vitro hepato-protective activity of *Bupleurum kaoi* leaf infusion, IFT Annual Meeting, Las Vegas, NV, July 12-16, (2004).
- [6] Lin C.C., Chiu H.F., Yen M.H., Wu C.C., Chen M.F., The pharmacological and pathological studies on Taiwan folk medicine (III): The effects of *Bupleurum kaoi* and cultivated *Bupleurum falcatum* var. *komarowi*, *Amer. J. Chinese Med.*, 18 (1990) 105-112.
- [7] Ohtsu S., Izumi S., Iwanaga S., Ohno N., Yadomae T., Analysis of mitogenic substances in *Bupleurum chinense* by ESR spectroscopy, *Biol. Pharm. Bull.*, 20 (1997) 97-100.
- [8] Muller F.L., Lustgarten M.S., Jang Y., Richardson A., Van Remmen H., Trends in oxidative aging theories, *Free Radic. Biol. Med.*, 43 (2007) 477-503.
- [9] Lin M.T., Beal M.F., The oxidative damage theory of aging, *Clin. Neurosci. Res.*, 2 (2003) 305-315.
- [10] Yen G.C., Duh P.D., Scavenging effect of methanolic extracts of peanut hulls on free-radical and active-oxygen species, *J. Agric. Food Chem.*, 42 (1994) 629-632.
- [11] Duh P.D., Antioxidant activity of burdock (*Arctium lapa* Linne): its scavenging effect on free radical and active oxygen, *J. Amer. Oil Chem. Soc.*, 75 (1998) 445-461.
- [12] Anonymous, Available at: [http://www2.cedgm.gov.tr/icd\\_raporlari/ispartaicd2008.pdf](http://www2.cedgm.gov.tr/icd_raporlari/ispartaicd2008.pdf), Retrieved May 20, 2011.
- [13] Bayram A., Isparta'nın korunan alanları, *Gülçevrem*, 1(1) (2007) 1-34.
- [14] Yıldızbakan A., Gündoğdu E., Fakir H., Akgün C., Ulusoy H., Cehennemdere yaban hayatı geliştirme sahasında yaban keçisi *Capra aegagrus* Erxleben 1777'nin yayılışı ve habitat kullanımı, Doğu Akdeniz Ormançılık Araştırma Enstitüsü, Çevre ve Orman Bakanlığı Yayın No: 433, DOA Yayın No:59, SBN 978-605-393-100-3, Tarsus., (2011) XI+43 s.
- [15] Cansaran A., Kaya Ö.F., Contributions of the ethnobotanical investigation carried out in Amasya district of Turkey (Amasya-Center, Bağlarüstü, Boğaköy and Vermiş villages; Yassıçal and Ziyaret towns), *Biological Diversity and Conservation*, 3(2) (2010) 97-116.
- [16] Kordali Ş., Zengin H., Bayburt ili buğday ekim alanlarında bulunan yabancı otların rastlama sıklığı, yoğunlukları ve topluluk oluşturma durumlarının saptanması, *Atatürk Üniv. Ziraat Fak. Derg.*, 38(1) (2007) 9-23.
- [17] Yıldırım A., Ekim T., Orta Anadolu Bölgesi yabancı ot florası, *Bitki Koruma Bülteni*, 43(1-4) (2003) 92-93.
- [18] Anonymous, Available at: [http://www2.cedgm.gov.tr/icd\\_raporlari/mersinidc2006.pdf](http://www2.cedgm.gov.tr/icd_raporlari/mersinidc2006.pdf), Retrieved May 20, 2011.
- [19] Tunalier Z., Öztürk N., Koşar M., Başer K.H.C., Duman H., Kırimer N., Bazı *Sideritis* türlerinin antioksidan etki ve fenolik bileşikler yönünden incelenmesi, 14. Bitkisel İlaç Hammaddeleri Toplantısı. Bildiriler, 29-31 Mayıs 2002, Eskişehir, (2002).
- [20] Wayne P.A., Performance standards for antimicrobial susceptibility testing; Ninth informational supplement, NCCLS document M100-S9. National Committee for Clinical Laboratory Standards, (2008) 120-126.
- [21] Slinkard K., Singelton V.L., Total phenolic analysis, automation and comparison with manual methods, *Amer. J. Enol. Vitic.*, 28 (1977) 49-55.

- [22] Gyamfi M.A., Yonamine M., Aniya Y., Free radical scavenging action of medical herbs from Ghane: *Thonningia sanguinea* on experimentally-induced liver injuries, *General Pharm.*, 32(6) (1999) 661-667.
- [23] Püskülcü H., İkiz F., Introduction statistic. Bornova-İzmir, Turkey: Bilgehan Press , (in Turkish) (1989).
- [24] Sökmen A., Jones B.M., Erturk M., Antimicrobial activity of extract from the cell cultures of some Turkish medicinal plants, *Phytother. Res.*, 13 (1999) 355-357.
- [25] Sökmen A., Jones B.M., Erturk M., The in vitro antibacterial activity of Turkish medicinal plants, *J. Ethnopharmacol.*, 67 (1999) 79-86.
- [26] Bazzaz B.S.F., Haririzadeh G., Screening of Iranian plants for antimicrobial activity, *Pharm. Biol.*, 41(8) (2003) 573-583.
- [27] Shafaghat A., Antioxidant, antimicrobial activities and fatty acid components of leaf and seed of *Bupleurum lancifolium* Hornem., *Journal of Medicinal Plants Research*, 5(16) (2011) 3758-3762.
- [28] Jaradat N., Al-Masri M., Al-Rimawi F., Zaid A.N., Saboba M.M., Hussein F., Aker A., Qasem D., Hejazi S.. Investigating the impacts of various solvents fractions of *Bupleurum lancifolium* on the antimicrobial and antioxidant potentials, *J. Intercult Ethnopharmacol.*, 6(4) (2017) 401-406.
- [29] Ertan S., *Bupleurum lycaonicum* Snogerup bitki türünün biyolojik aktivitesi, Yüksek lisans tezi, Gazi Üniversitesi, Fen Bilimleri Enstitüsü, (2017).
- [30] Wang B.J., Liu C.T., Tseng C.Y., Yu Z.R., Antioxidant activity of *Bupleurum kaoi* Liu (Chao et Chuang) fractions fractionated by supercritical CO<sub>2</sub>, *LWT-Food Sci Tech.*, 38 (2005) 281-287.

## Selection and Validation of Potential Reference Genes for Quantitative Real-Time PCR Analysis in *Blaptica Dubia* (Serville, 1838) (Blattidae, Blaberidae)

Emin Ufuk Karakaş<sup>1,a</sup>, Ayşe Nur Pektaş<sup>2,b</sup>, Şeyda Berk<sup>1,c,\*</sup>

<sup>1</sup> Department of Molecular Biology and Genetics, Faculty of Science, Sivas Cumhuriyet University, Sivas, Türkiye

<sup>2</sup> Advanced Technology Research Center (CUTAM), Sivas Cumhuriyet University, Sivas, Türkiye

\*Corresponding author

### Research Article

#### History

Received: 07/02/2022

Accepted: 03/06/2022

#### Copyright



©2022 Faculty of Science,  
Sivas Cumhuriyet University

### ABSTRACT

Reverse transcription-quantitative polymerase chain reaction (RT-qPCR) is an effective, reproducible, and dependable method for evaluating and targeting expression of genes. It is very important to normalize according to stably expressed housekeeping genes in order to facilitating gene expression studies and to acquire exact and meaningful results. The purpose of this study was to identify and validate six housekeeping genes (*GADPH*, *RPS18*,  $\alpha$ -*TUB*, *EF1 $\alpha$* , *ArgK* and *ACTB*) in adults of cockroach species *Blaptica dubia* employing five different algorithms (geNorm, Bestkeeper, Normfinder,  $\Delta$ Ct method and RefFinder) to assess putative housekeeping gene expression stability. Our study also showed that the geNorm, Normfinder  $\Delta$ Ct method and RefFinder algorithms identified *GADPH* as the most stable housekeeping gene in *B. dubia* adults. Additionally, *RPS18* was suggested as the most stable gene by GeNorm and BestKeeper. *ACTB* has been shown to be by far the least stable of all algorithms. In addition, since there are few validation studies for reference genes in cockroaches in the literature, it is considered that it would be beneficial to increase the number of studies related with RT-qPCR on the reference genes validation under biotic and abiotic conditions in cockroaches.

**Keywords:** *Blaptica dubia*, RT-qPCR, Reference genes, Validation, Normalization.

<sup>a</sup> [karakaseminufuk@hotmail.com](mailto:karakaseminufuk@hotmail.com)

<sup>b</sup> <https://orcid.org/0000-0001-5813-5678>

<sup>c</sup> [sberk@cumhuriyet.edu.tr](mailto:sberk@cumhuriyet.edu.tr)

<sup>d</sup> <https://orcid.org/0000-0003-4687-0223>

<sup>e</sup> [aysenur.pektas@gmail.com](mailto:aysenur.pektas@gmail.com)

<sup>f</sup> <https://orcid.org/0000-0001-5621-2844>

## Introduction

With the next-generation sequencing technologies development, it has provided in important increases in genomic and transcriptomic throughput for varied organism [1]. Normalization of gene expression has been imperative for evaluating and reporting these transcriptomic and genomic data quality [2,3]. Although RT-qPCR is a strong, reproducible and dependable method for targeting and measuring expression of genes [4], the quality and unity of RNA examples, reverse transcription, normalization, and this has become limited by PCR efficiency [5-7]. The characteristic method, normalization, is the evaluation of reference genes (housekeeping genes or internal control) expression levels that have important roles in major and common cellular functions and typically display consistent ubiquitous expression levels to measure simultaneously under varied biotic and abiotic conditions [4].

Gene expression normalization in RT-qPCR is accomplished by adding reference genes that are regularly expressed under various experimental conditions and act as endogenous controls [4, 6, 7]. The reference genes, described as "essential expressed to maintain cellular function", may not supply the necessary conditions for an ideal housekeeping gene expression at constant levels in a diversity of biotic and abiotic circumstances [2, 5, 7]. Many studies revealed that mostly used reference genes are expressed differently in numerous experimental circumstances have suggested

that multiple housekeeping genes need be included in the study for correct normalization [2, 5, 6].

There are many reference genes commonly used in the determination of mRNA levels by q-RT-PCR, such as ribosomal protein, glyceraldehyde-3-phosphate dehydrogenase (*GAPDH*),  $\beta$ -actin (*ACTIN*), elongation factor 1a (*EF1A*), and superoxide dismutase (*SOD*) [8-11]. Housekeeping genes are essential for survival, and it is generally considered that there is a slight variation in transcription of these genes. Ribosomal proteins, which are substantial parts of ribosomes, play crucial roles in many biological processes such as intracellular protein biosynthesis, DNA repair and cell differentiation [12]. *EF1A* is involved in translation by catalysing the binding of GTP-dependent aminoacyl-tRNA to the acceptor site of the ribosome. [13]. *SOD* serves as a metalloenzyme that can catalyse the dismutation of superoxide anion to hydrogen peroxide and elemental molecular oxygen [14]. While *ACTIN* is an essential component of the cellular skeleton providing structural unity and shapes cells [13], *GAPDH* joint in energy metabolism [15]. On the other hand, there are many studies showing differently expressed housekeeping genes under various experimental situations [13, 16]. Genes expressing differentially can often induce significant biological changes in tissues, sexes, and other samples at various developmental stages from a variety of experimental conditions, therefore, identification of genes with a consistent expression requires evaluation of specific

changes in gene expression. The smallest variation in successive stability levels of the analysed samples is defined as the stability of gene expression. Therefore, different software programs including GeNorm [4], BestKeeper [17], NormFinder [7],  $\Delta$ Ct Method [18], and RefFinder (<http://www.leonxie.com/referencegene.php>) have been improved to identify many of these stable genes.

Cockroaches are highly diverse insects with about 4500 species commonly found worldwide [19]. Most cockroaches live in terrestrial habitats and have good adaptations to survive in extreme conditions, but of the diversity that exists, only a small number have adapted to human habitats [19]. The Orange Spotted Cockroach/Argentine Wood Cockroach (*Blaptica dubia*) is a tropical cockroach species not native to human dwellings, although human exposure to *B. dubia* has increased with their widespread commercial reproduction as feeder insects [20]. Because cockroaches have ability to live in habitats containing varying quantity of toxic substances including environmental pollutants, insecticides, microbial toxins, they have been proposed as a good experimental model to study their stress response and detoxification abilities [21].

RT-qPCR has accelerated its progress in many fields and has become very important in entomology. Gene expression analysis has been used to study in gene expression changes between developmental stages, tissues, and other samples from varied experiments in insects, thus gene expression analyses have become of increasing importance in the field of insect molecular biology. Studies in the literature to assess the selection and validity of housekeeping genes in numerous biotic and abiotic situations in insects are summarized in the reviews by Lü et al. and Shakkell et al. [22, 23]. When the studies in the literature are examined, various traditional and new housekeeping genes have been selected in many studies to determine gene expression stability by RT-qPCR normalization in different insect species. Although RT-qPCR is widely used for the detection of gene expression in insects, there is no suitable housekeeping gene (HKGs) and consistent gene quantification system for *B. dubia*, yet. Our current study objectives are to determine appropriate reference genes and evaluate their expression stability in *B. dubia* before they are used as endogenous controls in effective genomic studies of six housekeeping genes commonly used to normalize qRT-PCR data in *B. dubia*.

## Material and Methods

### Sample and Ethics Statement

Adults of *Blaptica dubia* (Blattodea, Blaberidae) were commercially obtained from a producer in Antalya/Turkey (<https://www.antalyacekirge.net/>). *Blaptica dubia* adults were brought to the laboratory by controlled storage in the RNAlater® (Qiagen) that is RNA stabilization reagent and stored at freezer (-20°C) until used in further experiments.

### Total RNA Extraction and cDNA Synthesis

Total RNA was isolated from adult of *B. dubia* specimens using the commercially purchased RNA isolation kit (GeneAll® Hybrid-R™, Seoul, Korea) in accordance with the manufacturer's protocol. After RNA isolation from *B. dubia* adult samples evaluated in this study, A260/A280 and A260/A230 ratios were analysed to determine whether there was DNA or protein contamination. The A260/A280 ratio is between 1.90 and 2.12 for all samples; The A260/A230 ratio was found to be over 1.90, meaning that these ratios show that all samples do not contain DNA or protein contamination. The total RNA concentration of all samples was obtained as a value between 1210ng/μL and 2000ng/μL and was considered suitable for cDNA synthesis. cDNA synthesis was performed using first strand synthesis kit (GeneAll® HyperScript™, Seoul, Korea) to yield the cDNA product containing 1500 ng/μL RNA according to the manufacturer's recommendations.

### Reverse Transcription-Quantitative Polymerase Chain Reaction (RT-qPCR)

In present study, six candidate housekeeping genes (*GADPH*, *RPS18*,  $\alpha$ -*TUB*, *EF1 $\alpha$* , *ArgK* and *ACTB*) were selected among the most studied reference genes on insects in the literature. Primer's properties are given in Table 1. Correlation coefficients ( $R^2$ ) and efficiencies of PCR amplification (E) were determined for primer validation. Standard curves were generated using cDNA serial dilutions (1, 1/5, 1/25, 1/125 and 1/625) for each primer pair.

qPCR experiments were conducted based on the method previously described [11]. Briefly, a 5-fold cDNA dilution series of 1:625 from an undiluted *B. dubia* cDNA sample was used to identify the efficiencies of amplification and each primer pair specificity used in qPCR assays. For expression analysis of six putative reference genes, all experimental specimens for *B. dubia* were analysed simultaneously in the reverse transcription proceeding.

RT-qPCR analyses in 96-well plate (ABI- Type) using commercial qPCR Master Mix (iGreen, 2X, Biomatik, Canada) were conducted utilizing the StepOnePlus™ Real-Time PCR system (Applied Biosystems, USA). The reaction conditions are as follows, with 20 μL of final volume: [10 μL of Master Mix (2X), 0.7 μL of forward and reverse primers (10 μM), 2 μL of cDNA, and 6.6 μL of nuclease-free water].

The RT-qPCR schedule is as follows: initial denaturation at 95°C for 3 minutes, followed by 40 cycles of denaturation at 95°C for 10 seconds, annealing at 58°C for 30 seconds, and extension at 72°C for 15 seconds. For melting curve analysis, it is as follows: a cycle of decomposition steps (58°C -1 minute- followed by 0.5°C up to 95°C for 10 seconds). A melting curve was composed at per PCR reaction final to approve a single peak and eliminate the primer-dimer possibility and formation of non-specific product. Efficiency of PCR amplification (E)

was determined in accordance with the equalization:  $E = (10^{(-1/\text{slope})} - 1) \times 100$ .

### Data Interpretation

Cq values of six housekeeping genes were analysed using statistical analysis software GraphPad Prism 6.0 (GraphPad software, San Diego, C). A boxplot of Cq values was created. The stability of these six genes is determined by GeNorm [4], BestKeeper [17], NormFinder [7],  $\Delta\text{Ct}$  [18] and RefFinder (<https://www.Heartcure.com.au>), the comprehensive web-based analysis tool integrating all four software algorithms. Evaluated using /refinder/?type=reference). GeNorm reveals the mean expression stability value (M2) of each candidate (M

value) to demonstrate expression stability. The gene with the lowest M2 value is determined as the most stable gene [4]. BestKeeper evaluates the coefficient of variance (CV) and standard deviation (SD) of the Cq values of each housekeeping gene, and the gene with the lowest CV and SD is defined as the most constant gene [17]. In NormFinder, expression stability (M1) is revealed by the Cq values obtained by RT-qPCR analysis of candidate genes and are ranked. The gene with the lowest M1 value is the most stable [7]. RefFinder appoints a relevant weight to each gene and evaluates the geometric mean of these weights to make an overall final ranking (<https://www.heartcure.com.au/refinder/?type=reference>).

Table 1. Overview of housekeeping genes evaluated in RT-qPCR analysis

Symbol	Gene name	Description	Primer sequence (5'→3')	GenBank accession number	Length (bp)	R <sup>2</sup>	Ref.
<i>EF1α</i>	Elongation factor 1α	GTPase; Elongation factor translation	F: ACCAGATTTGATGGCTTTGG R: CACCCAGAGGAGCTTCAGAC	XM_003705302	194	0,989	[15]
<i>ACTB</i>	β-actin	Cytoskeleton	F: TCCATCATGAAGTGCATGT R: CCACATCTGTTGGAATGTCG	NM_001172372	228	0,982	[24]
<i>RPS18</i>	Ribosomal protein S18	Ribosomal protein; Ribonucleoprotein; rRNA-binding; RNA-binding;	F: TACACCTTTGATCGCTGTGAG R: GGCTCTGGTCATCCAGATAAG	XM_045615265	108	0,967	[25]
<i>ArgK</i>	Arginine Kinase	Phosphotransferase activity	F: CTCGTGTGGTGAACGAAGA R: GGTGGCTGAACGGGACTCT	NT_037436	130	0,951	[26]
<i>GADPH</i>	Glyceraldehyde-3-phosphate	Oxidoreductase in glycolysis; Gluconeogenesis	F: GCCAAGGTGATCCATGACAA R: GTCTTCTGAGTGGCAGTTGTAG	NC_007420	80	0,963	[27]
<i>α-TUB</i>	Alpha-tubulin	Microtubule	F: TCAAATGCGACCCACGTGAT R: GGCAATAGCCGCTGTGACAT	XM_970811	191	0,893	[28]

## Results and Discussion

### Expression Stability of Selected Reference Genes

Each primers PCR amplification was approved by the formation of only one peak in analyses of melting curve and the existence of specific band on agarose gel electrophoresis (1.5%). All primers evaluated in this study were found to have a correlation coefficient (R<sup>2</sup>) varying between 0.89 and 0.98. It also gave a primary efficiency value between 90% and 110% (Table 1). There was no fluorescent signal amplification in the negative control. This showed that both RNA isolation process and RNA clearance steps were effective.

The variation of Ct values among *B. dubia* adult samples for six reference genes is represented in Figure 1. Cycle threshold (Cq) values obtained amplifying the six candidate reference genes from *B. dubia* adults were plotted (Figure 1). Cq values for the six genes ranged from 20.92 to 36.67 in *B. dubia*. *GADPH* represented the lowest Cq values in *B. dubia* ( $24.95 \pm 2.70$ , mean Cq  $\pm$  std. dev.). Amplification of *α-TUB*, *RPS18*, *ArgK*, *ACTB* and *EF1α* showed mean Cqs of  $28.49 \pm 2.23$ ,  $29.64 \pm 1.12$ ,  $30.45 \pm 2.59$ ,  $32.28 \pm 4.18$  and  $32.45 \pm 2.59$ , respectively.

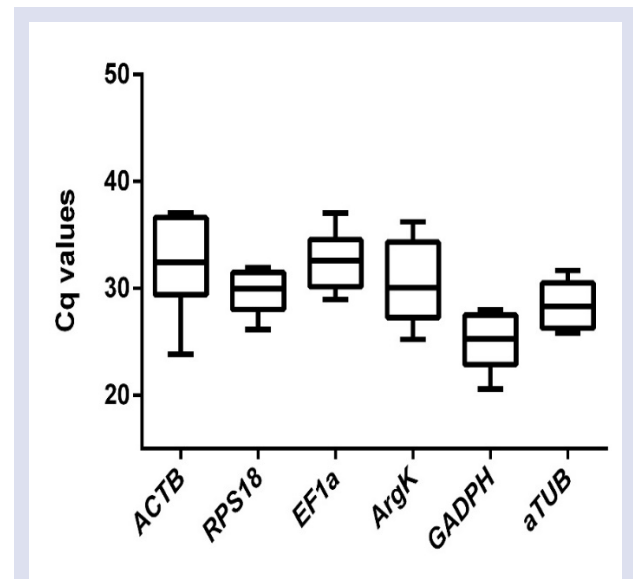


Figure 1. Amplification profiles of putative housekeeping genes. Box plot of qPCR cycle threshold values (Cq) of housekeeping genes in *Blaptica dubia*.

The smallest variation in successive stability levels of the analysed samples is defined as the stability of gene expression. Programs have been developed that identify most of these stable genes, including GeNorm [4], BestKeeper [17], NormFinder [7],  $\Delta$ Ct [18] and RefFinder.

In current study, to identify optimal reference genes in *B. dubia* adults, four statistical Excel macro programs (geNorm, BestKeeper, NormFinder, and  $\Delta$ -Ct method) and the web-based analysis tool RefFinder were used to assess the stability of six candidate genes (Table 2 and Figure 2).

Table 2. Stability of housekeeping gene expression in *Blaptica dubia* adults.

Reference genes	Genorm		Bestkeeper		Normfinder		Delta Ct		RefFinder		
	M	Rank	SD	r	Rank	SV	Rank	SD	Rank	Stability	Rank
<i>ACTB</i>	1.755	6	3.24	0.936*	6	2.245	6	2.47	6	6.000	6
<i>RPS18</i>	0.699	1	1.70	0.972*	1	1.050	3	1.54	3	1.730	2
<i>EF1<math>\alpha</math></i>	1.058	4	2.00	0.906*	2	1.307	4	1.80	4	3.360	4
<i>ArgK</i>	1.397	5	3.20	0.969*	5	1.486	5	1.95	5	5.000	5
<i>GADPH</i>	0.699	1	2.20	0.987*	4	0.350	1	1.32	1	1.410	1
<i><math>\alpha</math>-TUB</i>	0.715	3	2.00	0.966*	3	0.772	2	1.45	2	2.450	3

SD, standard deviation; r, Pearson correlation coefficient; SV, stability value; \*p $\leq$ 0.001.

The geNorm assuming candidate genes are not co-regulated, normally calculates M value (stability value of gene expression) for every housekeeping gene tested as the mean pairwise variation with other housekeeping genes for that gene. While the genes with low M are defined as having constant expression, the highest M value of gene is removed and this process continues until the two most stable genes remain, and this last gene pair is defined as the optimal reference gene pair. Therefore, it is recommended to use at least two reference genes to ensure correct normalization in geNorm. [4]. In *B. dubia* adults, geNorm ranked the set of candidate reference genes: *RPS18*, *GADPH* >  *$\alpha$ -TUB* > *EF1 $\alpha$*  > *ArgK* > *ACTB*. Based on this algorithm data, the M value was determined as 0.699 for both *RPS18* and *GADPH* and both genes were suggested as the two most stable genes. *ACTB* with an M value of 1.755 was determined as the gene with the least stable expression (Figure 2 and Table 2).

Normfinder, the analysis that takes into account systematic differences between sample subsets, is an ANOVA (analysis of variance) model identifying genes with the least variation of expression in all samples [7]. In *B. dubia* adults, Normfinder ranked the six reference genes as follows: *GADPH* >  *$\alpha$ -TUB* > *RPS18* > *EF1 $\alpha$*  > *ArgK* > *ACTB* with a stability value SV of 0.350, 0.772, 1.050, 1.307, 1.486, 2.245, respectively. *GADPH* was found to be the most constant with a stability value of 0.350 and *ACTB* the least constant with a stability value of 2.245 (Table 2 and Figure 2).

Reference genes that exhibit the lowest standard deviation (SD) according to BestKeeper analysis, which can calculate the candidate genes stability, the standard deviation (SD) based on the Cq values of all putative housekeeping genes, are taken as the most stable genes. Also, values exceeding the threshold value (SD < 1) are considered unstable in all samples. [17]. According to this analysis, all housekeeping genes [*RPS18* (SD: 1.70), *EF1 $\alpha$*  (SD: 2.0),  *$\alpha$ -TUB* (SD: 2.0), *GADPH*, (SD: 2.20), *ArgK* (SD: 3.20), *ACTB* (SD: 3.24)] exceeded the threshold in *B. dubia* adults (Table 2 and Figure 2).

In the  $\Delta$ Ct method, which calculates the mean SD of each gene cluster using the raw Ct values based on relative pairwise comparisons, the SD value is oppositely correlated to the gene expression stability. Standard deviation below 1

indicates appropriate stability [18]. As the mean SD of each gene set was over 1, none of the accessible housekeeping genes were found to be stable enough for *B. dubia* adults according to the  $\Delta$ CT method. The overall ranking based on the  $\Delta$ Ct method of reference genes was: *GADPH*,  *$\alpha$ -TUB*, *RPS18*, *EF1 $\alpha$* , *ArgK*, *ACTB* (Table 2 and Figure 2).

RefFinder is a comprehensive algorithm combining four software tools (geNorm, BestKeeper, NormFinder, and  $\Delta$ -Ct method) to order putative housekeeping genes stability. The overall ranking based on RefFinder of reference genes in *B. dubia* was: *GADPH*, *RPS18*,  *$\alpha$ -TUB*, *EF1 $\alpha$* , *ArgK*, and *ACTB* (Figure 2 and Table 2).

The sensitivity of RT-qPCR has made this analysis method the most important technique for the relative expression of mRNA quantities. However, the validity of RT-qPCR normalization studies is depending on the reference genes included in the study, and these reference genes expression stability may be affected by variances in the examined tissues, physiological or experimental situations [4]. On the other hand, there is no single "universal" housekeeping gene that is constantly expressed and viable for all cell and tissue types under various experimental cases [2, 10, 27, 29]. Therefore, several reports suggested that multiple stably expressed housekeeping genes need to be used, as the use of such genes for the experimental setup without prior and appropriate validation can induce estimation of inaccurate expression levels of target genes and thus interpretation of data incorrectly [4, 30, 31].

The result of a meta-analysis of control gene expression studies on insects by Lü et al. was that actin, RPL, GAPDH, Tub, 18S, TATA, RPS, EF1A, HSP and SDHA are among the mostly used housekeeping genes [23]. In many studies evaluating the stability of reference genes in various insect species such as *Liposcelis bostrychophila*, *Diabrotica virgifera virgifera*, *Chilo suppressalis* and *Spodoptera exigua*, actin has been reported to show high stability at varied developmental stages [15, 32, 33]; actin has also been determined to have fairly stable expression under numerous abiotic situations in *Liposcelis bostrychophila* (insecticide) [32], *Hippodamia convergens* (diet) [27].

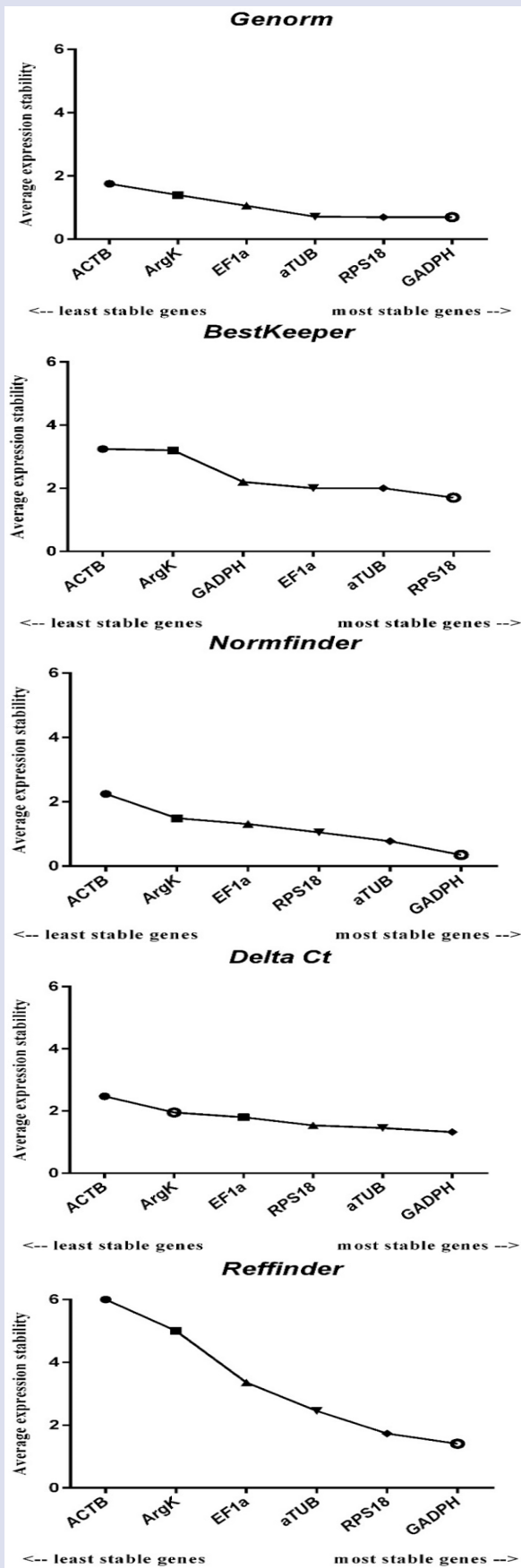


**Figure 2.** Stability of gene expression and ranking of the housekeeping genes evaluated by Genorm, Normfinder, Bestkeeper,  $\Delta$ Ct metod, RefFinder.

On the other hand, *ACTB* expression in some insect species was reported to be less stable [27, 34]. Ribosomal protein S genes (*RPS18*, *RPS15*, *RPS11* and *RPS3*), *C. maculata*, *S. inferens*, *N. lugens*, *M. domestica* and *H. armigera* were found to have high expression stability at varied developmental stages [25, 30, 35]. Tubulin ( $\alpha$ -,  $\beta$ -,  $\gamma$ -tubulin) encoding cytoskeletal structure proteins, another most studied reference gene, has been found to have highly stability under several biotic situations such as sex, tissues and developmental stages of *Sogatella furcifera*, *Coleomegilla maculata*, *Bactrocera dorsalis*, *Liposcelis bostsrychophila*, *Drosophila suzukii* [32, 36, 37] and abiotic conditions including temperature, photoperiod, insecticide and diet in *Nilaparvata lugens*, *Helicoverpa armigera*, *Bemisia tabaci* [29, 31, 36]. Similarly, *GADPH* expression showed high stability under different tissue and developmental stages of *Schistocerca gregaria*, *Tenebrio molitor*, *Rhodnius prolixus*, *Diabrotica virgifera virgifera*, *Hippodamia convergens*, *Bombyx mori*, *Chilo suppressalis*, *Sesamia inferens*, *Spodoptera litura* [8, 11, 15, 27, 30, 33]. Additionally, *GADPH* was found to be stable reference gene under abiotic conditions including viral infection in *Sogatella furcifera*, insecticide in *Liposcelis bostsrychophila*, photoperiod in *Hippodamia convergens*, diet in *Danaus plexippus*, mechanical injury and viral infection in *Helicoverpa armigera* [27, 32, 35, 36]. On the other hand, *GADPH* expression in some insect species was reported to be less stable [2, 27, 32, 37]. Furthermore, the *EF1A* gene showed high stability under different developmental stages and tissues of *Cimex lectularius* and *Bombus lucorum* [38, 39] whereas the *EF1A* gene was selected as the least constant housekeeping gene in *A. craccivora* in different temperatures and developmental stages [25]. Under starvation conditions, *ArgK*, *EF1A*, *RPS11* were recommended for *N. lugens* [31]. In summary, the expression of mostly used reference genes may alter under numerous experimental situations. Therefore, it would be beneficial to evaluate gene expression profiles widely in different biotic and abiotic cases and to determine gene stability.

In present study, a validation study was performed for reference genes (*GADPH*, *RPS18*,  *$\alpha$ -TUB*, *EF1 $\alpha$* , *ArgK*, and *ACTB*) in cockroach species *B. dubia* adults using five different algorithms ( $\Delta$ Ct method, geNorm, Bestkeeper, Normfinder and RefFinder) to assess the expression stability of selected housekeeping genes. Among the six putative housekeeping genes, *GADPH* was determined as the most stable housekeeping gene in *B. dubia* adults according to the geNorm, Normfinder  $\Delta$ Ct method and RefFinder algorithms. At the same time, *RPS18* was proposed by GeNorm and BestKeeper as the most stable gene. It has been shown that *ACTB* is by far the least stable of all algorithms. To the best of our knowledge, only one validation study [40] has been reported in cockroaches to date. In this study, only two algorithms (Normfinder and geNorm) were employed to assess eight housekeeping genes stability ( *$\beta$ -actin*, *GADPH*, *EF1 $\alpha$* , *RpL32*, *Arm*, *AnnIX*,  *$\alpha$ -Tub* and *SDHa*) in various developmental stages of

*Diploptera punctata*. The *a-Tub*, *EF1a*, and *Rpl32* genes have been suggested as the most stable genes for *D. punctata*. On the other hand, they suggested that *Actin* and *AnnIX* are the least stable genes and should not be used to normalize transcript levels. Our results suggested that *GADPH* and *RPS18* genes according to the five algorithms can be used for normalization of transcript levels in *B. dubia* adults, while *ACTB* should not be used to normalize transcript levels for cockroach *D. dubia*, as suggested in the study by Marchal *et al.* [40]. In the future planning of this study, as in other insect species, it is planned to investigate especially cockroaches under conditions of many biotic and abiotic conditions such as developmental stage, starvation, temperature, pesticide, diet. In addition, validation studies for reference genes in cockroaches are very few in the literature. Therefore, considering our current study and the studies in the literature, it is necessary to increase the number of studies to verify reference genes under biotic and abiotic conditions in q-RT-PCR studies in cockroaches.

## Acknowledgment

All analyses in this study were performed in the Molecular Biology laboratory of the Sivas Cumhuriyet University Advanced Technology and Research Center (CUTAM).

## Conflict of Interest

The authors state that did not have conflict of interests.

## References

- [1] Hudson M.E., Sequencing breakthroughs for genomic ecology and evolutionary biology, *Mol. Ecol. Resour.*, 8 (2008) 3-17.
- [2] Li R., Xie W., Wang S., Wu Q., Yang N., Yang X., Pan H., Zhou X., Bai L., Xu B., Zhou X., Zhang Y., Reference gene selection for qRT-PCR analysis in the sweetpotato whitefly, *Bemisia tabaci* (Hemiptera: Aleyrodidae), *PLoS One*, 8 (2013) e53006.
- [3] Lourenço A.P., Mackert A., Cristino A.d.S., Simões Z.L.P., Validation of reference genes for gene expression studies in the honey bee, *Apis mellifera*, by quantitative real-time RT-PCR, *Apidologie*, 39 (2008) 372-385.
- [4] Vandesompele J., De Preter K., Pattyn F., Poppe B., Van Roy N., De Paepe A., Speleman F., Accurate normalization of real-time quantitative RT-PCR data by geometric averaging of multiple internal control genes, *Genome biology*, 3 (2002) Research0034.
- [5] Strube C., Buschbaum S., Wolken S., Schnieder T., Evaluation of reference genes for quantitative real-time PCR to investigate protein disulfide isomerase transcription pattern in the bovine lungworm *Dictyocaulus viviparus*, *Gene*, 425 (2008) 36-43.
- [6] Guo J., Ling H., Wu Q., Xu L., Que Y., The choice of reference genes for assessing gene expression in sugarcane under salinity and drought stresses, *Scientific Reports*, 4 (2014) 7042.
- [7] Andersen C.L., Jensen J.L., Ørntoft T.F., Normalization of real-time quantitative reverse transcription-PCR data: a model-based variance estimation approach to identify genes suited for normalization, applied to bladder and colon cancer data sets, *Cancer Research*, 64 (2004) 5245-50.
- [8] Van Hiel M.B., Van Wielendaele P., Temmerman L., Van Soest S., Vuerinckx K., Huybrechts R., Broeck J.V., Simonet G., Identification and validation of housekeeping genes in brains of the desert locust *Schistocerca gregaria* under different developmental conditions, *BMC Mol Biol.*, 10 (2009) 56.
- [9] Pitino M., Coleman A.D., Maffei M.E., Ridout C.J., Hogenhout S.A., Silencing of aphid genes by dsRNA feeding from plants, *PLoS One*, 6 (2011) e25709.
- [10] Fu W., Xie W., Zhang Z., Wang S., Wu Q., Liu Y., Zhou X., Zhou X., Zhang Y., Exploring valid reference genes for quantitative real-time PCR analysis in *Plutella xylostella* (Lepidoptera: Plutellidae), *Int. J. Biol. Sci.*, 9 (2013) 792-802.
- [11] Berk S., and Pektas A., Selection and Validation of Reference Genes for Quantitative Real-time PCR in the Mealworm Beetle, *Tenebrio molitor*L. (Coleoptera: Tenebrionidae), *IOSR-JAVS.*, 13 (2020) 44-50.
- [12] Lador D.T., Frey B.L., Scalf M., Levenstein M.E., Artymiuk J.M., Smith L.M., Methylation of yeast ribosomal protein S2 is elevated during stationary phase growth conditions, *Biochemical and Biophysical Research Communications*, 445 (2014) 535-41.
- [13] Ponton F., Chapuis M.P., Pernice M., Sword G.A., Simpson S.J., Evaluation of potential reference genes for reverse transcription-qPCR studies of physiological responses in *Drosophila melanogaster*, *J. Insect Physiol.*, 57 (2011) 840-50.
- [14] Parker J.D., Parker K.M., Keller L., Molecular phylogenetic evidence for an extracellular Cu Zn superoxide dismutase gene in insects, *Insect Molecular Biology*, 13 (2004) 587-94.
- [15] Rodrigues T.B., Khajuria C., Wang H., Matz N., Cunha Cardoso D., Valicente F.H., Zhou X., Siegfried B., Validation of reference housekeeping genes for gene expression studies in western corn rootworm (*Diabrotica virgifera virgifera*), *PLoS One*, 9 (2014) e109825.
- [16] Lee P.D., Sladek R., Greenwood C.M., Hudson T.J., Control genes and variability: absence of ubiquitous reference transcripts in diverse mammalian expression studies, *Genome Research*, 12 (2002) 292-7.
- [17] Pfaffl M.W., Tichopad A., Prgomet C., Neuvians T.P., Determination of stable housekeeping genes, differentially regulated target genes and sample integrity: BestKeeper-Excel-based tool using pair-wise correlations, *Biotechnology Letters*, 26 (2004) 509-15.
- [18] Silver N., Best S., Jiang J., Thein S.L.J.B.m.b., Selection of housekeeping genes for gene expression studies in human reticulocytes using real-time PCR, 7 (2006) 1-9.
- [19] Pomés A., Arruda L.K., Investigating cockroach allergens: aiming to improve diagnosis and treatment of cockroach allergic patients, *Methods (San Diego, Calif.)*, 66 (2014) 75-85.
- [20] Wu H., Appel A.G., Hu X.P., Instar determination of *Blattella germanica* (Blattodea: Blattellidae) using Gaussian mixture models, *Annals of the Entomological Society of America*, 106 (2013) 323-328.
- [21] Zhang J., Zhang Y., Li J., Liu M., Liu Z., Midgut Transcriptome of the Cockroach *Periplaneta americana* and Its Microbiota: Digestion, Detoxification and Oxidative Stress Response, *PLoS One*, 11 (2016) e0155254.
- [22] Shakeel M., Rodriguez A., Tahir U.B., Jin F., Gene expression studies of reference genes for quantitative real-time PCR: an overview in insects, *Biotechnology Letters*, 40 (2018) 227-236.
- [23] Lü J., Yang C., Zhang Y., Pan H., Selection of Reference Genes for the Normalization of RT-qPCR Data in Gene Expression Studies in Insects: A Systematic Review, *Frontiers in Physiology*, 9 (2018) 1560.
- [24] Sang W., He L., Wang X.P., Zhu-Salzman K., Lei C.L., Evaluation of Reference Genes for RT-qPCR in *Tribolium castaneum* (Coleoptera: Tenebrionidae) Under UVB Stress, *Environmental Entomology*, 44 (2015) 418-25.
- [25] Yang C., Pan H., Noland J.E., Zhang D., Zhang Z., Liu Y., Zhou X., Selection of reference genes for RT-qPCR analysis in a predatory biological control agent, *Coleomegilla maculata* (Coleoptera: Coccinellidae), *Scientific Reports*, 5 (2015) 18201.
- [26] García-Reina A., Rodríguez-García M.J., Galián J., Validation of reference genes for quantitative real-time PCR in tiger beetles across sexes, body parts, sexual maturity and immune challenge, *Scientific Reports*, 8 (2018) 10743.
- [27] Pan H., Yang X., Siegfried B.D., Zhou X., A Comprehensive Selection of Reference Genes for RT-qPCR Analysis in a Predatory Lady



- Beetle, *Hippodamia convergens* (Coleoptera: Coccinellidae), *PLoS One*, 10 (2015) e0125868.
- [28] Altincicek B., Knorr E., Vilcinskis A., Beetle immunity: Identification of immune-inducible genes from the model insect *Tribolium castaneum*. *Developmental & Comparative Immunology*, 32 (2008) 585-595.
- [29] Liang P., Guo Y., Zhou X., Gao X., Expression profiling in *Bemisia tabaci* under insecticide treatment: indicating the necessity for custom reference gene selection, *PLoS One* 9 (2014) e87514.
- [30] Lu Y., Zheng X., Liang Q., Xu H., Yang Y., Tian J., He X., Lu Z., Evaluation and validation of reference genes for SYBR Green qRT-PCR normalization in *Sesamia inferens* (Lepidoptera: Noctuidae), *J. Asia-Pac. Entomol.*, 18 (2015) 669-675.
- [31] Yuan M., Lu Y., Zhu X., Wan H., Shakeel M., Zhan S., Jin B.R., Li J., Selection and evaluation of potential reference genes for gene expression analysis in the brown planthopper, *Nilaparvata lugens* (Hemiptera: Delphacidae) using reverse-transcription quantitative PCR, *PLoS One*, 9 (2014) e86503.
- [32] Jiang H.B., Liu Y.H., Tang P.A., Zhou A.W., Wang J.J., Validation of endogenous reference genes for insecticide-induced and developmental expression profiling of *Liposcelis bostrychophila* (Psocoptera: Liposcelididae), *Mol. Biol. Rep.*, 37 (2010) 1019-29.
- [33] Teng X., Zhang Z., He G., Yang L., Li F., Validation of reference genes for quantitative expression analysis by real-time rt-PCR in four lepidopteran insects, *J. Insect Sci.*, 12 (2012) 60.
- [34] Yang C., Pan H., Noland J.E., Zhang D., Zhang Z., Liu Y., Zhou X., Selection of reference genes for RT-qPCR analysis in a predatory biological control agent, *Coleomegilla maculata* (Coleoptera: Coccinellidae), *Scientific Reports*, 5 (2015) 1-11.
- [35] Zhang S., An S., Li Z., Wu F., Yang Q., Liu Y., Cao J., Zhang H., Zhang Q., Liu X., Identification and validation of reference genes for normalization of gene expression analysis using qRT-PCR in *Helicoverpa armigera* (Lepidoptera: Noctuidae), *Gene*, 555 (2015) 393-402.
- [36] An X.-k., Hou M.-l., Liu Y.-d., Reference gene selection and evaluation for gene expression studies using qRT-PCR in the white-backed planthopper, *Sogatella furcifera* (Hemiptera: Delphacidae), *J. Econ. Entomol.*, 109 (2016) 879-886.
- [37] Zhai Y., Lin Q., Zhou X., Zhang X., Liu T., Yu Y., Identification and validation of reference genes for quantitative real-time PCR in *Drosophila suzukii* (Diptera: Drosophilidae), *PLoS One*, 9 (2014) e106800.
- [38] Mamidala P., Rajarapu S.P., Jones S.C., Mittapalli O., Identification and validation of reference genes for quantitative real-time polymerase chain reaction in *Cimex lectularius*, *Journal of Medical Entomology*, 48 (2011) 947-51.
- [39] Hornáková D., Matoušková P., Kindl J., Valterová I., Pichová I., Selection of reference genes for real-time polymerase chain reaction analysis in tissues from *Bombus terrestris* and *Bombus lucorum* of different ages, *Analytical Biochemistry*, 397 (2010) 118-20.
- [40] Marchal E., Hult E.F., Huang J., Tobe S.S., Sequencing and validation of housekeeping genes for quantitative real-time PCR during the gonadotrophic cycle of *Diploptera punctata*, *BMC Research Notes*, 6 (2013) 237.

## The Role of Cisplatin Loaded Biocompatible Nanoparticles in Cancer Treatment

Tuğba Kumtepe <sup>1,a</sup>, Murat Doğan <sup>2,b,\*</sup>

<sup>1</sup> Faculty of Pharmacy, Sivas Cumhuriyet University, Sivas, Türkiye

<sup>2</sup> Department of Pharmaceutical Biotechnology, Faculty of Pharmacy, Sivas Cumhuriyet University, Sivas, Türkiye

\*Corresponding author

### Research Article

#### History

Received: 06/02/2022

Accepted: 03/06/2022

#### Copyright



©2022 Faculty of Science,  
Sivas Cumhuriyet University

[tbkumtepe@gmail.com](mailto:tbkumtepe@gmail.com)

<https://orcid.org/0000-0001-8687-6406>

[mdogan@cumhuriyet.edu.tr](mailto:mdogan@cumhuriyet.edu.tr)

<https://orcid.org/0000-0003-2794-0177>

### ABSTRACT

Chemotherapeutic treatments focusing on cisplatin, ovarian cancer, testicular cancer, breast cancer, colon cancer, lung cancer etc. seen in adults and children. Cisplatin is an antineoplastic agent frequently used in cancer types. Drug resistance to cisplatin has an effect on the success of the treatment. After cisplatin-administered treatments, patients may experience cisplatin-induced side effects of various toxic dimensions, such as nausea, nephrotoxicity, cardiotoxicity, hepatotoxicity, and neurotoxicity. As a result of the literature review, various studies have been carried out to reduce the side effects and toxic effects of cisplatin and other anticancer molecules without interfering with their activities. In this study, we planned to prepare a cisplatin-loaded chitosan nanoparticle formulation based on the ionic gelation method using chitosan and tripolyphosphate (TPP) with the information obtained from the literature. In this study, chitosan nanoparticles containing the same concentration of cisplatin were applied to MDA-MB-231 breast cancer cell lines obtained from the American Type Culture Collection (ATCC). As a result, biocompatible nanoparticles with similar cytotoxic effects cause less side effects in other cells and tissues than other nanoparticles.

**Keywords:** Cancer, Cisplatin, Chitosan, Nanoparticle, Cytotoxicity.

### Introduction

Cancer is one of the most important diseases that visibly affects living standards, requires long-term heavy treatment stages, has a very high mortality and morbidity rate, requires special care after diagnosis, and threatens human health today [1]. Many types of cancer usually begin with the uncontrolled division and proliferation of abnormal cells. Cancer types are mostly named according to the tissues and organs from which they originate [2]. Cancer cells accumulate over time to form tumors. Tumors may be benign or malignant according to their activity. Tumors that cause cancer are malignant tumors. The cells of such tumors are abnormal. Depending on their size, these tumors have the ability to compress, penetrate and destroy normal cells. When cancer cells leave the tumor of origin, they can reach the rest of the body through the blood or lymph circulation. They form colonies in these regions and continue their growth processes. The spread of cancer cells to the body in such a way is called metastasis, that is, the spread of cancer to other tissues and organs [3]. Patients with cancer are treated with either surgical treatment methods such as surgical interventions or newer treatment methods such as gene therapy, depending on the type of cancer and its stage. Radiation therapy is used dangerous doses of radiation to shrink or kill cancerous cells [4-6]. In addition to these, many drugs and drug active substances such as cisplatin are used in the treatment of cancer. Cisplatin is one of the first metal-based, widely used chemotherapeutic agents [7].

Cisplatin is one of the most widely used chemotherapeutic drugs for various tumors in the clinic due to its high activity and broad spectrum of action. [8, 9]. Cisplatin is an important chemotherapeutic agent widely used in the treatment of various diseases such as testis, ovary, breast, cervical, prostate, bladder, and lung [10]. Cisplatin is formed by the coordination of a central platinum atom in the "cis" position, two chlorine and two ammonia molecules. Molecular structure of cisplatin was shown in Figure 1.

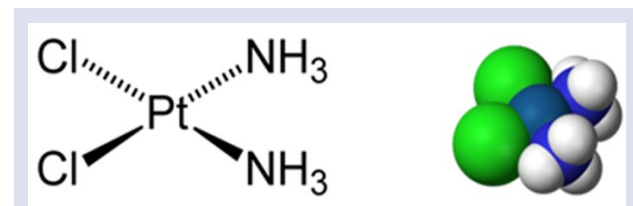


Figure 1. 2-dimensional and 3-dimensional structure of cisplatin [11]

Cisplatin generally binds to DNA from its genomic region to form gDNA or binds from its mitochondrial region to form mtDNA. It causes lesions in DNA. By acting on DNA, mRNA and proteins, it causes their inhibition and prevents their production. It activates multiple transduction pathways by interfering with the DNA replication mechanism. These events eventually lead to apoptosis and necrosis. [12-13]. Nephrotoxicity,

ototoxicity, gastrointestinal, neurotoxicity and hepatotoxicity often occur after cisplatin treatment [14]. It is known that cisplatin causes nephrotoxicity by contributing to the formation of free oxygen radicals such as superoxide and hydroxyl radical. Platinum response to combined cisplatin use is primarily high, however, many cancer patients will eventually resurface with cisplatin-resistant diseases. Therefore, significant resistance to the drug has been observed in many patients whose condition relapses due to cisplatin therapy. Suggested cisplatin-resistant mechanisms include differences in uptake and flux of cisplatin into cells, increased biotransformation and detoxification in the liver, and increased over DNA repair and anti-apoptotic mechanisms [15]. Cisplatin treatment is very beneficial on the life expectancy of breast cancer patients [16].

The MDA-MB-231 cell is an epithelial line of human breast cancer cells. Metastatic breast and adenocarcinoma from pleural effusion of a woman and is one of the breast cancer cell lines frequently used in research laboratories [17]. Many risk factors that cause breast cancer have been identified. Among these risk factors, hereditary factors are very important in the formation of breast cancer. Approximately 40% of human breast cancers are caused by mutations in the p53 gene [18]. In addition, cancer patients experience physical collapse such as nausea, loss of appetite, weight loss, hair loss, and psychological collapse such as depression and depression as a kind of side effect during chemotherapy treatment. These treatments are provided with psychological support [19]

Nanoparticles are used in cancer treatment. In general, as a result of the studies chitosan inhibits cell proliferation, induces apoptosis and has been shown to reduce its size. Therefore, it is widely used in breast cancer. Chitosan has many advantages such as bioavailability, biocompatibility, biodegradability, and mucoadhesiveness. It is distinguished from other nanoparticles by its properties [20]. It also has features such as antibacterial, antifungal, antitumor and hemostatic activities. It stimulates wound healing and immune system. Chitosan is one of the natural polysaccharides obtained from the shells of shellfish and fungal cell walls and is obtained as a result of deacetylation of chitin [20, 21]. Molecular structure of chitosan was shown in Figure 2 [22].

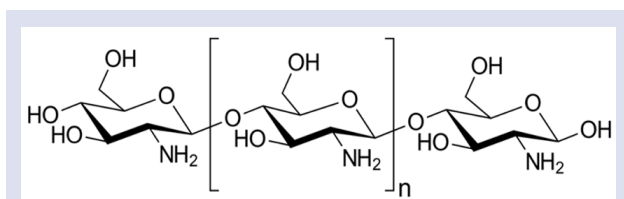


Figure 2. The structure of chitosan [22]

In this study, it was aimed to prepare nanoparticles with chitosan, a biocompatible polymer and cisplatin,

which has a cytotoxic effect on cancer cells. As seen in the studies, it has been stated that cisplatin has various toxic and side effects together with its use in cancer treatment. Our hypothesis is that the preparation of chitosan nanoparticles containing cisplatin in the concentration it is applied alone and that the biocompatible nanoparticles on cells and have more effective cytotoxic effect on MDA-MB-231 cancer cells.

## Materials and Methods

### Chemicals and Medical Consumables

MDA-MB-231 breast cancer (HTB-26™) cell line, penicillin/streptomycin (10,000U/mL), DMEM/Nutritional Mixture, Fetal Bovine Serum (FBS), Trypsin-EDTA solution and various consumables required for cell culture were used. In the preparation of chitosan nanoparticles, medium molecular weight chitosan, tripolyphosphate (TPP), glacial acetic acid were used.

### Preparation of Chitosan Nanoparticles

The ionic gelation method was used for the preparation of nanoparticles. It were dissolved in 0.05 % acetic acid, with a medium molecular weight chitosan concentration of 2,5 mg/ml. The dissolution process of chitosan was performed using a magnetic stirrer. The dilution of acetic acid was done with sterile bidistilled water. TPP was dissolved in sterile bidistilled water with stirring on a magnetic stirrer at a concentration of 2,5 mg/ml. The determined concentration of cisplatin were added to the dissolved TPP and mixed for 10-15 minutes to distribute it homogeneously. Afterwards, TPP containing cisplatin were dropped into the chitosan mixed in a magnetic stirrer with a certain dropping rate, and the mixing process were continued for 3 hours after the dropping process. Then, the chitosan-TPP mixture were added to a 50 ml centrifuge tube and centrifuged at 12.000 rpm for 15 minutes. After centrifugation, discarding the supernatant in the upper part, sterile bidistilled water were added and centrifugation were taken place again. After this process was repeated three times, the chitosan nanoparticles containing cisplatin at the bottom of the tube were maintained at -20 °C overnight. The next day, our frozen nanoparticles were lyophilized in the lyophilizer. Our lyophilized nanoparticles were put into an eppendorf tube and stored in a moisture-free environment after passing through the sieves used in nanoparticle preparation. Mechanical characterization studies of nanoparticles were performed using Malvern Zetasizer device [23].

### Cell Culture

MDA-MB 231 cells obtained from American Type Culture Collection (ATCC) were in an incubator at 37°C and 5% CO<sub>2</sub>, in flasks, in DMEM cell culture medium including 1% L-glutamine and penicillin-streptomycin, 10% fetal bovine serum were reproduced in vitro condition. When the cells reach a certain density (80%), the cells were passaged and work were started after a certain passage.

### XTT Cell Viability Assay

The effect of cisplatin and cisplatin-loaded nanoparticles on the viability of MDA-MB 231 cell line were investigated with the XTT cell viability assay. In this method, metabolically active cells reduce XTT, a tetrazolium salt, to orange colored formazan crystals. Because of the dye was water-soluble, the dye density can be read at certain wavelengths (450 nm) with the use of a spectrophotometer. The dye density in orange is proportional to the number of metabolically active cells. For cytotoxicity experiments, first of all,  $10 \times 10^3$  cells were taken from the medium containing 100  $\mu$ L of DMEM + 10% FBS + 1% antibiotic, and cells were seeded in a sterile 96-well microplate and incubated overnight for cells to adhere. The next day, the medium on the cells were removed, the wells were washed with PBS, fresh medium were added to the cells, different concentrations of cisplatin were applied to the cells and incubated for 24 hours. At the end of this period, the medium were removed and the cells were washed three times with PBS. Then, 100  $\mu$ l of clear (colorless) DMEM and 50  $\mu$ l of XTT solution were added to each well and incubated in a CO<sub>2</sub> incubator for 4 h. After the incubation, the optical density value were read at 450 nm in the microplate reader, the cell viability rate of the control group were considered as 100% [24].

### Results and Discussion

#### Mechanical Characterization Result of Nanoparticles

The zeta potential is known as the electrostatic interactions between particles and cells in a fluid medium. According to the results, the zeta potential values of the nanoparticles ranged between  $2.36 \pm 0.03$  mV and  $2.58 \pm 0.02$  mV (Table 1). Thanks to the positive zeta potential of nanoparticles, it is easier to adhere to the negatively charged cell membrane and enter the cell through receptors. The zeta potential values of the nanoparticles obtained at the end of the study can be evaluated as suitable for application. Particles above a certain molecular size are not able to pass through the cell membrane and show the desired effects in the target region. For this reason, it is desired that the nanoparticles have size in the specified ranges ( $< 400$  nm). In this study, nanoparticle sizes were observed to be between  $312.14 \pm 1.8$  nm and  $336.25 \pm 2.2$  nm. It can be concluded that nanoparticle sizes are appropriate for in vitro cell culture assay, hence its antiproliferative effect may be within the expected values in in vitro studies. The polydispersity index value is a significant parameter in the homogeneity of the size distribution of the nanoparticle and in the evaluation of the aggregation risk. This value is required to be less than 0.4 in terms of application.

Table 1. Particle size, zeta potential and polydisperse index values of chitosan nanoparticles

Formulations (Chitosan- TPP nanoparticles)	Zeta potential(mV) $\pm$ SD	Size (nm) $\pm$ SD	Polydispersity index $\pm$ SD
*NP1	$2.46 \pm 0.04$	$312.14 \pm 1.8$	$0.242 \pm 0.02$
*NP2	$2.58 \pm 0.02$	$334.22 \pm 2.6$	$0.273 \pm 0.04$
*NP3	$2.36 \pm 0.03$	$336.25 \pm 2.2$	$0.258 \pm 0.03$

\*All nanoparticles (NP1, NP2, NP3) containing medium molecular weight chitosan, tripolyphosphate and cisplatin.

When we evaluate the results, it can be said that the polydisperse index values of nanoparticles are lower than 0.4 and it is suitable for application. According to the results of the mechanical characterization study, the NP1 formulation has the most suitable particle size, zeta potential and polydisperse index values, so its applicability is higher in terms of in vitro studies.

#### Antiproliferative Activity Result of Cisplatin and Nanoparticles Loaded With Cisplatin

Nanoparticles loaded with cisplatin and only cisplatin were treated to the MDA-MB 231 cells at concentrations (2.5  $\mu$ g/ml, 5  $\mu$ g/ml, 10  $\mu$ g/ml, 25  $\mu$ g/ml, 50  $\mu$ g/ml) and the cytotoxic efficiencies and IC50 values of the samples were calculated and evaluated. Nanoparticles used in in vitro studies were prepared using the same method but mechanical features such as particle size, zeta potential and polydispersity index may differ owing to the differences arising from the experimental environment and minor mistake. Due to this difference, the antiproliferative activities of nanoparticles may also show slight differences. Concentration-dependent MDA-MB 231 antiproliferative activity of samples including only

cisplatin was calculated as 74.36 % at 2.5  $\mu$ g/mL concentration and 47.28 % at 50  $\mu$ g/mL concentration. Cell viability of NP1 samples 64.28 % at 2.5  $\mu$ g/mL concentration and 41.23 % at 50  $\mu$ g/mL concentration. If we evaluate the cell viability of NP2 samples on MDA-MB 231 cells, cell viability ranged between 68.87 % and 43.36 % depending on the concentration. In addition, cell proliferation of NP3 samples 69.22 % at least concentration and 45.52 % at highest concentration. According to XTT cell viability results, it was observed that NP samples including cisplatin had significantly more effective cytotoxic activity against MDA-MB 231 cells compared to cisplatin alone. Especially, the NP1 formulation showed the highest cytotoxic activity at all concentrations. According to the results of in vitro cell culture studies and XTT cytotoxicity studies, we can conclude that cisplatin has an important antiproliferative effect on MDA-MB 231 cells so has a cytotoxic effect. In addition, the main aim of preparing nanoparticles containing cisplatin in this study was to increase the antiproliferative activity of cisplatin on MDA-MB 231 cells and to obtain a more effective anticancer activity. According to the results, it can be said that nanoparticles show the desired efficiency in XTT cell viability assay.

Table 2. Concentration dependent MDA-MB 231 cell viability results of cisplatin and NPs including cisplatin

Samples/Concentration	MDA-MB 231 Cell Viability (%)				
	(2.5 µg/mL)	(5 µg/mL)	(10 µg/mL)	(25 µg/mL)	(50 µg/mL)
Cisplatin	74.36	71.12	63.74	57.78	47.28
NP1	64.28	61.35	54.28	49.57	41.23
NP2	68.87	63.37	57.58	51.36	43.36
NP3	69.22	64.12	57.86	54.78	45.52

In a study performed Alp et al. HeLa cells were treated with different concentrations of CDDP at 24 and 48 hours. The XTT technique was used to measure cell viability. Furthermore, using Real-Time PCR, the quantitative mRNA expression of the mTOR, AKT, CCND1, and STAT-3 genes was examined following treatment with various dosages of cisplatin. In summary, different mRNA expression pattern was found after CDDP treatment regarding to exposure time [25].

In another study performed Arslan et al. A549 and SK-MES-1 which had been kept as frozen form in the liquid nitrogen tank were prepared in order to use. The cytotoxicity was determined using XTT and MTT, and the apoptotic effects were assessed first by comparing the mRNA levels of the BAX, BCL-2, and CASPASE-3 genes, and then by counting the percentage of early apoptotic cells observed on the cell lines. When all of the data was analyzed properly, the effects of -Bgtx treatment with and without cisplatin were shown to be significant, particularly in the SK-MES-1 squamous lung cancer line, where tobacco use was the primary cause of cancer with a high percentage of cases. [26].

42 female patients were included in this study who were neoadjuvantly treated with the ETC combination (epirubicin 60 mg/m<sup>2</sup>, docetaxel 60 mg/m<sup>2</sup>, and cisplatin 60 mg/m<sup>2</sup>) every three weeks between March 2010 and March 2011 provided having the diagnosis of breast cancer. There wasn't any treatment related death. Combination of ETC chemotherapy can be preferred in neoadjuvant treatment of breast cancer because of high response rate and tolerability [27]. Unlike our study, cisplatin was used in combination. Epirubicin and docetaxal were used in combination.

Perez et al. reported a high response rate of up to 62% in a study they conducted with paclitaxel and carboplatin as the first choice treatment for patients with metastatic breast cancer. Based on the findings of these research, platinum compounds are becoming more popular as first-line treatments, particularly for triple-negative breast cancer. Cisplatin is utilized alone or in various combinations in these recent research. The inclusion of gemcitabine or capecitabine to anthracycline and taxanes-containing regimens is also being investigated [28].

The advantage of our study over other studies is that we used chitosan polymer in addition to cisplatin. Among

the features of chitosan; Biodegradable, biocompatible, antimicrobial activity, non-toxic, chemical and physical properties, can be converted into a wide variety of physical forms with appropriate technological methods. Since chitosan in cationic structure contains amino group that can react, it can easily react with ions in anionic structure. Chitosan has many advantages, especially with its ability to transform into microspheres, microparticles and nanoparticles. These forms can control the controlled release of active substances. Due to the biocompatible chitosan nanoparticle, it shows antiproliferative activity in cancer cells and prevents the progression of cancer cells. At the same time, it does not have any side effects and toxicity to healthy cells.

## Conclusion

The experiment was to investigate what kind of effect cisplatin has on breast cancer cells by observing its antiproliferative activity. It was aimed to prepare cisplatin-loaded chitosan nanoparticles and obtain better cytotoxic activity on cancer cells. In this study, nanoparticles with positive zeta potential showed the desired effect because they can easily adhere and pass through the cell membrane. The acceptable value of the polydisperse index value should be at most 0.4, and as a result of the experiment, it was found to be less than 0.4. Based on the results of the study, we can conclude that cisplatin loaded nanoparticle has a significant antiproliferative effect on MDA-MB 231 cells.

## Acknowledgements

I would like to state that I received support from the TUBITAK 2209 project numbered 1919B012002787 in this study. In addition, this study was performed at Cumhuriyet University Faculty of Pharmacy, Pharmaceutical Biotechnology Laboratory and Cumhuriyet University Faculty of Medicine Cancer Research Center.

## Conflicts of interest

The authors state that did not have conflict of interest.

## References

- [1] Zhang B., Pan X., Cobb GP., Anderson TA., MicroRNAs as Oncogenes and Tumor Suppressors, *Dev Biol.*, 302(1) (2007) 1-12.
- [2] Hanahan D., Weinberg R.A., Hallmarks of Cancer: the Next Generation, *Cell*, 144 (2011) 646-74.
- [3] American Cancer Society, Cancer Facts & Figures, Atlanta: American Cancer Society, 2012. Available at <https://www.cancer.org/research/cancer-facts-statistic>.
- [4] Lind M.J., Principles of Cytotoxic Chemotherapy, *Medicine*, 36(1) (2008) 19–23.
- [5] Eastman A., Improving Anticancer Drug Development Begins with Cell Culture: Misinformation Perpetrated by the Misuse of Cytotoxicity Assays, *Oncotarget*, 8 (2017) 8854–8866.
- [6] Donna S.S., Robert D.K., Introduction to Cancer Chemotherapeutics, *Chem. Rev.*, 109(7) (2009) 2859–2861.
- [7] Rosenberg B., Archie W.P., Stanley T., Stephen K.C., Cisplatin: Its History and Possible Mechanisms of action, *Academic Press*, (1980) 9–12.
- [8] Dasari S., Tchounwou P.B., Cisplatin in Cancer Therapy: Molecular Mechanisms of action, *European Journal of Pharmacology*, 740(3) (2014) 64-378.
- [9] Browning R.J., Reardon P.J.T., Parhizkar M., Pedley R.B., Edirisinghe M., Knowles J.C., Stride E., Drug Delivery Strategies for Platinum-Based Chemotherapy, *ACS Nano.*, 11(9) (2017) 8560-8578.
- [10] Tsimberidou A.M., Braiteh F., Stewart D.J., Kurzrock R., Ultimate Fate of Oncology Drugs Approved by the Us Food And Drug Administration without a Randomized Trial, *Journal of Clinical Oncology*, 27(36) (2009) 6243-6250.
- [11] Weiss R.B., Christian M.C., New Cisplatin Analogues in Development, *Drugs*, 46(3) (1993) 360-377.
- [12] Ciccarelli R.B., Solomon M.J., Varshavsky A., Lippard S.J., In vivo Effects of Cisand Trans- Diammine Dichloro Platinum (II) on Sv40 Chromosomes: Differential Repair, Dna-Protein Cross-Linking, and Inhibition of Replication, *Biochemistry*, (24) (1985) 7533–7540.
- [13] Florea A.M., Büsselberg D., Cisplatin as an Anti-Tumor Drug: Cellular Mechanisms of Activity, Drug Resistance and Induced Side Effects, *Cancers*, (3) (2011) 1351–1371.
- [14] Astolfi L., Ghiselli S., Guaran V., Chicca M., Simoni E., Olivetto E., Lelli G., Martini A., Correlation of Adverse Effects of Cisplatin Administration in Patients Affected by Solid Tumours: A Retrospective Evaluation, *Oncol. Rep.*, 29 (4) (2013) 1285–1292.
- [15] Gottesman M.M., Fojo T., Bates S.E., Multidrug Resistance in Cancer: Role of ATP-Dependent Transporters, *Nature Reviews Cancer*, 2(1) (2002) 48-58.
- [16] Decatris M.P., Sundar S., O'Byrne K.J., Platinum-based Chemotherapy in Metastatic Breast Cancer: Current Status, *Cancer Treat. Rev.*, (30) (2004) 53–81.
- [17] Liu H., Zang C., Fenner M.H., Possinger K., Elstner E., PPAR $\gamma$  Ligands and ATRA Inhibit the Invasion of Human Breast Cancer Cells in vitro, *Breast Cancer Research and Treatment*, 79(1) (2003) 63-74.
- [18] Libson S., Lippman M., A review of Clinical Aspects of Breast Cancer, *International Review of Psychiatry*, 26(1) (2014) 4-15.
- [19] Kim S., Competitive Biological Activities of Chitosan and its Derivatives Antimicrobial, Antioxidant, Anticancer, and Anti-Inflammatory Activities, *International Journal of Polymer Science*, 1708(172) (2018) 1-14.
- [20] Severino P., da Silva C.F., da Silva M.A., Santana M.H., Souto E.B., Chitosan Cross-Linked Pentasodium Tripolyphosphate Micro/Nanoparticles Produced by Ionotropic Gelation, *Sugar Tech.*, 18(1) (2016) 49-54.
- [21] Kutluturk S., Sozeri E., Uysal N., Bay F., Resilience and Burnout Status Among Nurses Working in Oncology, *Ann. Gen. Psychiatry*, 15(1) (2016) 1-9.
- [22] Jose S., Fanguero J. F., Smitha J., Cinu T.A., Chacko A.J., Premeletha K., Souto E.B., Cross-linked Chitosan Microspheres for Oral Delivery of Insulin: Taguchi Design and in vivo Testing, *Colloids and Surfaces B: Biointerfaces*, 92(3) (2012) 175-179.
- [23] Calvo, Pilar, et al. Novel Hydrophilic Chitosan-Polyethylene Oxide Nanoparticles as Protein Carriers, *Journal of Applied Polymer Science*, 63(1) (1997) 125-132.
- [24] Wolf Nadine B., Influences of Opioids and Nanoparticles on in vitro Wound Healing Models, *European Journal of Pharmaceutics and Biopharmaceutics*, 73(1) (2009) 34-42.
- [25] Alp E., Yılmaz, A., Önen H. İ., Konaç E., Ekmekçi A., Menevşe E. S., Menevşe A., HeLa Hücrelerinde Sisplatinin MTOR, AKT, CCND1 ve STAT3 mRNA İfadesi Üzerine Etkileri, 31 (2020) 5-9.
- [26] Arslan, Y., Balkan, A., Avcu, F., Uçar, E., Gümüş, S., Taşçı, C., Bilgiç, H., The Evaluation of the Effectiveness of Alpha Bungarotoxin Individually and Combined with Cisplatin on A549 Lung Adenocancer Cell Line and SK-MES-1 Lung Squamous Cell Cancer Cell Line, *Türk Toraks Dergisi*, 20 (2019) 35.
- [27] Avcı N., Lokal İleri Meme Kanserinin Neoadjuvan Kemoterapisinde Epirubisin, Doksetaksel ve Sisplatin Kombinasyonunun Etkinliği ve Güvenilirliği, Yüksek Lisans Tezi, Uludağ Üniversitesi, Tıp Fakültesi, (2012).
- [28] Vural B., Alkaç İ.M., Üçlü Negatif Meme Kanseri (Ünmk) Tedavisinde, Azd7762 İlacına Karşı Hassaslığın Rbfox2 Gen Ekspresyonu ile Araştırılması, *Türkiye Klinikleri Tıp Bilimleri Dergisi*, 41(4) (2021) 491-500.

## Analysis of Carvedilol in Pharmaceutical Preparations by Spectrofluorometric Method

Bilal Yılmaz<sup>1,a,\*</sup><sup>1</sup> Department of Analytical Chemistry, Faculty of Pharmacy, Atatürk University, Erzurum, Türkiye

\*Corresponding author

### Research Article

#### History

Received: 24/03/2022

Accepted: 02/06/2022

#### Copyright

©2022 Faculty of Science,  
Sivas Cumhuriyet University[yilmazb@atauni.edu.tr](mailto:yilmazb@atauni.edu.tr)<https://orcid.org/0000-0002-8574-7570>

### ABSTRACT

The goal of this research is to develop a spectrofluorometric method for analyzing carvedilol in pharmaceutical preparations and apply this method to the formulations. The method's calibration curve was plotted between 25 and 500 ng/mL. The mean calibration equation from six replicate experiments is  $y=1.8736x+7.7291$ . The correlation coefficient value was higher than 0.997 for the mean calibration curve. The trueness results were better than 2.09% and the precision results were less than 2.73% for carvedilol. The detection and quantitation limits were determined as 2.196 and 6.654 ng/mL, respectively. In addition, the method was used to study carvedilol in pharmaceutical preparations. The method had recovery values >98.4% for all samples in pharmaceutical preparations. The detection wavelength was optimized to maximize the sensitivity of the method. This method has good sensitivity with satisfactory results. Therefore, the method can be used in carvedilol analysis.

**Keywords:** Cocklebur, Biodiesel, Fatty acids, Linoleic acid.

## Introduction

Carvedilol is an antagonist of  $\alpha_1$  and  $\beta_1$ ,  $\beta_2$  receptors as cardiovascular agent [1-3]. In addition, it is used to treat congestive heart failure, myocardial infraction, high blood pressure and ischemic heart disease. The chemical formula structure of carvedilol is ( $\pm$ )-1-(carbazol-4-yloxy)-3-((2-(*o*-methoxyphenoxy)ethyl)amino)-2-propanol (Figure 1).

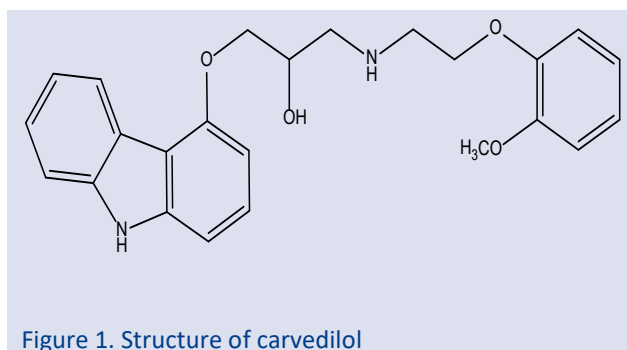


Figure 1. Structure of carvedilol

Carvedilol is available 12.5 mg and 25 mg varying doses in tablet formulations. Carvedilol has got C<sub>24</sub>H<sub>26</sub>N<sub>2</sub>O<sub>4</sub> molecular formula and of 406.474g/mol molecular mass [4]. Since it is polar, its solubility in polar solvents is good [5].

In literature research, UV-Visible spectrophotometry [6-13], spectrofluorometry [14], HPLC [15-21] and capillary electrophoresis [22,23], either as a single entity or with other drugs in methods for determining carvedilol in pharmaceutical formulations or biological fluids have been reached.

These methods, except spectrophotometric methods, offered the required sensitivity and selectivity for the analysis of carvedilol in biological fluids, however their sophisticated instrumentation and high-analysis cost limited their use in quality control laboratories for analysis of carvedilol in its pharmaceutical dosage forms. Moreover, these instruments are not available in most quality control laboratories specially, third world countries. In general, spectrofluorometry is considered one of the most convenient analytical techniques, because of its inherent simplicity, low cost, and wide availability in most quality control laboratories. For these reasons, the goal of this research is to develop a spectrofluorometry method for analyzing carvedilol in pharmaceutical preparations and apply this method to the formulations. The developed method was then validated with respect to the ICH Topic Q 2 (R1) guideline [24].

The presented method is based on a simple and single analysis step in a short time using inexpensive chemicals. At the same time, the approach was also used to examine carvedilol levels in pharmaceutical preparations.

## Materials and Methods

### Chemicals

Carvedilol standard (98% purity) and methanol were obtained from Sigma (Germany). From a pharmacy, Dilatrend, Carvexal and Coronis tablet that included 25 mg carvedilol was purchased.

### Spectrofluorometry System

Fluorescence analyses were performed with SHIMADSU RF-5301 PC spectrofluorometer system. In this work, a Xenon lamp was used. Excitation and emission wavelengths were as  $\lambda_{exc}=285$  nm and  $\lambda_{em}=335$  nm. Slit width was selected as 5.0 nm on spectrofluorometer system equipped with a 1 cm quartz cells.

### Preparation of Standard Solutions

Methanol was used to make a 1000 ng/mL carvedilol solution. Carvedilol standard solutions were diluted with methanol. Standard calibration samples were prepared 25-500 ng/mL (25, 50, 100, 200, 300, 400 and 500 ng/mL). The carvedilol solutions were all kept at 4 °C. Carvedilol quality control standard solutions were produced 75, 150 and 450 ng/mL.

### Statistical Analysis

The statistical analyses were done with SPSS V.15.0 version at computer program. Regression analyses were used in the preparation of the carvedilol standard line and calculations. For statistical significance, the results were given with the mean  $\pm$  standard error.

## Results and Discussion

### Development and Optimization of the Method

In this work, the various solvent systems (acetonitrile and methanol) were investigated for spectrofluorometry method. Methanol was selected as the solvent for sensitivity and stability. Excitation and emission spectra were recorded at  $\lambda_{exc}=285$  nm and  $\lambda_{em}=335$  nm, respectively.

### Validation of the Method

Spectrofluorometry method was validated with validation parameters according to CDER. These parameters were specificity, linearity, precision, trueness, recovery, limit of detection (LOD), limit of quantification (LOQ) and stability.

### Specificity

All the standard, quality control and tablet solutions were recorded at  $\lambda_{exc}=285$  nm and  $\lambda_{em}=335$  nm, respectively. The emission spectrum of carvedilol solutions showed maximum values. The spectrums of carvedilol standard were given in Figure 2.

The emission wavelengths of standard, quality control and tablet solutions did not changed at  $\lambda_{em}=335$  nm. The effects of common excipients and additives were tested for their possible interferences in the assay of carvedilol. The simulated and placebo samples were prepared and analyzed.

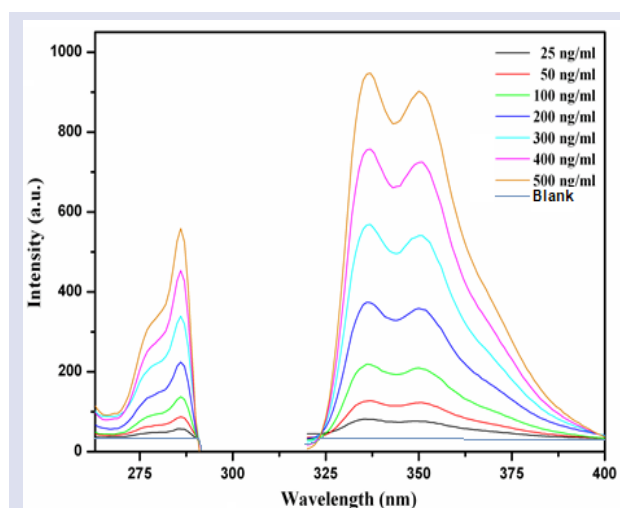


Figure 2. The spectrums of carvedilol.

It has not been determined any interference of these substances at the levels found in dosage forms. Excipient that was used in this preparation was the most commonly used by the pharmaceutical industry. The presence of titanium dioxide, talc, lactose, starch, and magnesium stearate did not appear interfere in the results of the analysis. Endogenous interference substances were not observed in spectra. According to the analysis results the method can be specific.

### Linearity

Standard calibration curve was drawn according to emission value ( $y$ ) of carvedilol versus carvedilol concentration. It was found to be linear over the 25-500 ng/mL concentration range for carvedilol. The mean calibration equation from three replicate experiments is  $y=1.8736x+7.7291$ . The correlation coefficient value was higher than 0.997 for the mean calibration curve. The results are listed in Table 1.

Table 1. Linearity values of carvedilol

Parameters	Carvedilol
$\lambda_{exc}$ (nm)	285
$\lambda_{em}$ (nm)	335
Linearity range (ng/mL)	25-500
Slope	18.736
Intercept	77.291
Correlation coefficient	0.997
Standard deviation of slope	0.002
Standard deviation of intercept	1.247
LOD (ng/mL)	2.196
LOQ (ng/mL)	6.654

### Precision and trueness

The %RSD value values were used to assess the proposed method's precision. Six replicates for each of three different concentrations were analyzed to determine intra-day precision. The same samples were analyzed in three successive days to measure the intermediate precision. In addition, the percentage relative error was used to assess the method's trueness. The results are listed in Table 2.



Table 2. Precision and trueness of carvedilol

Added (ng/mL)	Intra-day			Inter-day		
	Found $\pm$ SD <sup>a</sup>	Precision % RSD <sup>b</sup>	Trueness <sup>c</sup>	Found $\pm$ SD <sup>a</sup>	Precision % RSD <sup>b</sup>	Trueness <sup>c</sup>
75	74.6 $\pm$ 1.424	1.91	-0.53	75.2 $\pm$ 2.052	2.73	0.27
150	148.5 $\pm$ 3.121	2.10	1.00	152.2 $\pm$ 3.149	2.07	1.47
450	445.2 $\pm$ 4.243	0.95	-2.09	453.4 $\pm$ 5.325	1.17	0.76

In addition, the percentage relative error was used to assess the method's trueness. The results are listed in Table 2.

The precision and trueness for carvedilol from standard solution samples were gratifying. %RSD value is obtained as lower than 2.73%. In addition to this, trueness is detected to be within  $\pm$  2.09% with relative error. From the results obtained, it is understood that both the precision and the trueness of this method are good.

### Recovery

The percentage recovery was checked to study the formulation interference effects at three different concentrations. The recoveries were performed by adding known amount of pure drugs to pre-analyzed samples of carvedilol tablets. The percentage recoveries were calculated by comparing concentration obtained from the spiked samples with actual added concentrations. The results are listed in Table 3.

Table 3. Recovery of carvedilol in tablets (n=6)

Tablet	Added (ng/mL)	Found $\pm$ SD	Recovery (%)	RSD (%)
Dilatrend (150 ng/mL)	50	49.2 $\pm$ 1.312	98.4	2.67
	150	149.2 $\pm$ 3.124	99.5	2.09
	250	253.0 $\pm$ 6.847	101.2	2.71
Carvexal (150 ng/mL)	50	49.3 $\pm$ 1.097	98.6	2.23
	150	152.4 $\pm$ 3.473	101.6	2.28
	250	247.4 $\pm$ 3.146	98.9	1.27
Coronis (150 ng/mL)	50	49.6 $\pm$ 1.073	99.2	2.16
	150	147.8 $\pm$ 3.624	98.5	2.45
	250	252.7 $\pm$ 4.369	101.1	1.73

Also, the proposed method was compared with the official method [25]. Besides, the results of the proposed method were compared with the reported method [26]. The results revealed no significant difference between the

proposed and reference methods using F test at the 95% confidence level (Table 4). Also, the limit of quantitation of the proposed method is lower than those of the official method [25].

Table 4. Comparison of the methods

Parameters	Spectrofluorometry	Official method [25]	Reported method [26]
Trueness %	99.68	99.98	99.93
SD	0.847	0.012	-
% RSD	0.849	0.012	0.28
Variance	0.717	1.44x10 <sup>-4</sup>	
Standart error	0.346	4.89x10 <sup>-3</sup>	
Calculated F-value (F <sub>c</sub> )	1.76		
Tabulated F-value (F <sub>t</sub> )	3.00	F <sub>t</sub> > F <sub>c</sub> : (P > 0.05)	

### LOD and LOQ

The LOD and LOQ values were calculated using calibration standards as 3.3  $\sigma$ /S and 10  $\sigma$ /S, respectively [27,28]. (Where,  $\sigma$ : Standard deviation of the response, S: Slope of the calibration curve). The LOD and LOQ for the method were obtained as 2.196 and 6.654 ng/mL, respectively.

### Stability

Carvedilol stock solution stability was evaluated for at least 72 hours at room temperature. In addition, carvedilol standard sample solutions were stable at room temperature, 4 and -20 °C refrigeration temperature for 72 h. The trueness of carvedilol stability are within the acceptance range of 90-110%. No significant degradation product of carvedilol in these conditions. The results are also listed in Table 5.

Table 5. Stability of carvedilol in different temperatures (n=6)

Added (ng/mL)	Room temperature 24 h (Mean ± SD)	Room temperature 72 h (Mean ± SD)	Refrigeratory +4 °C, 72 h (Mean ± SD)	Frozen -20 °C, 72 h (Mean ± SD)
150	98.6 ± 2.65	98.6 ± 2.74	101.9 ± 1.47	98.6 ± 3.32
300	98.9 ± 1.62	98.9 ± 2.04	100.6 ± 1.79	98.2 ± 3.62
450	99.4 ± 3.61	101.2 ± 3.41	98.6 ± 2.64	101.9 ± 3.71

### Procedure for Pharmaceutical Preparations

The preparation of tablet sample solution was done by taking twenty tablets of carvedilol. Tablets were powdered in a mortar pestle. After, an amount of the powdered sample equivalent to 25 mg of drug was taken in a 25 mL volumetric flask and then solubilized with 25 mL methanol. Standard sample was prepared as 1.0 mg/mL. The tablet solution was filtered by Whatman No 42 paper. Then, it was diluted to get in the range of 100 and 400 ng/mL with methanol (Figure 3).

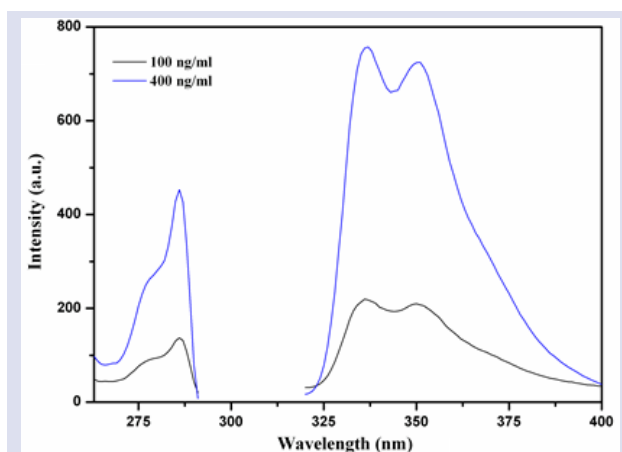


Figure 3. The spectrums of Dilatrend tablet containing carvedilol.

### Conclusions

In this work, a simple, new and fast spectrofluorometry method has been completely developed in order to analyze carvedilol in pharmaceutical preparations. Furthermore, the validation parameters were used to validate the procedure. The method was found to easy for the analysis of carvedilol. The carvedilol recoveries in tablets was in good agreement with their respective label claims. The method described has been effectively and efficiently used to analyze carvedilol pharmaceutical tablets without any interference from the pharmaceutical excipients. On the other hand, no extraction procedure is used. Therefore, the spectrofluorometric run time of 1 min allows the analysis of a large number of samples in a short period of time.

### Acknowledgment

The author would like to thank Semih Yilmaz for expert advice on the use of English.

### Conflicts of Interest

The author states that did not has conflict of interests.

### References

- [1] Karle C.A., Kreye V.A.W., Thomas D., Rockl K., Kathofer S., Zhang W., Kiehnet J., Antiarrhythmic Drug Carvedilol Inhibits HERG Potassium Channels, *Cardiovascular Res.*, 49 (2001) 361-370.
- [2] Chen J.J., Shih N.L., Carvedilol: An Anti-Inflammatory and Anti-Atherogenic  $\beta$ -blocker, *Acta Cardiol. Sin.*, 19 (2003) 93-94.
- [3] Franciosa J.A., Massie B.M., Lukas M.A., Nelson J.J., Lottes S., Abraham W.T., Fowler M., Gilbert E.M., Greenberg B.,  $\beta$ -blocker Therapy for Heart Failure Outside the Clinical Trial Setting: Findings of a Community-based Registry, *American Heart J.*, 148 (2004) 718-726.
- [4] Stoschitzky K., Koshucharova G., Lercher P., Maier R., Sakotnik A., Klein W., Liebmann P.M., Lindner W., Stereoselective Effects of (R)- and (S)-carvedilol in Humans, *Chirality.*, 13 (2001) 342-346.
- [5] Nath B., Nath L.K., Kumar P.Y., Preparation and In vitro Evaluation of Buccoadhesive Tablets of Carvedilol Using Dried Mucilage Powder of Aegle marmelose, *Research J. Pharm. Tech.*, 2 (2009) 762-767.
- [6] Desai D.C., Karkhanis V.V., Simple spectrophotometric estimation of carvedilol phosphate in bulk and tablet dosage forms, *Int. Res. J. Pharm.*, 3 (2012) 114-116.
- [7] Patel S.A., Patel N.J., Validated Spectrophotometric Methods for the Determination of Carvedilol in Tablets, *Int. Res. J. Pharm.*, 2 (2011) 171-175.
- [8] Theivarasu C., Santanu G., Indumarthi T., UV Spectrophotometric Determination of Carvedilol in Pharmaceutical Formulations, *Asian J. Pharm. Clin. Res.*, 3 (2010) 64-68.
- [9] Shinkar D.M., Dhake A.S., Setty C.M., Development of UV Spectrophotometric Method for estimation of Carvedilol in Bulk and Pharmaceutical Formulations, *Asian J. Res. Chem.*, 6 (2013) 956-959.
- [10] Vinod T., Sachin G., Omprakash B., Development, Validation and Stability Study of UV Spectrophotometric Method for Determination of Carvedilol Phosphate in Bulk and Pharmaceutical Dosage Forms, *Int. J. ChemTech Res.*, 10 (2017) 252-259.

- [11] Divya N.S., Narayana B., Simple Methods for the Spectrophotometric Determination of Carvedilol, *Int. Scholarly Res. Network*, 6 (2012) 373215.
- [12] Audumbar M., Vikas K., Rohan D., Sachin G., Ritesh B., Simultaneous UV Spectrophotometric Methods for Estimation of Carvedilol and Hydrochlorothiazide in Bulk and Tablet Dosage Form, *Asian J. Pharm. Tech.*, 6 (2016) 15-20.
- [13] Rajan V.R., Prathamesh P.T., UV Spectrophotometric Estimation of Carvedilol Hydrochloride by Second Order Derivative Methods in Bulk and Pharmaceutical Dosage Form, *Res. J. Pharm. Tech.*, 7 (2014) 1459-1462.
- [14] Sayed M.D., Mahmoud A.O., Mohamed A.K.A.L., Ahmed I.H., Development and Validation of a New Spectrofluorometric Method for the Determination of Some Beta-blockers through Fluorescence Quenching of Eosin Y, *Open Chem. J.*, 14 (2016) 258-266.
- [15] Sovan L.P., Utpal J.G., Mohanta P., Manna P.K., Method Development and Validation of Reverse Phase High Performance Liquid Chromatography Method to Determine Carvedilol in Pharmaceutical Formulations, *Der Pharm. Sin.*, 4 (2013) 22-27.
- [16] Sivakamasundari G., Kannappan N., Development and Validation of RP-UPLC Method for the Simultaneous estimation of Carvedilol and Hydrochlorothiazide in Pharmaceutical Dosage Form, *Int. Res. J. Pharm.*, 9 (2018) 23-26.
- [17] Rao U.V.M., Haritha G., Krishnaiah T., Saikiran T.G., Reddy T.A., Nikhil U.V.S., Veerabomma H.S., Veeram S.D.R., Method Development and Forced Degradation Studies of Carvedilol by RP-HPLC, *Int. J. Pharm. Anal. Res.*, 6 (2017) 457-468.
- [18] Patel H., Jivani N., Development of Validated RP-HPLC Method for Simultaneous Estimation of Carvedilol and Ivabradine, *World J. Pharm. Pharmaceut. Sci.*, 4 (2015) 630-639.
- [19] El-Adl S.M., Abdel-Aziz L.M., Mohamed M.A.M., HPLC Determination of Carvedilol and Atorvastatin Calcium in Their Bulk and Dosage Form, *Asian J. Pharm. Anal. Med. Chem.*, 4 (2016) 112-123.
- [20] Suganthi A., Ravi T.K., Development of RP-HPLC Method for the Estimation of Nebivolol and Carvedilol with selected NSAIDs and its Application to Drug Displacement Interaction Studies, *Malaysian J. Pharmaceut. Sci.*, 12 (2014) 47-65.
- [21] Mahaveer S., Kashkhedikar S.G., Soni L., Abhinav G., Tripti G., Amrish P., Development of RP-HPLC Method for Estimation of Carvedilol in Tablet Formulations, *Res. J. Pharm. Tech.*, 1 (2008) 18-21.
- [22] Clohs L., McErlane K.M., Development of a Capillary Electrophoresis Assay for the Determination of Carvedilol Enantiomers in Serum using Cyclodextrins, *J. Pharm. Biomed. Anal.*, 24 (2001) 545-554.
- [23] Samin H., Somaieh S., Abolghasem J., A dispersive liquid-liquid microextraction and chiral separation of Carvedilol in Human plasma using Capillary Electrophoresis, *Bioanalysis*, 7 (2015) 1107-1117.
- [24] ICH Topic Q 2 (R1) Validation of Analytical Procedures: Text and Methodology, Note for Guidance on Validation of Analytical Procedures: Text And Methodology (CPMP/ICH/381/95).
- [25] British Pharmacopoeia, The Stationery Office, London, (2009) 374.
- [26] Dogan B., Ozkan S.A., Electrochemical Behavior of Carvedilol and its Adsorptive Stripping Determination in Dosage Forms and Biological Fluids, *Electroanal.*, 17 (2005) 2074-2083.
- [27] Streim K., Sponer G., Muller B., Bartsch W., Pharmacological Profile of Caevdilol: A Compound with  $\beta$ -Blocking and Vasodilating Properties, *J. Cardiovas. Pharm.*, 10 (1987) 33-41.
- [28] Bartsch W., Sponer G., Muller B., Kling L., Bohm E., Martin U., Borbe H.O., Pharmacological Characteristics of the Stereoisomers of Carvedilol, *European J. Clin. Pharm.*, 38 (1990) 104-107.

## Syntheses of Hexaminomonoferrocenylspiro(N/O)cyclotetraphosphazenes: Spectral Properties and Antituberculosis Activities

Arzu Binici <sup>1,a,\*</sup><sup>1</sup> General Directorate of Public Health, Republic of Türkiye Ministry of Health, Ankara, Türkiye

\*Corresponding author

### Research Article

#### History

Received: 20/12/2021


Accepted: 09/04/2022

#### Copyright

©2022 Faculty of Science,  
Sivas Cumhuriyet University

### ABSTRACT

In this study, 3-(N-ferrocenylmethylamino)-1-propanol,  $\text{FcCH}_2\text{N}(\text{CH}_2)_3\text{OH}$ , is prepared by the reduction of Schiff base with  $\text{NaBH}_4$ , which is obtained from the condensation reaction of ferrocenecarboxaldehyde and 3-amino-1-propanol in methanol. Reaction of octachlorocyclotetraphosphazene (OCCP, tetramer,  $\text{N}_4\text{P}_4\text{Cl}_8$ , 1) and bidentate ligand (L), sodium 3-(N-ferrocenylmethylamino)-1-propanoxide, give hexachloromonoferrocenylspiro (2). Fully substituted mono-ferrocenylhexaamino(N/O) spirocyclotetraphosphazenes (2a and 2b) have been synthesized by the reaction of 2 with excesses of propylamine and butylamine, respectively. The structures of 2a and 2b were determined using elemental analysis, mass spectrometry (ESI-MS), FTIR,  $^1\text{H}$ ,  $^{13}\text{C}$  and  $^{31}\text{P}$  NMR data. In addition, antituberculosis activity studies of 2a and 2b against *Mycobacterium Tuberculosis* H37Rv reference strain were performed.

**Keywords:** Monoferrocenyl(N/O)spirocyclotetraphosphazenes, Spectroscopy, Antituberculosis activity. [yetik.arzu@gmail.com](mailto:yetik.arzu@gmail.com) <https://orcid.org/0000-0001-7470-4156>

## Introduction

Cyclophosphazenes are an inorganic ring system consisting of a skeleton  $(\text{N}=\text{PX}_2)_n$  ( $n = 3, 4, 5\dots$ ) linked by sequential binding of N and P atoms and two inorganic-organic and/or organometallic side groups (X) covalently bonded to each P atom [1,2]. Hexachlorocyclotriphosphazene (HCCP, trimer,  $\text{N}_3\text{P}_3\text{Cl}_6$ ) and octachlorocyclotetraphosphazene (OCCP, tetramer,  $\text{N}_4\text{P}_4\text{Cl}_8$ , 1) are the renowned starting reagents [3]. Both starting reagents have been widely used in the preparation of trimeric and tetrameric phosphazenes substituted with a lot of mono- and multifunctional heterocyclic reagents 4-6]. However, since the number of Cl atoms is higher in tetrameric phosphazene than in trimeric phosphazene, the number of geometrical and optical isomers that can be formed is also higher as expected. Thus, the products formed from the reactions of the tetramer are more difficult to separate. However, although the product variety is more interesting, the studies on the tetramer are very limited [7,8].

In phosphazenes, geometrical (nongeminal, cis/trans and geminal) and chiral isomers are formed depending on the number of replacements of Cl atoms with nucleophiles and the reaction conditions [9]. Moreover, the reaction of unsymmetrical bidentate ligands, such as sodium 3-amino-1-propanoxide and N-methyl-1,3 diaminopropane, with HCCP resulted in the formation of monospiro-, dispiro-, and trispirocyclotriphosphazenes [10, 11]. It was noticed that monospiro product was created stereoselectively in THF from the reaction of sodium 3-(N-ferrocenylmethylamino)-1-propanoxide (L) with an equimolar amount of HCCP [12].

In addition, it is stated in the literature that many cyclophosphazene derivatives can be used as biologically active materials [13], ionic liquids [14, 15], fluorescent indicators [16], lubricants [17], and organic light-emitting diodes (OLEDs) [18]. Moreover, some ferrocene compounds are of interest in various applications such as photoluminescent systems [19], drug release systems responsive to redox stimuli [20], electron-transfer mediators [21], organometallic catalysts [22]. Moreover, the antituberculosis and anticancer activities of ferrocene derivatives have been investigated against some reference strains and cancer cells [23, 24]. In addition, in recent years, there are studies in which trimeric and tetrameric phosphazenes containing ferrocenyl groups were obtained and their biological activities were investigated [25, 26].

In the last two decades, partially/fully substituted cyclophosphazene derivatives have received great attention for their potential as antituberculosis, antimicrobial and anticancer agents [27]. Ferrocenylcyclophosphazenes show antituberculous activity against *Mycobacterium tuberculosis* H37Rv [28].

In the present study, hexachloro(N/O) spirocyclotetraphosphazene containing monoferrocenyl pendant arm (2) was resynthesized as the starting compound [29,30]. In dry THF, the reaction of 2 with excess propyl and butylamine gave the hexaamino(N/O)spirocyclotetraphosphazene derivatives (2a and 2b) (Figure 1). These compounds were also synthesized to study their bioactivity.

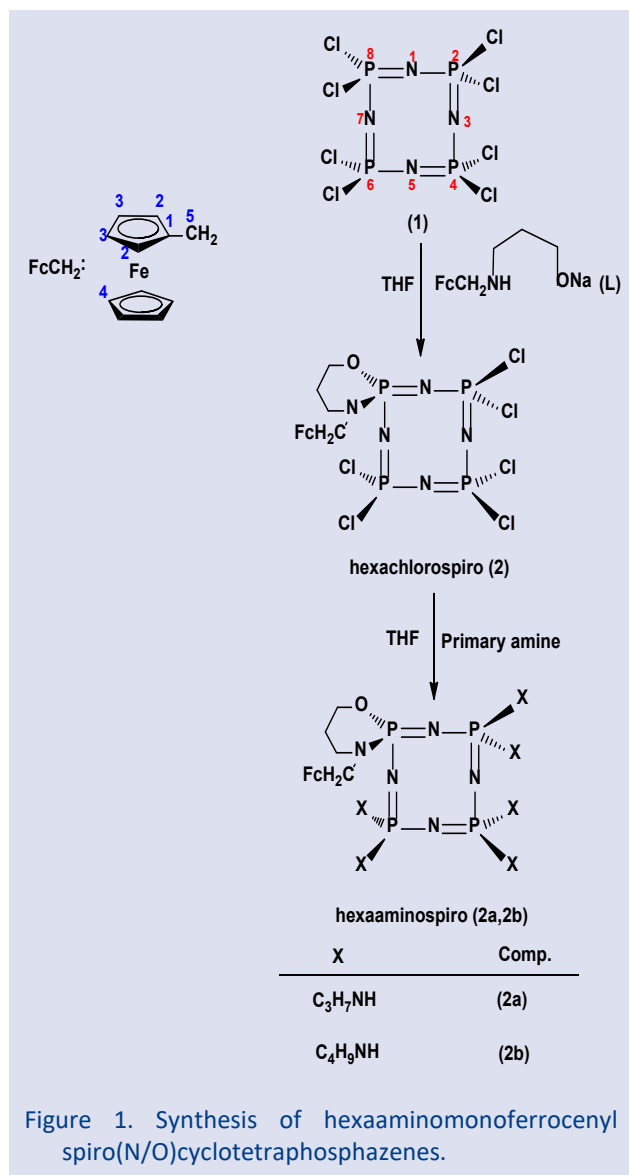


Figure 1. Synthesis of hexaaminomonoferrocenyl spiro(N/O)cyclotetraphosphazenes.

## Materials and Methods

### Apparatus

Nucleophilic substitution reactions were made under the Ar atmosphere. Necessary solvents were dried before use and purified by appropriate methods lit. N<sub>4</sub>P<sub>4</sub>Cl<sub>8</sub> (Otsuka Chemical Co. Ltd., crystallized from n-hexane), ferrocenecarboxaldehyde, (Aldrich), 3-amino-1-propanol, propylamine and butylamine (Merck) were procured. All the reactions were followed by TLC on Merck DC Alufolien Kiesegel 60 F254 plates in suitable solvents. Column chromatography was performed with Merck Kiesegel 60 (230-400 micronized ATSM) silica gel. The melting points of mono-ferrocenyl(N/O)cyclotetraphosphazenes were determined with a Gallenkamp instrument using a capillary tube. Micronalyses were performed with the Leco CHNS-932 instrument. FTIR spectra were recorded on KBr discs on a Jasco FTIR-430 spectrometer and reported in cm<sup>-1</sup> units. Electron spray ionization-mass spectra (ESI-MS) were taken with a Waters 2695 Alliance Micromass ZQ spectrometer. The <sup>1</sup>H and <sup>13</sup>C NMR spectra of the phosphazenes were recorded on the Varian

Mercury FT-NMR (400 MHz) spectrometer operating at 400.13 MHz and 100.62 MHz, respectively, and the <sup>31</sup>P NMR spectra were recorded on the Bruker Avance III HD (600 MHz) spectrometer operating at 242.94 MHz.

### Synthesis of Phosphazenes

#### Synthesis of compound 2

The starting compound, hexachloro(N/O)spirocyclo-tetraphosphazene (2), was synthesized from the reaction of OCCP (1) and equimolar amount of sodium L according to previous studies [29, 30].

#### Synthesis of Compound 2a

A propylamine solution (0.80 mL, 9.75 mmol) in dry THF (50 mL) was slowly added into a stirred solution of triethylamine (0.63 mL, 4.52 mmol) and 2 0.50 g, 0.75 mmol) in dry THF (100 mL) at room temperature. The mixture was refluxed for over 90 h. After the solvent was evaporated, the product was purified using column chromatography [THF-toluene (2:3)], and then it was purified by hexane: ethyl acetate (3:1) preparative thin-layer chromatography. Afterwards, the product was crystallized from n-hexane. Yield: (0.37 g, 62%). mp: 148 °C. Compound 2a: Anal. Calcd. for C<sub>32</sub>H<sub>65</sub>ON<sub>11</sub>P<sub>4</sub>Fe.2C<sub>7</sub>H<sub>8</sub>O: C, 47.88; H, 8.14; N, 15.35. Found: C, 48.38; H, 8.50; N, 15.20. ESI-MS (Ir %, Ir designates the fragment abundance percentage): *m/z* 801 ([M<sub>2</sub>H]<sup>+</sup>, 100). FTIR (KBr, cm<sup>-1</sup>): ν 2928, 2869 (C-H aliph.), 1265 (asymm.), 1113 (symm.) (P=N). <sup>1</sup>H NMR (400 MHz, CDCl<sub>3</sub>, ppm): δ 4.23 (m, 2H, H<sub>2</sub>), 4.16 (d, 2H, <sup>3</sup>J<sub>PH</sub>=13.2, <sup>3</sup>J<sub>HH</sub>=5.6 Hz, O-CH<sub>2</sub>), 4.10 (bp, 5H, H<sub>4</sub>), 4.06 (m, 2H, H<sub>3</sub>), 3.92 (d, 2H, <sup>3</sup>J<sub>PH</sub>=7.6 Hz, H<sub>5</sub>), 2.98 (m, 2H, Fc-CH<sub>2</sub>-N-CH<sub>2</sub>), 2.83 (m, 12H, P-NH-CH<sub>2</sub>), 2.38 (bp, 6H, P-NH), 1.63 (m, 2H, O-CH<sub>2</sub>-CH<sub>2</sub>), 1.49 (m, 12H, P-NH-CH<sub>2</sub>-CH<sub>2</sub>), 0.91 ve 0.89 (t, 18H, <sup>3</sup>J<sub>HH</sub>=6.8 ve <sup>3</sup>J<sub>HH</sub>=7.6 Hz, CH<sub>2</sub>-CH<sub>3</sub>). <sup>13</sup>C NMR (100 MHz, CDCl<sub>3</sub>, ppm): δ 85.27 (d, <sup>3</sup>J<sub>PC</sub>=10.8 Hz, C<sub>1</sub>), 69.82 (s, C<sub>2</sub>), 68.41 (s, C<sub>4</sub>), 67.69 (s, C<sub>3</sub>), 66.41 (d, <sup>2</sup>J<sub>PC</sub>=5.3 Hz, O-CH<sub>2</sub>), 53.42 (s, P-NH-CH<sub>2</sub>-CH<sub>2</sub>), 47.36 (s, C<sub>5</sub>), 45.56 (s, Fc-CH<sub>2</sub>-N-CH<sub>2</sub>), 42.96 ve 42.90 (s, P-NH-CH<sub>2</sub>), 25.72 (s, O-CH<sub>2</sub>-CH<sub>2</sub>), 11.70 ve 11.64 (s, CH<sub>2</sub>-CH<sub>3</sub>). <sup>31</sup>P NMR (242.94 MHz, H<sub>3</sub>PO<sub>4</sub> (85%), ppm): δ 3.32 (t, <sup>2</sup>J<sub>AC</sub>: 41.3 Hz, P<sub>A</sub>, OPN), 6.01 (t, <sup>2</sup>J<sub>BC</sub>: 26.7 Hz, P<sub>B</sub>, NPN), 5.80 (t, P<sub>C</sub>, PNN).

#### Synthesis of Compound 2b

The experimental procedure was similar to that of compound 2a, using 2 (0.50 g, 0.75 mmol), triethylamine (0.63 mL, 4.52 mmol) and butylamine (0.97 mL, 9.75 mmol). The mixture was refluxed for over 96 h. After the solvent was evaporated, the product was purified using column chromatography [THF-toluene (1:3)], and crystallized from n-hexane. Yield: (0.35 g, 53%). mp: 157 °C. Compound 2b: Anal. Calcd. for C<sub>38</sub>H<sub>77</sub>ON<sub>11</sub>P<sub>4</sub>Fe.2C<sub>7</sub>H<sub>8</sub>: C, 58.48; H, 8.77; N, 14.42. Found: C, 58.98; H, 8.99; N, 13.92. ESI-MS (Ir %, Ir designates the fragment abundance percentage): *m/z* 885 ([M+2H]<sup>+</sup>, 100). FTIR (KBr, cm<sup>-1</sup>): ν 2926, 2859 (C-H aliph.), 1271 (asymm.), 1117 (symm.) (P=N). <sup>1</sup>H NMR (400 MHz, CDCl<sub>3</sub>, ppm): δ 4.20 (m, 2H, H<sub>2</sub>), 4.17 (d, 2H, <sup>3</sup>J<sub>PH</sub>=11.6, <sup>3</sup>J<sub>HH</sub>=4.0 Hz, O-CH<sub>2</sub>), 4.11 (bp, 5H, H<sub>4</sub>), 4.06 (m, 2H, H<sub>3</sub>), 3.92 (d, 2H, <sup>3</sup>J<sub>PH</sub>=7.6 Hz, H<sub>5</sub>), 3.01 (m, 2H, Fc-CH<sub>2</sub>-N-CH<sub>2</sub>), 2.85 (m, 12H, P-NH-CH<sub>2</sub>), 2.68 (bp, 6H, P-NH), 1.61 (m, 2H, O-CH<sub>2</sub>-CH<sub>2</sub>), 1.53 (m, 12H, P-NH-

CH<sub>2</sub>-CH<sub>2</sub>-CH<sub>2</sub>) 1.47 (m, 12H, P-NH-CH<sub>2</sub>-CH<sub>2</sub>), 0.91 ve 0.89 (t, 18H, <sup>3</sup>J<sub>HH</sub>=7.2 ve <sup>3</sup>J<sub>HH</sub>=4.0 Hz, CH<sub>2</sub>-CH<sub>3</sub>). <sup>13</sup>C NMR (100 MHz, CDCl<sub>3</sub>, ppm): δ 83.88 (d, <sup>3</sup>J<sub>PC</sub>=11.2 Hz, C<sub>1</sub>), 70.11 (s, C<sub>2</sub>), 68.58 (s, C<sub>4</sub>), 68.32 (s, C<sub>3</sub>), 66.41 (d, <sup>2</sup>J<sub>PC</sub>=6.9 Hz, O-CH<sub>2</sub>), 53.45 (s, P-NH-CH<sub>2</sub>-CH<sub>2</sub>), 47.42 (s, C<sub>5</sub>), 45.60 (s, Fc-CH<sub>2</sub>-N-CH<sub>2</sub>), 41.41 ve 41.27 (s, P-NH-CH<sub>2</sub>), 30.39 ve 30.29 (s, N-CH<sub>2</sub>-CH<sub>2</sub>), 29.40 (d, <sup>3</sup>J<sub>PC</sub>=3.0 Hz, O-CH<sub>2</sub>-CH<sub>2</sub>), 26.39 ve 26.37 (m, P-NH-CH<sub>2</sub>-CH<sub>2</sub>-CH<sub>2</sub>) 13.84 ve 13.79 (s, CH<sub>2</sub>-CH<sub>3</sub>). <sup>31</sup>P NMR (242.94 MHz, H<sub>3</sub>PO<sub>4</sub> (85%), ppm): δ 3.20 (t, <sup>2</sup>J<sub>AC</sub>: 41.2 Hz, P<sub>A</sub>, OPN), 6.30 (t, <sup>2</sup>J<sub>BC</sub>: 36.4 Hz, P<sub>B</sub>, NPN), 5.62 (t, P<sub>C</sub>, PNN).

### Evaluation of Antituberculous Activity

The antituberculosis activities of the hexaamino(N/O)spirocyclo-tetraphosphazenes (2a and 2b) were evaluated against the reference strain *Mycobacterium tuberculosis* H37Rv (ATCC 27294) using the "Agar proportion method" in agar-based Middlebrook 7H10 medium with respect to the recommendations of the Clinical and Laboratory Standards Institute (CLSI). The final concentrations of each tetraphosphazene derivative in the medium were set at 5, 10, 20, 40 and 80 µg/mL, respectively. The rest of the experiments were carried out as stated in the literature [31].

## Results and Discussion

### Synthesis

It is known from previous studies that the replacement reaction of OCCP with an equimolar quantity of L yields two different types of products [29, 30]. These two products are mono-ferrocenyl-2-cis-4-dichloro-ansa- (2,4-ansa; yield 14%) and mono-ferrocenyl-spiro- (spiro; yield 35%) hexachlorocyclo-tetraphosphazene derivatives. In this study, monoferrocenylspiro-(2) with a higher yield was used as the starting reagent in this study. Compound 2 has six replaceable Cl atoms and is capable of substitution reactions with a wide variety of nucleophiles. In this study, hexapropylaminomonoferrocenylspiro(N/O) (2a) and hexabutylamino (2b) cyclo-tetraphosphazenes were obtained by reacting the spiro (2) (0.75 mmol) with excessive amounts of propylamine (9.75 mmol) and butylamine (9.75 mmol), respectively. Reactions during the formation of the spiro product are likely to proceed via the SN<sup>1</sup>(P) and/or SN<sup>2</sup>(P) reaction pathway (Fig. 2).

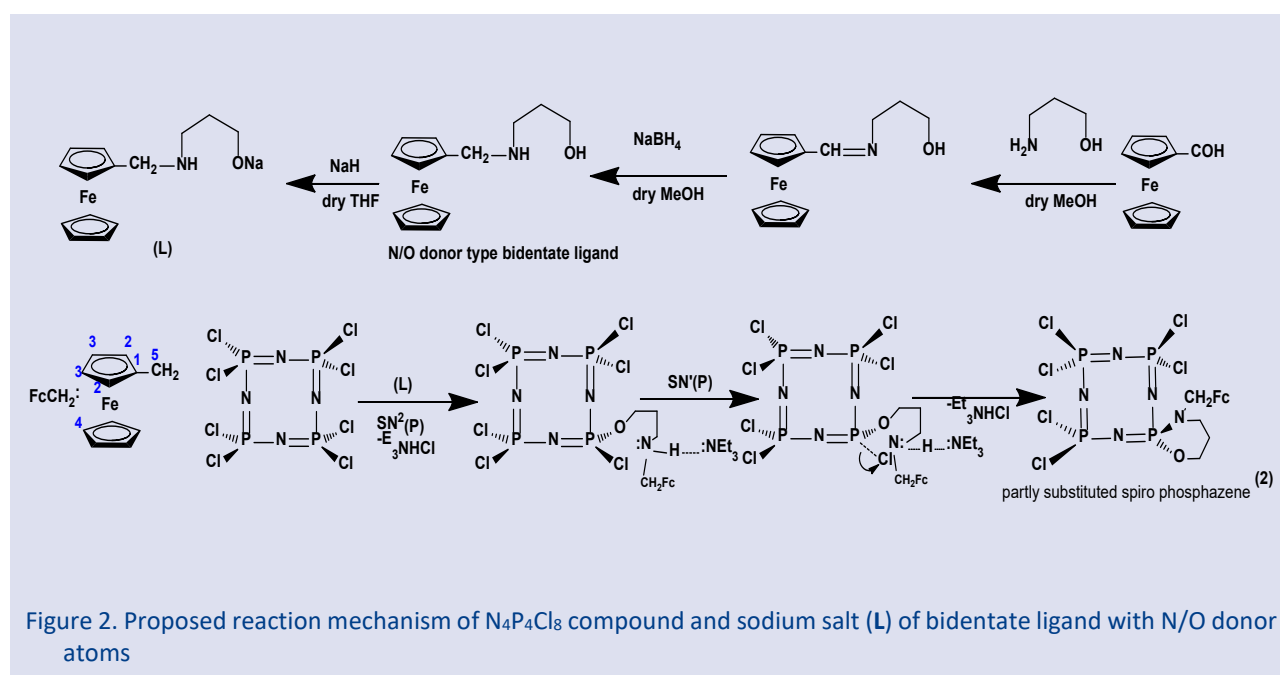


Figure 2. Proposed reaction mechanism of N<sub>4</sub>P<sub>4</sub>Cl<sub>8</sub> compound and sodium salt (L) of bidentate ligand with N/O donor atoms

Triethylamine (4.52 mmol) was used to keep the acid formed as a result of the replacement reaction of the tetramer with aminoloxide as the Et<sub>3</sub>N.HCl salt. The intramolecular hydrogen bond occurred between the N-H hydrogen of the Pendant FcCH<sub>2</sub> arm and triethylamine plays a significant role in increasing the reaction yield. The yields of 2a and 2b were calculated as 62% and 53%, respectively. The structures of the products were characterized using elemental analysis, FTIR, ESI-MS, <sup>1</sup>H-, <sup>13</sup>C- and <sup>31</sup>P-NMR data. These findings are consistent with the structures of hexaaminomonoferrocenyl(N/O) spirocyclo-tetraphosphazenes. Analytical data and NMR results were presented in the "Experimental Part".

### NMR and IR Spectroscopy

<sup>31</sup>P NMR results of monoferrocenylspiro (N/O)cyclo-tetraphosphazenes were given in Table 1. The starting compound 2 has ABCD spin system due to four different phosphorus environments in the molecule, while the spin systems of 2a and 2b are designated as ABC<sub>2</sub>. The δP chemical shifts of 2a and 2b were found to be greater than the starting compound 2 (Table 1).

Electron spray ionization-mass spectra (ESI-MS) of 2a and 2b were given in Figure 3. The molar masses of the compounds were calculated based on <sup>35</sup>Cl and <sup>56</sup>Fe isotopes. The mass spectrum of 2a and 2b gave a protonated molecular [M+2H]<sup>+</sup> ion peak.

Table 1.  $^{31}\text{P}$ NMR data of mono-ferrocenyl-(N/O)cyclotetraphosphazenes.

**ABCC' (2); ABC<sub>2</sub> (2a and 2b)**

Fc= Ferrocenyl ; X= Cl, propylamine and butylamine

Compound	Spin System	OPN	$\delta$ (ppm) CIPCI	NPN	$^2J_{PP}$ (Hz)	
2*	ABCD	-5.89 (P <sub>A</sub> )	-5.89 (P <sub>B</sub> ) -7.44 (P <sub>C</sub> ) -7.60 (P <sub>D</sub> )	-	$^2J_{AC}$ : 38.9 $^2J_{AD}$ : 41.3	$^2J_{BC}$ : 26.7 $^2J_{BD}$ : 29.2
2a	ABC <sub>2</sub>	3.32 (P <sub>A</sub> )	-	5.80 (P <sub>C</sub> ) 6.01 (P <sub>B</sub> )	$^2J_{AC}$ : 41.3	$^2J_{BC}$ : 26.7
2b	ABC <sub>2</sub>	3.20 (P <sub>A</sub> )	-	5.62 (P <sub>C</sub> ) 6.30 (P <sub>B</sub> )	$^2J_{AC}$ : 41.2	$^2J_{BC}$ : 36.4

<sup>a</sup> $^{31}\text{P}$ -NMR measurements were taken at 298 K in  $\text{CDCl}_3$  solution at 242.93 MHz.

<sup>\*</sup> $^{31}\text{P}$   $\{^1\text{H}\}$  NMR data are taken from the literature [31].

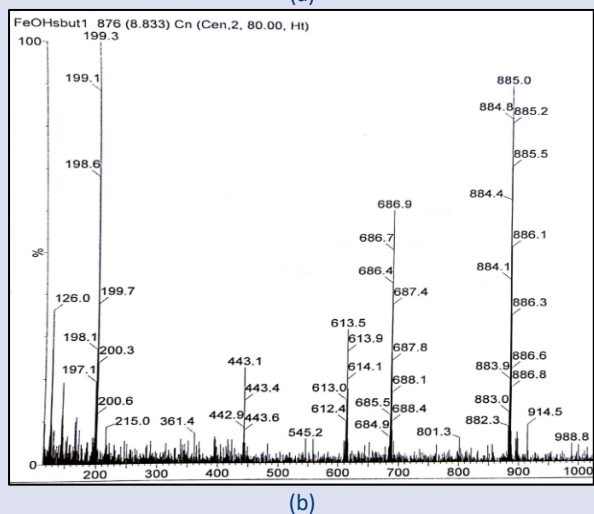
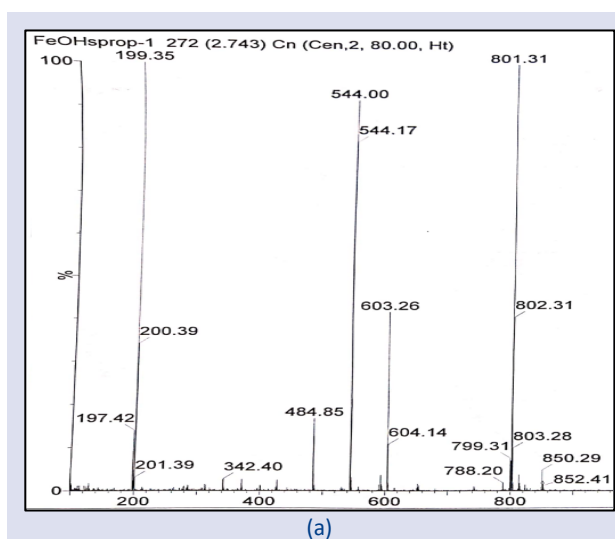


Figure 3. (a) Mass spectra of the compound hexapropylmonoferrocenylspiro (2a) and (b) hexabutylmonoferrocenylspiro (2b).

On the other hand, all  $\delta$  chemical shifts, J coupling constants and abundance of signals are evaluated from the  $^{13}\text{C}$  and  $^1\text{H}$  NMR spectra of monoferrocenyl(N/O)cyclotetraphosphazenes. These values are given in the "Experimental Part". The signals of O-CH<sub>2</sub> carbon of 2a and 2b are observed at 66.41 ppm and  $^2J_{POC}$  values are calculated as 5.3 and 6.9 Hz. Similarly, the  $^3J_{POCC}$  value for carbons O-CH<sub>2</sub>-CH<sub>2</sub> was observed only for 2b ( $^3J_{POCC}$  3.0 Hz). In addition, the expected carbon (C1-C4) peaks from ferrocene rings were determined from the  $^{13}\text{C}$  spectra of 2a and 2b. These results were found to be in agreement with literature findings for ferrocenylcyclotetraphosphazenes[32]. The ipso-C1 carbons of Fc of 2a and 2b were observed at 83.88 and 85.27 ppm, respectively, and the average value of  $^3J_{PNCC}$  was calculated as 11.0 Hz.

One of the best confirmations that the Cl atoms of the spiro (2) derivative are replaced by amines is the observation of the carbon signals of the amino groups in the  $^{13}\text{C}$  NMR spectra of 2a and 2b (Fig. 4).

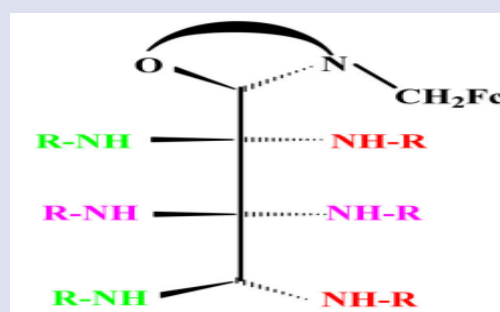


Figure 4. The stick diagram of hexaaminoferrocenyl(N/O)spirocyclotetraphosphazenes (2a and 2b)

From the integral ratios of the  $^1\text{H}$  spectra of 2a and 2b compounds, it is determined that six alkylamino groups are bonded to the P2, P4 and P6 atoms. The average  $\delta$  values of aliphatic  $\text{OCH}_2$ ,  $\text{O-CH}_2\text{-CH}_2$  and  $\text{NCH}_2$  protons were calculated as 4.16, 1.61 and 2.98 ppm, respectively. In addition, the expected proton ( $\text{H}_2\text{-H}_4$ ) peaks of ferrocene rings were observed in the  $^1\text{H}$  NMR spectra of aminocyclotetraphosphazenes. The results are consistent with the literature findings for ferrocenylphosphazenes [31].  $\text{Fc-CH}_2$  ( $\text{H}_5$ ) protons were determined as a doublet with an average value of 3.92 ppm, and the coupling constant ( $^3J_{\text{PH}}=7.6$  Hz) was calculated.

The characteristic FTIR frequencies of hexaminospiro(N/O)cyclotetraphosphazenes were also given in the "Experimental Part". The characteristic symmetric and asymmetric  $\nu_{\text{P=N}}$  bands of  $\text{P=N}$  bonds belong to the  $\text{P}_4\text{N}_4$  ring and appear at  $1113\text{-}1117\text{ cm}^{-1}$  and  $1265\text{-}1271\text{ cm}^{-1}$ , respectively [33, 34]. In addition,  $\nu_{\text{P-Cl}}$  stretching frequencies of the starting compound spiro (2) were observed at  $556\text{ cm}^{-1}$  (asymm.) and  $488\text{ cm}^{-1}$  (sym.), while these peaks disappeared in completely amino substituted products (2a and 2b) [35, 36, 37].

#### Antituberculosis Activity against *M. Tuberculosis* H37Rv Reference Strain

Tuberculosis is an infectious disease caused by *Mycobacterium Tuberculosis* and is known to cause death in large numbers of people. Although the disease is controlled with various treatment methods, many patients die from this disease every year and it is among the top 10 causes of death worldwide [38].

In this study, antituberculosis activities of 2a and 2b against *M. tuberculosis* H37Rv (ATCC 27294) reference strain were tested using the "Agar proportional method" [39] to contribute to the treatment of tuberculosis (TB). *M. tuberculosis* H37RV strain was found to be susceptible to two compounds [2a ( $35\text{ }\mu\text{g/mL}$ ) and 2b ( $70\text{ }\mu\text{g/mL}$ )]. The MIC value of compound 2a ( $35\text{ }\mu\text{g/mL}$ ) was found to be much smaller and more effective than compound 2b (Table 2) (Figure 5.). However, the MIC value of 2 was reported as  $80\text{ }\mu\text{g/mL}$  in the literature [29], which shows that the new compounds (2a and 2b) formed by binding to primary amines are more effective.

The MIC values of the drugs currently used against the reference strain of *M. tuberculosis* H37Rv are as follows; rifampicin ( $1.0\text{ }\mu\text{g/mL}$ ), isoniazid ( $1.0\text{ }\mu\text{g/mL}$ ), ethanebutol ( $10.0\text{ }\mu\text{g/kg}$ ) and streptomycin ( $10\text{ }\mu\text{g/mL}$ ). The MIC of 2a is closer to the MIC of streptomycin and ethanebutol. Therefore, it is thought that this compound can be used as a promising new drug in the treatment of TB at low doses.

As a result, it can be stated that the synthesized compounds contain elements such as chlorine, phosphorus and nitrogen in the body and when these compounds are decomposed, they will not harm living cells by transforming into ammonium and phosphate ions in the human body.

However, as a result of long-term use of first and second choice drugs used currently in the treatment of

tuberculosis, many serious side effects are encountered in patients.

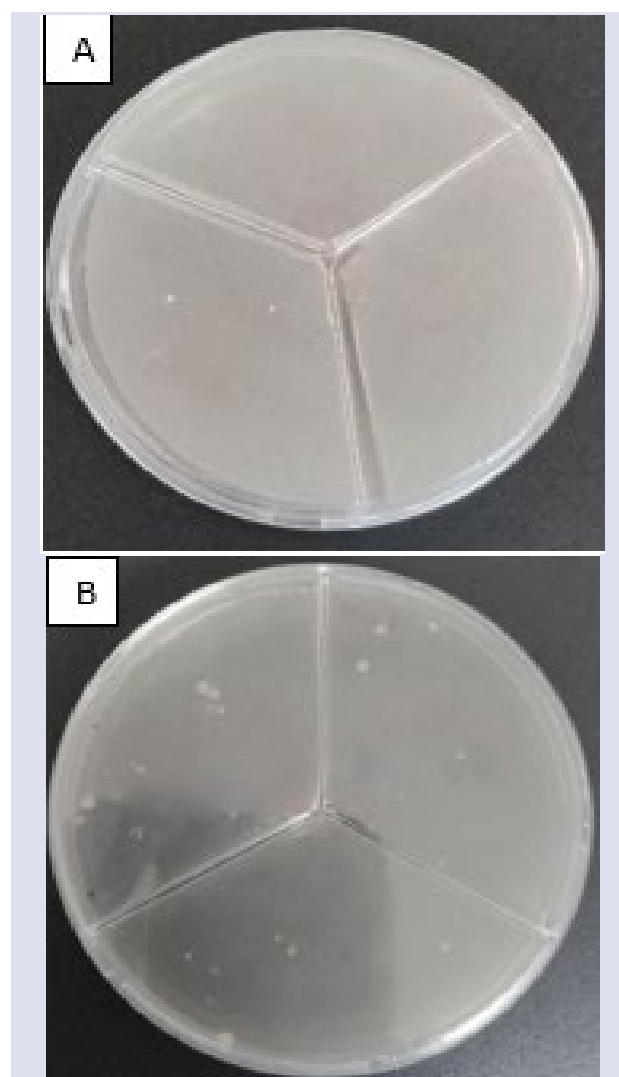


Figure 5. Anti-tuberculosis activity test of compound 2a against *M. tuberculosis* H37RV reference strain.

Bacterial growth (control) was observed for compound 2a in the first 3-compartment petri dish (control, 40 and  $35\text{ }\mu\text{g/mL}$ ) in A.. B was reproduced in the second petri dish with 3 compartments ( $30$ ,  $25$  and  $20\text{ }\mu\text{g/mL}$ ). In this case, the MIC of 2a is  $35\text{ }\mu\text{g/mL}$

Table 2. Effects of compounds (2a and 2b) in DMSO against *M. tuberculosis* H37Rv strain.

Comp.	Concentration ( $\mu\text{g/mL}$ )					MIC ( $\mu\text{g/mL}$ )
	80	40	20	10	5	
2a	S	S	R	R	R	35
2b	S	R	R	R	R	70

R: resistant, S: susceptible.



On the other hand, when the MIC values of the fully monoamine substituted monoferrocenylospirocyclophosphazene derivatives in the literature in antituberculosis activity studies against the reference strain

*M. tuberculosis* H37RV were compared: it was seen that the most effective compounds were monoferrocenyl (N/N)spirocyclophosphazene derivative pyrrolidine substituted derivatives (3 µg/mL) [26, 30, 31].

Table 3. MIC values of the compounds of fully substituted monoferrocenylospirocyclophosphazenes.

Test organism	<i>M. tuberculosis</i> H37Rv
Compounds	MIC (µg/mL)
<b>Monoamines-substituted monoferrocenyl (N/O)spirocyclophosphazenes:</b>	
Pyrrolidine-substituted [30]	65
Piperidine-substituted [30]	I
Morpholine-substituted [30]	70
DASD-substituted [30]	I
Hexylamine-substituted [31]	35
Benzylamine-substituted [31]	70
<b>Monoamines-substituted monoferrocenyl (N/N)spirocyclophosphazenes:</b>	
Pyrrolidine-substituted (4a) [26]	3
Pyrrolidine-substituted (5a) [26]	3
Pyrrolidine-substituted (6a) [26]	3
Morpholine-substituted (4b) [26]	I
Morpholine-substituted (5b) [26]	I
Morpholine-substituted (6b) [26]	I
DASD-substituted (4c) [26]	I
DASD-substituted (5c) [26]	70
DASD-substituted (6c) [26]	I

I: Ineffective

## Conclusion

In phosphorus-nitrogen chemistry, the replacement of Cl atoms in OCCP with various organic/inorganic mono- and bidentate ligands can enable the synthesis of organic-inorganic-based hybrid cyclophosphazene derivatives or their composite materials and thus their application in various fields. For this purpose, in this article, organic-inorganic based hybrid cyclophosphazenes; 2a and 2b were prepared. The structures of both tetraphosphazenes are elucidated using ESI-MS, FTIR and NMR data.

On the other hand, the antituberculosis activities of 2a and 2b were compared and it was observed that 2a with MIC value (35 µg/mL) had a more significant antituberculosis effect against *M. tuberculosis* H37RV reference strain than 2b. Also, since the MIC of 2 is greater than the amino-substituted derivatives (2a and 2b), this indicated that the antituberculosis activity increased when Cl atoms were replaced by amine groups.

As a result of these findings, these phosphazenes may have the chance to be used as promising new antituberculosis agents in medicine in the future.

## Acknowledgment

The author would like to thank Professors Zeynel Kılıç and Hülya Şimşek for their useful discussions on the spectroscopy and antituberculosis activity study.

## Conflicts of Interest

The author declares that there is no conflict of interest.

## References

- [1] Chandrasekhar V., Chakraborty A., Phosphazenes, *Organophosphorus Chem.*, 49 (2020) 349-376.
- [2] Stewart F. F., Phosphazenes, *Organophosphorus Chem.*, 44 (2015) 397-430.
- [3] Gleria M., Jaeger R. D., Phosphazenes: A Worldwide Insight. New York: Nova Science Publishers, (2004), 1047.
- [4] Medjdoub L., Mohammed B., New method for nucleophilic substitution on hexachlorocyclophosphazene by allylamine using an algerian proton exchanged montmorillonite clay (Maghnite-H+) as a green solid catalyst, *Bull. Chem. React. Eng. & Catal.*, 11(2) (2016) 151-160.
- [5] Elmas G., Syntheses and structural characterizations of 2-pyridyl(N/O)spirocyclophosphazene derivatives, *Phosphorus, Sulfur Silicon Relat. Elem.*, 194 (1-2) (2019) 13-24.
- [6] Elmas G., Okumuş A., Kılıç Z., Çam M., Açık L., Hökelek T., Phosphorus-nitrogen compounds. Part 40. The syntheses of (4-fluorobenzyl) pendant armed cyclophosphazene derivatives: spectroscopic, crystallographic and stereogenic properties, DNA interactions and antimicrobial activities, *Inorg. Chim. Acta*, 476 (2018) 110-122.
- [7] Mutlu G., Elmas G., Kılıç Z., Hökelek T., Koç L. Y., Türk M., Açık L., Aydın B., Dal H., Phosphorus-nitrogen Compounds: Part 31. Syntheses, structural and stereogenic properties,

- in vitro cytotoxic and antimicrobial activities, DNA interactions of novel bicyclic tetraphosphazenes containing bulky side group, *Inorg. Chim. Acta*, 436 (2015) 69-81.
- [8] Elmas G., Okumuş A., Sevinç P., Kılıç Z., Açık L., Atalan M., Türk M., Deniz G., Hökelek T., Phosphorus-nitrogen compounds. Part 37. Syntheses and structural characterizations, biological activities of mono and bis (4-fluorobenzyl) spirocyclo tetraphosphazenes, *New J. Chem.*, 41 (13) (2017) 5818-5835.
- [9] Chandrasekhar V., Thilagar P., Pandian B. M., Cyclophosphazene-based multi-site coordination ligands, *Coord. Chem. Rev.*, 251 (2007) 1045-1074.
- [10] Okumuş A., Elmas G., Kılıç Z., Ramazanoğlu N., Açık L., Türk M., Akça G., The reactions of  $N_3P_3Cl_6$  with monodentate and bidentate ligands: The syntheses and structural characterizations, In vitro antimicrobial activities and DNA interactions of 4-fluorobenzyl (N/O) spirocyclo triphosphazenes, *Turk. J. Chem.*, 41 (2017) 525-547.
- [11] Beşli S., Coles S. J., Davies D. B., Kılıç A., Shaw R. A., Bridged cyclophosphazenes resulting from deprotonation reactions bearing a P-NH group, *Dalton Trans.*, 40 (19) (2011) 5307-5315.
- [12] Tümer Y., Asmafiliz N., Kılıç Z., Hökelek T., Açık L., Solak A. O., Yola M. L., Phosphorus-nitrogen compounds: part 30. Syntheses and structural investigations, antimicrobial and cytotoxic activities and DNA interactions of vanillinato-substituted NN or NO spirocyclic monoferrocenyl cyclo triphosphazenes, *J. Biol. Inorg. Chem.*, 20(8) (2015) 165-178.
- [13] Xu L. C., Chen C., Zhu J., Tang M., Chen A., Allcock H. R., Siedlecki C. A., New cross-linkable poly[bis(octafluoropentoxy) phosphazene] biomaterials: Synthesis, surface characterization, bacterial adhesion, and plasma coagulation responses, *J. Biomed. Mater. Res.*, 108 (8) (2020) 3250-3260.
- [14] Elmas G., Okumuş A., Kılıç Z., Çelik S. P., Açık L., The Spectroscopic and Thermal Properties, Antibacterial and Antifungal Activity and DNA Interactions of 4-(Fluorobenzyl)Spiro(N/O) Cyclo triphosphazeneium Salts, *J. Turk. Chem. Soc. Sect. A: Chem.*, 4 (3) (2017) 993-1016.
- [15] Jimenez J., Pintre I., Gascon E., Sanchez-Somolinos C., Alcalá R., Cavero E., Serrano J. L., Oriol L., Photoresponsive Liquid-Crystalline Dendrimers Based on a Cyclo triphosphazene Core, *Macromol. Chem. Phys.*, 215 (2014) 1551-1562.
- [16] Selberg S., Pagano T., Tshepelevitsh S., Haljasorg T., Vahur S., Luik J., Saame J., Leito I., Synthesis and photophysics of a series of lipophilic phosphazene-based fluorescent indicators, *J. Phys. Org. Chem.*, 32 (7) (2019) e3950.
- [17] Wang X., Tan A. Y. X., Cho C. M., Ye Q., He C., Ji R., Xie H. Q., Tsai J. W. H., Xu J., Perfluoropolyether Boundary Lubricants Based on the Star Architecture, *Tribology Int.*, 9 (2015) 257-262.
- [18] Mucur S. P., Canımurbey B., Kavak P., Akbaş H., Karadağ A., Charge carrier performance of phosphazene-based ionic liquids doped hole transport layer in organic light-emitting diodes, *Appl. Phys. A*, 126 (12) (2020) 1-14.
- [19] Singh S. K., Kumar V., Drew M. G. B., Singh N., Syntheses, crystal structures and photoluminescent properties of new heteroleptic Ni(II) and Pd(II) complexes of ferrocene functionalized dithiocarbamate-and dipyrromethene ligands, *Inorg. Chem. Commun.*, 37 (2013) 151-154.
- [20] Haibin G., Shengdong M., Guirong Q., Xiong L., Li Z., Yanfei Y., Didier A., Redox-stimuli-responsive drug delivery systems with supramolecular ferrocenyl-containing polymers for controlled release, *Coord. Chem. Rev.*, 364 (2018) 51-85.
- [21] Lennox A. J. J., Nutting J. E., Stahl S. S., Selective electrochemical generation of benzylic radicals enabled by ferrocene-based electron-transfer mediators, *Chem. Sci.*, 9 (2018) 356-361.
- [22] Singh R. K., Kukrety A., Saxena R. C., Chouhan A., Jain S. L., Ray S. S., Phosphazene-based novel organo-inorganic hybrid salt: synthesis, characterization and performance evaluation as multifunctional additive in polyol, *RSC Adv.*, 7 (2017) 13390-13397.
- [23] Elmas G., Okumuş A., Cemaloğlu R., Kılıç Z., Çelik S. P., Açık L., Tunalı B. Ç., Türk M., Çerçi N. A., Güzel R., Hökelek T., Phosphorus-Nitrogen Compounds. Part 38. Syntheses, characterizations, cytotoxic, antituberculosis and antimicrobial activities and DNA interactions of spirocyclo tetraphosphazenes with bis-ferrocenyl pendant arms, *J. Organomet. Chem.*, 853 (2017) 93-106.
- [24] Elmas G., Kılıç Z., Çoşut B., Keşan G., Açık L., Çam M., Tunalı B. Ç., Türk M., Hökelek T., Synthesis of Bis(2,2,3,3-tetrafluoro-1,4-butanedioalkoxy)-2-trans-6-bis(4-fluorobenzyl)spiro cyclo tetraphosphazene: Structural Characterization, Biological Activity and DFT Studies, *J. Chem. Crystallogr.*, 51 (2020) 235-250.
- [25] Asmafiliz N., Kılıç Z., Öztürk A., Hökelek T., Koç L. Y., Açık L., Kisa Ö., Albay A., Üstündağ Z., Solak A. O., Phosphorus-Nitrogen Compounds. 18. Syntheses, stereogenic properties, structural and electrochemical investigations, biological activities, and DNA interactions of new spirocyclic Mono- and bisferrocenyl phosphazene derivatives, *Inorg. Chem.*, 48 (21) (2009) 10102-10116.
- [26] Okumuş A., Elmas G., Cemaloğlu R., Aydın B., Binici A., Şimşek H., Açık L., Türk M., Güzel R., Kılıç Z., Hökelek T., Phosphorus-Nitrogen Compounds. Part 35. Syntheses, spectroscopic and electrochemical properties, antituberculosis, antimicrobial and cytotoxic activities of mono-ferrocenyl-spirocyclo tetraphosphazenes, *New J. Chem.*, 40 (2016) 5588-5603.
- [27] Elmas G., Okumuş A., Kılıç Z., Özbeden P., Açık L., Tunalı B. Ç., Türk M., Çerçi N. A., Hökelek T., Phosphorus-nitrogen compounds. Part 48. Syntheses of the phosphazeneium salts containing 2-pyridyl pendant arm: Structural characterizations, thermal analysis, antimicrobial and cytotoxic activity studies, *Indian J. Chem. Sec. A*, 59A (2020) 533-550.
- [28] Elmas G., Okumuş A., Koç L. Y., Soltanzade H., Kılıç Z., Hökelek T., Dal H., Açık L., Üstündağ Z., Dündar D., Yavuz M., Phosphorus-Nitrogen Compounds. Part 29. Syntheses, crystal structures, spectroscopic and stereogenic properties, electrochemical investigations, antituberculosis, antimicrobial and cytotoxic activities and DNA interactions of ansa-spiro-ansa cyclo tetraphosphazenes, *Eur. J. Med. Chem.*, 87 (2014) 662-676.
- [29] Okumus A., Elmas G., Kılıç Z., Binici A., Ramazanoğlu N., Açık L., Çoşut B., Hökelek T., Güzel R., Tunalı B. Ç., Türk M., Şimşek H., The comparative reactions of 2- cis -4-ansa and spiro cyclo tetraphosphazenes with difunctional ligands: Structural and stereogenic properties, electrochemical, antimicrobial and cytotoxic activity studies, *App. Organomet Chem.*, e6150 (2021) 1-28.

- [30] Binici A., Okumus A., Elmas G., Kılıç Z., Ramazanoğlu N., Açık L., Şimşek H., Tunalı B. Ç., Türk M., Güzel R., Hökelek T., Phosphorus-nitrogen compounds. Part 42. The comparative syntheses of 2-cis-4-ansa(N/O) and spiro(N/O) cyclotetraphosphazene derivatives: spectroscopic and crystallographic characterization, antituberculosis and cytotoxic activity studies, *New J. Chem.*, 43 (2019) 6856-6873.
- [31] Binici A., Okumus A., Yakut M., Elmas G., Kılıç Z., Koyunoğlu D., Açık L., Şimşek H., Phosphorus-nitrogen compounds. Part 56. Comparative syntheses and spectral properties of multiheterocyclic 2-cis-4-ansa and spiro-ferrocenyl (N/O)cyclotetraphosphazenes: Antituberculosis and antimicrobial activity and DNA interaction studies, *Phosphorus, Sulfur Silicon Relat. Elem.*, (2021)
- [32] Elmas G., Okumuş A., Hökelek T., Kılıç Z., Phosphorus-Nitrogen Compounds. Part 52. The reactions of octachlorocyclotetraphosphazene with sodium 3-(N-ferrocenylmethylamino)-1-propanoxide: investigations of spectroscopic, crystallographic and stereogenic properties, *Inorg. Chim. Acta*, 497 (11) (2019) 119106.
- [33] Elmas G., The reactions of 2-trans-6-bis(4-fluorobenzyl)spirocyclotetraphosphazene with primary amines: spectroscopic and crystallographic characterizations, *Phosphorus Sulfur Silicon Relat. Elem.*, 192 (11) (2017) 1224-1232.
- [34] Carriedo G. A., Alonso F. G., Gonzalez P. A., Menendez J. R., Infrared and Raman spectra of the phosphazene high polymer  $[NP(O_2C_{12}H_8)]_n$ , *J. Raman Spectrosc.*, 29 (1998) 327-330.
- [35] Elmas G., Syntheses and spectroscopic investigations of 2-pyridyl(N/N)spirocyclotriphosphazenes, *J. Turk. Chem. Soc. Sect. A: Chem.*, 5(2) (2018) 621-634.
- [36] Mutlu Ö. F., Binici A., Okumuş A., Elmas G., Cosut B., Kılıç Z., Hökelek T., Phosphorus-nitrogen Compounds. Part 54. Syntheses of Chiral Amino-4-fluorobenzyl-spiro(N/O)cyclotriphosphazenes: Structural and Stereogenic Properties, *New J. Chem.*, 45 (2021) 12178-12192.
- [37] Binici A., Elmas G., Okumus A., Tayhan, S. E., Hökelek, T., Şeker, B. N., Açık, L., Kılıç Z., Phosphorus-nitrogen compounds. Part 58. Syntheses, structural characterizations and biological activities of 4-fluorobenzyl-spiro(N/O)cyclotriphosphazene derivatives, *J. Biomol. Struc. & Dyn.*, (2021).
- [38] World Health organization, Tuberculosis. Key facts. Available at: <https://www.who.int/news-room/fact-sheets/detail/tuberculosis>. Retrieved October 14, 2021.
- [39] Clinical and Laboratory Standards Institute, M24-A2, Susceptibility Testing of Mycobacteria, Nocardiae, and Other Aerobic Actinomycetes; Approved Standard-Second Edition, (2011).

## The Quality of Yıldız River Water and Determining Trace Elements by Liquid-Liquid Micro-Extraction Analytical Method

Gülşen Taşkın Çakıcı<sup>1,a,\*</sup>, Ergün Kasaka<sup>1,b</sup>, Nail Altunay<sup>2,c</sup>

<sup>1</sup> Department of Chemistry and Chemical Processing Technology, Yıldızeli Vocational School, Sivas Cumhuriyet University, Sivas, Türkiye

<sup>2</sup> Department of Chemistry, Faculty of Science, Sivas Cumhuriyet University, Sivas, Türkiye

\*Corresponding author

### Research Article

#### History

Received: 13/01/2022

Accepted: 09/04/2022

#### Copyright



©2022 Faculty of Science,  
Sivas Cumhuriyet University

### ABSTRACT

The present study was carried out between September 2019 and March 2020 in Yıldız River, which is located within the borders of the Yıldızeli district of Sivas province and used for agricultural irrigation purposes, to determine the chemical characteristics of river water and the trace elements. Water's alkalinity, chemical oxygen demand (COD), chloride (Cl<sup>-</sup>), calcium (Ca<sup>2+</sup>), total hardness, total phosphate (PO<sub>4</sub>-P), dissolved reactive phosphate (SRP), ammonium nitrogen (NH<sub>4</sub>-N), nitrate-nitrogen (NO<sub>3</sub>-N), nitrite-nitrogen (NO<sub>2</sub>-N), soluble reactive silica (SiO<sub>2</sub>-Si) concentrations, as well as trace elements (ferrous, lead, cadmium). Moreover, during the sampling process, also the water temperature, dissolved oxygen, conductivity, pH, and total dissolved solids measurements were performed. Before using the flame atomic absorption spectrometer (FAAS) in determining the Fe, Pb, and Cd in water samples, a simple, environment-friendly, and new ultrasonic liquid-liquid micro-extraction method was suggested. Several parameters (pH, ionic fluid amount, dispersive solvent volume, and temperature) influencing the performance of micro-extraction were optimized. Under the optimized conditions, the detection thresholds for Fe (II), Pb (II), and Cd (II) were found to be 0.6, 0.15, and 1.5 µg L<sup>-1</sup>, respectively.

**Keywords:** Yıldız River, Water chemistry, Ultrasonic supported sampling, Flame AAS.

<sup>a</sup> [gtaskin@cumhuriyet.edu.tr](mailto:gtaskin@cumhuriyet.edu.tr)

<sup>b</sup> <https://orcid.org/0000-0001-7564-9777>

<sup>c</sup> [naltunay@cumhuriyet.edu.tr](mailto:naltunay@cumhuriyet.edu.tr)

<sup>b</sup> <https://orcid.org/0000-0001-9053-7570>

<sup>b</sup> [ekasaka@cumhuriyet.edu.tr](mailto:ekasaka@cumhuriyet.edu.tr)

<sup>b</sup> <https://orcid.org/0000-0003-0786-0196>

## Introduction

Knowing the physical, chemical, and biological characteristics of the water, which is one of the necessities for our lives and activities (domestic use, industrial use, agricultural irrigation, recreational purposes, etc.), is very important [1]. Since the aquatic ecosystems and their near surroundings are important attraction centers for humans, as well as other organisms, they face the highest pollution pressure due to intensive settlement and use [2]. Water quality is affected by the wastes (canalization or toxic), intensive agriculture, and disposal of materials rich in phosphate or nitrogen [3]. It is important to identify the water quality by observing and determining the parameters (measurement locations, measurement times, and intervals) [4].

Clean water (containing no heavy metal, chemical materials, or pathogen microorganisms), which is a necessity for all vital activities, should be provided for humans. Heavy metals reaching risky levels especially due to technological advancements and increasing environmental pollution, accumulate within the bodies of plants, animals, and humans and pose a threat to human health [5,6]. It is also interesting that the number of studies examining water pollution and quality from this aspect has increased in the recent period.

Vegetables, which are widely consumed for their nutrient content and certain trace elements, have a significant contribution to human health [7]. Besides their

benefits, these products also have harmful effects due to the metals they contain. The amount of trace elements depends on various factors such as the cultivation and harvest of vegetables, the use of chemicals such as fertilizers and pesticides/herbicides, and storage conditions [8]. The elements' concentrations exceeding a specific limit in the human body create a toxic effect and cause undesired health results. In order to prevent such problems, it is necessary to perform the quality controls of water being used and to determine the concentrations of heavy metals. Various analytical methods are used in analyzing heavy metals. These methods include various atomic spectrometric methods such as high-resolution continuum source flame atomic absorption spectrometer (HR-CS-FAAS) [9], inductive coupled plasma mass spectrometry (ICP-MS) [10], inductive coupled plasma optical emission spectrometry (ICP-OES) [11], hydride generation atomic absorption spectrometer [12], and hydride generation atomic fluorescence spectrometry (HG-AFS) [13]. These methods are used in determining the metals such as zinc (Zn), cobalt (Co), manganese (Mn), nickel (Ni), ferrous (Fe), cadmium (Cd), lead (Pb), selenium (Se), and arsenic (As).

Since these metals are present in water and plant samples at trace concentrations, a preliminary isolation and enrichment process should be performed. The analysis of the sample without preliminary processing is

preferred because it would protect the sample from contamination. However, few instrumental methods can be used in procedures requiring very low concentrations. Since many instrumental methods have the same principle for technical concentration measurement, isolation-enrichment is used to increase the concentration to achieve the suitable analysis range during the measurements below the detection threshold of the analyte. Some of the methods frequently used in isolating and enriching the metals in real samples include cloud point extraction (CPE) [14], solid-phase extraction (SPE) [15], co-precipitation [16], liquid-liquid extraction (LLE) [17] and dispersive liquid-liquid micro-extraction (DLLME) [18], solid-phase micro-extraction (SPME) [19], liquid-liquid micro-extraction (LLME) [20], stir bar sorptive extraction (SBSE) [21], coacervate micro-extraction (CME) [22], hollow fiber-based liquid-phase micro-extraction (HF-LPME) [23], electrochemical accumulation [24], and vortex-assisted liquid-liquid micro-extraction (VA-LLME) [25]. The enrichment methods used before the trace analysis offers various advantages such as enrichment of detection capacity of the method by increasing the concentration of analyte, minimizing the matrix intervention, decreasing the detection threshold of the method, and increasing the selectivity.

In the present study, it was aimed to determine the Fe, Pb, and Cd metals in the water samples by using the ionic liquid dispersive liquid-liquid micro-extraction (IL-DLLME) method, which is an environment-friendly and useful method, to determine the water quality of Yıldız River located in Yıldızeli district of Sivas province.

## Materials and Methods

### Research Area and Sampling Points

Yıldız River is located in the northeastern side of Central Anatolia region, 27 km away from Sivas, flowing from north to south, and merges with Kızılırmak [26]. Water samples were collected from 3 sampling stations with an interval of 2 months between September 2019 and March 2020. The sampling stations were limited to the region between Yeniyanan hamlet and the merge point of Yıldız River and Kızılırmak and, their coordinates are given below;

Station I (Yeniyanan Hamlet Bridge); 39°49'23.27"K / 36°47'10.45"D, Altitude 1275 m.

Station II (Historical Yıldız Bridge); 39°45'31.30"K / 36°45'55.99"D, Altitude 1256 m.

Station III (Historical Yıldız Bridge); 39°42'49.63"K / 36°46'41.48"D, Altitude 1250 m

### Physicochemical Analyzes Related with Water Chemistry

The water samples obtained from the stations were taken into 1-liter brown bottles without an air gap. The samples were immediately taken to the laboratory and subjected to the preservation, storage, and filtration procedures. The chemical analyses were performed within 24 hours after the sampling. Water temperature,

electrical conductivity, dissolved oxygen, total suspended solids (TDS), and pH were measured during sampling. Chemical analyses (total phosphate, dissolved reactive phosphate ammonium, nitrate, nitrite, silica, chloride, alkalinity, water hardness, calcium, and COD) were performed in the laboratory.

COD measurement was performed using the titration-based Closed Reflux Method. Chloride was measured using titration method that is based on the brick red color created by silver nitrate with chloride or chromate ions [27], whereas total phosphate and dissolved reactive phosphate were determined spectrophotometrically using Ascorbic Acid Method [28] and, total alkalinity was measured using the weak acid titration between pH 4.5 and pH 8.4 limits [29]. Nitrate analysis was performed by spectrophotometrically measuring the color originating from the reaction between sulfosalicylic acid, which forms because of the addition of sodium silicate and sulfuric acid, and nitrate in alkali medium. Nitrite analysis was performed by spectrophotometrically measuring the color arising from the reaction between nitrite ions and reactive-diluted phosphoric acid-containing sulfonamide and N-1 naphthylenediamine dihydrochloride, whereas ammonium was analyzed by spectrophotometrically measuring the indophenol blue originating from the reaction with phenol-alkali hypochlorite with the catalyzer pH 11.3-11.7 sodium nitroprusside [30]. Silica analysis was performed using Molybdosilicate Method [31], while calcium and total hardness analyses were performed EDTA titration method [32].

### Chemicals

All the reactive materials were at analytical purity and obtained from Sigma (St. Louis, MO, USA) and Merck (Darmstadt, Germany) companies. Stock solutions of Fe (II), Pb (II), and Cd(II) were obtained from their nitrate salts. Calibration and standard working solutions were prepared by gradually diluting the stock solutions. Metal ions' complexes were obtained using Patent Blue V (Sigma). Patent Blue V ( $1 \times 10^{-4}$  M) solutions were prepared using ultrapure water and stock solutions. pH 6.5 phosphate buffer solution ( $0.1 \text{ mol L}^{-1}$ ) was prepared to mix sodium dihydrogen phosphate monohydrate and sodium hydroxide at sufficient amounts. 1-butyl-3-methylimidazolium bis (trifluorosulfonyl) imid [C4mim][Tf2N] was purchased from Sigma (St. Louis, MO, USA).

### Instruments

The measurements in the research field were performed using the "Hanna HI9829" model multiparameter device, whereas COD analysis was performed using the "HACH DRB 200" model thermoreactor and spectrophotometric measurements were performed using Cecil CE5502 model spectrophotometer. The ferrous, lead, and cadmium concentrations of water samples were determined using a flame atomic absorption spectrometer (FAAS) (Shimadzu AAS-6300 model, Kyoto, Japan) device equipped with deuterium background correction. The

measurement parameters of the device for each analyte are presented in Table 1. pH measurements of solutions were performed using a digital pH-meter (Sartorius Docu-model, North America). An ultrasonic bath (UCS-10 model, Seoul, Korea) was used to ease the phase separation and to increase the micelle formation of extraction solvent. During the the extraction experiments, the separation of the ionic fluid phase from the liquid phase was performed with a centrifuge (Universal Hettich, London, England). Ultrapure water with a resistance of 18.2 MΩ cm was obtained using a Milli-Q water purifier device (Millipore Corp., USA).

Table 1. FAAS operating parameters

Parameter	Ferrous	Lead	Cadmium
Wavelength (nm)	248.3	283.3	228.8
Lambda current (mA)	12	15	8
Spectral band width (nm)	0.2	0.2	0.7
Burning height (mm)	7.0	5	7
Acetylene and air flow rates (L min <sup>-1</sup> )	2.2/18	1.8/17	1.8/15

### Suggested Method

For the micro-extraction of Fe, Pb, and Cd, 10ml water samples containing 2-500 µg L<sup>-1</sup> Fe(II), 0.5-300 Pb(II) µg L<sup>-1</sup>, and 5-600 µg L<sup>-1</sup> Cd (II) were taken to 15 mL centrifuge tubes. The sample solution's pH was set to 6.5 by using phosphate-citrate buffer solution and 500 µL 1 x 10<sup>-3</sup> mol L<sup>-1</sup> Patent Blue V, 300 µL [C4mim] [Tf2N], and 500 µL ethanol (dispersive solvent) were added and the solution was diluted to 15 mL. Centrifuge tube was closed and sonication was performed using an ultrasonic bath at 40 °C for 10 minutes until IL droplets got completely dispersed and a cloudy solution was achieved. The triplet complexes containing Fe, Pb, and Cd were extracted into fine micro-droplets [C4mim] [Tf2N]. After centrifuging at 4000 rpm for 5 minutes, two phases including IL phase and liquid phase were obtained. The supernatant liquid phase was removed using a syringe. To increase the viscosity of IL phase and to ease the analysis process, IL phase was diluted to 2.0 mL using 0.1 mol L<sup>-1</sup> HNO<sub>3</sub> to protect the stability of triplet complexes based on the formation of ion couple and to ease the atomization of analytes. Then, it was aspirated to FAAS to determine the Fe, Pb, and Cd. All the experiments were repeated three times and the mean values of results were calculated.

### Results and Discussion

#### Water Quality

The parameters examined on the samples and the numerical data of these parameters were presented in Table 2.

Table 2. Physical and chemical analysis results of water samples taken from sampling stations on the Yıldız River

	09.30.2019			11.30.2019			01.30.2020			03.24.2020		
	STATIONS											
	I	II	III	I	II	III	I	II	III	I	II	III
Calcium (mg/L)	144	144	144	133	130	137	88	88	92	98	95	98
Hardness (Fr)	39.8	40.7	40.7	38.9	37.9	38.9	25.9	25.0	25.9	28.7	27.8	28.7
Alkalinity (mg CaCO <sub>3</sub> /L)	320	320	325	300	295	310	205	200	210	215	225	220
Ammonium(mg/L)	0.08	0.04	0.03	0.03	0.01	0.003	0.04	0.02	0.02	0.02	0.04	0.02
Nitrate (mg/L)	0.43	0.48	0.56	0.84	0.79	0.86	0.78	0.77	1.04	0.74	0.81	0.88
Nitrite (mg/L)	0.001	0.001	0.0004	0.002	0.002	0.002	0.013	0.012	0.010	0.014	0.021	0.017
Total Phosphate (mg/L)	0.001	0.001	0.008	0.012	0.020	0.024	0.025	0.019	0.027	0.006	0.016	0.022
SRP (mg/L)	0.002	0.002	0.002	0.013	0.002	0.005	0.016	0.018	0.02	0.01	0.01	0.01
Chloride (mg/L)	9.4	18.9	18.9	14.2	16.5	18.9	9.4	9.4	9.4	9.4	9.4	9.4
COD (mg O <sub>2</sub> /L)	16.0	48.1	32.1	32.1	3.2	16.0	32.1	32.1	16.0	32.1	32.1	16.0
Silica (mg/L)	9.8	9.9	10.4	9.4	8.3	9.0	9.6	9.8	9.2	9.9	9.8	9.8
Temperature (°C)	16.8	17.5	17.1	7.0	7.1	7.3	7.6	7.7	7.9	9.6	10	10
Dis. Oxygen (mg O <sub>2</sub> /L)	9.8	9.6	8.9	11.4	11.3	11.3	8.5	7.9	8.1	7.0	7.0	7.1
pH	7.9	8.1	7.9	8.0	8.0	8.0	8.2	8.2	8.2	8.2	8.2	8.2
Conductivity (µs/cm)	568	581	625	480	507	562	327	331	347	349	367	378
TDS (mg/L)	304	309	331	259	273	302	172	180	182	187	196	202

The mean value and total values of measurements and analyses were presented in Table 3.

Table 3. Physical and chemical average analysis results of star river water

	Mean of Station I	Mean of Station II	Mean of Station III	Total Mean
Calcium (mg/L)	116	114	118	116
Hardness (Fr)	33	33	34	33
Hardness (mg CaCO <sub>3</sub> /L)	326	323	328	326
Alkalinity	260	260	266	262
Ammonium (mg/L)	0.043	0.024	0.017	0.028
Nitrate (mg/L)	0.70	0.71	0.83	0.75
Nitrite (mg/L)	0.008	0.009	0.007	0.008
Total Phosphate (mg/L)	0.011	0.014	0.020	0.015
SRP (mg/L)	0.010	0.008	0.010	0.009
Chloride (mg/L)	10.6	13.6	14.2	12.8
COD (mg O <sub>2</sub> /L)	28	29	20	26
Silica (mg/L)	9.8	9.4	9.6	9.6
Temperature (°C)	10.3	10.6	10.6	10.5
Dis. Oxygen (mg O <sub>2</sub> /L)	9.2	9.0	8.9	9.0
pH	8.1	8.1	8.1	8.1
Conductivity (µS/cm)	431	447	478	452
TDS (mg/L)	231	240	254	241

Quality criteria of surface waters are presented in Table 4.

Table 4. Quality criteria according to the classes of surface water resources [32]

Water Quality Parameters	Water Quality Classes			
	I	II	III	IV
General Conditions				
Temperature (°C)	≤ 25	25	30	> 30
Dissolved Oxygen (mg O <sub>2</sub> /L)	> 8	6	3	< 3
Chloride Ion (mg/L)	25	200	400	400
pH	6.5-8.5	6.5-8.5	6.0-9.0	< 6.0 or > 9.0
Conductivity (µS/cm)	< 400	1000	3000	> 3000
Chemical oxygen demand (COD) (mg/L)	< 25	50	70	> 70
Ammonium nitrogen (mg NH <sub>4</sub> <sup>+</sup> -N/L)	< 0.2	1	2	> 2
Nitrate nitrogen (mg NO <sub>3</sub> <sup>-</sup> -N/L)	< 5	10	20	> 20
Nitrite nitrogen (mg NO <sub>2</sub> <sup>-</sup> -N/L)	< 0.01	0.06	0.12	> 0.3
Total phosphor (mg P/L)	< 0.03	0.16	0.65	> 0.65

According to the quality classes given in Table 4, the purposes of waters are:

- Class I – Very high-quality water (Very good water)
  - Class II – Less polluted water (Good water)
  - Class III – Polluted water (Moderate water)
  - Class IV – Very polluted water (Poor water; “Poor water”)
- Yıldız River’s physical and chemical measurement/analysis results and the quality criteria set in SWQMR [33] are compared in Table 5.

When comparing the water of Yıldız River to SWQMR as in Table 5, it was determined that the river has Class I water quality, except for COD. Class I water refers to “very good” water quality and, the waters in this class can be used as drinking water, for recreational purposes including body contact such as swimming, trout farming, animal husbandry/farming, and agricultural irrigation.

Considering the aspect of water hardness, the river has very hard water.

Table 5. Water quality of Yıldız River

Parameters	Total Mean	Quality Class in SWQMR 2008
Temperature (°C)	10.5	Class I
Dissolved Oxygen (mg O <sub>2</sub> /L)	9.0	Class I
Chloride (mg/L)	12.8	Class I
pH	8.1	Class I
Conductivity (µs/cm)	452	Class II
COD (Mg O <sub>2</sub> /L)	26	Class I-II
Ammonium (mg/L)	0.028	Class I
Nitrate (mg/L)	0.75	Class I
Nitrite (mg/L)	0.008	Class I
Total Phosphate (mg/L)	0.015	Class II

The hardness values of waters and Yıldız River's hardness are presented in Table 6.

Table 6. Hardness classification of Yıldız River water

Hardness level (°F)	mg CaCO <sub>3</sub> /L (ppm)	Water Class	Yıldız River
0-7	0-72	Very soft water	
7-14	72-145	Soft water	
14-22	145-215	Moderately hard water	
22-32	215-325	Hard water	
32-42	325-545	Very hard water	33 (°Fr) / 326 (mg CaCO <sub>3</sub> /L)
> 42	> 545	Excessively hard water	

### Optimization of Extraction Parameters

#### Effect of pH

Before the sample preparation, because of the effects on ionization status and analyte solubility, it is generally difficult to avoid the effect of sample pH. Since the pH of the medium affects the formation of the complex between metal ions and ligand and the enrichment procedure at the final step, pH optimization is important. Given the data presented in Figure 1, it can be seen that the best analytical signal for target analytes was achieved at pH 6.5.

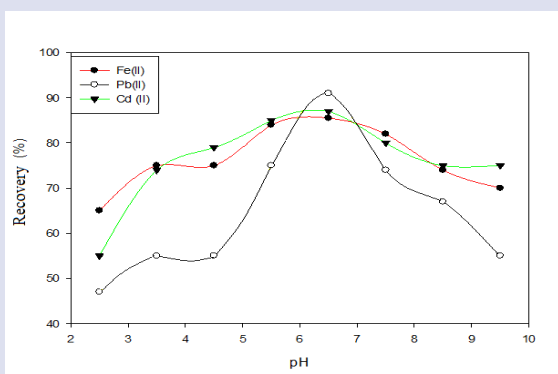


Figure 1. Effect of pH, amount on recovery of ions Fe (II), Pb (II), and Cd (II)

#### Effect of patent blue V volume

The rapid and stable complex structure of Fe(II), Pb(II), and Cd(II) ions were achieved using Patent Blue V. Together with pH, for metal ions in medium to establish a complex, the amount of complexing material should be sufficient. Patent Blue V solution ( $1 \times 10^{-3} \text{ mol L}^{-1}$ ) was added to the analyte solutions, pH of which was set to 6.5 by making use of a phosphate-citrate buffer, and the signals obtained after the enrichment process are presented in Figure 2. At 900 µL final volume of Patent Blue V, the highest signal among the absorbance values was achieved with 500 mL Patent Blue V. Thus, this amount was used as an optimal value in the next studies.

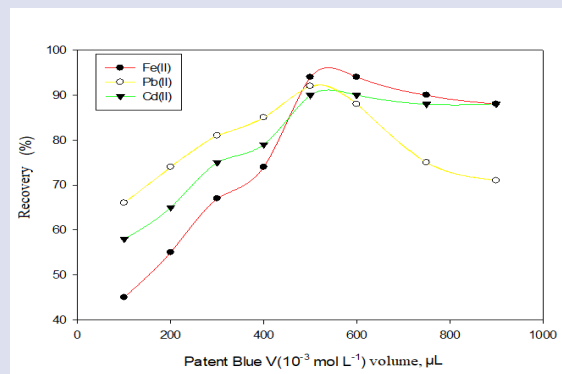


Figure 2. Effect of Patent Blue V volume on amount on recovery of ions Fe (II), Pb (II) and Cd (II)



### The effect of the amount of ionic liquid

In maximizing the extraction and increasing the selectivity of target analytes, the selection of an appropriate ionic liquid is a very important parameter for the micro-extraction process. To achieve these targets, an ionic liquid meeting the following criteria should be chosen; (i) high capacity for target analytes; (ii) low water-solubility; (iii) capacity of mixing with a solvent more dispersive and viscose than water; (iv) being present in liquid form; and (v) affordable. In conclusion, 1-butyl-3-methylimidazolium chloride [C4mim] [Tf2N] was used in the present study. After selecting the [C4mim] [Tf2N], its amount's effect on the analytical signal was analyzed between 100 and 700  $\mu\text{L}$  and in presence of ethanol (disperser solvent). According to Figure 3, the analytical signal for Fe, Pb, and Cd was increased between 100-300  $\mu\text{L}$  by increasing the amount of [C4mim] [Tf2N]. Thus, 300 $\mu\text{L}$  [C4mim] [Tf2N] was chosen for the next studies.

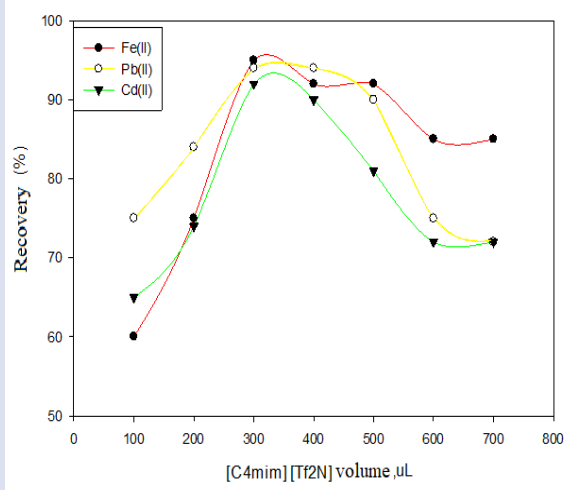


Figure 3. Effect of ionic liquid, [C6mim] [Tf2N], amount on recovery of ions Fe (II), Pb (II) and Cd (II).

### The effect of volume of dispersive solvent

In this micro-extraction process, the selection of dispersion solvent is very important for solubility in both IL and liquid phases because it acts as a bridge in dispersing the extraction solvent to achieve fine droplets. In presence of [C4mim] [Tf2N], a cloudy phase system was achieved using ethanol dispersion solvent. As seen in Figure 4, the best analytical signal was achieved when using 500  $\mu\text{L}$  ethanol as disperser solvent. In literature, the reasons for a decrease in analytical signal were reported to be related to (i) the increase in solubility of the complex in high volumes of water and (ii) the absence of complete cloudy phases at low volumes. In conclusion, 500  $\mu\text{L}$  ethanol volume was found to be suitable for use as a dispersive solvent in future studies.

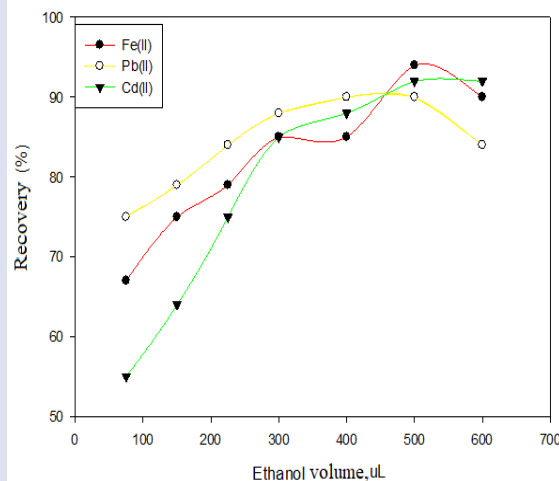


Figure 4. The effect of volume of dispersive solvent on recovery of ions Fe (II), Pb (II) and Cd (II).

### Effect of temperature

After the optimization of reactive materials influencing the extraction process, the balance temperature was optimized for the efficient separation of phases. The effect of balanced temperature on the recovery of trace elements was examined using ultrasonic force between 25 and 55  $^{\circ}\text{C}$ . It was found that the recovery of Fe (II), Pb(II), and Cd (II) increased with the increase in temperature between 25 and 40  $^{\circ}\text{C}$  and reached the maximum at 40  $^{\circ}\text{C}$ . The recovery of ions decreased after 40  $^{\circ}\text{C}$ . Since the complex including the analytes reversibly disperses into the aqueous solution depending on the increase in temperature, the recovery of analytes decreased at temperatures higher than 40  $^{\circ}\text{C}$ . Thus, the balance temperature of 40 $^{\circ}\text{C}$  was chosen as the optimum temperature for the extraction experiments.

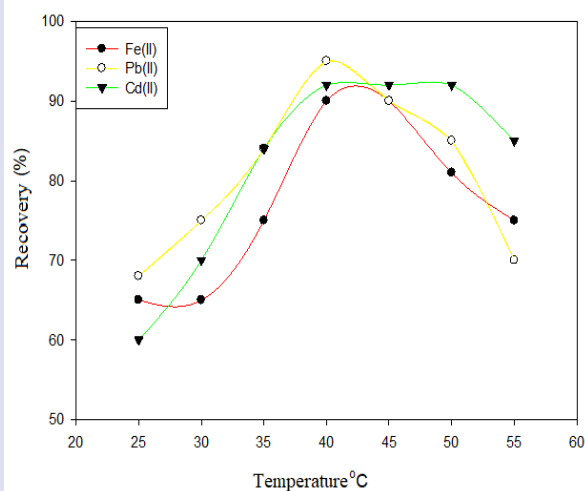


Figure 5. Effect of temperature on recovery of ions Fe (II), Pb (II) and Cd (II).

### Effect of ultrasonication time

One of the important parameters for obtaining the best analyte signal is the sample solutions' time in an ultrasonic bath. For this reason, the effect of sonication was investigated between 0 and 20 minutes. The results showed that the recovery of Fe (II), Pb(II), and Cd (II) increased with prolonging sonication time until 10 minutes but partially decreased with longer durations. Excessive length of ultrasonication time causes a decrease in absorbance [34]. For this reason, 10 minutes of sonication time was chosen to be the optimum value for extraction experiments.

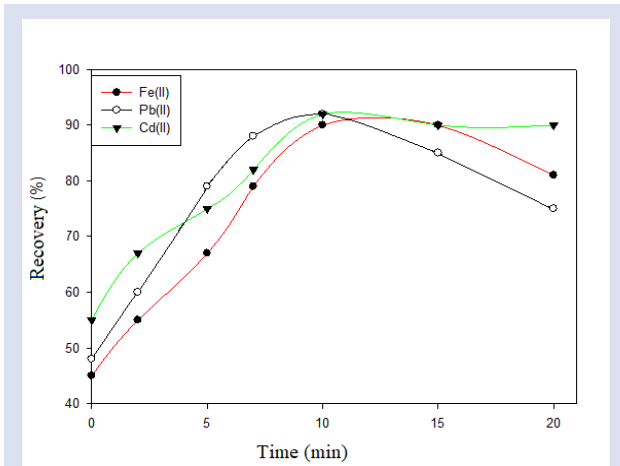


Figure 6. Effect of ultrasonication time on recovery of ions Fe (II), Pb (II) and Cd (II).

### Effect of foreign ions

To test the stability and selectivity of the suggested chemical method for Fe, Pb, and Cd ions, an interventional process was used. The results presented in Table 7 showed that the best tolerance limits and high recovery achievements were obtained in presence of various analyte ions. These results suggest that the suggested method has good selectivity for the analyte ions under the selected conditions.

Table 7. Selectivity of the method in the presence of foreign ions (n= 3)

Foreign ions	Ferrous		Lead		Cadmium	
	Tolerance limit	Recovery (%)	Tolerance limit	Recovery (%)	Tolerance limit	Recovery (%)
Ca <sup>2+</sup>	1500	97.5	1500	97.8	1000	97.5
K <sup>+</sup>	1500	96.1	1500	98.5	1000	97.2
Ba <sup>2+</sup>	1500	97.5	1000	97.3	1500	98.6
Mg <sup>+</sup>	1000	97.8	750	96.4	1500	98.5
F <sup>-</sup>	1000	96.2	750	96.1	500	96.2
Mn <sup>2+</sup>	750	96.0	750	97.5	500	96.9
Al <sup>3+</sup>	750	98.5	1000	96.2	100	95.5
Pb <sup>4+</sup>	750	97.8	100	95.4	250	96.4
CO <sub>3</sub> <sup>2-</sup>	750	96.3	500	96.8	250	96.8
Zn <sup>2+</sup>	500	95.4	500	97.2	1500	98.8
Fe <sup>3+</sup>	500	97.5	250	97.7	100	97.1
Cu <sup>2+</sup>	250	96.1	250	96.1	50	95.2
Co <sup>2+</sup>	250	95.2	50	95.0	750	96.7
Cr <sup>3+</sup>	100	95.0	100	96.4	750	97.6
As <sup>3+</sup>	100	96.7	250	97.6	750	97.1
VO <sup>2+</sup>	50	96.3	100	96.2	250	96.3

### Analytical performance

The analytical parameters of the suggested analyte method under the optimum conditions are listed in Table 8. The linear operational range of methods for Fe, Pb, and Cd are 2-500, 0.5-300, and 5-600 µg L<sup>-1</sup>, respectively.

Table 8. Analytical characteristics of the method

Analytical characteristics	Fe(II)	Pb(II)	Cd(II)
Calibration equation	A=0.0052[Fe(II)]+0.00085	A=0.00127[Pb(II)]+0.00103	A=0.00376[Cd(II)]+0.00053
Correlation coefficient (r <sup>2</sup> )	0.9913	0.9972	0.9953
Operational range (µg L <sup>-1</sup> )	2-500	0.5-300	5-600
Detection limit(3S <sub>empty</sub> /m, µg L <sup>-1</sup> )	0.6	0.15	1.5
Detection limit(10S <sub>empty</sub> /m, µg L <sup>-1</sup> )	2.0	0.5	5.0
%BSS (accuracy for day, n:5)	1.4	1.7	2.0
%BSS(accuracy for day, n:3x5)	2.3	2.6	3.2
% Recovery	95.8	97.8	96.3
Preliminary concentration factor	75	75	75
Sensitivity factor	94	105	87

### 3.2.8. Validation studies

To test the accuracy and validity of the suggested method, the analysis of the certified reference sample was performed using the suggested method and the results and reference values were compared. The results are presented in Table 9. It can be stated that the results obtained from the suggested method were in good harmony with the certified values at the confidence level of 95%.

After the reliability test of the suggested method, the applicability of the suggested method for detecting the ferrous, lead, and cadmium in the water samples of Yıldız River was investigated. The accuracy of suggested methods was tested by adding the samples with different concentrations of standard analyte solutions and analyzing the recovery values. The results are presented in Table 10. As seen in the results, the recovery values are at acceptable levels.

Table 9. Results of the method validation study

CRM	Fe			Pb			Cd		
	Result	%BSS, %Recovery	t <sub>exp</sub>	Result	%BSS, %Recovery	t <sub>exp</sub>	Result	%BSS, %Recovery	t <sub>exp</sub>
INCT-TL-1 (Tea leaves)	42.7±1.7	3.9 (98.8)	0.75	17.2±0. 7	4.0 (96.6)	1.38	29.6±1.4	4.7 (98.6)	0.96

Certified values were found to be 43.2±1.3 µg kg<sup>-1</sup> for ferrous, 17.8±2.4 µg kg<sup>-1</sup> for lead, and 30±4.0 µg kg<sup>-1</sup> for cadmium. For the confidence level of 95% and SD 4, t<sub>crit.</sub> = 2.78

Table 10. Analysis results of water samples by method (n: 3)

Samples	Months	Additive (µg L <sup>-1</sup> )			Result (µg L <sup>-1</sup> )			Recovery (%)			BSS (%)		
		Fe(II)/Pb(II)/Cd(II)			Fe	Pb	Cd	Cu	Pb	Cd	Cu	Pb	Cd
Station -1		-	45.7	14.3	6.8	-	-	-	2.4	1.8	2.4		
		100	140.4	111.4	102.3	94.7	97.1	95.5	2.2	1.7	2.2		
Station -2	09.30.2019	-	67.9	21.6	12.4	-	-	-	2.5	1.5	2.5		
		100	164.1	115.4	108.5	96.2	94.4	96.1	2.4	1.4	2.3		
Station -3		-	24.3	7.5	16.2	-	-	-	2.3	1.7	2.3		
		100	121.8	101.1	113.8	97.5	93.6	97.6	2.1	1.6	2.0		
Station -1		-	62.1	33.4	19.9	-	-	-	1.9	1.4	2.6		
		100	158.7	130.6	118.7	96.6	97.2	98.8	1.7	1.2	2.5		
Station -2	11.30.2019	-	100.2	21.9	26.7	-	-	-	1.8	1.6	2.4		
		100	195.1	120.4	119.2	94.9	98.5	92.5	1.5	1.4	2.4		
Station -3		-	44.8	11.6	8.1	-	-	-	2.3	1.5	2.5		
		100	142.1	109.4	105.0	97.3	97.8	96.9	2.1	1.4	2.3		
Station -1		-	65.8	33.6	9.5	-	-	-	2.1	1.5	1.9		
		100	160.5	131.7	102.5	94.7	98.1	93.0	2.0	1.3	1.7		
Station -2	01.30.2020	-	36.1	15.9	21.8	-	-	-	1.8	2.6	2.2		
		100	132.6	112.3	117.6	96.5	96.4	95.8	1.6	2.4	2.0		
Station -3		-	89.3	64.1	17.3	-	-	-	2.3	1.9	1.8		
		100	187.5	157.8	114.6	98.2	93.7	97.3	2.0	1.7	1.5		
Station -1		-	32.4	14.1	10.6	-	-	-	2.7	1.8	2.6		
		100	130.6	107.4	105.6	98.2	93.4	95.0	2.4	1.6	2.4		
Station -2	03.24.2020	-	76.5	26.8	31.7	-	-	-	2.4	1.9	2.5		
		100	173.6	122.8	128.9	97.1	96.5	97.2	2.3	1.7	2.3		
Station -3		-	65.8	42.9	17.3	-	-	-	2.4	1.7	2.1		
		100	162.5	137.8	110.9	96.7	94.9	93.6	2.5	1.6	2.0		

## Conclusions

As a result of the analyses of water samples taken from Yıldız River, the lowest calcium concentration in the river was found to be 88 mg/L, and the highest one was found to be 144 mg/L. Water hardness ranged between 250 and 400 mg/L. River water has an alkali character, and the maximum alkalinity was found to be 325 mg CaCO<sub>3</sub>/L. The highest values of ammonium, nitrate and nitrite parameters in the water were found to be 0.0846 mg/L, 0.857 mg/L, and 0.0004 mg/L, respectively. The highest total phosphate concentration in the present study was

found to be 0.0268 mg/L and the lowest one to be 0.0011 mg/L. During the sampling period, the water temperature ranged between 7 and 17.5 °C. The chloride concentration was found to range between 9.43 and 18.87 mg/L. pH values ranged between 7.94 and 8.18. The highest electrical conductivity in river water was found to be 625 µS/cm and the lowest one to be 327 µS/cm. Oxygen concentration, which is important for the water quality, did not fall below 7.03 mg/L during the sampling period, and the highest value was found to be 11.35 mg O<sub>2</sub>/L. The

silica concentration in the river water was found to be very high. The highest silica concentration was 10.39 mg O<sub>2</sub>/L and the lowest one was 8.33 mg O<sub>2</sub>/L. Moreover, even though the sulfate analysis was performed for the water samples, no sulfate could be detected. The water of Yıldız River was found to be Class I water quality, and the hardness class was found to be very hard water.

In the present study, a new, rapid, and simple method for preliminary concentration and isolation of ferrous, lead, and cadmium was optimized and then applied for measurements with FAAS. Fe (II), Pb (II), and Cd (II) ions become complex with [C4mim][Tf2N] at pH 6.5 and all the optimization procedures for the suggested method were completed. As a result of the experiment, it is predicted that, since the suggested method is simple, rapid, selective, highly sensitive, and suitable for the use at low concentrations, it would ease the observation, measurement, and identification of Fe (II), Pb(II), and Cd (II) heavy metals in water samples.

### Acknowledgment

The present study was supported by Sivas Cumhuriyet University's Scientific Research Project Coordination Unit (project number of RGD-018).

### Conflicts of interest

The authors state that did not have conflict of interests.

### References

- [1] Sayın B.T.C., Ministry of agriculture, forestry and rural affairs, 2nd Bandırma Bird Sanctuary and Bird Lake Symposium, (1987) 86-88.
- [2] Tekinalp O., Investigation of pollution and polluting factors of Yenişehir lake (Reyhanlı / HATAY), Dissertation, Mustafa Kemal University, (2005).
- [3] Moss B., Eutrophication and restoration of shallow and deep lakes, shallow lake wetlands, ecology, eutrophication and restoration. International Workshop, ODTÜ, (2001), 3-31-32.
- [4] Gündoğdu V., Özkan E.Y., Design of monitoring network and determination of water quality variables in Küçük Menderes River, *Ege J. Fisheries Aquatic Sci.*, 23 (3-4) (2006) 361-369.
- [5] Kumbur H., Özsoy H.D., Özer Z., Determination of the effects of chemicals used in agricultural area on water quality in Mersin Province, *Ecology*, 17(68) (2008) 54-58
- [6] Temamoğulları F., Dinçoğlu A.H., Selenium and zinc levels in well water in Sanlıurfa and vicinity. *Kafkas Uni. J. Faculty Vet. Med-Us*, 16 (2) (2010) 199-203.
- [7] Türkmen A., Türkmen M., Tepe Y., Naz M., Heavy metal concentrations in sea water of Iskenderun Bay and correlations between temperature, pH, oxygen and salinity values, *Turkish J. Aquatic Life*, 2 (3) (2004) 400-407.
- [8] Kahraman T., Alemdar S., Alişarlı M., Ağaoğlu S., Heavy metal levels in drinking water of Bitlis province, *Eurasian J. Vet. Sci.*, 28 (2012) 164-171.
- [9] Chirita L., Covaci E., Mot A., Ponta M., Gandeac A., Frentiu T., Determination of selenium in food and environmental samples by hydride generation high-resolution continuum source quartz furnace atomic absorption spectrometry, *J. Anal. Atom Spectrom.*, 36 (2021) 267-272.
- [10] Fernández Z.H., Álvarez J.R.E., Montero A., Ugarte Á.O.M., González I.P., González M.R., Júnior J.A.D.S., Freire M.B.C., Junior B. & O. P. D. S., Metal contaminants in rice from Cuba analyzed by ICP-MS, ICP-AES and CVAAS, *Food Addit Contam. B.*, 14 (2021) 59–65.
- [11] Ilin D.V., Pletnev I.V., Extraction and ICP-OES determination of heavy metals using tetrabutylammonium bromide aqueous biphasic system and oleophilic collector, *Talanta*, 221 (2021) 121485.
- [12] Masac J., Machynak L., Lovic J., Beinrohr E., Cacho F., On-line electrochemical preconcentration and electrochemical hydride generation for determination of antimony by high-resolution continuum source atomic absorption spectrometry, *Talanta*, 223 (2021) 121767.
- [13] Wei Y., Zhang J., Qiu S., Huang Q., Yuan L., Chen L., Dai T., Tu T., Zhang B., Yan H., Li W., Selenium species determination in se-enriched grain crops with foliar spray of sodium selenite by IP-RP-HPLC-UV-HG-AFS, *Food Anal. Method*, 14 (2021) 1345–1358.
- [14] Azooz E.A., Wannas F.A., Jawad S. K., Developed cloud point extraction coupled with onium system for separation and determination cobalt in biological samples, *Res. J. Pharm. Tech.*, 14(2) (2021) 594-598.
- [15] Juretic H., Montalbo-Lomboy M., Van Leeuwen J.H., Cooper W.J., Grewell D., Hydroxyl radical formation in batch and continuous flow ultrasonic systems. *Ultrason. Sonochem.*, 22 (2015) 600-606.
- [16] Feist B., Mikula B., Preconcentration of some metal ions with lanthanum-8-hydroxyquinoline co-precipitation system, *Food Chem.*, 147 (2014) 225-229
- [17] Fouladvand M.T., Asadi J., Lotfollahi M.N., Simulation and optimization of aromatic extraction from lube oil cuts by liquid-liquid extraction, *Chem. Eng. Res. Des.*, 165 (2021) 118-128.
- [18] Mandlate J.S., Soares B.M., Seeger T.S., Vecchia P.D., Mello P.A., Flores E.M.M., Duarte F.A., Determination of cadmium and lead at sub-ppt level in soft drinks: An efficient combination between dispersive liquid-liquid microextraction and graphite furnace atomic absorption spectrometry, *Food Chem.*, 221 (2017) 907–912.
- [19] Song X., Wu J., Pang J., Wu Y., Huang X., Task specific monolith for magnetic field-reinforced in-tube solid phase microextraction of mercury species in waters prior to online HPLC quantification, *J. Hazard Mater.*, 411 (2021) 125141.
- [20] Ji Y., Zhao M., Li A., Zhao L., Hydrophobic deep eutectic solvent-based ultrasonic-assisted dispersive liquid-liquid microextraction for preconcentration and determination of trace cadmium and arsenic in wine samples, *Microchem. J.*, 164 (2021) 105974.
- [21] Becker R., Heyn L., Jung C., Indoor exposure to airborne PAHs: A comparison of stir bar sorptive extraction and pump sampling, *Authorea Preprints* 14 January 2021 - authorea.com.
- [22] Melnyk A., Wolska L., Namieśnik J., Coacervative extraction as a green technique for sample preparation for the analysis of organic compounds, *J. Chromatogr. A.*, 1339 (2014) 1-12.
- [23] Mogaddam M.R.A., Farajzadeh M. A., Mohebbi A., Nemati M., Hollow fiber-liquid phase microextraction method based on a new deep eutectic solvent for extraction and

- derivatization of some phenolic compounds in beverage samples packed in plastics, *Talanta*, 216 (2020) 120986.
- [24] Armand M., Endres F., MacFarlane D.R., Ohno H., Scrosati B., Ionic-liquid materials for the electrochemical challenges of the future, *Mater. Sustain. Energy*, (2010) [https://doi.org/10.1142/9789814317665\\_0020](https://doi.org/10.1142/9789814317665_0020).
- [25] Ferreira V.J., Almeida J.S., Lemos V.A., Oliveira O.M.C., Garcia K.S., Teixeira L.S.G., Determination of Cu, Ni, Mn, and Pb in diesel oil samples using reversed-phase vortex-assisted liquid-liquid microextraction associated with energy dispersive X-ray fluorescence spectrometry, *Talanta*, 222 (2021) 121514.
- [26] Yıldırım M., Yılmaz I., Investigation of the usefulness of the Yıldız Irmak sediments as the cement aggregates, *Cumhuriyet Earth Sci.*, 19 (2002) 181-192.
- [27] Clesceri S., Greenberg E.A., Eaton D., Standard methods for examination of water and wastewater. 20. Edition, American Public Health Association, (1999).
- [28] Murphy J., Riley J.P., A single-solution method for the determination of soluble phosphate in sea water, *J. Marine Biol. Assoc. UK*, 37 (1958) 9-14.
- [29] Mackeret F.J.H., Heron J., Talling C.F., Water analysis: some revised methods for limnologists. *Sci. pub. Freshwater Biol. Assoc.*, (1978) 1-120.
- [30] Dişli M., Akkurt F., Alicılar A., Evaluation on water of Şanlıurfa balıklıgöl concerning chemical parameters, *J. Fac. Eng. Arch. Gazi Univ.*, 19 (3) (2004) 287-294.
- [31] Mullin J.D., Riley J.P., The colorimetric determination of silica in water. part 3. method for determining the total silica content, *Analyst. Lond.*, 88 (1955) 446-455.
- [32] West D.M., Skoog D.A., Holler F.J., Crouch S.R., Analitik Kimya Temel İlkeler. Esmâ Kılıç, Hamza Yılmaz (ed) Bilim yayınları, Ankara (2009).
- [33] Anonymous (2008) Water Pollution Control Regulation. 26786
- [34] Juretic H., Montalbo-Lomboy M., Van Leeuwen J.H., Cooper W.J., Grewell D., Hydroxyl radical formation in batch and continuous flow ultrasonic systems, *Ultrason Sonochem.*, 22 (2015) 600-606.

## Could Momordica Charantia Be Effective In The Treatment of COVID19?

Burak Tüzün <sup>1,a,\*</sup>, Koray Sayın <sup>2,b</sup>, Hilmi Ataseven <sup>3,c</sup>

<sup>1</sup> Plant and Animal Production Department, Technical Sciences Vocational School of Sivas, Sivas Cumhuriyet University, Sivas, Türkiye

<sup>2</sup> Department of Chemistry, Faculty of Science, Sivas Cumhuriyet University, Sivas, Türkiye

<sup>3</sup> Department of Gastroenterology, Faculty of Medicine, Sivas Cumhuriyet University, Sivas, Türkiye

\*Corresponding author

### Research Article

#### History

Received: 19/10/2021

Accepted: 22/05/2022

#### Copyright



©2022 Faculty of Science,  
Sivas Cumhuriyet University

[btuzun@cumhuriyet.edu.tr](mailto:btuzun@cumhuriyet.edu.tr)  
[hilmiataseven@yahoo.com](mailto:hilmiataseven@yahoo.com)

### ABSTRACT

One of the deadliest diseases is the SARS-CoV-2 virus, today. The rate of spread of this virus is very high. Momordica Charantia extracts studied for this virus. The inhibitory activities of 96 components in the extract of Momordica Charantia were compared against the SARS-CoV-2 virus. Molecular docking method was initially used for this comparison. ADME/T analysis of the inhibitors with the highest inhibitory activity was performed using the results obtained from these calculations. The molecular docking calculations of the molecule with the highest inhibitory activity were tried to be supported by MM-PBSA calculations. The molecular mechanics Poisson-Boltzmann surface binding free energy values of area (MM-PBSA) calculations study interactions between inhibitor molecules and SARS-CoV-2 virus proteins at 100 ps. Finally, the molecules with the highest inhibitory activity were compared with FDA approved drugs. As a result of the made molecular docking calculations, the docking score parameter is Karaviloside III with -9.36, among the extracts of momordica charantia, which has the most negative value. The Gibbs free energy value of the Karaviloside III against 6X6P protein with the best docking score value was calculated. This value is -477143.61±476.53. As a result of the comparison of inhibitory activities of extracts of Momordica charantia against SARS-CoV-2 virus, it has been observed that the Karaviloside III molecule has higher inhibitory activity than other melodies and FDA drugs.

**Keywords:** SARS-CoV-2, Molecular docking, COVID-19, Momordica charantia, ADME/T.

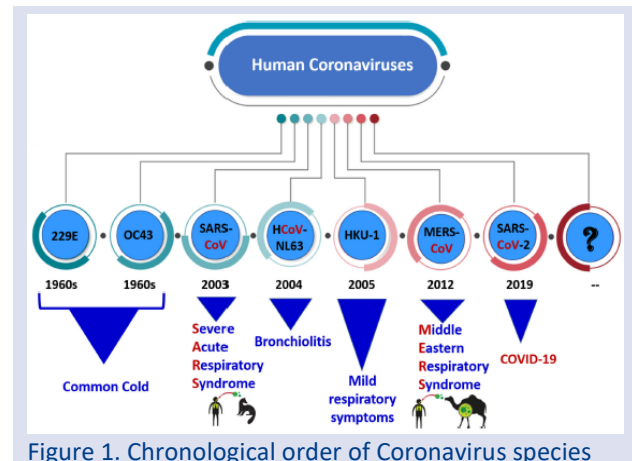
<https://orcid.org/0000-0002-0420-2043>  
<https://orcid.org/0123-4578-9012-3457>

[ksayin@cumhuriyet.edu.tr](mailto:ksayin@cumhuriyet.edu.tr) <https://orcid.org/0000-0001-6648-5010>

## Introduction

Severe Acute Respiratory Syndrome Coronavirus 2 (SARS-CoV-2), which started in Wuhan city of China and affected the whole world, is currently the most contagious and effective virus [1]. This virus started in the last month of 2019, infected 23 million people in 7 months, and caused the death of 850 thousand people. This infection was declared a pandemic by the world health organization (WHO) in March 2020. SARS-CoV-2 is an enveloped positive-sense single-stranded ribonucleic acid (RNA) virus. It is a dangerous virus that can spread from person to person through droplet exchange while coughing, talking, and sneezing. The upper respiratory tract's symptoms such as fever, dry cough, nausea, head and throat pain, and runny nose are in the foreground for this virus [2]. In patients, all of these symptoms appear between 3 and 14 days. People with low immune systems such as diabetes, heart problems, cancer, asthma, and organ transplantation are reported to show acute symptoms [2]. When the virus's incubation period ends, these mild symptoms worsen and begin to accumulate water in the lungs. Subsequently, the virus leads to respiratory failure and finally causes the patient to become pneumonia. When the disease reaches this level, it is challenging for the patient to recover [3].

Another name for SARS-CoV-2 disease is COVID-19. This disease is the seventh coronavirus transmitted to humans.



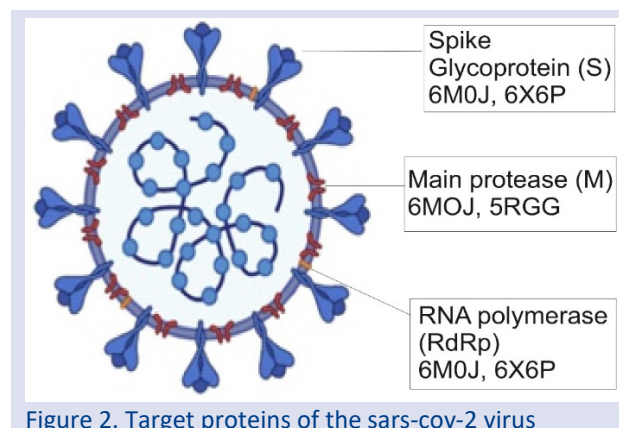
This virus is classified under four main headings: alfa, beta, gamma, and delta [4]. The order of the coronavirus types by years is shown in Figure 1. The six known before that are HCoV-229E (Human coronavirus 229E), HCoV-OC43 (Human coronavirus OC43), SARS-CoV (Severe acute respiratory syndrome- coronavirus), HCoV-NL63 (Human coronavirus NL63), HCoV-HKU-1 (Human coronavirus-HKU-1), MERS-CoV (Middle East respiratory syndrome coronavirus) [5]. Although SARS-CoV-2 triggers diseases in different and multiple organ systems in animals, it generally targets humans' respiratory systems. Although HCoV-229E, HCoV-OC43, SARS-CoV, HCoV-NL63, and

HCoV-HKU-1 cause upper respiratory tract discomfort with mild symptoms, SARS-CoV, MERS-CoV, and SARS-CoV-2 have serious and dangerous diseases. It is classified as the high pathogen that can cause [3,6]. The membrane receptor of host cells plays an essential role in the entry of coronaviruses into host cells and their pathogenesis. The coronavirus recognizes host receptors with its envelope-anchored spike (S) protein and binds with this protein's help. It then enters the cell by binding the host and viral membranes [7]. It was seen in many experimental and theoretical studies conducted before that, it was observed that the genome sequences of SARS-CoV-2 were 80% similar to other coronaviruses [8]. But SARS-CoV-2 infection rate is more than ten times higher [9]. The coronavirus genome consists of four main structural proteins. These are (1) the spike (S) protein, (2) nucleocapsid (N) protein, (3) membrane (M) protein, and (4) the envelope (E) protein [10].

Many theoretical studies have shown that it has been shown that four basic proteins within the SARS-CoV-2 virus are focused. The first is the main protease of the coronavirus 3CLpro and PLpro. The antiviral drug lopinavir [11,12] is used. The second is the RNA-dependent RNA polymerase [(RdRp), also called nsp12] protein of the coronavirus. Remdesivir [11], ribavirin [11,13], and favipiravir [14] are used as antiviral drugs. The third is the coronavirus s protein (viral spike glycoprotein). Arbidol [15] is used as an antiviral drug. The fourth and last is the ACE 2 protein of the coronavirus. Arbidol [15] is used as an antiviral drug.

Momordica charantia has many major components. The most important of these main components are cucurbitacins, sterols, triterpenoids, and vicine [16]. Momordica charantia has been used for centuries, particularly in the treatment of stomach diseases. The fruit of Momordica charantia is separated when ripe, giving orange-yellow fruits. In recent years, research has been carried out for cancer treatment with Momordica charantia, whose homeland is considered to be India. With Momordica charantia, natural support can be provided for digestive system diseases. The active ingredient called quarantine in Momordica charantia is effective in gastritis, stomach ulcer, reflux problems. Momordica charantia reduces the number of Helicobacter Pylori bacteria, suppressing their activity, and preventing their growth. It is effective against stomach and intestinal infections with its anti-inflammatory properties. An article published in "Current Molecular Medicine" in May 2011 wrote that Momordica charantia contains more than 20 bioactive compounds that increase its therapeutic value. Nearly 100 in vitro studies have proven the blood sugar lowering effect of Momordica charantia to date. In the June 2001 issue of the journal "Planta Medica" published a study demonstrating the capacity of Momordica charantia to inhibit HIV [17]. The June 2009 issue of the "Pharmaceutical Research" newsletter also reported that Momordica charantia inhibits cancer cells' growth and promotes cancer cell death without touching healthy cells [18]. The October 2010 issue of "Cancer Science" included

a study stating that Momordica charantia extract prevents carcinogenic cells from spreading from prostate tumors to the lung [19].



In the study of Ahamad et al., Momordica charantia found 96 components. These ninety-six molecules are given in supplementary data file. However, the inhibitory effects of 96 molecules of Momordica charantia against proteins of spike glycoprotein (PDB ID: 6M0J, 6X6P), main protease (PDB ID: 5RGG, 7BUY), and RNA dependent RNA polymerase (RdRp) (PDB ID: 7BV1, 7BV2) of the SARS-CoV-2 virus were compared by molecular docking calculations, are represented in Figure 2. The molecular mechanics Poisson-Boltzmann surface binding free energy values of area (MM-PBSA) calculations study interactions between inhibitor molecules and SARS-CoV-2 virus proteins at 100 ps. Afterward, ADME/T analysis of the molecules with the highest inhibitory activity among these 96 molecules was performed.

## Material and Methods

Previous theoretical studies show that the inhibitory properties of the molecules formed by many components of the Momordica Charantia against SARS-CoV-2 proteins were compared using molecular docking, which is one of the most used methods. Inhibitory activities were compared using the numerical value obtained from the interactions between molecules and SARS-CoV-2 proteins by molecular docking method. Active regions of many SARS-CoV-2 proteins are determined by calculations. In this study, molecular docking calculations were made to compare the inhibitory activities with the molecules of the Momordica Charantia.

Molecular docking calculations to calculate the inhibitory activities of 96 molecules studied were performed using the Maestro Molecular modeling platform (version 12.2) by Schrödinger. For these calculations, proteins and 96 pieces of Momordica Charantia molecules studied must be prepared. In docking calculations, a different process is performed for molecules at each stage. First, it was used from the Gaussian software program [20] to obtain optimized structures of molecules with extension \*.sdf were created using these structures.

All calculations were made with the Maestro Molecular modeling platform (version 12.2) by Schrödinger, LLC [21]. The Maestro Molecular modeling platform (version 12.2) by Schrödinger comes together from many modules. In the first module, the protein was prepared and the active site of the protein was found. The protein preparation module [22,23] is used. In the next module, the LigPrep module [24,25] was used to do the necessary operations for docking calculations of molecules.

For the next step, The Glide ligand docking module [26] was used to calculate interactions between the 96 therapeutic agents studied and the SARS-CoV-2 progeny. In this module, the OPLS3e method was used in all calculations for docking calculations of molecules and proteins. Numerical values of many parameters obtained as a result of molecular docking calculations using this module are used. After the docking calculations, studied 96 therapeutic agents were made ADME/T analysis (absorption, distribution, metabolism, excretion, and toxicity) so that they could become drugs in the future. The Qik-prop module [27] of the Schrödinger software was used for ADME/T analysis.

Molecular mechanics Poisson-Boltzmann surface area (MM-PBSA) calculations were performed for 6X6P protein and molecule 4a. For MM-PBSA calculations, Nanoscale Molecular Dynamics (NAMD) [28] and Visual Molecular Dynamics (VMD) [29] software programs were calculated all calculations. Binding free energy provides an overview of biomolecular interactions between protein and inhibitor. The binding energy of protein and inhibitor constitutes of potential energy, polar and non-polar solvation energies. In these calculations, the free binding energy and the total free energy of the protein, inhibitors, and inhibitor-protein complex were calculated respectively.

$$\Delta G_{\text{Binding}} = \Delta G_{\text{complex}} - (\Delta G_{\text{protein}} + \Delta G_{\text{inhibitor}})$$

where;  $\Delta G_{\text{Binding}}$  is the binding free energy,  $\Delta G_{\text{complex}}$ ,  $\Delta G_{\text{protein}}$ , and  $\Delta G_{\text{inhibitor}}$  demonstrates the total free energy of the protein-ligand complex and total free energies of the isolated protein and ligand, respectively. Each term in the above equation consists of the combination of many energy components. These are composed of many components such as van der Waals energy, electrostatic energy, and polar contribution.

## Results and Discussion

The ninety-three molecules of *Momordica charantia* will inhibit three different proteins of the SARS-CoV-2 virus. Three different SARS-CoV-2 virus proteins were taken into consideration, spike glycoprotein, main protease, and RNA dependent RNA polymerase proteins. It should be well known that the more that these 96 molecules interacts with the three different proteins of the SARS-CoV 2 virus, the most inhibition effect would be. The molecule with the most inhibition effect will stop the SARS-Cov-2 virus from entering the cell. Hence, replication of the SARS-Cov-2 virus in human metabolism would be inhibited.

Ninety-three molecules of the studied *Momordica charantia* were investigated by the molecular docking method against the SARS-CoV-2 virus's proteins. As a result of these calculations, many parameters about the inhibitors were calculated. These parameters provide much information about inhibitors' inhibitory properties against SARS-CoV-2 virus proteins [23]. As a result of molecular docking calculations, the most important parameter among the obtained parameters is the docking score parameter. This parameter is used to explain the interaction between inhibitors and proteins. It should be well known that if the interaction between the inhibitor and the proteins increases, the inhibitor's activity increases [25]. This increase in interaction causes the SARS-CoV-2 virus to inhibit the protein.

There are many more parameters obtained from docking calculations. These parameters are used to explain the interactions between the inhibitor and SARS-CoV-2 proteins. These parameters are Glide hbond, Glide evdw, and Glide ecoul. These parameters provide information about the number of chemical interactions that occur between the inhibitor and the proteins. These parameters give a numerical expression of hydrogen bonding, Van der Waals interactions, and Coulomb interactions occurring between inhibitors and proteins [30-32]. Apart from these parameters, there are Glide emodel, Glide energy, and Glide einternal parameters. All of these parameters explain the interaction of molecules with inhibitors. Table 1 shows the numerical values of the five inhibitors with the highest inhibitory activity among 96 inhibitors for all parameters [33].

As a result of molecular docking calculations, the best inhibitors for the three active protein regions of the SARS-CoV-2 virus are given in Table 1. These inhibitors are 4-Methoxybenzoic Acid (1a), Gypsogenin (2a), Momordicine I (3a), Karaviloside III (4a), and Charantoside II (5a). The interactions of the highest inhibitory activity molecules of 96 inhibitor molecules of *Momordica charantia* with the studied proteins are given in Figure 3-8.



Table 1. Numerical values of the docking parameters of molecule against enzymes

Protein	Parameters	1a	2a	3a	4a	5a
<b>6MOJ</b>	Docking score	-2.50	-3.34	-2.26	-	-
	Glide ligand efficiency	-0.23	-0.10	-0.07	-	-
	Glide evdw	-14.14	-18.81	-19.87	-	-
	Glide ecoul	-6.99	-7.75	-9.24	-	-
	Glide energy	-21.13	-26.55	-29.11	-	-
	Glide einternal	0.04	2.41	5.20	-	-
	Glide emodel	-24.41	-26.83	-36.67	-	-
	Glide hBond	-0.31	-2.09	-1.48	-	-
<b>6X6P</b>	Docking score	-3.63	-7.32	-7.17	-9.36	-8.57
	Glide ligand efficiency	-0.33	-0.22	-0.21	-0.21	-0.18
	Glide evdw	-11.83	-26.94	-32.43	-28.75	-22.25
	Glide ecoul	-5.27	-3.49	-1.61	-9.01	-11.31
	Glide energy	-17.10	-30.44	-34.04	-37.76	-33.55
	Glide einternal	3.35	7.70	0.00	15.62	0.00
	Glide emodel	-17.66	53.35	-46.09	10.46	26.41
	Glide hBond	-1.94	-1.95	-1.06	-2.96	-2.40
<b>5RGG</b>	Docking score	-2.65	-4.37	-6.44	-8.77	-7.09
	Glide ligand efficiency	-0.24	-0.13	-0.19	-0.19	-0.15
	Glide evdw	-15.39	-29.03	-32.83	-20.59	-31.84
	Glide ecoul	-2.62	-6.09	-7.87	-19.36	-11.57
	Glide energy	-18.01	-35.12	-40.70	-39.96	-43.41
	Glide einternal	0.83	2.27	5.20	13.26	11.53
	Glide emodel	-21.91	-44.43	-51.48	-58.62	-55.18
	Glide hBond	-0.60	-0.82	-1.33	-5.38	-3.05
<b>7BUY</b>	Docking score	-3.12	-4.71	-4.52	-7.35	-7.27
	Glide ligand efficiency	-0.28	-0.14	-0.13	-0.16	-0.15
	Glide evdw	-15.10	-21.68	-22.73	-31.55	-37.42
	Glide ecoul	-2.14	-8.80	-6.06	-12.79	-7.02
	Glide energy	-17.24	-30.48	-28.79	-44.33	-44.44
	Glide einternal	0.00	1.23	7.86	10.51	0.00
	Glide emodel	-21.91	-28.26	5.76	-32.36	-54.28
	Glide hBond	-0.35	-2.16	-1.32	-3.41	-3.03
<b>7BV1</b>	Docking score	-3.66	-4.64	-5.14	-8.42	-7.98
	Glide ligand efficiency	-0.33	-0.14	-0.15	-0.19	-0.17
	Glide evdw	-13.52	-33.47	-23.84	-26.83	-28.73
	Glide ecoul	-5.87	-0.58	-8.77	-18.24	-16.73
	Glide energy	-19.39	-34.05	-32.61	-45.07	-45.46
	Glide einternal	4.43	1.72	22.87	9.81	7.35
	Glide emodel	-21.47	-43.44	-18.74	-53.91	-55.02
	Glide hBond	-1.89	-1.41	-2.22	-3.55	-3.51
<b>7BV2</b>	Docking score	-1.70	-4.18	-4.68	-	-
	Glide ligand efficiency	-0.15	-0.12	-0.14	-	-
	Glide evdw	-14.92	-28.86	-18.62	-	-
	Glide ecoul	3.65	1.04	-5.51	-	-
	Glide energy	-11.28	-27.82	-24.13	-	-
	Glide einternal	0.43	0.49	5.70	-	-
	Glide emodel	-12.60	-32.52	-28.47	-	-
	Glide hBond	-0.30	-2.01	-1.92	-	-

After comparing the inhibitory activity of inhibitors against the protein, ADME/T analysis was performed to theoretically predict the five molecules' effects and responses with the highest inhibitory activity in human metabolism. To predict the effects and responses of inhibitors on organs and tissues in the human body from the numerical values obtained with this theoretical analysis. The numerical values of all the inhibitors' calculated parameters with this analysis are given in Table 2 in detail.

As a result of molecular docking calculations, there are two most essential parameters obtained due to ADME/T analysis for inhibitors, which are The RuleOfFive [34,35] and RuleOfThree [36] parameters. These two parameters constitute a combination of many parameters. Therefore, the numerical value of this parameter is required to be zero. Each other parameter gives the numerical value of the effects of inhibitor molecules on different organs and tissues.

Table 2. ADME properties of molecules

	1a	2a	3a	4a	5a	Reference Range
mol_MW	152	471	473	635	663	130-725
dipole (D)	3.9	4.7	4.0	7.1	6.4	1.0-12.5
SASA	347	703	779	979	986	300-1000
FOSA	93	534	613	789	797	0-750
FISA	107	151	148	178	146	7-330
PISA	147	17	17	11	43	0-450
WPSA	0	0	0	0	0	0-175
volume (A <sup>3</sup> )	539	1420	1526	1966	2008	500-2000
donorHB	1	1	3	5	4	0-6
accptHB	2.8	4.7	7.1	12.7	14.4	2.0-20.0
glob (Sphere =1)	0.9	0.9	0.8	0.8	0.8	0.75-0.95
QPpolrz (A <sup>3</sup> )	15.5	48.9	49.9	64.3	66.3	13.0-70.0
QPlogPC16	5.3	12.7	14.1	18.9	18.9	4.0-18.0
QPlogPoct	7.9	20.6	24.7	35.8	35.8	8.0-35.0
QPlogPw	6.0	8.0	12.3	20.3	20.5	4.0-45.0
QPlogPo/w	2.0	5.8	4.6	4.5	4.5	-2.0-6.5
QPlogS	-1.6	-6.8	-6.3	-6.9	-6.6	-6.5-0.5
CIQlogS	-1.6	-7.0	-5.9	-6.8	-6.9	-6.5-0.5
QPlogHERG	-1.7	-1.9	-4.5	-5.2	-5.3	*
QPPCaco (nm/sec)	243	92	387	202	410	**
QPlogBB	-0.4	-1.0	-1.4	-2.2	-1.8	-3.0-1.2
QPPMDCK (nm/sec)	136	48	177	88	189	**
QPlogKp	-2.8	-4.0	-3.4	-3.5	-2.8	Kp in cm/hr
IP (ev)	9.5	9.5	9.7	9.6	9.6	7.9-10.5
EA (eV)	0.4	-0.5	-0.6	-1.0	-0.9	-0.9-1.7
#metab	1	3	6	8	9	1-8
QPlogKhsa	-0.6	1.3	0.9	0.7	0.6	-1.5-1.5
Human Oral Absorption	3	1	1	1	1	-
Per. Human Oral Absorp.	81	83	100	82	87	***
PSA	59	94	84	125	116	7-200
RuleOfFive	0	1	0	1	1	Maximum is 4
RuleOfThree	0	1	1	2	2	Maximum is 3
Jm	9.6	0.0	0.0	0.0	0.0	-

Table 3. Representation of calculated parameters (kcal/mol) and standard deviation values of 6X6P protein and molecule 5a

Time (ps)	VDW		Kinetic		Potential		Gibbs binding free energy	
5000	37115.05	±6595.83	126302.61	±13544.26	-608437.17	±19585.05	-481644.11	±33037.00
10000	36094.54	±623.60	127085.12	±578.59	-603639.74	±998.39	-476081.47	±1441.35
15000	35723.95	±139.42	127073.28	±475.47	-603548.75	±488.83	-475969.93	±586.26
20000	36086.30	±620.05	127484.33	±347.71	-604501.37	±413.03	-476526.19	±462.71
25000	36155.52	±745.37	126908.49	±446.19	-604120.55	±421.86	-476727.22	±490.26
30000	34966.01	±571.37	127412.85	±383.23	-604979.05	±457.17	-477087.87	±515.18
35000	35187.36	±176.06	127982.60	±434.36	-603731.49	±595.22	-475245.12	±708.41
40000	34767.18	±42.96	127740.12	±366.03	-604973.83	±608.04	-476719.04	±657.72
45000	35430.36	±217.40	127164.10	±411.80	-604112.24	±547.16	-476449.45	±618.66
50000	35294.45	±647.40	126133.13	±473.90	-604967.54	±519.74	-478338.59	±583.24
55000	35355.61	±373.00	127982.63	±413.69	-604620.99	±626.82	-476140.86	±686.34
60000	35700.43	±356.67	127658.33	±417.18	-605190.27	±442.57	-477014.96	±392.80
65000	35845.87	±382.39	127679.02	±408.40	-605115.02	±415.79	-476944.97	±419.74
70000	35432.53	±381.52	127188.26	±345.76	-604172.07	±493.60	-476523.05	±469.70
75000	35632.89	±38.03	128005.92	±384.58	-605709.68	±474.10	-477214.31	±491.85
80000	35291.97	±217.59	127035.33	±389.65	-605856.03	±612.38	-478314.93	±531.02
85000	35446.23	±706.79	127629.78	±398.57	-606125.94	±405.27	-477988.34	±357.15
90000	35036.80	±230.09	127879.09	±425.58	-605938.91	±486.29	-477577.82	±452.78
95000	35100.63	±261.89	127409.73	±449.25	-606042.63	±515.98	-478126.02	±513.01
100000	34382.58	±572.34	127594.93	±376.68	-605226.04	±533.65	-477143.61	±476.53

Detailed analysis of these parameters is given in previous studies [37,38]. If these two parameters' numerical value becomes zero, it is expected that this inhibitor will be used as a drug in the future.

Molecular docking calculations for nanosecond-level binding calculations between molecule and protein have some drawbacks. In molecular docking calculations, although inhibitors are very flexible, proteins are not flexible at all. Molecular mechanics-Poisson-Boltzmann surface area (MM-PSBA) calculations are used to examine the interaction between molecule and protein in more detail. With these calculations, flexibility is given to both proteins and inhibitors. In these calculations, the protein and inhibitor are too surrounded by solvent molecules. In this study, the binding stability of protein-inhibitory structures was found for every five nanoseconds due to calculations. The Gibbs free energy value of the 4a inhibitor against 6X6P protein with the best docking score value was calculated. As a result of these calculations, the binding free energy changes and their deviations values were calculated for each five ns. There are many

interactions between protein and ligand. The most important interaction among these interactions is the hydrogen bond, which is one of the basic elements responsible for molecular interactions in biological systems [24]. The van der Waals energy (VDW), kinetic energy, potential energy, and Gibbs binding free energy changes of the inhibitor 4a against 6X6P protein were calculated. The final binding energy between protein and ligand is a cumulative sum of van der Waals, electrostatic, polar solvation, and SASA energy. An illustration of the interaction between protein and inhibitor is given at between 0-100 ns every 25 ns, in figure 9. These values are given in Table 3. Calculations made with molecular mechanics-Poisson-Boltzmann surface area (MM-PBSA) method were made to support molecular docking calculations. The more negative values obtained in these calculations indicate better binding [39-43]. The numerical values obtained from the calculations were plotted and given in Figure 10.

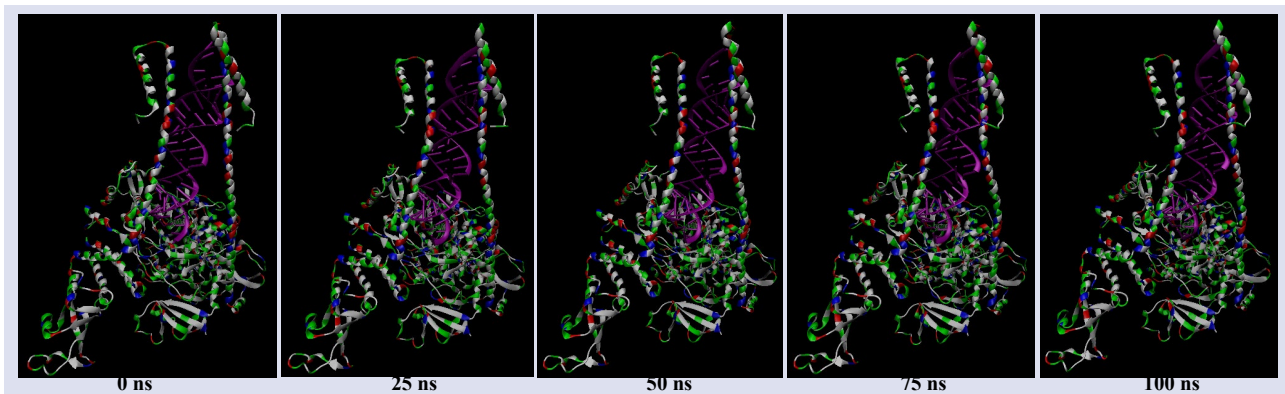


Figure 9. Representation of the interaction between protein and inhibitor is given at between 0-100 ns every 25 ns

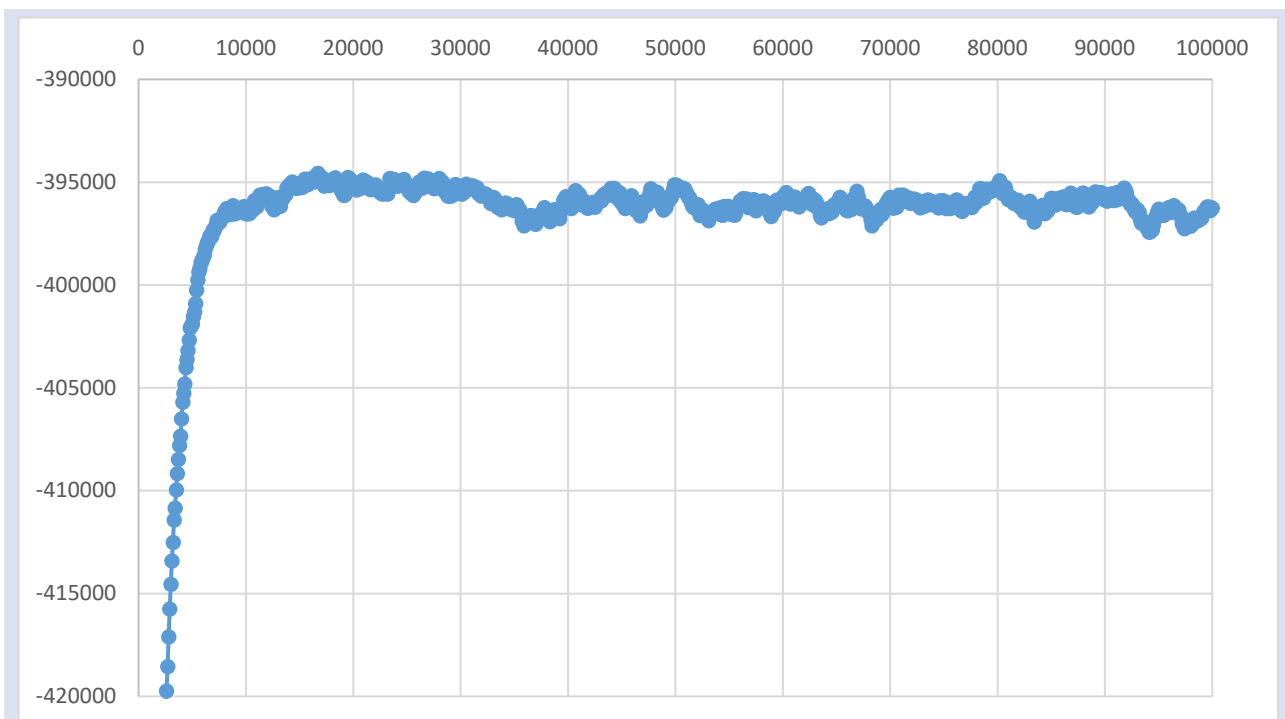


Figure 10. Change of Gibbs free energy values of 6X6P protein and molecule 5a in every five ns intervals.

As a result of the calculations, the inhibitory activities of 96 components of *Momordica Charantia* were compared against the SARS-CoV-2 virus. The calculated molecular dock results were compared with the values of corona drugs approved by the Food and Drug Administration (FDA) of the United States Ministry of

Health. Numerical values of FDA-approved drugs are given in Table 4. The structures of these FDA online drugs used were downloaded from the PubChem website (<https://pubchem.ncbi.nlm.nih.gov/>), and their calculations were made.

Table 4. Numerical values of the docking parameters of molecule against enzymes

Protein	Inhibitor	Docking score	Glide ligand efficiency	Glide evdw	Glide ecoul	Glide energy	Glide einternal	Glide emodel	Glide hBond
6X6P	37542	-5.59	-0.33	-21.05	-8.78	-29.83	3.00	-41.96	-2.62
6M0J	37542	-4.50	-0.26	-19.74	-5.20	-24.95	3.48	-37.19	-1.88
	84029	-2.57	-0.05	-20.46	-7.48	-27.94	15.61	10000	-1.18
	92727	-2.50	-0.05	-33.47	-11.57	-45.04	12.39	-58.92	-1.46
	131411	-1.38	-0.05	-27.55	-2.58	-30.12	3.80	-42.67	0.00
5RGG	37542	-4.26	-0.25	-12.66	-9.40	-22.06	4.27	-26.29	-2.68
	121304016	-3.19	-0.08	-37.43	-11.24	-48.66	9.35	-53.75	-1.63
	492405	-3.05	-0.28	-10.30	-7.91	-18.21	0.01	-21.00	-1.31
7BUY	92727	-6.13	-0.13	-45.13	-7.17	-52.30	13.77	-68.86	-1.18
	37542	-5.30	-0.31	-24.42	-8.92	-33.34	6.27	-40.09	-2.24
	492405	-4.53	-0.41	-17.50	-8.09	-25.59	0.01	-33.10	-1.79
7BV1	37542	-5.79	-0.34	-18.85	-15.86	-34.71	1.97	-43.45	-3.25
7BV2	37542	-6.94	-0.41	-15.81	-23.93	-39.74	3.44	-50.88	-4.38

These drugs are ribavirin (Pubchem number: 37542), arbidol (Pubchem number: 131411), favipiravir (Pubchem number: 492405), remdesivir (Pubchem number: 121304016), clarithromycin (Pubchem number: 84029), lopinavir (Pubchem number: 92727), and azithromycin (Pubchem number: 447043). These drugs are actively used against coronavirus. In the calculations for FDA approved drugs, the docking score of the ribavirin drug against the spike glycoprotein of the SARS-CoV-2 virus with 6X6P ID was -5.59, while the docking score value of the Karaviloside III (4a) inhibitor of *Momordica Charantia* was -9.36. Although the docking score of the ribavirin drug against the spike glycoprotein of the SARS-CoV-2 virus with 6M0J ID was -4.50, the docking score of *Momordica Charantia*'s Gypsogenin (2a) inhibitor was -3.34. In the next protein, the docking score value of the ribavirin drug against the main protease protein of the SARS-CoV-2 virus with 5RGG ID was -4.26, while the docking score value of the Karaviloside III (4a) inhibitor of *Momordica Charantia* was -6.20. Although the docking score of the lopinavir drug against the main protease protein of the SARS-CoV-2 virus with 7BUY ID was -6.13, the docking score value of the Karaviloside III (4a) inhibitor of *Momordica Charantia* was -7.35. In the next protein, the ribavirin drug's docking score against the RNA dependent RNA polymerase (RdRp) protein of the 7BV1 ID SARS-CoV-2 virus was -5.79 while the docking score value of *Momordica Charantia*'s Karaviloside III (4a) inhibitor was -8.42. Although the docking score value of ribavirin drug against RNA dependent RNA polymerase (RdRp) protein of SARS-CoV-

2 virus with 7BV2 ID was -4.68, *Momordica Charantia*'s momordicine I (3a) inhibitor had a docking score of -6.20.

As a result of the calculations, the covid-19 inhibitory activities of the molecules were compared. In many previous studies, the activity comparison of molecules was made. In the study of Aktaş et al. [44], RNA dependent RNA polymerase (RdRp) proteins were targeted, 3-Hydroxypyrazine-2-Carboxamide (CID 294642) and 2-oxo-(1,4-15N2)1H-pyrazine-3-(15N). The inhibitory activities of )carboxamide (CID 76973015) molecules were found to have higher inhibitory activity than the molecules studied. In the study of Ataseven et al. [45], the inhibitory activities of many boron molecules against spike glycoprotein, main protease and RNA dependent RNA polymerase of SARS-CoV-2 proteins were compared. ((R)-1-((S)-3-(4-(aminomethyl)phenyl)-2-benzamidopropanamido)-4-guanidinobutyl) boronic acid molecule was found to have higher inhibitory activity than other molecules. In the study by Tuzun et al. [46], the inhibitory activity of molecules in *Peganum harmala* extract was investigated to compare the inhibitory activities of SARS-CoV-2 against main protease, spike glycoproteins and RNA-dependent RNA polymerase proteins. It was observed that 1-methyl-1-Methyl-9H-beta-carbolin-7-ol molecule had higher inhibitory activity than other molecules against RNA-dependent RNA polymerase (RdRp) protein. In the study of Gedikli et al. [47], Inhibitory activities of SARS-CoV-2 virus against spike glycoprotein (PDB ID: 6M0J, 6LZG), main protease (PDB ID: 5RGG, 6WTT), and RNA dependent RNA polymerase (RdRp) (PDB ID: 6YYT, 7BV2) proteins were studied, Carvedilol molecule was found to have

higher inhibitory activity than other molecules. Çetiner et al. [48], in their study on boron-containing compounds, compared the inhibitory activities of SARS-CoV-2 against main protease, spike glycoproteins and RNA-dependent RNA polymerase proteins. The 4,6-di-tert-butyl-2-(4-methoxyphenyl) benzo[d][1,3,2] molecule was found to have higher inhibitory activity than other molecules. In the study of gedikli et al. [49], the inhibitory activities of clarithromycin, azithromycin and their analogues against the proteins of SARS-CoV2 virus were compared. In the comparison of SARS-CoV-2 virus against RNA-dependent RNA polymerase proteins, it is seen that Desosaminylazithromycin molecule has higher activity than other molecules. Many molecules have been studied in the above studies. Each molecule was found to have different activity in different SARS-CoV-2 protein regions.

## Conclusion

A comparison of the inhibitory activities of *Momordica Charantia* against SARS-CoV-2 was performed for 96 components found in the extract. ADME / T analysis of molecules with high inhibitory activity was performed using the molecular docking method used for this comparison. Based on these results, MM-PBSA calculations were made for the molecule with the highest inhibitory activity. MM-PBSA calculations confirmed molecular docking results. Finally, by making a comparison with FDA approved medicines; Results show that the Karaviloside III (4a) inhibitor is a better inhibitor than other inhibitors and FDA approved drugs. It is recommended that the Karaviloside III (4a) inhibitor be used as an inhibitor in future in vivo and in vitro studies.

## Acknowledgments

This work is supported by the Scientific Research Project Fund of Sivas Cumhuriyet University under the project number RGD-020. This research was made possible by TUBITAK ULAKBIM, High Performance, and Grid Computing Center (TR-Grid e-Infrastructure).

## Conflict of Interest

No potential conflict of interest was reported by the author(s).

## References

- [1] Gorbalenya A.E., Baker S.C., Baric R., Groot R.J.D., Drosten C., Gulyaeva A.A., ... Ziebuhr J., Severe acute respiratory syndrome-related coronavirus: Classifying 2019-NCoV and naming it SARS-CoV-2, *Nature Microbiology*, (2020) 1–9.
- [2] Alagaili A.N., Briese T., Mishra N., Kapoor V., Sameroff S.C., de Wit E., ... Lipkin W.I., Middle East respiratory syndrome coronavirus infection in dromedary camels in Saudi Arabia, *MBio*, 5(2) (2014) e00884-14.
- [3] Chen N., Zhou M., Dong X., Qu J., Gong F., Han Y., ... Zhang L., Epidemiological and clinical characteristics of 99 cases of 2019 novel coronavirus pneumonia in Wuhan, China: a descriptive study, *The Lancet*, 395(10223) (2020) 507-513.
- [4] Ahmed F.S., Quadeer A.A., McKay R.M., Preliminary identification of potential vaccine targets for the COVID-19 coronavirus (SARS-CoV-2) based on SARS-CoV immunological studies, *Viruses*, 12(3) (2020) 254.
- [5] Tao Y., Shi M., Chommanard C., Queen K., Zhang J., Markotter W., ... Tong S., Surveillance of bat coronaviruses in Kenya identifies relatives of human coronaviruses NL63 and 229E and their recombination history, *Journal of Virology*, 91(5) (2017) e01953–16.
- [6] Wang D., Hu B., Hu C., Zhu F., Liu X., Zhang J., ... Peng Z., Clinical characteristics of 138 hospitalized patients with 2019 novel coronavirus-infected pneumonia in Wuhan, China, *JAMA*, 323(11) (2020) e201585.
- [7] Wang M., Cao R., Zhang L., Remdesivir and chloroquine effectively inhibit the recently emerged novel coronavirus (2019-nCoV) in vitro, *Cell Res.*, 30(3) (2020) 269-271.
- [8] Gallagher T.M., Buchmeier M.J., Coronavirus spike proteins in viral entry and pathogenesis, *Virology*, 279(2) (2001) 371–374.
- [9] Ahn D.G., Shin H.J., Kim M.H., Lee S., Kim H.S., Myoung J., ... Kim S.J., Current status of epidemiology, diagnosis, therapeutics, and vaccines for novel coronavirus disease 2019 (COVID-19), *Journal of Microbiology and Biotechnology*, 30(3) (2020) 313–324.
- [10] Schoeman D., Fielding B.C., Coronavirus envelope protein: Current knowledge, *Virology Journal*, 16(1) (2019) 69.
- [11] Sheahan T.P., Sims A.C., Leist S.R., Schäfer A., Won J., Brown A.J., ... Baric R.S. Comparative therapeutic efficacy of remdesivir and combination lopinavir, ritonavir, and interferon beta against MERS-CoV Nat., *Commun.*, 11(1) (2020) 1-14.
- [12] Maxmen A., More than 80 clinical trials launch to test coronavirus treatments, *Nature*, 578(7795) (2020) 347–348.
- [13] Arabi Y.M., Shalhoub S., Mandourah Y., Al-Hameed F., Al-Omari A., Al Qasim E., ... Fowler R., Ribavirin and Interferon Therapy for Critically Ill Patients with Middle East Respiratory Syndrome: A Multicenter Observational Study, *Clin. Infect. Dis.*, 70(9) (2019) 1837-1844.
- [14] Lakhri Y., Rbaa M., Tuzun B., Hichar A., Ounine K., Almalki F., Lakhri B., Synthesis, structural confirmation, antibacterial properties and bio-informatics computational analyses of new pyrrole based on 8-hydroxyquinoline, *Journal of Molecular Structure*, 1259 (2022) 132683.
- [15] Al-Janabi I.A.S., Yavuz S.Ç., Köprü S., Tapera M., Kekeçmuhammed H., Akkoç S., ... Sarıpinar, E. Antiproliferative activity and molecular docking studies of new 4-oxothiazolidin-5-ylidene acetate derivatives containing guanylhydrazone moiety, *Journal of Molecular Structure*, 1258 (2022) 132627.
- [16] Ahamad J., Amin S., Mir S.R., *Momordica charantia* Linn.(Cucurbitaceae): Review on phytochemistry and pharmacology, *Phytochemistry*, 11(2) (2017) 53-65.
- [17] Jiratchariyakul W., Wiwat C., Vongsakul M., Somanabandhu A., Leelamanit W., Fujii I., ... Ebizuka Y., HIV inhibitor from Thai bitter gourd, *Planta Medica*, 67(04) (2001) 350-353.
- [18] Nerurkar P., Ray R.B. Bitter melon: antagonist to cancer, *Pharmaceutical Research*, 27(6) (2010) 1049-1053.
- [19] Pitchakarn P., Ogawa K., Suzuki S., Takahashi S., Asamoto M., Chewonarin T., Shirai T., *Momordica charantia* leaf extract suppresses rat prostate cancer progression in vitro and in vivo, *Cancer Science*, 101(10) (2010) 2234-2240.

- [20] Frisch M.J., Trucks G.W., Schlegel H.B., Scuseria G.E., Robb M.A., Cheeseman J.R., Scalmani G., Barone V., Mennucci B., Petersson G.A., Nakatsuji H., Caricato M., Li X., Hratchian H.P., Izmaylov A.F., Bloino J., Zheng G., Sonnenberg J.L., Hada M., Ehara M., Toyota K., Fukuda R., Hasegawa J., Ishida M., Nakajima T., Honda Y., Kitao O., Nakai H., Vreven T., Montgomery J.A., Peralta J.E., Ogliaro F., Bearpark M., Heyd J.J., Brothers E., Kudin K.N., Staroverov V.N., Kobayashi R., Normand J., Raghavachari K., Rendell A., Burant J.C., Iyengar S.S., Tomasi J., Cossi M., Rega N., Millam J.M., Klene M., Knox J.E., Cross J.B., Bakken V., Adamo C., Jaramillo J., Gomperts R., Stratmann R.E., Yazyev O., Austin A.J., Cammi R., Pomelli C., Ochterski J.W., Martin R.L., Morokuma K., Zakrzewski V.G., Voth G.A., Salvador P., Dannenberg J.J., Dapprich S., Daniels A.D., Farkas O., Foresman J.B., Ortiz J.V., Cioslowski J., Fox D.J. (2009) Gaussian 09, revision D.01. Gaussian Inc, Wallingford CT.
- [21] Schrödinger L. (2019). Small-Molecule Drug Discovery Suite 2019-4.
- [22] Schrödinger Release (2019) 2019-4: Protein Preparation Wizard; Epik, Schrödinger, LLC, New York, NY, 2016; Impact, Schrödinger, LLC, New York, NY, 2016; Prime, Schrödinger, LLC, New York, NY.
- [23] Rbaa M., Haida S., Tuzun B., El Hassane A., Kribii A., Lakhrissi Y., ... Berdimurodov E., Synthesis, characterization and bioactivity of novel 8-hydroxyquinoline derivatives: Experimental, molecular docking, DFT and POM analyses, *Journal of Molecular Structure*, 1258 (2022) 132688.
- [24] Schrödinger Release (2019) 2019-4: LigPrep, Schrödinger, LLC, New York, NY, 2019.
- [25] Kökbudak Z., Akkoç S., Karataş H., Tüzün B., Aslan G. In Silico and In Vitro Antiproliferative Activity Assessment of New Schiff Bases, *Chemistry Select*, 7(3) (2022) e202103679.
- [26] Koçyiğit Ü.M., Taslimi P., Tüzün B., Yakan H., Muğlu H., Güzel E., 1, 2, 3-Triazole substituted phthalocyanine metal complexes as potential inhibitors for anticholinesterase and antidiabetic enzymes with molecular docking studies, *Journal of Biomolecular Structure and Dynamics*, (2020) 1-11.
- [27] Schrödinger Release 2020-1: QikProp, Schrödinger, LLC, New York, NY, 2020.
- [28] Nelson M.T., Humphrey W., Gursoy A., Dalke A., Kalé L.V., Skeel R.D., Schulten K., NAMD: A parallel, object-oriented molecular dynamics program, *The International Journal of Supercomputer Applications and High-Performance Computing*, 10(4) (1996) 251–268.
- [29] Humphrey W., Dalke A., Schulten K., VMD: Visual molecular dynamics, *Journal of Molecular Graphics*, 14(1) (1996) 33–38.
- [30] Celebioglu H.U., Erden Y., Hamurcu F., Taslimi P., Şentürk O.S., Özmen, Ü.Ö., ... Gulçin İ., Cytotoxic effects, carbonic anhydrase isoenzymes,  $\alpha$ -glycosidase and acetylcholinesterase inhibitory properties, and molecular docking studies of heteroatom-containing sulfonyl hydrazone derivatives, *Journal of Biomolecular Structure and Dynamics*, (2020) 1-12.
- [31] Huseynova A., Kaya R., Taslimi P., Farzaliyev V., Mammadyarova X., Sujayev, A., ... Gulçin İ. Design, synthesis, characterization, biological evaluation, and molecular docking studies of novel 1, 2-aminopropanthiols substituted derivatives as selective carbonic anhydrase, acetylcholinesterase and  $\alpha$ -glycosidase enzymes inhibitors, *Journal of Biomolecular Structure and Dynamics*, (2020) 1-13.
- [32] Taslimi P., Erden Y., Mamedov S., Zeynalova L., Ladokhina N., Tas R., ... Gulçin İ., The Biological Activities, Molecular Docking Studies, and Anticancer Effects of 1-Arylsulphonylpyrazole Derivatives, *Journal of Biomolecular Structure and Dynamics*, (2020) 1-20.
- [33] Demir Y., Taslimi P., Koçyiğit Ü. M., Akkuş M., Özaslan M. S., Duran H. E., et al., Determination of the inhibition profiles of pyrazolyl-thiazole derivatives against aldose reductase and  $\alpha$ -glycosidase and molecular docking studies, *Archiv der Pharmazie*, (2020) e2000118.
- [34] Lipinski C. A., Lead-and drug-like compounds: the rule-of-five revolution, *Drug Discovery Today: Technologies*, 1(4) (2004) 337-341.
- [35] Lipinski C. A., Lombardo F., Dominy B. W., Feeney P. J., Experimental and computational approaches to estimate solubility and permeability in drug discovery and development settings, *Advanced Drug Delivery Reviews*, 23 (1997) 3-25.
- [36] Jorgensen W.J., Duffy E.M., Prediction of drug solubility from structure, *Advanced Drug Delivery Reviews*, 54(3) (2002) 355-366.
- [37] Kısa D., Korkmaz N., Taslimi P., Tuzun B., Tekin Ş., Karadağ A., Şen F., Bioactivity and Molecular Docking Studies of Some Nickel Complexes: New Analogues for the Treatment of Alzheimer, Glaucoma and Epileptic Diseases, *Bioorganic Chemistry*, (2020) 104066.
- [38] Türkan F., Taslimi P., Abdalrazaq S. M., Aras A., Erden Y., Celebioglu H. U., et al., Determination of anticancer properties and inhibitory effects of some metabolic enzymes including acetylcholinesterase, butyrylcholinesterase, alpha glycosidase of some compounds with molecular docking study, *Journal of Biomolecular Structure and Dynamics*, (2020) 1-17.
- [39] Alici E.H., Bilgiçli A.T., Tüzün B., Günşel A., Arabaci G., Yarasir M.N., Alkyl chain modified metalophthalocyanines with enhanced antioxidant-antimicrobial properties by doping Ag<sup>+</sup> and Pd<sup>2+</sup> ions, *Journal of Molecular Structure*, 1257 (2022) 132634.
- [40] Erdogan M.K., Gundogdu R., Yapar Y., Gecibesler I.H., Kirici M., Behcet L., ... Taslimi P., The Evaluation of Anticancer, Antioxidant, Antidiabetic and Anticholinergic Potentials of Endemic Rhabdosciadium microcalycinum Supported by Molecular Docking Study, *ChemistrySelect*, 7(17) (2022) e202200400.
- [41] Majumdar D., Tüzün B., Pal T.K., Das S., Bankura K., Architectural View of Flexible Aliphatic-OH Group Coordinated Hemi-Directed Pb (II)-Salen Coordination Polymer: Synthesis, Crystal Structure, Spectroscopic Insights, Supramolecular Topographies, and DFT Perspective, *Journal of Inorganic and Organometallic Polymers and Materials*, (2022) 1-18.
- [42] Shafiee S., Davaran S., A mini-review on the current COVID-19 therapeutic strategies, *Chemical Review and Letters*, 3(1) (2020) 19-22.
- [43] Majedi S., Majedi S., Existing drugs as treatment options for COVID-19: A brief survey of some recent results, *Journal of Chemistry Letters*, 1(1) (2020) 2-8.
- [44] Aktaş A., Tüzün B., Aslan R., Sayin K., Ataseven H., New anti-viral drugs for the treatment of COVID-19 instead of favipiravir, *Journal of Biomolecular Structure and Dynamics*, 39(18) (2021) 7263-7273.

- [45] Ataseven H., Sayin K., Tüzün B., Gedikli M., Could boron compounds be effective against SARS-CoV-2?, *Bratislava Medical Journal-Bratislavské Lekárske Listy*, 122(10) (2021) 753-758.
- [46] Tuzun B., Nasibova T., Garaev E., Sayin K., Ataseven H. Could *Peganum harmala* be effective in the treatment of COVID-19?, *Bratislavské Lekárske Listy*, 122(9) (2021) 670-679.
- [47] Gedikli M.A., Tuzun B., Sayin K., Ataseven H., Determination of inhibitor activity of drugs against the COVID-19, *Bratislavské Lekárske Listy*, 122(7) (2021) 497-506.
- [48] Cetiner E., Sayin K., Tuzun B., Ataseven H., Could boron-containing compounds (BCCs) be effective against SARS-CoV-2 as anti-viral agent?, *Bratislavské Lekárske Listy*, 122(4) (2021) 263-269.
- [49] Gedikli M., Tuzun, B., Aktas A., Sayin K., Ataseven H., Are clarithromycin, azithromycin and their analogues effective in the treatment of COVID19, *Bratislava Medical Journal-Bratislavské Lekárske Listy*, 122(2) (2021) 101-110.

## Quantum Chemical Benchmark Study on Valdecoxib, a Potent and Selective Inhibitor of COX-2, and its Hydroxylated Derivative

Sümeyya Serin<sup>1,a,\*</sup>, Öznur Doğan Ulu<sup>1,b</sup><sup>1</sup> Scientific and Technological Research Center, İnönü University, Malatya, Türkiye

\*Corresponding author

### Research Article

#### History

Received: 11/03/2022



Accepted: 27/05/2022

#### Copyright

©2022 Faculty of Science,  
Sivas Cumhuriyet University

### ABSTRACT

In this work, quantum chemical calculations were performed on valdecoxib (VLB), a highly selective and potent COX-2 inhibitor, and its hydroxylated derivative (1H-VLB), an active metabolite. The geometry optimizations and frequency calculations were carried out by using density functional theory (DFT)/B3LYP functional with the 6-311++G (d, p) basis set. To define water phase behaviors, calculations were renewed by using universal SMD solvation model for both molecules. Structural and thermodynamic parameters, FT-IR analysis, Mulliken population analysis (MPA), frontier molecular orbital (FMO) analysis, natural bond orbital (NBO) analysis, and electrostatic surface properties were investigated in detail. Quantum chemical reactivity identifiers were calculated separately for both vacuum and water environment in order to evaluate the bioactivity tendency of both mentioned compounds. When the bioactivity of VLB and 1H-VLB molecules were compared based on quantum chemical reactivity identifiers, it was observed that the VLB molecule was more active. Moreover, drug-likeness properties of studied molecules were predicted by means of Molinspiration cheminformatics software. Molecular lipophilicity potential (MLP) maps that exhibit the accumulative lipophilic contributions of each atom in studied molecules were visualized.

**Keywords:** Valdecoxib, DFT, Lipophilicity, NBO [sumeyya.alatas@inonu.edu.tr](mailto:sumeyya.alatas@inonu.edu.tr) <https://orcid.org/0000-0002-4637-1734> [oznur.dogan@inonu.edu.tr](mailto:oznur.dogan@inonu.edu.tr) <https://orcid.org/0000-0002-5561-227X>

## Introduction

The increasing severity and prevalence of chronic diseases caused by inflammatory disorders pose challenges to both the health system and the economy. Therefore, there is a need for the development of environmentally friendly drugs with high efficacy and selectivity, as well as suitable toxic properties. Non-steroidal anti-inflammatory drugs (NSAIDs), commonly used in the treatment of inflammation, pain and fever inhibit cyclooxygenase (COX), also called prostaglandin synthase (PG) [1]. PGs produced from fatty acids in human organs and tissues lead symptoms such as pain, fever and redness in inflammation and injuries. COX enzymes have two different isomers called COX-1 and COX-2 [2,3]. COX-1 is involved in physical functions such as kidney function and gastrointestinal integrity, while COX-2 is responsible for proinflammatory conditions [4,5]. It was observed that the amount of PG in inflamed tissues was higher than in normal tissues [6]. The gastrointestinal side effects seen as a result of long-term use of NSAIDs necessitated the development of different drugs.

Heterocyclic compounds are widely used in organometallic chemistry, catalysis and drug chemistry for the synthesis of new and effective compounds [7,8]. Nitrogen heterocyclic compounds containing oxygen atoms have an important place in pharmaceutical chemistry. In particular, isoxazole, which has a five-membered ring containing oxygen and nitrogen atoms, attracts attention due to its biological and medicinal

properties [9]. Many anti-inflammatory drugs such as flucloxacillin, dicloxacillin, cloxacillin and valdecoxib contain an isoxazole core in their structure (Figure 1).

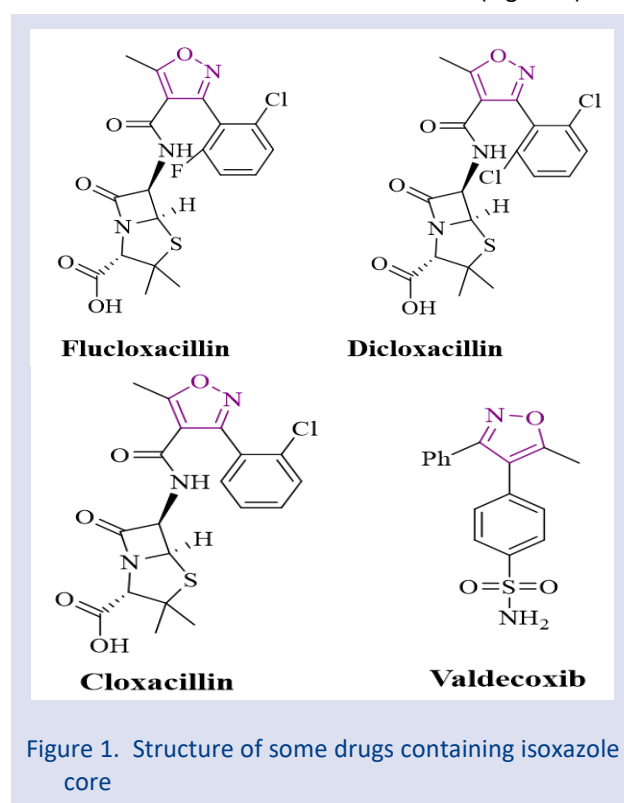


Figure 1. Structure of some drugs containing isoxazole core



Isoxazole has unsaturated double bonds and hydrogen bonds, and this unique structure makes it an important unit in the production of new compounds [9]. Valdecoxib (4-(5-methyl-3-phenyl-4-isoxazolyl) benzenesulfonamide, brand name Bextra, VLB) is an effective COX-2 inhibitor and is widely used for the treatment of pain, rheumatoid arthritis and inflammation [10]. Due to the selectivity of valdecoxib in inhibiting COX-2, different analogues were synthesized and their effects were investigated [11,12].

In general, drug design studies consist of a multi-step and time-consuming series of synthesis processes and in vivo testing steps. Then, promising compounds are investigated for their absorption, distribution, metabolism, excretion, and toxicity (ADMET) properties [13]. As the synthesis and bioactivity screenings of new drug candidates have increased significantly, the demands for the early determination of ADMET properties are also increasing. On the other hand, today, computer-aided quantum chemical calculations are frequently used to predict the values of interest for a particular molecule without performing experimental studies [14,15]. Therefore, the use of quantum chemical computational methods is very advantageous both to save time and to focus on the most promising drug candidates. Based on this information, in this study, it is aimed to perform comparative quantum chemical analysis of valdecoxib (VLB) molecule, which is a potent and selective COX-2 inhibitor, and its hydroxylated derivative (1H-VLB).

## Computational Details

The whole DFT computations of VLB and 1H-VLB were performed by using GAUSSIAN 16 software package [16]. Moreover, Gauss View 6 molecular visualization software [17] was utilized in order to visualize FMO plots and ESP maps. The geometry optimizations and frequency calculations of mentioned molecules were carried out in vacuum and also water phase by means of DFT/ B3LYP functional with 6-311++G(d,p) [18-20]. The universal SMD (Solvent Model based on Density) model was used to simulate the water phase ( $\epsilon=78.4$ ) [21]. Molinspiration Cheminformatics software [22] was used in order to calculate polar surface area (PSA), molecular volume and logPow values (logarithm of n-octanol/water partition coefficient) for lipophilicity evaluation. In addition, molecular lipophilicity potential (MLP) maps of studied molecules were visualized in Molinspiration Galaxy 3D Structure Generator v2018.01 beta [23].

In Koopmans' theorem, HOMO and LUMO energy values are associated with ionization energy (I) (Equation (1)) and electron affinity (A) (Equation (2)) [24]. In addition, kinetic stability and chemical reactivity predictions can be made by interpreting the energy gap value ( $\Delta E$ ) (Equation (3)) obtained from the difference of HOMO and LUMO energy values. HOMO-LUMO energy values are obtained from the molecular orbital energy levels. Therefore, if the HOMO and LUMO energies are known, parameters called quantum chemical reactivity identifiers, which ensure significant information about the

activity of the molecule, can be computed. The parameters, proposed by Parr et al. [25-29] and the corresponding formulas are given below (Equations (4)-(8)):

$$\text{Ionization Energy (I)} \quad I = -E_{HOMO} \quad (1)$$

$$\text{Electron Affinity (A)} \quad A = -E_{LUMO} \quad (2)$$

$$\text{Energy Gap } (\Delta E) \quad \Delta E = E_{LUMO} - E_{HOMO} \quad (3)$$

$$\text{Chemical Potential } (\mu) \quad \mu = \frac{E_{HOMO} + E_{LUMO}}{2} \quad (4)$$

$$\text{Chemical Hardness } (\eta) \quad \eta = \frac{I - A}{2} \quad (5)$$

$$\text{Softness (S)} \quad S = \frac{1}{2\eta} \quad (6)$$

$$\text{Electronegativity } (\chi) \quad \chi = \frac{I + A}{2} \quad (7)$$

$$\text{Electrophilicity index } (\omega) \quad \omega = \frac{\mu^2}{2\eta} \quad (8)$$

In another part of study, NBO analysis of mentioned molecules was explored with NBO 3.1 program integrated into Gaussian program by using B3LYP/6-311++G (d, p) level of theory. For each donor (i) and acceptor (j) NBO, the stabilization energy  $E^{(2)}$  value is calculated according to the formula as follows (Equation (9)):

$$E^{(2)} = \Delta E_{ij} = qi \left[ \frac{(F_{ij})^2}{(\epsilon_j - \epsilon_i)} \right] \quad (9)$$

$E^{(2)}$ : Stabilization energy.  $qi$ : Donor orbital occupancy.  $F_{ij}$ : off diagonal Fock matrix

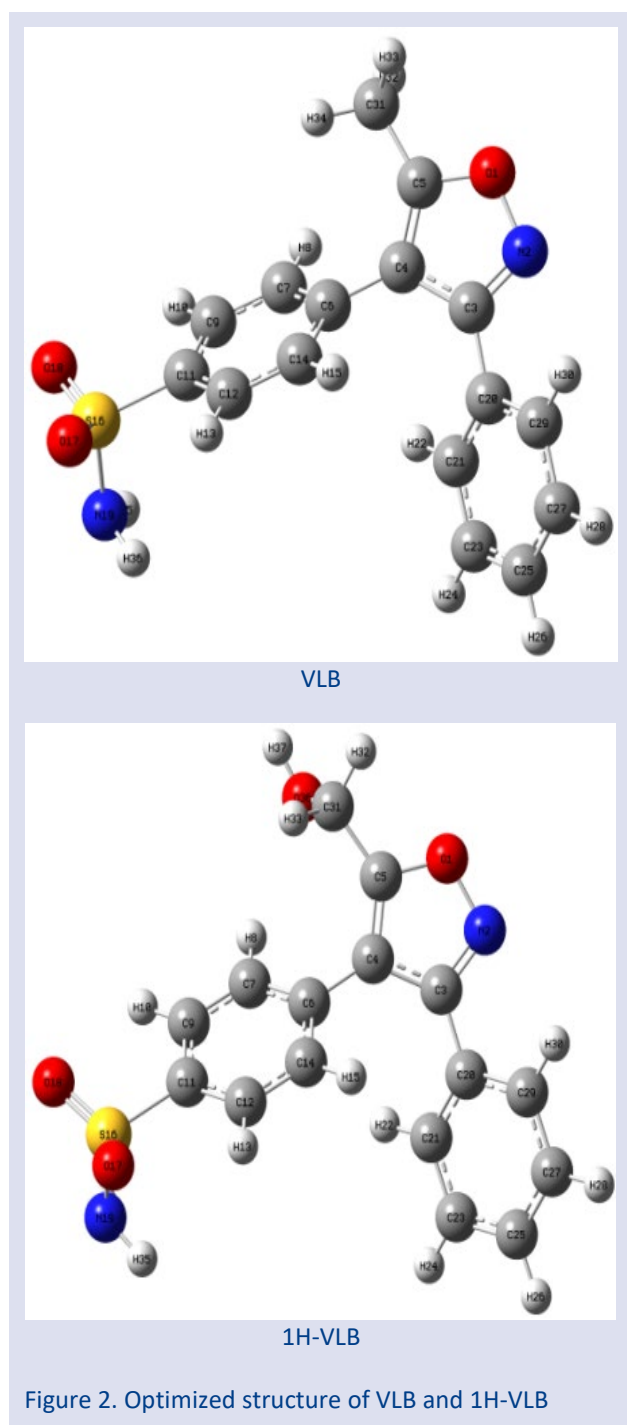
$\epsilon_i$  and  $\epsilon_j$ : diagonal element. donor and acceptor orbital energies

## Results and Discussion

### Molecular Structure and Vibrational Analysis

The crystal structure of valdecoxib was acquired from the Cambridge Crystallographic Data Center (CCDC 262463). It has Pbc<sub>a</sub> space group and orthorhombic crystal. The crystal structure parameters of VLB were found to be  $a = 12.872$  (2) Å,  $b = 9.282$  (3) Å,  $c = 24.761$  (7) Å, and  $V = 2958.4$  (14) Å<sup>3</sup> [30]. The optimized molecular structures of VLB and its 1-hydroxy analogue 1H-VLB with numbering and labeling scheme are represented in Figure 2. Structural parameters like bond lengths, bond angles, and dihedral angles of mentioned molecules were calculated by using B3LYP/6-311++G (d, p) level. 1H-VLB is a similar compound with VLB as structural features. Because of this, structural parameters of the 1H-VLB obtained from geometric optimization calculation checked with those of the crystal structure of the VLB. The selected experimental [30] and theoretical values are presented in Table 1.

According to Table 1, from the crystalline structure of VLB, the N2=C3 and C4=C5 bond lengths were determined as 1.317 Å and 1.347 Å, respectively. These values were calculated as 1.313 Å and 1.369 Å for VLB, 1.314 Å and 1.368 Å for 1H-VLB.



While the C3-C4 bond length was found to be 1.441 Å experimentally, it was calculated as 1.442 Å for VLB and 1H-VLB theoretically. Considering bond angles, while the bond angles of C5-O1-N2 and C3-N2-O1 were determined experimentally as 108.7° and 106.0°, they were calculated as 109.6° and 106.0° for VLB, 109.4° and 106.3° for 1H-VLB, respectively. For sulfonamide group, O17-S16-N19 and O18-S16-N19 bond angles were calculated as 105.4° and 105.3° for VLB and 105.4° for 1H-VLB. X-ray values of these angles were defined as 107.9° and 106.1° respectively. When all the bond length, bond angle, and dihedral angle values given in Table 1 are examined, it is striking that the calculation results are in good agreement with the experimental results.

Table 1. Selected geometric parameters of studied molecules

Bond Lengths (Å)	X-ray value	VLB	1H-VLB
O1-C5	1.348	1.346	1.345
O1-N2	1.404	1.395	1.389
N2-C3	1.317	1.313	1.314
C3-C4	1.441	1.442	1.442
C3-C20	1.479	1.477	1.478
C4-C5	1.347	1.369	1.368
C4-C6	1.482	1.475	1.473
C5-C31	1.486	1.487	1.490
C6-C14	1.391	1.404	1.404
C6-C7	1.385	1.402	1.404
C7-C9	1.382	1.391	1.392
C9-C11	1.383	1.392	1.393
C11-C12	1.384	1.394	1.394
C11-S16	1.768	1.803	1.804
S16-O17	1.424	1.457	1.457
S16-O18	1.430	1.458	1.457
S16-N19	1.603	1.681	1.682
Bond Angles (°)			
C5-O1-N2	108.7	109.6	109.4
C3-N2-O1	106.0	106.0	106.3
N2-C3-C4	110.8	111.2	111.1
N2-C3-C20	117.5	119.2	119.1
C4-C3-C20	131.6	129.6	129.8
C5-C4-C3	104.0	103.6	103.3
C5-C4-C6	125.8	127.1	126.9
C3-C4-C6	130.2	129.2	129.8
C4-C5-O1	110.5	109.6	110.0
C4-C5-C31	133.9	133.9	133.2
O1-C5-C31	115.5	116.5	116.8
O17-S16-O18	118.5	123.1	122.9
O17-S16-N19	107.9	105.4	105.4
O18-S16-N19	106.1	105.3	105.4
O17-S16-C11	107.7	107.4	107.4
O18-S16-C11	107.8	107.3	107.4
N19-S16-C11	108.6	107.5	107.5
Dihedral Angles (°)			
C5-O1-N2-C3	-0.7	-0.6	-0.4
O1-N2-C3-C4	0.4	0.6	0.2
O1-N2-C3-C20	179.1	179.9	179.4
N2-C3-C4-C5	0.1	-0.4	0.03
C20-C3-C4-C5	-178.4	-179.6	-179.0
N2-C3-C4-C6	-178.0	-177.2	-177.3
C20-C3-C4-C6	3.6	3.6	3.7
C6-C4-C5-O1	177.7	176.9	177.1
C3-C4-C5-C31	-177.2	-177.5	-178.9
S16-C11-C9-C7	-177.7	-179.2	-179.2
C25-C27-C29-C20	-0.1	0.1	0.2

Table 2 shows the experimental and calculated vibrational frequencies of studied molecules. Experimental data for VLB were obtained from reference [31]. The vibrational modes were multiplied by 0.983 for vibrations less than 1700 cm<sup>-1</sup> and the larger ones were multiplied by 0.958 scale factors for B3LYP/6-311++G (d,

p) level of theory [32]. According to Table 2, while the N-H stretching vibration of VLB experimentally arised at  $3377\text{ cm}^{-1}$  and  $3249\text{ cm}^{-1}$ , theoretically it was observed at  $3481\text{ cm}^{-1}$  and  $3371\text{ cm}^{-1}$  for VLB, and  $3480\text{ cm}^{-1}$  and  $3370\text{ cm}^{-1}$  for 1H-VLB. Symmetric and asymmetric stretching vibrations of S=O for VLB were calculated as  $1112\text{ cm}^{-1}$  and  $1312\text{ cm}^{-1}$ , respectively. Similarly, the same vibrations were calculated as  $1113\text{ cm}^{-1}$  and  $1313\text{ cm}^{-1}$  for 1H-VLB. It is known that O-H groups give a strong absorption peak in  $3700\text{-}3500\text{ cm}^{-1}$  [33]. The characteristic O-H stretching vibration for 1H-VLB was calculated as  $3667\text{ cm}^{-1}$ . In general, it was concluded that the calculated values complied with those of the experimental data.

Table 2. The experimental and calculated vibrational frequencies of VLB and 1H-VLB

Vibration	Exp. ( $\text{cm}^{-1}$ )	VLB	1H-VLB
N-H stretch	3377	3481	3480
	3249	3371	3370
N-H bend	1544	1555	1555
S=O asym stretch	1334	1312	1313
S=O sym stretch	1150	1112	1113
C-H stretch ( $\text{CH}_3$ )	2929	2999	3040
	2874	2908	3031
C-H stretch (Ar ring)	3091	3064	3066
O-H stretch	-	-	3667
C-H asym stretch ( $\text{CH}_2$ )	-	-	2932
C-H sym stretch ( $\text{CH}_2$ )	-	-	2888

### Thermodynamic Parameters

The physicochemical and thermodynamic parameters such as dipole moment, total energy, enthalpy and

entropy, have a crucial act in the assessment of the related chemical process in experimental and also theoretical sciences [34]. In the optimization process made with Gaussian software, the thermodynamic parameters of the chemical systems are also obtained. In this context, the results of the calculations for VLB and 1H-VLB in vacuum and water environment were given in Table 3.

It can be seen from Table 3 that the dipole moment (DM) and polarizability ( $\alpha$ ) values increase while passing from the vacuum medium to the water phase. Besides, it is seen that the heat capacity ( $C_v$ ) value increases from  $74.289\text{ cal/molK}$  to  $74.310\text{ cal/molK}$  for VLB, and from  $77.775\text{ cal/molK}$  to  $77.976\text{ cal/molK}$  for 1H-VLB while going from vacuum environment into water environment. Considering the entropy (S) values, it was observed that the entropy increased with the addition of an OH group to the structure of VLB. At the same time, it is clearly seen from the Table 3 that while the entropy value is calculated as  $146.971\text{ cal/molK}$  by decreasing for the VLB molecule in the water environment, the entropy for the 1H-VLB molecule is calculated as  $155.059\text{ cal/molK}$  by increasing in the water environment. Also, for VLB, the  $\Delta E$  values were calculated as  $-1351.384971\text{ a.u.}$  and  $-1351.417042\text{ a.u.}$  for vacuum and water phase, respectively.  $\Delta H$  and  $\Delta G$  values were also observed to give close results. Similarly, for 1H-VLB,  $\Delta E$  values were found as  $-1426.611857\text{ a.u.}$ ,  $-1426.651455\text{ a.u.}$  for vacuum and water medium whereas the  $\Delta H$  values were calculated as  $-1426.610913\text{ a.u.}$ ,  $-1426.650510\text{ a.u.}$ , respectively.

Table 3. The calculated physicochemical and thermodynamic parameters of studied molecules

	VLB		1H-VLB	
	Vacuum	Water	Vacuum	Water
DM (Debye)	3.78	5.57	3.08	3.85
$\Delta E$ (a.u.)	-1351.384971	-1351.417042	-1426.611857	-1426.651455
$\Delta H$ (a.u.)	-1351.384027	-1351.416098	-1426.610913	-1426.650510
$\Delta G$ (a.u.)	-1351.454246	-1351.485929	-1426.683527	-1426.724184
$\Delta E_{\text{thermal}}$ (kcal/mol)	183.528	183.143	187.498	187.051
$C_v$ (cal/molK)	74.289	74.310	77.775	77.976
S (cal/molK)	147.789	146.971	152.829	155.059
$\alpha$ (a.u.)	233.16	340.69	238.78	345.92
$\Delta E_{\text{solv}}$ (kJ/mol)	-	-84.20	-	-103.97
$\Delta H_{\text{solv}}$ (kJ/mol)	-	-84.20	-	-103.96
$\Delta G_{\text{solv}}$ (kJ/mol)	-	-83.18	-	-106.75

### HOMO-LUMO Analysis and Quantum Chemical Reactivity Identifiers

HOMOs (Highest Occupied Molecular Orbital) and LUMOs (Lowest Unoccupied Molecular Orbital), known as frontier molecular orbitals, play a substantial role in chemical reactivity as well as in UV-Vis absorption spectra and optical properties [35]. Besides, HOMO-LUMO diagrams which provide a visual advantage for the interpretation of the electronic properties of a wide variety of molecular systems in many fields are frequently used in computational chemistry [36]. The HOMO-LUMO

diagrams of VLB and 1H-VLB computed at B3LYP/6-311++G (d, p) level of theory corresponding to the vacuum and water medium are shown in the Figure 3 and Figure 4. For both molecules, it is clear that HOMO is spread over almost the entire molecule for not only gas phase but also water phase. Similarly, for both molecules, it is seen that LUMOs are predominantly concentrated on the benzenesulfonamide and isoxazole ring.

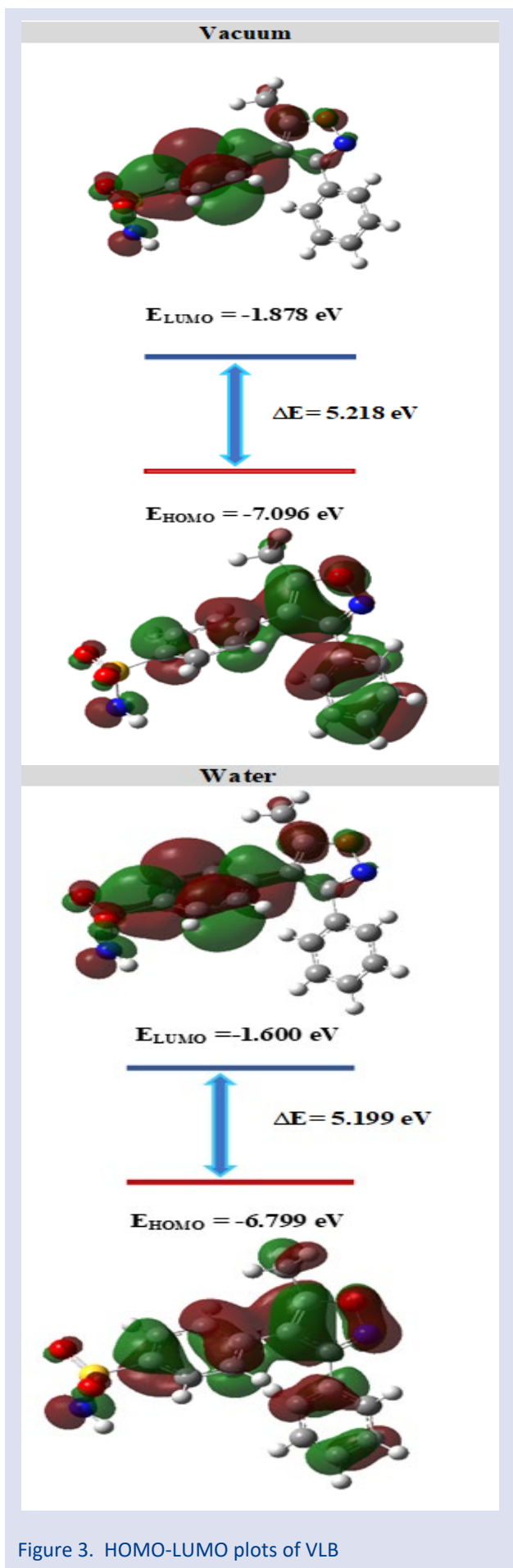


Figure 3. HOMO-LUMO plots of VLB

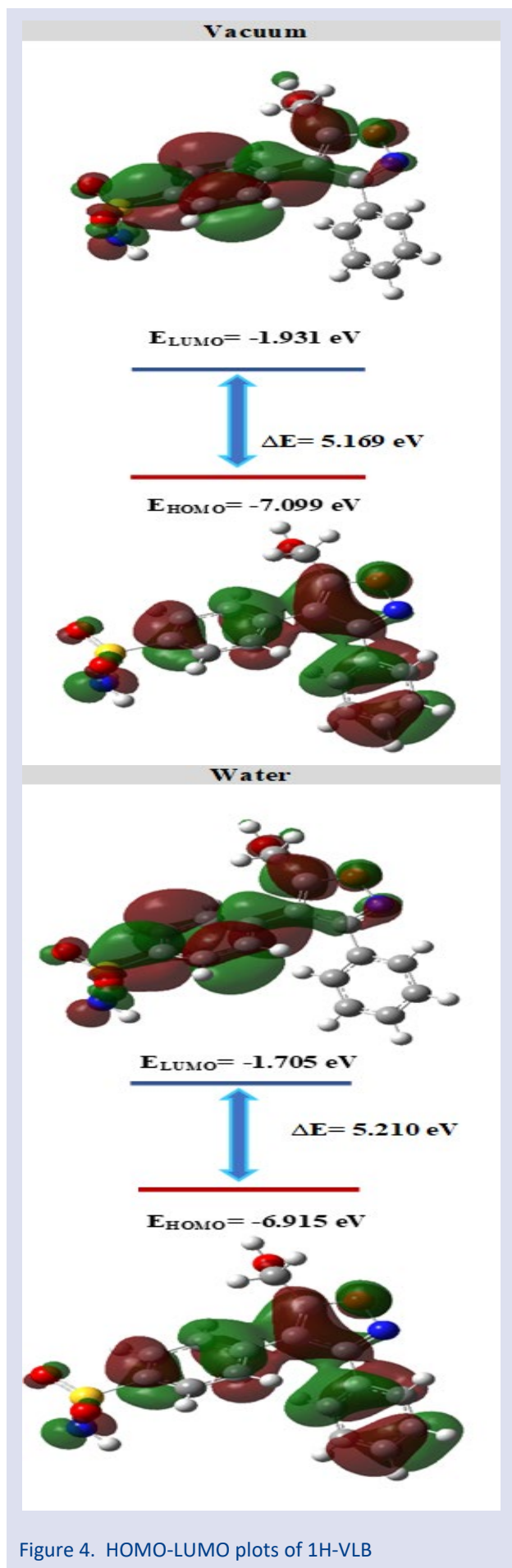


Figure 4. HOMO-LUMO plots of 1H-VLB

The calculated quantum chemical parameters for the vacuum and water environment of the studied molecules are listed in Table 4. According to Table 4, energy gap values were calculated as 5.218 eV and 5.199 eV for VLB in vacuum and water environment and as 5.169 eV and 5.210 eV for 1H-VLB, respectively. With the help of calculated quantum chemical reactivity identifiers of a given molecule, important information can be obtained about the general trend of its biological activity. There are several studies in the literature to explain the stability and

reactivity of molecules using quantum chemical computational methods. [37,38]. In this context, if we compare the bioactivity of VLB and 1H-VLB molecules in water based on quantum chemical reactivity identifiers, it is concluded that VLB molecule is more active for all parameters except ELUMO. The results obtained here support the conclusion that the VLB molecule has an excellent oral activity in animal models used to develop NSAIDs compared to the 1H-VLB molecule [12].

Table 4. Calculated quantum chemical parameters of studied molecules in eV (S: eV<sup>-1</sup>)

		E <sub>HOMO</sub>	E <sub>LUMO</sub>	ΔE	η	S	μ	χ	ω
Vacuum	VLB	-7.096	-1.878	5.218	2.609	0.192	-4.487	4.487	3.859
	1H-VLB	-7.099	-1.931	5.169	2.584	0.193	-4.515	4.515	3.944
Water	VLB	-6.799	-1.600	5.199	2.599	0.192	-4.200	4.200	3.393
	1H-VLB	-6.915	-1.705	5.210	2.605	0.192	-4.310	4.310	3.566

### Molinspiration Analysis

Rapid and accurate prediction of molecular transport properties is one of the principal agents speeding up the drug discovery and development process [39]. The parameter commonly used for this purpose is the n-octanol/water partition coefficient, which expresses lipophilicity. However, in recent years, several different descriptors have been introduced to predict the absorption, distribution, metabolism and excretion (ADME) characteristics of drug candidates. In particular, the limiting parameters known as Lipinski's rule of five have been very popular [40]. On the other hand, in this study, polar surface area (PSA) and molecular lipophilicity potential (MLP) descriptors, which are very useful parameters, were calculated separately for VLB and 1H-VLB. Physicochemical parameter computations were performed by means of Molinspiration cheminformatics software in order to evaluate the structure-activity relationships for VLB and its hydroxy analogue. The results are listed in Table 5. According to the Table 5, the numbers of hydrogen bond donors and acceptors increase with the addition of a hydroxy group to the VLB molecule. Similarly,

the molecular volume and polar surface area values were calculated as 263.55 Å<sup>3</sup> and 86.20 Å<sup>2</sup> for VLB, respectively, and increased to 271.81 Å<sup>3</sup> and 106.42 Å<sup>2</sup> for 1H-VLB.

Table 5. Molinspiration computations of molecular properties of studied molecules

	VLB	1H-VLB
PSA (Å <sup>2</sup> )	86.20	106.42
Volume (Å <sup>3</sup> )	263.55	271.81
LogP <sub>calc</sub>	2.73	2.09
Formula weight (g/mol)	314.37	330.37
Number of rotatable bonds	3	4
Number of H-bond donors	2	3
Number of H-bond acceptors	5	6

Furthermore, as a visual identifier of lipophilicity, the molecular lipophilicity potential (MLP) maps of studied molecules were illustrated in Figure 5. The MLP map defines the 3D distribution of hydrophilic/lipophilic potential on the molecular surface via color codes. 3D CPK images were used to make the MLP map more understandable in Figure 5.

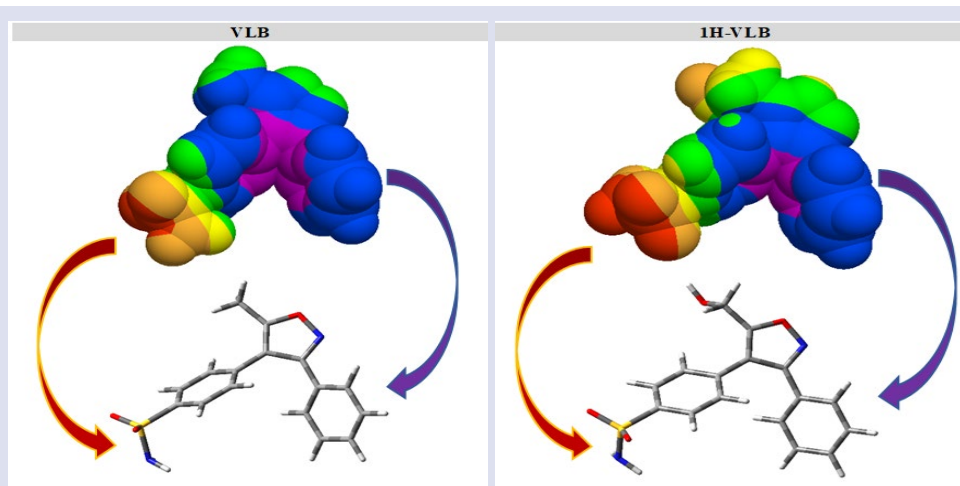


Figure 5. 3D CPK view of MLP maps of VLB and 1H-VLB

Orange and red regions represent hydrophilic surfaces, while regions coded with purple and blue indicate the most lipophilic surfaces. Additionally, regions coded in yellow and green indicate intermediate lipophilic surfaces. As can be seen from the MLP maps, the blue and purple regions in the VLB molecule are more intense than in 1H-VLB. On the other hand, in 1H-VLB molecule, it is observed that the area of the red and orange regions increases with the addition of the -OH group. Based on this information, it is concluded that the VLB molecule is more lipophilic than 1H-VLB. As can be seen from Table 5, while the  $\log P_{ow}$  value was calculated as 2.73 for VLB, it was calculated as 2.09 for 1H-VLB. Molinspiration calculation results indicate that phenyl rings of VLB and 1H-VLB support predominantly lipophilic interactions, and sulfonamide and hydroxyl groups support hydrophilic interactions.

### Mulliken Population Analysis

The total atomic charges of VLB and 1H-VLB obtained by Mulliken [41] population analysis with B3LYP/ 6-311++G (d, p)

level of theory were presented in Table 6 and Figure 6. Natural charges [42] are given in NBO analysis section. According to Mulliken population analysis, there are both positively charged and negatively charged carbon atoms in both structures. While the charges of C3 bound to N2 and C5 bound to O1 atoms were calculated as 0.168e and -0.212e for VLB, they were calculated as 0.504e and 0.106e for 1H-VLB, respectively. C6 and C20 atoms were found to have the highest positive charge of 0.578e and 1.362e for VLB, 0.550e and 1.402e for 1H-VLB, respectively. It was determined that while the charges of O1 and S16 atoms from O, S, and N heteroatoms in the structures were positive, N2, N19, O17, O18 and O36 atoms were negatively charged. Furthermore, it is clear from the Mulliken histogram that all hydrogens are positively charged. It was determined that H35 and H36 atoms attached to N19 in the VLB molecule have the highest positive value (0.286e and 0.287e) due to the electron withdrawing property of the nitrogen atom. The same is true for H34 and H35 atoms (0.286e and 0.287e) in the 1H-VLB molecule.

Table 6. Mulliken atomic charge values of VLB and 1H-VLB

Atom	VLB	1H-VLB	Atom	VLB	1H-VLB
O1	0.300	0.319	C20	1.362	1.402
N2	-0.459	-0.476	C21	-0.406	-0.434
C3	0.168	0.504	H22	0.167	0.168
C4	-0.315	-0.853	C23	-0.275	-0.282
C5	-0.212	0.106	H24	0.182	0.185
C6	0.578	0.550	C25	-0.356	-0.359
C7	-0.477	-0.594	H26	0.154	0.154
H8	0.208	0.275	C27	-0.294	-0.316
C9	-0.257	-0.224	H28	0.181	0.183
H10	0.265	0.259	C29	-0.049	0.067
C11	-0.214	-0.200	H30	0.218	0.220
C12	-0.394	-0.350	C31	-0.614	-0.676
H13	0.261	0.261	H32	0.199	0.189
C14	-0.553	-0.584	H33	0.181	0.166
H15	0.194	0.192	H34	0.154	0.286
S16	0.201	0.217	H35	0.286	0.287
O17	-0.178	-0.181	H36	0.287	-
O18	-0.188	-0.182	O36	-	-0.228
N19	-0.301	-0.303	H37	-	0.252

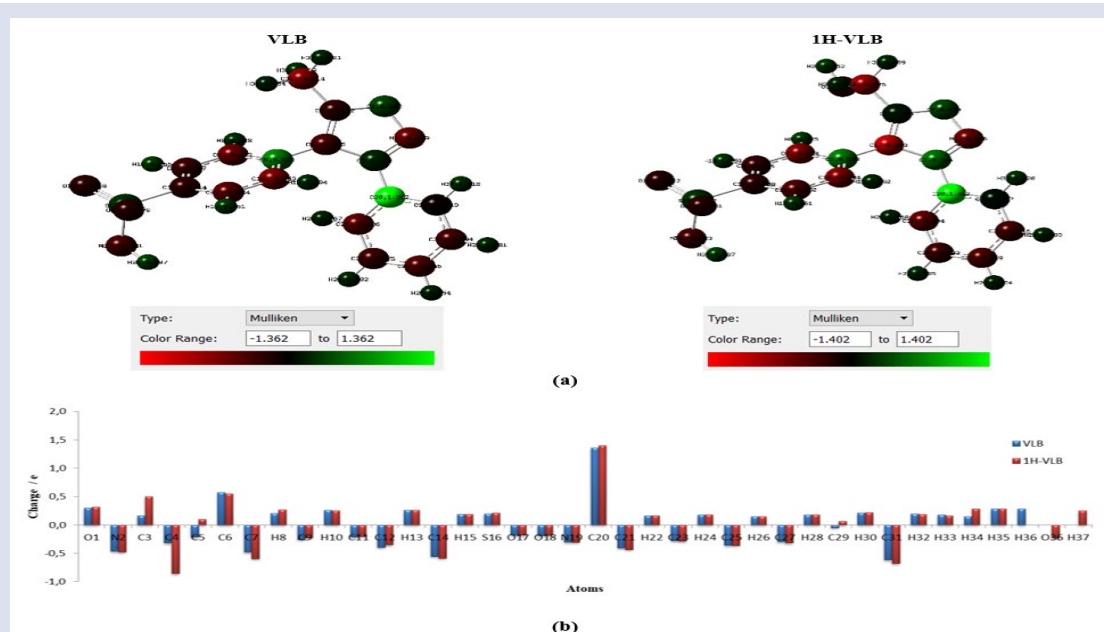


Figure 6. (a) Mulliken atomic charge distributions and (b) Mulliken histogram of VLB and 1H-VLB

**Natural Bond Orbital (NBO) Analysis**

The natural bond orbital (NBO) analysis ensures detailed information about interactions between donor and acceptor orbitals. In order to estimate stabilization energies ( $E^{(2)}$ ), second order Fock matrix is utilized [43, 44]. The stabilization energy,  $E^{(2)}$ , expresses the intensity of electron delocalization between the bonding (BD) or lone pair (LP) orbitals and anti-bonding (BD\*) orbitals. The

higher  $E^{(2)}$  value means that the interaction between the donor and acceptor orbitals is more intensive.

The calculated natural charges and effective valence electron configurations (NEC) for each atom except hydrogens of VLB and 1H-VLB are summarized in Table 7. Additionally, the second order perturbation theory results of Fock matrix in NBO basis for studied molecules are represented in Table 8 and Table 9.

Table 7. Summary of natural charges and natural electron configurations

VLB			1H-VLB		
Atom	Natural Charge	Natural Electron Configuration	Atom	Natural Charge	Natural Electron Configuration
O1	-0.32474	[core]2S <sup>1.62</sup> 2p <sup>4.68</sup> 3p <sup>0.01</sup> 3d <sup>0.01</sup>	O1	-0.31100	[core]2S <sup>1.62</sup> 2p <sup>4.67</sup> 3p <sup>0.01</sup> 3d <sup>0.01</sup>
N2	-0.13784	[core]2S <sup>1.48</sup> 2p <sup>3.63</sup> 3d <sup>0.01</sup> 4p <sup>0.01</sup>	N2	-0.12899	[core]2S <sup>1.48</sup> 2p <sup>3.62</sup> 3d <sup>0.01</sup> 4p <sup>0.01</sup>
C3	0.16930	[core]2S <sup>0.84</sup> 2p <sup>2.96</sup> 3d <sup>0.01</sup> 4p <sup>0.02</sup>	C3	0.16607	[core]2S <sup>0.84</sup> 2p <sup>2.96</sup> 3d <sup>0.01</sup> 4p <sup>0.02</sup>
C4	-0.18434	[core]2S <sup>0.86</sup> 2p <sup>3.30</sup> 3p <sup>0.01</sup> 4p <sup>0.01</sup>	C4	-0.14774	[core]2S <sup>0.86</sup> 2p <sup>3.26</sup> 4p <sup>0.01</sup>
C5	0.38330	[core]2S <sup>0.85</sup> 2p <sup>2.75</sup> 3p <sup>0.01</sup> 3d <sup>0.01</sup> 4p <sup>0.01</sup>	C5	0.35263	[core]2S <sup>0.85</sup> 2p <sup>2.77</sup> 3d <sup>0.01</sup> 4p <sup>0.02</sup>
C6	-0.02421	[core]2S <sup>0.86</sup> 2p <sup>3.15</sup> 3p <sup>0.01</sup>	C6	-0.04373	[core]2S <sup>0.87</sup> 2p <sup>3.15</sup> 4p <sup>0.01</sup>
C7	-0.18976	[core]2S <sup>0.94</sup> 2p <sup>3.23</sup> 4p <sup>0.01</sup>	C7	-0.18641	[core]2S <sup>0.95</sup> 2p <sup>3.22</sup> 4p <sup>0.01</sup>
C9	-0.19018	[core]2S <sup>0.95</sup> 2p <sup>3.22</sup> 4p <sup>0.01</sup>	C9	-0.19026	[core]2S <sup>0.95</sup> 2p <sup>3.22</sup> 4p <sup>0.01</sup>
C11	-0.28008	[core]2S <sup>0.98</sup> 2p <sup>3.27</sup> 4p <sup>0.02</sup>	C11	-0.27900	[core]2S <sup>0.98</sup> 2p <sup>3.27</sup> 4p <sup>0.02</sup>
C12	-0.18841	[core]2S <sup>0.95</sup> 2p <sup>3.22</sup> 4p <sup>0.01</sup>	C12	-0.19116	[core]2S <sup>0.95</sup> 2p <sup>3.23</sup> 4p <sup>0.01</sup>
C14	-0.17535	[core]2S <sup>0.94</sup> 2p <sup>3.22</sup> 4p <sup>0.01</sup>	C14	-0.17300	[core]2S <sup>0.94</sup> 2p <sup>3.22</sup> 4p <sup>0.01</sup>
S16	2.19601	[core]3S <sup>1.05</sup> 3p <sup>2.54</sup> 3d <sup>0.17</sup> 5p <sup>0.04</sup>	S16	2.19544	[core]3S <sup>1.05</sup> 3p <sup>2.54</sup> 3d <sup>0.17</sup> 5p <sup>0.04</sup>
O17	-0.90874	[core]2S <sup>1.83</sup> 2p <sup>5.07</sup> 3d <sup>0.01</sup>	O17	-0.90975	[core]2S <sup>1.83</sup> 2p <sup>5.07</sup> 3d <sup>0.01</sup>
O18	-0.91026	[core]2S <sup>1.83</sup> 2p <sup>5.07</sup> 3d <sup>0.01</sup>	O18	-0.91029	[core]2S <sup>1.83</sup> 2p <sup>5.07</sup> 3d <sup>0.01</sup>
N19	-1.02481	[core]2S <sup>1.50</sup> 2p <sup>4.50</sup> 3p <sup>0.01</sup>	N19	-1.02457	[core]2S <sup>1.50</sup> 2p <sup>4.50</sup> 3p <sup>0.01</sup>
C20	-0.08117	[core]2S <sup>0.86</sup> 2p <sup>3.20</sup> 4p <sup>0.01</sup>	C20	-0.08331	[core]2S <sup>0.86</sup> 2p <sup>3.20</sup> 4p <sup>0.01</sup>
C21	-0.17228	[core]2S <sup>0.93</sup> 2p <sup>3.23</sup> 4p <sup>0.01</sup>	C21	-0.17060	[core]2S <sup>0.93</sup> 2p <sup>3.22</sup> 4p <sup>0.01</sup>
C23	-0.20539	[core]2S <sup>0.95</sup> 2p <sup>3.24</sup> 4p <sup>0.01</sup>	C23	-0.20512	[core]2S <sup>0.95</sup> 2p <sup>3.23</sup> 4p <sup>0.01</sup>
C25	-0.19220	[core]2S <sup>0.95</sup> 2p <sup>3.22</sup> 4p <sup>0.01</sup>	C25	-0.19142	[core]2S <sup>0.95</sup> 2p <sup>3.22</sup> 4p <sup>0.01</sup>
C27	-0.20359	[core]2S <sup>0.95</sup> 2p <sup>3.23</sup> 4p <sup>0.01</sup>	C27	-0.20362	[core]2S <sup>0.95</sup> 2p <sup>3.23</sup> 4p <sup>0.01</sup>
C29	-0.15533	[core]2S <sup>0.93</sup> 2p <sup>3.21</sup> 4p <sup>0.01</sup>	C29	-0.15601	[core]2S <sup>0.93</sup> 2p <sup>3.21</sup> 4p <sup>0.01</sup>
C31	-0.62508	[core]2S <sup>1.09</sup> 2p <sup>3.53</sup>	C31	-0.07752	[core]2S <sup>1.01</sup> 2p <sup>3.05</sup> 3p <sup>0.01</sup> 4S <sup>0.01</sup> 3d <sup>0.01</sup>
			O36	-0.72760	[core]2S <sup>1.69</sup> 2p <sup>5.02</sup> 3p <sup>0.01</sup>

Table 8. Second-order perturbation theory results of Fock matrix in NBO basis for VLB

Donor(i)	ED <sub>i</sub> /e	Acceptor(j)	ED <sub>j</sub> /e	E <sup>(2)</sup> kcal/mol	E(j)-E(i)/a.u	F(i,j)/a.u
π N2-C3	1.90673	π* C4-C5	0.28248	8.27	0.36	0.051
		π* C20-C21	0.36957	5.20	0.36	0.042
π C4-C5	1.78536	π* N2-C3	0.31719	26.03	0.29	0.080
		π* C6-C7	0.35208	6.74	0.30	0.041
π C6-C7	1.63703	π* C9-C11	0.38412	24.03	0.27	0.072
		π* C12-C14	0.29223	18.31	0.28	0.065
π C9-C11	1.68575	π* C6-C7	0.35208	16.70	0.30	0.064
		π* C12-C14	0.29223	21.20	0.30	0.071
σ S16-O18	1.98735	π* C23-C25	0.33092	9.41	0.61	0.074
σ C20-C21	1.96888	π* C23-C25	0.33092	13.34	0.33	0.064
π C23-C25	1.65558	π* C20-C21	0.36957	21.01	0.28	0.069
π C27-C29	1.65536	π* C20-C21	0.36957	20.37	0.28	0.068
LP (2) O1	1.70777	π* N2-C3	0.31719	16.36	0.42	0.074
LP (2) O17	1.81964	σ* C11-S16	0.20565	15.54	0.44	0.074
		σ* S16-N19	0.23205	11.04	0.41	0.061
LP (3) O17	1.78060	σ* S16-N19	0.23205	13.21	0.52	0.074
LP (2) O18	1.82021	σ* C11-S16	0.20565	16.15	0.44	0.076
		σ* S16-N19	0.23205	10.92	0.41	0.061
LP (3) O18	1.78122	σ* S16-N19	0.23205	13.69	0.41	0.067
LP (1) N19	1.92211	σ* C11-S16	0.20565	5.33	0.49	0.047

According to Table 8 and Table 9, it is observed that there are interactions between the same donor-acceptor orbitals for VLB and 1H-VLB molecules and the stabilization energies are close to each other.

For example, the stabilization energies for the interactions between the  $\pi$  (N2-C3) donor and the  $\pi^*$  (C4-C5) acceptor orbital were calculated as 8.27 kcal/mol for VLB and 9.10 kcal/mol for 1H-VLB. Similarly, another interaction is between  $\pi$  (C4-C5)  $\rightarrow$   $\pi^*$  (N2-C3) orbitals and stabilization energies are calculated as 26.03 kcal/mol

for VLB and 24.65 kcal/mol for 1H-VLB. Furthermore, this interaction is the strongest observed for the VLB molecule. For 1H-VLB, the strongest interaction is observed between  $\pi$  (C23-C25) donor orbital ( $E_{Di} = 1.65380e$ ) and  $\pi^*$ (C20-C21) acceptor orbital ( $E_{Dj} = 0.36972e$ ) with stabilization energy of 64.68 kcal/mol. For VLB,  $E(2)$  of this interaction was calculated as 21.01 kcal/mol. In addition, the most important lone pair interactions were given in Table 8 and 9 for both molecules.

Table 9. Second-order perturbation theory results of Fock matrix in NBO basis for 1H-VLB

Donor(i)	$E_{Di}/e$	Acceptor(j)	$E_{Dj}/e$	$E^{(2)}$ kcal/mol	$E(j)-E(i)/a.u$	$F(i,j)/a.u$
$\sigma$ N2-C3	1.98612	$\pi^*$ C20-C21	0.36972	7.98	0.76	0.077
$\pi$ N2-C3	1.89731	$\pi^*$ C4-C5	0.28104	9.10	0.37	0.054
		$\sigma^*$ S16-O17	0.14138	9.35	0.44	0.058
		$\pi^*$ C20-C21	0.36972	11.39	0.23	0.049
$\pi$ C4-C5	1.77906	$\pi^*$ N2-C3	0.31513	24.65	0.29	0.078
		$\pi^*$ C6-C7	0.35105	7.41	0.31	0.044
$\pi$ C9-C11	1.68516	$\pi^*$ C6-C7	0.35105	16.72	0.30	0.064
		$\pi^*$ C12-C14	0.29410	20.58	0.30	0.071
$\pi$ C12-C14	1.65250	$\pi^*$ C6-C7	0.35105	21.08	0.29	0.069
		$\pi^*$ C9-C11	0.38450	19.78	0.27	0.066
$\pi$ C20-C21	1.65008	$\pi^*$ N2-C3	0.31513	12.36	0.26	0.051
		$\pi^*$ C23-C25	0.33041	19.83	0.29	0.068
$\sigma$ C21-C23	1.97641	$\sigma^*$ S16-O17	0.14138	21.36	0.88	0.126
$\pi$ C23-C25	1.65380	$\pi^*$ C20-C21	0.36972	64.68	0.14	0.086
$\sigma$ C25-H26	1.98041	$\pi^*$ C20-C21	0.36972	20.29	0.44	0.093
$\pi$ C27-C29	1.65456	$\pi^*$ C20-C21	0.36972	38.80	0.14	0.066
		$\pi^*$ C23-C25	0.33041	20.78	0.28	0.069
$\sigma$ C31-O36	1.98988	$\sigma^*$ S16-N19	0.23220	13.34	0.83	0.099
$\sigma$ O36-H37	1.98738	$\sigma^*$ S16-N19	0.23220	19.95	0.49	0.094
LP (2) O1	1.69685	$\pi^*$ N2-C3	0.31513	14.10	0.38	0.066
		$\pi^*$ C4-C5	0.28104	29.77	0.40	0.098
		$\sigma^*$ S16-O17	0.14138	15.76	0.47	0.080
LP (2) O17	1.82000	$\sigma^*$ C11-S16	0.20522	16.41	0.44	0.076
		$\sigma^*$ S16-N19	0.23220	11.77	0.39	0.061
LP (3) O17	1.78106	$\pi^*$ C20-C21	0.36972	11.43	0.19	0.043
LP (2) O18	1.82016	$\sigma^*$ S16-N19	0.23220	21.00	0.41	0.083
		$\pi^*$ C20-C21	0.36972	24.42	0.19	0.065
LP (3) O18	1.78136	$\sigma^*$ S16-O17	0.14138	28.43	0.39	0.096
		$\sigma^*$ S16-N19	0.23220	14.30	0.39	0.067

### Molecular Electrostatic Potential (MEP) Surfaces

Interpretation of molecular electrostatic potential (MEP) surface maps obtained by quantum chemical methods is seen as one of the effective ways to evaluate

the chemical reactivity of a molecule towards positively or negatively charged reagents [45].

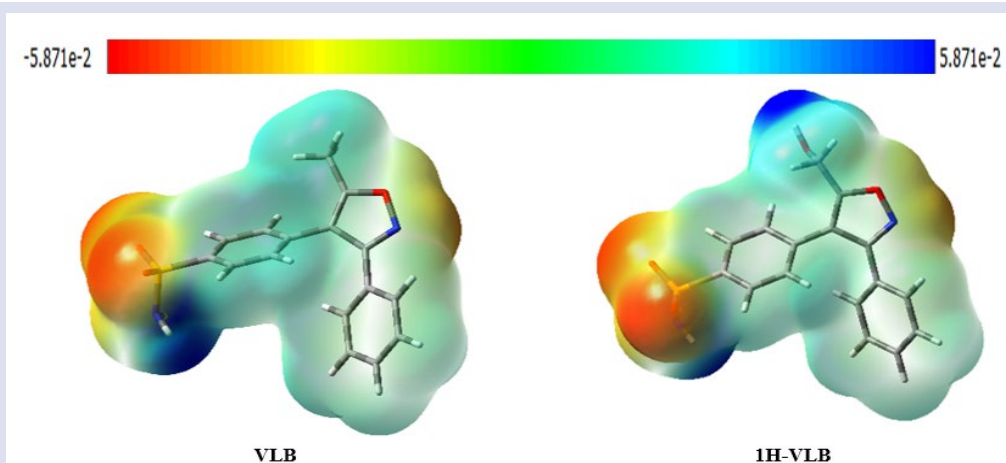


Figure 7. 3D molecular mapped surfaces of studied molecules at B3LYP/6-311++G (d, p) level



Figure 7 shows the MEP maps of studied molecules at B3LYP/6-311++G (d, p) theory level. In 3D charge distribution of MEP, nucleophilic centers are shown in blue, while electrophilic centers are shown in red. The electrostatic potential decreases according to the order blue > green > yellow > orange > red. The MEP maps of the mentioned molecules are in the ranges  $-0.05871$  a. u. (red) and  $+0.05871$  a. u. (blue). From Figure 7, it is seen that the region with the highest electron density is around the oxygen O17 and O18 atoms. On the other hand, the positive regions are the regions where the blue color intensity is the majority on the hydrogen atoms. The N-H and O-H regions show the regions with the lowest electron density.

## Conclusions

In this study, inspired by studies to identify drug candidates with potent and specific anti-inflammatory properties, quantum chemical computations for both vacuum and water phase were performed on valdecoxib and its active metabolite, hydroxy valdecoxib compounds. The results obtained from this research study can be presented as follows:

- Structural parameters calculated at the theory level of B3LYP/6-311++G (d, p) and FT-IR analysis results are in good agreement with the experimental results.
- When the bioactivity of VLB and 1H-VLB molecules were compared based on quantum chemical reactivity identifiers, it was concluded that all parameters except  $E_{LUMO}$  supported the conclusion that VLB molecule was more active.
- Molinspiration calculation results indicate that phenyl rings of VLB and 1H-VLB support predominantly lipophilic interactions, and sulfonamide and hydroxyl groups support hydrophilic interactions.
- The changes in atomic charges with the addition of an -OH group to the structure of VLB were investigated by Mulliken population analysis.
- In the next segment, second-order perturbative predictions of interactions between donor-acceptor (bond-antibond) orbitals on the basis of NBO were presented. Accordingly, for VLB, the strongest interaction is observed between  $\pi$  (C4-C5)  $\rightarrow$   $\pi^*$  (N2-C3) orbitals with stabilization energy of 26.03 kcal/mol. On the other hand, for 1H-VLB, the strongest interaction is observed between  $\pi$  (C23-C25) donor orbital ( $ED_i = 1.65380e$ ) and  $\pi^*$  (C20-C21) acceptor orbital ( $ED_j = 0.36972e$ ) with stabilization energy of 64.68 kcal/mol.
- From the molecular electrostatic potential maps, it is seen that the regions with the highest electron density are around the oxygen O17 and O18 atoms, while the regions with the lowest electron density are concentrated around the N-H and O-H atoms.

It was concluded that the results obtained from this study are quite compatible with the literature and support each other.

## Acknowledgment

The numerical calculations reported in this paper were fully performed at TUBITAK ULAKBIM, High Performance and Grid Computing Center (TRUBA resources).

## Conflicts of interest

The authors declare that they have no conflict of interest.

## References

- [1] Vane J.R., Inhibition of Prostaglandin Synthesis as a Mechanism of Action for Aspirin-like Drugs, *Nature New Biol.*, 231 (1971) 232–235.
- [2] Fu J. R., Masferrer J. L., Seibert K., Raz A., Needleman P., The induction and suppression of prostaglandin H2 synthase (cyclooxygenase) in human monocytes, *J. Biol. Chem.*, 265 (1990) 265 16737-16740.
- [3] Battistini B., Botting B., Bakhle Y., SCOX-1 and COX-2: Toward the development of more selective NSAIDs, *Drug News Perspect.*, 7 (1994) 501.
- [4] Sayed G., Abou-seri S.M., Kamel G., Moawad M., Celecoxib analogs bearing ben-zofuran moiety as cyclooxygenase-2 inhibitors: design, synthesis and evaluation as potential anti-inflammatory agents, *Eur. J. Med. Chem.*, 76 (2014) 482–493.
- [5] Abdelall E.K.A., Lamie P.F., Ahmed A.K.M., El-nahass E., COX-1/COX-2 inhibition assays and histopathological study of the new designed anti-inflammatory agent with a pyrazolopyrimidine core, *Bioorg. Chem.*, 86 (2019) 235–253.
- [6] Raz A., Wyche A., Siegel N., Needleman P., Regulation of fibroblast cyclooxygenase synthesis by interleukin-1, *J. Biol. Chem.*, 263 (1988) 263 3022-3028.
- [7] Wang C., Chen F., Qian P., Cheng J., Recent advances in the Rh-catalyzed cascade arene C–H bond activation/annulation toward diverse heterocyclic compounds, *Org. Biomol. Chem.*, 19 (2021) 1705-1721.
- [8] Mermer A., Keleş T., Şirin Y., Recent studies of nitrogen containing heterocyclic compounds as novel antiviral agents: A review, *Bioorg. Chem.*, 114 (2021) 105076.
- [9] Zhu Jun J., Hong-zhi M., Yao L., Chen Y., Sun H., The recent progress of isoxazole in medicinal chemistry, *Bioorg. Med. Chem.*, 26 (2018) 3065–3075.
- [10] Scheen A.J., Malaise M., Le médicament du mois. Valdecoxib (Bextra), *Rev. Med. Liege*, 59 (2004) 251-254.
- [11] Erdelyi P., Fodor t., Varga A.K., Czugler M., Gere A., Fischer J., Chemical and biological investigation of N-hydroxy-valdecoxib: An active metabolite of valdecoxib, *Bioorg. Med. Chem.*, 16 (2008) 5322–5330.
- [12] Talley J.J., Brown D.L., Carter J.S., Graneto M.J., Koboldt C.M., Masferrer J.L., Perkins W.E., Rogers R.S., Shaffer A.F., Zhang Y.Y., Zweifel B.S., Seibert K., 4-[5-Methyl-3-phenylisoxazol-4-yl]-benzenesulfonamide, Valdecoxib: A potent and selective inhibitor of COX-2, *J. Med. Chem.*, 43 (2000), 775-777.
- [13] Van De Waterbeemd H., Gifford E., ADMET in silico modelling: towards prediction paradise?, *Nat. Rev. Drug Discov.*, 3 (2003) 192-204.

- [14] Borges R. M., Colby S. M., Das S., Edison A. S., Fiehn O., Kind T., Lee J., Merrill A. T., Merz K. M. Jr., Metz T. O., Nunez J. R., Tantillo D. J., Wang L. P., Wang S., Renslow R. S., Quantum chemistry calculations for metabolomics, *Chem. Rev.*, 121 (2021), 5633–5670.
- [15] Genç F., Kandemirli S. G., Kandemirli F., Theoretical B3LYP study on electronic structure of contrast agent iopamidol, *Acta Chim. Slov.*, 68 (2021) 320-331.
- [16] Frisch M.J., Trucks G.W., Schlegel H.B., Scuseria G.E., Robb M.A., Cheeseman J.R., Scalmani G., Barone V., Petersson G.A., Nakatsuji H., et.al., Gaussian 16 Rev. B.01, Wallingford, CT, 2016.
- [17] Dennington R., Keith T.A., Millam J.M., GaussView, Version 6 Semichem Inc., Shawnee Mission, KS, 2016.
- [18] Becke A.D., A new mixing of Hartree–Fock and local density-functional theories, *J. Chem. Phys.*, 98 (1993) 1372–1377.
- [19] Lee C., Yang W., Parr R.G., Development of the Colle-Salvetti correlation-energy formula into a functional of the electron density, *Phys. Rev. B.*, 37 (1988) 785–789.
- [20] Becke A.D., Density-functional thermochemistry. III. The role of exact exchange, *J. Chem. Phys.*, 98 (1993) 5648–5652.
- [21] Marenich A.V., Cramer C.J., Truhlar D.G., universal solvation model based on solute electron density and on a continuum model of the solvent defined by the bulk dielectric constant and atomic surface tensions, *J. Phys. Chem. B.*, 113 (8) (2009) 6378-6396.
- [22] Molinspiration Cheminformatics free web services, <https://www.molinspiration.com>, Slovensky Grob, Slovakia.
- [23] Gaillard P., Carrupt P.A., Testa B., Boudon A., Molecular lipophilicity potential, a tool in 3D QSAR: method and applications, *J. Comput. Aided Mol. Des.*, 8 (1994) 83–96.
- [24] Koopmans T., Über die zuordnung von wellenfunktionen und eigenwerten zu den einzelnen elektronen eines atoms, *Physica*, 1(6) (1934) 104-113.
- [25] Parr R. G., Pearson R. G., Absolute hardness: companion parameter to absolute electronegativity, *J. Am. Chem. Soc.*, 105 (1983) 7512-7516.
- [26] Pearson R. G., Absolute electronegativity and hardness correlated with the molecular orbital theory, *Proc. Natl. Acad. Sci. U.S.A.*, 83 (1986) 8440-8441.
- [27] Parr R. G., Szentpaly L. V., Liu, S., Electrophilicity Index, *J. Am. Chem. Soc.*, 121 (1999) 1922-1924.
- [28] Perdew J. P., Levy M., Physical content of the exact Kohn-Sham orbital energies: band gaps and derivative discontinuities, *Phys. Rev. Lett.*, 51(20) (1983). 1884-1887.
- [29] Perdew J. P., Parr R. G., Levy M., Balduz J. L. Jr., Density functional theory for fractional particle number: derivative discontinuities of the energy, *Phys. Rev. Lett.*, 49 (23) (1982) 1691-1694.
- [30] Malathy Sony S. M., Charles P., Ponnuswamy M. N., Yathirajan H. S., Valdecobix, a non-steroidal anti-inflammatory drug, *Acta Cryst.*, 61 (2005) 108-110.
- [31] Kaushal A.M., Chakraborti A.K., Bansal A.K., FTIR Studies on differential intermolecular association in crystalline and amorphous states of structurally related non-steroidal anti-inflammatory drugs, *Molecular Pharmaceutics*, 6 (2008) 937–945.
- [32] Sundaraganesan N., Ilakiamani S., Salem H., Wojciechowski P. M., Michalska D., FT-Raman and FT-IR spectra, vibrational assignments and density functional studies of 5-bromo-2-nitropyridine, *Spectrochim. Acta A Mol. Biomol. Spectrosc.*, 61 (2005) 2995–3001.
- [33] Anı K., Vibrational Spectra of 4-hydroxy-3-cyano-7-chloroquinoline by density functional theory and ab initio Hartree-Fock Calculations, *Int. J. Chem. Technol.*, 1 (2017) 24-29.
- [34] Erdoğan M., Serdaroglu G., New Hybrid (E)-4-((pyren-1-ylmethylene) amino)-N-(thiazol-2-yl)benzenesulfonamide as a potential drug candidate: Spectroscopy, TD-DFT, NBO, FMO, and MEP studies, *ChemistrySelect*, 6 (2021) 9369–938.
- [35] Fukui K., Role of frontier orbitals in chemical reactions, *Science.*, 218 (1982) 747–754.
- [36] Baybas D., Serdaroglu G., Semerci B., The composite microbeads of alginate, carrageenan, gelatin, and poly(lactic-co-glycolic acid): Synthesis, characterization and density functional theory calculations, *Int. J. Biol. Macromol.*, 181 (2021) 322–338.
- [37] Sayin K., Üngördü A., Investigations of structural, spectral and electronic properties of enrofloxacin and boron complexes via quantum chemical calculation and molecular docking, *Spectrochim. Acta A Mol. Biomol. Spectrosc.*, 220 (2019)117102.
- [38] Brahmia A., Bejaoui L., Rolicek J., Hassen R.B., Serdaroglu G., Kaya S., Synthesis, crystal structure, Hirshfeld surface analysis and DFT calculations of 2, 2, 2-tribromo-1-(3,5-dibromo-2-hydroxyphenyl)ethanone, *J. Mol. Struct.*, 1248 (2022) 131313.
- [39] Blake J. F., Chemoinformatics - predicting the physicochemical properties of 'drug-like' molecules, *Curr. Opin. Biotechnol.*, 11 (2000) 104-107.
- [40] Lipinski C. A., Lombardo F., Dominy B. W., Feeney, P. J., Experimental and computational approaches to estimate solubility and permeability in drug discovery and development settings, *Adv. Drug Delivery Rev.*, 23 (1997) 3-25.
- [41] Mulliken R.S., Electron population analysis on LCAO-MO molecular wave functions, *J. Chem. Phys.*, (1955) 1833-1841.
- [42] Reed A.E., Weinstock R.B., Weinhold F., Natural atomic orbitals and natural population analysis, *J. Chem. Phys.*, 83 (1985) 735–746.
- [43] Weinhold F., Landis C.R., Glendening E.D., What is NBO analysis and how is it useful?, *Int. Rev. Phys. Chem.*, 35 (2016) 399-440.
- [44] Reed A.E., Curtiss L.A., Weinhold F., Intermolecular interactions from a natural bond orbital, donor-acceptor viewpoint, *Chem. Rev.*, 88(1988) 899-926.
- [45] Murray J.S., Politzer P., The electrostatic potential: an overview, *Wiley Interdiscip. Rev. Comput. Mol. Sci.*, 1 (2011) 153-163.

## Investigation of In Vitro Effect and Molecular Docking of Aluminum on Glucose-6-Phosphate Dehydrogenase Activity

Dilara Ülger Özbek <sup>1,a,\*</sup>, Deniz Kuruçay <sup>2,b</sup>

<sup>1</sup> Advanced Technology Research and Application Center, Sivas Cumhuriyet University, Sivas, Türkiye

<sup>2</sup> Biochemistry Laboratory, Medical Faculty Hospital, Sivas Cumhuriyet University, Sivas, Türkiye

\*Corresponding author

### Research Article

#### History

Received: 17/03/2021

Accepted: 28/05/2022

#### Copyright



©2022 Faculty of Science,  
Sivas Cumhuriyet University

### ABSTRACT

Aim: Aluminum is one of the elements that is widely used in many sectors and is the most abundant element in nature. The harm of aluminum, which was thought to be harmless until recently and is actively used in daily life, is open to discussion. In this study, it was aimed to investigate the effect of Aluminum Sulphate [Al<sub>2</sub>(SO<sub>4</sub>)<sub>3</sub>] on Glucose-6-Phosphate Dehydrogenase (G6PDH) activity, which is a key enzyme that catalyzes the first step of the pentose phosphate pathway (PPF). In addition, enzyme activity are detailed with molecular docking studies. For the purpose of examining in vitro effect of Aluminium on G6PDH, 4 different concentration of substrate (D-glucose-6-P) (0.1M, 0.08M, 0.05M, 0.03M) prepared and 10mM, 30mM Al<sub>2</sub>(SO<sub>4</sub>)<sub>3</sub> was added G6PDH envoriment. G6PDH activity was measured by spectrofotometrically. Molecular docking studies were performed with DockingServer and HEX 8.0.0 programs. With the data obtained, the Vmax of G6PDH was calculated as 3.33 and Km=0.0323. When 10 mM and 30mM Al<sub>2</sub>(SO<sub>4</sub>)<sub>3</sub> were added to the reaction environment, it was observed that there was a decrease in enzyme activity by 24.92% and 57.06%, respectively. It was observed that the increase in Al<sub>2</sub>(SO<sub>4</sub>)<sub>3</sub> concentration was an uncompetitive inhibition due to a significant decrease in both Km and Vmax values of the enzyme.

**Keywords:** Aluminium, Glucose 6-Phosphat dehydrogenase, Uncompetitive inhibition, Enzyme.

[dilaraulger@cumhuriyet.edu.tr](mailto:dilaraulger@cumhuriyet.edu.tr)

<https://orcid.org/0000-0002-6834-020X>

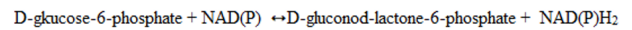
[denizkirucay@gmail.com](mailto:denizkirucay@gmail.com)

<https://orcid.org/0000-0002-9255-3301>

## Introduction

Nowadays, the rapid development of industry, the change in production methods in agriculture (use of artificial fertilizers, pesticides, etc.), the unhealthy storage of solid wastes and wastewater, and the contamination of some heavy minerals used in food storage conditions to living things [1]. Aluminum (Al) is widely used in many industrial fields (electricity, petroleum, chemistry, space, furniture, household), food and pharmaceutical industries. Al is taken into the body through diet, respiration and skin [2,3]. Normally, the accumulation of Al in the body is prevented, but in pathological conditions, the body Al load increases and leads to toxicity [4]. Most of the Al in the body is excreted through the urine. Studies have shown that Al accumulates in tissues such as liver, kidney, brain and lung in renal dysfunction and in some pathological conditions [5,6]. Although Al is one of the most abundant elements in nature, many of its forms are not harmful to living things. However, it turns into harmful derivatives at low pH [7,8]. It is reported that the accumulation of Al and its derivatives in the body plays an important role in the pathogenesis of many diseases, especially Alzheimer's [3,9].

Glucose-6-Phosphate Dehydrogenase (EC 1.1.1.49) is an important enzyme with its coenzyme NADP<sup>+</sup>, which plays a role in the rate-limiting step of PFY [10] and is widely found in all tissues and erythrocyte cells (RBC).



G6PDH enzyme deficiency is the most common hereditary enzyme deficiency in the world [11]. G6PDH deficiency, which is the most common and clinically important enzyme in the world, causes hemolytic anemia [12]. Since changes in this enzyme activity will negatively affect metabolism, it is of vital importance.

Molecular docking process allows to examine the biological activities and enzyme inhibition properties of molecules at the molecular level. With the molecular docking process, the interactions between the minimalized protein structure of cell lines and the drug candidate can be examined at the molecular level. By molecular docking, the binding energies, binding modes and types of secondary chemical interactions between the target protein and the molecule under study can be determined [13].

In this study, it was aimed to investigate the in vitro effect of Al and its derivatives, which are widely used in various pharmaceutical, food, agriculture and many industrial areas, on the vitally important G6PDH enzyme activity. Molecular docking studies are of great importance in cell biology, as they are performed by interacting a target protein or enzyme (cell line) with a ligand molecule. It is a key step in drug development. The docking results can be used to find the inhibitor of the

target protein and the biological activities of the studied chemical species can be studied at the molecular level.

## Materials and Methods

### Chemicals and Apparatus

Tris-HCL, NADP, G6PDH, D-glucose-6-P were purchased from Sigma Aldrich (Steinheim, Germany), Glycine,  $Al_2(SO_4)_3$ ,  $MgCl_2$  were purchased from MERCK (Darmstadt, Germany), BSA was purchased from Amresco (USA). All chemicals used are of analytical purity. All solutions used in this study were prepared with deionized Milli-Q water (Millipore, Bedford, MA, USA). Dual beam path Spectrophotometer (Labmed. Inc) and electronic precision balance (Sartorius 000032) were used. Experimental studies were carried out at room temperature ( $25.0 \pm 0.5$ ) °C.

### Measuring G6PDH Activity

Experimental method steps in the Worthington Enzyme Manual [14] were followed to examine the effect of aluminum against the kinetic behavior of the G6PDH enzyme. The activity values against 4 different (0.1, 0.08, 0.05, 0.03 mM) substrate concentrations were calculated and the Lineweaver-Burk plot with  $1/Activity$  versus  $1/concentration$  plot was drawn. In the presence of  $Al_2(SO_4)_3$  with 10 mM and 30 mM concentrations, it was added to each of the 4 different concentrations of substrate medium as inhibitor. Activity values were recorded. Activity experiments were repeated three times. The average of the data obtained here was transferred to the Lineweaver-Burk graph. Maximum velocity ( $V_{max}$ ) and Michaelis-Menten constant ( $K_m$ ) of the enzyme were calculated (Table-1). The reaction rate of the G6PDH enzyme was determined by the reduction of absorbance at 340 nm as a result of reduction of NADP. The reduction of  $1\mu mol$  NADP per minute at pH 7.8 and 30°C was determined as one unit of activity. The specific activity values of the G6PDH enzyme were calculated with the help of the following equation [14]. With the help of these data, the in vitro effect of  $Al_2(SO_4)_3$  on G6PDH activity was evaluated.

$$\text{Units /mg} = \frac{\Delta A_{340}/\text{min}}{6,22 \times \text{mg enzyme/mL reaction mix}}$$

### Molecular Docking Calculation

Docking Server was used as the docking program. For this, the geometry optimization of the ligands was done again with the MMFF94 method. The load calculation method was chosen as Gasteiger. pH = 7.0 was taken for all calculations. In docking calculations, grid maps are  $90 \times 90 \times 90 \text{ \AA}$  (x, y and z) and Lamarckian genetic algorithm (LGA) and Solis & wet local search method was used [15]. During docking, the population size was set to 150. A translation step of 0.2 Å and a 5 Å quaternion and torsion steps were applied during the search for the appropriate region of the target protein of the molecules studied. HEX

8.0.0 [16] was preferred for the overall exposure of the studied compound.

## Results

Lineweaver-Burk graph was drawn according to the data obtained using D-glucose-6-P at 4 different concentrations (0.1, 0.08, 0.05, 0.03 mM). The  $V_{max}$  value of G6PDH was calculated as 3.33 /mg protein/min, and the  $K_m$  value was calculated as 0.0323 mM (Figure-1). G6PDH activity was measured by adding  $Al_2(SO_4)_3$  solution prepared at two different concentrations (10 mM and 30 mM) to the reaction medium. Lineweaver-Burk curve was drawn according to the obtained data (Figure-2). In the presence of 10 mM, the  $Al_2(SO_4)_3$   $K_m$  value was calculated as 0.029 and the  $V_{max}$  as 2.5 ( $\mu mol$  D-G6P/mg protein)/min. In the presence of 30 mM, the  $Al_2(SO_4)_3$   $K_m$  value was calculated as 0.0271 and the  $V_{max}$  as 1.43 ( $\mu mol$  D-G6P/mg protein)/minute. It was observed that there was a 24.9% decrease in G6PDH activity in the presence of 10 mM  $Al_2(SO_4)_3$  and a 57.06% decrease in the presence of 30 mM  $Al_2(SO_4)_3$  (Table 1).

Looking at the data obtained, it was seen that  $Al_2(SO_4)_3$  inhibited the G6PDH enzyme uncompetitively.

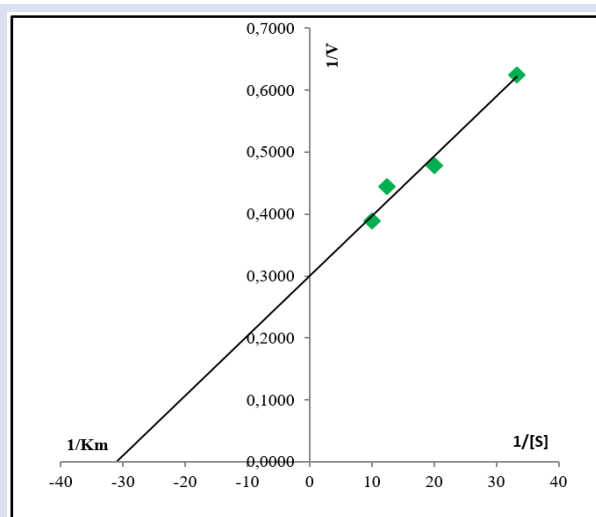


Figure 1. Lineweaver-Burk plot of G6PDH without inhibitor

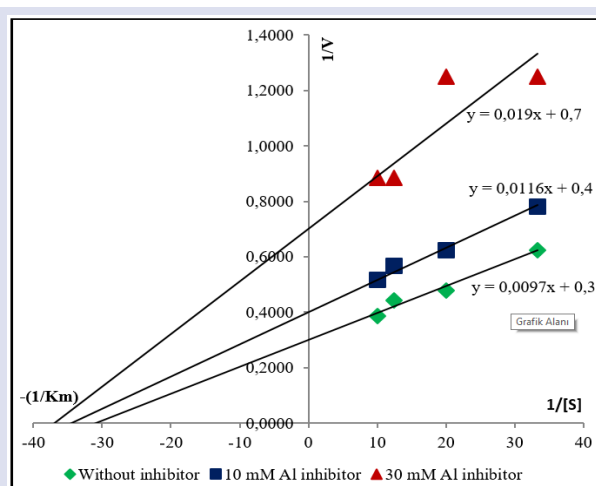


Figure 2. Lineweaver-Burk plot of the effect of  $Al_2(SO_4)_3$  on G6PDH enzyme activity

**Table 1.** Kinetic Properties of G6PDH Enzyme and Al<sub>2</sub>(SO<sub>4</sub>)<sub>3</sub>

	G6PDH Enzyme				
	No Inhibitor	10mM Al <sub>2</sub> (SO <sub>4</sub> ) <sub>3</sub>		30mM Al <sub>2</sub> (SO <sub>4</sub> ) <sub>3</sub>	
K <sub>m</sub> (mM)	0.0323	0.029	10.22%	0.0271	16.10%
V <sub>max</sub> (µmol D-G6P/mg protein/dk.)	3.33	0.0323	24.92%	1.43	57.06%

Molecular docking is of great importance in cell biology because it is done by interacting a target protein with a ligand molecule. It is very important in terms of determining the interactions that take place in biological processes. The docking results can be used to find the

inhibitor of the target protein. Target proteins were determined in the protein database. PDB ID=1DPG [17] target proteins were selected for the glucose 6-phosphate dehydrogenase (G6PDH) enzyme. Geometry optimization for Al<sub>2</sub>(SO<sub>4</sub>)<sub>3</sub> and selected target proteins was done by MMFF94 method. Docking processes were repeated with both programs. An important parameter used while giving molecular docking results is the binding energy. Binding energy includes interactions such as van der Waals interactions, electrostatic interactions, hydrogen bonds, and hydrophobic interactions. The magnitude of the binding energy is a measure of the stability of the ligand-receptor complex [18]. The affinity of two molecules can be estimated using the binding energy. Interaction types, docking poses and binding modes of Al<sub>2</sub>(SO<sub>4</sub>)<sub>3</sub> with target proteins representing G6PDH enzyme are given in the Figure 3.

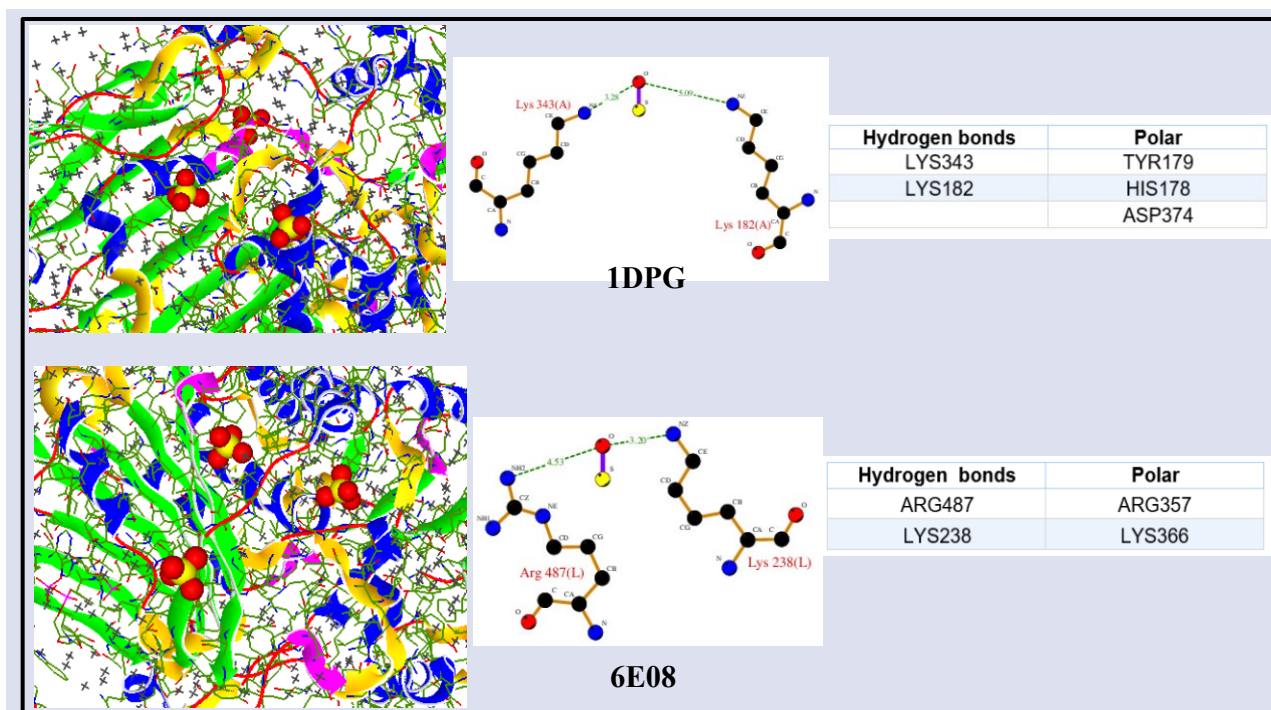


Figure 3. Binding modes, docking poses and interaction types between investigated ligand and target proteins.

When the interaction types between Al<sub>2</sub>(SO<sub>4</sub>)<sub>3</sub> and the target proteins, whose docking poses are given in Figure 3, are examined, there are H-bond and polar interactions. The studied ligand forms H-bond with amino acid residues LYS343 and LYS182 of the 1DPG target protein. TYR179 is in polar interaction with amino acid residues HIS178 and ASP374. Al<sub>2</sub>(SO<sub>4</sub>)<sub>3</sub> ligand 6E08 forms an H-bond with amino acid residues ARG487, LYS238 and polar interaction with amino acid residues ARG357, LYS366 of the target protein. The binding energy (BE), intermolecular energy (IE), van der Waals interactions, vdW + Hbond + desolved Energy (WHDE), interaction surface (IS) and inhibition constant (K<sub>i</sub>) values to estimate enzyme inhibition activity between ligand-target proteins are given in Table 2.

**Table 2.** Docking results between Al<sub>2</sub>(SO<sub>4</sub>)<sub>3</sub> and target proteins

	1DPG	6E08
BE (kcal/mol)	-2.29	-4.93
IE (kcal/mol)	-2.29	-4.93
WHDE (kcal/mol)	-0.82	-1.04
IS	187.645	226.149
K <sub>i</sub> (µM)	210.80	245.03

As seen in Table 2, negative values of BE, IE and WHDE energies provide inhibition of both 1DPG and 6E08 enzymes of Al<sub>2</sub>(SO<sub>4</sub>)<sub>3</sub> at molecular level. More negative interaction energy indicates higher inhibition efficiency [19]. According to the calculated docking results here, considering the energies, it is thought that Al<sub>2</sub>(SO<sub>4</sub>)<sub>3</sub>

inhibits a small molecule AG1, which corrects it in the 6E08 target protein, more since there is no drug available to treat G6PDH deficiency. On the other hand, when the interaction surfaces (IS) of  $Al_2(SO_4)_3$  with target proteins are examined, the interactions with both target proteins are almost close. The high interaction surface also increases the ligand-protein interaction and causes an increase in enzyme inhibition activity [20]. The inhibition constant ( $K_i$ ) is a data about the amount of drug to be used in the treatment. The smaller this value, the smaller the amount of drug used in the treatment [21]. In addition, the results of the two docking programs show that only sulfur and oxygen atoms interact with amino acid residues. However, it is remarkable that it is included in the target protein in the form of a compound.

## Discussion

Erythrocytes are among the most abundant cell types in an adult human, with a gross volume of 2 L and accounting for ~10% of the total cell number. The lifespan of erythrocytes is about 100-120 days, meaning that more than 200 billion erythrocytes containing about 20 mL of filled cell volume need to be replaced every day [22]. Eryptosis can occur due to various cellular stresses such as osmotic shock, oxidative stress and energy deficiency [23]. Oxidative stress or insufficient antioxidative defense activates  $Ca^{2+}$  and  $Cl^-$  channels, causing the concentration of these intracellular ions to change [24]. In addition, oxidative stress causes eryptosis by causing the activation of aspartyl and cysteinyl proteases in erythrocytes [25]. In erythrocytes, NADPH+H is synthesized in PFY, the only source, in the rate-limiting step catalyzed by the G6PDH enzyme. Necessary for the production of reduced glutathione (GSH), which is important for protection against oxidative damage in NADPH. Fico et al. clearly stated the role of G6PDH in protection from apoptosis and necrosis induced by redox imbalance [26]. In our study, we found that  $Al_2(SO_4)_3$  caused uncompetitive inhibition of the G6PDH enzyme.

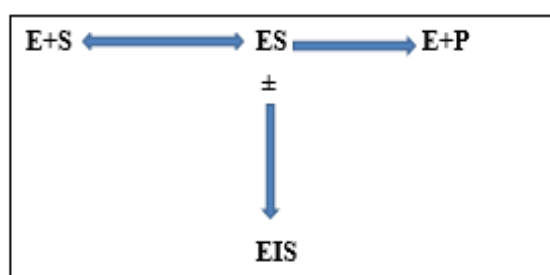


Figure 4. Uncompetitive Enzyme Inhibition (E:Enzyme S:Substrate I:Inhibitor P:Protein)

It is thought that exposure to Al or its compounds for a long time will cause triggering of eryptosis due to the increase in blood concentration. They showed that ROS-producing agents affect peripheral mononuclear cells (PBMC) of patients with G6PDH deficiency, leading to apoptosis due to insufficient protection from oxidative damage by low glutathione [27]. Therefore, inhibition of

G6PDH will cause activation of the apoptotic pathway not only for erythrocytes but also within PBMC.

Many researchers have investigated the activator or inhibitory effects of heavy metals on the enzyme system in living organisms [28,29,30]. Although aluminum is not in the heavy metals group, it has been defined as a potentially toxic element in recent years [31]. Although most forms of aluminum are not harmful to living things, they tend to form harmful derivatives at low pH's [32]. Tolerable levels of Al determined by 'The Joint FAO/WHO Expert Committee on Food Additives (JECFA)' for human body is 2 mg/kg/week [33]. Aluminum salts (such as aluminum hydroxide, phosphate, carbonate) are also used for treatment in the field of medicine such as humoral immunity, peptic ulcer and dialysis [34-37]. Several studies have been conducted on aluminum exposure. For example, it is a controversial issue whether the role of aluminum in Alzheimer's disease is due to Al accumulation in the patient's brain or due to Al-induced oxidative stress [38], in a study in rats,  $Al_2(SO_4)_3$  was found to cause germinative damage and renal degeneration [39]. Again, in an experimental animal study, it was shown that Al causes anemia with the damage it causes to the hematological system [40]. Sucralfate is an aluminum-containing drug recently approved by the Food and Drug Administration (FDA) for the short-term (up to eight week) treatment of duodenal peptic ulcers. This drug was used in different doses and durations for therapeutic purposes, and it was found that the serum Al levels of the patients increased after the treatment [41]. Aluminum especially can affect important biomolecules of metabolism such as AMP, ATP, ADP, inositol phosphate, Glucose-6-Phosphate, 2,3-diphosphoglycerate. In the relationship between ATP and  $Mg^{2+}$ , which takes place in most biological reactions,  $Mg^{2+}$  is irreversibly replaced and forms a more stable complex. In addition, it can decrease  $Ca^{2+}$  ATPase activity, disrupt intracellular  $Ca^{2+}$  movement and inhibit many enzymes [42]. It is known that deficiency or inhibition of G6PDH, the most common and clinically important enzyme in the world, causes hemolytic anemia [12]. NADPH+H produced in the pentose phosphate pathway is required to reduce erythrocytes oxidized (GSSG) glutathione to reduced glutathione (GSH). Changes in G6PDH enzyme activity will cause hemolysis due to increased GSSG level as NADPH+H production will be affected significantly [12.]

In this study, it was determined that aluminum sulfate is an uncompetitive inhibitor of  $Al_2(SO_4)_3$  G6PDH enzyme and affects both  $K_m$  and  $V_{max}$  levels (Figure-2). It is thought that as a result of the increase of aluminum in tissues and blood circulation, G6PDH enzyme will be inhibited and erythrocytes will be affected the most. Insufficient functioning of this enzyme means slowing of PFY and incomplete production of NADPH+H in the cell. The only production pathway of NADPH+H in erythrocytes is the pentose phosphate pathway. Oxidized glutathione (GSSH) is reduced to reduced glutathione (GSH) by the enzyme glutathione reductase, whose coenzyme is NADPH+H.  $H_2O_2$ 's occurring in living organisms are

converted to water by the enzymes catalase (CAT) and glutathione peroxidase (GPx). GPx needs reduced glutathione (GSH) to perform this reaction. In this case, there is not enough NADPH+H for the antioxidant enzymes involved in the reduction of free radicals to work efficiently [43]. Free radicals, especially reactive oxygen species (ROS), are compounds that can react very actively. It is known that ROT interacts with lipid, protein and DNA, disrupting the structure of these biomolecules and causing many metabolic diseases.

In our study, aluminum sulfate was found to be an uncompetitive inhibitor of the G6PDH enzyme. Mainly aluminum; It is known to bind to phosphate, carboxylate, amines, amino acids, nucleic acids and nucleotides [42]. We believe that the G6PDH enzyme inhibits by binding to these molecules in its structure. As a result of this inhibition, it will not be possible to eliminate free radicals since NADPH+H cannot be produced by pentose phosphate. This will cause hemolysis due to the deterioration of the structure of many biomolecules and damage to cell membranes.

As a result, when the data of our study is evaluated, it is seen that aluminum salts have negative effects on the antioxidant defense system. Accordingly, we think that it is important for people with low plasma G6PDH enzyme levels not to use aluminum-containing food and industrial products if possible, and to inform their physicians if they are given aluminum-containing drugs. With molecular docking studies, for the first time, the glucose-6-phosphate dehydrogenase (G6PDH) enzyme inhibition of  $Al_2(SO_4)_3$  was investigated at the molecular level and its inhibition efficiency was theoretically supported.

## Conflicts of Interest

The authors state that did not have conflict of interests

## References

- [1] Yılmaz E., Farklı Dozlardaki Alüminyum Klorür'ün Galleria Mellonella (Lepidoptera: pyralidae)'nın Biyolojisine ve Hemosit Sayılarına Etkileri (Doctoral dissertation), Marmara Üniversitesi, (2013).
- [2] Ak Uysal H., Ergene N.B., Alüminyum ve İnsan Sağlığı, *SÜ Tıp Fakültesi Dergisi*, 6(2) (1990) 230-237.
- [3] Yenigül E., Alüminyum ve Bazı Organik Asitlerin Etkileşiminin Spektrometrik ve Kromatografik Yöntemlerle Tayini, (2006).
- [4] Alfrey A.C., Aluminum, *Advances in Clinical Chemistry*, 23 (1983) 69-91.
- [5] Ojeda C. B., Rojas F.S., Pavón J.C., Torres A.G., Automated Online Separation Preconcentration System For Platinum Determination by Electrothermal Atomic Absorption Spectrometry, *Analytica Chimica Acta*, 494 (1-2) (2003) 97-103.
- [6] Akpolat T., Utaş C., Hemodiyaliz Hekimi El Kitabı, Kayseri, Anadolu Yayıncılık (2001).
- [7] Becaria A., Campbell A., Bondy S. C., Aluminum as a Toxicant, *Toxicology and Industrial Health*, 18(7) (2002) 309-320.
- [8] Haberhauer G., Ja A.A., Tunega D., Gerzabek Martin H., Lischka H., Potential of Theoretical Calculations to Estimate the Stability of  $Al^{3+}$ /Citrate, Oxalate and Acetate Complexes, In 17. World congress of Soil Science, Bangkok (Thailand), August (2002).
- [9] Savory J., Opening of the Mitochondrial Permeability Transition Pore by Reactive Oxygen Species is a Basic Event Neurodegeneration, Virginia Univ Charlottesville, (2001).
- [10] Telefoncu A., Telefoncu F., Glukoz-6-fosfat Dehidrogenaz Aktivitesine Primaquine'nin Etkisi, *Tr. J. Medical Sci.*, 14 (1989) 57-63.
- [11] Greer J. P., Arber D.A., Glader B., List A.F., Means R.T., Paraskevas F., Rodgers G.M., Wintrobe's Clinical Hematology, Lippincott Williams & Wilkins (2013).
- [12] Sodeman W. A., TM., Sodeman's Pathologic Physiology Mechanisms of Disease, 1 (1992).
- [13] Kaya S., Erkan S., Karakaş D., Computational Investigation of Molecular Structures, Spectroscopic Properties and Antitumor-Antibacterial Activities of Some Schiff Bases. *Spectrochimica Acta Part A: Molecular and Biomolecular Spectroscopy*, 244 (2021) 118829.
- [14] Von Worthington, Worthington Enzyme Manual; Enzymes And Related Biochemicals, 1.1.1.49 Glucose-6-Phosphate Dehydrogenase, (1993) 189-190.
- [15] Bikadi Z., Hazai E., Application of the PM6 Semi-empirical Method to Modeling Proteins Enhances Docking Accuracy of AutoDock, *Journal of Cheminformatics*, 1(1) (2009) 1-16.
- [16] Ritchie D., Orpailleur T., Hex 8.0. 0 User Manual. Protein Docking Using Spherical Polar Fourier Correlations Copyright c (2013).
- [17] Rowland P., Basak A.K., Gover S., Levy H.R., Adams M.J., The Three Dimensional Structure of Glucose 6-Phosphate Dehydrogenase from Leuconostoc Mesenteroides Refined At 2.0 Å Resolution, *Structure*, 2(11) (1994) 1073-1087.
- [18] Erkan S., Activity of the Rocuronium Molecule and its Derivatives: A Theoretical Calculation, *Journal of Molecular Structure*, 1189 (2019) 257-264.
- [19] Erkan S., Structural, Spectroscopic and Anti-Cancer Properties of Hydroxy-and Sulfonamide-Azobenzene Platinum (II) Complexes: DFT and Molecular Docking Studies, *Cumhuriyet Science Journal*, 39(4) (2018) 1036-1051.
- [20] Erkan S., Kaya S., Sayin K., Karakaş D., Structural, Spectral Characterization and Molecular Docking Analyses of Mer-Ruthenium (II) Complexes Containing the Bidentate Chelating Ligands, *Spectrochimica Acta Part A: Molecular and Biomolecular Spectroscopy*, 224 (2020) 117399.
- [21] Merugu R., Neerudu U.K., Dasa K., Singh K.V., Molecular Docking Studies of Deacetyl-bisacodyl with Intestinal Sucrase-Maltase Enzyme, *Int. J. Adv. Sci. Res.*, 2(12) (2016) 191-193.
- [22] Bosman G., Willekens F., Werre J., Erythrocyte Aging: a More Than Superficial Resemblance to Apoptosis, *Cellular Physiology and Biochemistry*, 16(1-3) (2005) 1-8.
- [23] Lang K. S., Durantón C., Poehlmann H., Myssina S., Bauer C., Lang F., Huber S.M., Cation Channels Trigger Apoptotic Death of Erythrocytes, *Cell Death & Differentiation*, 10(2) (2003) 249-256.
- [24] Durantón C., Huber S. M., Lang F., Oxidation Induces a Cl-Dependent Cation Conductance in Human Red Blood Cells, *The Journal of Physiology*, 539(3) (2002) 847-855.
- [25] Matarrese P., Straface E., Pietraforte D., Gambardella L., Vona R., Maccaglia A., Malorni W., Peroxynitrite Induces Senescence and Apoptosis of Red Blood Cells Through the Activation of Aspartyl and Cysteiny Proteases, *The FASEB Journal*, 19(3) (2005) 1-27.

- [26] Fico A., Paglialonga F., Cigliano L., Abrescia P., Verde P., Martini G., Filosa S., Glucose-6-Phosphate Dehydrogenase Plays a Crucial Role in Protection From Redox-Stress-Induced Apoptosis, *Cell Death & Differentiation*, 11(8) (2004) 823-831.
- [27] Spitz D.R., Azzam E.I., Jian Li J., Gius D., Metabolic Oxidation/Reduction Reactions and Cellular Responses to Ionizing Radiation: a Unifying Concept in Stress Response Biology, *Cancer and Metastasis Reviews*, 23(3) (2004) 311-322.
- [28] Fairbanks V.F., Copper Sulfate-induced Hemolytic Anemia: Inhibition of Glucose-6-Phosphate Dehydrogenase and Other Possible Etiologic Mechanisms, *Archives of Internal Medicine*, 120(4) (1967) 428-432.
- [29] Danielyan K. E., Babayan L. A., Chailyan S. G., Impact of the Heavy Metals on the Activity of Xanthine Oxidoreductase, *Appl Clin Pharmacol Toxicol*, 3(123) (2019) 2577-0225.
- [30] Budak H., Ceylan H., Kocpinar E.F., Gonul N., Erdogan O., Expression of Glucose-6-Phosphate Dehydrogenase and 6-Phosphogluconate Dehydrogenase in Oxidative Stress Induced by Long-Term Iron Toxicity in Rat Liver, *Journal of Biochemical and Molecular Toxicology*, 28(5) (2014) 217-223.
- [31] Exley C., Korchazhkina O.V., Promotion of formation of Amyloid Fibrils By Aluminium Adenosine Triphosphate (AlATP), *Journal of Inorganic Biochemistry*, 84(3-4) (2001) 215-224.
- [32] Merian E., Anke M., Ihnat M., Stoepler M., Elements and Their Compounds in the Environment, Occurrence, Analysis and Biological Relevance 2nd ed. Wiley-VCH Verlag GmbH and Co. KGaA (2004). (<https://www.cabdirect.org/cabdirect/abstract/20043118056>).
- [33] Serencam H., Arslaner A., Müge K., Civil Peynirde Ağır Metal Kontaminasyon Kaynağı ve Düzeyinin Belirlenmesi Üzerine Bir Araştırma, *Engineering Sciences*, 13(1) (2018) 21-26.
- [34] Onur E. Alüminyum Toksikitesinin Kalite Kontrol Açısından Değerlendirilmesi, *Türk Nefroloji Diyaliz ve Transplantasyon Dergisi*, 1(2) (1997).
- [35] Recker R.R., Blotcky A.J., Leffler J.A., Rack, E.P., Evidence of Aluminum Absorption from the Gastrointestinal Tract and Bone Deposition by Aluminum Carbonate Ingestion with Normal Renal Function, *The Journal of Laboratory and Clinical Medicine*, 90(5) (1977) 810-815.
- [36] Clapp T., Siebert P., Chen D., Braun L.J., Vaccines with Aluminum-Containing Adjuvants: Optimizing Vaccine Efficacy and Thermal Stability, *Journal of Pharmaceutical Sciences*, 100(2) (2011) 388-401.
- [37] Klaassen C.D. (Ed.), Casarett and Doull's Toxicology: The Basic Science of Poisons. New York: McGraw-Hill, 1236 (2013) 189.
- [38] Bakar C., Baba A., Metaller ve İnsan Sağlığı: Yirminci Yüzyıldan Bugüne ve Geleceğe Miras Kalan Çevre Sağlığı Sorunu, 1. Tıbbi Jeoloji Çalıştayı, (2009).
- [39] Kutlubay R., Oğuz E.O., Güven C., Can B., Sinik Z., Tuncay Ö.L., Histological and Ultrastructural Evidence for Protective Effects on Aluminium-induced Kidney Damage by Intraperitoneal Administration of  $\alpha$ -Tocopherol, *International Journal of Toxicology*, 26(2) (2007) 95-101.
- [40] Oğuz E. O., Yüksel H., Havane E., Yaşar E., Zorbozan O., Zuhul C., Turgut G., Alüminyum Sülfat'ın "Ross" Cinsi Term Besi Civivi Karaciğerinde Yarattığı Toksik Ve İnflamatuar Hasar, *Ankara Üniversitesi Tıp Fakültesi Mecmuası*, 61(1) (2008) 1-6.
- [41] Pai S., Melethil S., Cuddy P., Hall T., Elevation of Serum Aluminum in Humans on a two-day Sucralfate Regimen, *The Journal of Clinical Pharmacology*, 27(3) (1987) 213-215.
- [42] Günaydin N., Uzun Süreli Alüminyum Kaplarda Yapılan Yoğurtlarla Beslenenlerde Plazma Alüminyum Seviyeleri ile Oksidatif Durum Arasındaki İlişkinin Araştırılması (Master thesis), Sağlık Bilimleri Enstitüsü, (2005).
- [43] Fridovich I., The Biology of Oxygen Radicals: The Superoxide Radical is an Agent of Oxygen Toxicity; Superoxide Dismutases Provide an Important Defense, *Science*, 201(4359) (1978) 875-880.



## In Silico Studies of Synthetic Sulfatide as a Potential Drug Candidate Against Covid-19

Samet Kocabay<sup>1,a,\*</sup>, M. Abdullah Alagöz<sup>2,b</sup>, H. Gökhan Bakır<sup>1,c</sup>, Birnur Akkaya<sup>3,d</sup>

<sup>1</sup> Department of Molecular Biology and Genetics, Science and Literature Faculty, İnönü University, Malatya, Türkiye

<sup>2</sup> Department of Pharmaceutical Chemistry, Faculty of Pharmacy, İnönü University, Malatya, Türkiye

<sup>3</sup> Department of Molecular Biology and Genetics, Science Faculty, Sivas Cumhuriyet University, Sivas, Türkiye

\*Corresponding author

### Research Article

#### History

Received: 02/03/2022

Accepted: 03/06/2022

#### Copyright



©2022 Faculty of Science,  
Sivas Cumhuriyet University

### ABSTRACT

Sulfatides play various roles in many biological processes such as cancer metastasis, viral infections and regulation in nerve cells. The sulfatide molecules are related with hypertension diseases in which ACE2 (Angiotensin converting enzyme) is important for regulating blood pressure. ACE2 is also a key receptor for Covid-19 and highly expressed many different tissue types. Understanding the interaction between the sulfatides and ACE2 might be a key factor to develop potential novel treatments against Covid-19. Here we studied the interaction of main protease enzyme (6LU7) of Covid-19 with native sulfatide(A), chitosan based synthetic sulfatide(B) and inhibitor N3, through in silico studies such as molecular docking, molecular dynamics, ADMET prediction and target selection analysis. The compounds A, B and N3 bind the virus protease enzyme with docking score of -5.420, -6.009, -6.161 kcal/mol respectively indicates synthetic sulfatide binds better than native sulfatide and comparable to N3. Besides, molecular dynamics studies were carried out to reveal the stability of the complexes of interest. ADMET and target prediction studies carried out to reveal pharmacological properties and toxicity of the complexes and synthetic sulfatide found to be a drug-like molecule. We anticipate that computational investigation of virus interaction mechanisms will be an important starting point for experimental research in drug development efforts against Covid-19.

**Keywords:** Sulfatide, Covid-19, Drug design, Molecular docking, MD simulation.

<sup>a</sup> [samet.kocabay@inonu.edu.tr](mailto:samet.kocabay@inonu.edu.tr)

<sup>b</sup> <https://orcid.org/0000-0002-0120-2910>

<sup>b</sup> [mehmet.alagoz@inonu.edu.tr](mailto:mehmet.alagoz@inonu.edu.tr)

<sup>d</sup> <https://orcid.org/0000-0001-5190-7196>

<sup>c</sup> [hincal.bakir@inonu.edu.tr](mailto:hincal.bakir@inonu.edu.tr)

<sup>d</sup> <https://orcid.org/0000-0003-0974-1481>

<sup>d</sup> [bakkaya@cumhuriyet.edu.tr](mailto:bakkaya@cumhuriyet.edu.tr)

<sup>d</sup> <https://orcid.org/0000-0001-9139-1884>

## Introduction

The recent outbreak emerged in the late 2019, named Covid-19 by the World Health Organization (WHO), have been a global challenge for scientific community to find an immediate cure[1]. Phylogenetical analysis show that the newly emerged virus is similar to the early versions including the SARS-CoV (Severe acute respiratory syndrome–coronavirus) and MERS-CoV (Middle East respiratory syndrome coronavirus) which were emerged in 2002 and 2012 respectively, so that the new virus is named as SARS-CoV-2 because of genetic similarity[2]. It is found that most of the Covid-19 infected patients show symptoms in a broad range such as difficulty in breathing, weakness, fever, vomiting, loss of taste and smell and dry cough[3-6]. In order to enter to host cell, the SARS-CoV-2 uses ACE2 receptors which are type I membrane proteins found on the surface of mammalian cells, especially in lungs, heart, kidneys, and intestine. These receptors are associated with the metabolism of angiotensin (Ang), a peptide hormone that regulates vasoconstriction and blood pressure[2, 7, 8]. The hypertensive patients use the ACE inhibitor drugs to control their blood pressure; however, they express the ACE2 more than normal due to the inhibitor drug consuming[9]. As a result, hypertensive patients having Covid-19 are at more risk than normal individuals[10]. In addition, differences in expression

levels of ACE2 between children and adults is suggested recently to explain why Covid-19 is milder in children than adults[11]. Therefore, computational efforts to shed light on sulfatides' interactions will be helpful to understand the underlying mechanisms of Covid-19.

The sulfatides are expressed in liver tissue and found abundantly in neural systems [6,12]. The sulfatide prevents human paravirus influenza type 3 to enter COS-7 cells [13]. It has been reported that the concentration of sulfatide in the blood of children may be higher than in adults [14]. The low sulfatide concentration increases hypertension risk two times than having high amount of sulfatide in blood[15-17]. Changes in the expression of hepatic cerebroside sulfotransferase (CST), the key enzyme involved in sulfatide synthesis, are the primary determinants of serum sulfatide amount [16]. Regarding Covid-19, it could be that high amount of the sulfatide might reduce the infection ability or disease severity and vice-verse[6, 18]. In their cell culture experiments Davies et al. observed that fenofibrate drug decreased Covid-19 infection significantly and fenofibrate is thought to increase the amount of sulfatide in the blood[19]. We synthesized and characterized chitosan based synthetic sulfatide both chemically and biologically and have published elsewhere[12].

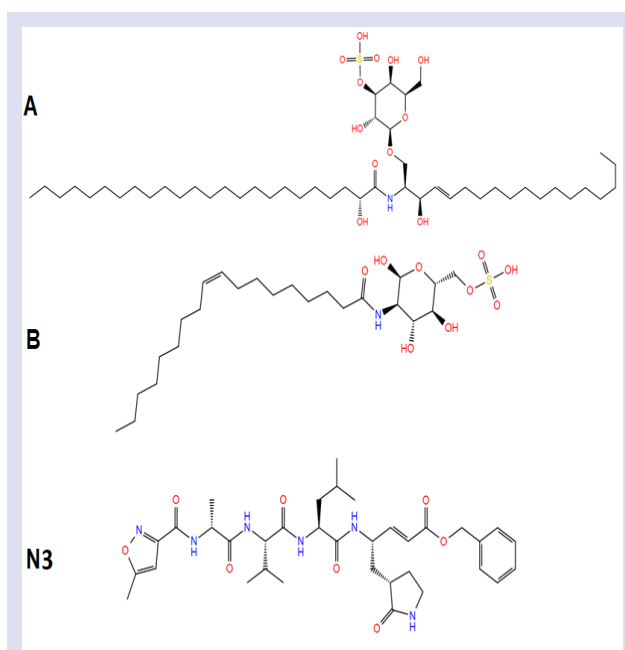


Figure 1. 2D structures of compounds A, B, and N3

Molecular docking studies were performed in order to reveal and compare the binding properties of the natural ligand (A), the synthetic derivative (B) under investigation and the N3, ligand of crystallized form for comparison[20]. In addition, molecular dynamics simulations were employed to verify the stability of protein-ligand complexes. Both studies showed that chitosan based synthetic sulfatide can play an important role for inhibition ACE2 as receptor for Covid-19.

## Material and Methods

### Docking Studies

Maestro 12.8 of Schrödinger (Schrödinger Release 2021-4: Maestro, Schrödinger, LLC, New York, NY, 2021) software was used in all molecular docking studies. The structures of the ligands were drawn with 2D Sketcher software. The ligands were minimized using LigPrep, a utility of Schrödinger (Schrödinger Release 2021-4: Maestro, Schrödinger, LLC, New York, NY, 2021). The X-ray structure of the target protein (PDB ID: 6LU7) was downloaded from the RCSB Protein Data Bank ([www.rcsb.org](http://www.rcsb.org))[21, 22]. Schrödinger's modules, Protein Preparation Wizard Prime, Impact, Epik, Prime (Schrödinger Release 2021-4: Protein Preparation Wizard; Epik, Schrödinger, LLC, New York, NY, 2021; Impact, Schrödinger, LLC, New York, NY; Prime, Schrödinger, LLC, New York, NY, 2021.)[22] and Propka[23] were used for removing ligands and solvent molecules in protein, adding hydrogens, assigning charges and deleting polar hydrogens for clarity. Grid maps were created with the Maestro (Schrödinger Release 2021-4: MacroModel, Schrödinger, LLC, New York, NY, 2021). grid generation panel, and prepared ligands were docked in this grid map

100 times in standard precision (SP) mode using the Glide software[24, 25]

### Molecular Dynamics Simulations

MD simulations were carried out by the Desmond (Schrödinger Release 2021-4: Desmond Molecular Dynamics System, D. E. Shaw Research, New York, NY, 2021. Maestro-Desmond Interoperability Tools, Schrödinger, New York, NY, 2021.)[26] module through Maestro of Schrödinger suite in order to investigate stability and interaction profiles of protein-ligand complexes for 50ns. Backbone RMSDs, the average distance between the backbone atoms of the protein-ligand structures, were plotted to compare the structural and dynamical properties[27].

Table 1. Program parameters of MD stimulation studies

Force Field	OPLS3E[28]
Solvation	Crystallographic Water (TIP3P)
Counter Ions	Na + Cl-
Ensemble	(Npt) Of Nose-Hoover Thermostat 300k Barostat 1bar
Boundary Conditions	Orthorhombic Periodic Boundary Conditions
Buffer Region	10 Å
Any Deleted Molecules	Water, Etc.
Minimization Algorithm	1000 Steps Of Steepest Descent Followed By Conjugate Gradient
Adjusting The Concentration Of The System	0,15M NaCl

### ADME Prediction

ADME (Adsorption, Distribution, Metabolism and Excretion) evaluation is a key step to analyze the pharmacodynamics properties of the molecules to be used as a drug. The 2D structures of the compounds were drawn using the 2D Sketcher module of the Maestro program. Smiles data of the compounds were transferred to the SWISS-ADME[29] online program and various physicochemical parameters, Lipophilicity, Water Solubility, Lipinski rules, and drug likeness scores of the given compounds were calculated[30].

### Target Prediction

Molecular target studies are used to predict the effects of small molecules in the body. These may cause cross-reactivity with other proteins or cause side effects[31]. Using the Swiss Target Prediction website[29] (<https://www.swisstargetprediction.ch>), the smile formula of the molecules was examined by applying it to the search bar.

### Toxicity Prediction

The toxicology prediction of small drug candidates must be known before applying them to the animal or human model. In this case, pkCSM [24] database (is used for details of toxicological effects such as AMES Toxicity, human maximum tolerance dose, hERG-I inhibitor, hERG-II inhibitor, LD50, LOAEL, Hepatotoxicity, Skin Toxicity, T. pyriformis toxicity, and Minnow toxicity). The website was accessed and SMILES of the sulfatides were entered into the website search bar and the toxicity mode was selected[32].

## Results and Discussion

### Molecular Docking and MD Simulations

Molecular docking studies were carried out to examine the interactions of ligands with residues in the active site of the target protein (6LU7). For the validation of the docking studies, the N3 in the crystal structure of the protein was removed, minimized, redocked and the RMSD value was calculated 0.526 Å. The compounds A, B

and N3 bind the virus protease enzyme with docking score of -5.420, -6.009, -6.161 kcal/mol respectively (Table 2).

Table 2. Docking scores of compounds, A, B, and N3 with 6LU7 PDB encoded protein

Compounds	Docking Scores (kcal/mol)
A	-5.420
B	-6.009
N3	-6.161

The molecular docking score of the compound B was higher than the scores of compound A and also very close to the docking score of N3. Similar to N3, compound B interacted hydrogen bonded in the active site of the enzyme with GLU166, GLN189 and hydrophobically with LEU27, MET49, LEU141, PHE140, CYS145, MET165, LEU167, PRO168, ALA191. It made polar interactions with THR190, and charged (positive) interaction with ARG188. It also made a hydrogen bond with THR190 (Figure 2).

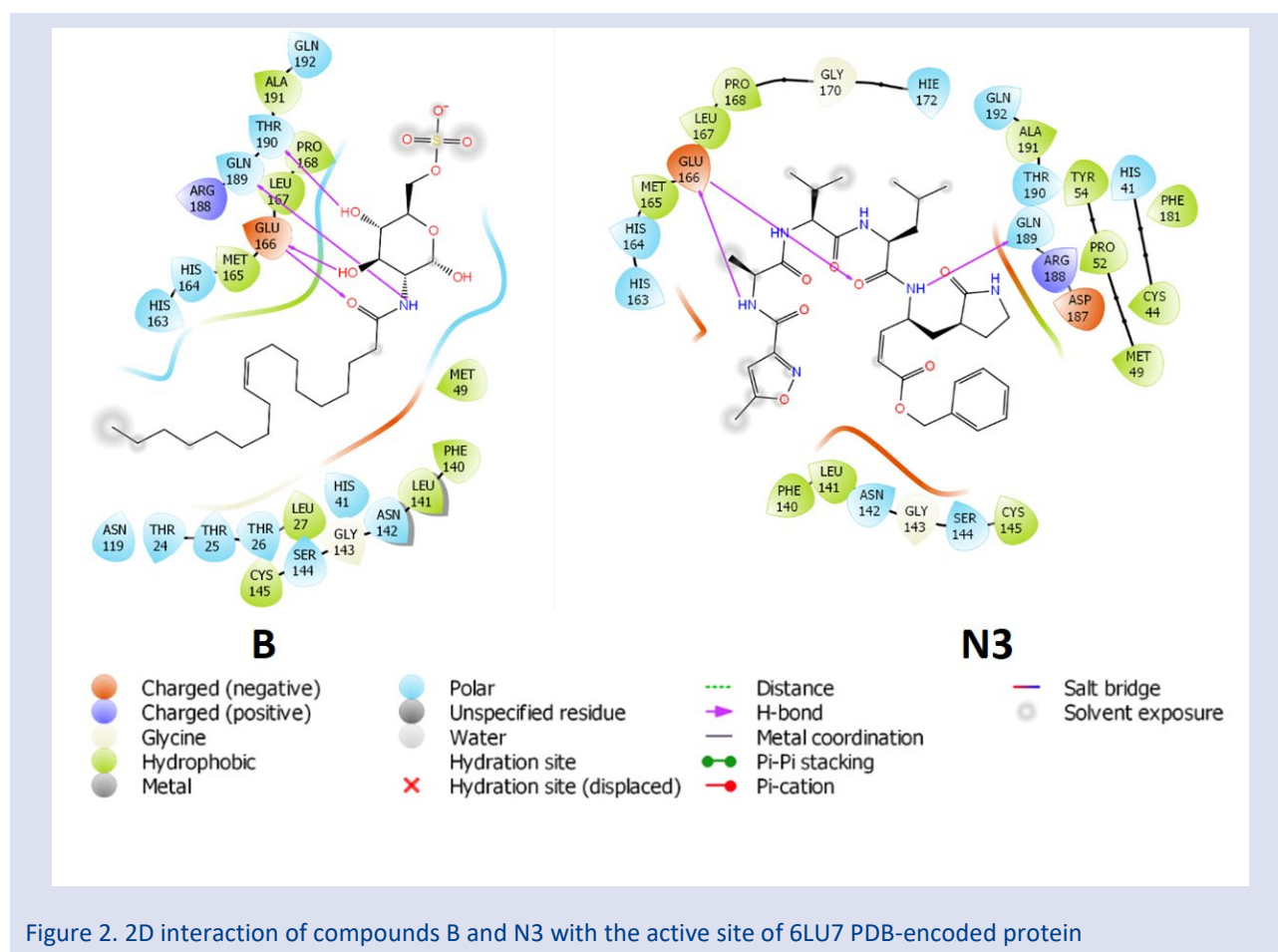


Figure 2. 2D interaction of compounds B and N3 with the active site of 6LU7 PDB-encoded protein

In addition to molecular docking studies, and MD Simulation studies were carried out with compounds A, B, and N3. RMSD values of compounds A, B, and N3 to analyze structural deviations and stability are shown in Figure 3. Simulations performed for 50 ns and RMSD

values of the alpha carbons ( $C\alpha$ ) of the enzyme (6LU7) in all three analyzes were seen to vary up to 3.2 Å (Figure 3). Despite the slight shifts observed, synthetic sulfatide complex B reached stability after 20 ns, with less deviations compared to compound A. Compound B and

native ligand-protein compound N3 show similar RMSD values.

The interaction of residues in the active site of the enzyme with compounds A and B were also investigated. In Figure 4, the residues interact with the ligands are

shown and they are observed to be constant throughout the simulation. In particular, it was determined that GLU166 and GLU189 distinctly took place in binding with both compounds.

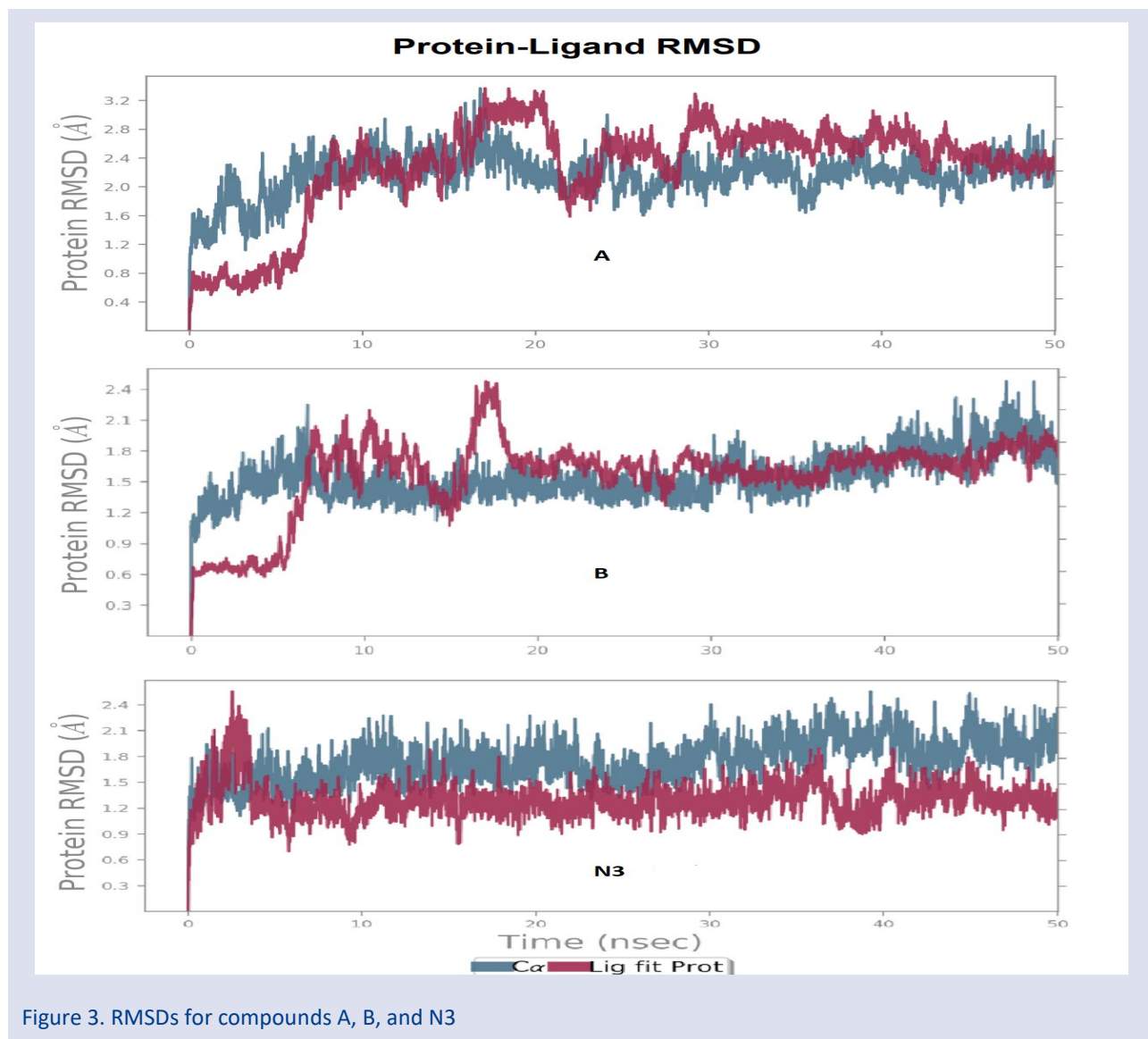


Figure 3. RMSDs for compounds A, B, and N3

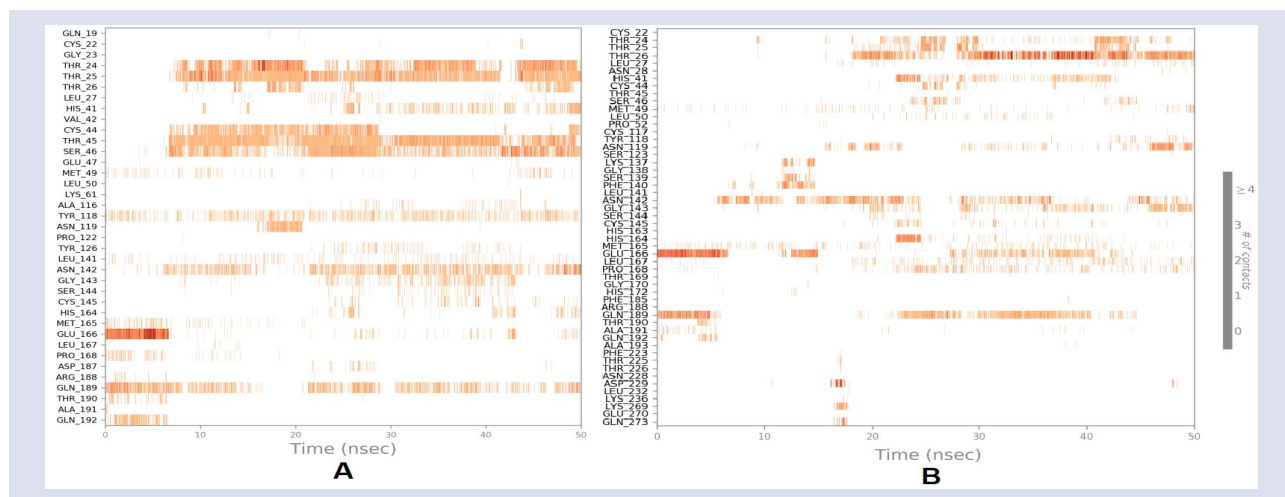


Figure 4. The residues interact with compounds A and B

**ADME Prediction**

After submission of the ligand molecules to SWISSADME database, the results were obtained in Table 3.

Table 3: Estimated Physicochemical, Lipophilicity, Water Solubility, Pharmacokinetics, Drug likeness, ADMET properties of A, B and N3

<b>Physicochemical Properties</b>	<b>A</b>	<b>B</b>	<b>N3</b>
Molecular weight	908.32 g/mol	523.68 g/mol	680.79 g/mol
Num. H-bond acceptors	12	9	9
Num. H-bond donors	7	5	5
TPSA	220.69 Å <sup>2</sup>	171.00 Å <sup>2</sup>	197.83 Å <sup>2</sup>
<b>Lipophilicity</b>	<b>A</b>	<b>B</b>	<b>N3</b>
Log $P_{o/w}$ (iLOGP)	7.74	3.39	3.94
Consensus Log $P_{o/w}$	9.25	2.90	2.73
<b>Water Solubility</b>	<b>A</b>	<b>B</b>	<b>N3</b>
Log $S$ (ESOL) ; Class	-11.69; Insoluble	-4.26; Moderately soluble	-4.89; Moderately soluble
Log $S$ (Ali) ; Class	-19.21; Insoluble	-7.24; Poorly soluble	-7.18; Poorly soluble
<b>Pharmacokinetics</b>	<b>A</b>	<b>B</b>	<b>N3</b>
GI absorption	Low	Low	Low
BBB permeant	No	No	No
P-gp substrate	Yes	Yes	Yes
CYP1A2 inhibitor	No	No	No
CYP2C19 inhibitor	No	No	No
CYP2C9 inhibitor	No	No	No
CYP2D6 inhibitor	No	No	No
CYP3A4 inhibitor	No	No	Yes
<b>Drug likeness</b>	<b>A</b>	<b>B</b>	<b>N3</b>
Lipinski	No; 3 violations: MW>500, NorO>10, NHorOH>5	Yes; 1 violation: MW>500	No; 2 violations: MW>500, NorO>10
<b>ADMET</b>	<b>A</b>	<b>B</b>	<b>N3</b>
AMES toxicity	No	No	No
Categorical (Yes/No)			
Max. tolerated dose (human)	0.435	0.299	-0.424
Numeric (log mg/kg/day)			
hERG I inhibitor Categorical (Yes/No)	No	No	No
hERG II inhibitor Categorical (Yes/No)	No	No	Yes

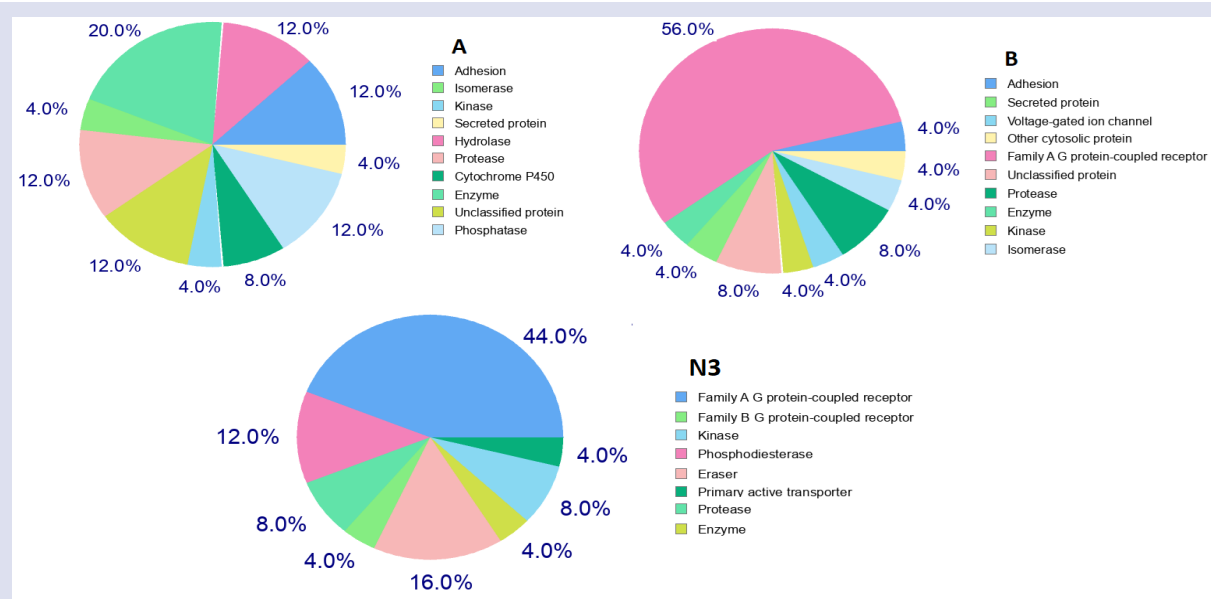


Figure 5. Top-25 targets predicted for A, B, and N3

The pie-chart graphs of the target prediction analysis are given in Figure 5 for the top-25 targets as displayed in the website. The pie chart predicts the following observations for native sulfatide (Figure 5): 12% of adhesion, 4% of isomerases, 4% of Kinase, 4% of Secreted protein, 12% of hydrolases, 12% of protease, 8% of cytochrome p450, 20% of Enzymes, 12% of unclassified protein and 12% of phosphatases. The pie chart also predicts for chitosan based synthetic sulfatide (Figure 5): 4% of Adhesion, 4% of Secreted protein, 4% Voltage-gated ion channel, 4% Other cytosolic protein, 56% of Family A G protein-coupled receptor, 8% Unclassified protein, 8% of Protease, 4% of Enzyme, 4% of Kinase, 4% of Isomerase. Target prediction analysis for N3 is as follows (Figure 5): 44% of Family A G protein-coupled receptor, 4% of Family B G protein-coupled receptor, 8% Kinase, 12% Phosphodiesterase, 16% Eraser, 4% Primary active transporter, 8% of protease, 4% of Enzymes. Native and chitosan based sulfatides are specific to only P-selectin.

Preliminary estimates of different properties of drugs (such as physicochemical properties, toxicity, absorption, distribution, metabolism, and excretion from the body, solubility in water and fat, and interaction with some enzymes in the body) can be obtained through various computer programs. These properties are evaluated by considering whether the obtained numerical results fall within the reference ranges. Bioavailability is an important criterion for evaluating any synthetic drug for clinical trials. Transportation properties can be determined by the TPSA value [33, 34].  $TPSA < 140 \text{ \AA}^2$  is the standard value for gastrointestinal absorption[35] and  $TPSA > 90 \text{ \AA}^2$  means low blood brain barrier (BBB) penetration[36]. Absorption percent (%ABS) was calculated by using  $\%ABS = 109 - (0.345 \times TPSA)$  is another factor for bioavailability ( $\%Abs > 50$  high,  $\%Abs < 30$  low) is low or high[37, 38].  $\log BB$  term is used to predict brain penetration for compounds of interest. For the compounds of interest values greater than 0.3 means a penetration, while values less than -1.0 indicate a poor diffusion[39]. Toxicity for *T. Pyriformis*, a protozoa bacteria, is predicted by the  $pIGC50 (> -0.5 \mu\text{g/L}$  toxic) and Minnow toxicity is predicted by the  $LC50 (\log LC50 < -0.3$  toxic) respectively. In addition, lipophilicity determined by  $\log P_{o/w}$  - Consensus  $\log P_{o/w}$  values and water solubility determined by  $\log S$  (ESOL) and  $\log S$  (Ali) values are important predictors for drug-delivery properties[40-42]. Some of the cytochrome P450 enzymes (CYP1A2, CYP3A4, CYP2C19, CYP2D6 and CYP2C9) are essential to metabolize many drugs[43], so pharmacokinetic interactions with these enzymes are also predicted.

The toxicity of drugs is a key factor and should be of great concern[44]. For toxicity, the maximum tolerated dose is important that it is used to estimate the starting dose in phase I clinical trials of drugs. For the maximum tolerated dose, values less than or equal to 0.477 are considered to be low and vice versa[45]. The toxicity of

drugs is highly related to the interaction with some important proteins in the body, the chemical nature and dose of the any given drug, and the stage of infection. For example, drugs sold in markets such as cisapride, sertindole, terfanadine inhibit human (hERG)  $K^+$  channels, causing cardiac arrhythmias and ultimately death and for this reason their sale has been stopped[44]. By measuring the toxicity tests using the ProTox-II - Prediction of Toxicity of Chemicals program, more detailed information about the drug can be obtained with computer data[44].

In our study,  $i\log P_{o/w}$  and consensus  $\log P_{o/w}$  values for compound A are 7.74 and 9.25 respectively, so it is weak in terms of lipophilicity. On the contrary these values are 2.90-3.39 and 2.73-3.94 for B and N3 indicating both are lipophilic and exhibit good GI properties. Both the ESOL  $\log S$  and Ali  $\log S$  values, suggest that compound A is insoluble, while the others are moderately soluble (see Table 3). The GI is low for all three compounds and all three cannot exceed the BBB. The three drugs do not inhibit any of the p450 inhibitors, except N3 inhibits CYP3A4. This eliminates an important concern in terms of the toxicity of the synthetic drug. The drug likeness property is positive only for B. It only violates the molecular weight rule. However there are many drugs of high molecular weight in phase III[46, 47]. Three drugs can be excreted from the cell as they are substrates of P-gp (see Table 3). Ames toxicity is negative for all three components, which suggest that the molecules are non-carcinogenic in nature. Maximum tolerated doses ( $\log \text{mg/kg/day}$ ) for all show eligibility for human use (Table 3). Except N3 gives positive result for hERG II, none exhibit hERG I and hERG II inhibitory property. All these results promise that the synthetic molecule (B) can be safely used as drug.

## Conclusion

It has been observed that sulfatide molecules may be of high importance in viral infections. The synthetic sulfatide showed great binding than native sulfatide due to their binding affinity scores. Structural mimic of the compound B was investigated by molecular docking and MD simulation studies. In addition, it was observed that compound B interacts with residues in the active site of the target enzyme similar to N3. ADMET studies showed that compound B did not have a significant predicted toxic effect and was in accordance with Lipinski's five-point rule.

Development of drugs or vaccines against Covid-19 in a short time is a great challenge for scientific community. The novel vaccines are currently been used in many countries. However, viruses can change their genetic material via mutations rapidly, so the vaccines don't keep us protected for a long time against mutated viruses. Efforts for developing anti-viral drugs studies for Covid-19 are slower and less promising than vaccine development. Although there are some drugs used in Covid-19 treatment protocols, there is currently no drug whose

effectiveness has been proven and approved by authorized institutions. Therefore, rapid development of alternative drug molecules is of vital importance and computational efforts can guide experimental and clinical studies in this field.

While obtaining huge amounts of biological sulfatides can be difficult, synthetic sulfatide is relatively easy to be produced in laboratory. These molecules are candidates to be the starting point for successful drug development against COVID-19.

### Conflicts of Interest

The author declares that there is no conflict of interest.

### References

- [1] Xu H., Zhong L., Deng J., Peng J., Dan H., High Expression Of Ace2 Receptor Of 2019-Ncov On The Epithelial Cells Of Oral Mucosa, *International Journal of Oral Science*, 12(1) (2020) 1-5.
- [2] Yan R., Zhang Y., Li Y., Xia L., Guo Y., Structural Basis for the Recognition of SARS-CoV-2 by Full-Length Human ACE2, *Science*, 367(6485) (2020) 1444-1448.
- [3] Dawson P., Rabold E.M., Laws R.L., Connors E.E., Gharpure R., Loss of Taste and Smell as Distinguishing Symptoms of COVID-19, *Clinical Infectious Diseases*, 72(4) (2021) 682-685.
- [4] Gautier J-F., Ravussin Y., A New Symptom of COVID-19: Loss of Taste and Smell, *Obesity (Silver Spring)*, 28(5) (2020) 848.
- [5] Yuki K., Fujiogi M., Koutsogiannaki S., COVID-19 Pathophysiology: A review, *Clinical Immunology*, 215 (2020) 108427.
- [6] Buschard K., Fenofibrate increases the amount of sulfatide which seems beneficial against Covid-19, *Medical Hypotheses*, 143 (2020) 110127.
- [7] Donoghue M., Hsieh F., Baronas E., Godbout K., Gosselin M., UltraRapid Communication, *Circulation Research*, 87 (2000) e1-e9.
- [8] Zhangh K., The Digestive System Is A Potential Route Of 2019 Ncovinfection: A Bioinformatics Analysis Based On Single Cell Transcriptomes, *BioRxiv*, 2020.
- [9] South A.M., Brady T.M., Flynn J.T., ACE2 (Angiotensin-Converting Enzyme 2), COVID-19, and ACE Inhibitor and Ang II (Angiotensin II) receptor blocker use during the pandemic: The pediatric perspective, *Hypertension*, 76(1) (2020) 16-22.
- [10] Pranata R., Lim M.A., Huang I., Raharjo S.B., Lukito A.A., Hypertension is Associated with Increased Mortality and Severity of Disease in COVID-19 Pneumonia: a Systematic Review, Meta-Analysis and Meta-Regression, *Journal of the Renin-angiotensin-aldosterone System: JRAAS*, 21(2) (2020) 1470320320926899.
- [11] Yuki K., Fujiogi M., Koutsogiannaki S., COVID-19 Pathophysiology: A review., *Clinical Immunology*, 215 (2020) 108427.
- [12] Kocabay S., Akkaya B., Preparation of Sulfatide Mimicking Oleic Acid Sulfated Chitosan as a Potential Inhibitor for Metastasis, *International Journal of Biological Macromolecules*, 147 (2020) 792-798.
- [13] Takahashi T., Ito K., Fukushima K., Takaguchi M., Hayakawa T., Sulfatide Negatively Regulates the Fusion Process of Human Parainfluenza Virus Type 3, *J. Biochem.*, 152(4) (2012) 373-380.
- [14] Blomqvist M., Kaas A., Månsson J.E., Formby B., Rynmark B.M., Developmental Expression of the Type I Diabetes Related Antigen Sulfatide and Sulfated Lactosylceramide in Mammalian Pancreas, *Journal of Cellular Biochemistry*, 89(2) (2003) 301-310.
- [15] Buschard K., Fredman P., Bøg-Hansen E., Blomqvist M., Hedner J., Low Serum Concentration of Sulfatide and Presence of Sulfated Lactosylceramid are Associated with Type 2 Diabetes. The Skaraborg Project, *Diabetic Medicine* 22(9) (2005) 1190-1198.
- [16] Guo R., Hu X., Yamada Y., Harada M., Nakajima T., Effects of Hypertension and Antihypertensive Treatments on Sulfatide Levels in Serum and its Metabolism, *Hypertension Research*, 42(5) (2019) 598-609.
- [17] Buschard K., Høy M., Bokvist K., Olsen H.L., Madsbad S., Sulfatide Controls Insulin Secretion by Modulation of ATP-Sensitive K<sup>+</sup>-channel Activity and Ca<sup>2+</sup>-dependent Exocytosis in Rat Pancreatic  $\beta$ -cells, *Diabetes*, 51(8) (2002) 2514-2521.
- [18] Yasmin F., Zeeshan M.H., Ullah I., The Role of Fenofibrate in the Treatment of COVID-19, *Annals of Medicine and Surgery*, 74 (2022) 102974.
- [19] Davies S.P., Mycroft-West C.J., Pagani I., Hill H.J., Chen Y-H., The Hyperlipidaemic Drug Fenofibrate Significantly Reduces Infection by SARS-CoV-2 in Cell Culture Models, *Frontiers in Pharmacology*, 12(660490) (2021) 1755.
- [20] Wang K.Y., Liu F., Jiang R., Yang X., You T., Structure of Mpro from COVID-19 Virus and Discovery of its Inhibitors, *Nature*, 2020.
- [21] Peele K.A., Durthi C.P., Srihansa T., Krupanidhi S., Ayyagari V.S., Molecular Docking and Dynamic Simulations for Antiviral Compounds Against SARS-CoV-2: A Computational Study, *Informatics in Medicine Unlocked*, 19 (2020) 100345.
- [22] Sastry G.M., Adzhigirey M., Day T., Annabhimoju R., Sherman W., Protein and Ligand Preparation: Parameters, Protocols, and Influence on Virtual Screening Enrichments, *Journal of Computer-Aided Molecular Design*, 27(3) (2013) 221-234.
- [23] Olsson M.H., Søndergaard C.R., Rostkowski M., Jensen J.H., PROPKA3: consistent treatment of internal and Surface Residues in Empirical p K a Predictions, *Journal of Chemical Theory and Computation*, 7(2) (2011) 525-537.
- [24] Friesner R.A., Banks J.L., Murphy R.B., Halgren T.A., Klicic J.J., Glide: a New Approach for Rapid, Accurate Docking and Scoring. 1. Method and Assessment of Docking Accuracy, *Journal of Medicinal Chemistry*, 47(7) (2004) 1739-1749.
- [25] Algul O., Ersan R.H., Alagoz M.A., Duran N., Burmaoglu S., An Efficient Synthesis of Novel Di-Heterocyclic Benzazole Derivatives and evaluation of Their Antiproliferative Activities, *Journal of Biomolecular Structure and Dynamics*, 39(18) (2021) 6926-6938.
- [26] Bowers K.J., Chow D.E., Xu H., Dror R.O., Eastwood M.P., Scalable Algorithms for Molecular Dynamics Simulations on Commodity Clusters. SC'06: Proceedings of the 2006 ACM/IEEE Conference on Supercomputing; 0-7695-2700-0/06 (2006) IEEE.
- [27] Ozten O., Kurt B.Z., Sonmez F., Dogan B., Durdagi S. Synthesis, Molecular Docking and Molecular Dynamics Studies of novel tacrine-carbamate derivatives as Potent Cholinesterase Inhibitors, *Bioorganic Chemistry*, 115 (2021) 105225.

- [28] Harder E., Damm W., Maple J., Wu C., Reboul M., OPLS3: a Force Field Providing Broad Coverage of Drug-Like Small Molecules And Proteins, *Journal of Chemical Theory and Computation*, 12(1) (2016) 281-296.
- [29] Daina A., Michielin O., Zoete V., SwissTargetPrediction: Updated Data and New Features for Efficient Prediction of Protein Targets of Small Molecules, *Nucleic Acids Research*, 47(W1) (2019) W357-W364.
- [30] Vardhan S., Sahoo S.K., In Silico ADMET and Molecular Docking Study on Searching Potential Inhibitors from Limonoids and Triterpenoids for COVID-19, *Computers in Biology and Medicine*, 124 (2020) 103936.
- [31] Gfeller D., Grosdidier A., Wirth M., Daina A., Michielin O., SwissTargetPrediction: a Web Server for Target Prediction of Bioactive Small Molecules, *Nucleic Acids Research*, 42(W1) (2014) W32-W38.
- [32] Halgren T.A., Murphy R.B., Friesner R.A., Beard H.S., Frye L.L., Glide: a New Approach for Rapid, Accurate Docking and Scoring. 2. Enrichment Factors in Database Screening, *Journal of Medicinal Chemistry*, 47(7) (2004) 1750-1759.
- [33] Chidambaram S.K., Ali D., Alarifi S., Radhakrishnan S., Akbar I., In Silico Molecular Docking: Evaluation of Coumarin Based Derivatives Against SARS-CoV-2, *Journal of Infection and Public Health*, 13(11) (2020) 1671-1677.
- [34] Ertl P., Rohde B., Selzer P., Fast Calculation of Molecular Polar Surface Area as a Sum of Fragment-Based Contributions and its Application to the Prediction of Drug Transport Properties. *Journal of Medicinal Chemistry*, 43(20) (2000) 3714-3717.
- [35] Palm K., Stenberg P., Luthman K., Artursson P., Polar Molecular Surface Properties Predict the Intestinal Absorption of Drugs in Humans, *Pharmaceutical Research*, 14(5) (1997) 568-571.
- [36] Hitchcock S.A., Pennington L.D., Structure– brain Exposure Relationships, *Journal of Medicinal Chemistry*, 49(26) (2006) 7559-7583.
- [37] Zhao Y.H., Abraham M.H., Le J., Hersey A., Luscombe C.N., Rate-limited Steps of Human Oral Absorption and QSAR Studies, *Pharmaceutical Research*, 19(10) (2002) 1446-1457.
- [38] Wang R., Fu Y., Lai L., A New Atom-additive Method for Calculating Partition Coefficients, *Journal of Chemical Information and Computer Sciences*, 37(3) (1997) 615-621.
- [39] Abraham M.H., Takács-Novák K., Mitchell R.C., On the Partition of Ampholytes: Application to Blood–Brain Distribution, *Journal of Pharmaceutical Sciences*, 86(3) (1997) 310-315.
- [40] Lipinski C.A., Lombardo F., Dominy B.W., Feeney P.J., Experimental and Computational Approaches to Estimate Solubility and Permeability in Drug Discovery and Development Settings, *Advanced Drug Delivery Reviews*, 23(1-3) (1997) 3-25.
- [41] Delaney J.S., ESOL: Estimating Aqueous Solubility Directly from Molecular Structure, *Journal of Chemical Information and Computer Sciences*, 44(3) (2004) 1000-1005.
- [42] Ali J., Camilleri P., Brown M.B., Hutt A.J., Kirton S.B., Revisiting the General Solubility equation: in silico Prediction of Aqueous Solubility Incorporating the Effect of Topographical Polar Surface Area, *Journal of Chemical Information and Modeling*, 52(2) (2012) 420-428.
- [43] Zanger U.M., Schwab M., Cytochrome P450 Enzymes in Drug Metabolism: regulation of gene expression, Enzyme Activities, and Impact of Genetic Variation, *Pharmacology & Therapeutics*, 138(1) (2013) 103-141.
- [44] Sepay N., Sekar A., Halder U.C., Alarifi A., Afzal M., Anti-COVID-19 Terpenoid from marine sources: A Docking, Admet and Molecular Dynamics Study, *Journal of Molecular Structure*, 1228 (2021) 129433.
- [45] Pires D.E., Blundell T.L., Ascher D.B., pkCSM: Predicting Small-Molecule Pharmacokinetic and Toxicity Properties Using Graph-Based Signatures, *Journal of Medicinal Chemistry*, 58(9) (2015) 4066-4072.
- [46] Basche M., Gustafson D.L., Holden S.N., O'Bryant C.L., Gore L., A Phase I Biological and Pharmacologic Study of the Heparanase Inhibitor PI-88 in patients with Advanced Solid Tumors, *Clinical Cancer Research*, 12(18) (2006) 5471-5480.
- [47] Kudchadkar R., Gonzalez R., Lewis K.D., PI-88: a Novel Inhibitor of Angiogenesis, *Expert Opinion on Investigational Drugs*, 17(11) (2008) 1769-1776.



## Computational Structure Characterization of 1,2,3-Selendiazole Isomers, Investigation of Some Molecular Properties and Biological Activities

Sultan Erkan <sup>1,a,\*</sup>, Doğan Can Dikyol <sup>1,b</sup><sup>1</sup> Department of Chemistry, Faculty of Science, Sivas Cumhuriyet University, 58140, Sivas, Türkiye

\*Corresponding author

### Research Article

#### History

Received: 07/01/2022



Accepted: 09/06/2022

#### Copyright

©2022 Faculty of Science,  
Sivas Cumhuriyet University

### ABSTRACT

Four different selendiazole compounds were handled by computational chemistry methods. Compounds 1,2,3-selendiazole, 1,2,5-selendiazole, 1,2,4-selendiazole and 1,3,4-selendiazole were optimized at the B3LYP/6-31G(d) level. Structural parameters were examined. In the structural determination, IR and NMR techniques, which are spectroscopic methods, were applied. Quantum chemical parameters giving global properties such as the highest occupied molecular orbital (HOMO) energy, the lowest unoccupied molecular orbital (LUMO) energy, hardness ( $\eta$ ), softness ( $\sigma$ ), chemical potential ( $\mu$ ), electronegativity ( $\chi$ ), electrophilicity index ( $\omega$ ), nucleophilicity index ( $\epsilon$ ), the electron accepting power ( $\omega^+$ ), electron donating power ( $\omega^-$ ) and polarizability were investigated for biological activities of selendiazoles. Local electrophilic and nucleophilic regions were determined using Fukui index functionals. Docking studies of the studied selendiazoles were performed with proteins representing the cervical cancer cell line and the MCF-7 breast cancer cell line.

**Keywords:** Selendiazoles, Fukui index, Molecular docking. [sultanerkan58@gmail.com](mailto:sultanerkan58@gmail.com) <https://orcid.org/0000-0001-6744-929X> [dikyoldogukan@gmail.com](mailto:dikyoldogukan@gmail.com) <https://orcid.org/0000-0000-0000-0000>

## Introduction

Organoselenium compounds, which are found in trace amounts in nature, contain carbon (C), selenium (Se) and sulfur (S) in their skeleton structure. The two nitrogenous atoms of the mentioned skeletal structure are called selenadiazole. There are basically four known types of selenadiazole heterocycles, with atoms in different positions in the ring structure. These are 1,2,3-selenadiazole with C–Se–N–N bond order, 1,2,4-selenadiazole with N–C–Se–N bond order, 1,2,5-selenadiazole with N–C–Se–C–N bond order and 1,3,4-selenadiazole with N–Se–N bond order given in Figure 1.

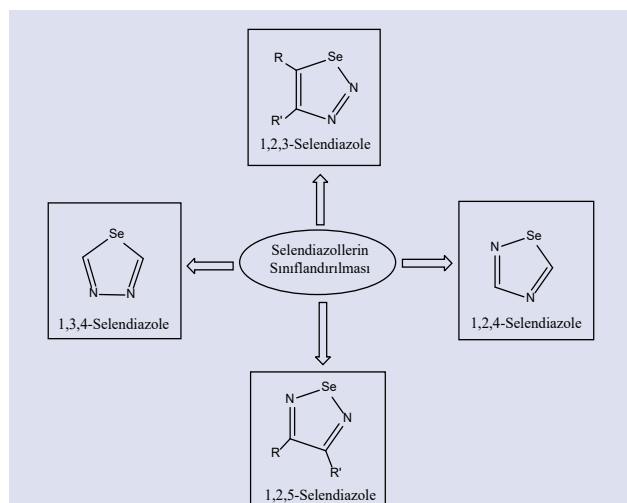


Figure 1. Classification of selenadiazoles according to the position of nitrogen and selenium atoms.

1,2,3-Selenadiazoles are a class of selendiazoles whose pharmacological applications have been widely studied. Their derivatives have been evaluated in many studies such as anti-bacterial and anti-cancer [1,2]. The biological activity of 1,2,3-selenadiazoles depends on the electron-accepting and electron-donating properties of the substituents attached to the carbon atoms in the ring structure. As in the nature of most chemicals, differences in functional groups have created differences in their biological potentials. 1,2,3-selenadiazole derivatives act as microbial agents such as antifungal [3], antibacterial [4], antitumor [5], cytotoxic [6] and enzyme inhibitors [7], as well as having important applications in chemotherapy and pharmacology [3-7]. In particular, the benzopyrano-1,2,3-selenadiazole derivatives exhibited antitumor activity against human cell lines such as MCF-7, VERO (African green monkey kidney cells), WI-38 (fibroblast cells) and HEPG-2 (hepatoma cells) [5]. Thioacetanilide derivatives of 1,2,3-selenadiazole showed anti-HIV activity against HIV-1 [6]. There are fewer chemical studies of 1,2,4-selenadiazoles than other selenadiazoles [8-15]. 1,2,5-Selenadiazoles are a type of selenadiazole that contains more information in the literature, thanks to the advantage of the synthesis steps. 1,2,5-selenadiazole compounds exhibit both biological activity and organic light-emitting diode properties [16]. 1,3,4-selendiazoles exhibited physical and biological activity properties on fungi and MAO-B [10]. In addition to these biological properties, organo selenium compounds also act as nonlinear optical potential candidates for electro-optical properties and sensor application [18,19].

In this study, the differences of the basic seleniazole compounds in terms of their structural and molecular properties are discussed. For this purpose, selendiazole compounds are studied by computational chemistry methods. The energy stability of 1,2,3-selendiazole, 1,2,5-selendiazole, 1,2,4-selendiazole and 1,3,4-selendiazole compounds is investigated. For structural analysis, bond lengths, bond angles, differences between IR and NMR data are examined. Quantum chemical parameters are compared to predict the biological activities of the studied compounds. Local electrotophic and nucleophilic regions are determined using the Fukui index functionals. The biological activities of the studied selendiazoles with proteins representing the cervical cancer cell line and the MCF-7 breast cancer cell line are docked with the help of simulation.

### Calculation Method

Selendiazole compounds were plotted in the program GaussView 6.0.16 [20]. All calculations were made in Gaussian 09:AS64L-G09RevD.01 program and an imaginary frequency could not be obtained [21]. The B3LYP method was used in the calculations [22-24]. The basis set selection is 6-31G(d) [25].

With the Density Functional Theory, it allows the approximation of quantum chemical descriptors such as hardness ( $\eta$ ), softness ( $\sigma$ ), chemical potential ( $\mu$ ), and electronegativity ( $\chi$ ). In order to correlate the ground state ionization energy ( $I$ ) and electron affinity ( $A$ ) values of chemical compounds, parameters, finite difference approach was considered and finally, the following equations were obtained [26-27].

$$I = -E_{HOMO}$$

$$A = -E_{LUMO}$$

$$\mu = -\chi = \left[ \frac{\partial E}{\partial N} \right]_{v(r)} = -\left( \frac{I + A}{2} \right)$$

$$\eta = \frac{1}{2} \left[ \frac{\partial^2 E}{\partial N^2} \right]_{v(r)} = \frac{I - A}{2}$$

$$\sigma = 1/\eta$$

$$\omega = \chi^2 / 2\eta = \mu^2 / 2\eta$$

$$\varepsilon = 1/\omega$$

$$\omega^+ = (I + 3A)^2 / (16(I - A))$$

$$\omega^- = (3I + A)^2 / (16(I - A))$$

$$\langle \alpha \rangle = 1/3 [\alpha_{xx} + \alpha_{yy} + \alpha_{zz}]$$

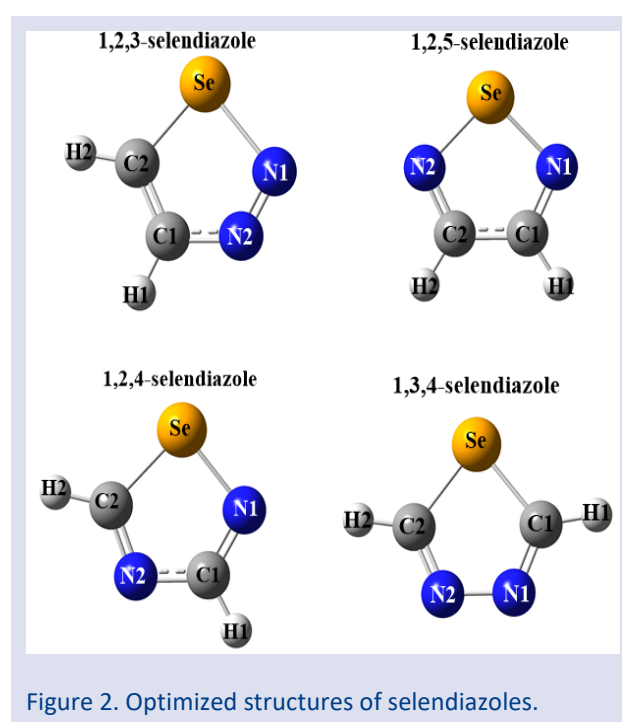
In docking studies, compounds and proteins examined in the MMFF94 method were optimized with

DockingSever [28]. Charge calculations were made using the Gasteiger method. Neutral media (pH = 7.0) was used in all calculations. The dimensions of the grid maps were  $90 \times 90 \times 90 \text{ \AA}$  (x, y and z) and were calculated by Solis & Wets local search method and Lamarckian genetic algorithm [29].

## Results and Discussion

### Optimized Structures

Derivatives of the selendiazoles in the literature, consisting of differences in sulfur, nitrogen and carbon locations, were optimized at the B3LYP/6-31G(d) level. The optimized structures obtained are given in Figure 2. Some bond lengths and bond angles obtained from the optimized structures of selendiazoles are given in Table 1.



When the bond lengths and angles given in Table 1 are examined, it is generally in the range of 1.845-1.963 Å of Se-C and Se-N bonds. Selenium bonds were found to be the shortest in 1,2,5-selendiazole compound. In 1,2,5-selendiazole, selenium is bonded to two more electronegative nitrogen atoms than carbon. It is expected that nitrogen atoms will attract bond electrons to themselves and the bond they form with selenium is shorter than the others. The lengths of the N-C bonds in the studied compounds are around 1.3 Å. According to the derivatives of the compounds, there is not much difference between C-C bonds and C-H bonds. When their geometric structures are evaluated according to bond angles, there are deviations from the cyclopentadienyl structure.

Table 1. Selected bond lengths and bond angles for seleno compounds studied at B3LYP/6-31G(d) level in the gas phase

1,2,3-selendiazole		1,2,5-selendiazole		1,2,4-selendiazole		1,3,4-selendiazole	
<b>Bonds (Å)</b>							
Se-N1	1.963	Se-N1	1.807	Se-N1	1.814	Se-C2	1.872
Se-C2	1.845	Se-N2	1.807	Se-C2	1.867	Se-C1	1.872
N1-N2	1.249	N2-C2	1.310	N1-C1	1.308	C2-N2	1.298
N2-C1	1.381	N1-C1	1.310	C1-N2	1.378	C1-N1	1.298
C1-C2	1.377	C1-C2	1.461	N2-C2	1.302	N1-N2	1.370
C2-C4	1.500	C2-C4	1.503	C1-H1	1.086	C1-H1	1.083
C1-C5	1.504	C1-C3	1.503	C2-H2	1.084	C2-H2	1.083
<b>Bond angles (°)</b>							
Se-N1-N2	108.7	Se-N1-C1	107.8	Se-N1-C1	107.4	Se-C1-N1	114.8
N1-N2-C1	120.0	N1-C1-C2	115.9	N1-C1-N2	122.5	C1-N1-N2	114.4
N2-C1-C2	115.0	C1-C2-N2	115.9	C1-N2-C2	110.3	N1-N2-C2	114.4
C1-C2-Se	110.2	C2-N2-Se	107.8	N2-C2-Se	112.5	N2-C2-Se	114.8
C2-Se-N1	85.84	N2-Se-N1	92.4	C2-Se-N1	87.1	C2-Se-C1	81.4

### Stability of Selendiazoles

By examining the thermodynamic parameters of compounds with the same number of electrons, their stability can be predicted. The total energy (E) and Gibbs free energy ( $G^\circ$ ) taken into account in predicting the stability of the selendiazoles were calculated at the B3LYP/6-31G(d) level and are given in Table 2.

Table 2. Total and Gibbs free energies of Selendiazoles ( $\text{kJ}\cdot\text{mol}^{-1}$ ).

Compounds	E ( $\text{kJ}\cdot\text{mol}^{-1}$ )	$G^\circ$ ( $\text{kJ}\cdot\text{mol}^{-1}$ )
1,2,3-selendiazole	-6790280.119660	-6790245.113860
1,2,4-selendiazole	-6790355.014670	-6790316.958053
1,2,5-selendiazole	-6790337.838650	-6790300.519796
1,3,4-selendiazole	-6790281.629322	-6790245.830627

The stability of the Selendiazoles can be determined by decreasing the Total and Gibbs free energies. Selendiazole, which has the lowest energy, has the most stability [30]. Thus, the order of stability of the selendiazoles should be:

1,2,4- selendiazole > 1,2,5-selendiazole > 1,3,4-selendiazole > 1,2,3-selendiazole

Considering E and  $G^\circ$ , the most unstable selendiazole is 1,2,3-selendiazole. However, 1,2,3-selendiazole and 1,3,4-selendiazole E and  $G^\circ$  values are close to each other. Therefore, 1,2,3-selendiazole compounds appear in the literature as derivatives too. The 1,2,4-selendiazoles may have had fewer chemical investigations than other selendiazoles due to their stability.

### IR Spectrum

Infrared spectra of molecules are one of the most important methods in structural characterization. The IR spectra of the four derivatives constituting the basic structures of selendiazoles were calculated at the B3LYP/6-31G(d) level. Obtained spectra are given in Figure 2. The peaks in the vibrational spectra of the Selendiazole compounds were numbered. The frequencies in the spectra were examined in detail with the VEDA program and listed in Table 3 and Table 4.

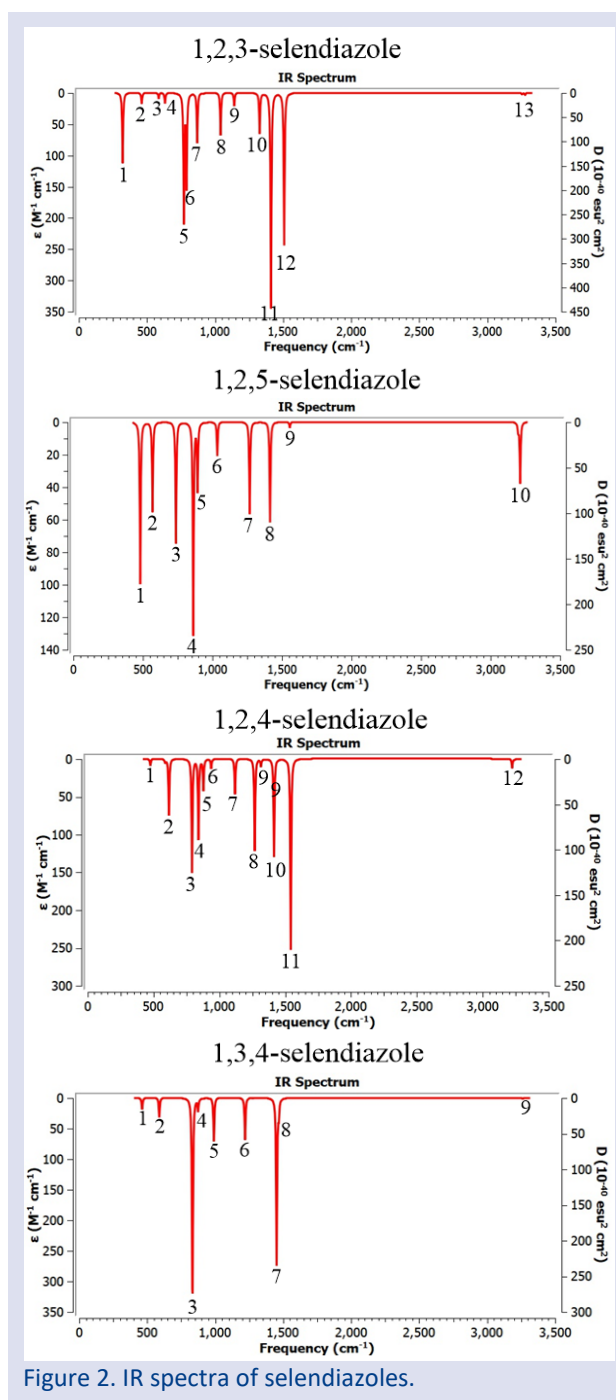


Figure 2. IR spectra of selendiazoles.

Table 3. Calculated frequencies and labeling of 1,2,3 and 1,2,4-selendiazoles

1,2,3 selendiazole			1,2,4 selendiazole		
Mod	Freq. (cm <sup>-1</sup> )	Label	Mod	Freq. (cm <sup>-1</sup> )	Label
1	321	BEND (SeCC)	1	480	STRE (SeN)
		BEND (NNC)			BEND (SeNC)
		BEND (NCC)			
2	461	TORS (NNCC)	2	616	TORS (CNCN)
		TORS (NCCSe)			
3	586	STRE (SeC)	3	792	BEND (CNC)
		BEND (NNC)			BEND (NCN)
		BEND (NCC)			BEND (SeNC)
4	632	TORS (HCNN)	4	841	TORS (HCNC)
		TORS (NNCC)			TORS (CNCN)
		TORS (NCCSe)			
5	771	TORS (HCSeN)	5	878	BEND (CNC)
		TORS (HCNN)			BEND (NCN)
		TORS (NNCC)			
6	790	STRE (SeC)	6	937	TORS (CNCN)
		BEND (NNC)			
		BEND (NCC)			
7	869	BEND (SeCC)	7	1119	BEND (HCN)
		BEND (NNC)			BEND (NCN)
		BEND (NCC)			
8	1040	STRE (NC)	8	1268	BEND (HCN)
		BEND (HCSe)			
9	1141	STRE (CC)	9	1315	STRE (NC)
		STRE (NC)			BEND (HCN)
		BEND (HCSe)			BEND (NCN)
		BEND (HCN)			
10	1327	STRE (NC)	10	1415	STRE (NC)
		BEND (HCSe)			
		BEND (HCN)			
		BEND (NCC)			
11	1411	STRE (NN)	11	1542	STRE (NC)
		STRE (CC)			
12	1507	STRE (NN)	12	3224	STRE (CH)
		STRE (CC)			
		BEND (HCN)			
13	3254	STRE (CH)			

Table 4. Calculated frequencies and labeling of 1,2,5 and 1,3,4-selendiazoles

1,2,5 selendiazole			1,3,4 selendiazole		
Mod	Freq. (cm <sup>-1</sup> )	Label.	Mod	Freq. (cm <sup>-1</sup> )	Label
1	480	TORS (SeNCC)	1	460	STRE (SeC)
2	568	STRE (SeN)	2	590	BEND (SeCN)
		BEND (SeNC)			STRE (SeC)
3	737	STRE (CC)	3	832	BEND (SeCN)
		BEND (NCC)			TORS (HCNN)
4	862	TORS (HCNSe)	4	874	BEND (CNN)
5	893	BEND (NCC)	5	990	STRE (NN)
		BEND (CCN)			
6	1035	STRE (CC)	6	1219	BEND (HCN)
		BEND (HCN)			
7	1268	BEND (HCN)	7	1451	STRE (NC)
8	1414	STRE (NC)	8	1467	STRE (NC)
		STRE (CC)			
		BEND (HCN)			
9	1556	STRE (NC)	9	3258	STRE (CH)
10	3212	STRE (CH)			

In Tables 3 and 4, the bond stresses corresponding to the peaks given in the IR spectra of the selendiazoles and their labeling are given. It is seen that the bond stress modes correspond to one or more vibrational transitions with the labels made with the VEDA 4 program, which considers the calculated frequencies potential energy distribution (PED) contributions. Therefore, the high oscillatory strength bond strain modes of the related compounds were investigated. In general, stretching (STRE), bending (BEND) and torsional (TORS) vibrations are also present in selendiazole compounds. Bond stretching frequencies of selenium and selene-bound atoms are at low frequency values. The bond stretch frequencies of 1,2,3-, 1,2,4-, 1,2,5- and 1,3,4-selendiazoles differ slightly from each other. For example, the N-C bond stretching frequency in 1,2,3-selendiazole is not alone in the range of 1040, 1141 and 1327  $\text{cm}^{-1}$ , but is seen in a peak that includes more than one bond stretching vibrations. C-H bond stretching frequency in 1,2,3-selendiazole is 3254  $\text{cm}^{-1}$ . The 1,2,4-selendiazole

compound has only the N-C bond stretching frequency at 1415 and 1542  $\text{cm}^{-1}$ . The C-H vibrational frequency for 1,2,4-selendiazole is at 3224  $\text{cm}^{-1}$ . In the vibration spectrum of 1,2,5-selendiazole, the N-C and C-H vibrational spectra correspond to 1556 and 3212  $\text{cm}^{-1}$ , respectively. N-C bond stretching frequencies for 1,3,4-selendiazole are clearly seen at 1467 and 1451  $\text{cm}^{-1}$ . The C-H bond stretching frequency for the mentioned compound is 3258  $\text{cm}^{-1}$ .

### $^1\text{H}$ and $^{13}\text{C}$ -NMR Spectrum

NMR spectra of molecules are one of the most essential spectroscopic methods for the identification of skeletal structure. The chemical shifts of the molecules examined by computational chemistry methods were calculated at the B3LYP/6-31G(d) level relative to the reference tetramethylsilane. Atomic labeling and  $^1\text{H}$  and  $^{13}\text{C}$ -NMR spectra of selendiazole compounds are given in Figure 3.

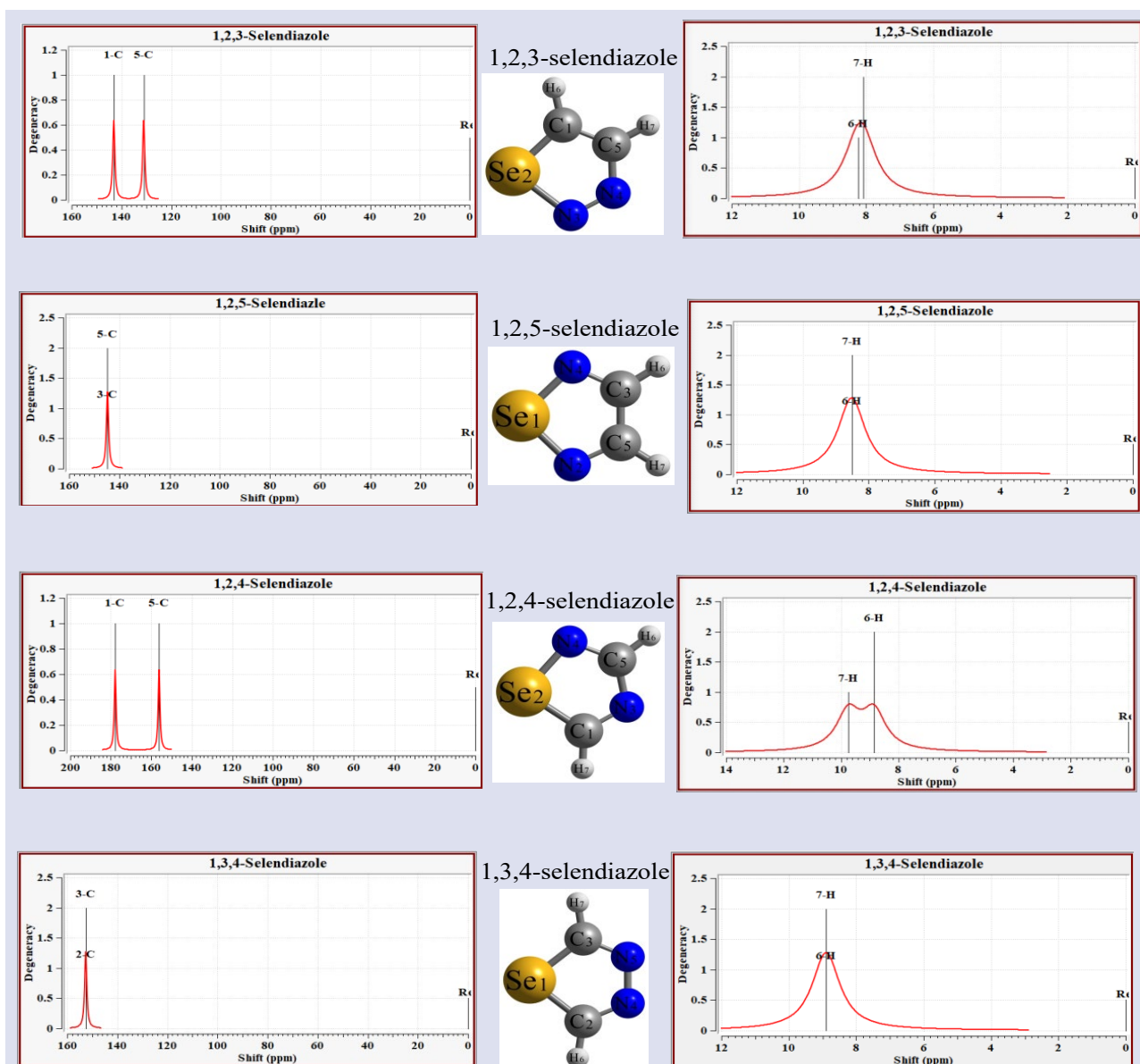


Figure 3. Atomic labeling and  $^{13}\text{C}$ - and  $^1\text{H}$ -NMR spectra of selendiazoles

The data shown in Figure 3 give  $^{13}\text{C}$  chemical shifts for the 1,2,3-selendazole molecule. For 1,2,3-selendazole molecule, it is 143.1 and 131.0 ppm at C1 and C5 atoms, respectively. The  $^1\text{H}$  chemical shifts are 8.2 and 8.1 ppm for H6 and H7 atoms, respectively.  $^{13}\text{C}$  chemical shifts for 1,2,5-selendazole molecule were calculated as 144.7 ppm at C3 and C5 atoms. The  $^1\text{H}$  chemical shifts are 23.5 ppm for the H6 and H7 atoms. The  $^{13}\text{C}$  chemical shifts for the 1,2,4-selendazole molecule are 177.8 and 156.1 ppm at the C1 and C5 atoms, respectively. The  $^1\text{H}$  chemical shifts are 9.7 and 8.8 ppm for H6 and H7 atoms, respectively.  $^{13}\text{C}$  chemical shifts for the 1,3,4-selendazole molecule were determined as 152.6 ppm at C2 and C3 atoms.  $^1\text{H}$  chemical shifts were found to be 8.9 ppm for H6 and H7 atoms. The calculation results meet the theoretical expectations. Nitrogen is an electronegative atom and attracts more electrons than neighboring carbon atoms with lower electronegativity. This results in less shielding of carbon

nuclei. Less shielded nuclei exhibit higher chemical shift values. For this reason, there are differences in the chemical shift values of the carbon atoms and subsequently the hydrogen atoms in the molecules.

### Quantum Chemical Parameters

Quantum chemical parameters such as the highest occupied molecular orbital (HOMO) energy, the lowest unoccupied molecular orbital (LUMO) energy, hardness ( $\eta$ ), softness ( $\sigma$ ), chemical potential ( $\mu$ ), electronegativity ( $\chi$ ), electrophilicity index ( $\omega$ ), nucleophilicity index ( $\epsilon$ ), the electron accepting power ( $\omega^+$ ) and electron donating power ( $\omega^-$ ) have an important place in biological activity studies. The quantum chemical parameters calculated at the B3LYP/6-31G(d) level for the studied selendazole molecules are given in Table 5 in detail.

**Table 5.** Quantum chemical parameters calculated for selendazole compounds

Parameters	1,2,3-selendazole	1,2,5-selendazole	1,2,4-selendazole	1,3,4-selendazole
$E_{\text{HOMO}}$ (eV)	-6.5969	-6.8146	-7.6647	-7.6114
$E_{\text{LUMO}}$ (eV)	-2.0760	-1.8901	-1.7059	-1.8640
$\Delta E$	4.5209	4.9245	5.9588	5.7474
$\eta$ (eV)	2.2605	2.4622	2.9794	2.8737
$\sigma$ (eV $^{-1}$ )	0.4424	0.4061	0.3356	0.3480
$\chi$ (eV)	4.3364	4.3524	4.6853	4.7377
$\mu$ (eV $^{-1}$ )	-4.3364	-4.3524	-4.6853	-4.7377
$\omega$	4.1595	3.8467	3.6840	3.9054
$\epsilon$	0.2404	0.2600	0.2714	0.2561
$\omega^+$	1.5583	1.4296	1.3323	1.4315
$\omega^-$	6.610	6.331	6.399	6.633
$\alpha$	84.1150	82.9273	57.0193	57.8453

The HOMO and LUMO orbital energies can provide a comparison of the electron-donating and electron-accepting abilities of molecules, respectively. It has been noted that the HOMO orbital represents the electron-donating ability and its high values belong to a good inhibitor. Low LUMO molecular orbital energy and energy gap values between HOMO and LUMO orbitals indicate that the molecule does not want to donate electrons and that electron exchange is easy, respectively. It is clear from the data presented for the energies of the leading molecular orbitals in the table above that the biological activity trends of the studied molecules follow the following order:

1,2,3-selendazole > 1,2,5-selendazole > 1,3,4-selendazole > 1,2,4-selendazole

Hardness, softness and polarizability, which are among the quantum chemical parameters, can be illuminated in the light of numerical values with electronic structure principles of the molecule's activity behaviors. Chemical hardness is reported as resistance to electron cloud polarization or deformation of molecules [31]. According to Pearson, hard molecules have energy gap values between the high-energy HOMO and LUMO orbitals and are visualized in Figure 4 by contour diagrams. The shapes of the HOMO and LUMO molecular orbitals indicate that

the electron-donating orbitals of the compounds are different, but the electron acceptor regions can be generally taken into similar lobes. The global softness of the molecules is equal to the opposite sign of their hardness. Soft and polarizable molecules have high activities. Electronegativity represents the electron-withdrawing forces of molecules and chemical potential electron-donating forces. The electrophilicity index reflects the tendency to accept electrons from electron-rich chemical species. The nucleophilicity index indicates the tendency to donate electrons to chemical species. It can be said that molecules with low electronegativity and electrophilicity index and high chemical potential and nucleophilicity index are more advantageous in terms of biological activities. Moreover, the parameters known as electron donation strength and electron-accepting strength provide important clues about the electron-donating and electron-accepting abilities of molecules. A molecule with effective biological activity should easily donate electrons.

In this case, the activity order of the selendazoles examined according to the mentioned parameters can be evaluated as follows.

1,2,3-selendiazole > 1,2,5-selendiazole > 1,3,4-selendiazole > 1,2,4-selendiazole

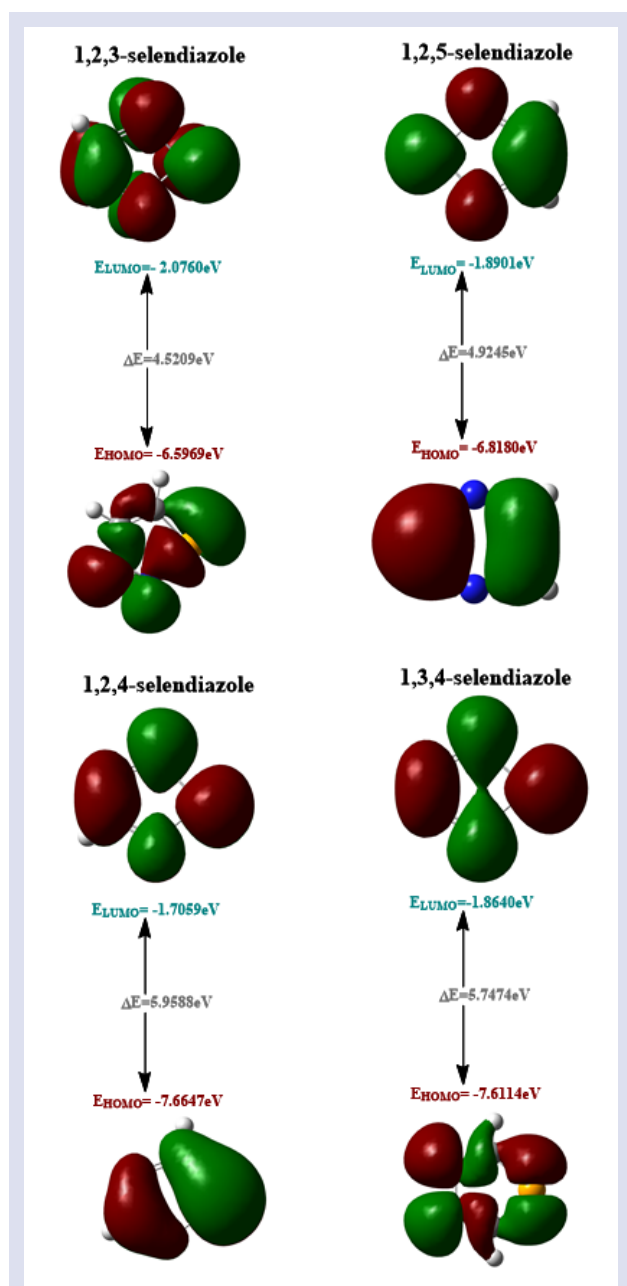


Figure 4. Frontier molecular orbital contour diagrams of selendiazoles

### Fukui Indexes

Fukui indices are very important for the analysis of the local atomic activities of Selendiazoles. The calculated Fukui indices of the examined molecules are presented visually in Figure 5. It is important to note that higher  $f^-$  values represent sites of electrophilic attack, while a higher  $f^+$  value corresponds to sites suitable for nucleophilic attack. From the presented image, suitable regions for electrophilic and nucleophilic attacks of the studied molecules can be seen. In addition, electrophilic and nucleophilic indices of atom-sized selendiazoles are given in Table 6.

Table 6 shows that 4(N) is the most suitable site for electrophilic attack for selendiazole compounds. However, the nucleophilic attack sites of the selendiazole compounds vary according to the derivatives of the compounds.

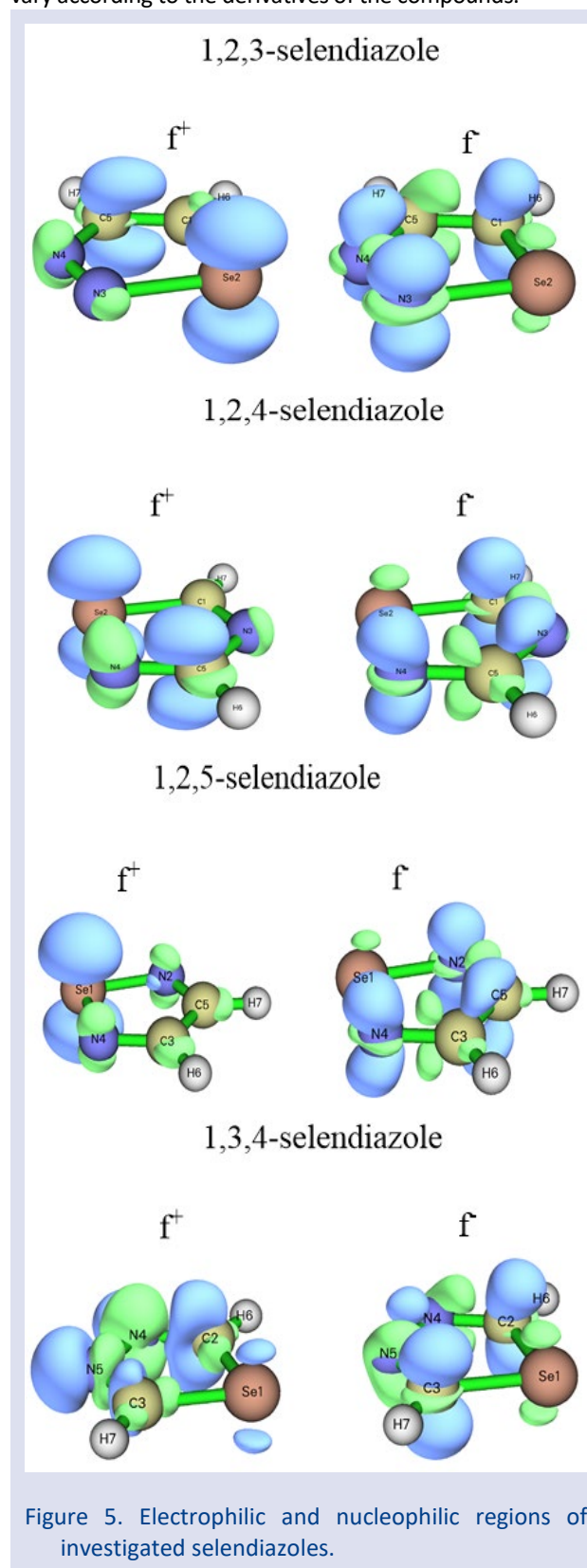


Figure 5. Electrophilic and nucleophilic regions of investigated selendiazoles.

As a result, it has been observed that heteroatoms are the most active atoms. This highlights the important role

of selenidazole molecules in their activity and interaction ability.

**Table 6.** Fukui function indices of the selenidazoles

1,2,3-selenidazole			1,2,5-selenidazole		
Atoms	Electrophilicity	Nucleophilicity	Atoms	Electrophilicity	Nucleophilicity
1(C)	-0.03340	-0.51984	1(Se)	-1.03668	-0.25482
2(Se)	-0.67610	-0.32125	2(N)	-0.00094	-0.55512
3(N)	-0.06783	-0.68865	3(C)	-0.03585	-0.21159
4(N)	0.00095	-0.35577	4(N)	-0.00094	-0.55512
5(C)	-0.31700	-0.00336	5(C)	-0.03585	-0.21159
6(H)	-0.05410	-0.17575	6(H)	-0.06002	-0.11449
7(H)	-0.08148	-0.09374	7(H)	-0.06002	-0.11449
1,2,4-selenidazole			1,3,4-selenidazole		
Atoms	Electrophilicity	Nucleophilicity	Atoms	Electrophilicity	Nucleophilicity
1(C)	-0.02217	-0.57550	1(Se)	-0.43817	-0.29090
2(Se)	-0.74968	-0.27509	2(C)	-0.22625	-0.55817
3(N)	-0.02516	-0.18116	3(C)	-0.11865	-0.55817
4(N)	0.02114	-0.53582	4(N)	0.07060	-0.07091
5(C)	-0.27691	-0.13805	5(N)	-0.28278	-0.07091
6(H)	-0.07471	-0.09915	6(H)	-0.06359	-0.16308
7(H)	-0.05237	-0.17724	7(H)	-0.05620	-0.16308

### Molecular Docking

In recent years, molecular docking studies have been very popular in biological activity studies. Thanks to the determined protein sequences of biological systems, the activity studies of the drug candidate molecules examined can be predicted. In this way, information about the interaction energies and binding modes of the biological system with the chemical species can be obtained without loss of time and matter. For this purpose, biological activities of selenidazole derivatives, which basically contain structural differences, against cervical cancer cells and human MCF-7 breast cancer cells were investigated by molecular docking studies. The protein representing the cervical cancer cell line from the protein data bank was identified as PDB ID: 3F81 [32]. Loss of VHR phosphatase induces cell cycle arrest in HeLa carcinoma cells, suggesting that VHR inhibition may be a useful approach to arrest the growth of cancer cells. The 3F81 target protein

contains multidentate small molecule VHR inhibitors that inhibit enzymatic activity at anomolar concentrations and exert antiproliferative effects on cervical cancer cells. For the protein representative of the human MCF-7 breast cancer cell line, the target protein PDB ID: 3HY3 [33] was preferred. 5,10-Methenyltetrahydrofolate synthetase (MTHFS) regulates carbon flux through a one-carbon metabolic network that supplies essential components for cell growth and proliferation. Inhibition of MTHFS in human MCF-7 breast cancer cells has been shown to arrest the growth of cells. The lack of three-dimensional structure of human MTHFS (hMTHFS) has hindered the rational design and optimization of drug candidates. The 3HY3 target protein was chosen to examine this deficiency. The interaction energies between selenidazoles and selected target proteins and secondary chemical interactions during binding are given in Tables 7 and 8, respectively. The binding modes obtained from the docking results are given in Figure 6.

**Table 7.** Docking energies (kcal/mol) between selenidazoles and target proteins

Target proteins Compounds	3F81			3HY3		
	E <sub>BIND</sub>	E <sub>SECONDARY</sub>	E <sub>TOTAL</sub>	E <sub>BIND</sub>	E <sub>SECONDARY</sub>	E <sub>TOTAL</sub>
1,2,3-selenidazol	-4.37	-4.10	-4.37	-4.32	-4.27	-4.32
1,2,5-selenidazol	-3.60	-3.49	-3.60	-3.77	-3.71	-3.77
1,2,4-selenidazol	-3.38	-3.23	-3.38	-3.75	-3.69	-3.75
1,3,4-selenidazol	-4.18	-3.99	-4.18	-4.17	-4.11	-4.17

The energies obtained from the docking results; binding energy (E<sub>BIND</sub>), secondary chemical interaction energy (E<sub>SECONDARY</sub>) and total interaction energy (E<sub>TOTAL</sub>). According to these energy values, it is seen that 1,2,3-selenidazole interacts better with the target protein representing the cervical cancer

cell line and its biological activity is higher than other selenidazoles. A similar situation shows that the biological activity of 1,2,3-selenidazole compound against the target protein representing the MCF-7 breast cancer cell line is high.



In addition, the results show that there is a general trend in the biological activity ranking of selendiazole.

1,2,3-selendiazole > 1,3,4-selendiazole > 1,2,5-selendiazole > 1,2,4-selendiazole

Table 8. Binding modes between selendiazoles and target proteins

Target Proteins	3F81				3HY3			
	Compounds	H-bond	Polar	Hydrophobic	Pi-Pi	H-bond	Polar	Hydrophobic
1,2,3-selendiazole	CYS124	ARG125 ARG130	-	TYR128	-	-	PRO81 ILE111	-
1,2,5-selendiazole	-	ARG125 ARG130	MET69	-	GLY136 LEU173 GLN178	-	ILE62 PRO135	PHE55
1,2,4-selendiazole	ASP92 CYS124	ASP92 ARG130	CYS124	-	PRO81 PRO112	GLN113	LEU56 PRO81 ILE111	-
1,3,4-selendiazole	CYS124	ARG125 ARG130	-	-	-	-	LEU56 PRO81 ILE111	-

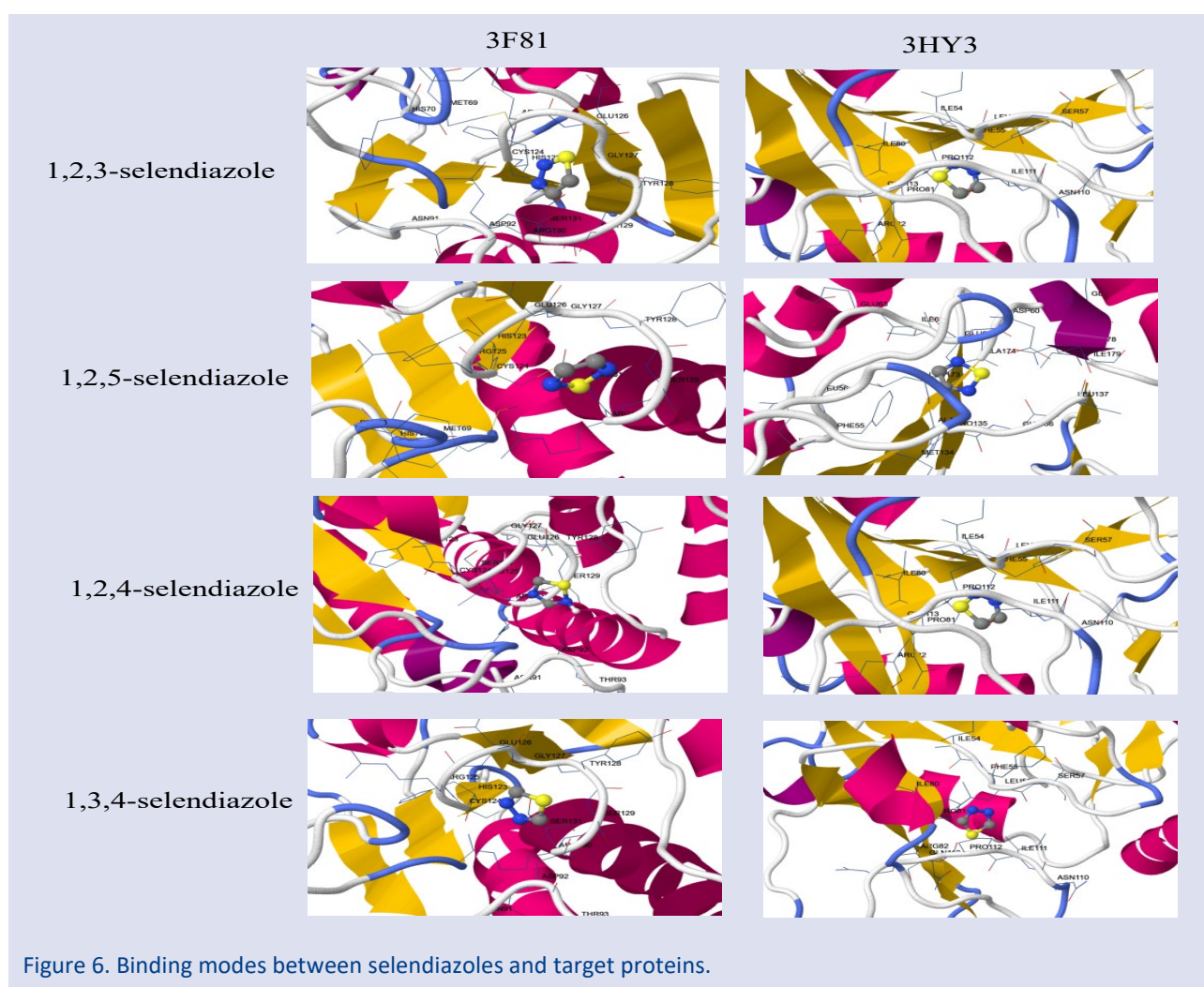


Figure 6. Binding modes between selendiazoles and target proteins.

## Conclusion

1,2,3-selendiazole, 1,2,5-selendiazole, 1,2,4-selendiazole and 1,3,4-selendiazole compounds, which are the basic structures of the selendiazole compounds, were optimized at the B3LYP/6-31G(d) level. The obtained structural parameters showed differences in the cyclopentadienyl ring with respect to the selendiazole derivative. The stability of the derivatives of Selendiazole

compounds was investigated. The most stable structure was determined as 1,2,4-selendiazole and the most unstable structure was 1,2,3-selendiazole. For structural characterization, IR and NMR techniques, which are spectroscopic methods, were applied in detail and the differences between the obtained spectra were compared. Activity estimations were made according to

quantum chemical parameters such as the highest occupied molecular orbital (HOMO) energy, the lowest unoccupied molecular orbital (LUMO) energy, hardness ( $\eta$ ), softness ( $\sigma$ ), chemical potential ( $\mu$ ), electronegativity ( $\chi$ ), electrophilicity index ( $\omega$ ), nucleophilicity index ( $\epsilon$ ), the electron accepting power ( $\omega^+$ ), electron donating power ( $\omega^-$ ) and polarizability. It is predicted that the activity will increase according to the order of indecision. The local electrophilic and nucleophilic regions were examined using the Fukui index functionals, and the active regions of heteroatoms were obtained from calculations. Selenodiazole derivatives were found to exhibit activity parallel to quantum chemical parameters as a result of docking studies with proteins representing cervical cancer cell line and MCF-7 breast cancer cell line.

### Conflicts of interest

All authors declare that they have no conflict of interest.

### Referanslar

- Joshi P. G., More M. S., Jadhav A. A., Khanna P. K., Materials and biological applications of 1, 2, 3-selenodiazoles: a review, *Materials Today Chemistry*, 16 (2020) 100255.
- Khanna P. K., Materials chemistry of 1, 2, 3-Selenodiazoles, *Phosphorus, Sulfur, and Silicon and the Related Elements*, 180(3-4) (2005) 951-955.
- Moawad E. B., Yousif M. Y., Metwally M. A., Synthesis of certain heteroaryl-fused pyrimidines and pyridines and seleno- and thia-diazoles with naphthyl substituent as potential antifungal agents, *Die Pharmazie*, 44(12) (1989) 820-822.
- Al-qatrani N. H. K., Essa A. H., Al-Jadaan S. A., Synthesis, Characterization and Antibacterial Activity of Some New 1, 2, 3-Selenodiazole derived from 4-amino acetophenone, *Journal of Physics: Conference Series*, 1279(1) (2019) 012036.
- Atta S. M. S., Farrag D. S., Sweed A. M., Abdel-Rahman A. H., Preparation of new polycyclic compounds derived from benzofurans and furochromones. An approach to novel 1, 2, 3-thia-, and seleno-diazolofurochromones of anticipated antitumor activities, *European Journal of Medicinal Chemistry*, 45(11) (2010) 4920-4927.
- Arsenyan P., Rubin K., Shestakova I., Domracheva I., 4-Methyl-1, 2, 3-selenodiazole-5-carboxylic acid amides: antitumor action and cytotoxic effect correlation. *European Journal of Medicinal Chemistry*, 42(5) (2007) 635-640.
- Al-Balas Q. A., Al-Smadi M. L., Hassan M. A., Al Jabal G. A., Almaaytah A. M., Alzoubi K. H., Multi-Armed 1, 2, 3-Selenodiazole and 1, 2, 3-Thiadiazole Benzene Derivatives as Novel Glyoxalase-I Inhibitors, *Molecules*, 24(18) (2019) 3210.
- Abramov M. A., Dehaen W., D'hooge B., Petrov M. L., Smeets S., Toppet S., Voets M., Nucleophilic intramolecular cyclization reactions of alkynychalcogenolates, *Tetrahedron*, 56(24) (2000) 3933-3940.
- Rocha J. B., Piccoli B. C., Oliveira, C. S. (2017). Biological and chemical interest in selenium: a brief historical account, *ARKIVOC: Online Journal of Organic Chemistry*, 2017.
- Mhizha S., Młochowski J., Synthesis of 2-acyl- and 2-sulfonylbenzisoselenazol-3 (2H)-ones, *Synthetic Communications*, 27(2) (1997) 283-291.
- Fischer H., Kalbas C., Hofmann J., Dichalcogenolanes by ring-expansion of transition metal-coordinated thietanes and selenetanes, *Journal of the Chemical Society, Chemical Communications*, (15) (1992) 1050-1051.
- Asmus S. M., Bergstraesser U., Regitz M., Organophosphorus compounds; 142: A simple approach to 1, 2, 4-seleno- and telluradiphospholes from phosphalkynes and the chalcogen elements and a first study of their reactivity, *Synthesis*, 1999(09) (1999) 1642-1650.
- Ito M., Tokito N., Okazaki R., 1, 3, 2, 4-Diselenastannaboretane, a novel selenium-containing four-membered boracycle: synthesis, structure and thermal cycloreversion into a selenoxoborane, *Chemical Communications*, (22) (1998) 2495-2496.
- Kodani M., Takimiya K., Aso Y., Otsubo T., Nakayashiki T., Misaki Y., Effective Synthesis of 1, 3-Diselenole-2-selone-4, 5-diselenolate (dsis) and its Utilization for the Synthesis of Selenocycle-fused Tetraselenafulvalene (TSF) Derivatives, *Synthesis*, 2001(11) (2001) 1614-1618.
- Osajda M., Bisbenzisoselenazol-3 (2H)-ones, a new group of ebselen analogues, *Polish Journal of Chemistry*, 75(6) (2001) 823-830.
- Bertini V., Synthesis of 1, 2, 5-Selenodiazole and some of its Derivatives, *Angewandte Chemie International Edition in English*, 6(6) (1967) 563-564.
- El-Sadek M. M., El-Dayem, N. S. A., Hassan S. Y., Yacout G. A., 1, 3, 4-oxadiazole and selenodiazole derivatives as new C-glycosyl analogs with MAO-B, antibacterial and antifungal activities, *Int. Res. J. Microbiol.*, 4 (2013) 204-219.
- Velusamy M., Thomas K. J., Lin J. T., Wen Y. S., Benzo [1, 2, 5] selenodiazole bridged amines: electro-optical properties, *Tetrahedron Letters*, 46(44) (2005) 7647-7651.
- Ostrowski J. C., Susumu K., Robinson M. R., Therien M. J., Bazan G. C., Near-Infrared Electroluminescent Light-Emitting Devices Based on Ethyne-Bridged Porphyrin Fluorophores, *Advanced Materials*, 15(15) (2003) 1296-1300.
- Dennington R.D., Keith T.A., Millam J.M., GaussView 6.0. 16, Semichem. Inc., Shawnee Mission KS, 2016.
- Frisch M.J., Trucks G.W., Schlegel H.B., Scuseria G.E., Robb M.A., Cheeseman J.R., Nakatsuji H., Gaussian09 Revision D. 01, Gaussian Inc., Wallingford CT, 2009. <http://www.gaussian.com>.
- Becke A. D., Perspective: Fifty years of density-functional theory in chemical physics, *The Journal of Chemical Physics*, 140(18) (2014) 18A301.
- Lee C., Yang W., Parr R. G., Development of the Colle-Salvetti correlation-energy formula into a functional of the electron density, *Physical Review B*, 37(2) (1988) 785.
- Zhao Y., Truhlar D. G., The M06 suite of density functionals for main group thermochemistry, thermochemical kinetics, noncovalent interactions, excited states, and transition elements: two new functionals and systematic testing of four M06-class functionals and 12 other functionals, *Theoretical Chemistry Accounts*, 120(1-3) (2008) 215-241.
- Rassolov V.A., Ratner M.A., Pople J.A., Redfern P.C., Curtiss L.A., 6-31G\* basis set for third-row atoms, *J. Comput. Chem.*, 22 (9) (2001) 976-984.
- EL Aatiaoui, A., Koudad, M., Chelfi, T., ERKAN, S., Azzouzi, M., Aouniti, A., & Oussaid, A., Experimental and

- theoretical study of new Schiff bases based on imidazo (1, 2-a) pyridine as corrosion inhibitor of mild steel in 1M HCl, *Journal of Molecular Structure*, (2021) 1226 129372.
- [27] Al-Otaibi J. S., Mary Y. S., Mary Y. S., Kaya S., Erkan S., Spectral analysis and DFT investigation of some benzopyran analogues and their self-assemblies with graphene, *Journal of Molecular Liquids*, 317 (2020) 113924.
- [28] Bikadi Z., Hazai E., Application of the PM6 semi-empirical method to modeling proteins enhances docking accuracy of AutoDock, *Journal of Cheminformatics*, 1(1) (2009) 1-16.
- [29] Güzel E., Koçyiğit Ü. M., Taslimi P., Erkan S., Taskin, O. S., Biologically active phthalocyanine metal complexes: Preparation, evaluation of  $\alpha$ -glycosidase and anticholinesterase enzyme inhibition activities, and molecular docking studies, *Journal of Biochemical and Molecular Toxicology*, (2021) e22765.
- [30] Köse M., Kurtoglu N., Gümüşsu Ö., Tutak M., McKee V., Karakaş D., Kurtoglu M., Synthesis, characterization and antimicrobial studies of 2-((E)-[(2-hydroxy-5-methylphenyl) imino] methyl)-4-[(E)-phenyldiazenyl] phenol as a novel azo-azomethine dye, *Journal of Molecular Structure*, 1053 (2013) 89-99.
- [31] Kaya S., Kaya C., A new method for calculation of molecular hardness: a theoretical study, *Computational and Theoretical Chemistry*, 1060 (2015) 66-70.
- [32] Wu S., Vossius S., Rahmouni S., Miletic A. V., Vang T., Vazquez-Rodriguez J., ... Tautz L. Multidentate small-molecule inhibitors of vaccinia H1-related (VHR) phosphatase decrease proliferation of cervix cancer cells, *Journal of Medicinal Chemistry*, 52(21) (2009) 6716-6723.
- [33] Wu D., Li Y., Song G., Cheng C., Zhang R., Joachimiak A., ... Liu Z. J., Structural basis for the inhibition of human 5, 10-methenyltetrahydrofolate synthetase by N10-substituted folate analogues, *Cancer Research*, 69(18) (2009) 7294-7301.

## The Effect of Mullite Addition on Wear Properties of SiO<sub>2</sub> Doped ZrO<sub>2</sub> Ceramics

Mehmet Akif Hafizoğlu<sup>1,a,\*</sup>, Tahsin Boyraz<sup>2,b</sup>, Ahmet Akkuş<sup>3,c</sup>

<sup>1</sup> Department of Mechanical Engineering, Faculty of Engineering, Dicle University, Diyarbakır, Türkiye.

<sup>2</sup> Department of Metallurgical and Materials Engineering, Faculty of Engineering, Sivas Cumhuriyet University, Sivas, Türkiye.

<sup>3</sup> Department of Mechanical Engineering, Faculty of Engineering, Sivas Cumhuriyet University, Sivas, Türkiye.

\*Corresponding author

### Research Article

#### History

Received: 29/10/2021

Accepted: 18/04/2022

#### Copyright



©2022 Faculty of Science,  
Sivas Cumhuriyet University

### ABSTRACT

Mullite (3Al<sub>2</sub>O<sub>3</sub>.2SiO<sub>2</sub>) and 10 mol% silica added zirconia (10 mol% SiO<sub>2</sub> - 90 mol% ZrO<sub>2</sub>) ceramic powders were synthesized by conventional ceramic processing route. The mixtures were prepared by mechanical alloying method using zirconia ball mill in acetone environment. To synthesize mullite, Al<sub>2</sub>O<sub>3</sub> and SiO<sub>2</sub> powders mixture was prepared with stoichiometric proportions and fired it in the air at 1600 °C for 3 h. And the silica added zirconia composites were fired at 1300 °C for 2 h. Thus, silica - zirconia and mullite composite phases were obtained and milling and sieving processes were carried out. Then, mullite-free and 10% by weight mullite reinforced silicon oxide added zirconia mixtures were prepared by powder metallurgy method. The powders were compacted by uniaxial pressing. The formed samples were sintered in a high temperature furnace in air conditions for 1 and 5 h at 1500 and 1600 °C sintering temperatures. Finally, microstructure examinations of the composites with SEM, phase analysis with XRD, hardness, three-point bending and wear tests were performed. In addition, the results of water absorption, porosity and density from physical properties and the effect of mullite additive on the mechanical and especially wear properties of this mixture were investigated.

**Keywords:** Wear, Zirconia, Mullite, Silica, Characterization.

<sup>a</sup> [makif.hafizoglu@dicle.edu.tr](mailto:makif.hafizoglu@dicle.edu.tr)  
<sup>c</sup> [aakkus@cumhuriyet.edu.tr](mailto:aakkus@cumhuriyet.edu.tr)

<sup>ID</sup> <https://orcid.org/0000-0002-9689-3004>  
<sup>ID</sup> <https://orcid.org/0000-0002-6881-9333>

<sup>b</sup> [tahsinboyraz@cumhuriyet.edu.tr](mailto:tahsinboyraz@cumhuriyet.edu.tr) <sup>ID</sup> <https://orcid.org/0000-0003-4404-6388>

## Introduction

Among ceramics, zirconia (ZrO<sub>2</sub>) and its composites have become very popular for technological and many scientific studies because of their good mechanical properties, corrosion resistance, low thermal conductivities, higher temperature stabilities and higher chemical stabilities [1]. They are preferred as significant materials for refractory materials, high temperature furnaces, components that are resistant to wear, various cutting tools, dental studies and a lot of fields. High-purity zirconia (ZrO<sub>2</sub>) exhibits three polymorphs depending on temperature: monoclinic phase is stable up to about 1170 °C. After this temperature, the conversion from the monoclinic phase to the tetragonal phase begins and the tetragonal phase is stable up to 2370 °C. From this temperature to the melting temperature of 2680 °C, it is in the cubic zirconia phase [2]. Depending on the cooling processes, conversion from the t-ZrO<sub>2</sub> phase to the m-ZrO<sub>2</sub> phase takes place. Transformation is very important as it causes volumetric changes of around 3% to 5% and thus cracks. Due to preventing this transformation and stabilizing the zirconia, it is common to use stabilizers. Addition of stabilizers to zirconia, lowers temperature of the transformations, reduces volumetric growth or shrinking and blocks the polymorphic transformations. By using stabilizers, it is possible to make stable the high-temperature phases at low temperatures too [3]. Different stabilizers, such as, Al<sub>2</sub>O<sub>3</sub> [4], CaO [5], CeO<sub>2</sub> [6,7], MgO [8–10], SiO<sub>2</sub> [11-13], TiO<sub>2</sub> [14,15], Y<sub>2</sub>O<sub>3</sub> [16,17] and

even a combination of them [18,19], stabilize and hold stable the ZrO<sub>2</sub> in the tetragonal and/or cubic forms at room temperature. It is possible to produce materials including only t-ZrO<sub>2</sub> or c-ZrO<sub>2</sub> or a mixture of these with m-ZrO<sub>2</sub> phases by adding different quantities of stabilizer. If less than sufficient stabilizing oxide is added, partially stabilized zirconia (PSZ) is obtained instead of fully stabilized zirconia. PSZ usually consists of two or more closely mixed phases. As a result of using stabilizers and obtaining fully or partially stabilized zirconia, could be achieved superb mechanical properties for example bending strength, hardness, fracture toughness [20,21]. Zirconia exhibits better mechanical properties than other ceramics. However, like all other ceramics, it is fragile and cannot be formed at room temperature. Therefore, it is desirable to increase the toughness of these materials. So, some energy absorbing mechanisms such as transformation toughening and fiber reinforcement are used in ceramic matrices [22-25].

Powder metallurgy method is frequently used in the shaping and sintering processes of powder matrix alloy and reinforcement materials after mixing. In order to obtain a good microstructure, it is very important to distribute all the particles homogeneously within the structure. So, mechanical alloying method has an important place in powder metallurgy. Mechanical alloying is a solid-state powder production and synthesis method that enables the production of homogeneous

materials. Mechanical alloying is the process of powder mixing and grinding in a dry or aqueous environment (acetone, alcohol, water, etc. is used as liquid) used to produce composite powders with small crystal grains and controlled microstructures. This method is one of the common techniques for producing ceramic powders by mechanical methods [26].

In the literature, mullite ( $3\text{Al}_2\text{O}_3 \cdot 2\text{SiO}_2$ ) is described as the matchless stable middle crystalline phase for  $\text{Al}_2\text{O}_3$ - $\text{SiO}_2$  binary system, cost-friendly and exhibiting good refractory ability [27]. Mullite has received significant attention for technological applications because of its well properties like low coefficient of thermal expansion, high melting temperature, good resistance to creep, good chemical stability and satisfactory hardness [28]. In short, fracture toughness of zirconia can be advanced with mullite reinforcement as the secondary phase into the  $\text{ZrO}_2$  matrix and so, the other mechanical properties can be improved too [22]. In addition, the temperature of sintering is also important, because of affecting some properties of ceramics through changing of the crystalline phases and microstructure [29].

Aguilar, D. H. et al., examined the crystallization properties by adding 2 - 80%  $\text{SiO}_2$  into  $\text{ZrO}_2$  matrix and stated that m- $\text{ZrO}_2$ , t- $\text{ZrO}_2$  and  $\text{ZrSiO}_4$  phases were formed in different proportions of compositions [11]. Vasanthavel, S. et al., mixing  $\text{SiO}_2$  with  $\text{ZrO}_2$  in varying proportions by sol-gel method, examined the effect of  $\text{SiO}_2$  addition on phase behavior and stated that m- $\text{ZrO}_2$ , t- $\text{ZrO}_2$  and c- $\text{ZrO}_2$  phases were formed in the structure [12]. Again, Vasanthavel, S. et al. prepared  $\text{ZrO}_2$ - $\text{SiO}_2$ -Dysprosium mixtures in different proportions by sol-gel method and stated that m- $\text{ZrO}_2$ , t- $\text{ZrO}_2$ , c- $\text{ZrO}_2$ , c- $\text{SiO}_2$ ,  $\text{ZrSiO}_4$  phases were formed in the structure [13].

Also the wear properties of zirconia and mullite ceramics are investigated in many studies. In the study conducted by Akkuş and Boyraz [30], the wear properties of the samples prepared and produced with CaO, MgO and  $\text{ZrO}_2$  oxide powders in different compositions and ratios were investigated. They reported that the wear values obtained by applying different wear loads and wear times to the samples increase in parallel with the increase in the applied load and wear time. Huang et al [31] stated that hardness, porosity, density and bending strength of the samples had important effects on the wear properties in their study to examine the wear properties of the composites produced by adding mullite additives at 0-10 mole ratios to zirconia (3Y-TZP). Especially adhesive and abrasive wear were observed in the samples.

In this study, mullite ( $3\text{Al}_2\text{O}_3 \cdot 2\text{SiO}_2$ ) and 10 mol % silica doped zirconia ( $\text{SiO}_2$ - $\text{ZrO}_2$ ) ceramic powders were synthesized by conventional ceramic production processing route. Then, the effect of mullite additive on the properties of this mixture was investigated.

## Materials and Methods

Mullite ( $3\text{Al}_2\text{O}_3 \cdot 2\text{SiO}_2$ ) and silica doped zirconia ( $\text{SiO}_2$ - $\text{ZrO}_2$ ) ceramic powders were produced by conventional ceramic production processing route in this study. All

precursory powder materials were obtained from Company Eczacıbaşı ( $\text{Al}_2\text{O}_3$  and  $\text{SiO}_2$  powders) and Chemicals of Handan Yaxiang Trading Co. ( $\text{ZrO}_2$ ). The powders were mixed in acetone environment by mechanical alloying method. The powders were heated for 24 hours in oven at  $110\text{ }^\circ\text{C}$  before and after mixing. Mullite ( $3\text{Al}_2\text{O}_3 \cdot 2\text{SiO}_2$ ) and 10 mol% silica doped zirconia ( $\text{SiO}_2$ - $\text{ZrO}_2$ ) powders were synthesized by sintering from the powders prepared with stoichiometric ratios of  $\text{Al}_2\text{O}_3$ ,  $\text{SiO}_2$  and  $\text{ZrO}_2$  powders after homogenized in ball mill. Mullite ( $3\text{Al}_2\text{O}_3 \cdot 2\text{SiO}_2$ ) was synthesized for 3h at  $1600\text{ }^\circ\text{C}$  and 10 mol% silica doped zirconia ( $\text{SiO}_2$ - $\text{ZrO}_2$ ) composite powders were synthesized for 2 h at  $1300\text{ }^\circ\text{C}$ . Thus, silica - zirconia and mullite composite phases were obtained and milling and sieving processes were carried out. Then, mullite-free and 10% by weight mullite reinforced silicon oxide added zirconium oxide composites were prepared by powder metallurgy technique (named SiZ00M and SiZ10M respectively). The sample was coded as SiZ10M16005 (SiZ: Silica doped zirconia; 10M: 10% by weight mullite addition and 16005:  $1600\text{ }^\circ\text{C}$  sintering temperature and 5 hours sintering time). After the composite powders were milled for 24 h in acetone environment with zirconia ball mill, sieved and dried. Then, the composite mixtures were pressed to 56x12 mm sizes mold gap by uniaxial pressing machine at 200 MPa load. The pressed samples were sintered in a high temperature furnace (Protherm™ Furnace) and in air conditions for 1-5 h sintering times and  $1500$ - $1600\text{ }^\circ\text{C}$  temperatures. The heating rate was  $5\text{ }^\circ\text{C}/\text{min}$ . Then, microstructure investigations with SEM, phase analysis with XRD, the hardness, 3-point bending and wear tests and physical properties that are water absorption, porosity, shrinkage and density results were examined on the composites.

The three-point flexural strength tests were executed with crosshead speed of 0.5 mm/min in a Shimadzu brand tensile-compression device. For each sample, measurements were taken five times and their average were taken as the bending strength results of the samples. The strength calculations were made with the formula (1):

$$\sigma = 3/2 * P * L / (b * h^2) \quad (1)$$

(In (1) the letters mean that, P: maximum load, L: distance of between supports, b: width, h: height).

After 180, 320, 600, 1200 and 2500 grit sanding process, polishing is done for each sample. With Vickers hardness tester that was Mitutoyo brand, the measurements of hardness were executed by 1 kg load for 10 seconds. For each sample, measurements were taken five times and their average were taken as the hardness results of the samples [32-35]. The wear tests of samples were executed with Plint brand wear tester. For wear tests, steel discs were used. For each sample, wear tests were executed at 400 rpm rate, 5, 10 and 15 min wear durations and 50 N, 100 N, 150 N forces. The samples were measured with a precision scale of  $10^{-4}$  g. After the assigned wear times, the samples were scaled again and

the wear amounts were calculated [30,36,37]. To determine the phases, XRD with Cu K $\alpha$  radiation (Bruker AXS D8 Advance; 20kV-60kV, 6mA-80mA and  $\theta = 10^{\circ}$ - $90^{\circ}$ , 0.002 $^{\circ}$ ) was used. The phases of the samples seen in XRD patterns were defined with the Panalytical X'Pert program. The microstructural characterization of the samples was done with the Mira3XMU FE-SEM (Tescan, Czech Republic) brand scanning electron microscope machine and energy dispersion spectrum. The results were presented in various graphics and tables and some comments on these results were made.

Physical (shrinkage, water absorption, density and porosity tests) and mechanical (hardness, 3-point bending and wear) tests, SEM, EDS and XRD analysis results were included in this section. Calculations and measurements were repeated 5 times and arithmetic averages were taken. The shrinkage, porosity, water absorption, relative density and bulk density results are shown in Table 1, and also Fig. 1. In Fig. 1, the relative density values were taken at the rate of 1/3 of the actual values for the graph.

Table 1. Physical test results of SiZ00M and SiZ10M samples

Samples	Bulk density (g/cm <sup>3</sup> )	Relative density (%)	Water absorption (%)	Porosity (%)	Shrinkage (%)
SiZ00M15001	4,04	75,15	6,56	24,85	8,58
SiZ00M15005	4,40	81,78	4,40	18,22	10,68
SiZ00M16001	4,85	90,11	2,16	9,89	13,54
SiZ00M16005	5,13	95,34	1,08	5,66	14,98
SiZ10M15001	3,60	70,53	8,26	29,47	6,28
SiZ10M15005	3,76	73,69	6,93	26,31	7,76
SiZ10M16001	4,57	89,55	3,02	10,45	12,85
SiZ10M16005	4,68	91,69	1,97	8,31	14,20

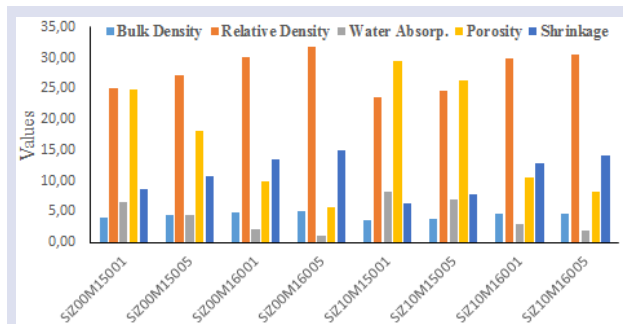


Figure 1. Physical test results graph of SiZ00M and SiZ10M samples.

When the results were examined, it was found that the shrinkage values increased with increasing sintering temperature and time in all samples, and accordingly the water absorption and porosity values decreased; it is seen that the experimental density and relative density values increase. In addition, it is seen that shrinkage, experimental density and relative density values are lower, water absorption and porosity values are higher in mullite added samples [36,37].

Table 2, Figure 2 and Figure 3 indicated the hardness and three-point flexural or bending strength results of SiZ00M and SiZ10M samples.

According to the results, it is seen that the hardness values for all samples increase with increasing sintering temperature and time. In addition, in the samples coded as 1500, the hardness values of the samples with mullite additives are lower than the samples without additives.

Table 2. Hardness and 3-point bending strength values of SiZ00M and SiZ10M samples

Samples	Hardness (HV)	3-Point bending strength (MPa)
SiZ00M15001	166,80	50,374
SiZ00M15005	197,70	52,565
SiZ00M16001	297,10	55,527
SiZ00M16005	375,53	62,268
SiZ10M15001	140,73	42,375
SiZ10M15005	172,43	44,842
SiZ10M16001	395,25	48,394
SiZ10M16005	425,56	50,056

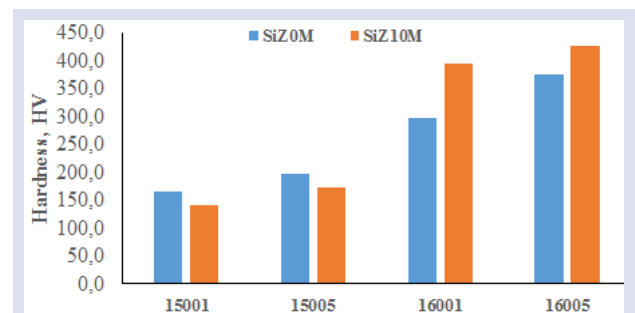


Figure 2. Hardness graph of samples.

In the samples coded as 1600, it is seen that the hardness values of the samples with mullite additives are higher than the samples without additives. We think that this is a result of possible phase changes in the microstructure.

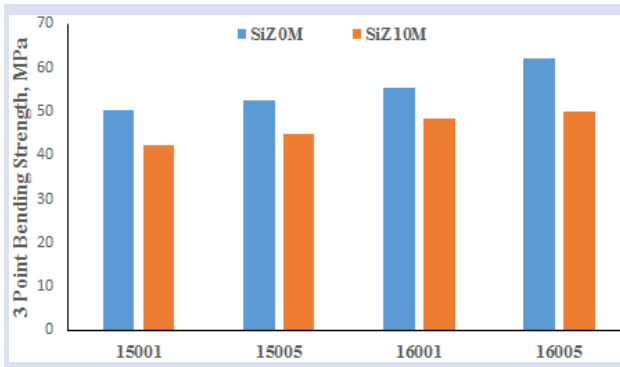


Figure 3. 3-Point bending strength graph of samples.

When we look for the flexural strength results, we see that the three-point flexural strength values increase with increasing sintering temperature and time in all samples, and the three-point flexural strength values of the mullite-added samples are lower than the un-doped samples.

The wear tests of samples were executed with Plint brand wear tester. For wear tests, steel discs were used. For each sample, wear tests were executed at 400 rpm rate, 5, 10 and 15 min wear durations and 50 N, 100 N, 150 N forces. The samples were measured with a precision scale of  $10^{-4}$  g. After the assigned wear times, the samples were scaled again and the wear amounts were calculated. Wear results are shown in Table 3, 4, 5 and Figure 4, 5, 6. In addition, graphs showing the load-dependent wear volume of the samples coded as 16005 are also presented in Figure 7.

Table 3. Wear results of SiZ00M and SiZ10M samples at 50 N load

Samples	Wear Volume (mm <sup>3</sup> ), 50 N		
	5 min.	10 min.	15 min.
SiZ00M15001	3,99	8,68	16,77
SiZ00M15005	3,53	8,27	15,88
SiZ00M16001	2,40	5,36	9,33
SiZ00M16005	1,72	4,15	8,23
SiZ10M15001	5,35	10,86	18,70
SiZ10M15005	4,99	9,22	16,55
SiZ10M16001	1,51	6,09	9,86
SiZ10M16005	1,28	2,89	4,65

Table 4. Wear results of SiZ00M and SiZ10M samples at 100 N load

Samples	Wear Volume (mm <sup>3</sup> ), 100 N		
	5 min.	10 min.	15 min.
SiZ00M15001	5,24	12,82	18,69
SiZ00M15005	3,79	11,15	17,25
SiZ00M16001	2,76	6,21	10,21
SiZ00M16005	1,99	4,87	8,79
SiZ10M15001	8,57	15,25	21,58
SiZ10M15005	7,96	13,75	19,57
SiZ10M16001	1,93	3,57	5,58
SiZ10M16005	1,56	3,18	5,12

Table 5. Wear results of SiZ00M and SiZ10M samples at 150 N load

Samples	Wear Volume (mm <sup>3</sup> ), 150 N		
	5 min.	10 min.	15 min.
SiZ00M15001	12,56	29,58	43,92
SiZ00M15005	7,68	11,45	28,56
SiZ00M16001	3,27	7,01	11,96
SiZ00M16005	2,25	5,50	9,42
SiZ10M15001	15,74	31,26	45,21
SiZ10M15005	13,78	29,16	38,76
SiZ10M16001	2,62	3,70	6,00
SiZ10M16005	2,13	3,57	5,75

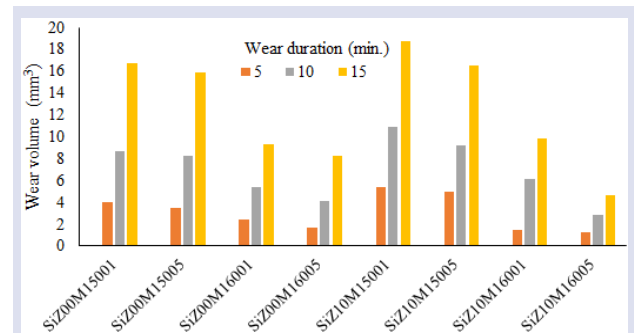


Figure 4. Wear test results graph for 50 N load.

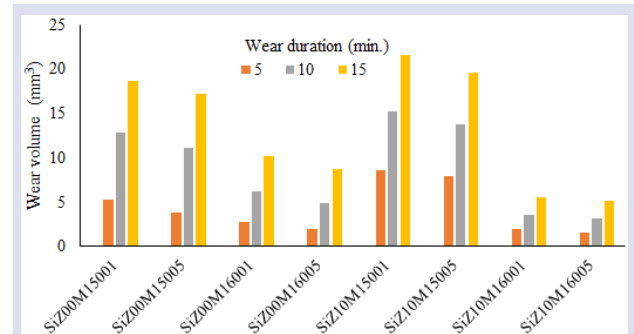


Figure 5. Wear test results graph for 100 N load.

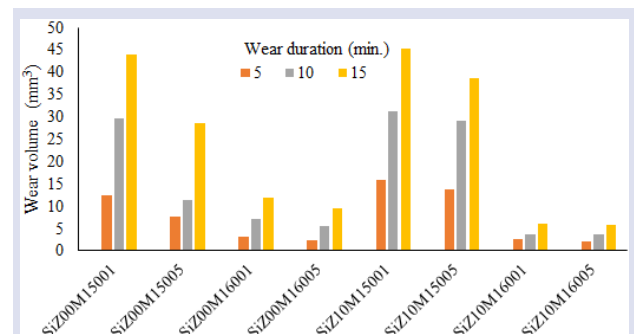


Figure 6. Wear test results graph for 150 N load.

When the results given in the tables are examined, it is seen that the wear resistances increase and the wear volume values decrease with increasing sintering temperature and time in all samples.

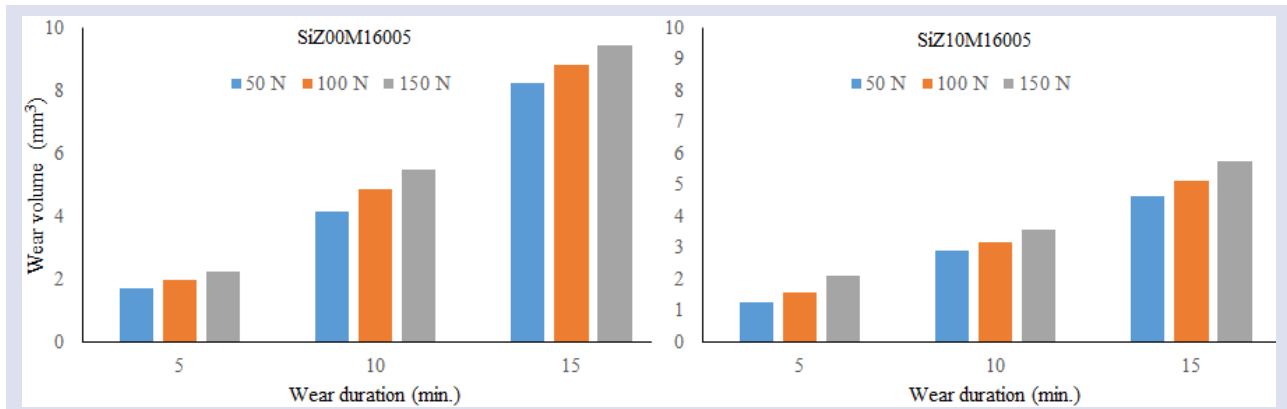


Figure 7. Wear results graphs of SiZ00M16005 and SiZ10M16005 samples.

In addition, while the wear resistance of the samples with mullite additive coded as 1500 is lower than the samples without additives; In the samples coded as 1600, it is seen that the wear resistance of the samples with mullite additive is higher than the samples without additives. We think that this is related to hardness values. Although adhesive type wear is observed in the samples in general, it has been observed that with the increase in the wear time in some samples, cracks occur on the worn

surface and very small pieces break off and cause abrasive wear.

The phase changes in the sample structure depending on the sintering temperature and time of SiZ00M and SiZ10M samples were analyzed and the basic phases that emerged in the structure were shown in Figure 8 and Figure 9.

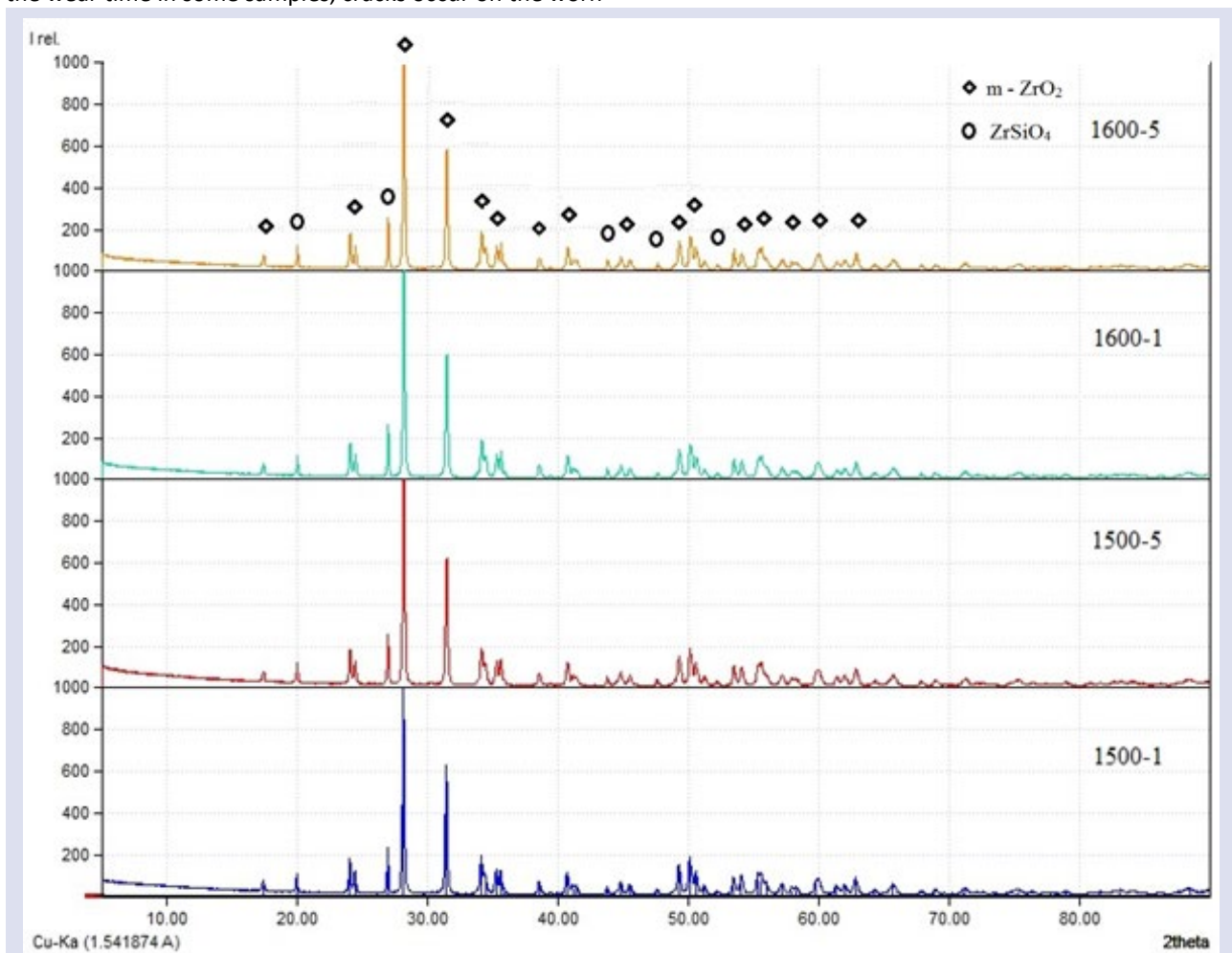


Figure 8. XRD patterns of SiZ00M samples.



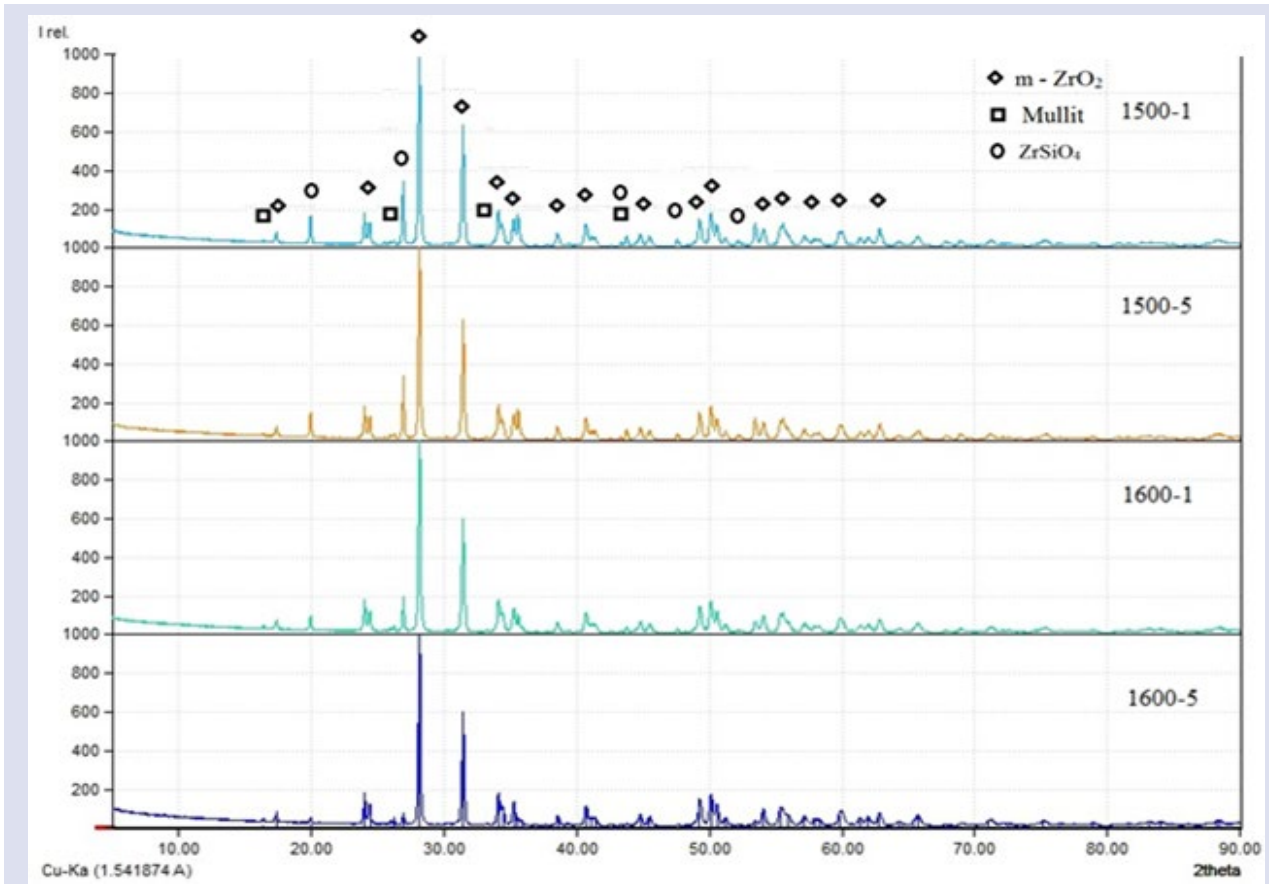


Figure 9. XRD patterns of SiZ10M samples.

As can be seen from Figure 8 and Figure 9, while  $m\text{-ZrO}_2$  and  $\text{ZrSiO}_4$  phases are detected in the samples without mullite additives, it is seen that there is a mullite phase in addition to these phases in the samples with mullite additives. When the XRD patterns given in Figure 8 and Figure 9 are compared, it is understood that the higher hardness value of the samples coded as 1600 mullite-added samples compared to the un-doped samples coded as 1600, depends on the zircon ( $\text{ZrSiO}_4$ ) phase in the structure. The fact that the zircon phase of samples coded as 1600 with mullite additives was less

than the samples without additives increased the hardness values of these samples.

The microstructure image of SiZ00M16005 and SiZ10M16005 samples is given in Figure 10.

As can be seen from the SEM image given in Figure 10, the amount and size of the pores on the surface decreased with the addition of mullite and a more homogeneous surface was obtained. It can be predicted that this will have a positive effect on the hardness values of the samples and may increase the hardness value of the mullite added sample.

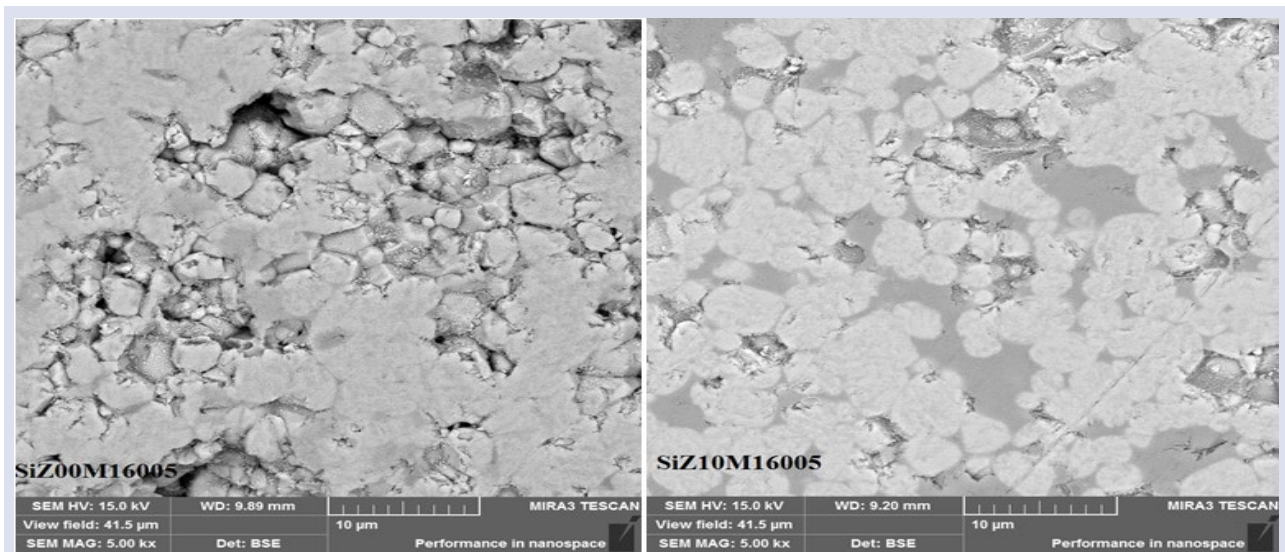


Figure 10. SEM images of SiZ00M16005 and SiZ10M16005 samples.

As a matter of fact, in the experimental results, the hardness value of the SiZ10M16005 sample was found to be higher than the hardness value of the SiZ00M16005 sample.

Elemental analyzes of SiZ00M16005 and SiZ10M16005 samples with EDS are given in Figure 11 and Figure 12.

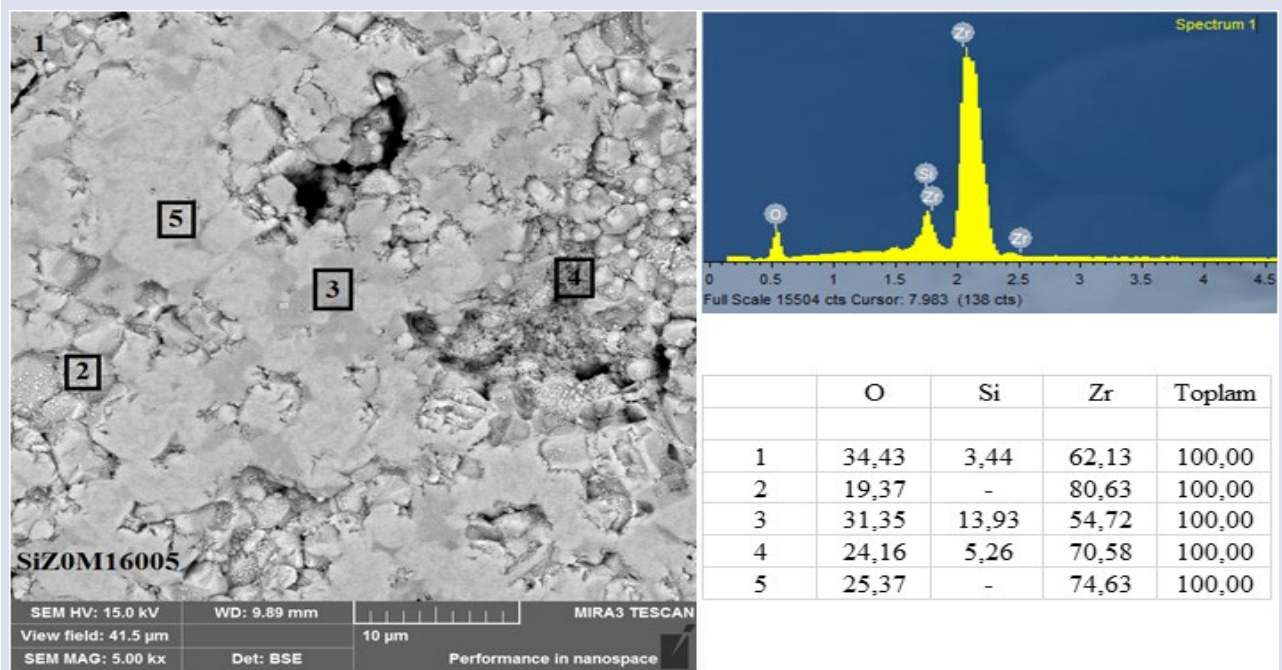


Figure 11. EDS analyses of SiZ00M16005 samples.

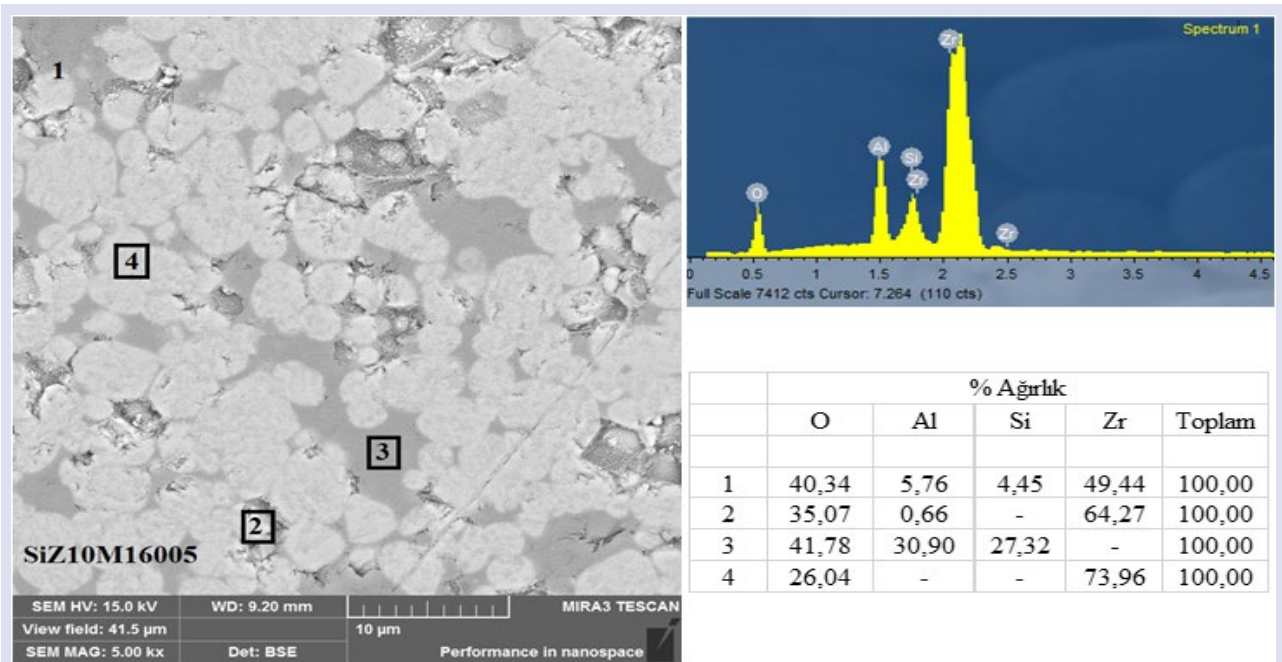


Figure 12. EDS analyses of SiZ10M16005 samples.

According to the EDS analyzes given in Figure 11 and Figure 12, the evaluation of the EDS analysis results on the SiZ00M16005 and SiZ10M16005 samples was made from general (1) and parts 2, 3, 4, 5. It has been observed that the results of the EDS elemental analysis made from the general field survey (1) and other parts are compatible with the contribution rates and XRD results made to the samples.

### Conclusion

In our study, utilization of mullite in the production of silica doped zirconia was explored. The effect of SiO<sub>2</sub> and mullite contribution to ZrO<sub>2</sub> main matrix was evaluated.

In all SiZ00M and SiZ10M coded samples, shrinkage, experimental density, relative density, hardness values, three-point bending strength values and wear resistance increase with increasing sintering temperature and time.

It is observed that the water absorption and porosity values decrease.

While the mullite additive reduces the shrinkage, experimental density, relative density and three-point bending strength values of the samples; It is observed that the water absorption and porosity values increase. The reason for this is that the density value of the mullite additive is lower than the  $ZrO_2 - SiO_2$  composite and it is more stable in terms of shrinkage value at high temperatures compared to this composite. Therefore, in mullite added samples, shrinkage, experimental density and relative density are lower, whereas water absorption and porosity values are higher.

The hardness values and wear resistance of the mullite added samples in 1500 samples are lower than the mullite-free samples. But in the samples coded as 1600, it is seen that the hardness values and wear resistance of the samples with mullite additives are higher than the samples without additives. When the XRD patterns are compared, it is understood that the higher hardness values of the samples coded as 1600 mullite-added samples compared to the samples coded as 1600 undoped samples, depend on the  $ZrSiO_4$  (zircon) phase in the structure. The fact that the amount of zircon phase in samples coded as 1600 with mullite additive is less compared to the samples without additive, increases the hardness values of these samples.

While  $m-ZrO_2$  and  $ZrSiO_4$  phases are detected in the samples without mullite additives, it is determined that there was a mullite phase in addition to these phases in the samples with mullite additives.

## Acknowledgment

This work is supported by the Scientific Research Project Fund of Sivas Cumhuriyet University under the project number M-767. Authors would like to acknowledge Scientific Research Project Fund of Sivas Cumhuriyet University.

## Conflicts of interest

All authors declare that they have no conflict of interest.

## References

- [1] Kim I.H., Singh B., Lim J.W., Song S.J., Determination of partial conductivities and electrolytic domain of yttrium-doped zirconia prepared from Indonesian zircon sand, *Journal of Ceramic Processing Research*, 19(2) (2018) 134-141.
- [2] Kosmač T., Oblak C., Jevnikar P., Funduk N., Marion L., The effect of surface grinding and sandblasting on flexural strength and reliability of Y-TZP zirconia ceramic, *Dental Materials*, 15(6) (1999) 426-433.
- [3] Gupta T.K., Bechtold J.H., Kuznicki R.C., Cadoff L.H., Rossing B.R., Stabilization of tetragonal phase in polycrystalline zirconia, *Journal of Materials Science*, 12(12) (1977) 2421-2426.
- [4] Rao P.G., Iwasa M., Tanaka T., Kondoh I., Inoue T., Preparation and mechanical properties of  $Al_2O_3-15wt.\% ZrO_2$  composites, *Scripta Materialia*, 48(4) (2003) 437-441.
- [5] Garvie R.C., Nicholson P.S., Phase analysis in zirconia systems, *Journal of the American Ceramic Society*, 55(6) (1972) 303-305.
- [6] Tsukuma K., Shimada M., Strength, fracture toughness and Vickers hardness of  $CeO_2$ -stabilized tetragonal  $ZrO_2$  polycrystals (Ce-TZP), *Journal of Materials Science*, 20(4) (1985) 1178-1184.
- [7] Deville S., El Attaoui H., Chevalier J., Atomic force microscopy of transformation toughening in ceria-stabilized zirconia, *Journal of the European Ceramic Society*, 25(13) (2005) 3089-3096.
- [8] Hughan R.R., Hannink R.H., Precipitation During Controlled Cooling of Magnesia-Partially-Stabilized Zirconia, *Journal of the American Ceramic Society*, 69(7) (1986) 556-563.
- [9] Sakuma T., Microstructural aspects on the cubic-tetragonal transformation in zirconia, *In Key Engineering Materials*, 153 (1998) 75-96.
- [10] Czeppe T., Zięba P., Pawłowski A., Crystallographic and microchemical characterization of the early stages of eutectoid decomposition in  $MgO$ -partially stabilized  $ZrO_2$ , *Journal of the European Ceramic Society*, 22(8) (2002) 1389-1394.
- [11] Aguilar D.H., Torres-Gonzalez L.C., Torres-Martinez L.M., Lope T., Quintana P., A study of the crystallization of  $ZrO_2$  in the sol-gel system:  $ZrO_2-SiO_2$ , *Journal of Solid State Chemistry*, 158(2) (2001) 349-357.
- [12] Vasanthavel S., Nandha Kumar P., Kannan S., Quantitative analysis on the influence of  $SiO_2$  content on the phase behavior of  $ZrO_2$ , *Journal of the American Ceramic Society*, 97(2) (2014) 635-642.
- [13] Vasanthavel S., Derby B., Kannan S., Tetragonal to cubic transformation of  $SiO_2$ -stabilized  $ZrO_2$  polymorph through dysprosium substitutions, *Inorganic Chemistry*, 56(3) (2017) 1273-1281.
- [14] Lin C.L., Gan D., Shen P., Stabilization of zirconia sintered with titanium, *Journal of the American Ceramic Society*, 71(8) (1988) 624-629.
- [15] Bukhari S.B., Imran M., Bashir M., Riaz S., Naseem S., Room temperature stabilized  $TiO_2$  doped  $ZrO_2$  thin films for teeth coatings—A sol-gel approach, *Journal of Alloys and Compounds*, 767 (2018) 1238-1252.
- [16] Annenkov Y.M., Aparov N.N., Frangul'yan T.S., Voznya A.V., Gornostaev A.M., Effect of a stabilizing  $\gamma$   $ZrO_2$  additive on the strength properties of zirconia ceramics sintered from plasma chemical powders, *Glass and ceramics*, 54(11-12) (1997) 401-403.
- [17] Yoshimura M., Oh S.T., Sando M., Niihara K., Crystallization and microstructural characterization of  $ZrO_2$  (3 mol%  $Y_2O_3$ ) nano-sized powders with various  $Al_2O_3$  contents, *Journal of Alloys and Compounds*, 290(1-2) (1999), 284-289.
- [18] Moon J., Choi H., Kim H., Lee C., The effects of heat treatment on the phase transformation behavior of plasma-sprayed stabilized  $ZrO_2$  coatings, *Surface and Coatings Technology*, 155(1) (2002) 1-10.
- [19] Zhang Y.L., Jin X. J., Rong Y.H., Hsu T.Y., Jiang D.Y., Shi J.L., On the  $t \rightarrow m$  martensitic transformation in Ce-Y-TZP ceramics, *Acta Materialia*, 54(5) (2006) 1289-1295.
- [20] Cutler R.A., Reynolds J.R., Jones A., Sintering and characterization of polycrystalline monoclinic, tetragonal, and cubic zirconia, *Journal of the American Ceramic Society*, 75(8) (1992) 2173-2183.

- [21] Govila R.K., Strength characterization of yttria-partially stabilized zirconia, *Journal Of Materials Science*, 30(10) (1995) 2656-2667.
- [22] Liu P.F., Li Z., Xiao P., Luo H., Jiang T.H., Microstructure and mechanical properties of in-situ grown mullite toughened 3Y-TZP zirconia ceramics fabricated by gelcasting, *Ceramics International*, 44(2) (2018) 1394-1403.
- [23] Duszová A., Dusza J., Tomášek K., Blugan G., Kuebler, J., Microstructure and properties of carbon nanotube/zirconia composite, *Journal of the European Ceramic Society*, 28(5) (2008) 1023-1027.
- [24] Eichler J., Rödel J., Eisele U., Hoffman M., Effect of grain size on mechanical properties of submicrometer 3Y-TZP: fracture strength and hydrothermal degradation, *Journal of the American Ceramic Society*, 90(9) (2007) 2830-2836.
- [25] Sun J., Gao L., Iwasa M., Nakayama T., Niihara K., Failure investigation of carbon nanotube/3Y-TZP nanocomposites, *Ceramics International*, 31(8) (2005) 1131-1134.
- [26] Şenel M.C., Fabrication of aluminum matrix hybrid composites reinforced with graphene-ceramic particles by powder metallurgy method and investigation of their mechanical and microstructural properties, PhD thesis, Ondokuz Mayıs University, Graduate School of Natural and Applied Sciences, 2018.
- [27] Kucuk I., Boyraz T., Structural and mechanical characterization of mullite and aluminium titanate reinforced yttria stabilized zirconia ceramic composites, *Journal of Ceramic Processing Research*, 20(1) (2019) 73-79.
- [28] Kumar P., Nath M., Ghosh A., Tripathi H.S., Enhancement of thermal shock resistance of reaction sintered mullite-zirconia composites in the presence of lanthanum oxide, *Materials Characterization*, 101 (2015) 34-39.
- [29] Denry I., Kelly J.R., State of the art of zirconia for dental applications, *Dental materials*, 24(3) (2008) 299-307.
- [30] Akkus A., Boyraz T., Investigation of wear properties of CaO, MgO added stabilized zirconia ceramics produced by different pressing methods, *J. Ceram. Process Res.*, 19(3) (2018) 249-52.
- [31] Huang Y.Q., Li Z., Liu P.F., Huan T.X., Li Y., Xiao P., Tribological properties of Mullite/3Y-TZP ceramics with different content of mullite fabricated by gel-casting, *Applied Surface Science*, 476 (2019) 232-241.
- [32] Boyraz T., An investigation on physical and electrical properties of CaO/MgO-stabilized zirconia ceramics formed with different methods, PhD thesis, Istanbul Technical University, Graduate School of Natural and Applied Sciences, 2008.
- [33] Boyraz T., Thermal Properties and Microstructural Characterization of Aluminium Titanate (Al<sub>2</sub>TiO<sub>5</sub>)/La<sub>2</sub>O<sub>3</sub>-Stabilized Zirconia (ZrO<sub>2</sub>) Ceramics, *Cumhuriyet Science Journal*, 39(1) (2018) 243-249.
- [34] Çitak E., Boyraz T., Microstructural characterization and thermal properties of aluminium titanate/YSZ Ceramics, *Acta Physica Polonica A*, 125(2) (2014) 465-468.
- [35] Boyraz T., Akkuş A., Investigation of wear properties of mullite and aluminium titanate added porcelain ceramics, *Journal of Ceramic Processing Research*, 22(2) (2021) 226-231.
- [36] Hafizoğlu M.A., Boyraz T., Akkuş A., Fabrication, characterization and wear properties of mullite reinforced silica-doped zirconia ceramic composites, 4. International Conference on Materials Science, Mechanical and Automotive Engineerings and Technology (IMSMATEC'21), Nevşehir, 2021, 175-180.
- [37] Hafizoğlu M.A., Akkuş A., Boyraz T., Fabrication, characterization and wear properties of mullite reinforced Al<sub>2</sub>O<sub>3</sub>-doped ZrO<sub>2</sub> ceramic composites, Global Conference on Engineering Research (GLOBECER'21), Bandırma (Balıkesir), 2021, 673-686.

## The Effects of Cooking Temperatures and Times on the Formation of Aromatic Amines of Meatballs Derived from Sivas Province

Özlem Pelin Can <sup>1,a,\*</sup>, Ayşegül Demir <sup>1,b</sup>

<sup>1</sup> Department of Food Hygiene and Technology, Faculty of Veterinary, Sivas Cumhuriyet University, Sivas, Türkiye

\*Corresponding author

### Research Article

#### History

Received: 21/11/2021

Accepted: 03/06/2022

#### Copyright





©2022 Faculty of Science,  
Sivas Cumhuriyet University


### ABSTRACT

In this study, nine different experimental groups were prepared by cooking meatball samples 5, for 7,5 and 10 minutes at 150, 200 and 250 °C. Some chemical analysis including fat, protein, thiobarbituric acid contents and pH were applied to samples. The amount of Heterocyclic Aromatic Amines (HAA) of the samples treated by heat at 250 °C for 7,5 minutes had highest value, 0.42 ng/g. IQ (2-amino-3-metilimidazo[4,5-f]kinolin) and PhIP (2-amino-1-metil-6-fenilimidazo[4,5-b]piridin) were detected for the samples subjected to 250 °C heat treatment. HAA was not detected in the samples cooked at 7,5 for 10 minutes and 200 °C, whereas MeQlx was found to be 0.17 ng/g for the samples baked for 5 minutes. Consequently, it was detected that the amount of HAA in all groups was below the 1 ng/g, which makes possible to comment chosen parameters for cooking meatballs is appropriate for formation of HAA.

**Keywords:** Heterocyclic aromatic amines, Meatball, Heat treatment, Time.

 [ozlempelincan@gmail.com](mailto:ozlempelincan@gmail.com)

 <https://orcid.org/0000-0001-8769-4823>

 [aysgl\\_aytkn@hotmail.com](mailto:aysgl_aytkn@hotmail.com)

 <https://orcid.org/0000-0003-4060-9710>

### Introduction

Meat and meat products are widely preferred to consume after cooking in whole world. When meat and meat products are cooked, a noticeable changes could be occurred in their sensory, chemical and microbiological properties. The changes in the sensory properties of a meat product after cooking mostly defined as satisfied and aromatic by consumers. The bright red color turns into brown with the effect of heat, depending on the denaturation of the proteins, especially connective tissue/ligament proteins get brittle related to collagen denaturation.

The meat products prepared with different forms from fresh ground beef patties to meatball dough, mostly cooked as a grill called as meatballs [1]. In Turkey, the meatballs are prepared with different formulas depending on locality (İnegöl, Akçaabat, Sivas, etc.). Sivas meatball is one of most popular type that have great demand of consumer in Sivas region and also has a geographic patent.. The production of Sivas meatball comprises in three main stages as choosing raw material, preparation of dough and cooking. In order to provide the special taste and aroma of Sivas meatball, the meat should be provided from cattle or sheep meat which were grown in plateaus in the unique flora of Sivas region and fed by clover, vetch and thyme in natural environment. The meat obtained from the ribs, butt, scapula of the at least two years old calves raised in natural habitats and the meat from the butt of the sheep is used as raw material. Twenty grams of salt (NaCl) per kilogram is added and drawn in a meat grinder..The NaCl is the only ingredient that used in the production of Sivas meatball. Prepared meatballs are

cooked in the oak coal fire, flameless and with dense ember by turning them at short intervals so that both sides will be cooked or they are cooked in the oven and then served hot [2].

The consumers mostly prefer to consume meat and meat products after cooking to be certain of safety and flavor of the products. Ripened meat tastes like lactic acid due to the presence of some components such as aldehydes, amino acids, carbonyls. Increasing flavor by cooking in meat products occurred by maillard reaction on the surface with the effect of heat applied to the surface of the meat and free radicals are formed at high temperatures. These free radicals have negative effects on health and they can cause unwanted taste and taste changes on the product by reacting with food components (protein, carbohydrate, fat and vitamin). Heterocyclic aromatic amines (HAA) form an is the most important groups of these compounds. HAAs are usually formed by the exposure of animal-derived products containing nitrogenous compounds such as protein and creatine to heat. Meat contains creatine and creatinine which can react with free amino acids and sugars during cooking and they form the HAAs depending on time and temperature [3]. They are present in significant amounts in heated meat and fish when the cooking temperature over 150°C [4]. In addition, HAAs can also occur in longer cooking times even at lower temperatures [5]. It has been known that HAA's are formed in very small quantities with boiling in the meat, but their formation after roasting, grilling, baking etc. has increased greatly [4].

The cooking of food might be resulted in formation of HAAs in different kinds and quantities. The patterns of formations or concentrations of HAAs depend on various factors including cooking time and temperature, water activity, pH value, effect and amount of precursors required for formation (creatine/creatinine, free amino acids, sugars, peptides, proteins), fats, oil oxidation, antioxidants, amount of available inhibitor and activator components, heat and mass transfer, type of heat-treated food, cooking equipment and method [6].

HAAs can also be found in ready-to eat foods which generally cooked by using traditional frying methods. [4]. The most identified HAAs in cooked meat products are; 2-amino-3,8-dimethylimidazo [4,5-f] quinoxaline (MeIQx), 2-amino-3,4,8-trimethylimidazo [4,5f] quinoxaline (4,8-DiMeIQx) and 2-amino-1-methyl-6-phenylimidazo [4,5-b] pyridine (PhIP) [7].

In this current study, it was aimed to determine the amount HAAs that were occurred during the cooking process of the Sivas Meatballs which were highly consumed by the people with pleasure.

## Materials and Methods

### Raw Materials

Sivas Meatballs used in the research (consist of beef and 2% (NaCl)) was obtained from a local company in Sivas province that is offered for sale in commercial and brought to the laboratory under the cold chain. Meatballs are standard size, 8 cm in diameter and 1 cm thickness.

### Chemicals

Ethylenediaminetetraacetic acid disodium, trichloroacetic acid, thiobarbituric acid (TBA), diacetyl, diethyl ether, hydrochloric acid were obtained from Merck KGaA (Darmstadt, Germany). Chemicals for HAA analysis, including ethyl acetate, methanol, acetone, sodium hydroxide, hydrochloric acid, glacial acetic acid, acetonitrile, and ammonium hydroxide solution (25%) were purchased from Merck KGaA (Darmstadt, Germany). For solid phase extraction, Extrelut NT packing material (Merck, Darmstadt, Germany), Oasis MCX cartridge (Waters, Milford, Massachusetts, USA), SPE manifold (Supelco Visiprep, St. Louis, Missouri, USA), and Oasis HLB cartridge (Waters, Milford, Massachusetts, USA) were used. HAA standards were purchased from Riedel-de Haën Chemicals: IQ (CAS no:76180-96-6, 2-amino-3-methylimidazo[4,5-f]quinoline), IQx (CAS no:108354-47-8; 2-amino-3-methylimidazo[4,5-f]quinoxaline), MeIQ (CAS no:77094-11-2; 2-amino-3,4-dimethylimidazo[4,5-f]quinoline), MeIQx (CAS no:77500-04-0; 2-amino-3,8-dimethylimidazo[4,5-f]quinoxaline), 4,8-DiMeIQx (CAS no:95896-78-9; 2-amino-3,4,8-trimethylimidazo[4,5-f]quinoxaline), 7,8-DiMeIQx (CAS no:92180-79-5; 2-amino-3,7,8-trimethylimidazo[4,5-f]quinoxaline), PhIP (CAS no:105650-23-5; 2-amino-1-methyl-6-phenylimidazo[4,5-f]pyridine), harman (CAS no:486-84-0; 1-methyl-9H-pyrido[3,4-b] indole), norharman (CAS no:244-63-3; 9H-pyrido[3,4-b]indole), AαC (CAS

no:26148-68-5; 2-amino-9H-pyrido[2,3-b]indole), MeAαC (CAS no: 68006-83-7; 2-amino-3-methyl-9H-pyrido[2,3-b]indole), and 4,7,8-TriMeIQx (CAS no:132898-07-8; 2-amino-3,4,7,8-tetramethylimidazo[4,5-f]quinoxaline).

Chemicals and solvents were of high-performance liquid chromatography (HPLC) or analytical grade. All solutions, except the HPLC-grade solutions, were passed through a 0.45 µm filter (Millipore, Billerica, Massachusetts, USA) before use.

## Methods

### Cooking process

Cooking temperature grades and times are determined as a result of preliminary studies conducted at the cooking areas commercially available for consumption (restaurants). The temperatures were setted as 150°C, 200°C and 250°C for cooking. The cooking times were specified as 5, 7.5 and 10 minutes. The oven temperature and the central temperatures of the cooked meatballs in the oven (İnoksan FKG 042) were measured by a termocouple (Datalog Termometer, RS-232 and Exttech HD200) during the cooking time. In the study 9 experimental groups were composed of 3 replicates and 4 meatball samples were prepared for each group (9x3x4, total 108 meatballs).

The cooked samples were cooled at ambient temperature and then homogenized with a household mixer and stored in aluminum foil at -18°C until the proposed analyses achieved.

### The determination of chemical

The protein and lipid contents were determined according to AOAC (1990) methods [8]. The lipid content was determined via the Soxhlet method and the protein content was analyzed via the Kjeldahl method. The pH of samples was measured using a digital pH meter (Hanna, Vohringen, Germany) calibrated with standard buffers of pH 4.0 and 7.0 at room temperature.

Lipid oxidation was measured by analyzing TBARS. TBARS were determined reported by AOAC (1990) [8]. TBARS values were expressed as mg of malondialdehyde mg MDA/kg of meatball.

### Heterocyclic aromatic amine analysis

#### Extraction of heterocyclic aromatic amines

HAAs were extracted from the meatball using the method described by Murkovic [4] which is a modified method originally developed by Öz (2010) [9]. According to the method, 1 g of meatball was dissolved in 12 mL NaOH (1 M). The suspension was homogenized using a magnetic stirrer for 1 h at 500 rpm at room temperature. The alkaline solution was mixed with 13 g diatomaceous earth (Extrelut NT packaging material, Merck, Darmstadt, Germany) and then poured into empty Extrelut columns. The extractions were performed by using ethyl acetate and the eluate was passed through coupled Oasis MCX cartridges. The cartridge was washed with 2 mL of 0.1 M HCl and 2 mL MeOH. The analytes were eluted with 2 mL

MeOH-concentrated (25%) ammonia (19/1, v/v). The eluted mixtures were evaporated to dryness at 50 °C and the final extracts were dissolved in 100 µL MeOH just before measurements were taken.

### HPLC analyses

HAAs were identified and quantified by HPLC (Thermo Ultimate 3000, Thermo Scientific, USA) with Diode Array Detector (DAD-3000), an auto-sampler (WPS-3000), a column oven (TCC-3000) and a pump (LPG-3400SD). Separation was carried out on a reverse phase analytical column (Acclaim™ 120 C18 3 µm (4.6 × 150 mm)) from Tosoh Bioscience GmbH (Stuttgart, Germany) at 35 °C with a mobile phase of methanol / acetonitrile / water / acetic acid (8/14/76/2, v/v/v/v) at pH 5.0 (adjusted with ammonium hydroxide 25%) as solvent A and acetonitrile as solvent B at a flow rate of 0.7 mL/min. The gradient program was: 0% B, 0–10 min; 0–23% B, 11–20 min; 23% B, 21–30 min; 0% B, 31–45 min. The injection volume was 10 µL (25% was an internal standard) from the final extract (dissolved in 100 µL of MeOH of the sample extract) as mentioned by Öz [9]. The identification of HAAs was carried out by comparing retention time and UV spectra (at 264 nm) recorded for standards and HAA standard spiked samples. Recovery rates for the different HAAs in the samples were determined by the standard addition method before extraction of the HAAs. The samples were spiked with HAA mixtures at four spiking levels (0.5, 1, 2, and 2.5 ng/g frozen meatball) by adding different volumes of a methanolic solution of the analytes [10]. The concentration of the HAAs in the samples was calculated by a standard curve running with different concentrations (0.5, 1, 2.5, 5, and 10 ng/g) of standards. Quantitative determination was performed by using an external calibration curve method. Linear regression (nanograms of compound against peak area) was performed for individual HAAs in mix stock solutions. Coefficients of the regression line ( $r^2$ ) for HAA standard curves were 0.9995 for IQx, 0.9995 for IQ, 0.9995 for MeIQx, 0.9994 for MeIQ, 0.9995 for 7,8-DiMeIQx, 0.9995 for 4,8-DiMeIQx, 0.9994 for PhIP, 0.9994 for AαC and 0.9995 for MeAαC.

### Statistical analysis

Statistical analyses were performed by using the Minitab 15 statistic program with ANOVA. Significant differences between two factors (GTE or MC) and two-way interactions (GTE × MC) were also analyzed based on the Duncan test (significance  $P < 0.05$ ) using the Mstat-C statistic program.

## Results and Discussion

### Heat Treatment Results of Meatball Samples

Worked with three replications for each temperature-time combinations on the samples of meatballs cooked with three different combinations of temperature and time. The code number for each meatball sample, the cooking temperature, the

cooking time and the internal temperature reached by the cooked meatballs are given in the following chart (Table 1).

Table 1. The code number for each meatball sample, the cooking temperature, the cooking time and the internal temperature

Code Number	Cooking Temperature (°C)	Internal Temperature (°C)	Cooking Time (min)
A	150	78.2	5
B	150	85.1	7.5
C	150	92.5	10
K	200	88.8	5
L	200	97	7.5
M	200	97.5	10
X	250	96.8	5
Y	250	98.5	7.5
Z	250	100.3	10

### Chemical Analysis Results

The fat, protein, pH and TBARs results of the experimental samples are also shown in the Table 2. The average values of fat, protein, pH and TBARs of the samples without heat treatment were 15.8%, 32.13%, 5.3 and 0.13 MDA/kg, respectively. In experimental samples, depending on increase in temperature time the changes in the amount of fat, pH value and TBARs in the samples were not found significant ( $p > 0.05$ ). As the experimental samples were evaluated in terms of protein content, since the cooking time and temperature were increased and meatball samples were cooked for 10 minutes at 250°C due to water loss the protein concentration reached 36.19%. The statistical difference was found to be insignificant in between the samples cooked at 150°C and 200°C temperatures ( $p > 0.05$ ).

Table 2. Chemical composition of meatball samples

Groups	Total fat (%)	Protein (%)	pH	TBARs (MDA mg/kg)
	M±SE	M±SE	M±SE	M±SE
A	14.00±1.13 <sup>a</sup>	33.51±0.71 <sup>a</sup>	5.28±0.96 <sup>a</sup>	0.12±0.02 <sup>a</sup>
B	14.30±1.56 <sup>a</sup>	32.19±1.03 <sup>a</sup>	5.29±0.87 <sup>a</sup>	0.14±0.05 <sup>a</sup>
C	15.10±0.98 <sup>a</sup>	34.15±0.86 <sup>a</sup>	5.33±0.35 <sup>a</sup>	0.16±0.02 <sup>a</sup>
K	14.40±2.01 <sup>a</sup>	35.17±0.98 <sup>a</sup>	5.31±0.46 <sup>a</sup>	0.19±0.06 <sup>a</sup>
L	14.90±1.16 <sup>a</sup>	36.11±1.11 <sup>a</sup>	5.26±0.63 <sup>a</sup>	0.15±0.05 <sup>a</sup>
M	14.70±0.83 <sup>a</sup>	35.41±0.96 <sup>a</sup>	5.33±0.29 <sup>a</sup>	0.14±0.02 <sup>a</sup>
X	15.20±2.26 <sup>a</sup>	36.10±0.76 <sup>a</sup>	5.21±0.33 <sup>a</sup>	0.24±0.03 <sup>a</sup>
Y	14.90±1.93 <sup>a</sup>	35.93±0.98 <sup>a</sup>	5.37±0.51 <sup>a</sup>	0.18±0.02 <sup>a</sup>
Z	15.20±1.43 <sup>a</sup>	36.19±1.14 <sup>a</sup>	5.30±0.69 <sup>a</sup>	0.19±0.05 <sup>a</sup>

### HAA content results

The recoveries obtained depended on the sample nature and the spiked concentration level. The limits of detection (LOD) and limits of quantification (LOQ) for standard solutions were calculated with a signal to noise ratio of 3 (S/N = 3) and 10 (S/N = 10), respectively. The lowest detected concentrations for each compound within the sample were: IQx = 0.004 ng/g, IQ = 0.009 ng/g, MeIQx = 0.024 ng/g, MeIQ = 0.014 ng/g, 7,8-DiMeIQx = 0.005 ng/g, 4,8-DiMeIQx = 0.008 ng/g, PhIP = 0.025 ng/g, AαC = 0.012, and MeAαC = 0.010 ng/g. The lowest quantified concentrations for each compound within the sample were: IQx = 0.013 ng/g, IQ = 0.029 ng/g,

MeIQx = 0.081 ng/g, MeIQ = 0.047 ng/g, 7,8-DiMeIQx = 0.018 ng/g, 4,8-DiMeIQx = 0.025 ng/g, PhIP = 0.085 ng/g, AαC = 0.039, and MeAαC = 0.035 ng/g. Figure 1 shows an HPLC chromatogram of the mix stock solution (10 ng/g).

HAA quantities of experimental meatballs cooked at different temperatures and at different times are given in the following chart (Table 3). According to the results; 7,8-DiMeIQx, 4,8-DiMeIQx, AαC and MeAαC were not determined as numerical values at any temperature and time. Other HAAs were determined in varying amounts depending on the cooking temperature and duration.

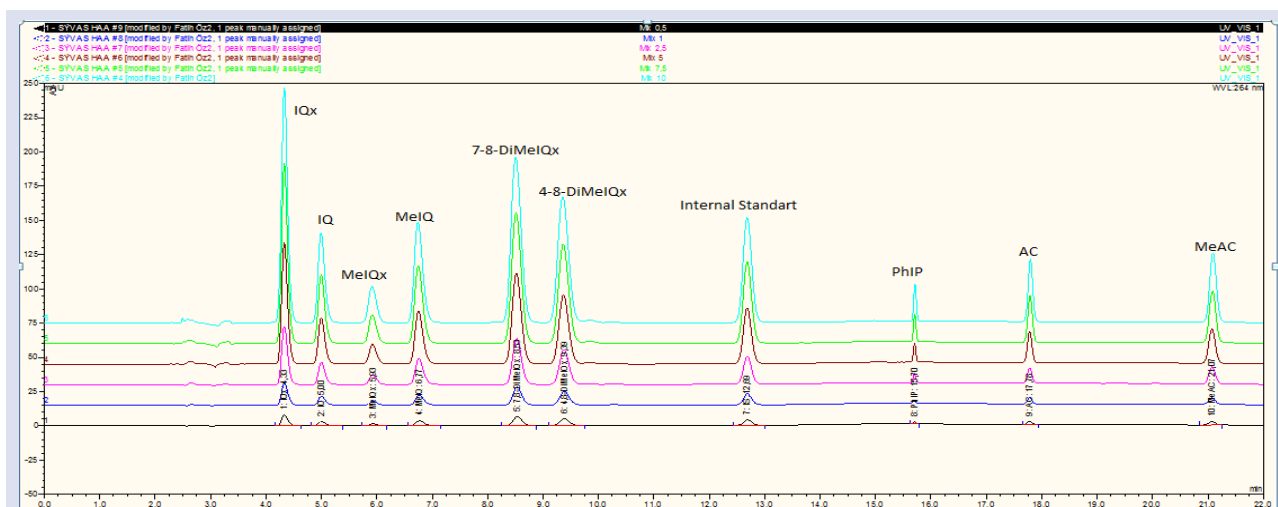


Figure 1. HAA chromatogram of standard mix 10 ng/g)

The IQx compound in the experimental samples was determined to be between 0-0.06 ng/g. The highest IQx content was determined in the meatballs cooked at 0,06 ng/g in a convection oven at 150°C for 7.5 min. Kizil [11]

has determined that the IQx content of meatballs cooked in the oven at different temperatures varied between 0-0,60 ng/g and that the highest IQx content was in the case of meatballs cooked 90 minutes at 150°C.

Table 3. The quantities of HAA (ng/g) resulting from the cooking of experimental meatball samples at different temperatures and time.

Temperature (°C)	150			200			250		
Time (min)	5	7.5	10	5	7.5	10	5	7.5	10
IQx	0.05	0.06	0.03	nd	nd	nd	nd	nd	nd
IQ	nd	nd	nd	nd	nd	nd	nd	0.15	0.11
MeIQx	nq	0.08	nq	0.17	nd	nd	nd	nd	nd
MeIQ	nq	nq	nd	nd	nd	nd	nq	0.05	nd
7,8-DiMeIQx	nq	nq	nq	nq	nq	nq	nq	nq	nq
4,8-DiMeIQx	nd	nq	nd	nd	nd	nd	nd	nq	nd
PhIP	nd	nd	0.18	nd	nd	nd	nd	0.22	0.17
AαC	nd	nd	nd	nd	nd	nd	nd	nd	nq
MeαAC	nd	nd	nd	nd	nd	nd	nd	nd	nq
Total HAA	0.05	0.14	0.21	0.17	-	-	-	0.42	0.28

nd: not detected (<LOD), nq: not quantities (LOD<...<LOQ).



Öz [10], they were unable to identify IQx in beef samples cooked at 200°C for 3-12 minutes with oven cooking method. Zikirov [12] determined the IQx compound between 0-0,156 ng/g in beef samples cooked in different methods. Turesky [13], they found IQx at levels of 0.2 ng/g and 0.03 ng/g in barbecued beef and roast beef steaks, respectively.

In this study, it was determined that the samples of the meatballs cooked with the convection oven contain IQ

compounds in the range of nd-0,15 ng/g. The highest IQ content detected is; (0.15 ng/g) in the meatball samples cooked for 7.5 minutes at 250°C (Figure 2). When IQ contents of meatball samples are examined, at 150°C and 200°C, no IQ compound was formed, at 250°C, IQ compounds were detected in the amounts of 0,15 ng/g ve 0,11 ng/g, respectively, at 7,5 and 10 min cooked meatballs.

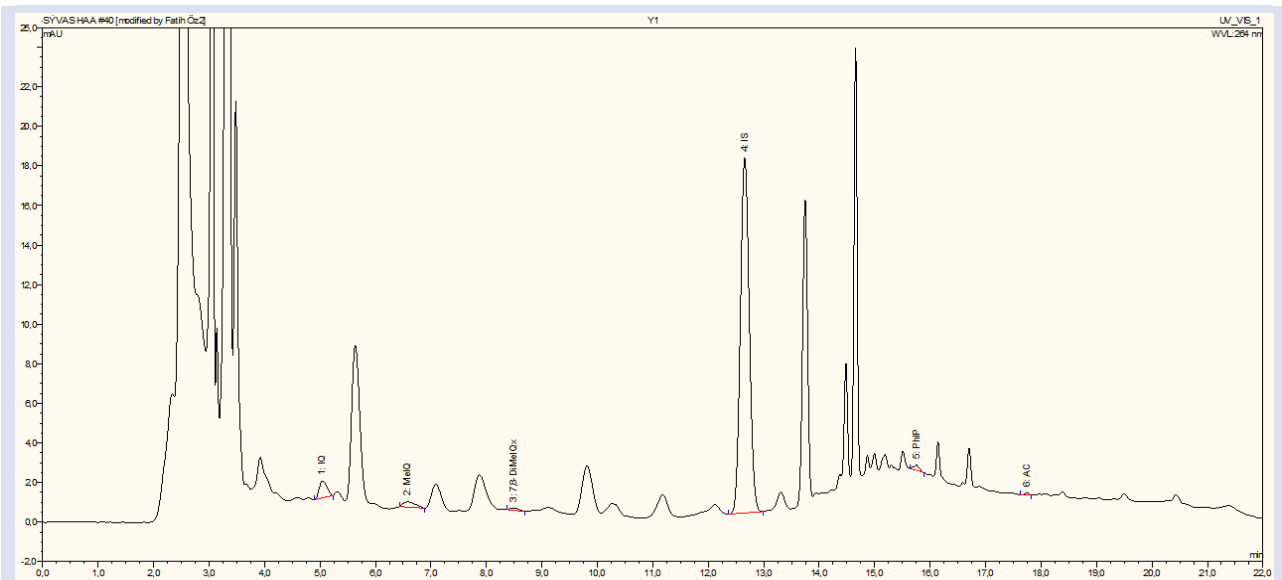


Figure 2. HPLC chromatogram of the sample baked for 7.5 min at 250°C

Kızıl [11] has found nd-1.26 ng/g IQ in the meat samples cooked at different temperatures in the oven. The highest IQ value was detected in the meatball cooked for 20 minutes at 150°C. In a study performed, in the examples cooked at 75°C and 85°C with sous-vide cooking method and with frying method (75°C internal temperature), it has been reported that IQ compound could not be determined but in the examples which were fried in a pan with internal temperature upto 95°C 0.037 ng/g IQ compound was detected [13]. In another study, in meatballs cooked at 175°C and 200°C (12 and 20 min), the IQ compound was reported as 0.7 ng/g, 1.3 ng/g, 1.7 ng/g and 4.4 ng/g, respectively [14]. Abdulkarim and Smith [15] have detected IQ up to 4.11ng/g in beef samples cooked in barbecue for 7-12 min at 200-240°C. Sinha [16] could not detect the IQ compound in beef samples cooked at different temperatures in the oven. Öz [17], in the study found 0.86 ng/g IQ in chops samples fried at 225°C but in samples at cooking temperatures of 175°C and 200°C, it was not possible to detect the IQ compound.

The contents of MeIQx of the analyzed samples were determined to be between 0-0.17 ng/g. The highest MeIQx content (0.17) was detected in the convection oven at 200°C temperature for 5 minute. 0.015 ng / g MeIQx compound was detected in samples cooked for 7.5 min at 150°C. No MeIQx compound was detected in any of the other samples. In a research

done, it has been reported that MeIQx quantities of pork meat samples cooked in pan and in the oven are; between 0.4-4.3 ng/g in fried cooked samples and between 0-4 ng/g in the cooked in oven samples [18]. Even though HAA quantities for cooking in the oven are generally at low levels, in a study by Skog [19] they found out that the amount of MeIQx of the pork meat samples cooked in the oven was 3.2 ng/g. These values were reported to be the highest reported values for cooking in the oven. In their study Turesky [20], they found 2.7 ng/g, 4.2 ng/g and 12.3 ng/g MeIQx compounds in meatballs at which were fried at 275°C for 5, 10 and 15 minutes. Gross [21] reported that they detected a MeIQx compound of between 1.1 and 1.4 ng/g in 10 minutes of fried pork meat. Balogh [22] have found 0.5 ng/g and 0.8 ng/g at 175°C respectively and 1.5 ng/g and 4.2 ng/g MeIQx at 200°C, respectively in cooked meatball samples at 175°C and 200°C (12 and 20 min). The increase in temperature and time has led to an increase in the amount of MeIQx compound [14]. When the MeIQx results of the analyzed meatball samples were compared with the literature results, seems to be compliance provided.

In the experimental meatball samples, MeIQ was detected between nd-0.05 ng/g. The highest MeIQ amount was found as 0.05 ng/g in the meatballs cooked for 7.5 min at 250°C. In the study of Zikirov [12], MeIQ was detected between nd-0.068 ng/g in pan-fried beef

samples. Klassen [23] found that the content of MeIQ in hamburger beef samples was less than 0.1 ng/g. Abdulkarim and Smith [15] found 0.38 ng/g MeIQ compound in the grilled meats at 200 and 240°C. In their study Felton [24] found no MeIQ compound in meatball samples cooked for 12 minutes at 200°C.

When the experimental meatball samples were evaluated for 7,8-DiMeIQx and 4,8-DiMeIQx, both compounds were found, but the amount could not be determined in any sample (LOD <... LOQ). In some studies, 7,8-DiMeIQx was not found and the findings were found to be consistent with the present study [23, 25]. The 4,8-DiMeIQx compound was found in different amounts in different studies. For example, Öz [17], it could not detect 4,8-DiMeIQx in roasted chops samples (15 min) at 200°C but, found 1.77 ng/g 4,8-DiMeIQx in fried chops (15 min) at 225°C temperature. Again Öz [10] in another study they did, reported that they could not detect the 4,8-DiMeIQx compound in beef 3-12 min cooked at 200°C.

Gross [21] were unable to determine the amount of 4,8-DiMeIQx since they were below the detectable value (0.5 ppb) in the beef meatballs cooked on a grill. In another study they did, 4,8-DiMeIQx was not detected in 10 min fried beef at 250°C. However, they found 1.3 ng/g 4,8-DiMeIQx in 190°C 6 min pan fried steak.

PhIP is the most common heterocyclic aromatic amine in food and it is indicated that the formation in the food is largely depends on the cooking temperature and it occurs in excess amounts at high temperatures. In meatball samples, nd-0.22 PhIP compound was detected. The highest PhIP content was detected in samples cooked for 7.5 min at 250°C. With PhIP at 0.22 ng/g value, it is the HAA that can be detected in the highest amount among the HAAs analyzed in this study. In a study done, hamburger meatballs were cooked by using grill/ barbecue, frying pan, oven cooking method and 16.8 ng/g (grill/barbecue), 2.3 ng/g (frying pan) PhIP levels have been detected. As a reason for the formation of more PhIP in hamburger meatballs cooked using frying and grilling/barbecue methods, it has been reported that compared to cooking in the oven the same internal temperature was reached in a shorter time [23].

MeAxC and AxC compounds were not detected in any sample cooked using convection oven at different temperatures and times. MeAxC and AxC were found at the highest temperature studied but their amounts could not be determined. Öz [10] reported that MeAxC and AxC compounds could not be detected in beef samples cooked in the oven at 200°C (3-12 min), grilled (2-8 min) and fried (1.5-6 min).

As a result, it was observed that the total HAA amounts of the samples cooked in the convection oven using different temperatures and times were between 0-0.42 ng/g (Table 5). HAA was not detected at any temperature and any time for meatball samples cooked 7.5 min at 200°C, 10 min at 200°C and 5 min at 250°C.

It is possible to say that sample of meatballs are safe in terms of HAA amounts according to the temperature and time they are cooked.

**Table 5.** The total quantities of HAA (ng/g) resulting from the cooking of experimental meatball samples at different temperatures and time

Temperatures (°C)	Time (min)	Total HAA (ng/g)
150	5	0.05
	7.5	0.14
	10	0.21
200	5	0.17
	7.5	-
	10	-
250	5	-
	7.5	0.42
	10	0.28

Based on the results of this study, it was determined that the formation of MeIQx compound increased with increasing cooking temperature. It has been observed that there are fluctuations in the amount of formation of other HAAs.

## Conclusion

Heterocyclic aromatic amines are chemicals known with mutagenic and carcinogenic effects on human health and produced by the cooking process in meat products that are rich in terms of protein. For this reason, the detection and prevention of HAA in meat and meat products has been the main objectives of recent studies. As a result of our study, it was determined that the application different cooking methods for cooking meatballs is suitable. Also, it was determined that the formation of MeIQx compound increased with increasing cooking temperature. It has been observed that there are fluctuations in the amount of other HAAs., This current work will be guiding for further studies researching formation of HAAs in meatballs obtained from different meat products. From this point of view, our study contributes to the literature. Moreover, the reduction techniques could be developed for detection HAAs in meat products.

## Acknowledgment

This work is summarized in the master's thesis. This work was supported financially by the University of Cumhuriyet scientific research projects CUBAP(Project number: M 630).

## Conflicts of Interest

The authors state that did not have conflict of interests.

## References

- [1] Alaejos M., Pino V., Afonso A., Metabolism and Toxicology of Heterocyclic Aromatic Amines When Consumed in Diet: Influence of The Genetic Susceptibility to Develop Human Cancer A review, *Int. Food Res.*, 41 (2008) 327-340.
- [2] Skog K., Solyakov A., Heterocyclic Amines in Poultry Products: A Literature Review, *Food Chem. Toxicol.*, 40 (2002) 1213-1221.
- [3] Jägerstad M., Skog K., Arvidsson P., Solyakov A., Chemistry, Formation and Occurrence of Genotoxic Heterocyclic Amines Identified in Model Systems and Cooked Foods, *Z Lebens Unters Forsch A.*, 207 (1998) 419-427.
- [4] Murkovic M., Formation of Heterocyclic Aromatic Amines in Model Systems, *J. Chromatogr. B Biomed. Appl.*, 802 (2004) 3-10.
- [5] Jägerstad M., Laser Reuterswärd A., Olsson R., Grivas S., Nyhammar T., Olsson K., Dahlgvist A., Creatin(in)e and Maillard Reaction Products as Precursors of Mutagenic Compounds: Effects of Various Amino Acids, *Food Chem.*, 12 (1983) 255-264.
- [6] Bermudo E., Ruiz-Calero V., Puignou L., Galceran M.T., Analysis of Heterocyclic Amines in Chicken by Liquid Chromatography with Electrochemical Detection, *Anal. Chim. Acta.*, 536 (2005) 83-90.
- [7] Puignou L., Casal J., Santos F., Galceran M., Determination of Heterocyclic Aromatic Amines by Capillary Zone Electrophoresis in A Meat Extract, *J. Chromatogr. A*, 797 (1997) 293-299.
- [8] AOAC, Official Methods of Analysis of Association of Official Chemists, 15th Ed., AOAC Inc., (1990) Arlington.
- [9] Öz F., Kaban G., Kaya M., Effect of Cooking Methods and Levels On Formation of Heterocyclic Aromatic Amines in Chicken and Fish Wüth Oasis Extraction Method. *LWT-Food Sci. Technol.*, 43(9) (2010) 1345-1350.
- [10] Öz F., Kaban G., Kaya M., Heterocyclic Aromatic Amine Contents of Beef and Lamb Chops Cooked by Different Methods to Varying Levels, *J. Anim. Vet. Adv.*, 9(10) (2010) 1436-1440.
- [11] Kızıl M., Ankara'da Toplu Beslenme Yapılan Kurumlardan Alınan Farklı Pişirme Yöntemleri Uygulanmış Köfte Örneklerinin Heterosiklik Aromatik Amin İçeriklerinin Değerlendirilmesi Üzerine Bir Araştırma, PHD Thesis, University of Hacettepe, Health Science Ankara (2012).
- [12] Zikirov E., Sous-vide Pişirme Yönteminin Sığır Etinde Heterosiklik Aromatik Amin Oluşumu ve Bazı Kalitatif Kriterler Üzerine Etkisi, PHD Thesis, University of Atatürk, Institute of Science, Erzurum, 2014.
- [13] Turesky R. J., Taylor J., Schnackenberg L., Freeman J.P., Holland R.D., Quantitation of Carcinogenic Heterocyclic Aromatic Amines and Detection of Novel Heterocyclic Aromatic Amines in Cooked Meats and Grill Scrapings by HPLC/ESI-MS, *J. Agric. Food Chem.*, 53(8) (2005) 3248-3258.
- [14] Fay L.B., Ali S., Gross G.A., Determination of Heterocyclic Aromatic Amines in Food Products: Automation of The Sample Preparation Method Prior to HPLC and HPLC-MS Quantification, *Mutat. Res-Fund. Mol. M.*, 376(1-2) (1997) 29-35.
- [15] Abdulkarim B.G., Smith J.S., Heterocyclic Amines in Fresh and Processed Meat Products, *J. Agric. Food Chem.*, 46(11) (1998) 4680-4687.
- [16] Sinha R., Rothman N., Salmon C.P., Knize M.G., Brown E.D., Swanson C.A., Rhodes D., Rossi S., Felton J.S., Levander O.A., Heterocyclic Amine Content in Beef Cooked by Different Methods to Varying Degrees of Doneness and Gravy made from Meat Drippings, *Food and Chem. Toxicol.*, 36 (1998) 279-287.
- [17] Öz F., Farklı Sıcaklıklarda Pişirilen Taze Et Ürünlerinde Baharat Kullanımının Heterosiklik Aromatik Aminlerin Oluşumu Üzerine Etkisi, PHD Thesis, University of Atatürk, Institute of Science, Erzurum, 2006.
- [18] Gibis M., Heterocyclic Aromatic Amines in Cooked Meat Products: Causes, Formation, Occurrence, and Risk Assessment, *Compr. Rev. Food Sci. Food Saf.*, 15 (2006) 269-302.
- [19] Skog K., Blue cotton, Blue Rayon and Blue Chitin in The Analysis of Heterocyclic Aromatic Amines-A review, *J. Chromatogr. B Biomed. Appl.*, 802 (2004) 39-44.
- [20] Turesky R.J., Bur H., Huynh-Ba T., Aeschbacher H.U., Milon H., Analysis of Mutagenic Heterocyclic Amines in Cooked Beef Products by High-Performance Liquid Chromatography in Combination with Mass Spectrometry, *Food Chem. Toxicol.*, 26(6) (1998) 501-509.
- [21] Gross G.A., Turesky R.J., Fay L.B., Stillwell W.G. I., Skipper P.L., Tannenbaum S.R., Heterocyclic Aromatic Amine Formation in Grilled Bacon, Beef and Fish and Grill Scrapings, *Carcinogenesis*, 14(11) (1993) 2313-2318.
- [22] Balogh Z., Gray J.I., Gomaa E.A., Booren A.M., Formation and Inhibition of Heterocyclic Aromatic Amines in Fried Ground Beef Patties, *Food Chem. Toxicol.*, 38(5) (2000) 395-401.
- [23] Klassen R.D., Lewis D., Lau B.P.Y., Sen N.P., Heterocyclic Aromatic Amines in Cooked Hamburgers and Chicken Obtained from Local Fast Food Outlets in the Ottawa Regio, *Int. Food Res. J.*, 35(9) (2002) 837-847.
- [24] Felton J.S., Knize M.G., Salmon C.P., Malfatti M.A., Kulp K.S., Human Exposure to Heterocyclic Amine Food Mutagens/Carcinogens: Relevance to Breast Cancer, *Environ. Mol. Mutagen*, 39 (2002) 112-118.
- [25] Toribio F., Busquets R., Puignou L., Galceran M.T., Heterocyclic Amines in Griddled Beef Steak Analysed Using A Single Extract Clean-up Procedure, *Food Chem. Toxicol.*, 45(4) (2007) 667-675.

## On the Associated Curves of a Frenet Curve in $R_1^4$

Esra Çiçek Çetin <sup>1,a,\*</sup>, Mehmet Bektaş <sup>1,b</sup>, Münevver Yıldırım Yılmaz <sup>1,c</sup>

<sup>1</sup> Department of Mathematics, Faculty of Science, Firat University, 23119 Elazığ, Türkiye.

\*Corresponding author

### Research Article

#### History

Received: 23/02/2021

Accepted: 29/03/2022

#### Copyright



©2022 Faculty of Science,  
Sivas Cumhuriyet University

### ABSTRACT

In the present work, we have dealt with the properties of associated curves of a Frenet curve in  $R_1^4$ . In addition to this, we define principal direction curve,  $B_1$  –direction curve,  $B_2$  – direction curve of a given Frenet curve by using integral curves of 4-dimensional Minkowski space. Then we introduce some characterizations for general helix and slant helix. Finally, some new associated curves and theorems obtained for space-like curves and time-like curves in  $R_1^4$ . Also, an example is given.

**Keywords:** Frenet curve, Associated curve, Principal -direction curve,  $B_1$  –direction curve,  $B_2$  – direction curve.

<sup>a</sup> [esracek23@gmail.com](mailto:esracek23@gmail.com)  
<sup>c</sup> [myildirim@firat.edu.tr](mailto:myildirim@firat.edu.tr)

<sup>b</sup> <https://orcid.org/0000-0001-8213-0156>  
<sup>d</sup> <https://orcid.org/0000-0003-1278-3981>

<sup>b</sup> [mbektas@firat.edu.tr](mailto:mbektas@firat.edu.tr)

<sup>d</sup> <https://orcid.org/0000-0002-5797-4944>

## Introduction

One of the important and productive area of differential geometry is curve theory for many researchers. The special defined curves such as helices, slant helices, rectifying curves, Bertrand and Mannheim curve pairs are characterized by their curvatures, in many ways. Also, among these special defined curves an interesting one is associated curves obtained by the integral curves of the Frenet elements.

In general, we denominate these curves by the name of Frenet elements, ea. principal direction curve, binormal direction. The researchers focus on the subject from the different point of view and most of them based on the different dimension and different spaces because of the variety of the Frenet equations.

In [1] Babaarslan, Tandoğan and Yaylı defined Bertrand curves and constant slope surfaces according to Darboux frame. Moreover, Bektaş, Ergüt and Öğrenmiş in [2], mentioned a special curves of 4D Galilean space. Also, in [3] author introduced special helices on equiform differential geometry of time-like curves in  $E_1^4$ . In [4-5], authors defined associated curves on different spaces and researched their applications. Following the studies above the geometers introduce associated directional curves in various spaces in [6-9]. According to these studies, in [10] Sahiner obtained characterizations for quaternionic direction curve and some special dual direction in  $R^3$ . Due to the popularity of the special defined curves these are numerous works related to this subject in different aspects [11-12].

Inspired by the above studies, we have focused on the associated curves of a Frenet curve in  $R_1^4$  which is another famous research area for mathematicians.

## Preliminaries

Let  $R_1^4$  be 4-dimensional vector space endowed with the scalar product  $\langle, \rangle$  defined as

$$\langle x, y \rangle = x_1y_1 + x_2y_2 + x_3y_3 + x_4y_4 \quad (1)$$

where  $(x_1, x_2, x_3, x_4)$  is a rectangular coordinate system in  $R_1^4$ .  $R_1^4$  is 4-dimensional vector space equipped with the scalar product  $\langle, \rangle$  then  $R_1^4$  is called Lorentzian 4-space or 4-dimensional Minkowski space. A vector  $v \in R_1^4$  can have one of the three casual characters called space-like ( $\langle v, v \rangle > 0$  or  $v = 0$ ), time-like ( $\langle v, v \rangle < 0$ ) and light-like (or null) ( $\langle v, v \rangle = 0$  and  $v \neq 0$ ). Similarly, an arbitrary curve  $\alpha = \alpha(s)$  in  $R_1^4$  is called space-like, time-like or light-like respectively.

If all of velocity vector  $\alpha'(s)$  are space-like, time-like or light-like respectively. The norm of a vector  $v \in R_1^4$  is given by  $\|v\| = \sqrt{|\langle v, v \rangle|}$ . Therefore,  $v$  is a unit vector  $\langle v, v \rangle = \pm 1$ . A curve (space-like, or time-like) is parametrized by the arc length if  $\alpha'(s)$  is unit vector for any  $s$ . Also, we say that the vectors  $v, w \in R_1^4$  are orthogonal if  $\langle v, w \rangle = 0$ . [10]

For any three vectors  $a = (a_1, a_2, a_3, a_4), b = (b_1, b_2, b_3, b_4), c = (c_1, c_2, c_3, c_4) \in R_1^4$  the Lorentzian vector product is defined by

$$a \times b \times c = \begin{vmatrix} -e_1 & e_2 & e_3 & e_4 \\ a_1 & a_2 & a_3 & a_4 \\ b_1 & b_2 & b_3 & b_4 \\ c_1 & c_2 & c_3 & c_4 \end{vmatrix}$$

Here  $e_1, e_2, e_3$  and  $e_4$  are orthogonal vectors satisfying equations

$e_1 \wedge e_2 \wedge e_3 = e_4, e_2 \wedge e_3 \wedge e_4 = e_1, e_3 \wedge e_4 \wedge e_1 = e_2, e_4 \wedge e_1 \wedge e_2 = -e_3.$  [12].

Let  $\gamma$  be a space-like curve in  $R_1^4$  with the curvatures  $k_1, k_2, k_3$ . Then Frenet formulae are given as follows

$$\begin{bmatrix} T' \\ N' \\ B_1' \\ B_2' \end{bmatrix} = \begin{bmatrix} 0 & k_1 & 0 & 0 \\ -k_1 & 0 & k_2 & 0 \\ 0 & -k_2 & 0 & k_3 \\ 0 & 0 & k_3 & 0 \end{bmatrix} \begin{bmatrix} T \\ N \\ B_1 \\ B_2 \end{bmatrix}$$

Let  $\gamma$  be a time-like curve in  $R_1^4$  with the curvatures  $k_1, k_2, k_3$ . Then Frenet formulae are given as follows:

$$\begin{bmatrix} T' \\ N' \\ B_1' \\ B_2' \end{bmatrix} = \begin{bmatrix} 0 & k_1 & 0 & 0 \\ k_1 & 0 & k_2 & 0 \\ 0 & -k_2 & 0 & k_3 \\ 0 & 0 & -k_3 & 0 \end{bmatrix} \begin{bmatrix} T \\ N \\ B_1 \\ B_2 \end{bmatrix}$$

For a detailed information we refer to [10].

### Associated Curves of a Frenet Curve in $R_1^4$

In this section we have focused on the associated curves of a Frenet curve in  $R_1^4$ .

**Definition 3.1.** Let us consider an admissible  $\gamma$  Frenet curve  $\{T, N, B_1, B_2\}$  with Frenet frame in  $R_1^4$ .

The integral curve of the principal normal vector field of  $\gamma$  is defined as principal direction curve of  $\gamma$ .

The integral curve of the first binormal vector field of  $\gamma$  is defined as  $B_1$  -direction curve of  $\gamma$ .

The integral curve of the second binormal vector field of  $\gamma$  is defined  $B_2$  -direction curve of  $\gamma$ .

**Theorem 3.1.** Let  $\gamma$  be a space-like curve whose curvatures are  $k_1, k_2, k_3$  and  $\bar{\gamma}$  be the principal direction curve of  $\gamma$  in  $R_1^4$ . Then the curvatures of  $\bar{\gamma}$  are as follows

$$\begin{aligned} \bar{k}_1(s) &= |k_1 - k_2| \\ \bar{k}_2(s) &= 0 \end{aligned}$$

**Proof.** Let  $\{\bar{T}, \bar{N}, \bar{B}_1, \bar{B}_2, \bar{k}_1, \bar{k}_2, \bar{k}_3\}$  be the Frenet elements of  $\bar{\gamma}$ . We find from the definition (3.1.a) as, we can easily obtain ,

$$\begin{aligned} N(s)|_{\bar{\gamma}(s)} &= \bar{\gamma}'(s) = \bar{T}(s) \\ \text{Then,} \\ \bar{N}(s) &= \frac{\bar{\gamma}''(s)}{\|\bar{\gamma}''(s)\|} = \frac{N'(s)}{\|N'(s)\|} = \frac{-k_1T + k_2B_1}{\|-k_1T + k_2B_1\|} \\ &= \frac{-k_1T + k_2B_1}{|k_1 - k_2|} \end{aligned}$$

$$\bar{B}_2 = \frac{\bar{\gamma}' \times \bar{\gamma}'' \times \bar{\gamma}'''}{\|\bar{\gamma}' \times \bar{\gamma}'' \times \bar{\gamma}'''\|} = \frac{k_1B_1 + k_2T}{k_1 + k_2}$$

and ,

$$\bar{B}_1 = \bar{B}_2 \times \bar{T} \times \bar{N} = \frac{k_1^2 + k_2^2}{|k_1 + k_2||k_1 - k_2|} B_2$$

Then the curvatures of  $\bar{\gamma}$  are given by

$$\begin{aligned} \bar{k}_1(s) &= \langle \bar{T}', \bar{N} \rangle = \frac{k_1^2 + k_2^2}{|k_1 - k_2|} \\ \bar{k}_2(s) &= \langle \bar{N}', \bar{B}_1 \rangle = 0 \end{aligned}$$

**Theorem 3.2.** Let  $\gamma$  be a space-like curve whose curvatures are  $k_1, k_2, k_3$  and  $\bar{\gamma}$  be the  $B_1$  - direction curve of  $\gamma$  in  $R_1^4$ , the curvatures of  $\bar{\gamma}$  are as follows

$$\begin{aligned} \bar{k}_1(s) &= \sqrt{k_2^2 - k_3^2} \\ \bar{k}_2(s) &= -\frac{k_1k_2(k_2^2 + k_3^2)}{(k_3^2 - k_2^2)^{\frac{3}{2}}} \end{aligned}$$

**Proof.** The proof is similar to the proof of Theorem 3.1 , so it is omitted.

**Theorem 3.3.** Let  $\gamma$  be a space-like curve whose curvatures are  $k_1, k_2, k_3$  and  $\bar{\gamma}$  be the  $B_2$  - direction curve of  $\gamma$ , in  $R_1^4$ , the curvatures of  $\bar{\gamma}$  are as follows

$$\begin{aligned} \bar{k}_1(s) &= k_3 \operatorname{sgn}(k_3) \\ \bar{k}_2(s) &= k_2 \operatorname{sgn}(k_3) \end{aligned}$$

**Proof.** Let  $\{\bar{T}, \bar{N}, \bar{B}_1, \bar{B}_2, \bar{k}_1, \bar{k}_2, \bar{k}_3\}$  be the Frenet elements of  $\bar{\gamma}$ . We find from the definition (3.1.c) , we get,

$$B_2(s) = \bar{\gamma}'(s) = \bar{T}(s)$$

Using the Frenet vector fields, we find,

$$\begin{aligned} \bar{N}(s) &= \operatorname{sgn}(k_3)B_1 \\ \bar{B}_2(s) &= T \\ \bar{B}_1 &= -\operatorname{sgn}(k_3)N \end{aligned}$$

Then, the curvatures of  $\bar{\gamma}$  are given by

$$\begin{aligned} \bar{k}_1(s) &= k_3 \operatorname{sgn}(k_3) \\ \bar{k}_2(s) &= k_2 \operatorname{sgn}(k_3) \end{aligned}$$

**Theorem 3.4.** Let  $\gamma$  be a space-like curve in  $R_1^4$  and  $\bar{\gamma}$  be the principal direction curve of  $\gamma$  is a slant helix  $\Leftrightarrow \bar{\gamma}$  is a general helix.

**Proof.** Let  $\{T, N, B_1, B_2\}$  be the Frenet frame of  $\gamma$ . From the definition (3.1.a) , we can write,

$$\begin{aligned} N(s)|_{\bar{\gamma}(s)} &= \bar{\gamma}'(s) = \bar{T}(s) \\ \text{thus,} \end{aligned}$$

$\gamma$  is a slant helix  $\Leftrightarrow \langle N, u \rangle = c$  here  $u$  is a constant vector and  $c = \text{const.}$

$$\begin{aligned} \Leftrightarrow \langle \bar{T}, u \rangle &= c \\ \Leftrightarrow \gamma &\text{ is a general helix.} \end{aligned}$$

**Theorem 3.5.** Let  $\gamma$  be a space-like curve in  $R_1^4$  and  $\bar{\gamma}$  be the  $B_2$  - direction of  $\gamma$ . Then  $\gamma$  is a  $B_2$  - slant helix  $\Leftrightarrow \bar{\gamma}$  is a general helix.

**Proof:** Let  $\{T, N, B_1, B_2\}$  be the Frenet frame of  $\gamma$ . From the definition (3.1.c), we may write,

$$B_2(s)|_{\bar{\gamma}(s)} = \bar{\gamma}'(s) = \bar{T}(s)$$

Thus,

$\gamma$  is  $B_2$  slant helix  $\Leftrightarrow \langle B_2, v \rangle = c$  here  $v$  is a constant vector and  $c = const.$

$\Leftrightarrow \langle \bar{T}, v \rangle = c$  here  $v$  is a constant vector and  $c = const.$

$\Leftrightarrow \gamma$  is a general helix.

From now on we have focused on the time-like curve in  $R_1^4$ .

**Theorem 3.6.** Let  $\gamma$  be a time-like curve in  $R_1^4$  with the curvatures  $k_1, k_2, k_3$  and  $\bar{\gamma}$  be the principal direction curve of  $\gamma$ . Then the curvatures of  $\bar{\gamma}$  are as follows

$$\bar{k}_1(s) = \sqrt{k_2^2 - k_1^2}$$

$$\bar{k}_2(s) = -(k_1^2 - k_2^2)^{3/2}$$

**Proof.** Let  $\{\bar{T}, \bar{N}, \bar{B}_1, \bar{B}_2, \bar{k}_1, \bar{k}_2, \bar{k}_3\}$  be the Frenet elements of  $\bar{\gamma}$ . We find from the definition (3.1.a), we can easily obtain,

$$N(s)|_{\bar{\gamma}(s)} = \bar{\gamma}'(s) = \bar{T}(s)$$

Then,

$$\bar{N}(s) = \frac{\bar{\gamma}''(s)}{\|\bar{\gamma}''(s)\|} = \frac{N'(s)}{\|N'(s)\|} = \frac{k_1 T + k_2 B_1}{\|k_1 T + k_2 B_1\|}$$

$$= \frac{k_1 T + k_2 B_1}{\sqrt{k_2^2 - k_1^2}}$$

$$\bar{B}_2 = \frac{\bar{\gamma}' \times \bar{\gamma}'' \times \bar{\gamma}'''}{\|\bar{\gamma}' \times \bar{\gamma}'' \times \bar{\gamma}'''\|} = \frac{-k_1 B_1 + k_2 T}{\sqrt{k_1^2 - k_2^2}}$$

and,

$$\bar{B}_1 = \bar{B}_2 \times \bar{T} \times \bar{N} = \frac{k_1^2 + k_2^2}{(k_2^2 - k_1^2)i} B_2$$

Then the curvatures of  $\bar{\gamma}$  are given by

$$\bar{k}_1(s) = \langle \bar{T}', \bar{N} \rangle = \frac{k_1^2 + k_2^2}{\sqrt{k_2^2 - k_1^2}}$$

$$\bar{k}_2(s) = \langle \bar{N}', \bar{B}_1 \rangle = -(k_1^2 - k_2^2)^{3/2}$$

**Theorem 3.7.** Let  $\gamma$  be a time-like curve whose curvatures are  $k_1, k_2, k_3$  and  $\gamma$  be the  $B_1$  - direction curve of  $\gamma$  in  $R_1^4$ . Then the curvatures of  $\gamma$  are as follows

$$\bar{k}_1(s) = k_2 - k_3$$

$$\bar{k}_2(s) = |k_2 - k_3|$$

**Proof.** The proof is similar to the proof of Theorem 3.7, so it is omitted.

**Theorem 3.8.** Let  $\gamma$  be a time-like curve whose curvatures are  $k_1, k_2, k_3$  and  $\bar{\gamma}$  be the  $B_2$  - direction curve of  $\gamma$ , in  $R_1^4$ , the curvatures of  $\bar{\gamma}$  are as follows

$$\bar{k}_1(s) = k_3 \operatorname{sgn}(k_3)$$

$$\bar{k}_2(s) = (k_2 + k_3) \operatorname{sgn}(k_3)$$

**Proof.** Let  $\{\bar{T}, \bar{N}, \bar{B}_1, \bar{B}_2, \bar{k}_1, \bar{k}_2, \bar{k}_3\}$  be the Frenet elements of  $\bar{\gamma}$ . From the (3.1.c), we get,

$$B_2(s) = \bar{\gamma}'(s) = \bar{T}(s)$$

Using the Frenet vector fields, we find,

$$\bar{N}(s) = -\operatorname{sgn}(k_3) B_1$$

$$\bar{B}_2(s) = T$$

$$\bar{B}_1 = \operatorname{sgn}(k_3) N$$

Finally, the curvatures of  $\bar{\gamma}$  are given by

$$\bar{k}_1(s) = k_3 \operatorname{sgn}(k_3)$$

$$\bar{k}_2(s) = (k_2 + k_3) \operatorname{sgn}(k_3)$$

**Theorem 3.9.** Let  $\gamma$  be a time-like curve in  $R_1^4$  and  $\bar{\gamma}$  be the principal direction curve of  $\gamma$  is a slant helix  $\Leftrightarrow \bar{\gamma}$  is a general helix.

**Proof.** Let  $\{T, N, B_1, B_2\}$  be the Frenet frame of  $\gamma$ . From the definition (3.1.a), we also know,

$$N(s)|_{\bar{\gamma}(s)} = \bar{\gamma}'(s) = \bar{T}(s)$$

Thus,

$\gamma$  is a slant helix  $\Leftrightarrow \langle N, u \rangle = c$  here  $u$  is a constant vector and  $c = const.$

$\Leftrightarrow \langle \bar{T}, u \rangle = c$

$\Leftrightarrow \gamma$  is a general helix.

**Theorem 3.10.** Let  $\gamma$  be a space-like curve in  $R_1^4$  and  $\bar{\gamma}$  be the  $B_2$  - direction of  $\gamma$ . Then  $\gamma$  is a  $B_2$  - slant helix  $\Leftrightarrow \bar{\gamma}$  is a general helix.

**Proof:** Let  $\{T, N, B_1, B_2\}$  be the Frenet frame of  $\gamma$ . From the definition (3.1.c), we may write,

$$B_2(s)|_{\bar{\gamma}(s)} = \bar{\gamma}'(s) = \bar{T}(s)$$

Thus,

$\gamma$  is  $B_2$  slant helix  $\Leftrightarrow \langle B_2, v \rangle = c$  here  $v$  is a constant vector and  $c = const.$

$\Leftrightarrow \langle \bar{T}, v \rangle = c$  here  $v$  is a constant vector and  $c = const.$

$\Leftrightarrow \gamma$  is a general helix.

### Example

In this section, an example of directional associated curves of space-like curve are given as follows:

Consider a space-like curve

$$\alpha(s) = (\sin 2s, \cos 2s, \sqrt{3}s, \sqrt{3})$$

The Frenet frame vectors and curvatures are obtained by

$$T = (2 \cos 2s, -2 \sin 2s, \sqrt{3}, 0)$$

$$N = (-\sin 2s, -\cos 2s, 0, 0)$$

$$B_1 = \frac{1}{\sqrt{113}}(8 \cos 2s - \sin 2s, -\cos 2s - 8 \sin 2s, 4\sqrt{3}, 0)$$

$$B_2 = (0, 0, 0, 0)$$

$$k_1 = 4, \quad k_2 = \sqrt{113}$$

We obtain principal-direction,  $B_1$ -direction and  $B_2$ -direction,

$$N(s)|_{\bar{\gamma}(s)} = \bar{\gamma}'(s) = \bar{T}(s) = \left( \frac{1}{2} \cos 2s, -\frac{1}{2} \sin 2s, \frac{\sqrt{3}}{4}, 0 \right)$$

$$\bar{N}(s) = \frac{\bar{\gamma}''(s)}{\|\bar{\gamma}''(s)\|} = (-\sin 2s, -\cos 2s, 0, 0)$$

$$\bar{B}_2 = \frac{\bar{\gamma}' \times \bar{\gamma}'' \times \bar{\gamma}'''}{\|\bar{\gamma}' \times \bar{\gamma}'' \times \bar{\gamma}'''\|} = \left( 0, 0, 0, -\frac{\sqrt{3}}{2} \right)$$

$$\bar{B}_1 = \bar{B}_2 \times \bar{T} \times \bar{N} = \left( \frac{\sqrt{3}}{4} \cos 2s, \frac{\sqrt{3}}{2} \sin 2s, -\frac{\sqrt{3}}{3}, 0 \right)$$

Then we get the curvatures of  $\bar{\gamma}$  as

$$\bar{k}_1(s) = \langle \bar{T}', \bar{N} \rangle = 1$$

$$\bar{k}_2(s) = \langle \bar{N}', \bar{B}_1 \rangle = -\frac{\sqrt{3}}{2} \cos^2 2s + \sqrt{3} \sin^2 2s$$

### Acknowledgment

The author would like to thank to Prof. Dr. Mihriban KÜLAHCI from Fırat University and referees owing to enlightening ideas.

### Conflicts of interest

The authors state that did not have conflict of interests.

### References

- [1] Babaarslan M., Tandoğan Y. A., Yaylı Y. A., A note on Bertrand curves and constant slope surfaces according to Darboux frame, *Journal of Advanced Mathematical Studies*, 5 (2012) 87-96.
- [2] Bektaş M., Ergüt M., Öğrenmiş A., A special curves of 4D Galilean space, *International Journal of Mathematical Engineering and Science*, 2(3) (2013) 2277-6982.
- [3] Bulut F., Special helices on equiform differential geometry of time-like curves in  $E_1^4$ , *Cumhuriyet Science Journal* 42(4) (2021) 906-905.
- [4] Choi J. H., Kim Y.H., Ali A.T. Some associated curves of Frenet non-light-like curves in  $E_1^3$ , *Journal of Mathematical Analysis and Applications*, 394 (2012) 712-723.
- [5] Choi J. H., Kim Y.H., Associated curves of a Frenet curve and their applications, *Applied Mathematics and Computation*, 218 (2012) 9116-9124.
- [6] Macit N., Akbıyık M., Yüce S., Some New Associated Curves of An Admissible Frenet Curve In 3-dimensional and 4-dimensional Galilean Spaces, *Romanian Journal of Mathematics and Computer Science*, 7 (2017) 110-122.
- [7] Macit N., Döldül M., Some New Associated Curves of a Frenet curve in  $E^3$  and  $E^4$ , *Turkish Journal of Mathematics*, 38 (2014) 1023-1037.
- [8] Mak M., Altınbaş H., Some Special Associated Curves of Non-Degenerate Curve in Anti de Sitter 3-Space, *Mathematical Sciences and Applications*, 5(27) (2017) 89-97.
- [9] Körpınar T., Sarıaydın M. T., Turhan E., Associated curves to Bishop frame in Euclidean 3-space, *Advanced Modelling and Optimization*, 15 (2013) 713-717.
- [10] Sahiner B., Some Special Dual Direction Curves, *Erzincan Üniversitesi Fen Bilimleri Dergisi*, (2018) 509-517.
- [11] T.Ali A., Lopez R., Turgut M., k-type null and pseudo null slant helices in Minkowski 4-space, *Math. Commun.*, 17 (2012) 93-103.
- [12] Yılmaz S., Turgut M., On the Differential Geometry of Curves in Minkowski space-time I, *Int. J. Contemp. Math. Sci.*, 3(27) (2008) 1343-1349.

## On Gaussian Jacobsthal-Padovan Numbers

Nusret Karaaslan <sup>1,a,\*</sup>

<sup>1</sup> Kalkandere Dağdibi Secondary School, Rize, Türkiye.

\*Corresponding author

### Research Article

#### History

Received: 18/11/2021

Accepted: 13/04/2022

#### Copyright




©2022 Faculty of Science,  
Sivas Cumhuriyet University

### ABSTRACT

Gaussian Jacobsthal-Padovan numbers have been the central focus of this paper and firstly this number sequence has defined. Later, we have given the proof of the generating function of the Gaussian Jacobsthal-Padovan sequence. After that by using generating function, we have given the proof of the Binet formula for this number sequence. Additionally, we have investigated some properties such as Simson identity, summation formulas of this sequence. Finally, we have obtained some matrices whose elements are Gaussian Jacobsthal-Padovan numbers.

**Keywords:** Jacobsthal numbers, Jacobsthal-Padovan numbers, Gaussian Jacobsthal-Padovan numbers, Generating function, Binet formula

 [nusret5301@gmail.com](mailto:nusret5301@gmail.com)

 <https://orcid.org/0000-0002-0244-1286>

## Introduction

In recent years, there have been many studies on a variety of number sequences in the literature. Some of the famous examples are Fibonacci, Lucas, Pell, Pell-Lucas, Jacobsthal and Jacobsthal-Lucas etc. Details can be found in [1-5]. In [4], Jacobsthal and Jacobsthal-Lucas number sequences are given respectively by

$$\begin{aligned} J_n &= J_{n-1} + 2J_{n-2}, & J_0 &= 0, J_1 = 1, & n &\geq 2, \\ j_n &= j_{n-1} + 2j_{n-2}, & j_0 &= 2, j_1 = 1, & n &\geq 2. \end{aligned}$$

Gaussian forms of these sequences are also available in the literature. Gaussian forms of these sequences as well as their properties have been inquired into by many authors, see [6-10] for details. In [9], Jacobsthal and Jacobsthal-Lucas sequences' Gaussian forms are defined by the recursion formulas

$$\begin{aligned} GJ_n &= GJ_{n-1} + 2GJ_{n-2}, & GJ_0 &= \frac{i}{2}, GJ_1 = 1, & n &\geq 2, \\ Gj_n &= Gj_{n-1} + 2Gj_{n-2}, & Gj_0 &= 2 - \frac{i}{2}, Gj_1 = 1 + 2i, & n &\geq 2, \end{aligned}$$

respectively.

Also, Cerda-Morales [11] defined Gauss third-order Jacobsthal numbers and investigated some properties of this sequence.

Additionally, the Padovan (sequence A000931 in [12]), Pell-Padovan (sequence A066983 in [12]) and Jacobsthal-Padovan (sequence A159284 in [12]) sequences are given, respectively, by the third-order recurrence relations

$$\begin{aligned} P_n &= P_{n-2} + P_{n-3}, & P_0 &= P_1 = P_2 = 1, & n &\geq 3, \\ R_n &= 2R_{n-2} + R_{n-3}, & R_0 &= R_1 = R_2 = 1, & n &\geq 3, \\ JP_n &= JP_{n-2} + 2JP_{n-3}, & JP_0 &= JP_1 = JP_2 = 1, & n &\geq 3. \end{aligned}$$

Also, Taşçı [13] defined Gaussian Padovan and Gaussian Pell-Padovan sequences as follows:

$$\begin{aligned} GP_n &= GP_{n-2} + GP_{n-3}, & GP_0 &= 1, & GP_1 &= 1 + i, \\ GP_2 &= 1 + i, & & & n &\geq 3, \end{aligned}$$

$$\begin{aligned} GR_n &= 2GR_{n-2} + GR_{n-3}, & GR_0 &= 1 - i, \\ GR_1 &= 1 + i, GR_2 = 1 + i, & & & n &\geq 3, \end{aligned}$$

respectively.

Moreover, in [13], some properties of these sequences are investigated. In addition, Yaşar Kartal [14] studied the Gaussian Padovan sequence.

In this study, we extended the Jacobsthal-Padovan sequence to Gaussian Jacobsthal-Padovan sequence. Then, we have derived generating function and the Binet formula for this sequence. Also, we have found numerous sums and various equalities for Gaussian Jacobsthal-Padovan sequence.

## Main Results

First, we give the definition of Gaussian Jacobsthal-Padovan number sequence based on the recurrence relation.

**Definition 1.** The sequence  $\{GJP_n\}_{n=0}^{\infty}$  of Gaussian Jacobsthal-Padovan numbers satisfies the following third-order recurrence relation:

$$GJP_n = GJP_{n-2} + 2GJP_{n-3}$$

with initial conditions  $GJP_0 = 1, GJP_1 = 1 + i, GJP_2 = 1 + i$  and  $n \geq 3$ .



Then we get the Gaussian Jacobsthal-Padovan sequence

$$\{GJP_n\} = \{1, 1 + i, 1 + i, 3 + i, 3 + 3i, 5 + 3i, 9 + 5i, \dots\}.$$

Also, note that for  $n \geq 0$

$$GJP_n = JP_n + iJP_{n-1}$$

where  $JP_n$  is the  $n$ -th Jacobsthal-Padovan numbers.

Theorem 1. The sequence  $\{GJP_n\}_{n \geq 0}$  can be extended to negative subscripts by defining

$$GJP_{-n} = -\frac{1}{2}GJP_{-(n-1)} + \frac{1}{2}GJP_{-(n-3)}$$

for  $n \geq 1$ .

Proof. From the recurrence relation of Gaussian Jacobsthal-Padovan sequence, we have

$$GJP_{n-3} = \frac{1}{2}GJP_n - \frac{1}{2}GJP_{n-2}.$$

Then, for  $n = -n + 3$ , we obtain

$$\begin{aligned} GJP_{-n} &= \frac{1}{2}GJP_{-n+3} - \frac{1}{2}GJP_{-n+1} \\ &= \frac{1}{2}GJP_{-(n-3)} - \frac{1}{2}GJP_{-(n-1)} \\ &= -\frac{1}{2}GJP_{-(n-1)} + \frac{1}{2}GJP_{-(n-3)} \end{aligned}$$

as required.

Presently, we deliver the generating function of Gaussian Jacobsthal-Padovan sequence with next theorem.

Theorem 2. The generating function of Gaussian Jacobsthal-Padovan sequence is obtained as

$$g(x) = \frac{1 + (1 + i)x + ix^2}{1 - x^2 - 2x^3}.$$

Proof. Assume that  $g(x)$  the generating function of  $\{GJP_n\}_{n=0}^\infty$ . By considering the recurrence relation of Gaussian Jacobsthal-Padovan sequence, and deriving  $x^2 \sum_{n=0}^\infty GJP_n x^n$  and  $2x^3 \sum_{n=0}^\infty GJP_n x^n$  from  $\sum_{n=0}^\infty GJP_n x^n$  we get

$$\begin{aligned} (1 - x^2 - 2x^3) \sum_{n=0}^\infty GJP_n x^n &= \sum_{n=0}^\infty GJP_n x^n - x^2 \sum_{n=0}^\infty GJP_n x^n - 2x^3 \sum_{n=0}^\infty GJP_n x^n \\ &= \sum_{n=0}^\infty GJP_n x^n - \sum_{n=0}^\infty GJP_n x^{n+2} - 2 \sum_{n=0}^\infty GJP_n x^{n+3} \\ &= \sum_{n=0}^\infty GJP_n x^n - \sum_{n=2}^\infty GJP_{n-2} x^n - 2 \sum_{n=3}^\infty GJP_{n-3} x^n \\ &= (GJP_0 + GJP_1 x + GJP_2 x^2) - GJP_0 x^2 + \sum_{n=3}^\infty (GJP_n - GJP_{n-2} - 2GJP_{n-3}) x^n \\ &= GJP_0 + GJP_1 x + (GJP_2 - GJP_0) x^2. \end{aligned}$$

Thus, by using the initial conditions, we obtain

$$\sum_{n=0}^{\infty} \text{GJP}_n x^n = \frac{1 + (1+i)x + ix^2}{1 - x^2 - 2x^3}$$

which is desired.

We now find the Binet formula for Gaussian Jacobsthal-Padovan sequence in the following theorem.

Theorem 3.  $n^{\text{th}}$  Gaussian Jacobsthal-Padovan number is

$$\text{GJP}_n = \frac{(x_1 + 1)(x_1 + i)}{(x_1 - x_2)(x_1 - x_3)} x_1^n + \frac{(x_2 + 1)(x_2 + i)}{(x_2 - x_1)(x_2 - x_3)} x_2^n + \frac{(x_3 + 1)(x_3 + i)}{(x_3 - x_1)(x_3 - x_2)} x_3^n$$

where  $x_1, x_2$  and  $x_3$  are the different roots of the equation  $x^3 - x - 2 = 0$  and whose roots are

$$x_1 = \sqrt[3]{1 + \frac{\sqrt{78}}{9}} + \sqrt[3]{1 - \frac{\sqrt{78}}{9}}, \quad x_2 = \omega \sqrt[3]{1 + \frac{\sqrt{78}}{9}} + \omega^2 \sqrt[3]{1 - \frac{\sqrt{78}}{9}}, \quad x_3 = \omega^2 \sqrt[3]{1 + \frac{\sqrt{78}}{9}} + \omega \sqrt[3]{1 - \frac{\sqrt{78}}{9}}$$

where  $\omega = \frac{-1+i\sqrt{3}}{2}$ .

Proof. Suppose that  $g(x) = 1 - x^2 - 2x^3$ . Then using the roots  $x_1, x_2$  and  $x_3$  of the equation, we can write  $g(x)$  as

$$g(x) = (1 - x_1x)(1 - x_2x)(1 - x_3x),$$

namely,

$$1 - x^2 - 2x^3 = (1 - x_1x)(1 - x_2x)(1 - x_3x) \tag{1}$$

Thus, we find all roots of  $g(x)$  as which  $\frac{1}{x_1}, \frac{1}{x_2}$  and  $\frac{1}{x_3}$ .

Now, we write the equation (1) and the generating function of  $\{\text{GJP}_n\}_{n=0}^{\infty}$  as:

$$\begin{aligned} \sum_{n=0}^{\infty} \text{GJP}_n x^n &= \frac{1 + (1+i)x + ix^2}{1 - x^2 - 2x^3} \\ &= \frac{1 + (1+i)x + ix^2}{(1 - x_1x)(1 - x_2x)(1 - x_3x)} \\ &= \frac{A}{1 - x_1x} + \frac{B}{1 - x_2x} + \frac{C}{1 - x_3x} \end{aligned} \tag{2}$$

Hence,

$$1 + (1+i)x + ix^2 = A(1 - x_2x)(1 - x_3x) + B(1 - x_1x)(1 - x_3x) + C(1 - x_1x)(1 - x_2x).$$

Then, for  $x = \frac{1}{x_1}$ , we have  $1 + (1+i)\frac{1}{x_1} + i\frac{1}{x_1^2} = A\left(1 - \frac{x_2}{x_1}\right)\left(1 - \frac{x_3}{x_1}\right)$ . From here, we find

$$A = \frac{x_1^2 \left[ 1 + (1+i)\frac{1}{x_1} + i\frac{1}{x_1^2} \right]}{(x_1 - x_2)(x_1 - x_3)} = \frac{x_1^2 + (1+i)x_1 + i}{(x_1 - x_2)(x_1 - x_3)} = \frac{(x_1 + 1)(x_1 + i)}{(x_1 - x_2)(x_1 - x_3)}$$

In a similar way, we obtain

$$B = \frac{(x_2 + 1)(x_2 + i)}{(x_2 - x_1)(x_2 - x_3)}, \quad C = \frac{(x_3 + 1)(x_3 + i)}{(x_3 - x_1)(x_3 - x_2)}.$$

Consequently, we can write the equation (2) as in the following way

$$\sum_{n=0}^{\infty} \text{GJP}_n x^n = A(1 - x_1x)^{-1} + B(1 - x_2x)^{-1} + C(1 - x_3x)^{-1}$$

$$= A \sum_{n=0}^{\infty} x_1^n x^n + B \sum_{n=0}^{\infty} x_2^n x^n + C \sum_{n=0}^{\infty} x_3^n x^n$$

$$= \sum_{n=0}^{\infty} (Ax_1^n + Bx_2^n + Cx_3^n)x^n.$$

Thus, we obtain for all  $n \geq 0$

$$GJP_n = Ax_1^n + Bx_2^n + Cx_3^n$$

$$= \frac{(x_1 + 1)(x_1 + i)}{(x_1 - x_2)(x_1 - x_3)} x_1^n + \frac{(x_2 + 1)(x_2 + i)}{(x_2 - x_1)(x_2 - x_3)} x_2^n + \frac{(x_3 + 1)(x_3 + i)}{(x_3 - x_1)(x_3 - x_2)} x_3^n$$

as required.

The following theorem gives the Simson formula for Gaussian Jacobsthal-Padovan sequence.

Theorem 4. For  $n \in \mathbb{Z}$ , we have

$$\begin{vmatrix} GJP_{n+2} & GJP_{n+1} & GJP_n \\ GJP_{n+1} & GJP_n & GJP_{n-1} \\ GJP_n & GJP_{n-1} & GJP_{n-2} \end{vmatrix} = -2^n(1 - i).$$

Proof. We show the proof of this theorem by induction over  $n$ . For  $n = 1$ , the statement is true. In fact

$$\begin{vmatrix} GJP_3 & GJP_2 & GJP_1 \\ GJP_2 & GJP_1 & GJP_0 \\ GJP_1 & GJP_0 & GJP_{-1} \end{vmatrix} = -2 + 2i = -2^1(1 - i).$$

Now, let this statement be true for  $n = k$ . That is,

$$\begin{vmatrix} GJP_{k+2} & GJP_{k+1} & GJP_k \\ GJP_{k+1} & GJP_k & GJP_{k-1} \\ GJP_k & GJP_{k-1} & GJP_{k-2} \end{vmatrix} = -2^k(1 - i).$$

Finally, we must show that the statement is correct for  $n = k + 1$ . We obtain from induction hypothesis and the properties of determinant function.

$$\begin{vmatrix} GJP_{k+3} & GJP_{k+2} & GJP_{k+1} \\ GJP_{k+2} & GJP_{k+1} & GJP_k \\ GJP_{k+1} & GJP_k & GJP_{k-1} \end{vmatrix} = \begin{vmatrix} GJP_{k+1} + 2GJP_k & GJP_{k+2} & GJP_{k+1} \\ GJP_k + 2GJP_{k-1} & GJP_{k+1} & GJP_k \\ GJP_{k-1} + 2GJP_{k-2} & GJP_k & GJP_{k-1} \end{vmatrix}$$

$$= \begin{vmatrix} GJP_{k+1} & GJP_{k+2} & GJP_{k+1} \\ GJP_k & GJP_{k+1} & GJP_k \\ GJP_{k-1} & GJP_k & GJP_{k-1} \end{vmatrix} + \begin{vmatrix} 2GJP_k & GJP_{k+2} & GJP_{k+1} \\ 2GJP_{k-1} & GJP_{k+1} & GJP_k \\ 2GJP_{k-2} & GJP_k & GJP_{k-1} \end{vmatrix}$$

$$= 2 \begin{vmatrix} GJP_k & GJP_{k+2} & GJP_{k+1} \\ GJP_{k-1} & GJP_{k+1} & GJP_k \\ GJP_{k-2} & GJP_k & GJP_{k-1} \end{vmatrix}$$

$$= -2 \begin{vmatrix} GJP_{k+2} & GJP_k & GJP_{k+1} \\ GJP_{k+1} & GJP_{k-1} & GJP_k \\ GJP_k & GJP_{k-2} & GJP_{k-1} \end{vmatrix}$$

$$= 2 \begin{vmatrix} GJP_{k+2} & GJP_{k+1} & GJP_k \\ GJP_{k+1} & GJP_k & GJP_{k-1} \\ GJP_k & GJP_{k-1} & GJP_{k-2} \end{vmatrix}$$

$$\begin{aligned}
 &= 2[-2^k(1 - i)] \\
 &= -2^{k+1}(1 - i).
 \end{aligned}$$

Therefore, the statement is also correct for  $n = k + 1$ . □

In the next theorem, we give some summation formulas of Gaussian Jacobsthal-Padovan sequence.

Theorem 5. For  $n \geq 1$ , we have the following sums:

$$\begin{aligned}
 \text{i. } \sum_{k=1}^n \text{GJP}_k &= \frac{1}{2}(\text{GJP}_{n+2} + \text{GJP}_{n+3}) - (2 + i), \\
 \text{ii. } \sum_{k=1}^n \text{GJP}_{2k} &= \frac{1}{2}\text{GJP}_{2n+3} - (3 + i), \\
 \text{iii. } \sum_{k=1}^n \text{GJP}_{2k-1} &= \frac{1}{2}\text{GJP}_{2n+2} - (1 + i).
 \end{aligned}$$

Proof (i). From the recursive relation of Gaussian Jacobsthal-Padovan sequence, we have

$$\text{GJP}_{n-3} = \frac{1}{2}\text{GJP}_n - \frac{1}{2}\text{GJP}_{n-2}. \tag{3}$$

Thus, we have from the equation (3)

$$\begin{aligned}
 \text{GJP}_1 &= \frac{1}{2}\text{GJP}_4 - \frac{1}{2}\text{GJP}_2 \\
 \text{GJP}_2 &= \frac{1}{2}\text{GJP}_5 - \frac{1}{2}\text{GJP}_3 \\
 \text{GJP}_3 &= \frac{1}{2}\text{GJP}_6 - \frac{1}{2}\text{GJP}_4 \\
 &\vdots \\
 \text{GJP}_n &= \frac{1}{2}\text{GJP}_{n+3} - \frac{1}{2}\text{GJP}_{n+1}.
 \end{aligned}$$

After performing necessary calculations, we obtain

$$\begin{aligned}
 \sum_{k=1}^n \text{GJP}_k &= \frac{1}{2}(\text{GJP}_{n+2} + \text{GJP}_{n+3}) - \frac{1}{2}(\text{GJP}_2 + \text{GJP}_3) \\
 &= \frac{1}{2}(\text{GJP}_{n+2} + \text{GJP}_{n+3}) - (2 + i)
 \end{aligned}$$

which is desired.

The proof of (ii) and (iii) can be done similarly to the proof of (i).

Theorem 6. For  $n \in \mathbb{Z}^+$ , we have

$$\begin{pmatrix} 0 & 1 & 2 \\ 1 & 0 & 0 \\ 0 & 1 & 0 \end{pmatrix}^n \cdot \begin{pmatrix} 1+i \\ 1+i \\ 1 \end{pmatrix} = \begin{pmatrix} \text{GPJ}_{n+2} \\ \text{GPJ}_{n+1} \\ \text{GPJ}_n \end{pmatrix}.$$

Proof. We can prove the theorem by induction on  $n$ . For  $n = 1$ , we get

$$\begin{pmatrix} 0 & 1 & 2 \\ 1 & 0 & 0 \\ 0 & 1 & 0 \end{pmatrix}^1 \cdot \begin{pmatrix} 1+i \\ 1+i \\ 1 \end{pmatrix} = \begin{pmatrix} 3+i \\ 1+i \\ 1+i \end{pmatrix} = \begin{pmatrix} \text{GPJ}_3 \\ \text{GPJ}_2 \\ \text{GPJ}_1 \end{pmatrix}.$$

Assume that the equality holds for  $n = k$ , namely,

$$\begin{pmatrix} 0 & 1 & 2 \\ 1 & 0 & 0 \\ 0 & 1 & 0 \end{pmatrix}^k \cdot \begin{pmatrix} 1+i \\ 1+i \\ 1 \end{pmatrix} = \begin{pmatrix} GPJ_{k+2} \\ GPJ_{k+1} \\ GPJ_k \end{pmatrix}.$$

Now, we need to show that it is true for  $n = k + 1$ . Hence, we obtain

$$\begin{aligned} \begin{pmatrix} 0 & 1 & 2 \\ 1 & 0 & 0 \\ 0 & 1 & 0 \end{pmatrix}^{k+1} \cdot \begin{pmatrix} 1+i \\ 1+i \\ 1 \end{pmatrix} &= \begin{pmatrix} 0 & 1 & 2 \\ 1 & 0 & 0 \\ 0 & 1 & 0 \end{pmatrix} \cdot \left[ \begin{pmatrix} 0 & 1 & 2 \\ 1 & 0 & 0 \\ 0 & 1 & 0 \end{pmatrix}^k \cdot \begin{pmatrix} 1+i \\ 1+i \\ 1 \end{pmatrix} \right] \\ &= \begin{pmatrix} 0 & 1 & 2 \\ 1 & 0 & 0 \\ 0 & 1 & 0 \end{pmatrix} \cdot \begin{pmatrix} GPJ_{k+2} \\ GPJ_{k+1} \\ GPJ_k \end{pmatrix} \\ &= \begin{pmatrix} GPJ_{k+1} + 2GPJ_k \\ GPJ_{k+2} \\ GPJ_{k+1} \end{pmatrix} \\ &= \begin{pmatrix} GPJ_{k+3} \\ GPJ_{k+2} \\ GPJ_{k+1} \end{pmatrix}. \end{aligned}$$

The proof is completed.

### Conflicts of interest

The authors state that did not have conflict of interests.

### References

- [1] Koshy T., Fibonacci and Lucas numbers with applications. New York: John Wiley and Sons Inc., (2001).
- [2] Hoggatt V.E. Jr., Fibonacci and Lucas numbers. Boston: Houghton Mifflin Company, (1969).
- [3] Koshy T., Pell and Pell-Lucas numbers with applications. New York: Springer, (2014).
- [4] Horadam A.F., Jacobsthal Representation Numbers, *Fibonacci Quarterly*, 34 (1) (1996) 40-54.
- [5] Koshy T., Jacobsthal and Jacobsthal-Lucas numbers with applications. New York: John Wiley and Sons Inc., (2001).
- [6] Jordan J.H., Gaussian Fibonacci and Lucas Numbers, *Fibonacci Quarterly*, 3 (1965) 315-318.
- [7] Halıcı S., Öz S., On Some Gaussian Pell and Pell-Lucas Numbers, *Ordu University Journal of Science and Technology*, 6 (1) (2016) 8-18.
- [8] Gökbaş H., Köse H., On Complex K-Horadam and Gaussian K-Horadam Sequences, *International Journal of Mathematics and Computer Science*, 6 (11) (2018) 1938-1942.
- [9] Aşçı M., Gürel E., Gaussian Jacobsthal and Gaussian Jacobsthal-Lucas Numbers, *Ars Combinatoria*, 111 (2013) 53-63.
- [10] Özkan E., Taştan M., A New Families of Gauss k-Jacobsthal Numbers and Gauss k-Jacobsthal-Lucas Numbers and Their Polynomials, *Journal of Science and Arts*, 4 (53) (2020) 893-908.
- [11] Cerda-Morales G., On Gauss Third-Order Jacobsthal Numbers and Their Applications, *Annals of the Alexandru Ioan Cuza University-Mathematics*, 67 (2) (2021) 231-241.
- [12] Sloane N.J.A., The Online Encyclopedia of Integer Sequences. Available at: <http://oeis.org/>.
- [13] Taşçı D., Gaussian Padovan and Gaussian Pell-Padovan Sequences, *Communications Faculty of Sciences University of Ankara Series A1 Mathematics and Statistics*, 67 (2) (2018) 82-88.
- [14] Kartal M.Y., Gaussian Padovan and Gaussian Perrin Numbers and Properties of Them, *Asian-European Journal of Mathematics*, 12 (6) (2019) 2040014.

## A New Decomposition Method for Integro-Differential Equations

Morufu Oyedunsi Olayiwola <sup>1,a</sup>, Kabiru Oyeleye Kareem <sup>1,b,\*</sup><sup>1</sup> Department of Mathematical Sciences, Osun State University, Osogbo, Nigeria

\*Corresponding author

### Research Article

#### History

Received: 22/08/2021

Accepted: 17/04/2022

#### Copyright

©2022 Faculty of Science,  
Sivas Cumhuriyet University

### ABSTRACT

This present study developed a new Modified Adomian Decomposition Method (MADM) for integro-differential equations. The modification was carried out by decomposing the source term function into series. The terms in the series were then selected in pairs to form the initials for the prevailing approximation. The newly modified Adomian decomposition method (MADM) accelerates the convergence of the solution faster than the Standard Adomian Decomposition Method (SADM). This study recommends the use of the MADM for solving integro-differential equations

**Keywords:** Adomian polynomials, Integro-differential equations, Taylor series. [olayiwola.oyedunsi@unosun.edu.ng](mailto:olayiwola.oyedunsi@unosun.edu.ng) <https://orcid.org/0000-0001-6101-1203> [kareemkabiruoeyeleye@gmail.com](mailto:kareemkabiruoeyeleye@gmail.com) <https://orcid.org/0000-0002-7457-5945>

## Introduction

Integro-differential equations have been investigated in many fields, including biology, physics, and engineering. Integro-differential equations, on the other hand, are widely used in science and engineering to simulate a variety of physical phenomena. As a result, scientists and applied mathematicians have focused their efforts on finding exact and approximate solutions to integro-differential equations [1-7].

The fractional calculus is a powerful tool in applied mathematics for studying a variety of problems from various fields of science and engineering, with many breakthrough results in mathematical physics, finance, hydrology, biophysics, thermodynamics, control theory, statistical mechanics, astrophysics, cosmology, and bioengineering [8]. Since the fractional calculus piqued the interest of mathematicians and other scientists, the solutions of fractional integro-differential equations have been studied frequently in recent years [9-19], other approaches of the least squares with shifted Chebyshev polynomials [20], least-squares method using Bernstein polynomials [21], fractional residual power series method [22], Taylor matrix method [23].

Laguerre polynomials are used to solve some integer order integro-differential equations. The Altarelli-Parisi equation [24], the Pantograph-type Volterra integro-differential equation [25] and the linear Fredholm integro-differential equation are examples of these. In addition, Laguerre polynomials are used to solve fractional integro-differential equations [20]. Algebraic equations, differential equations, integral equations, and other functional equations are frequently the result of mathematical modeling of real-life problems [26].

In many domains of science and engineering, differential and integral equations are often used. However, research

into these areas has uncovered novel subtopics in which both differential and integral operators appear in the same equation. This new type of equation is known as integro-differential equation.

Integro-differential equations are equations that are known to emerge in both the derivatives and anti-derivatives of a function [27]. It is an equation in which the unknown function  $u(x)$  appears under the integral sign and has yet to be identified [28]. To solve polynomial issues, various types of analytical methods have been applied. Hirota's bilinear approach, Darboux transformation, symmetry method, inverse scattering transformation, variational iteration method used by [29-30]. The Adomian Decomposition Method (ADM) is a dependable and practical method for dealing with various equations, both linear and non-linear.

Differential equations, such as Boundary Value Problems (BVPs), have also been solved using this method in other sectors of science and engineering. For nonlinear operators, the method relies on the calculation of Adomian polynomials. The usage of the Adomian decomposition approach has various drawbacks that can develop due to the nature of the issues being considered, such as a relatively poor convergence rate and a huge functional evaluation for non-linear problems. [30] solved certain linear and nonlinear integral equations using a modified version of this ADM. Using Adomian Polynomials, this paper proposes a new version of the Adomian Decomposition Method for integro-differential equations.

This new decomposition modification introduces a change in the formulation of Adomian polynomials, which is superior to the usual Adomian technique. The novel modified Adomian Decomposition Method (MADM) improves the accuracy, speed of convergence, and reduces the number of functional calculations.

### Methodology

Assuming that the nonlinear function is  $F(y(x))$  therefore, below are few of Adomian polynomials.

$$A_0 = F(y_0), \tag{1}$$

$$A_1 = y_1 F'(y_0), \tag{2}$$

$$A_2 = y_2 F'(y_0) + \frac{1}{2!} y_1^2 F''(y_0), \tag{3}$$

$$A_3 = y_3 F'(y_0) + y_1 y_2 F''(y_0) + \frac{1}{3!} y_1^3 F'''(y_0), \tag{4}$$

$$A_4 = y_4 F'(y_0) + \left(\frac{1}{2!} y_2^2 + y_1 y_3\right) F''(y_0) + \frac{1}{2!} y_1^2 y_2 F'''(y_0) + \frac{1}{4} y_1^4 F^{(iv)}(y_0), \tag{5}$$

Two important observations can be made here. First,  $A_0$  depends only on  $y_0$ ,  $A_1$  depends only on  $y_0$  and  $y_1$ ,  $A_2$  depends only on  $y_0$ ,  $y_1$  and  $y_2$ , and so on. Secondly, substituting these  $A_j$ 's in (3) gives:

$$\begin{aligned} F(y) &= A_0 + A_1 + A_2 + A_3 + \dots \\ &= F(y_0) + (y_1 + y_2 + y_3 + \dots) F'(y_0) + \frac{1}{2!} (y_1^2 + 2y_1 y_2 + 2y_1 y_3 + y_2^2) F''(y_0) \\ &\quad + \frac{1}{3!} (y_1^3 + 3y_1^2 y_3 + 6y_1 y_2 y_3 + \dots) F'''(y_0) + \dots \\ &= F(y_0) + (y - y_0) F'(y_0) + \frac{1}{2!} (y - y_0)^2 F''(y_0) + \dots \end{aligned}$$

In the following, we will calculate Adomian polynomials for several linear terms that may arise in nonlinear integral equations.

#### Case 1.

The first four Adomian polynomials for  $F(y) = y^2$  are given by

$$A_0 = y_0^2$$

$$A_1 = 2y_0 y_1$$

$$A_2 = 2y_0 y_2 + y_1^2$$

$$A_3 = 2y_0 y_3 + 2y_1 y_2$$

#### Case 2.

The first four Adomian polynomials for  $F(y) = y^3$  are given by

$$A_0 = y_0^3,$$

$$A_1 = 3y_0^2 y_1,$$

$$A_2 = 3y_0^2 y_2 + 3y_0 y_1^2,$$

$$A_3 = 3y_0^2 y_3 + 6y_0 y_1 y_2 + y_1^3$$

#### Case 3.

The first four Adomian polynomials for  $F(y) = y^4$  are given by

$$A_0 = y_0^4,$$

$$A_1 = 4y_0^3 y_1,$$

$$A_2 = 4y_0^3 y_2 + 6y_0^2 y_1^2,$$

$$A_3 = 4y_0^3 y_3 + 4y_1^3 y_0 + 12y_0^2 y_1 y_2$$

#### Case 4.

The first four Adomian polynomials for  $F(y) = \sin y$  are given by

$$A_0 = \sin y_0,$$

$$A_1 = y_1 \cos y_0,$$

$$A_2 = y_2 \cos y_0 - \frac{1}{2!} y_1^2 \sin y_0,$$

$$A_3 = y_3 \cos y_0 - y_1 y_2 \sin y_0 - \frac{1}{3!} y_1^3 \cos y_0$$

#### Case 5.

The first four Adomian polynomials for  $F(y) = \cos y$  are given by

$$A_0 = \cos y_0,$$

$$A_1 = -y_1 \sin y_0,$$

$$A_2 = -y_2 \sin y_0 - \frac{1}{2!} y_1^2 \cos y_0,$$

$$A_3 = -y_3 \sin y_0 - y_1 y_2 \cos y_0 + \frac{1}{3!} y_1^3 \sin y_0,$$

#### Case 6.

The first four Adomian polynomials for  $F(y) = \exp(y)$  are given by

$$A_0 = \exp(y_0),$$

$$A_1 = y_1 \exp(y_0),$$

$$A_2 = \left(y_2 + \frac{1}{2!} y_1^2\right) \exp(y_0),$$

$$A_3 = \left(y_3 + y_1 y_2 + \frac{1}{3!} y_1^3\right) \exp(y_0),$$

The modification was carried out by decomposing the source term function into series of the form

$$g(x) = \sum_{j=0}^{+\infty} g_j(x)$$

and the new recursive relation was obtained as:

$$y_0(x) = g_0(x),$$

$$y_1(x) = g_1(x) + g_2(x) + \lambda \int_a^x k(x, t) (L(y_0(x)) + A_0) dt,$$

$$y_2(x) = g_3(x) + g_4(x) + \lambda \int_a^x k(x, t) (L(y_0(x) + y_1(x)) + A_1) dt,$$

$$y_{j+1}(x) = g_{2(j+1)}(x) + g_{2(j+1)-1}(x) + \lambda \int_a^x k(x, t) (L(y_j(x) + y_{j-1}(x)) + A_1) dt.$$

### Numerical Examples

#### Example 1:

Consider the standard integro-differential equation;

$$y'(x) = 1 - \frac{1}{3}x + \int_0^1 xy(t)dt; \quad y(0) = 0, \quad y(x) = x$$

Let

$$a_0 = 1$$

$$a_0 = \int_0^x adx$$

$$a_0 = x$$

$$y_0 = t$$

$$g_0 = -\frac{1}{6}x^2$$

$$a_1 = g_0 + \int_0^x x \int_0^1 ty_0 dt dx$$

$$a_1 = 0$$

$$y_1 = 0$$

$$g_1 = 0$$

Then;

$$y_n = y_0 + y_1 + y_2 + y_3 + y_4$$

$$y_n(t) = t$$

$$y_n(x) = x$$

#### Example 2:

Consider the standard integro-differential equation;

$$y''(x) = \frac{1}{2}e^x + \frac{1}{2} \int_0^1 e^{x-2t} y^2(t) dt; \quad y(0) = 1, \quad y'(0) = 1$$

Applying two fold integral linear operator defined by:

$$L^{-1} = \int_0^x \int_0^x (\cdot) dx dx$$

The differential equation is transformed to:

$$y(x) = \frac{1}{2} + \frac{1}{2}x + \frac{1}{2}e^x + \frac{1}{2}L^{-1} \left[ \int_0^1 e^{(x-2t)} y^2(t) dt \right] dx dx$$

Let

$$r = \frac{1}{2} + \frac{1}{2}x + \frac{1}{2}e^x$$

Using Taylor (r, from x to 10)

$$1 + x + \frac{1}{4}x^2 + \frac{1}{12}x^3 + \frac{1}{48}x^4 + \frac{1}{120}x^5 + \frac{1}{1440}x^6 + \frac{1}{10080}x^8 + \frac{1}{725760}x^9 + 0(x^{10})$$

Then;

$$a_0 = 1$$

$$y_0 = 1$$

$$g_0 = x + \frac{1}{4}x^2$$

We have,

$$a_1 = g_0 + \frac{1}{2} \int_0^x e^x \int_0^x \left[ \int_0^1 e^{(-2t)} y_0^2 dt \right] dx dx$$

$$a_1 = x + \frac{1}{4}x^2 + 0.2161661792 + 0.2161661792e^x x - 0.2161661792e^x$$

$$y_1 = t + \frac{1}{4}t^2 + 0.2161661792 + 0.2161661792e^t t - 0.2161661792e^t$$

Then,

$$g_1 = \frac{1}{12}x^3 + \frac{1}{48}x^4$$

$$a_4 = g_3 + \frac{1}{2} \int_0^x e^x \int_0^x \left[ \int_0^1 e^{(-2t)} a_{iv} dt \right] dx dx$$

$$a_4 = \frac{1}{1080}x^7 + \frac{1}{80640}x^8 + 0.02183314121 + 0.02183314121e^x x - 0.02183314121e^x$$

$$y_4 = \frac{1}{1080}t^7 + \frac{1}{80640}t^8 + 0.02183314121 + 0.02183314121e^t t - 0.02183314121e^t$$

Then;



$$y_n = y_0 + y_1 + y_2 + y_3 + y_4$$

$$y_n(t) = 1.5044983400 + t + \frac{1}{4}t^2 + 0.5049834007e^t t - 0.5049834007e^t + \frac{1}{12}t^3 + \frac{1}{48}t^4 + \frac{1}{120}t^5 + \frac{1}{1440}t^6 + \frac{1}{1080}t^7 + \frac{1}{80640}t^8$$

$$y_n(x) = 1.5044983400 + x + \frac{1}{4}x^2 + 0.5049834007e^x x - 0.5049834007e^x + \frac{1}{12}x^3 + \frac{1}{48}x^4 + \frac{1}{120}x^5 + \frac{1}{1440}x^6 + \frac{1}{1080}x^7 + \frac{1}{80640}x^8$$

Table 1. Table of Absolute Errors for Example 2

X	Exact	NADM	Absolute Error
0.0	1.000.000.000	0.999514939	0.000485061
0.1	1.105.170.918	1.105.285.188	0.000114270
0.2	1.221.402.758	1.222.254.295	0.000851537
0.3	1.349.858.808	1.352.753.581	0.002894773
0.4	1.491.824.698	1.498.889.078	0.007064380
0.5	1.648.721.271	1.663.062.055	0.014340784
0.6	1.822.118.800	1.848.010.030	0.025891230
0.7	2.013.752.707	2.056.854.272	0.043101565
0.8	2.225.540.928	2.293.154.795	0.067613867
0.9	2.459.603.111	2.560.973.914	0.101370803
1.0	2.718.281.828	2.864.949.506	0.146667678

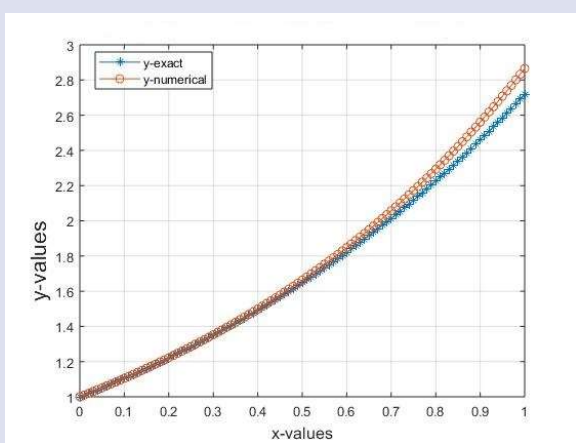


Figure 1. Graph of Comparison of the New ADM and the Exact for Example 2

**Example 3:**

$$y'(x) = e^x + \frac{1}{16}(3 + e^2)x + \frac{1}{4} \int_0^1 xt(1 + u(t) - y^2(t))dt ;$$

Which subject to the initial condition?

$$u(0) = 2$$

Applying a one-fold integral linear operator defined by:

$$L^{-1} = \int_0^x (\cdot) dx$$

The differential equation is transformed to

$$y(x) = 1 + \exp(x) + \frac{1}{32}(3 + \exp(2))x + \frac{1}{4}L^{-1} \left[ \int_0^1 xt(1 + y(t) - y^2(t))dt \right] dx$$

By using Taylor Series

$$\left( 1 + \frac{973}{2997}x^2 + \exp(x) \text{ from } x \text{ to } 10 \right)$$

We have;

$$2 + x + \frac{4943}{5994}x^2 + \frac{1}{6}x^3 + \frac{1}{24}x^5 + \frac{1}{720}x^6 + \frac{1}{5040}x^7 + \frac{1}{40320}x^8 + \frac{1}{362880}x^9 + (0)x^{10}$$

Then;

$$a_0 = 2$$

$$y_0 = 2$$

and

$$a_i ; a_{ii} ; a_{iii} ; a_{iv} \text{ represent } y_0^2 ; y_1^2 ; y_2^2 ; y_3^2$$

Then;

Integrate  $y_0$ ;

$$a_1 = -0.3827304872x^2$$

$$y_1 = -0.3827304872t^2$$

$$a_{ii} = 2y_0y_1$$

$$a_{ii} = -0.7654609744(1 + e^t + 0.3246580031t^2)t^2$$

$$a_2 = \frac{1}{4} \int_0^x \int_0^1 t(1 + y_1 - a_{ii})dt dx$$

$$a_2 = 0.1335487491x^2$$

$$y_2 = 0.1335487491t^2$$

Then; the sum of  $y_0$  to  $y_4$ ;

$$y_n = y_0 + y_1 + y_2 + y_3 + y_4$$

We have

$$y_n(t) = 2 + t + \frac{2955595512151}{4120514592768}t^2 + \frac{1}{6}t^3 + \frac{1}{24}t^4 + \frac{1}{120}t^5 + \frac{1}{720}t^6 + \frac{1}{5040}t^7 + \frac{1}{40320}t^8$$

$$y_n(x) = 2 + x + \frac{2955595512151}{4120514592768}x^2 + \frac{1}{6}x^3 + \frac{1}{24}x^4 + \frac{1}{120}x^5 + \frac{1}{720}x^6 + \frac{1}{5040}x^7$$

Table 2. Table of Absolute Errors for Example 2

X	Exact	NADM	Absolute Error
0.0	2.000.000.000	2.000.000.000	0.000000000
0.1	2.105.170.918	2.107.343.798	0.002172880
0.2	2.221.402.759	2.230.094.277	0.008691518
0.3	2.349.858.807	2.369.414.725	0.019555918
0.4	2.491.824.697	2.526.590.771	0.034766074
0.5	2.648.721.265	2.703.043.255	0.054321990
0.6	2.822.118.771	2.900.342.437	0.078223666
0.7	3.013.752.588	3.120.223.689	0.106471101
0.8	3.225.540.527	3.364.604.822	0.139064295
0.9	3.459.601.938	3.635.605.188	0.176003250
1.0	3.718.278.771	3.935.566.732	0.217287961

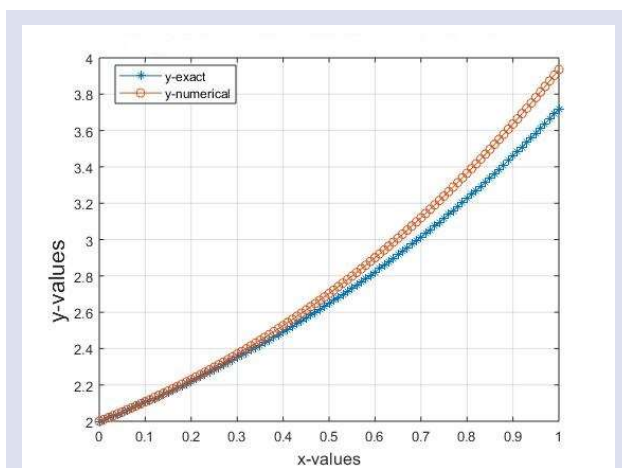


Figure 2. Graph of Comparison of the New ADM and the Exact for Example 3

## Results and Discussion

The new Modified Adomian Decomposition Method (MADM) for integro-differential equations was introduced in this paper. This new approach converges faster, and it can be seen that the source term expansion should be as lengthy as feasible. The decomposed source term's convergence is improved by a little increase in the terms of decomposed source terms. The addition of more terms in the integral sign improves accuracy and, as a result, the Adomian polynomials.

## Acknowledgment

The authors would like to express their gratitude to everyone who helped make this study a success.

## Conflicts of interest

With respect to this work, the authors state that there are no conflicts of interest.

## References

- [1] Dzhumabaev D.S., New general solutions to linear Fredholm integro-differential equations and their applications on solving the boundary value problems, *Journal of Computational and Applied Mathematics*, 327 (2018) 79-108.
- [2] Fairbairn A.I., Kelmanson, M.A., Error analysis of a spectrally accurate Volterra-transformation method for solving 1-D Fredholm integro-differential equations, *International Journal of Mechanical Sciences*, 144 (2018) 382-391.
- [3] Hendi F.A., Al-Qarni M.M., The variational Adomian decomposition method for solving nonlinear two-dimensional Volterra-Fredholm integro-differential equation, *Journal of King Saud University – Science*, 31(1) (2017) 110-113.
- [4] Kürçü Ö.K., Aslan, E., Sezer, M., A novel collocation method based on residual error analysis for solving integro-differential equations using Hybrid Dickson and Taylor polynomials, *Sains Malaysiana*, 46(2) (2017) 335-347.
- [5] Rahimkhani P., Ordokhani Y., Babolian E., Fractional-order Bernoulli functions and their applications in solving fractional Fredholm-Volterra integro-differential equations, *Applied Numerical Mathematics*, 122 (2017) 66-81.
- [6] Rohaninasab N., Maleknejad K., Ezzati R., Numerical solution of high-order Volterra-Fredholm integro-differential equations by using Legendre collocation method, *Applied Mathematics and Computation*, 328 (2018) 171-188.
- [7] Yüzbaşı Ş., Karaçayır M., A Galerkin-like scheme to solve two-dimensional telegraph equation using collocation points in initial and boundary conditions. *Computers and Mathematics with Applications* 74 (2017) 3242-3249.
- [8] Abbas S., Benchohra M., N'Guerekata G.M., *Advanced Fractional Differential and Integral Equations*. New York: Nova Science Publishers, (2015).
- [9] Alkan S., Hatipoglu V.F. Approximate solutions of Volterra-Fredholm integro-differential equations of fractional order, *Tbilisi Mathematical Journal*, 10(2) (2017) 1-13.
- [10] Hamoud A.A., & Ghadle K.P., The approximate solutions of fractional Volterra-Fredholm integro-differential equations by using analytical techniques, *Problemy Analiza Issues of Analysis*, 7(25) (2018a) 41-58.
- [11] Hamoud A.A., Ghadle K.P., Modified Laplace decomposition method for fractional Volterra-Fredholm integro-differential equations, *Journal of Mathematical Modeling*, 6(1) (2018b) 91-104.
- [12] Ibrahim, H., Ayoo P. V., Approximation of systems of Volterra integro-differential equations using the new iterative method, *International Journal of Science and Research*, 4(5) (2015) 332-336.
- [13] Kumar K., Pandey R.K., Sharma, S., Comparative study of three numerical schemes for fractional integro-differential equations, *Journal of Computational and Applied Mathematics*, 315(2017) 287-302.
- [14] Ma X., Huang, C., Spectral collocation method for linear fractional integro-differential equations, *Applied Mathematical Modelling*, 38 (2014) 1434-1448.
- [15] Nemati S., Sedaghat S., Mohammadi, I., A fast numerical algorithm based on the second kind Chebyshev polynomials for fractional integro-differential equations with weakly singular kernels, *Journal of Computational and Applied Mathematics*, 308 (2016) 231-242.

- [16] Ordokhani Y., Dehestani H., Numerical solution of linear Fredholm-Volterra integro-differential equations of fractional order, *World Journal of Modelling and Simulation*, 12(3) (2016) 204-216.
- [17] Turmetov B., Abdullaev J., Analytic solutions of fractional integro-differential equations of Volterra type, *IOP Conference Series, Journal of Physics: Conference Series*, 890 (2017) 012113.
- [18] Wang Y., Zhu L., SCW method for solving the fractional integro-differential equations with a weakly singular kernel, *Applied Mathematics and Computation*, 275 (2016) 72-80.
- [19] Yi M., Wang L., Huang, J., Legendre wavelets method for the numerical solution of fractional integro-differential equations with weakly singular kernel, *Applied Mathematical Modelling*, 40 (2016) 3422-3437.
- [20] Mahdy A.M.S., Shwayyeh R.T., Numerical solution of fractional integro-differential equations by least squares method and shifted Laguerre polynomials pseudo-spectral method, *International Journal of Scientific & Engineering Research*, 7(4) (2016) 1589-1596.
- [21] Oyedepo T., Taiwo O.A., Abubakar J.U., Ogunwobi Z.O., Numerical studies for solving fractional integro-differential equations by using least squares method and Bernstein polynomials, *Fluid Mechanics: Open Access*, 3(3) (2016) 1000142.
- [22] Syam M.I., Analytical solution of the fractional Fredholm integrodifferential equation using the fractional residual power series method, *Complexity* 2017, 4573589.
- [23] Gülsu M., Öztürk Y., Anapalı A., Numerical approach for solving fractional Fredholm integro-differential equation, *International Journal of Computer Mathematics*, 90(7) (2013) 1413-1434.
- [24] Kobayashi R., Konuma M., Kumano, S., Fortran program for a numerical solution of the nonsinglet Altarelli-Parisi equation, *Computer Physics Communications*, 86 (1995) 264-278.
- [25] Pandey P.K., Numerical Solution of Linear Fredholm Integro-Differential Equations by Non-standard Finite Difference Method, *Applications and Applied Mathematics: An International Journal*, 10(2) (2015) 1019-1026.
- [26] Yüzbaşı Ş., Laguerre approach for solving pantograph-type Volterra integro-differential equations, *Applied Mathematics and Computation*, 232 (2014) 1183-1199.
- [27] Karim M.F., Mohamad M., Rusiman M.S., Che-HIM N., Roslan, R., Khalid, K., ADM for solving linear second-order fredholm integro- differential equations. *IOP Conf. Series: Journal of Physics*, 995 (2018) Doi: 10.1088/1742-6596/995/1/012009.
- [28] Wazwaz A.M., First course in integral equations, 2<sup>nd</sup>. Ed. Singapore: World Scientific Publishing Co. Pte. Ltd., (2015) 596224
- [29] Olayiwola M. O., Ogunniran M. O., Variational iteration method for solving higher-order integro-differential equations, *Nigerian Journal of Mathematics and Application*, B29 (2019) 18-23.
- [30] Olayiwola M. O., Adedokun K. A., Gbolagade A. W., Solving linear and non linear integro-differential equations using modified Adomian decomposition method, *Islamic University Multidisciplinary Journal* 6(3) (2019) 202-209.

## On Fixed Point Results for Generalized Contractions in Non-Newtonian Metric Spaces

Demet Binbaşıoğlu<sup>1,a,\*</sup>

<sup>1</sup> Department of Mathematics, Faculty of Arts and Sciences, Tokat Gaziosmanpaşa University, Tokat, Türkiye.

\*Corresponding author

### Research Article

#### History

Received: 11/10/2021

Accepted: 19/04/2022

#### Copyright



©2022 Faculty of Science,  
Sivas Cumhuriyet University

### ABSTRACT

The work of non-Newtonian calculus was begun in 1972. This calculus provides a different area to the classical one. Non-Newtonian metric concept was defined in 2002 by Basar and Cakmak. Then Binbaşıoğlu et al. had given the metric spaces of non-Newtonian in 2016. Also, they started to the fixed-point theory by defining some topological properties in non-Newtonian metric spaces.

In this work, we give some fixed-point theorems and results for self-mappings satisfying certain conditions in the non-Newtonian metric spaces.

**Keywords:** Fixed point, Non-Newtonian metric space, Contraction mapping, Generalized contraction mapping.

 [demet.binbasioğlu@gop.edu.tr](mailto:demet.binbasioğlu@gop.edu.tr) |  <https://orcid.org/0000-0001-7041-5277>

### Introduction

There exist too many studies on fixed-point theory in different spaces [1-12]. Also, there are many applications of the theory and mappings that meet certain conditions of contraction and have been a crucial area of different research works.

The non-Newtonian calculus is alternative to what is customary. The non-Newtonian calculus in various fields including information technology, fractal geometry, economic growth, finance, wave theory, quantum physics, in medicine for examples tumor therapy, cancer-chemotherapy, in mathematics for examples functional analysis, differential equations, approximation theory, problems of decision making, and chaos theory has many applications. The non-Newtonian metric concept was defined in 2002 by Basar et al. and then Binbaşıoğlu et al. gave the metric spaces of non-Newtonian in 2016. Also, they started to study on the fixed-point theory in non-Newtonian metric spaces.

In this work, we present fixed-point theorems and results for self-mappings satisfying certain conditions in the non-Newtonian metric spaces.

### Preliminaries

We mention that some basic knowledge related to structure of non-Newtonian calculus.

#### Definition

A generator is called as an injective function from  $\mathbb{R}$  to a subset of  $\mathbb{R}$  [6].

#### Remark

Every generator generates an arithmetic. An arithmetic is generated by a generator [6].

#### Remark

Let us take the function  $\beta: \mathbb{R} \rightarrow \mathbb{R}^+, a \rightarrow \beta(a) = e^a = b$ . If  $\beta = \exp$ , then the function generates the geometrical arithmetics [6].

#### Remark

Assume that the function  $\beta$  is a generator, i.e., if  $\beta = I$ , then  $\beta$  generates the usual arithmetic, where  $I$  is an identity mapping [6].

#### Definition

The  $\beta$ -integers are produced as follows;  $\beta$ -zero,  $\beta$ -one and similarly all  $\beta$ -integers are denoted as,  $\dots, \beta(-1), \beta(0), \beta(1), \dots$

Let us take any generator  $\beta$  with range  $A$ . Then for  $a, b \in \mathbb{R}$ , the operations  $\beta$ -addition,  $\beta$ -subtraction,  $\beta$ -multiplication,  $\beta$ -division and  $\beta$ -order are defined as follows,

$$\begin{aligned} a \dot{+} b &= \beta\{\beta^{-1}(a) + \beta^{-1}(b)\}, \\ a \dot{-} b &= \beta\{\beta^{-1}(a) - \beta^{-1}(b)\}, \\ a \dot{\times} b &= \beta\{\beta^{-1}(a) \times \beta^{-1}(b)\}, \\ a \dot{\div} b &= \beta\{\beta^{-1}(a) \div \beta^{-1}(b)\}, \\ a \dot{<} b &= \beta(a) < \beta(b). \end{aligned}$$

The set  $\mathbb{R}(N) = \{\beta(a): a \in \mathbb{R}\}$ , is non-Newtonian real numbers set.

For  $a \in A \subset \mathbb{R}(N)$ , the  $\beta$ -square is described as  $a \dot{\times} a$  and denoted with  $a^{2N}$ . The notation  $\sqrt{a}^{-N}$  denotes

$k = \beta\{\sqrt{\beta^{-1}(a)}\}$ . The  $\beta$ -square is equal to  $a$  and which means  $k^{2N} = a$ .

During this work,  $a^{pN}$  denotes the concept of  $p$ th non-Newtonian exponent.

$|a|_N$  denotes the  $\beta$  –absolute value for a number  $a \in A \subset \mathbb{R}(N)$  defined by  $\beta(|\beta^{-1}(a)|)$  and so

$$\sqrt{a^{2N}} = |a|_N = \beta(|\beta^{-1}(a)|).$$

Thus,

$$|a|_N = \beta(|\beta^{-1}(a)|) = \begin{cases} a, & \beta(0) \leq a, \\ \beta(0), & \beta(0) = a, \\ \beta(0) \cdot a, & \beta(0) > a. \end{cases}$$

Let us take any  $c \in \mathbb{R}(N)$ . If  $c \leq \beta(0)$ , then  $c$  is called a positive non-Newtonian real number. If  $c > \beta(0)$ , then  $c$  is called a non-Newtonian negative real number. If  $c = \beta(0)$ , then  $c$  is called an unsigned non-Newtonian real number. Non-Newtonian positive and negative real numbers are denoted by  $\mathbb{R}^+(N)$  and  $\mathbb{R}^-(N)$  respectively [6].

**Definition**

Let us take  $X \neq \emptyset$  and suppose that  $d_N: X \times X \rightarrow \mathbb{R}^+(N)$  satisfies the following conditions for  $a, b, c \in X$ ;

- (NM1)  $d_N(a, b) = \beta(0)$  iff  $a = b$ ,
- (NM2)  $d_N(a, b) = d_N(b, a)$ ,
- (NM3)  $d_N(a, b) \leq d_N(a, c) \cdot d_N(c, b)$ .

Then  $d_N$  is a non-Newtonian metric on  $X$ . Also  $(X, d_N)$  is a non-Newtonian metric space [6].

**Example**

Assume that  $d_N$  is defined as  $d_N(a, b) = |a \cdot b|_N$  for all  $a, b \in \mathbb{R}(N)$ , then  $(\mathbb{R}(N), d_N)$  is a non-Newtonian metric space [6].

**Main Results**

**Theorem**

Let  $d_N$  be a non-Newtonian complete metric on  $X$  and  $c, d$  be positive integers. If a mapping  $K: X \rightarrow X$  satisfies

$$d_N(K^c a, K^d b) \leq k \cdot d_N(a, b) \cdot l \cdot d_N(a, K^c a) \cdot m \cdot d_N(b, K^d b) \cdot n \cdot d_N(a, K^d b) \cdot p \cdot d_N(b, K^c a)$$

for all  $a, b \in X$ , where  $k, l, m, n, p$  are non-Newtonian positive real numbers with  $k \cdot l \cdot m \cdot n \cdot p \leq \beta(1)$ ,  $l = m, n = p$ , then  $K$  has a unique fixed-point.

**Proof**

Take  $a_0 \in X, t \geq \beta(0)$ , we construct

$$a_{2t+1} = K^c a_{2t}, \\ a_{2t+2} = K^d a_{2t+1}.$$

Then

$$d_N(a_{2t+1}, a_{2t+2}) = d_N(K^c a_{2t}, K^d a_{2t+1}) \\ \leq k \cdot d_N(a_{2t}, a_{2t+1}) \cdot l \cdot d_N(a_{2t}, K^c a_{2t}) \cdot m \cdot d_N(a_{2t+1}, K^d a_{2t+1}) \\ \cdot n \cdot d_N(a_{2t}, K^d a_{2t+1}) \cdot p \cdot d_N(a_{2t+1}, K^c a_{2t}) \\ \leq (k \cdot l) \cdot d_N(a_{2t}, a_{2t+1}) \cdot m \cdot d_N(a_{2t+1}, a_{2t+2}) \cdot n \cdot d_N(a_{2t}, a_{2t+2}) \\ \leq (k \cdot l \cdot n) \cdot d_N(a_{2t}, a_{2t+1}) \cdot (m \cdot n) \cdot d_N(a_{2t+1}, a_{2t+2}).$$

**Definition**

A sequence  $(a_n)$  in a non-Newtonian metric space  $X = (X, d_N)$  is non-Newtonian convergent if taken any  $n_0 = n_0(\varepsilon) \in \mathbb{N}, a \in X$  there exists  $\varepsilon \leq \beta(0)$  such that for all  $n > n_0, d_N(a_n, a) \leq \varepsilon$  and it is shown with  $\lim_{n \rightarrow \infty} a_n = a$  or  $a_n \rightarrow a, n \rightarrow \infty$  [5].

**Definition**

A sequence  $(a_n)$  in a non-Newtonian metric space  $X = (X, d_N)$  is non-Newtonian Cauchy if taken any  $n_0 = n_0(\varepsilon) \in \mathbb{N}, a \in X$  there exists  $\varepsilon \leq \beta(0)$  such that for all  $m, n > n_0, d_N(a_n, a_m) \leq \varepsilon$ . The non-Newtonian metric space  $(X, d_N)$  is non-Newtonian complete if every non-Newtonian Cauchy sequence is non-Newtonian convergent [5].

**Remark**

Let  $k, l, m, n, p$  be non-Newtonian positive real numbers with  $k \cdot l \cdot m \cdot n \cdot p \leq \beta(1), l = m, n = p$ .

If  $r = (k \cdot l \cdot n) \cdot (\beta(1) \cdot m \cdot n)^{-1}$  and  $s = (k \cdot m \cdot p) \cdot (\beta(1) \cdot l \cdot p)^{-1}$ , then  $r \cdot s \leq \beta(1)$ . If  $l = m$  then

$$r \cdot s = \frac{k \cdot l \cdot n}{\beta(1) \cdot m \cdot n} \cdot \frac{k \cdot m \cdot p}{\beta(1) \cdot l \cdot p} = \frac{k \cdot m \cdot n}{\beta(1) \cdot l \cdot p} \cdot \frac{k \cdot l \cdot p}{\beta(1) \cdot m \cdot n} \leq \beta(1),$$

and if  $n = p$  then

$$r \cdot s = \frac{k \cdot m \cdot n}{\beta(1) \cdot m \cdot n} \cdot \frac{k \cdot m \cdot p}{\beta(1) \cdot l \cdot p} = \frac{k \cdot m \cdot n}{\beta(1) \cdot m \cdot n} \cdot \frac{k \cdot m \cdot n}{\beta(1) \cdot l \cdot p} \leq \beta(1).$$

It implies that

$$\leq (\beta(1) \dot{-} m \dot{-} n) \dot{\times} d_N(a_{2t+1}, a_{2t+2}) \leq (k \dot{+} l \dot{+} n) \dot{\times} d_N(a_{2t}, a_{2t+1}).$$

So

$$d_N(a_{2t+1}, a_{2t+2}) \leq r \dot{\times} d_N(a_{2t}, a_{2t+1}), \text{ where } r = \frac{(k \dot{+} l \dot{+} n)}{\beta(1) \dot{-} m \dot{-} n}.$$

$$\begin{aligned} d_N(a_{2t+2}, a_{2t+3}) &= d_N(K^c a_{2t+2}, K^d a_{2t+1}) \\ &\leq k \dot{\times} d_N(a_{2t+2}, a_{2t+1}) \dot{+} l \dot{\times} d_N(a_{2t+2}, K^c a_{2t+2}) \dot{+} m \dot{\times} d_N(a_{2t+1}, K^d a_{2t+1}) \\ &\quad \dot{+} n \dot{\times} d_N(a_{2t+2}, K^d a_{2t+1}) \dot{+} p(a_{2t+1}, K^c a_{2t+2}) \\ &\leq k \dot{\times} d_N(a_{2t+2}, a_{2t+1}) \dot{+} l \dot{\times} d_N(a_{2t+2}, a_{2t+3}) \dot{+} m \dot{\times} d_N(a_{2t+1}, a_{2t+2}) \\ &\quad \dot{+} n \dot{\times} d_N(a_{2t+2}, a_{2t+2}) \dot{+} p \dot{\times} d_N(a_{2t+1}, a_{2t+3}) \\ &\leq (k \dot{+} m \dot{+} p) \dot{\times} d_N(a_{2t+1}, a_{2t+2}) \dot{+} (l \dot{+} p) \dot{\times} d_N(a_{2t+2}, a_{2t+3}), \end{aligned}$$

implies that

$$d_N(a_{2t+2}, a_{2t+3}) \leq s \dot{\times} d_N(a_{2t+1}, a_{2t+2}),$$

where  $s = \frac{(k \dot{+} m \dot{+} p)}{\beta(1) \dot{-} l \dot{-} p}$ .

Therefore, we get for each  $t = 0, 1, 2, \dots$

$$\begin{aligned} d_N(a_{2t+1}, a_{2t+2}) &\leq r \dot{\times} d_N(a_{2t}, a_{2t+1}) \\ &\leq r \dot{\times} s \dot{\times} d_N(a_{2t-1}, a_{2t}) \\ &\leq r \dot{\times} (r \dot{\times} s) \dot{\times} d_N(a_{2t-2}, a_{2t-1}) \\ &\leq \dots \leq r \dot{\times} (r \dot{\times} s)^{tN} \dot{\times} d_N(a_0, a_1), \\ d_N(a_{2t+2}, a_{2t+3}) &\leq s \dot{\times} d_N(a_{2t+1}, a_{2t+2}) \\ &\leq \dots \leq (r \dot{\times} s)^{(t \dot{+} 1)N} \dot{\times} d_N(a_0, a_1). \end{aligned}$$

So, for  $y < z$  we have

$$\begin{aligned} &d_N(a_{2y+1}, a_{2z+1}) \leq d_N(a_{2y+1}, a_{2y+2}) \\ &\quad \dot{+} d_N(a_{2y+2}, a_{2y+3}) \dot{+} \dots \dot{+} d_N(a_{2z}, a_{2z+1}) \\ &\leq [r \dot{\times} \sum_{i=y}^{z-1} (r \dot{\times} s)^{iN} \dot{+} \sum_{i=y+1}^z (r \dot{\times} s)^{iN}] \dot{\times} d_N(a_0, a_1) \\ &\leq [\frac{r \dot{\times} (r \dot{\times} s)^{yN}}{\beta(1) \dot{-} r \dot{\times} s} \dot{+} \frac{(r \dot{\times} s)^{(y+1)N}}{\beta(1) \dot{-} r \dot{\times} s}] \dot{\times} d_N(a_0, a_1) \\ &\leq (\beta(1) \dot{+} r) \dot{\times} [\frac{(r \dot{\times} s)^{yN}}{\beta(1) \dot{-} r \dot{\times} s}] \dot{\times} d_N(a_0, a_1). \end{aligned}$$

Then we deduced

$$\begin{aligned} d_N(a_{2y}, a_{2z+1}) &\leq (\beta(1) \dot{+} r) \dot{\times} [\frac{(r \dot{\times} s)^{yN}}{\beta(1) \dot{-} r \dot{\times} s}] \dot{\times} d_N(a_0, a_1), \\ d_N(a_{2y}, a_{2z}) &\leq (\beta(1) \dot{+} r) \dot{\times} [\frac{(r \dot{\times} s)^{yN}}{\beta(1) \dot{-} r \dot{\times} s}] \dot{\times} d_N(a_0, a_1), \\ d_N(a_{2y+1}, a_{2z}) &\leq (\beta(1) \dot{+} r) \dot{\times} [\frac{(r \dot{\times} s)^{yN}}{\beta(1) \dot{-} r \dot{\times} s}] \dot{\times} d_N(a_0, a_1). \end{aligned}$$

For  $0 < w < v$ ,  $d_N(a_w, a_v) \leq q_w$ , where

$$q_w = (\beta(1) \dot{+} r) \dot{\times} [\frac{(r \dot{\times} s)^{yN}}{\beta(1) \dot{-} r \dot{\times} s}] \dot{\times} d_N(a_0, a_1) \text{ with an integer part of } \frac{w}{2}.$$

So  $\{a_w\}$  is non-Newtonian Cauchy. Since  $(X, d_N)$  is non-Newtonian complete, there exists  $x \in X$  such that

$$a_w \xrightarrow{N} x.$$

For a non-Newtonian real number  $0 \leq \beta(e)$ , choose  $d_0 \in \mathbb{N}$  such that

$$d_N(x, a_{2t}) \leq \frac{\beta(e)}{\beta(3) \dot{\times} A} d_N(a_{2t-1}, a_{2t}) \leq \frac{\beta(e)}{\beta(3) \dot{\times} A} d_N(x, a_{2t-1}) \leq \frac{\beta(e)}{\beta(3) \dot{\times} A}$$

for all  $t \geq d_0$ , where

$$A = \max\left\{\frac{\beta(1) \dot{+} n}{\beta(1) \dot{-} l \dot{-} p}, \frac{k \dot{+} p}{\beta(1) \dot{-} l \dot{-} p}, \frac{m}{\beta(1) \dot{-} l \dot{-} p}\right\}.$$

Now,

$$\begin{aligned} d_N(x, K^v a) &\leq d_N(x, a_{2t}) \dot{+} d_N(a_{2t}, K^v x) \\ &\leq d_N(x, a_{2t}) \dot{+} d_N(K^w a_{2t-1}, K^v x) \\ &\leq d_N(x, a_{2t}) \dot{+} k \dot{\times} d_N(x, a_{2t-1}) \dot{+} l \dot{\times} d_N(x, K^v x) \dot{+} m \dot{\times} d_N(a_{2t-1}, K^w a_{2t-1}) \\ &\quad \dot{+} n \dot{\times} d_N(x, K^w a_{2t-1}) \dot{+} p \dot{\times} d_N(a_{2t-1}, K^v x) \\ &\leq d_N(x, a_{2t}) \dot{+} k \dot{\times} d_N(x, a_{2t-1}) \dot{+} l \dot{\times} d_N(x, K^v x) \dot{+} m \dot{\times} d_N(a_{2t-1}, a_{2t}) \\ &\quad \dot{+} n \dot{\times} d_N(x, a_{2t}) \dot{+} p \dot{\times} d_N(a_{2t-1}, x) \dot{+} p \dot{\times} d_N(x, K^v x) \\ &\leq (\beta(1) \dot{+} n) \dot{\times} d_N(x, a_{2t}) \dot{+} (k \dot{+} p) \dot{\times} d_N(x, a_{2t-1}) \\ &\quad \dot{+} m \dot{\times} d_N(a_{2t-1}, a_{2t}) \dot{+} (l \dot{+} p) \dot{\times} d_N(x, K^v x). \\ d_N(x, K^v x) &\leq A \dot{\times} d_N(x, a_{2t}) \dot{+} A \dot{\times} d_N(x, a_{2t-1}) \dot{+} A \dot{\times} d_N(a_{2t-1}, a_{2t}) \\ &\leq \frac{\beta(e)}{\beta(3)} \dot{+} \frac{\beta(e)}{\beta(3)} \dot{+} \frac{\beta(e)}{\beta(3)} = \beta(e). \end{aligned}$$

Therefore

$d_N(x, K^v x) \leq \frac{\beta(e)}{\beta(\gamma)}$  for every  $y \in \mathbb{N}$ . From  $\frac{\beta(e)}{\beta(\gamma)} \dot{-} d_N(x, K^v x) \geq \beta(0)$  we have  $d_N(x, K^v x) = \beta(0)$ . This implies that  $x = K^v x$ .

By using the inequality,

$$d_N(x, K^w x) \leq d_N(x, a_{2t+1}) \dot{+} d_N(a_{2t+1}, K^w x),$$

now we show that  $x = K^w x$ .

$$\begin{aligned} d_N(Kx, x) &= d_N(KK^v x, K^w x) = d_N(K^v Kx, K^w x) \\ &\leq k \dot{\times} d_N(Kx, x) \dot{+} l \dot{\times} d_N(Kx, K^v Kx) \\ \dot{+} m \dot{\times} d_N(x, K^v x) \dot{+} n \dot{\times} d_N(Kx, K^w x) \dot{+} p \dot{\times} d_N(x, K^v Kx) \\ &\leq k \dot{\times} d_N(Kx, x) \dot{+} l \dot{\times} d_N(Kx, Kx) \\ \dot{+} m \dot{\times} d_N(x, x) \dot{+} n \dot{\times} d_N(Kx, x) \dot{+} p \dot{\times} d_N(x, Kx) \\ &= (k \dot{+} n \dot{+} p) \dot{\times} d_N(Kx, x). \end{aligned}$$

So  $x$  is a fixed-point of  $K$ .

We suppose that for some  $x^*$ , there exists another point  $x^* \in X$  such that  $x^* = Kx^*$ . Thus, we have

$$\begin{aligned} d_N(x, x^*) &= d_N(K^v x, K^w x^*) \\ &\leq k \dot{\times} d_N(x, x^*) \dot{+} l \dot{\times} d_N(x, K^v x) \\ \dot{+} m \dot{\times} d_N(x^*, K^w x^*) \dot{+} n \dot{\times} d_N(x, K^w x^*) \dot{+} p \dot{\times} d_N(x^*, K^v x) \\ &\leq k \dot{\times} d_N(x, x^*) \dot{+} l \dot{\times} d_N(x, x) \\ \dot{+} m \dot{\times} d_N(x^*, x^*) \dot{+} n \dot{\times} d_N(x, x^*) \dot{+} p \dot{\times} d_N(x, x^*) \\ &\leq (k \dot{+} n \dot{+} p) \dot{\times} d_N(x, x^*). \end{aligned}$$

Consequently,  $x^*$  is equal to  $x$ .

**Theorem**

Let  $d_N$  be non-Newtonian complete metric on  $X$ . If  $K: X \rightarrow X$  satisfies

$$\begin{aligned} d_N(Ka, Kb) &\leq k \dot{\times} d_N(a, b) \dot{+} l \dot{\times} d_N(a, Ka) \\ \dot{+} m \dot{\times} d_N(b, Kb) \dot{+} n \dot{\times} d_N(a, Kb) \dot{+} p \dot{\times} d_N(b, Ka) \end{aligned}$$

for all  $a, b \in X$ , where  $k, l, m, n, p$  are non-Newtonian positive real numbers with  $k \dot{+} l \dot{+} m \dot{+} n \dot{+} p \dot{<} \beta(1)$ , then  $K$  has a unique fixed-point.

**Proof**

Since  $d_N$  is a non-Newtonian metric, the above inequality implies that

$$d_N(Ka, Kb) \leq k \cdot d_N(Ka, Kb) + \frac{l+m}{\beta(2)} \cdot [d_N(a, Ka) + d_N(b, Kb)] + \frac{n+p}{\beta(2)} \cdot [d_N(a, Kb) + d_N(b, Ka)].$$

If we substitute  $K^v = K^w = K$  in the above theorem, we get the required result.

**Corollary**

Let  $(X, d_N)$  be a non-Newtonian complete metric space and  $v, w$  be positive integers. If a self-mapping  $K$  on  $X$  satisfies

$$d_N(K^v a, K^w b) \leq k \cdot d_N(a, b) + l \cdot d_N(a, K^v a) + m \cdot d_N(b, K^w b) + n \cdot d_N(a, K^w b) + p \cdot d_N(b, K^v a)$$

for all  $a, b \in X$ , where  $k, l, m, n, p$  be non-Newtonian positive real numbers with  $k + l + m + n + p < \beta(1)$ ,  $l = m, n = p$ , then  $K$  has a unique fixed-point.

**Conclusion**

In this paper, we use the concept of non-Newtonian metric space and present some new fixed-point theorems. We expect that our research results can offer a mathematical basis. In the future research, we will explore so concrete applications of the obtained results, here.

**Acknowledgements**

The author wishes to thank the referee for valuable suggestions and comments which improved the paper considerably.

**Conflicts of Interest**

The author states that did not has conflict of interests.

**References**

- [1] Alar R., Yigit Dakmaz E., Sola Erduran F., Gezici A., On Soft Fuzzy Metric Spaces and Topological Structure, *Journal of Advanced Studies in Topology*, 9 (2018) 61-70.
- [2] Aslantas M., Some Best Proximity Point Results via a New Family of F-Contraction and an Application to Homotopy Theory, *Journal of Fixed Point Theory and Applications*, 23 (4) (2021).
- [3] Aslantas M., Sahin H., Sadullah U., Some Generalizations for Mixed Multivalued Mappings, *Applied General Topology*, 23 (1) (2022) 169-178.
- [4] Aslantas M., Sahin H., Turkoglu D., Some Caristi Type Fixed-Point Theorems, *The Journal of Analysis*, 29 (2021) 89-103.
- [5] Binbasioglu D., Demiriz S., Turkoglu D., Fixed-Points of non-Newtonian Metric Spaces, *J. Fixed Point Theory Appl.*, 18 (2016) 213-224.
- [6] Cakmak A. F., Basar F., Some New Results on Sequence Spaces with respect to non-Newtonian Calculus, *J. Inequal. Appl.*, 2012 (2012) 228.
- [7] Cevik C., Altun I., Sahin H., Ozeken C. C., Some Fixed-Point Theorems for Contractive Mapping in Ordered Vector Metric Spaces, *Journal of Nonlinear Sciences and Applications*, 10 (4) (2017) 1424-1432.
- [8] Choudhary B., Nanda S., *Functional Analysis with Applications*. Newyork: John Wiley and Sons, (1990).
- [9] Grossman M. and Katz R., *Non-Newtonian Calculus*, Lowell Technological Institute (1972).
- [10] He X., Song M. and Chen D., Common Fixed-Points for Weak Commutative Mappings on a Multiplicative Metric Space, *Fixed Point Theory Appl.*, 2014 (2014) 48.
- [11] Sola Erduran F., Yigit Dakmaz E., Alar R., Gezici A., Soft Fuzzy Metric Spaces, *General Letters in Mathematics*, 3 (2017) 91-101.
- [12] Uzer A., Multiplicative Type Complex Calculus as an Alternative to the Classical Calculus, *Comput. Math. Appl.*, 60 (2010) 2725-2737.



## Properties of $J_p$ -Statistical Convergence

Canan Sümbül<sup>1,a</sup>, Cemal Belen<sup>2,b</sup>, Mustafa Yıldırım<sup>1,c,\*</sup>

<sup>1</sup> Department of Mathematics, Faculty of Science, Sivas Cumhuriyet University, Sivas, Türkiye.

<sup>2</sup> Department of Mathematics Education, Ordu University, Ordu, Türkiye.

\*Corresponding author

### Research Article

#### History

Received: 08/02/2022

Accepted: 19/04/2022

#### Copyright



©2022 Faculty of Science,  
Sivas Cumhuriyet University

### ABSTRACT

In this study, different characterizations of  $J_p$ -statistically convergent sequences are given. The main features of  $J_p$ -statistically convergent sequences are investigated and the relationship between  $J_p$ -statistically convergent sequences and  $J_p$ -statistically Cauchy sequences is examined. The properties provided by the set of bounded and  $J_p$  statistical convergent sequences is shown. It is given that the statistical limit is unique. Furthermore, a sequence that  $J_p$ -statistical converges to the number  $L$  has a subsequence that converges to the same number of  $L$ , is shown. The analogs of  $J_p$  statistical convergent sequences is studied.

**Keywords:** Power series method,  $J_p$ -statistical convergence,  $J_p$ -statistical Cauchy

<sup>a</sup> [cnnhs@gmail.com](mailto:cnnhs@gmail.com)  
<sup>c</sup> [yildirim@cumhuriyet.edu.tr](mailto:yildirim@cumhuriyet.edu.tr)

<sup>ib</sup> <https://orcid.org/0000-0002-8905-1247>  
<sup>id</sup> <https://orcid.org/0000-0002-8880-5457>

<sup>b</sup> [cbelen52@gmail.com](mailto:cbelen52@gmail.com)

<sup>id</sup> <https://orcid.org/0000-0002-8832-1524>

## Introduction

Statistical convergence is a generalization of the concept of convergence in the Cauchy sense. The idea of statistical convergence was introduced under the name of "almost convergence" in the first edition [1] of Zygmund's monograph, published in 1935. The term "statistical convergence" was used by Fast [2] and Steinhaus [3] independently of each other. Also, statistical convergence was studied by Buck [4] in 1953 with the expression of "convergence in density".

Fridy [5] introduced the concept of the statistical Cauchy sequence and presented a characterization of statistical convergence without needing to know the statistical limit. Statistical convergence was considered as a regular summability method, and it was discussed in Schoenberg [6], Connor [7] and [8].

Although statistical convergence is a new field of study, it has become an active area of research in recent years (see Belen et al [9], [10], Burgin and Duman [11], Connor and Kline [12], Çakallı and Khan [13], Et and Şengül [14], Freedman and Sember [15], Miller [16], Salat [17], Savaş and Mohiuddine [18]). Many researchers have done and still do studies on statistical convergence ([19], [20], [21], [22]).

Ünver [23] defined the new density concept using the Abel method and presented a definition of a new version of statistical convergence via this density. Ünver and Orhan [24] gave a new density concept according to the power series method and the definitions of  $P_p$ -statistical convergence and strong  $P_p$ -convergence via this density. In the study, they gave a Krovkin-type approximation theorem. Belen et al. [25] defined the concepts of  $J_p$ -convergence respect to a power series method and strong  $J_p$ -convergence via a modulus function  $f$ . They examined

the relationship between them. In addition, in the study, the concepts of  $J_p$ -statistical convergence and  $f$ - $J_p$ -statistical convergence were given and the relationships between them were examined.

Now, let us remind the basic concepts used in this study.

Let  $E \subset \mathbb{N}_0$ ,  $E(n) = \{k \leq n : k \in E\}$  and  $|E(n)|$  denote the cardinality of the set  $E(n)$ . If the limit  $\delta(E) = \lim_{n \rightarrow \infty} \frac{|E(n)|}{(n+1)}$  exists, then the set  $E \subset \mathbb{N}_0$  is said to have the usual density  $\delta(E)$  [4]. The real number sequence  $x = (x_k)$  is said to be statistically convergent to the number  $L$ , if the limit  $\lim_{n \rightarrow \infty} \frac{1}{n+1} |\{k \leq n : |x_k - L| \geq \varepsilon\}| = 0$  for each  $\varepsilon > 0$ ; i.e.,  $\delta(E_\varepsilon) = 0$  where  $E_\varepsilon := \{k \leq n : |x_k - L| \geq \varepsilon\}$  and denoted by  $\text{st-lim} x = L$  [5].

Now let's introduce the  $J_p$  convergence given in Boss [26].

Let  $\mathbb{N}_0$  be the set of non-negative integers. Let  $(p_k)_{k \in \mathbb{N}_0}$  be a sequence of non-negative integers where  $p_0 > 0$ , satisfying

$$P_n = \sum_{k=1}^n p_k \rightarrow \infty, (n \rightarrow \infty) \quad (1)$$

and

$$p(t) = \sum_{k=1}^{\infty} p_k t^k < \infty, (\text{for } 0 < t < 1) \quad (2)$$

(In other words,  $p(t)$  has radius of convergence  $R = 1$ ).

Let  $x = (x_k)_{k \in \mathbb{N}_0}$  be a sequence of real numbers. In this case, the power series method  $J_p$  is defined as follows:

If for every  $0 < t < 1$ ,  $p_x(t) = \sum_{k=1}^{\infty} p_k t^k x_k$  converges and  $\lim_{t \rightarrow 1^-} \frac{p_x(t)}{p(t)} = L$ , then  $(x_k)$  is called  $J_p$ -convergent to

L the sequence via the power series method and it is denoted as  $x_k \rightarrow L (J_p)$ . If  $x_k \rightarrow L (J_p)$  as  $x_k \rightarrow L$ , the  $J_p$ -method is called regular. It is known that condition (1) or, equivalently, condition  $p(t) \rightarrow \infty$  when  $t \rightarrow 1^-$  guarantees the regularity of method  $J_p$  (see, [4]). Therefore, assuming (1), we will consider only regular  $J_p$ -methods.

Let  $E \subset \mathbb{N}_0$  be any set. If  $\delta_{J_p}(E) = \lim_{t \rightarrow 1^-} \frac{1}{p(t)} \sum_{k \in E} p_k t^k = 0$  exists, then  $\delta_{J_p}(E)$  is called the  $J_p$ -density of the set  $E$ . If  $\lim_{t \rightarrow 1^-} \frac{1}{p(t)} \sum_{k \in E_\varepsilon} p_k t^k = 0$  for every  $\varepsilon > 0$ , i.e.,  $\delta_{J_p}(E_\varepsilon) = 0$ , then the number  $L$  of the sequence  $x = (x_k)$  is said to be  $J_p$ -statistically convergent. The set of all  $J_p$ -statistically convergent sequences will be denoted by  $st_{J_p}$  [24].

In this study, some expected properties of the  $J_p$ -statistical convergent sequence space are examined.

### Main Results

In this section, we prove that if a sequence  $x = (x_k)$  is  $J_p$ -statistical convergent then there is a subsequence of  $x = (x_k)$  which is convergence to the same number in ordinary sense. Also, we show that the  $J_p$ -statistical limit is unique, and we give the relationship between  $J_p$ -statistical Cauchy sequences and  $J_p$ -statistical convergent sequences.

**Theorem 2.1** A real sequence  $x = (x_k)$  is  $J_p$ -statistical convergent to a number  $\ell$  if and only if there exists a subset  $K = \{k \in \mathbb{N} : k = 1, 2, \dots\}$  such that  $\delta_{J_p}(K) = 1$  and

$$\lim_{\substack{k \rightarrow \infty \\ k \in K}} x_k = \ell$$

Proof. Necessity. Let  $x = (x_k)$  be  $J_p$ -statistical convergent to  $\ell$ .

$$K_r := \left\{ k \in \mathbb{N} : |x_k - \ell| \geq \frac{1}{r} \right\}$$

and

$$M_r := \left\{ k \in \mathbb{N} : |x_k - \ell| < \frac{1}{r} \right\}, r = 1, 2, \dots$$

In this case, we get  $\delta_{J_p}(K_r) = 0$  and

$$M_1 \supset M_2 \supset \dots \supset M_i \supset M_{i+1} \supset \dots \tag{3}$$

$$\delta_{J_p}(M_r) = 1. \tag{4}$$

Now, we have to show that  $(x_k)$  converges to  $\ell$  for  $k \in M_r$ . Assume that  $(x_k)$  is not convergent to  $\ell$ . In this case, there is an  $\varepsilon > 0$  for the infinitely many terms, such that

$$|x_k - \ell| \geq \varepsilon.$$

Define

$$M_\varepsilon = \{k : |x_k - \ell| < \varepsilon\} \text{ and } \varepsilon > \frac{1}{r} \quad (r = 1, 2, \dots).$$

Hence

$$\delta_{J_p}(M_\varepsilon) = 0 \tag{5}$$

and  $M_r \subset M_\varepsilon$  from (3). So we have  $\delta_{J_p}(M_r) = 0$ , which is a contradiction with (4). Then  $(x_k)$  is convergent to  $\ell$ .

Sufficiency. Suppose that there is a subset  $K = \{k \in \mathbb{N} : k = 1, 2, \dots\}$  such that  $\delta_{J_p}(K) = 1$  and

$$\lim_{\substack{k \rightarrow \infty \\ k \in K}} x_k = \ell$$

Therefore, for every  $\varepsilon > 0$  there is a  $N \in \mathbb{N}$  such that

$$|x_k - \ell| < \varepsilon, \forall k \geq N \text{ and } k \in K.$$

Since

$$K_\varepsilon = \{k : |x_k - \ell| \geq \varepsilon\} \subseteq \mathbb{N} - \{k_{N+j} : j \in \mathbb{N} \text{ and } k_{N+j} \in K\}$$

we have

$$\delta_{J_p}(K_\varepsilon) \leq 1 - 1 = 0.$$

Thus,  $x = (x_k)$  is statistically convergent to  $\ell$ .

**Theorem 2.2** Let the sequence  $x = (x_k)$  be  $J_p$ -statistical convergent to a number  $L$ . In this case, there is a sequence  $y$  that converges to the number  $L$  and a sequence  $z$  that  $J_p$ -statistical convergences to zero such that  $x = y + z$ .

Proof. Let the sequence  $x = (x_k)$  be  $J_p$ -statistical convergent to a number  $L$ . For the set

$$E_j = \left\{ k \leq n : |x_k - L| \geq \frac{1}{j} \right\}$$

with  $N_0 = 0$  and  $n \geq N_j (j = 1, 2, \dots)$ , we can find an increasing sequence of positive numbers  $(N_j)$  such that  $\delta_{J_p}(E_j) < \frac{1}{j}$ . Now let's define the  $y$  and  $z$  sequences as follows. Take  $z_k = 0$  and  $y_k = x_k$  when  $N_0 < k \leq N_1$ . For  $\frac{1}{j} \geq 1$ , let  $N_j < k \leq N_{j+1}$ .  $z_k = 0$  and  $y_k = x_k$  when  $|x_k - L| < \frac{1}{j}$  and finally, when  $|x_k - L| \geq \frac{1}{j}$ , let  $z_k = x_k - L$  and  $y_k = L$ . It is clear that we can write  $x = y + z$ . Now, we claim that the sequence  $y$  is convergent to  $L$ . Let  $\varepsilon > 0$  be given, let us choose  $j$  such that  $\varepsilon > \frac{1}{j}$ . For  $k \leq N_j$ , if  $|x_k - L| \geq \frac{1}{j}$  then  $|y_k - L| = |L - L| = 0$

and if

$$|x_k - L| < \frac{1}{j} \text{ then } |y_k - L| = |x_k - L| < \frac{1}{j} < \varepsilon$$

so  $\lim_{k \rightarrow \infty} y_k = L$  is obtained. Now, let us see  $st_{J_p} - \lim z = 0$ . We should show that

$$\lim_{t \rightarrow 1^-} \frac{1}{p(t)} \sum_{k \in E_z} p_k t^k = 0$$

for  $E_z = \{k \leq n: z_k \neq 0\}$ . Since

$$\{k \leq n: |z_k| \geq \varepsilon\} \subset \{k \leq n: z_k \neq 0\}$$

for every  $\varepsilon > 0$ , we have

$$\delta_{J_p}(\{k \leq n: |z_k| \geq \varepsilon\}) \leq \delta_{J_p}(\{k \leq n: z_k \neq 0\}).$$

Now if  $\delta > 0$ ,  $j \in \mathbb{N}$  and  $\frac{1}{j} < \delta$  we have to show that  $\delta_{J_p}(\{k \leq n: z_k \neq 0\}) < \delta$  for every  $n > N_j$ . Let  $N_j < k \leq N_{j+1}$ , then  $z_k \neq 0$  is possible only with  $|x_k - L| \geq \frac{1}{j}$ . So if  $N_j < k \leq N_{j+1}$  then

$$\{k \leq n: z_k \neq 0\} = \left\{k \leq n: |x_k - L| \geq \frac{1}{j}\right\}.$$

Therefore, if  $N_v < k \leq N_{v+1}$  and  $v > j$  implies that

$$\delta_{J_p}(\{k \leq n: z_k \neq 0\}) \leq \delta_{J_p}\left(\left\{k \leq n: |x_k - L| \geq \frac{1}{v}\right\}\right) < \frac{1}{v} < \frac{1}{j} < \delta.$$

Thus, the proof is complete.

**Corollary 2.1** If the sequence  $x = (x_k)$  is  $J_p$ -statistical convergent to the number  $L$ , then  $\exists(x_{n_k}) \subset (x_n) \ni x_{n_k} \rightarrow L$ .

**Theorem 2.3** If  $x = (x_k)$  be a sequence such that  $st_{J_p} - \lim x = L$ , then  $L$  is determined uniquely.

Proof. Assume that  $x = (x_k)$  is  $J_p$ -statistically convergent to two different numbers  $L$  and  $K$ . i.e.,  $st_{J_p} - \lim x = L$  and  $st_{J_p} - \lim x = K$ . Let us choose  $L < K$ . If we choose  $\varepsilon = \frac{K-L}{3}$ , then

$$(L - \varepsilon, L + \varepsilon) \cap (K - \varepsilon, K + \varepsilon) = \emptyset.$$

Also, since  $st_{J_p} - \lim x = L$  and  $st_{J_p} - \lim x = K$

$$\delta_{J_p}(\{k \leq n: |x_k - L| \geq \varepsilon\}) = 0$$

$$\delta_{J_p}(\{k \leq n: |x_k - K| \geq \varepsilon\}) = 0$$

then

$$\delta_{J_p}(\{k \leq n: |x_k - L| < \varepsilon\}) = 1$$

$$\delta_{J_p}(\{k \leq n: |x_k - K| < \varepsilon\}) = 1.$$

Hence, we get  $\{k \leq n: |x_k - L| < \varepsilon\} \cap \{k \leq n: |x_k - K| < \varepsilon\} \neq \emptyset$ . This is a contradiction, as the sets are disjoint.

Hence the theorem is proved.

The following theorem shows that the statistical convergence method is linear.

**Theorem 2.4** Let  $x = (x_k)$  and  $y = (y_k)$  be two real sequences.

(i)  $st_{J_p} - \lim x = L_1$  and  $st_{J_p} - \lim y = L_2$  implies  $st_{J_p} - \lim(x + y) = L_1 + L_2$ .

(ii)  $st_{J_p} - \lim x = L_1$  and  $\alpha \in \mathbb{R}$  implies  $st_{J_p} - \lim(\alpha x) = \alpha L_1$ .

Proof. (i) Let  $st_{J_p} - \lim x = L_1$  and  $st_{J_p} - \lim y = L_2$ . For the set  $A_1 = \left\{k \leq n: |x_k - L_1| \geq \frac{\varepsilon}{2}\right\}$  since  $\delta_{J_p}(A_1) = 0$ , there is  $k_1 \in \mathbb{N}$  such that  $|x_k - L_1| < \frac{\varepsilon}{2}$  for every  $k > k_1$  and  $k \in (\mathbb{N} - A_1)$  when  $\varepsilon > 0$ . For the set  $A_2 = \left\{k \leq n: |y_k - L_2| \geq \frac{\varepsilon}{2}\right\}$  since  $\delta_{J_p}(A_2) = 0$ , there is  $k_2 \in \mathbb{N}$  such that  $|y_k - L_2| < \frac{\varepsilon}{2}$  for every  $k > k_2$  and  $k \in (\mathbb{N} - A_2)$  when  $\varepsilon > 0$ . Let define  $k_0 := \max\{k_1, k_2\}$ . Let show  $|x_k + y_k - L_1 - L_2| < \varepsilon$  for every and every  $k \in (\mathbb{N} - (A_1 \cap A_2))$  and every  $k > k_0$ . Since  $\delta_{J_p}(A_1) = 0$  and  $\delta_{J_p}(A_2) = 0$ , then  $\delta_{J_p}(A_1 \cap A_2) = 0$ . In that case for  $k > k_0$

$$|x_k + y_k - L_1 - L_2| < |x_k - L_1| + |y_k - L_2| < \frac{\varepsilon}{2} + \frac{\varepsilon}{2} = \varepsilon$$

and for every  $\varepsilon > 0$

$$\delta_{J_p}(\{k \leq n: |x_k + y_k - L_1 - L_2| \geq \varepsilon\}) = 0.$$

This gives  $st_{J_p} - \lim(x + y) = L_1 + L_2$

(ii) If  $\alpha = 0$ , we have nothing to prove. Let us assume that  $\alpha \neq 0$ .

$$\begin{aligned} \delta_{J_p}(\{k \leq n: |\alpha x_k - \alpha L_1| \geq \varepsilon\}) &= \delta_{J_p}(\{k \leq n: |\alpha| |x_k - L_1| \geq \varepsilon\}) \\ &\leq \delta_{J_p}\left(\left\{k \leq n: |x_k - L_1| \geq \frac{\varepsilon}{|\alpha|}\right\}\right) \\ &= 0 \end{aligned}$$

So  $st_{J_p} - \lim(\alpha x) = \alpha L_1$  is obtained.

**Theorem 2.5** The space  $st_{J_p} \cap \ell_\infty$  is a closed subspace of the normed space  $\ell_\infty$ .

Proof. Let  $x^{(n)} \in st_{J_p} \cap \ell_\infty$  and  $x^{(n)} \rightarrow x \in \ell_\infty$ . Since  $x_k \in st_{J_p} \cap \ell_\infty$  there are real numbers  $a_n$  such that

$$st_{J_p} - \lim x_k^{(n)} = a_n (n = 1, 2, \dots).$$

Since  $x^{(n)} \rightarrow x$ , for every  $\varepsilon > 0$ , there is a number  $N = N(\varepsilon) \in \mathbb{N}$  such that

$$|x^{(p)} - x^{(n)}| < \varepsilon/3 \tag{6}$$

where  $p \geq n \geq N$ . Here,  $|\cdot|$  denotes the norm in a vector space. From Theorem 2.1,  $\mathbb{N}$  has a subset of  $K_1$  with  $\delta_{J_p}(K_1) = 1$  and

$$\lim_{k \in K_1} x_k^{(n)} = a_n. \tag{7}$$

Since  $\delta_{J_p}(K_1) = 1$ , let us take  $k_1 \in K_1$ . From (7),

$$|x_{k_1}^{(p)} - a_p| < \varepsilon/3. \tag{8}$$

Thus, for every  $p \geq n \geq N$  from (6), we have

$$|a_p - a_n| \leq |a_p - x_{k_1}^{(p)}| + |x_{k_1}^{(p)} - x_{k_1}^{(n)}| + |x_{k_1}^{(n)} - a_n| < \frac{\varepsilon}{3} + \frac{\varepsilon}{3} + \frac{\varepsilon}{3} = \varepsilon.$$

Therefore  $(a_n)$  is a Cauchy sequence and hence  $(a_n)$  is convergent. Let

$$\lim_n a_n = a. \tag{9}$$

We should show that  $x$  is  $J_p$ -statistical convergence to  $a$ . Since  $x^{(n)} \rightarrow x$ , for every  $\varepsilon > 0$ , there is a  $N_1(\varepsilon)$  such that

$$|x_j^{(n)} - x_j| < \varepsilon/3$$

where every  $j \geq N_1(\varepsilon)$ . Also, from (9), for every  $\varepsilon > 0$  there is a  $N_2(\varepsilon) \in \mathbb{N}$  such that

$$|a_j - a| < \varepsilon/3$$

where every  $j \geq N_2(\varepsilon)$ . Again, since  $st_{J_p} \lim x^{(n)} = a_n$ , there is a set  $K \subseteq \mathbb{N}$  with  $\delta_{J_p}(K) = 1$  and  $N_3(\varepsilon) \in \mathbb{N}$  for every  $\varepsilon > 0$  such that

$$|x_j^{(n)} - a_n| < \varepsilon/3$$

when  $j \in K$  and all  $j \geq N_3(\varepsilon)$ . Let us say  $\max\{N_1(\varepsilon), N_2(\varepsilon), N_3(\varepsilon)\} = N_4(\varepsilon)$ . In this case

$$|x_j - a| \leq |x_j^{(n)} - x_j| + |x_j^{(n)} - a_n| + |a_j - a| < \frac{\varepsilon}{3} + \frac{\varepsilon}{3} + \frac{\varepsilon}{3} = \varepsilon$$

is obtained for a given  $\varepsilon > 0$  and all  $j \geq N_4(\varepsilon)$ ,  $j \in K$ . Therefore  $st_{J_p} \lim x = a$ , i.e.,  $x \in st_{J_p} \cap \ell_\infty$ . So  $st_{J_p} \cap \ell_\infty$  is a closed subspace of  $\ell_\infty$ .

**Theorem 2.6** The space  $st_{J_p} \cap \ell_\infty$  is nowhere dense in  $\ell_\infty$ . Proof. Since every closed subspace of an arbitrary normed space  $S$  different from  $S$  is nowhere dense in  $S$  (Neubrum et al. 1968), it is sufficient to show that it is only  $st_{J_p} \cap \ell_\infty \neq \ell_\infty$ . Let

$$p_k = \begin{cases} 1, & k = n^2, n \in \mathbb{N}_0 \\ 0, & \text{otherwise.} \end{cases}$$

and

$$x_k = \begin{cases} 1, & k = n^2, n \in \mathbb{N}_0 \\ 0, & \text{otherwise.} \end{cases}$$

Then  $x$  is not  $J_p$ -statistical convergent but bounded. Hence,  $st_{J_p} \cap \ell_\infty \neq \ell_\infty$ .

**Definition 2.1**  $x = (x_k)$  is said to be  $J_p$ -statistical Cauchy sequence if for every  $\varepsilon > 0$  there exists a  $N(\varepsilon) \in \mathbb{N}$  such that  $\delta_{J_p}(\{k \leq n: |x_k - x_N| < \varepsilon\}) = 1$ .

**Theorem 27** A sequence  $x = (x_k)$  is  $J_p$ -statistical convergent if and only if  $x = (x_k)$  is  $J_p$ -statistical Cauchy.

Proof. Let  $(x_k)$  be  $J_p$ -statistical convergent to  $L$ . In this case,  $\delta_{J_p}(\{k \leq n: |x_k - \ell| \geq \varepsilon\}) = 0$  for every  $\varepsilon > 0$ . Let us choose  $N$  as  $|x_N - \ell| \geq \varepsilon$  and define the sets as

$$A_\varepsilon = \{k \leq n: |x_k - x_N| \geq \varepsilon\}, \\ B_\varepsilon = \{k \leq n: |x_k - \ell| \geq \varepsilon\}, \\ C_\varepsilon = \{k = N \leq n: |x_N - \ell| \geq \varepsilon\}$$

In this case, it is clear that  $A_\varepsilon \subseteq B_\varepsilon \cup C_\varepsilon$ . From here,  $\delta_{J_p}(A_\varepsilon) \leq \delta_{J_p}(B_\varepsilon) + \delta_{J_p}(C_\varepsilon) = 0$  is obtained. So  $x$  is  $J_p$ -statistical Cauchy sequence. Conversely, let  $x$  be  $J_p$ -statistical Cauchy, but not  $J_p$ -statistical convergent. In this case, there exists  $N$  such that  $\delta_{J_p}(A_\varepsilon) = 0$ . Therefore,

$$\delta_{J_p}(\{k \leq n: |x_k - x_N| < \varepsilon\}) = 1.$$

Specifically, if  $|x_k - \ell| < \varepsilon/2$  we can write

$$|x_k - x_N| \leq 2|x_k - \ell| < \varepsilon. \tag{10}$$

Since  $x$  is not  $J_p$ -statistical convergent,  $\delta_{J_p}(B_\varepsilon) = 1$ . That is

$$\delta_{J_p}(\{k \leq n: |x_k - \ell| < \varepsilon\}) = 0.$$

Thus from (10),

$$\delta_{J_p}(\{k \leq n: |x_k - x_N| < \varepsilon\}) = 0$$

i.e.,  $\delta_{J_p}(A_\varepsilon) = 1$ . This is a contradiction. So,  $x$  is  $J_p$ -statistical convergent.

### Conclusion

In this study, different characterizations of  $J_p$ -statistically convergent sequences are given. The main features of  $J_p$ -statistical convergent sequences are investigated and the relationship between  $J_p$ -statistical convergent sequences and  $J_p$ -statistical Cauchy sequences is examined.

### Acknowledgment

The authors would like to thank the anonymous reviewers for their suggestions about paper.

### Conflicts of interest

The author states that did not have conflict of interests

## References

- [1] Zygmund A., Trigonometric Series. 3<sup>rd</sup>.ed. London: Cambridge Univ. Press, (2003),
- [2] Fast H., Sur la convergence statistique, *Colloq. Math.*, 2 (1951) 241-244.
- [3] Steinhaus H., Sur la convergence ordinaire et la convergence asymptotique, *Colloq. Math.*, 2 (1951) 73-74.
- [4] Buck R. C., Generalized asymptotic density, *Amer. J. Math.*, 75 (2) (1953) 335-346.
- [5] Fridy, J. A., On statistical convergence, *Analysis* 5 (1985) 301-313.
- [6] Schoenberg I. J., The integrability of certain functions and related summability methods, *Amer. Math. Monthly*, 66(5) (1959) 361-375.
- [7] Connor J., The statistical and strong  $p$ -Cesàro convergence of sequences, *Analysis*, 8 (1988) 47-63.
- [8] Connor J., On strong matrix summability with respect to a modulus and statistical convergence, *Canad. Math. Bull.*, 32 (1989) 194-198.
- [9] Belen C., Mursaleen M., Yildirim M., Statistical A-summability of double sequences and a Korovkin type approximation theorem, *Bull. Korean Math. Soc.*, 49 (4) (2012) 851-861.
- [10] Belen C., Some Tauberian theorems for weighted means of bounded double sequences, *An. Ştiinţ. Univ. Al. I. Cuza Iaşi. Mat. (N.S.)*, 63 (1) (2017) 115-122.
- [11] Burgin M., Duman O., Statistical convergence and convergence in statistics, <http://arxiv.org/abs/math/0612179>. Retrieved, 2006.
- [12] Connor J., Kline J., On statistical limit points and the consistency of statistical convergence, *J. Math. Anal. Appl.*, 197 (2) (1996) 392-399.
- [13] Çakallı H. and Khan M. K., Summability in topological spaces, *Appl. Math. Lett.* 24(3) (2011) 348-352.
- [14] Et M. and Şengul H., Some Cesàro-type summability spaces of order and lacunary statistical convergence of order, *Filomat*, 28(8) (2014), 1593-1602.
- [15] Freedman, A. R., Sember, J. J., Densities and summability, *Pacific J. Math.*, 95(2) (1981) 293-305.
- [16] Miller H. I., A measure theoretical subsequence characterization of statistical convergence, *Trans. Amer. Math. Soc.*, 347(5) (1995) 1811-1819.
- [17] Šalát, T., On statistically convergent sequences of real numbers, *Math. Slovaca*, 30 (1980) 139--150.
- [18] Savas E., Mohiuddine S. A.,  $\lambda$ -statistically convergent double sequences in probabilistic normed spaces, *Math. Slovaca*, 62(1) (2012), 99-108.
- [19] Et M., Baliarsingh P., Şengül Kandemir H., Küçükaslan M., On  $\mu$ -deferred statistical convergence and strongly deferred summable functions, *Rev. R. Acad. Cienc. Exactas Fís. Nat. Ser. A Mat. RACSAM*, 115(1-34) (2021).
- [20] Sengül H., Et M., Lacunary statistical convergence of order  $(\alpha, \beta)$  in topological groups, *Creat. Math. Inform.*, 26(3), (2017), 339-344.
- [21] Sengul H., Et M., f-lacunary statistical convergence and strong f-lacunary summability of order  $\alpha$ , *Filomat*, 32(13) (2018) 4513-4521.
- [22] Sengul H., Et M., On  $(\lambda, l)$ -statistical convergence of order  $\alpha$  of sequences of function, *Proc. Nat. Acad. Sci. India Sect. A*, 88(2) (2018) 181--186.
- [23] Ünver M., Abel summability in topological spaces, *Monatsh. Math.*, 178(4) (2015) 633-643.
- [24] Ünver M., Orhan C., Statistical convergence with respect to power series methods and applications to approximation theory, *Numer. Func. Anal Opt.*, 40(5) (2019) 535-547.
- [25] Belen C., Yildirim M., Sümbül C., On Statistical and Strong Convergence with Respect to a Modulus Function and a Power Series Method, *Filomat*, 34 (12) (2020) 3981-3993.A.
- [26] Boos J., Classical and modern methods in summability, Oxford University Press, Oxford (2000).

## Kinematic Analysis in 3-Dimensional Generalized Space

Ümit Ziya Savcı<sup>1,a,\*</sup><sup>1</sup> Department of Mathematics and Science Education, Faculty of Education, Kütahya Dumlupınar University, Kütahya, Türkiye.

\*Corresponding author

### Research Article

#### History

Received: 07/01/2022

Accepted: 22/04/2022

#### Copyright

©2022 Faculty of Science,  
Sivas Cumhuriyet University

### ABSTRACT

In this paper, we have first obtained the derivatives of spherical and spatial motions by using the special matrix group in generalized space  $E^3(\alpha, \beta)$ . The rotation matrices and tangent operators were found by using derivatives of one- and multi-parameters motions in  $E^3(\alpha, \beta)$ . Also, we obtained the angular velocity matrix of the moving body and its linear velocity vector. Finally, we gave some examples including applications of tangent operators and rotation matrices in support of our results.

**Keywords:** Generalized space, Rigid motion, Kinematics, Tangent operators, Matrix group.

[ziyasavci@hotmail.com](mailto:ziyasavci@hotmail.com)<https://orcid.org/0000-0003-2772-9283>

## Introduction

Kinematics is a Greek word that means 'motion', and it is one of the branches of mechanics that deals with the analysis of the motion of particles and rigid bodies. The rigid body is a set of the points that the distance between two of the points never varies after motion [1].

In order to represent a rigid motion in Euclidean or Lorentzian space equipped with multiple coordinate frames, it is required to determine the concept of a rotation matrix and a translation axis. These concepts are used to construct homogeneous transformation matrices that are used to represent the position and orientation of a coordinate frame relative to the other. These transformations allow us to navigate from one to another coordinate frame [2-6].

Recent studies on robot kinematics are dealing with the establishment of different coordinate systems to represent the positions and orientations of rigid bodies. Also, Robot kinematics is concerned with the transformations between these coordinate systems [7-10].

To obtain frame M from frame F, it is needed to first apply a rotation determined by R and then a translation (with respect to F) given as t. This transformation called coordinates transformation is denoted as  $T:F \rightarrow M$ , and it is determined as  $x^M = R \cdot x^F + t$ . In this notation, R is an  $n \times n$  orthogonal matrix called a rotation matrix, and t is an n-dimensional vector called a translation. This transformation is denoted by  $T=(R,t)$  and defined as a matrix-vector pair [11,12].

The derivative of a motion represents the velocity of a point from the fixed frame F to the moving frame M. Linear velocity is the instantaneous rate of change in the linear position of a point relative to some frame. The angular velocity is  $\omega$ , which describes the rotational motion of M with respect to F. The relationship between

the angular velocity vector  $\omega$  and time-varying rotation matrix  $R(t)$  is defined by  $[\dot{R}] = [R\dot{R}^T]$  [6,11,12].

The rotation matrix, which is used to represent relative orientations between coordinate frames, is an orthogonal matrix in Euclidean or Lorentzian space. In Euclidean and Lorentzian spaces, if A is an orthogonal matrix,  $\det A = 1$  denotes rotation and  $\det A = -1$  denotes reflection [11-14].

The generalized quaternions  $H(\alpha, \beta)$  are four-dimensional algebra that is associative but not commutative. This algebra is a pair of sub-algebras of Clifford algebra of three-dimensional generalized space  $E^3(\alpha, \beta)$ , where  $E^3(\alpha, \beta)$  is a real vector space  $R^3$  equipped with the metric  $\langle u, v \rangle_G = \alpha u_1 v_1 + \beta u_2 v_2 + u_3 v_3$ ,  $\alpha, \beta \in R$ . For 3-dimensional non-degenerate vector space,  $E^3(\alpha, \beta)$  with an orthonormal basis  $\{e_1, e_2, e_3\}$ , the Clifford algebra  $Cl(E^3(\alpha, \beta)) = Cl(p, q)$ ,  $p+q=2$  has the basis  $\{1, e_1=i, e_2=j, e_1 e_2=k\}$ , where  $e_1^2 = -\alpha$ ,  $e_2^2 = -\beta$  and  $e_1 e_2 = -e_2 e_1$ . General information about generalized space and their algebraic properties can be found from [15-21].

Beggs (1965) gave a derivation for a screw matrix by using two different coordinate systems [3]. By defining the pitch for a finite screw as the ratio of one-half the translation to the tangent of one-half the rotation, Parkin has shown that the finite screw cylindroid can be represented by the linear combinations of two bases screws in 1992 [22]. In 1994, Huang and Roth showed the finite displacement of a rigid body can be represented completely by six independent parameters [23]. Knosow, Ronfard, and Horaud showed that the tangent operator can be used to explain the human body kinematic chain and robotics motion in 2008 [24]. In 2017 Durmaz, Aktaş and Gundogan computed the derivative and the tangent operator of motion in Lorentzian space [25]. In 2021 Ata and Savcı obtained the generalized Cayley formula,

Rodrigues equation, and Euler parameters of a generalized orthogonal matrix in 3-dimensional generalized space  $E^3(\alpha, \beta)$  [16].

Due to the definition of the generalized space  $E^3(\alpha, \beta)$ , it is Euclidean space  $E^3(1, 1)$  if  $\alpha = \beta = 1$ , and it is semi-Euclidean space  $E^3(1, -1)$  if  $\alpha = 1$  and  $\beta = -1$ . Therefore, this space  $E^3(\alpha, \beta)$  allows us to define more general algebraic structures and study them. In this study, for all situations of  $\alpha$  and  $\beta$  except zero, derivatives of spherical and spatial motion and tangent operators have been obtained for one- and multi-parameter motions in generalized space. We get ordinary differential equations using these derivatives. The rotation matrix is obtained from the solution of these equations. In addition, Lie product of tangent operators and some properties provided by Lie product is defined.

**Preliminaries**

In this section, we provide some fundamental properties of the generalized space, the transformation and the rotation.

**Definition 1:** Let  $u = (u_1, u_2, u_3)$ ,  $v = (v_1, v_2, v_3)$  be two vectors in  $\mathbb{R}^3$  and  $\alpha, \beta \in \mathbb{R}$ . Then the generalized metric tensor product is defined by

$$\langle u, v \rangle_G = \alpha u_1 v_1 + \beta u_2 v_2 + \alpha \beta u_3 v_3.$$

This can be written as  $\langle u, v \rangle_G = u^T \begin{bmatrix} \alpha & 0 & 0 \\ 0 & \beta & 0 \\ 0 & 0 & \alpha\beta \end{bmatrix} v.$

The vector space  $\mathbb{R}^3$  equipped with the generalized scalar product, is called as 3 –dimensional generalized space and is denoted by  $E^3(\alpha, \beta) = (R^3, \langle \cdot, \cdot \rangle_G)$ . The generalized cross product in  $E^3(\alpha, \beta)$  is defined by

$$u \wedge_G v = \beta(u_2 v_3 - u_3 v_2)i - \alpha(u_1 v_3 - u_3 v_1)j + (u_1 v_2 - u_2 v_1)k,$$

where  $i \wedge_G j = k, j \wedge_G k = \beta i,$  and  $k \wedge_G i = -\alpha j$  [18].

If  $\langle u, v \rangle_G$  is a generalized semi-Euclidean inner product, then  $E^3(\alpha, \beta)$  is a 3 –dimensional generalized semi-Euclidean space  $E_2^3$ . If  $\langle u, v \rangle_G$  is an Euclidean inner product, then  $E^3(\alpha, \beta)$  space is known as  $E^3$  Euclidean space.

**Definition 2:** Let  $E^3(\alpha, \beta)$  be a generalized semi-Euclidean space with a generalized semi-Euclidean inner product. A vector  $w \in E^3(\alpha, \beta)$  is called generalized spacelike vector, if  $\langle v, v \rangle_G > 0$  or  $v = 0$ , generalized timelike vector, if  $\langle v, v \rangle_G < 0$ , generalized null vector, if  $\langle v, v \rangle_G = 0$  and  $v \neq 0$ .

$\|v\| = \sqrt{|\alpha v_1 + \beta v_2 + \alpha \beta v_3|}$  represents the norm of a vector  $v \in E^3(\alpha, \beta)$  [13,14,18].

**Definition 3:** The set of the  $3 \times 3$  invertible matrices, denoted  $GL(\alpha, \beta)(3)$ , is an algebraic group under the operation of matrix multiplication in generalized space  $E^3(\alpha, \beta)$  [17].

**Definition 4:** A matrix  $C = \begin{bmatrix} 0 & \beta s_3 & \beta s_2 \\ \alpha s_3 & 0 & -\alpha s_1 \\ -s_2 & s_1 & 0 \end{bmatrix}$  called a

generalized skew-symmetric matrix if  $C^T \varepsilon = -\varepsilon C$ , where

$$\varepsilon = \begin{bmatrix} \alpha & 0 & 0 \\ 0 & \beta & 0 \\ 0 & 0 & \alpha\beta \end{bmatrix} \text{ and } \alpha, \beta \in \mathbb{R} - \{0\} \text{ [18].}$$

**Definition 5:** A matrix  $R$  is called a generalized orthogonal matrix if  $R^T \varepsilon R = |\varepsilon| \varepsilon$  where

$$\varepsilon = \begin{bmatrix} \alpha & 0 & 0 \\ 0 & \beta & 0 \\ 0 & 0 & \alpha\beta \end{bmatrix} \text{ and } \alpha, \beta \in \mathbb{R} - \{0\}.$$

The set of all generalized orthogonal matrices with the operation of matrix multiplication is called the rotation group in  $E^3(\alpha, \beta)$  [14].

A rotation about the origin can be given with the equation of  $x' = R \cdot_G x$ , where  $R$  is  $3 \times 3$  G-orthogonal matrix and  $x \in E^3(\alpha, \beta)$ . Generalized Cayley formula is defined as  $R = (I - C)^{-1} \cdot (I + C) = (I + C) \cdot (I - C)^{-1}$ , where  $C$  is a G-skew symmetric matrix. By using G-Cayley formula, any G-orthogonal matrix can be obtained by a G-skew symmetric matrix  $C$ , where

$$C = \begin{bmatrix} 0 & -\beta c_3 & \beta c_2 \\ \alpha c_3 & 0 & -\alpha c_1 \\ -c_2 & c_1 & 0 \end{bmatrix}$$

the matrix  $C$  obtained the vector  $c = (c_1, c_2, c_3)$  and satisfying the equation  $C \cdot_G y = c \wedge_G y$  [16].

The rotations in the three-dimensional space are represented by  $3 \times 3$  rotation matrices, i.e. by means of 9 parameters. Since constrained by the orthogonality conditions  $R^T \varepsilon R = |\varepsilon| \varepsilon$  these parameters are not independent. Only three independent parameters are needed to obtain a minimal representation of rotations in space.

If frame  $M$  is obtained from frame  $F$  by first applying a rotation specified by  $R$  followed by a translation given (with respect to  $F$ ) by  $t$ , then the coordinates are given by

$$x' = R \cdot_G x + t \tag{1}$$

Since the displacement is not a linear transformation it not be represented by  $3 \times 3$  matrix transformation.

**Definition 6:** A transformation of the form given in eq. (1) is called a rigid motion if  $R$  is generalized orthogonal matrix.

Since the set of displacements of an 3-dimensional generalized space  $E^3(\alpha, \beta)$  is an algebraic group. If  $T_1: F \rightarrow M_1$  and  $T_2: M_1 \rightarrow M_2$  are displacements, then  $T = T_1 T_2: F \rightarrow M_2$  is also a displacement [26].

A combination of those two displacements with the matrices identity;

$$\begin{bmatrix} R_1 & t_1 \\ 0 & 1 \end{bmatrix} \cdot \begin{bmatrix} R_2 & t_2 \\ 0 & 1 \end{bmatrix} = \begin{bmatrix} R_1 \cdot R_2 & R_1 \cdot t_2 + t_1 \\ 0 & 1 \end{bmatrix}$$

where  $0$  denotes the row vector  $(0,0,0)$ , shows that the rigid motions can be represented by the set of matrices of the form;

$$G - H(4) = \begin{bmatrix} R & t \\ 0 & 1 \end{bmatrix}; R \in SO(\alpha, \beta)(3) \quad (2)$$

Transformation matrices of the form eq. (2) are called homogeneous transformation in  $E^3(\alpha, \beta)$  space and denote by  $[g] = [R, t]$ . The displacement is not a linear transformation, but the homogeneous transformation  $[g] = [R, t]$  is a linear transformation. The homogeneous representation eq. (2) is a special case of homogeneous coordinates, which have been extensively used in the field of computer graphics. The most general homogeneous transformation takes the form;

$$G - H(4) = \begin{bmatrix} R_{3 \times 3} & t_{3 \times 1} \\ f_{1 \times 3} & s_{1 \times 1} \end{bmatrix} = \begin{bmatrix} \text{Rotation} & | & \text{Translation} \\ \hline \text{perspective} & | & \text{scale factor} \end{bmatrix}$$

From the definition of the metric tensor, all possible selections of  $\alpha$  and  $\beta$  can be covered by two conditions given above. From now on we take these two cases into consideration.

### The Derivative of a Motion and G-Tangent Operators in Generalized Space

We will use G-tangent operator instead of tangent operator in generalized space for appropriate notation. The continuous motion of a rigid body is the parametrized set of linear transformations,  $[g(s)]: \mathbb{R} \rightarrow GL(\alpha, \beta)(3)$ . In particular, spherical motion define by  $[g(s)]: \mathbb{R} \rightarrow SO(\alpha, \beta)(3)$  and spatial motion define by  $[g(s)]: \mathbb{R} \rightarrow G - H(4)$  in generalized space  $E^3(\alpha, \beta)$ .

Generally, since elements  $s_{ij}$  of  $[g(s)]: \mathbb{R} \rightarrow GL(\alpha, \beta)(3)$  are continuous functions of a real parameter, derivative of this matrix function is the matrix of derivatives of its elements and defined by  $[\dot{g}(s)]$ . The tangent direction of the motion at  $[g(s_0)]$  defined by  $[\dot{g}(s_0)]$ .

The matrix function  $[g(s)]: \mathbb{R} \rightarrow GL(\alpha, \beta)(3)$  generates a continuous set of points

$$B(s) = [g(s)] \cdot b$$

is called the trajectory of  $b$ . The direction of the tangent to the trajectory  $B(s)$  at  $s = s_0$  is the derivative

$$\dot{B}(s_0) = [\dot{g}(s_0)] \cdot b = [\dot{g} \cdot g^{-1}(s_0)] \cdot B(s_0)$$

From the equation above we can see that  $[\dot{g} \cdot g^{-1}]$  calculates the derivative of  $\dot{B}(s)$  by using the the trajectory  $B(s)$ . Also, from the following equation, we can see that  $[\dot{g} \cdot g^{-1}]$  also computes the derivative of  $[g(s)]$ .

$$[\dot{g}(s)] = [\dot{g} \cdot g^{-1}] \cdot [g(s)].$$

**Definition 7:**  $[\dot{g} \cdot g^{-1}]$  matrix is called G-tangent operator on  $GL(\alpha, \beta)(3)$ . We now determine the motion

$[A(s)]$  that has a constant matrix  $[w]$  as its tangent operator. As the matrix  $[w]$  calculates the derivative  $[\dot{A}(s)]$  at every point  $[A(s)]$  we obtain the matrix differential equation

$$[\dot{A}(s)] = [w] \cdot [A(s)]$$

If the initial condition is  $[A(0)] = [A_0]$ , then it has the solution

$$[A(s)] = [A_0] \cdot e^{s[w]} = [A_0](I + s[w] + \frac{(s[w])^2}{2!} + \frac{(s[w])^3}{3!} + \dots).$$

The last equation has the initial condition  $[A(0)] = [I]$ , becomes simplified as

$$[R(t)] = e^{s[w]}.$$

Notice that in this case, the tangent operator  $[w]$  is the derivative of  $[A(s)]$  at  $[A(0)] = [I]$ . Thus, the set of tangent operators on  $GL(\alpha, \beta)(3)$  is identical to the tangent directions at the identity  $[I]$ .

If the set of tangent directions at the identity  $[A(0)] = [I]$  is  $[\dot{A}(0)]$  then,

$$[\dot{A}(0)] = [w] \cdot e^{s[w]} = [w] \cdot [A(s)]$$

$$[\dot{A}(0)] = [w] \cdot [A(0)] = [w].$$

Lie product is defined for the tangent operators  $[g]$  and  $[w]$  as  $[g] \wedge [w]$  is also tangent operator

$$[g] \wedge [w] = [g \cdot w - w \cdot g] \quad (3)$$

where  $g \cdot w$  denotes the matrix product in generalized space.

### The Tangent Operators of $SO(\alpha, \beta)(3)$

The condition defining the tangent operators of  $SO(\alpha, \beta)(3)$  is obtained from the relation  $[R^T \varepsilon R] = [\varepsilon]$  which must be satisfied by all rotation matrices in  $E^3(\alpha, \beta)$ . Differentiating both sides, we obtain

$$[\dot{R}^T \varepsilon R] + [R^T \varepsilon \dot{R}] = [0]$$

which can be written as

$$[R^T \varepsilon \dot{R}] = -[R^T \varepsilon \dot{R}]^T$$

the last equation shows that  $[R^T \varepsilon \dot{R}] = [\theta]$  is a skew-symmetric matrix that is called G-angular velocity matrix of the rotation  $[A(s)]$  in  $E^3(\alpha, \beta)$ . If we can calculate that  $[\dot{R}] = [R \varepsilon^{-1} \theta]$ , let  $[\varepsilon^{-1} \theta] = [\Phi]$ , then  $[\dot{R}] = [R] \cdot [\Phi]$ . Note that  $[\Phi]$  is a G-skew-symmetric matrix.

For a given matrix  $[\Phi]$  we obtain a one parameter group of rotations from the matrix differential equation

$$[\dot{R}(s)] = [R(s)] \cdot [\Phi]$$

the equation has solution



$$[R(s)] = e^{s[\Phi]}$$

so  $[R(s)] = e^{s[\Phi]} = \sum_{n=0}^{\infty} \frac{(s[\Phi])^n}{n!}$  note, we assume

$$[R(0)] = [I].$$

Let  $k = (c_1, c_2, c_3) \in E^3(\alpha, \beta)$  be vector corresponding to G-skew-symmetric matrix in  $E^3(\alpha, \beta)$ , then

$$[\Phi] = \begin{bmatrix} 0 & -\beta c_3 & \beta c_2 \\ \alpha c_3 & 0 & -\alpha c_1 \\ -c_2 & c_1 & 0. \end{bmatrix}$$

The norm of  $k = (c_1, c_2, c_3)$  is  $\|k\| = \sqrt{\alpha c_1^2 + \beta c_2^2 + \alpha \beta c_3^2}$ . We can obtain the unit vector in direction of  $\phi$  as  $t = \frac{k}{\phi} = (t_1, t_2, t_3)$ . Thus, we get  $\frac{[\Phi]}{\phi} = [T]$

$$[T] = \begin{bmatrix} 0 & -\beta t_3 & \beta t_2 \\ \alpha t_3 & 0 & -\alpha t_1 \\ -t_2 & t_1 & 0. \end{bmatrix}$$

$$[R(s)] = e^{(\phi s)[T]} = \sum_{n=0}^{\infty} \frac{((\phi s)[T])^n}{n!}$$

$$= I + \frac{(\phi s)[T]}{1!} + \frac{((\phi s)[T])^2}{2!} + \frac{((\phi s)[T])^3}{3!} + \frac{((\phi s)[T])^4}{4!} + \frac{((\phi s)[T])^5}{5!} + \frac{((\phi s)[T])^6}{6!} + \dots \tag{4}$$

$$= I + \frac{(\phi s)[T]}{1!} + \frac{(\phi s)^2[T^2]}{2!} + \frac{(\phi s)^3[T^3]}{3!} + \frac{(\phi s)^4[T^4]}{4!} + \frac{(\phi s)^5[T^5]}{5!} + \frac{(\phi s)^6[T^6]}{6!} + \dots$$

Let  $t = (t_1, t_2, t_3) \in E^3(\alpha, \beta)$  be unit vector corresponding to G-skew-symmetric matrix in  $E^3(\alpha, \beta)$ , then

$$[T] = \begin{bmatrix} 0 & -\beta t_3 & \beta t_2 \\ \alpha t_3 & 0 & -\alpha t_1 \\ -t_2 & t_1 & 0. \end{bmatrix}$$

We get  $[T^2]$  and  $[T^3]$  as;

$$[T^2] = \begin{bmatrix} -\beta t_2^2 - \alpha \beta t_3^2 & \beta t_1 t_2 & \alpha \beta t_1 t_3 \\ \alpha t_1 t_2 & -\alpha t_1^2 - \alpha \beta t_3^2 & \alpha \beta t_2 t_3 \\ \alpha t_1 t_3 & \beta t_2 t_3 & -\alpha t_1^2 - \beta t_2^2 \end{bmatrix}$$

and

$$[T^3] = \begin{bmatrix} 0 & \beta t_3(\alpha t_1^2 + \beta t_2^2 + \alpha \beta t_3^2) & -\beta t_2(\alpha t_1^2 + \beta t_2^2 + \alpha \beta t_3^2) \\ -\alpha t_3(\alpha t_1^2 + \beta t_2^2 + \alpha \beta t_3^2) & 0 & \alpha t_1(\alpha t_1^2 + \beta t_2^2 + \alpha \beta t_3^2) \\ t_2(\alpha t_1^2 + \beta t_2^2 + \alpha \beta t_3^2) & -t_1(\alpha t_1^2 + \beta t_2^2 + \alpha \beta t_3^2) & 0 \end{bmatrix}$$

**case 1:** Let  $\alpha > 0$  and  $\beta > 0$ . Since norm of unit vector  $t = (t_1, t_2, t_3)$  is  $\|t\| = 1$ , we have

$$[T^3] = -[T]$$

$$[T^4] = [T] \cdot [T^3] = -[T] \cdot [T] = -[T^2]$$

$$[T^5] = [T] \cdot [T^4] = -[T^3] = [T] \tag{5}$$

$$[T^6] = [T] \cdot [T^5] = [T] \cdot [T] = [T^2].$$

if we use eq. (5) in eq. (4), we obtain

$$[R(s)] = I + \frac{(\phi s)[T]}{1!} + \frac{(\phi s)^2[T^2]}{2!} - \frac{(\phi s)^3[T]}{3!} - \frac{(\phi s)^4[T^2]}{4!} + \frac{(\phi s)^5[T]}{5!} + \frac{(\phi s)^6[T^2]}{6!} + \dots$$

$$= I + \left(\frac{(\phi s)}{1!} - \frac{(\phi s)^3}{3!} + \frac{(\phi s)^5}{5!} - \dots\right)[T] + \left(\frac{(\phi s)^2}{2!} - \frac{(\phi s)^4}{4!} + \frac{(\phi s)^6}{6!} - \dots\right)[T^2]$$

$$= I + \left(\sum_{n=0}^{\infty} \frac{(-1)^n (\phi s)^{2n+1}}{(2n+1)!}\right)[T] + \left(1 - \sum_{n=0}^{\infty} \frac{(-1)^n (\phi s)^{2n}}{(2n)!}\right)[T^2]$$

$$[R(s)] = I + \sin(\phi s)[T] + (1 - \cos(\phi s))[T^2] \tag{6}.$$

**case 2:** Let  $\alpha > 0$  and  $\beta < 0$ . We should consider two subcases such that the unit vector  $t$  is a spacelike or timelike vector. If  $t$  is a spacelike, then we have the same result in case 1. If  $t$  is a timelike, then norm of the unit timelike vector is  $\|t\| = -1$ . Thus, we get

$$[T^3] = [T]$$

$$[T^4] = [T] \cdot [T^3] = [T] \cdot [T] = [T^2]$$

$$[T^5] = [T] \cdot [T^4] = [T^3] = [T] \tag{7}$$

$$[T^6] = [T] \cdot [T^5] = [T] \cdot [T] = [T^2].$$

if we use eq. (7) in eq. (4), we have

$$\begin{aligned} [R(s)] &= I + \frac{(\phi s)[T]}{1!} + \frac{(\phi s)^2[T^2]}{2!} + \frac{(\phi s)^3[T]}{3!} + \frac{(\phi s)^4[T^2]}{4!} + \frac{(\phi s)^5[T]}{5!} + \frac{(\phi s)^6[T^2]}{6!} + \dots \\ &= I + \left(\frac{(\phi s)}{1!} + \frac{(\phi s)^3}{3!} + \frac{(\phi s)^5}{5!} + \dots\right)[T] + \left(\frac{(\phi s)^2}{2!} + \frac{(\phi s)^4}{4!} + \frac{(\phi s)^6}{6!} + \dots\right)[T^2] \\ &= I + \left(\sum_{n=0}^{\infty} \frac{(\phi s)^{2n+1}}{(2n+1)!}\right)[T] + \left(\sum_{n=0}^{\infty} \frac{(\phi s)^{2n}}{(2n)!} - 1\right)[T^2] \end{aligned}$$

$$[R(s)] = I + \sinh(\phi s)[T] + (\cosh(\phi s) - 1)[T^2] \tag{8}.$$

**Example 1:** Let G-skew symmetric matrix  $C$  given as;

$$C = \begin{bmatrix} 0 & 0 & \beta t \\ 0 & 0 & 0 \\ -t & 0 & 0 \end{bmatrix}$$

We can obtain G-orthogonal matrix  $R$  from the matrix  $C$  using by G-Cayley formula as

$$R = (I - C)^{-1}(I + C) = \frac{1}{1 + \beta t^2} \begin{bmatrix} 1 - \beta t^2 & 0 & 2\beta t \\ 0 & 1 + \beta t^2 & 0 \\ -2t & 0 & 1 - \beta t^2 \end{bmatrix}$$

Let  $\cos\theta = \frac{1 - \beta t^2}{1 + \beta t^2}$  and  $\sin\theta = \frac{2\sqrt{\beta}t}{1 + \beta t^2}$ , then

$$R = \begin{bmatrix} \cos\theta & 0 & \sqrt{\beta}\sin\theta \\ 0 & 1 & 0 \\ -\frac{\sin\theta}{\sqrt{\beta}} & 0 & \cos\theta \end{bmatrix}$$

we see that  $R$  is a G-orthogonal matrix that it is the  $\theta$  –degree rotation about  $y$  –axis in  $E^3(\alpha, \beta)$  space. If we calculate  $[\theta] = [R^T \varepsilon \dot{R}]$

$$[\theta] = [R^T \varepsilon \dot{R}] = \begin{bmatrix} \frac{1 - \beta t^2}{1 + \beta t^2} & 0 & -\frac{2t}{1 + \beta t^2} \\ 0 & 1 & 0 \\ \frac{2\beta t}{1 + \beta t^2} & 0 & \frac{1 - \beta t^2}{1 + \beta t^2} \end{bmatrix} \begin{bmatrix} \alpha & 0 & 0 \\ 0 & \beta & 0 \\ 0 & 0 & \alpha\beta \end{bmatrix} \begin{bmatrix} -\frac{4\beta t}{(1 + \beta t^2)^2} & 0 & \frac{2\beta - 2\beta^2 t^2}{(1 + \beta t^2)^2} \\ 0 & 0 & 0 \\ \frac{-2 + 2\beta t^2}{(1 + \beta t^2)^2} & 0 & -\frac{4\beta t}{(1 + \beta t^2)^2} \end{bmatrix}$$

we get the tangent operator of  $R(t)$ ;

$$[\theta] = \begin{bmatrix} 0 & 0 & \frac{2\alpha\beta}{(1 + \beta t^2)^2} \\ 0 & 0 & 0 \\ -\frac{2\alpha\beta}{(1 + \beta t^2)^2} & 0 & 0 \end{bmatrix}.$$

**Example 2:** Let  $\alpha > 0$  and  $\beta < 0$ . The G-skew symmetric matrix  $C$  corresponding to the vector  $c = (0, 3, 0)$ ;

$$C = \begin{bmatrix} 0 & 0 & 3\beta \\ 0 & 0 & 0 \\ 3 & 0 & 0 \end{bmatrix}$$

The norm of  $c = (0, 3, 0)$  is  $\|c\| = 3\sqrt{-\beta}$ . The unit vector in direction of  $c$  is  $t = \frac{c}{3\sqrt{-\beta}} = (0, \frac{1}{\sqrt{-\beta}}, 0)$ . So G-skew symmetric matrix  $T$  corresponding to the vector  $s$ ;

$$T = \begin{bmatrix} 0 & 0 & \sqrt{-\beta} \\ 0 & 0 & 0 \\ -\frac{1}{\sqrt{-\beta}} & 0 & 0 \end{bmatrix}$$

We can obtain the rotation matrix  $R$  from eq. (7)

$$\begin{aligned} R &= I + \sinh(3\sqrt{-\beta}t)[S] + (\cosh(3\sqrt{-\beta}t) - 1)[S^2] \\ &= \begin{bmatrix} \cosh(3\sqrt{-\beta}t) & 0 & \sqrt{-\beta}\sinh(3\sqrt{-\beta}t) \\ 0 & 1 & 0 \\ \frac{\sinh(3\sqrt{-\beta}t)}{\sqrt{-\beta}} & 0 & \cosh(3\sqrt{-\beta}t) \end{bmatrix} \end{aligned}$$

### The Tangent Operators of $G - H(4)$

In this chapter, we study the operations of rotation and translation and introduce the notion of homogeneous transformations.

The tangent operators of  $G - H(4)$  must satisfy the relation

$$\begin{aligned} [\dot{g} \cdot g^{-1}] &= \begin{bmatrix} \dot{R} & \dot{t} \\ 0 & 0 \end{bmatrix} \begin{bmatrix} R^{-1} & -R^{-1} \cdot t \\ 0 & 1 \end{bmatrix} \\ &= \begin{bmatrix} \dot{R}R^{-1} & -\dot{R} \cdot R^{-1} \cdot t + \dot{t} \\ 0 & 0 \end{bmatrix} \end{aligned}$$

or

$$[\dot{g} \cdot g^{-1}] = \begin{bmatrix} \Omega & v \\ 0 & 0 \end{bmatrix} = [\Omega, v]$$

where  $[\Omega] = [\dot{R}R^{-1}]$  is the  $3 \times 3$  G-angular velocity matrix of the moving body and  $v = -[R] \cdot t + \dot{t}$  is its 3-dimensional G-linear velocity vector.

Let us consider a special case of the equation  $[\dot{g}(s) \cdot g^{-1}(s)] = [B(s)]$  when the  $[B(s)]$  is a constant matrix. Thus, the one parameter subgroup of  $G - H(4)$  can be obtained from ordinary differential equation

$$[\dot{g}(s)] = [B] \cdot [g(s)] \tag{9}$$

where  $[B] = [A, s]$ . Let us consider a special case of the eq. (9) when the  $[B]$  is a constant matrix. Assuming that a fixed frame and a moving frame coincide at the moment  $t = 0$ , so  $[g(0)] = [I]$ . We may conclude that:

$$[g(s)] = e^{s[B]}.$$

We can decompose G-linear velocity vector  $v$  into components. Let  $c$  be a point on the G-screw axis, then  $v^\perp = c \wedge w$  and  $kw = v - v^\perp$  perpendicular and G-angular velocity vector  $w$ , respectively.

We consider the case  $v^\perp = 0$ , then  $v = pw$ . Since  $[\Omega] \cdot w = 0$ , we have

$$[B^2] = \begin{bmatrix} \Omega^2 & 0 \\ 0 & 0 \end{bmatrix}$$

therefore,

$$[g(s)] = e^{s[B]} = \begin{bmatrix} e^{s[\Omega]} & pws \\ 0 & 1 \end{bmatrix} = \begin{bmatrix} R(s) & pws \\ 0 & 1 \end{bmatrix}$$

where  $[R(s)]$  is the rotation matrix.

### Vector Associated with Tangent Operators

The tangent operator of  $SO(\alpha, \beta)(3)$  is  $3 \times 3$  G-skew symmetric matrix has only three independent elements of nine elements, likewise, the tangent operator of  $G - H(4)$  is  $4 \times 4$  has only six independent elements of sixteen elements.

**Definition 8:** The components of a tangent operator of  $[R] = [\Psi, v]$  are assembled into the 6 –dimensional vector  $R = (\psi, v)$ , called a screw.

Lie product defined in eq. (3) provides a product operation for the vectors associated with each of these tangent operators. For  $SO(\alpha, \beta)(3)$ ,  $\psi$  and  $\phi$  are corresponding vectors of the G-skew symmetric matrices  $[\Psi]$  and  $[\Phi]$ , then we find that vectors corresponding vectors the G-skew symmetric matrices obtained from the Lie product

$$[\Psi] \wedge [\Phi] = [\Psi \cdot \phi - \phi \cdot \Psi]$$

is  $\psi \times_G \phi$ .

For homogeneous transformation  $G - H(4)$ , Lie product of the tangent operators  $[R] = [\Psi, r]$  and  $[S] = [\Phi, s]$  is defined by

$$\begin{aligned} [R] \wedge [S] &= [R \cdot S - S \cdot R] \\ &= [\Psi, r][\Phi, s] - [\Phi, s][\Psi, r] \\ &= [\Psi \cdot \phi - \phi \cdot \Psi, [\Psi] \cdot s - [\Phi] \cdot r] \\ &= (\psi \wedge \phi, \psi \wedge s - \phi \wedge r), \end{aligned}$$

where  $[R]$  and  $[S]$  as follow respectively;

$$[R] = \begin{bmatrix} 0 & -\beta\psi_3 & \beta\psi_2 & r_1 \\ \alpha\psi_3 & 0 & -\alpha\psi_1 & r_2 \\ -\psi_2 & \psi_1 & 0 & r_3 \\ 0 & 0 & 0 & 0 \end{bmatrix} \text{ and } [S] = \begin{bmatrix} 0 & -\beta\phi_3 & \beta\phi_2 & s_1 \\ \alpha\phi_3 & 0 & -\alpha\phi_1 & s_2 \\ -\phi_2 & \phi_1 & 0 & s_3 \\ 0 & 0 & 0 & 0 \end{bmatrix}.$$

### Multi-Parameter Motion in Generalized Space

The matrix function  $[g(s)]: \mathbb{R} \rightarrow GL(\alpha, \beta)(3)$  defines a motion of a body that is parameterized by a single variable, we now consider the motions parameterized by  $n$  variables  $\theta = (\theta_1, \dots, \theta_n)$ , denoted  $[F(\theta)]: \mathbb{R}^n \rightarrow GL(\alpha, \beta)(3)$ .

The partial derivative of  $[F(\theta)] = [f_1(\theta_1, \dots, \theta_n), f_2(\theta_1, \dots, \theta_n), f_3(\theta_1, \dots, \theta_n)]$  with respect to a variable  $\theta_i$  is the  $3 \times n$  matrix

$$\left[ \frac{\partial F}{\partial \theta_i} \right] = \left[ \frac{\partial f_1}{\partial \theta_i}, \frac{\partial f_2}{\partial \theta_i}, \frac{\partial f_3}{\partial \theta_i} \right].$$

If the variables  $\theta_i$  are functions of a variable  $\iota$ , that  $\theta = \theta(\iota)$ , then the chain rule the partial derivatives  $\frac{\partial F}{\partial \theta_i}$  to the derivative

$\left[ \dot{F} \right]$  by the relation

$$\left[ \dot{F} \right] = \left[ \frac{\partial F}{\partial \theta_1} \right] \dot{\theta}_1 + \dots + \left[ \frac{\partial F}{\partial \theta_n} \right] \dot{\theta}_n.$$

Multiplying on the right by  $[F^T \varepsilon]$ , we obtain the tangent operator

$$[F^T \varepsilon \dot{F}] = \left[ F^T \varepsilon \frac{\partial F}{\partial \theta_1} \right] \dot{\theta}_1 + \dots + \left[ F^T \varepsilon \frac{\partial F}{\partial \theta_n} \right] \dot{\theta}_n.$$

The matrices  $\left[ F^T \varepsilon \dot{F} \right]$  are partial tangent operators associated with each of the parameters  $\theta_i$ , individually.

Now, let's obtain the tangent operator of two parameters motion.

**Example 3:** Let G-skew symmetric matrix  $C$  given as

$$C = \begin{bmatrix} 0 & 0 & \beta t \\ 0 & 0 & -\alpha s \\ -t & s & 0 \end{bmatrix}$$

We can obtain rotation matrix  $R$  from the matrix  $C$  using by G-Cayley formula as,

$$R = (I + C)(I + C)^{-1} = \frac{1}{1 + \alpha s^2 + \beta t^2} \begin{bmatrix} 1 + \alpha s^2 - \beta t^2 & 2\beta st & 2\beta t \\ 2\alpha st & 1 - \alpha s^2 - \beta t^2 & 0 \\ -2t & 0 & 1 - \alpha s^2 - \beta t^2 \end{bmatrix}$$

The derivatives of the rotation matrix  $[R]$  with respect to  $t$  and  $s$ , respectively;

$$\frac{\partial F}{\partial t} = \begin{bmatrix} \frac{-4\beta t(1 + \alpha s^2)}{(1 + \alpha s^2 + \beta t^2)^2} & \frac{2\beta s(1 + \alpha s^2 - \beta t^2)}{(1 + \alpha s^2 + \beta t^2)^2} & \frac{2\beta(1 + \alpha s^2 - \beta t^2)}{(1 + \alpha s^2 + \beta t^2)^2} \\ \frac{2\alpha s(1 + \alpha s^2 - \beta t^2)}{(1 + \alpha s^2 + \beta t^2)^2} & \frac{4\alpha\beta s^2 t}{(1 + \alpha s^2 + \beta t^2)^2} & \frac{4\alpha\beta st}{(1 + \alpha s^2 + \beta t^2)^2} \\ \frac{-2(1 + \alpha s^2 - \beta t^2)}{(1 + \alpha s^2 + \beta t^2)^2} & \frac{-4\beta st}{(1 + \alpha s^2 + \beta t^2)^2} & \frac{-4\beta t}{(1 + \alpha s^2 + \beta t^2)^2} \end{bmatrix}$$

and

$$\frac{\partial F}{\partial s} = \begin{bmatrix} \frac{4\alpha\beta st^2}{(1 + \alpha s^2 + \beta t^2)^2} & \frac{2\beta t(1 - \alpha s^2 + \beta t^2)}{(1 + \alpha s^2 + \beta t^2)^2} & \frac{-4\alpha\beta st}{(1 + \alpha s^2 + \beta t^2)^2} \\ \frac{2\alpha t(1 - \alpha s^2 + \beta t^2)}{(1 + \alpha s^2 + \beta t^2)^2} & \frac{-4\alpha s(1 + \beta t^2)}{(1 + \alpha s^2 + \beta t^2)^2} & \frac{-2\alpha(1 - \alpha s^2 + \beta t^2)}{(1 + \alpha s^2 + \beta t^2)^2} \\ \frac{4\alpha st}{(1 + \alpha s^2 + \beta t^2)^2} & \frac{2(1 - \alpha s^2 + \beta t^2)}{(1 + \alpha s^2 + \beta t^2)^2} & \frac{-4\alpha s}{(1 + \alpha s^2 + \beta t^2)^2} \end{bmatrix}$$

If we calculate components of the tangent operator;

$$[\Phi]_t = \left[ R^T \varepsilon \frac{\partial R}{\partial t} \right] = \begin{bmatrix} 0 & \frac{2\alpha\beta s}{1 + \alpha s^2 + \beta t^2} & \frac{2\alpha\beta}{1 + \alpha s^2 + \beta t^2} \\ \frac{-2\alpha\beta s}{1 + \alpha s^2 + \beta t^2} & 0 & 0 \\ \frac{-2\alpha\beta}{1 + \alpha s^2 + \beta t^2} & 0 & 0 \end{bmatrix}$$

and

$$[\Phi]_s = \left[ R^T \varepsilon \frac{\partial R}{\partial s} \right] = \begin{bmatrix} 0 & \frac{-2\alpha\beta t}{1 + \alpha s^2 + \beta t^2} & 0 \\ \frac{2\alpha\beta t}{1 + \alpha s^2 + \beta t^2} & 0 & \frac{-2\alpha\beta}{1 + \alpha s^2 + \beta t^2} \\ 0 & \frac{2\alpha\beta}{1 + \alpha s^2 + \beta t^2} & 0 \end{bmatrix}$$

we get the tangent operator of the two parameters motion as;

$$[R^T \varepsilon F] = \left[ R^T \varepsilon \frac{\partial R}{\partial t} \right] \frac{\partial}{\partial t} + \left[ R^T \varepsilon \frac{\partial R}{\partial s} \right] \frac{\partial}{\partial s}.$$

## Conclusion

Since the solutions obtained for generalized space cover both Lorentzian and Euclidean spaces, it is an undeniable fact that the results obtained in generalized space are valid in both spaces. Therefore, the data obtained as a result of the situations examined within the scope of this study provide the necessary conditions for both spaces. It is important in terms

of enabling researchers to perform calculations in generalized space and then go to specific instead of making separate calculations for two different spaces. The generalization of the space studied in this study to  $n$  dimensions is also foreseen as an advanced research topic.

## Conflicts of interest

The author state that did not have conflict of interests.

## References

- [1] Awrejcewicz J., Classical Mechanics; Kinematics and Statics, New York: Springer, (2012).
- [2] Agrawal O.P., Hamilton Operators and Dual-number-quaternions in Spatial Kinematics, *Mech Mach Theory*, 22 (1987) 569-575.
- [3] Beggs J.S., Advanced Mechanisms, New York: The Macmillan Company Collier-Macmillan, London (1965).
- [4] Herve J.M., The mathematical group structure of the set of displacements, *Mech. Mach. Theory*, 29 (1994) 73-81.
- [5] Hiller M., Woernle C., A Unified Representation of Spatial Displacements, *Mech. Mach. Theory*, 19(1984) 477-486.
- [6] Spong M.W., Hutchison S., Vidyasagar M., Robot Modeling and Control. Hoboken: NJ John Wiley & Sons, (2006).
- [7] Altmann S.L., Rotations, Quaternions and Double Groups. Oxford: Oxford University Press, (1986).
- [8] Aragon G., Aragon J.L., Rodriguez M.A., Clifford Algebras and Geometric Algebra, *Adv Appl Clifford Al.*, 7(2) (1997) 91-102.
- [9] Rosenfeld B., Geometry of Lie Groups. Dordrecht: Kluwer Academic Publishers, (1997).
- [10] Uicker J.J., Pennock G.R., Shigley J., Theory of Machines and Mechanisms. New York: Oxford University Press, (2011).
- [11] Bottema O., Roth, B., Theoretical Kinematics. New York: North-Holland Press, (1979).
- [12] McCarthy J.M., An Introduction to Theoretical Kinematics. Cambridge: MIT Press, (1990).
- [13] O'Neill B., Semi-Riemannian Geometry With Applications to Relativity. New York: Academic Press Inc., (1983).
- [14] Ryan P.J., Euclidean and non-Euclidean geometry; an analytic approach. Cambridge, New York: Cambridge Univ. Press, (1986).
- [15] Ata E., Yıldırım Y.A., Different Polar Representation for Generalized and Generalized Dual Quaternions, *Adv Appl Clifford Al.*, 28 (2010) 193-202.
- [16] Ata E., Savcı Ü.Z., Spherical Kinematics in 3-Dimensional Generalized Space *Int J Geom Meth Mod Phys.*, 18(3) (2020) 2150033.
- [17] Erdmann K., Skowronski A., Algebras of generalized quaternion type, *Advances in Mathematics*, 349 (2019) 1036-1116.
- [18] Jafari M., Yaylı Y., Generalized Quaternions and Rotation in 3-Space  $E^3_{\alpha\beta}$ , *TWMS J. Pure Appl. Math.*, 6(2) (2015) 224-232.
- [19] Lam T.Y., Introduction to Quadratic Forms Over Fields, *American Mathematical Society*, USA (2005).
- [20] Pottman H., Wallner J., Computational line geometry. Berlin Heidelberg, New York: Springer-Verlag, (2000).
- [21] Savcı Ü.Z., Generalized Dual Quaternions and Screw Motion in Generalized Space, *Konuralp Journal of Mathematics*, 10 (1) (2022) 197-202.
- [22] Parkin I.A., A third conformation with the screw systems: finite twist displacements of a directed line and point, *Mech. Mach. Theory*, 27(2) (1992) 177- 188.
- [23] Huang C., Roth B., Analytic expressions for the finite screw systems, *Mech. Mach. Theory*, 29(2) (1994) 207-222.
- [24] Knossow D., Ronfard R., Horaud R., Human motion tracking with a kinematic parameterization of extremal contours, *International Journal of Computer Vision*, 79 (2008) 247-269.
- [25] Durmaz O., Aktaş B., Gündogan H., The derivative and tangent operators of a motion in Lorentzian space, *Int. J. Geom. Meth. Mod. Phys.*, 14(4) (2017) 1750058.
- [26] Ward J.P., Quaternions and Cayley numbers algebra and applications. London: Kluwer Academic Publishers, (1997).

## Singularities of the Ruled Surfaces According to RM Frame and Natural Lift Curves

Emel Karaca <sup>1,a,\*</sup><sup>1</sup> Department of Mathematics, Polatlı Faculty of Science and Arts, Ankara Hacı Bayram Veli University, Ankara, Türkiye.

\*Corresponding author

### Research Article

#### History

Received: 13/01/2022



Accepted: 05/05/2022

#### Copyright

©2022 Faculty of Science,  
Sivas Cumhuriyet University

### ABSTRACT

In this study, the ruled surface generated by the natural lift curve in  $\mathbb{R}^3$  is obtained by using the isomorphism between unit dual sphere,  $DS^2$  and the subset of the tangent bundle of unit 2-sphere,  $\overline{TM}$ . Then, exploiting E. Study mapping and the isomorphism mentioned below, each natural lift curve on  $\overline{TM}$  corresponds the ruled surface in  $\mathbb{R}^3$ . Moreover, the singularities of this ruled surface are examined according to RM vectors and these ruled surfaces have been classified. Some examples are given to support the main results.

**Keywords:** Ruled surface, Dual space, Natural lift curve, RM vectors. [emel.karaca@hbv.edu.tr](mailto:emel.karaca@hbv.edu.tr) <https://orcid.org/0000-0003-0703-939X>

### Introduction

In geometry, there are many orthonormal frames such as Frenet, Bishop, RM frames, etc. for investigating the geometric structures of curves and surfaces, [1-4]. These frames describe the kinematic properties of a particle moving along a continuous, differentiable curve in Euclidean space. Furthermore, they have several advantages and application areas in differential geometry, engineering, surface modeling, etc. For example, due to minimal twist, the rotation minimizing frame (RMF) is extensively used in computer graphics, surface modeling, motion design and control in computer animation and robotics, streamline visualization, and tool path planning in CAD/CAM, [5-7].

The theory of curves is a significant subject in differential geometry. Considering the relation among Frenet vectors, some special curves such as natural lift curve, some curve couples like Bertrand, Mannheim, Involute-evolute pairs, etc. have attracted many mathematicians in literature. Among these special curves, the well-known curve, which is called the natural lift curve, has firstly been encountered in J. A. Thorpe's book, [8]. In this book, the natural lift curve is defined as a curve obtained by the endpoints of the unit tangent vectors of the given curve. Taking into consideration the definition of the natural lift curve, the fundamental properties of this curve is examined in [9]. Then, the Frenet vector fields of the natural lift curve are calculated in [10]. Moreover, Frenet operators of the natural lift curve are calculated by using the Frenet operators of the main curve in detail.

In addition to the theory of curves, the surface theory is an important subject in differential geometry. There are several special surfaces such as minimal surfaces, ruled surfaces, parallel surfaces, circular surfaces, etc. One of the well-known surfaces is the ruled surface which consists the union of one parametric family of lines. The

lines of this family are called the generators of the ruled surface. In literature, the properties of these surfaces have been studied in different spaces, [11-15]. Moreover, by using the theorems and definitions of dual space in [16], the isomorphism among unit dual sphere, the tangent bundle of unit 2-sphere, and non-cylindrical ruled surfaces are investigated in [17]. In the light of this study, a one-to-one correspondence between and is mentioned in [18]. In that study, according to E. Study mapping, to each curve on corresponds a ruled surface in Euclidean 3-space, Furthermore, exploiting this relation, each curve on corresponds a ruled surface in Then, inspired by [18], the isomorphism among , the subset of the tangent bundle of unit 2-sphere, and the ruled surface generated by natural lift curves in are examined in [19]. Furthermore, the developability condition of this ruled surface is given in the same study.

The problem of singularities for surfaces has attracted many mathematicians such as [20-22] in literature. In [21], basic notations and properties of space curves have been described. Also, the classification of singularities of the rectifying developable and the Darboux developable of a space curve are reviewed in detail. In [22], Legendre curves in unit tangent bundle by using rotation minimizing vector fields have been investigated. Then, ruled surfaces corresponding to these curves are specified. Additionally, the singularities of these ruled surfaces have been analyzed and classified.

In literature, there has not been any research about the singularities of the ruled surface generated by the natural lift curve according to RM frame. In order to fill this gap, this study is organized as follows: In Section 2, the properties of natural lift curves and RM vector fields are denoted. In Section 3, the isomorphism among , the subset of the tangent bundle of unit 2-sphere, and the

ruled surface generated by natural lift curves in is examined in detail. Furthermore, the singularities of the ruled surfaces generated by the natural lift curves according to RM vectors are mentioned. Some examples are given to illustrate the main theorems. In Section 4, the obtained results are discussed.

### Natural Lift Curves and RM Vector Fields

In this section, we recall some basic definitions and theorems about the tangent bundle of unit 2-sphere and properties of the natural lift curve of the given curve. Moreover, the difference between the Frenet frame and RM frame of natural lift curve has been mentioned.

Assume that  $S^2$  is the unit 2-sphere in  $\mathbb{R}^3$ . The tangent bundle of  $S^2$  is denoted as

$$TS^2 = \{(\gamma, \nu) \in \mathbb{R}^3 \times \mathbb{R}^3 : |\gamma| = 1, \langle \gamma, \nu \rangle = 0\}, \tag{1}$$

where " $\langle \cdot, \cdot \rangle$ " is the inner product and " $|\cdot|$ " is the norm in  $\mathbb{R}^3$ , respectively, [18]. Also, the unit tangent bundle of  $S^2$  is

$$UTS^2 = \{(\gamma, \nu) \in \mathbb{R}^3 \times \mathbb{R}^3 : |\gamma| = |\nu| = 1, \langle \gamma, \nu \rangle = 0\}. \tag{2}$$

Let  $T\bar{M}$  be a subset of  $TS^2$ , defined by

$$T\bar{M} = \{(\bar{\gamma}, \bar{\nu}) \in \mathbb{R}^3 \times \mathbb{R}^3 : |\bar{\gamma}| = 1, \langle \bar{\gamma}, \bar{\nu} \rangle = 0\}, \tag{3}$$

where  $\bar{\gamma}$  and  $\bar{\nu}$  represent the derivatives of  $\gamma$  and  $\nu$ , respectively, [19]. Moreover,

$$UT\bar{M} = \{(\bar{\gamma}, \bar{\nu}) \in \mathbb{R}^3 \times \mathbb{R}^3 : |\bar{\gamma}| = |\bar{\nu}| = 1, \langle \bar{\gamma}, \bar{\nu} \rangle = 0\}. \tag{4}$$

**Definition 1** For the curve  $\gamma$ ,  $\bar{\gamma}$  is called the natural lift of  $\gamma$  on  $T\bar{M}$ , which produces in the following equation, [19]:

$$\bar{\Gamma}(s) = (\bar{\gamma}(s), \bar{\nu}(s)) = (\gamma'(s)|_{\Gamma(s)}, \nu'(s)|_{\nu(s)}). \tag{5}$$

Accordingly, we can write

$$\frac{d\bar{\Gamma}(s)}{ds} = \frac{d}{ds}(\Gamma'(s)|_{\Gamma(s)}) = D_{\Gamma'(s)}\Gamma'(s).$$

Here,  $D$  refers the Levi-Civita connection in  $\mathbb{R}^3$ . We have

$$T\bar{M} = \bigcup_{p \in \bar{M}} T_p\bar{M},$$

where  $T_p\bar{M}$  is the tangent space of  $\bar{M}$  at  $p$ , [9].

Additionally, the Frenet formulas along the natural lift curve  $\bar{\Gamma}(s)$  are

$$\begin{pmatrix} \nabla_{\bar{T}}\bar{T}(s) \\ \nabla_{\bar{N}}\bar{N}(s) \\ \nabla_{\bar{B}}\bar{B}(s) \end{pmatrix} = \begin{pmatrix} 0 & 1 & 0 \\ \bar{\kappa}(s)/|\bar{W}(s)| & 0 & \bar{\tau}(s)/|\bar{W}(s)| \\ \bar{\tau}(s)/|\bar{W}(s)| & 0 & \bar{\kappa}(s)/|\bar{W}(s)| \end{pmatrix} \begin{pmatrix} \bar{T}(s) \\ \bar{N}(s) \\ \bar{B}(s) \end{pmatrix},$$

where  $\bar{W}(s)$  is Darboux vector field of the mean curve  $\Gamma(s)$  in [10].

Assume that  $\bar{\gamma}$  is a smooth curve in  $(M, g)$ . A normal vector field  $\bar{N}$  over  $\bar{\gamma}$  is called a rotation minimizing vector field (in short, RM vector field) if it is parallel with respect to the normal connection of  $\bar{\gamma}$ . That is,  $\nabla_{\bar{\gamma}}\bar{N}$  and  $\bar{\gamma}'$  are proportional.

The orthonormal frame which consists of the tangent vectors  $\bar{T}$  and two normal vector fields  $\bar{N}_1$  and  $\bar{N}_2$  is called RM frame along a curve  $\bar{\gamma} = \bar{\gamma}(s)$ . The Frenet type equations are defined as

$$\begin{pmatrix} \nabla_{\bar{T}}\bar{T}(s) \\ \nabla_{\bar{T}}\bar{N}_1(s) \\ \nabla_{\bar{T}}\bar{N}_2(s) \end{pmatrix} = \begin{pmatrix} 0 & \bar{\kappa}_1(s) & \bar{\kappa}_2(s) \\ -\bar{\kappa}_1(s) & 0 & 0 \\ -\bar{\kappa}_2(s) & 0 & 0 \end{pmatrix} \begin{pmatrix} \bar{T}(s) \\ \bar{N}_1(s) \\ \bar{N}_2(s) \end{pmatrix}.$$

Here,  $\bar{\kappa}_1(s)$  and  $\bar{\kappa}_2(s)$  are called natural curvatures of RM frame which provide the following equations given below, [22]:

$$\bar{\kappa}(s) = \sqrt{\bar{\kappa}_1^2(s) + \bar{\kappa}_2^2(s)}$$

and

$$\bar{\tau}(s) = \theta'(s) = \frac{\bar{\kappa}_1(s)\bar{\kappa}_2'(s) - \bar{\kappa}_1'(s)\bar{\kappa}_2(s)}{\bar{\kappa}_1^2(s) + \bar{\kappa}_2^2(s)}.$$

Here,  $\theta(s) = \arg(\bar{\kappa}_1(s), \bar{\kappa}_2(s)) = \arctan(\frac{\bar{\kappa}_2(s)}{\bar{\kappa}_1(s)})$ .  $\theta'$  denotes

the derivative of  $\theta$  according to arc-length parameter  $s$ , [22]. Furthermore, the following theorem is denoted:

**Theorem 1** Let  $\bar{\gamma} : I \subseteq \mathbb{R} \rightarrow S^2$  be a regular smooth curve with the Frenet apparatus  $\{\bar{T}, \bar{N}, \bar{B}, \bar{\kappa}, \bar{\tau}\}$ . The following assumptions are satisfied:

(i) If  $\bar{T}(s)$  and  $\bar{N}_1(s)$  are RM vector fields of the curve  $\bar{\gamma}$ , the curve  $\bar{\Gamma}(s) = (\bar{T}(s), \bar{N}_1(s))$  is natural lift  $\bar{\gamma}$  on  $T\bar{M}$



(ii) If  $\bar{T}(s)$  and  $\bar{N}_2(s)$  are RM vector fields of the curve  $\bar{\gamma}$ , the curve  $\bar{\Gamma}(s) = (\bar{T}(s), \bar{N}_2(s))$  is natural lift curve on  $T\bar{M}$ . **Proof.** Using the definition of natural lift curve, the proof can be easily seen.

From the definition of  $UT\bar{M}$ , we may introduce the new frame satisfying  $\bar{\mu}(s) = \bar{\nu}(s) \times \bar{v}(s)$ . It can be simply seen that  $\langle \bar{\nu}(s), \bar{v}(s) \rangle = \langle \bar{\nu}(s), \bar{\mu}(s) \rangle = 0$ . Moreover, the Frenet frame along  $\bar{\gamma}(s)$  can be expressed as

$$\begin{pmatrix} \bar{\nu}'(s) \\ \bar{v}'(s) \\ \bar{\mu}'(s) \end{pmatrix} = \begin{pmatrix} 0 & \bar{l}(s) & \bar{m}(s) \\ -\bar{l}(s) & 0 & \bar{n}(s) \\ -\bar{m}(s) & -\bar{n}(s) & 0 \end{pmatrix} \begin{pmatrix} \bar{\nu}(s) \\ \bar{v}(s) \\ \bar{\mu}(s) \end{pmatrix},$$

where

$$\begin{aligned} \bar{l}(s) &= \langle \bar{\nu}'(s), \bar{v}(s) \rangle, \bar{m}(s) = \langle \bar{\nu}'(s), \bar{\mu}(s) \rangle \text{ and} \\ \bar{n}(s) &= \langle \bar{v}'(s), \bar{\mu}(s) \rangle \text{ are curvature functions of } \bar{\Gamma}(s). \end{aligned}$$

**Theorem 2** Let  $\bar{\Gamma}(s) = (\bar{\nu}(s), \bar{v}(s))$  be the natural lift curve on  $T\bar{M}$ . If  $\bar{l}(s) = 0$ , the vectors  $(\bar{\nu}(s), \bar{v}(s))$  are the RM vector fields of the  $\bar{\mu}$ -direction curve  $\bar{\beta}$  (i.e.,  $\bar{\beta}(s) = \int \bar{\mu}(s) ds$ ), the set  $\{\bar{\nu}, \bar{v}, \bar{\mu}\}$  is RM frame.

**Proof.** Let  $\bar{\Gamma}(s) = (\bar{\nu}(s), \bar{v}(s))$  be the natural lift curve on  $T\bar{M}$ . If  $\bar{l}(s) = 0$ , we write

$$\begin{pmatrix} \bar{\mu}'(s) \\ \bar{\nu}'(s) \\ \bar{v}'(s) \end{pmatrix} = \begin{pmatrix} 0 & -\bar{m}(s) & -\bar{n}(s) \\ \bar{m}(s) & 0 & 0 \\ \bar{n}(s) & 0 & 0 \end{pmatrix} \begin{pmatrix} \bar{\mu}(s) \\ \bar{\nu}(s) \\ \bar{v}(s) \end{pmatrix}.$$

Hence, we conclude that  $\{\bar{\nu}(s), \bar{v}(s), \bar{\mu}(s)\}$  is RM frame along the natural lift curve  $\bar{\Gamma}$ . The proof is completed.

### Natural Lift Curves and Singularities of the Ruled Surfaces According to RM Frame

In this section, firstly, we mention the isomorphism among the subset of tangent bundle of unit 2-sphere,  $T\bar{M}$ , unit dual sphere,  $DS^2$  and the ruled surface in  $\mathbb{R}^3$ . Secondly, exploiting this isomorphism, we examine the singularities of two ruled surfaces, which are obtained by natural lift curves, according to RM frame. Thirdly, some examples are given to support the main results.

The set of dual numbers is defined as

$$ID = \{X = x + \epsilon x^* : (x, x^*) \in \mathbb{R} \times \mathbb{R}, \epsilon^2 = 0\}.$$

The combination of  $\bar{x}$  and  $\bar{x}^*$  is called dual vectors in  $\mathbb{R}^3$ . These vectors are real part and dual part of  $\bar{X}$ , respectively. If  $\bar{x}$  and  $\bar{x}^*$  are vectors in  $\mathbb{R}^3$ , then  $\bar{X} = \bar{x} + \epsilon \bar{x}^*$  is defined as dual vector. Assume that  $\bar{X} = \bar{x} + \epsilon \bar{x}^*$  and  $\bar{Y} = \bar{y} + \epsilon \bar{y}^*$  are dual vectors. The addition, inner product and vector product are presented as follows:

The addition is

$$\bar{X} + \bar{Y} = (\bar{x} + \bar{y}) + \epsilon(\bar{x}^* + \bar{y}^*)$$

and their inner product is

$$\langle \bar{X}, \bar{Y} \rangle = \langle \bar{x}, \bar{y} \rangle + \epsilon(\langle \bar{x}^*, \bar{y} \rangle + \langle \bar{x}, \bar{y}^* \rangle).$$

Also, the vector product is given as

$$\bar{X} \times \bar{Y} = \bar{x} \times \bar{y} + \epsilon(\bar{x} \times \bar{y}^* + \bar{x}^* \times \bar{y}).$$

The norm of  $\bar{X} = \bar{x} + \epsilon \bar{x}^*$  is defined as

$$|\bar{X}| = \sqrt{\langle \bar{x}, \bar{x} \rangle} + \epsilon \frac{\langle \bar{x}, \bar{x}^* \rangle}{\sqrt{\langle \bar{x}, \bar{x} \rangle}}. \tag{6}$$

The norm of  $\bar{X}$  exists only for  $\bar{x} \neq 0$ . If the norm of  $\bar{X}$  is equal to 1, the dual vector is called unit dual vector. The unit dual sphere which consists of the all unit dual vectors is defined as

$$DS^2 = \{\bar{X} = \bar{x} + \epsilon \bar{x}^* \in D^3 : |\bar{X}| = 1\}. \tag{7}$$

Here,  $D^3$  is called the  $D$ -module which consists of the dual vectors. For detailed information for dual vectors in [16]. The correspondence between the unit dual sphere and the subset of the tangent bundle of unit 2-sphere of the natural lift curve is given via Eqs. (3) and (7):

$$T\bar{M} \rightarrow DS^2,$$

$$\bar{\Gamma} = (\bar{q}, \bar{v}) \mapsto \bar{\bar{\Gamma}} = \bar{q} + \epsilon \bar{v}.$$

Here  $\bar{q}$  and  $\bar{v}$  are  $\bar{q}'$  and  $\bar{v}'$ , respectively.

**Theorem 3** (E. Study mapping) There exists one-to-one correspondence between the oriented lines in  $\mathbb{R}^3$  and the points of  $DS^2$ , [16].

**Theorem 4** Let  $\bar{\Gamma}(s) = \bar{q}(s) + \varepsilon\bar{v}(s)$  be a natural lift curve on  $DS^2$ . In  $\mathbb{R}^3$ , the ruled surface obtained by the natural lift curve  $\bar{\Gamma}(s)$  can be represented as

$$\bar{\phi}_{(\bar{\beta}, \bar{\gamma})}(s, u) = \bar{\beta}(s) + u\bar{\gamma}(s), \tag{8}$$

where

$$\bar{\beta}(s) = \bar{\gamma}(s) \times \bar{v}(s) \tag{9}$$

is the base curve of  $\bar{\phi}$ . Consequently, the isomorphism among  $T\bar{M}$ ,  $DS^2$  and  $\mathbb{R}^3$  can be given as

$$T\bar{M} \rightarrow DS^2 \rightarrow \mathbb{R}^3,$$

$$\bar{\Gamma}(s) = (\bar{q}(s), \bar{v}(s)) \mapsto \bar{\Gamma}(s) = \bar{q}(s) + \varepsilon\bar{v}(s) \mapsto \bar{\phi}_{(\bar{\beta}, \bar{\gamma})}(s, u) = \bar{\beta}(s) + u\bar{\gamma}(s).$$

Here  $\bar{\phi}_{(\bar{\beta}, \bar{\gamma})}(s, u)$  is the ruled surface in  $\mathbb{R}^3$  corresponding to the dual curve  $\bar{\Gamma}(s) = \bar{q}(s) + \varepsilon\bar{v}(s) \in DS^2$  (or to the natural lift curve  $\bar{\Gamma}(s) \in T\bar{M}$ ) in [19]. Considering the ruled surface given in Eq. (8), the striction curve of ruled surface is expressed as

$$\hat{\beta}(s) = (\bar{\gamma}(s) \times \bar{v}(s)) + \frac{\langle \bar{\gamma}(s) \times \bar{v}(s), \bar{\gamma}'(s) \rangle}{\langle \bar{\gamma}'(s), \bar{\gamma}'(s) \rangle} \bar{\gamma}(s).$$

The ruled surface  $\bar{\phi}_{(\bar{\beta}, \bar{\gamma})}(s, u) = \bar{\beta}(s) + u\bar{\gamma}(s)$ , is called developable if  $\det(\bar{\beta}(s), \bar{\gamma}(s), \bar{\gamma}'(s)) = 0$ . Exploiting the RM frame for  $\mu$ - direction curve  $\bar{\beta}(s)$ , the following six ruled surfaces may be defined as

$$\bar{\phi}_{(\bar{\beta}_{1i}, \bar{\gamma}_{1i})}(s, u) = \bar{\beta}_{1i}(s) + u\bar{\gamma}_{1i}(s), i = 1, 2, \dots, 6. \tag{10}$$

**Corollary 5**

All ruled surfaces  $\bar{\phi}_{(\bar{\beta}_{1i}, \bar{\gamma}_{1i})}(s, u) = \bar{\beta}_{1i}(s) + u\bar{\gamma}_{1i}(s)$

generated by natural lift curves are developable for  $i = 1, 2, \dots, 6$ .

In Corollary 5, the dral of these ruled surfaces equals to zero. That is,

$$P_{\bar{\phi}} = \frac{\det\left(\frac{d\bar{\beta}'_{1i}}{ds}, \bar{\gamma}_{1i}, \frac{d\bar{\gamma}'_{1i}}{ds}\right)}{\left|\frac{d\bar{\phi}}{ds}\right|^2} = 0.$$

This verifies that these ruled surfaces are developable.

Let's mention the parametric equations of three type surfaces in  $\mathbb{R}^3$ , [21]:

- (i) Cuspidal edge;  $C \times \mathbb{R} = \{(x_1, x_2) : x_1^2 = x_2^3\} \times \mathbb{R}$ .
- (ii) Swallowtail;  
 $SW = \{(x_1, x_2, x_3) : x_1 = 3u^4 + u^2v, x_2 = 4u^3 + 2uv, x_3 = v\}$ .
- (iii) Cuspidal crosscap;  
 $CCR = \{(x_1, x_2, x_3) : x_1 = u^3, x_2 = u^3v^3, x_3 = v^2\}$ .

Now, we investigate the local classification of singularities of the ruled surfaces in the following theorem:

**Theorem 6** Let  $\bar{\Gamma}(s) = (\bar{q}(s), \bar{v}(s))$  be the natural lift curve on  $UT\bar{M}$ . Then, we have the following assertions with the RM frame  $\{\bar{\mu}, \bar{\nu}, \bar{v}\}$  for  $\bar{\mu}$ - direction curve  $\bar{\beta}(s)$ :

1. The ruled surface  $\bar{\phi}_{(\bar{\beta}, \bar{\gamma})}(s, u) = \bar{\beta}(s) + u\bar{\gamma}(s)$ , where  $\bar{\beta}(s) = \bar{\gamma}(s) \times \bar{v}(s)$  is the base curve of  $\bar{\phi}$  which is generated by the natural lift curve is locally diffeomorphic to;
  - (i) Cuspidal edge at  $\bar{\phi}_{(\bar{\beta}, \bar{\gamma})}(s_0, u_0)$  if and only if  $u_0 = -\bar{m}(s_0)^{-1} \neq 0$  and  $\bar{m}'(s_0) \neq 0$ .
  - (ii) Swallowtail at  $\bar{\phi}_{(\bar{\beta}, \bar{\gamma})}(s_0, u_0)$  if and only if  $u_0 = -\bar{m}(s_0)^{-1} \neq 0, \bar{m}'(s_0) = 0$  and  $(\bar{m}''(s_0))^{-1} = 0$ .
2. The ruled surface  $\bar{\phi}_{(\bar{\beta}, \bar{\gamma})}(s, u) = \bar{\beta}(s) + u\bar{v}(s)$ , where  $\bar{\beta}(s) = \bar{\gamma}(s) \times \bar{v}(s)$  is the base curve of  $\bar{\phi}$  which is generated by the natural lift curve is locally diffeomorphic to;
  - (i) Cuspidal edge at  $\bar{\phi}_{(\bar{\beta}, \bar{\gamma})}(s_0, u_0)$  if and only if  $u_0 = -\bar{n}(s_0)^{-1} \neq 0$  and  $u_0'(s_0) \neq 0$ .
  - (ii) Swallowtail at  $\bar{\phi}_{(\bar{\beta}, \bar{\gamma})}(s_0, u_0)$  if and only if  $u_0 = -\bar{n}(s_0)^{-1} \neq 0, \bar{n}'(s_0) = 0$  and  $(\bar{n}''(s_0))^{-1} = 0$ .
3. The ruled surface  $\bar{\phi}_{(\bar{\beta}, \bar{\gamma})}(s, u) = \bar{\beta}(s) + u\bar{\gamma}(s)$  (resp.  $\bar{\phi}_{(\bar{\beta}, \bar{\gamma})}(s, u) = \bar{\beta}(s) + u\bar{v}(s)$ ) which is generated by the natural lift curve that is a cone surface if and only if  $\bar{m}$  (resp.  $\bar{n}$ ) is constant.

**Proof.** Let  $\bar{\Gamma}(s) = (\bar{q}(s), \bar{v}(s))$  be the natural lift curve on  $UT\bar{M}$ . with the RM frame  $\{\bar{\mu}, \bar{\nu}, \bar{v}\}$  for  $\bar{\mu}$  direction curve  $\bar{\beta}(s)$ . Then, we have

$$\frac{\partial \bar{\phi}_{(\bar{\beta}, \bar{\nu})}^{\bar{\nu}}(s, u)}{\partial s} = (1 + u\bar{m}(s))\bar{\mu},$$

$$\frac{\partial \bar{\phi}_{(\bar{\beta}, \bar{\nu})}^{\bar{\nu}}(s, u)}{\partial u} = \bar{v}.$$

The vector product of  $\frac{\partial \bar{\phi}_{(\bar{\beta}, \bar{\nu})}^{\bar{\nu}}(s, u)}{\partial s}$  and  $\frac{\partial \bar{\phi}_{(\bar{\beta}, \bar{\nu})}^{\bar{\nu}}(s, u)}{\partial u}$  is calculated as  $(1 + u\bar{m}(s))\bar{v}$ . Singularities of the normal vector field of  $\bar{\phi}_{(\bar{\beta}, \bar{\nu})}^{\bar{\nu}} = \bar{\phi}_{(\bar{\beta}, \bar{\nu})}^{\bar{\nu}}(s, u)$  is

$$u = -\frac{1}{\bar{m}(s)}.$$

In [5], if there is a parameter  $s_0$  such that

$$u_0 = -\frac{1}{\bar{m}(s_0)} \neq 0 \text{ and } u_0' = -\frac{\bar{m}'(s_0)}{\bar{m}^2(s_0)} \neq 0, \bar{\phi}_{(\bar{\beta}, \bar{\nu})}^{\bar{\nu}}(s, u)$$

locally diffeomorphic to  $C \times R$  at  $\bar{\phi}_{(\bar{\beta}, \bar{\nu})}^{\bar{\nu}}(s_0, u_0)$ . This completes the assertions of 1. (i). Again from [10], if there is a parameter  $s_0$  such that  $u_0 = -\frac{1}{\bar{m}(s_0)} \neq 0,$

$$u_0' = -\frac{\bar{m}'(s_0)}{\bar{m}^2(s_0)} = 0, \text{ and } (\bar{m}(s_0)^{-1})'' = 0, \bar{\phi}_{(\bar{\beta}, \bar{\nu})}^{\bar{\nu}}$$

is locally diffeomorphic to  $SW$  at  $\bar{\phi}_{(\bar{\beta}, \bar{\nu})}^{\bar{\nu}}(s_0, u_0)$ . This completes the assertions of 1. (ii). Likewise, proof of assertion 2 could be done as proof of assertion 1. The proof of assertion 3 is that the singular point equals to the striction curve of  $\bar{\phi}$ . Then, we write

$$\bar{\phi}_{(\bar{\beta}, \bar{\nu})}^{\bar{\nu}}(s, u) = \bar{\phi}_{(\bar{\beta}, \bar{\nu})}^{\bar{\nu}}\left(s, -\frac{1}{\bar{m}(s)}\right) = \bar{\beta}(s) - \frac{1}{\bar{m}(s)}\bar{v}(s)$$

$$\text{(resp. } \bar{\phi}_{(\bar{\beta}, \bar{\nu})}^{\bar{\nu}}(s, u) = \bar{\phi}_{(\bar{\beta}, \bar{\nu})}^{\bar{\nu}}\left(s, -\frac{1}{\bar{m}(s)}\right) = \bar{\beta}(s) - \frac{1}{\bar{m}(s)}\bar{v}(s) \text{).}$$

Hence, we get

$$\bar{\phi}_{(\bar{\beta}, \bar{\nu})}^{\bar{\nu}}(s, u) = \left(-\frac{1}{\bar{m}(s)}\right)' \bar{v}(s)$$

$$\text{(resp. } \bar{\phi}_{(\bar{\beta}, \bar{\nu})}^{\bar{\nu}}(s, u) = \left(-\frac{1}{\bar{m}(s)}\right)' \bar{v}(s) \text{).}$$

It is concluded that if  $\bar{m}(s)$  is constant,  $\bar{\phi}_{(\bar{\beta}, \bar{\nu})}^{\bar{\nu}}(s, u) = \bar{\phi}_{(\bar{\beta}, \bar{\nu})}^{\bar{\nu}}(s, u) = 0$ . Finally, we say that

$\bar{\phi}_{(\bar{\beta}, \bar{\nu})}^{\bar{\nu}}(s, u)$  (or  $\bar{\phi}_{(\bar{\beta}, \bar{\nu})}^{\bar{\nu}}$ ) has only one singularity point. It is a cone surface. Hence, the proof is completed.

**Example 7.** Let us consider

$$\bar{\nu}(s) = \left(\frac{-1}{\sqrt{5}} \sin\left(\frac{s}{\sqrt{5}}\right), \frac{1}{\sqrt{5}} \cos\left(\frac{s}{\sqrt{5}}\right), \frac{2}{\sqrt{5}}\right) \text{ and}$$

$$\bar{v}(s) = \left(\frac{2}{\sqrt{5}} \sin\left(\frac{s}{\sqrt{5}}\right), \frac{-2}{\sqrt{5}} \cos\left(\frac{s}{\sqrt{5}}\right), \frac{1}{\sqrt{5}}\right). \text{ Since}$$

$|\bar{v}(s)| = |\bar{v}(s)| = 1$  and  $\langle \bar{v}(s), \bar{v}(s) \rangle = 0$ , the natural lift curve  $\bar{\Gamma}(s) = (\bar{\nu}(s), \bar{v}(s)) \in UT\bar{M}$ . The ruled surface generated by  $\bar{\Gamma}(s)$  is

$$\bar{\phi}_{(\bar{\nu}, \bar{v})}^{\bar{v}}(s, u) = \frac{1}{\sqrt{5}} \left( (2-u) \sin\left(\frac{s}{\sqrt{5}}\right), (u-2) \cos\left(\frac{s}{\sqrt{5}}\right), (1+2u) \right),$$

where the base curve is

$$\bar{\beta}(s) = \left(\frac{2}{\sqrt{5}} \sin\left(\frac{s}{\sqrt{5}}\right), \frac{-2}{\sqrt{5}} \cos\left(\frac{s}{\sqrt{5}}\right), \frac{1}{\sqrt{5}}\right).$$

The normal vector of  $\bar{\phi}_{(\bar{\beta}, \bar{\nu})}^{\bar{\nu}}$  is

$$\left(\frac{1}{5\sqrt{5}}(u-2) \sin\left(\frac{s}{\sqrt{5}}\right), \frac{-2}{5\sqrt{5}}(2-u) \cos\left(\frac{s}{\sqrt{5}}\right), \frac{1}{5\sqrt{5}}(2-u)\right).$$

Hence, the ruled surface  $\bar{\phi}_{(\bar{\beta}, \bar{\nu})}^{\bar{\nu}}$  is a cone surface.

Additionally,  $u = 2$  is a singular point.

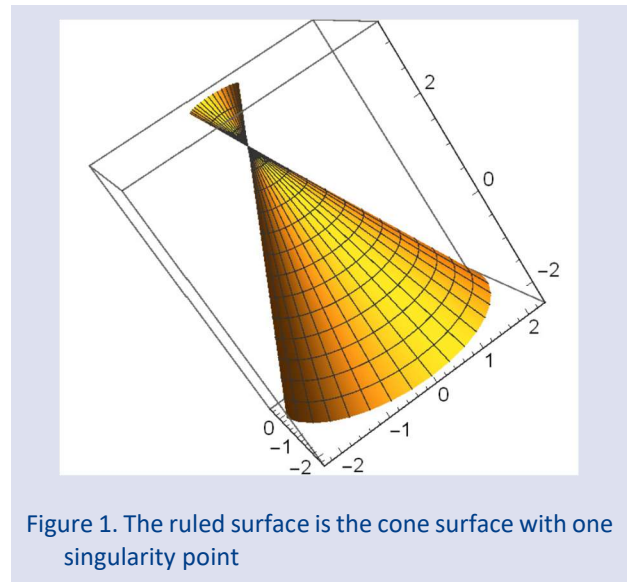


Figure 1. The ruled surface is the cone surface with one singularity point

**Theorem 8.** Let  $\bar{\Gamma}(s) = (\bar{q}(s), \bar{v}(s))$  be the natural lift curve on  $UT\bar{M}$ . Then, we have the following assertions with the RM frame  $\{\bar{\mu}, \bar{\nu}, \bar{v}\}$  for  $\bar{\mu}$  - direction curve  $\bar{\beta}(s)$ :

1. The ruled surface  $\bar{\phi}_{(\bar{\nu}, \bar{\beta})}(s, u) = \bar{\nu}(s) + u\bar{\beta}(s)$  which is generated by the natural lift curve is locally diffeomorphic to;

- (i) Cuspidal edge at  $\bar{\phi}_{(\bar{\nu}, \bar{\beta})}(s_0, u_0)$  if and only if  $u_0 = -\bar{m}(s_0) \neq 0$  and  $\bar{m}'(s_0) \neq 0$ .
- (ii) Swallowtail at  $\bar{\phi}_{(\bar{\nu}, \bar{\beta})}(s_0, u_0)$  if and only if  $u_0 = -\bar{m}(s_0) = 0, \bar{m}'(s_0) \neq 0$ .
- (iv) Cuspidal crosscap at  $\bar{\phi}_{(\bar{\nu}, \bar{\beta})}(s_0, u_0)$  if and only if  $u_0 = -\bar{m}(s_0) \neq 0, \bar{m}'(s_0) = 0$  and  $\bar{m}''(s_0) \neq 0$ .

2. The ruled surface  $\bar{\phi}_{(\bar{\nu}, \bar{\beta})}(s, u) = \bar{\nu}(s) + u\bar{\beta}(s)$  which is generated by the natural lift curve is locally diffeomorphic to;

- (i) Cuspidal edge at  $\bar{\phi}_{(\bar{\nu}, \bar{\beta})}(s_0, u_0)$  if and only if  $u_0 = -\bar{n}(s_0) \neq 0$  and  $\bar{n}'(s_0) \neq 0$ .
- (ii) Swallowtail at  $\bar{\phi}_{(\bar{\nu}, \bar{\beta})}(s_0, u_0)$  if and only if  $u_0 = -\bar{n}(s_0) = 0, \bar{n}'(s_0) = 0$  and  $\bar{n}''(s_0) \neq 0$ .
- (iii) Cuspidal crosscap at  $\bar{\phi}_{(\bar{\nu}, \bar{\beta})}(s_0, u_0)$  if and only if  $u_0 = -\bar{n}(s_0) = 0, \bar{n}'(s_0) \neq 0$

3. The ruled surface  $\bar{\phi}_{(\bar{\nu}, \bar{\beta})}(s, u) = \bar{\nu}(s) + u\bar{\beta}(s)$  (resp.  $\bar{\phi}_{(\bar{\nu}, \bar{\beta})}(s, u) = \bar{\nu}(s) + u\bar{\beta}(s)$ ) which is generated by the natural lift curve that is a cone surface if and only if  $\bar{m}$  (resp.  $\bar{n}$ ) is constant.

**Proof.** Similarly, this theorem can be simply proved by using the method of the proof in Theorem 6.

**Example 9.**

Let us consider  $\bar{\nu}(s) = (\frac{-1}{\sqrt{2}} \sin(\frac{s}{\sqrt{2}}), \frac{1}{\sqrt{2}} \cos(\frac{s}{\sqrt{2}}), \frac{1}{\sqrt{2}})$  and

$\bar{\nu}(s) = (\frac{1}{\sqrt{2}} \sin(\frac{s}{\sqrt{2}}), \frac{1}{\sqrt{2}} \cos(\frac{s}{\sqrt{2}}), \frac{1}{\sqrt{2}})$ . Since

$|\bar{\nu}(s)| = |\bar{\nu}(s)| = 1$  and  $\langle \bar{\nu}(s), \bar{\nu}(s) \rangle = 0$ , the natural lift curve  $\bar{\Gamma}(s) = (\bar{\nu}(s), \bar{\nu}(s)) \in UT\bar{M}$ . The ruled surface generated by  $\bar{\Gamma}(s)$  is

$$\bar{\phi}_{(\bar{\beta}, \bar{\nu})}(s, u) = \frac{1}{\sqrt{2}} ((1-u)\sin(\frac{s}{\sqrt{2}}), (u+1)\cos(\frac{s}{\sqrt{2}}), (1+u)),$$

where the base curve is

$$\bar{\beta}(s) = (\frac{1}{\sqrt{2}} \sin(\frac{s}{\sqrt{2}}), \frac{1}{\sqrt{2}} \cos(\frac{s}{\sqrt{2}}), \frac{1}{\sqrt{2}}).$$

The normal vector of  $\bar{\phi}_{(\bar{\beta}, \bar{\nu})}$  is

$$(\frac{1}{2\sqrt{2}}(u+1)\sin(\frac{s}{\sqrt{2}}), \frac{-1}{2\sqrt{2}}(1-u)\cos(\frac{s}{\sqrt{2}}), \frac{1}{2\sqrt{2}}\cos(\frac{2s}{\sqrt{2}})).$$

Hence, the ruled surface  $\bar{\phi}_{(\bar{\beta}, \bar{\nu})}$  is a cone surface.

Additionally,  $u = 1$  is a singular point.

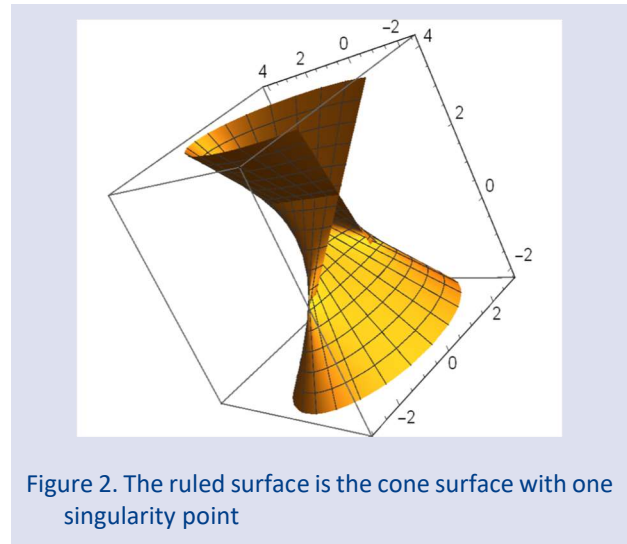


Figure 2. The ruled surface is the cone surface with one singularity point

**Theorem 10.** Let  $\bar{\Gamma}(s) = (\bar{q}(s), \bar{\nu}(s))$  be the natural lift curve on  $UT\bar{M}$ . Then, we have the following assertions with the RM frame  $\{\bar{\mu}, \bar{\nu}, \bar{\nu}\}$  for the curvature functions  $\bar{m}$  and  $\bar{n}$  :

1. The ruled surface  $\bar{\phi}_{(\bar{\nu}, \bar{\nu})}(s, u) = \bar{\nu}(s) + u\bar{\nu}(s)$  which is generated by the natural lift curve is locally diffeomorphic to;

- (i) Cuspidal edge at  $\bar{\phi}_{(\bar{\nu}, \bar{\nu})}(s_0, u_0)$  if and only if  $u_0 = -\frac{\bar{m}}{\bar{n}}(s_0) = 0$  and  $(\frac{\bar{m}}{\bar{n}})'(s_0) \neq 0$ .
- (ii) Swallowtail at  $\bar{\phi}_{(\bar{\nu}, \bar{\nu})}(s_0, u_0)$  if and only if  $u_0 = -\frac{\bar{m}}{\bar{n}}(s_0) \neq 0, (\frac{\bar{m}}{\bar{n}})'(s_0) = 0$  and  $(\frac{\bar{m}}{\bar{n}})''(s_0) \neq 0$ .
- (iii) Cuspidal crosscap at  $\bar{\phi}_{(\bar{\nu}, \bar{\nu})}(s_0, u_0)$  if and only if  $u_0 = \frac{\bar{m}}{\bar{n}}(s_0) = 0$  and  $(\frac{\bar{m}}{\bar{n}})'(s_0) \neq 0$ .

2. The ruled surface  $\bar{\phi}_{(\bar{\nu}, \bar{\nu})}(s, u) = \bar{\nu}(s) + u\bar{\nu}(s)$  which is generated by the natural lift curve is locally diffeomorphic to;

(i) Cuspidal edge at  $\bar{\phi}_{(\bar{v}, \bar{v})}(s_0, u_0)$  if and only if  $u_0 = -\frac{\bar{n}}{\bar{m}}(s_0) \neq 0$  and  $(\frac{\bar{n}}{\bar{m}})'(s_0) \neq 0$ .

(ii) Swallowtail at  $\bar{\phi}_{(\bar{v}, \bar{v})}(s_0, u_0)$  if and only if  $u_0 = -\frac{\bar{n}}{\bar{m}}(s_0) \neq 0, (\frac{\bar{n}}{\bar{m}})'(s_0) = 0$  and  $(\frac{\bar{n}}{\bar{m}})''(s_0) \neq 0$ .

(iii) Cuspidal crosscap at  $\bar{\phi}_{(\bar{v}, \bar{v})}(s_0, u_0)$  if and only if  $u_0 = -\bar{n}(s_0) = 0, \bar{n}'(s_0) \neq 0$ .

3. The ruled surface  $\bar{\phi}_{(\bar{v}, \bar{v})}(s, u) = \bar{v}(s) + u\bar{v}(s)$  (resp.  $\bar{\phi}_{(\bar{v}, \bar{v})}(s, u) = \bar{v}(s) + u\bar{v}(s)$ ) which is generated by the natural lift curve that is a cone surface if and only if  $\frac{\bar{n}}{\bar{m}}(s)$  (resp.  $\frac{\bar{m}}{\bar{n}}(s)$ ) is constant.

**Proof.** Similarly, this theorem can be simply proved by using the method of the proof in Theorem 6.

**Example 11.** Let us consider  $\alpha : [0, B] \rightarrow \mathbb{R}^3 (0 < B < 2\pi)$  as smooth curve defined by

$$\begin{aligned} \bar{v}(s) &= (\frac{\sqrt{3}}{2} \cos 2s, \frac{\sqrt{3}}{2} \sin 2s, \frac{-1}{2}), \\ \bar{v}(s) &= (-\sqrt{3} \sin 2s, \sqrt{3} \cos 2s, 0), \\ \bar{\mu}(s) &= (\frac{\sqrt{3}}{2} \cos 2s, \frac{-\sqrt{3}}{2} \sin 2s, \frac{3}{2}). \end{aligned}$$

Since  $|\bar{v}(s)| = |\bar{v}(s)| = 1$  and  $\langle \bar{v}(s), \bar{v}(s) \rangle = 0$ , the natural lift curve  $\bar{\Gamma}(s) = (\bar{v}(s), \bar{v}(s)) \in UT\bar{M}$ . Moreover,  $\bar{\Gamma}(s) = (\bar{v}(s), \bar{v}(s))$  is the natural lift curve with the curvature  $\bar{m}(s) = \frac{-3}{2} \sin 4s$ .

Hence, we have the following assertions:

1. If  $B = \frac{\pi}{8}$ , we write  $\bar{m}(\frac{\pi}{8}) = \frac{-3}{2} \neq 0, \bar{m}'(\frac{\pi}{8}) = 0$  and  $\bar{m}''(\frac{\pi}{8}) = \frac{3}{2} \neq 0$ . Thus, the ruled surface is

$$\begin{aligned} \bar{\phi}_{(\bar{\beta}, \bar{v})}(s, u) &= \bar{\beta}(s) + u\bar{v}(s), \\ \bar{\phi}_{(\bar{\beta}, \bar{v})}(s, u) &= (\frac{\sqrt{3}}{4} \sin 2s, \frac{\sqrt{3}}{4} \cos 2s, \frac{-s}{2}) + u(\frac{\sqrt{3}}{2} \cos 2s, \frac{\sqrt{3}}{2} \sin 2s, \frac{-1}{2}). \end{aligned}$$

Furthermore, this ruled surface is locally diffeomorphic to the cuspidal edge at  $\bar{\phi}_{(\bar{\beta}, \bar{v})}(\frac{\pi}{8}, \frac{2}{3})$ .

2. If  $B = \pi$ , we write  $u_0 = \bar{m}^{-1}(s_0) \neq 0$  and  $(\bar{m}^{-1})'(s_0) \neq 0$ . The ruled surface is given above is locally diffeomorphic to swallowtail at  $\bar{\phi}_{(\bar{\beta}, \bar{v})}(\frac{\pi}{8}, u_0)$ .

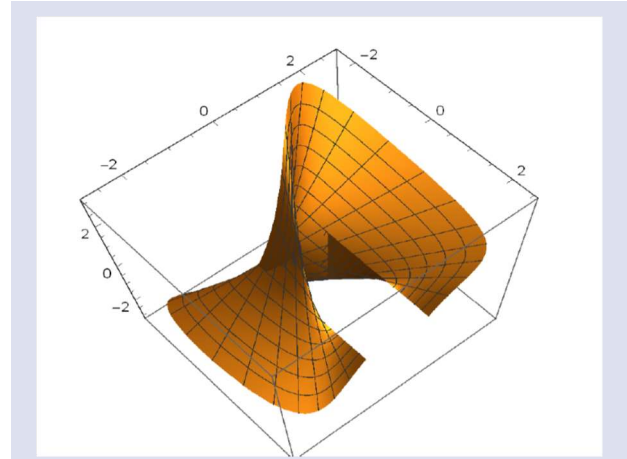


Figure 3. The cuspidal edge at  $\bar{\phi}_{\bar{\beta}, \bar{v}}(\frac{\pi}{8}, \frac{2}{3})$

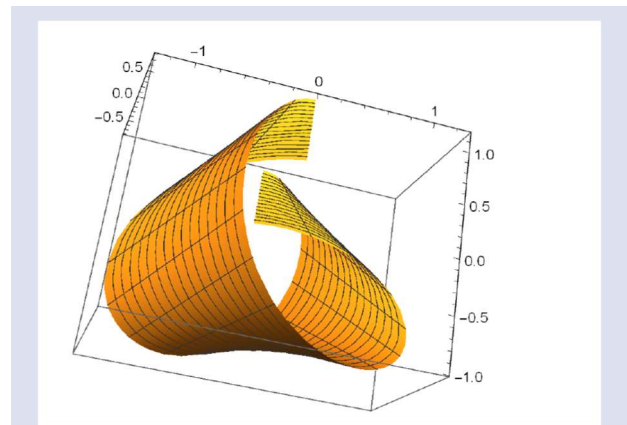


Figure 4. The cuspidal edge at  $\bar{\phi}_{\bar{\beta}, \bar{v}}(\frac{\pi}{8}, \mu_0)$

### Conclusion

In this paper, we have dealt with the singularities of the ruled surface generated by the natural lift curve. Moreover, we classify the singularities and examine the conditions of being locally diffeomorphic to cuspidal edge, swallowtail or cuspidal crosscap. Additionally, some theorems are verified by giving examples. This study opens new horizons to mathematicians who study the singularities of special curves.

## Acknowledgment

The authors are thankful to the referees for their valuable comments, opinions and suggestions.

## Conflicts of interest

The authors state that did not have conflict of interests.

## References

- [1] Wang W., Juttler B., Zheng D., Liu Y., Computation of Rotation Minimizing Frame, *ACM Trans. Graph.*, 27(1) (2008) 1-18.
- [2] Bishop R.L., There is More Than One Way to Frame A Curve, *Amer. Math. Monthly*, 8(246) (1975) 1, 2.
- [3] Do Carmo M.P., *Differential Geometry of Curves and Surfaces*. Prentice Hall, Englewood Cliffs, NJ, (1976).
- [4] Dede M., Why Flc- Frame is Better than Frenet Frame? DOI: 10.13140/RG.2.2.23418.24002 (2019).
- [5] Ravani R., Meghdari A., Ravani B., Rational Frenet-Serret Curves and Rotation Minimizing Frames in Spatial Motion Design, *IEEE International Conference on Intelligent Engineering Systems, INES* (2004) 186-192.
- [6] Wang W., Joe B., Robust Computation of The Rotation Minimizing Frame for Sweep Surface Modeling, *Computer Aided Design*, 29(5) (1997) 379-391.
- [7] Farouki R.T., Rational Rotation-Minimizing Frames Recent Advances and Open Problems, *Applied Mathematics and Computation*, 272(1) (2016) 80-91.
- [8] Thorpe J.A., *Elementary Topics in Differential Geometry*. New York, HeidelbergBerlin: Springer Verlag, (1979).
- [9] Ergün E., Çalışkan M., On Natural Lift of A Curve, *Pure Mathematical Sciences*, 2 (2012) 81-85.
- [10] Ergün E., Bilici M., Çalışkan M., The Frenet Vector Fields and The Curvatures of The Natural Lift Curve, *The Bulletin Society for Mathematical Services and Standarts*, 2 (2012) 38-43.
- [11] Mert T., Timelike Ruled Surface in de-Sitter 3-Space, *Turkish Journal of Mathematics and Computer Science*, 2(12) (2020) 166-175.
- [12] Mert T., Atçeken M., Spacelike Ruled Surface in de-Sitter 3-Space, *Asian Journal of Mathematics and Computer Research*, 27(4) (2020) 37-53.
- [13] Mert T., Atçeken M., Special Ruled Surfaces in de-Sitter 3-Space, *Fundamental Journal of Mathematics and Applications*, 4(3) (2021) 195-209.
- [14] Altın M., Kazan A., Karadağ H.B., Ruled Surfaces Constructed by Planar Curves in Euclidean 3-Space with Density, *Celal Bayar University Journal of Science*, 16(1) (2020) 81-88.
- [15] Altın M., Kazan A., Yoon Woon D., 2-Ruled hypersurfaces in Euclidean 4-space, *Journal of Geometry and Physics*, 166 (2021) 1-13.
- [16] Fischer I.S., *Dual-Number Methods in Kinematics, Statics and Dynamics*. Boca Raton, London, New York, Washington DC: CRC Press, (1999).
- [17] Karakaş B., Gündoğan H., A Relation among  $DS^2$ ,  $TS^2$  and Non-Cylindrical Ruled Surfaces, *Mathematical Communications*, 8 (2003) 9-14.
- [18] Hathout F., Bekar M., Yaylı Y., Ruled Surfaces and Tangent Bundle of Unit 2-Sphere, *Int. J. of Geo. M. M. Phy.*, 14(10) (2017).
- [19] Karaca E., Çalışkan M., Ruled Surfaces and Tangent Bundle of Unit 2-Sphere of Natural Lift Curves, *Gazi University Journal of Science*, 33(5) (2020) 751-759.
- [20] Bruce J.W., Giblin P.J., *Curves and Singularities*. 2nd ed. Cambridge: Cambridge Univ. Press, (1992) 1, 2,5.
- [21] Izumiya S., Takeuchi N., New Special Curves and Developable Surfaces, *Turk J Math*, 28 (2004) 153-163.
- [22] Bekar M., Hathout F., Yaylı Y., Legendre Curves and The Singularities of Ruled Surfaces Obtained by Using Rotation Minimizing Frame, *Ukrainian Mathematical Journal*, 5(73) (2021) 589-601.

## A Study On Generalized Absolute Matrix Summability

Ahmet Karakaş<sup>1,a,\*</sup>

<sup>1</sup> Department of Mathematics, Faculty of Science, Erciyes University, 38039 Kayseri, Türkiye.

\*Corresponding author

### Research Article

#### History

Received: 04/11/2021

Accepted: 17/05/2022

#### Copyright



©2022 Faculty of Science,  
Sivas Cumhuriyet University

### ABSTRACT

In the present paper, generalized absolute matrix summability method of infinite series has been studied. A known theorem on  $|M|_k$  summability method has been generalized using the  $|M, p_\eta, \lambda; \mu|_k$  summability method of infinite series. So a new theorem has been established and proved. Some results related to the new theorem also have been obtained.

**Keywords:** Summability factors, Absolute matrix summability, Infinite series, Hölder inequality, Minkowski inequality.

<sup>a</sup> [ahmetkarakas1985@gmail.com](mailto:ahmetkarakas1985@gmail.com)  <https://orcid.org/0000-0001-7043-1445>

### Introduction

Summability theory is important for analysis, applied mathematics and engineering sciences. The purpose of this theory is to bring an appropriate value to the indefinite divergent series. Various summability methods have been defined by some researchers to find the value. Some of these methods are Cesàro [1], Abel [2], Nörlund [3], Riesz [4], matrix summability [5].

A significant increase began in studies on the summability theory in the second half of the 19<sup>th</sup> century. In 1890, Cesàro published a paper on the multiplication of series [1]. Das gave the definition of absolute summability [6]. Then Kishore and Hotta defined the summability factor [7]. The definition of  $|M|_k$  summability was given by Tanović-Miller [8]. Later Bor defined  $|\bar{N}, p_\eta|_k$  and  $|\bar{N}, p_\eta; \mu|_k$  summability of an infinite series [9, 10]. The definition of  $|M, p_\eta; \mu|_k$  summability of an infinite series was defined by Özarslan and Ögdük [11]. The definition of  $|M, p_\eta, \lambda; \mu|_k$  summability was given by Özarslan and Karakaş [12]. In this paper a theorem on absolute matrix summability is obtained using  $|M, p_\eta, \lambda; \mu|_k$  summability method. Now we give some definitions related to the summability which are used in this article.

**Definition 1** [13]. Let  $(s_\eta)$  be partial sums of the infinite series  $\sum m_\eta$ .  $(p_\eta)$  is a sequence such that

$$p_\eta > 0 \text{ and } P_\eta = \sum_{v=0}^{\eta} p_v \rightarrow \infty \text{ as } \eta \rightarrow \infty \text{ (} P_{-j} = p_{-j} = 0, j \geq 1 \text{)}. \quad (1)$$

$(\mathcal{G}_\eta)$  is the  $(\bar{N}, p_\eta)$  means of the sequence  $(s_\eta)$  such that

$$\mathcal{G}_\eta = \frac{1}{P_\eta} \sum_{v=0}^{\eta} p_v s_v. \quad (2)$$

**Definition 2** [9]. The series  $\sum m_\eta$  is called summable  $|\bar{N}, p_\eta|_k, \kappa \geq 1$ , if

$$\sum_{\eta=1}^{\infty} \left( \frac{P_\eta}{p_\eta} \right)^{\kappa-1} |\mathcal{G}_\eta - \mathcal{G}_{\eta-1}|^\kappa < \infty. \quad (3)$$

**Definition 3** [8]. Let  $M = (m_{\eta\nu})$  be a normal matrix, i.e. a lower triangular matrix of nonzero diagonal entries. By  $M = (m_{\eta\nu})$ , a transformation from sequence  $s = (s_\eta)$  to  $Ms = (M_\eta(s))$  can be constituted where

$$M_\eta(s) = \sum_{v=0}^{\eta} m_{\eta\nu} s_v, \eta = 0, 1, \dots \quad (4)$$

The series  $\sum m_\eta$  is called summable  $|M|_k, \kappa \geq 1$ , if

$$\sum_{\eta=1}^{\infty} \eta^{\kappa-1} |\bar{\Delta} M_\eta(s)|^\kappa < \infty, \quad (5)$$

where

$$\bar{\Delta} M_\eta(s) = M_\eta(s) - M_{\eta-1}(s). \quad (6)$$

**Definition 4** [14]. The series  $\sum m_\eta$  is called summable  $|M, p_\eta|_k, \kappa \geq 1$ , if

$$\sum_{\eta=1}^{\infty} \left( \frac{p_{\eta}}{\rho_{\eta}} \right)^{\kappa-1} \left| \bar{\Delta} M_{\eta}(s) \right|^{\kappa} < \infty. \tag{7}$$

**Definition 5** [12]. The series  $\sum m_{\eta}$  is called summable

$|M, p_{\eta}, \lambda; \mu|_{\kappa}$ ,  $\kappa \geq 1$ ,  $\mu \geq 0$  and  $\lambda$  is a real number if

$$\sum_{\eta=1}^{\infty} \left( \frac{p_{\eta}}{\rho_{\eta}} \right)^{\lambda(\mu\kappa+\kappa-1)} \left| \bar{\Delta} M_{\eta}(s) \right|^{\kappa} < \infty. \tag{8}$$

Here, if we choose  $\lambda=1$  and  $\mu=0$ ,  $|M, p_{\eta}, \lambda; \mu|_{\kappa}$  summability reduces to  $|M, p_{\eta}|_{\kappa}$  summability. Also, by taking  $\lambda=1$ ,  $\mu=0$  and  $p_{\eta}=1$  for  $\forall \eta \in \mathbb{N}$ ,  $|M, p_{\eta}, \lambda; \mu|_{\kappa}$  summability reduces to  $|M|_{\kappa}$  summability.

**Known Results**

The following lemmas and theorem on  $|M|_{\kappa}$  summability of the series  $\sum m_{\eta} \lambda_{\eta} X_{\eta}$  have been proved by Sulaiman in [15].

**Lemma 1.** If  $\sum \eta^{-1} \lambda_{\eta}$  is convergent, then  $(\lambda_{\eta})$  is non-negative and decreasing,  $\lambda_{\eta} \log \eta = O(1)$ , and  $\eta \Delta \lambda_{\eta} = O(1 / (\log \eta)^2)$ .

**Lemma 2.** If  $\sum \eta^{-1} \lambda_{\eta} X_{\eta}$  is convergent, such that

$$\eta \Delta \lambda_{\eta} = O(\lambda_{\eta}) \text{ as } \eta \rightarrow \infty, \tag{9}$$

$$\sum_{v=1}^{\eta} \lambda_v = O(\eta \lambda_{\eta}) \text{ as } \eta \rightarrow \infty, \tag{10}$$

then

$$\eta \lambda_{\eta} \Delta X_{\eta} = O(1), \tag{11}$$

$$\sum_{\eta=1}^q \lambda_{\eta} \Delta X_{\eta} = O(1) \text{ as } q \rightarrow \infty, \tag{12}$$

$$\sum_{\eta=1}^q \eta \lambda_{\eta} \Delta^2 X_{\eta} = O(1) \text{ as } q \rightarrow \infty. \tag{13}$$

**Theorem 1.** Let  $(\lambda_{\eta})$ ,  $(X_{\eta})$  be two sequences such that

$\sum_{\eta=1}^{\infty} \eta^{-1} \lambda_{\eta} X_{\eta}$  is convergent, and the conditions (9), (10) are satisfied. Let  $M=(m_{\eta\nu})$  be a normal matrix with non-negative entries satisfying

$$\bar{m}_{\eta 0} = 1, \quad \eta = 0, 1, \dots, \tag{14}$$

$$m_{\eta-1, \nu} \geq m_{\eta\nu}, \text{ for } \eta \geq \nu + 1, \tag{15}$$

$$\eta m_{\eta\eta} = O(1), \quad 1 = O(\eta m_{\eta\eta}), \tag{16}$$

$$\sum_{v=1}^{\eta-1} m_{\eta\nu} \hat{m}_{\eta\nu} = O(m_{\eta\eta}). \tag{17}$$

If  $u_{\nu}^{\kappa} = O(1) (C, 1)$ , where  $u_{\nu} = \frac{1}{\nu+1} \sum_{i=1}^{\nu} i m_i$ , then the series  $\sum m_{\eta} \lambda_{\eta} X_{\eta}$  is summable  $|M|_{\kappa}$ ,  $\kappa \geq 1$ .

**Lemma 3.** According to Theorem 1, we have

$$\sum_{v=0}^{\eta-1} \left| \Delta_v(\hat{m}_{\eta\nu}) \right| = m_{\eta\eta}, \tag{18}$$

$$\hat{m}_{\eta, \nu+1} \geq 0, \tag{19}$$

$$\sum_{\eta=\nu+1}^{q+1} \hat{m}_{\eta, \nu+1} = O(1). \tag{20}$$

**Main Result**

There are many studies on absolute matrix summability of infinite series [16-29]. This study provides a generalization of above mentioned theorem to  $|M, p_{\eta}, \lambda; \mu|_{\kappa}$  summability under some suitable conditions. For the convenience of the reader, we give some further notations.

Let  $M=(m_{\eta\nu})$  be a normal matrix. The definition of two lower semi-matrices  $\bar{M}=(\bar{m}_{\eta\nu})$  and  $\hat{M}=(\hat{m}_{\eta\nu})$  are as follows.

$$\bar{m}_{\eta\nu} = \sum_{i=\nu}^{\eta} m_{\eta i}, \quad \eta, \nu = 0, 1, \dots \tag{21}$$

and

$$\hat{m}_{00} = \bar{m}_{00} = m_{00}, \quad \hat{m}_{\eta\nu} = \bar{m}_{\eta\nu} - \bar{m}_{\eta-1, \nu}, \quad \eta = 1, 2, \dots \tag{22}$$

It is well-known that

$$M_{\eta}(s) = \sum_{v=0}^{\eta} m_{\eta\nu} s_{\nu} = \sum_{v=0}^{\eta} \bar{m}_{\eta\nu} m_{\nu} \tag{23}$$

and

$$\bar{\Delta} M_{\eta}(s) = \sum_{v=0}^{\eta} \hat{m}_{\eta\nu} m_{\nu}. \tag{24}$$

Now, let's give the main theorem.

**Theorem 2.** Let  $(\lambda_{\eta})$  and  $(X_{\eta})$  be two sequences such that  $\sum_{\eta=1}^{\infty} \eta^{-1} \lambda_{\eta} X_{\eta}$  is convergent. The conditions (9), (10), (14)-(17) and



$$m_{\eta\eta} = O\left(\frac{p_\eta}{P_\eta}\right), \tag{25}$$

$$= O(1) \sum_{\eta=2}^{q+1} \left(\frac{p_\eta}{P_\eta}\right)^{\lambda(\mu\kappa+\kappa-1)} \left(\sum_{v=1}^{\eta-1} \frac{1}{v^\kappa} u_v^\kappa m_{vv}^{1-\kappa} \widehat{m}_{\eta v} \phi_v^\kappa\right) \left(\sum_{v=1}^{\eta-1} m_{vv} \widehat{m}_{\eta v}\right)^{\kappa-1}$$

$$\sum_{\eta=v+1}^{q+1} \left(\frac{p_\eta}{P_\eta}\right)^{\lambda(\mu\kappa+\kappa-1)-\kappa+1} \widehat{m}_{\eta,v+1} = O(1) \text{ as } q \rightarrow \infty, \tag{26}$$

$$\sum_{\eta=v+1}^{q+1} \left(\frac{p_\eta}{P_\eta}\right)^{\lambda(\mu\kappa+\kappa-1)-\kappa+1} |\Delta_v(\widehat{m}_{\eta v})| = O(m_{vv}) \text{ as } q \rightarrow \infty, \tag{27}$$

$$\sum_{v=1}^{\eta-1} m_{vv} \widehat{m}_{\eta,v+1} = O(m_{\eta\eta}) \tag{28}$$

are satisfied.

If  $\left(\frac{p_v}{P_v}\right)^{\lambda(\mu\kappa+\kappa-1)-\kappa+1} u_v^\kappa = O(1) (C, 1)$ , where  $(u_v)$  as in Theorem 1, then the series  $\sum m_\eta \lambda_\eta X_\eta$  is summable  $|M, p_\eta, \lambda; \mu|_\kappa$ ,  $\kappa \geq 1$ ,  $\mu \geq 0$  and  $-\lambda(\mu\kappa + \kappa - 1) + \kappa > 0$ .

**Proof of Theorem 2**

Let  $\phi_\eta = \lambda_\eta X_\eta$  and  $(W_\eta)$  be  $M$  – transform of the series  $\sum m_\eta \phi_\eta$ . By (23) and (24), we get

$$\bar{\Delta} W_\eta = \sum_{v=1}^{\eta} \widehat{m}_{\eta v} m_v \phi_v = \sum_{v=1}^{\eta} \frac{\widehat{m}_{\eta v} \phi_v}{v} m_v v.$$

Using Abel's transformation, we obtain the following.

$$\begin{aligned} \bar{\Delta} W_\eta &= \sum_{v=1}^{\eta-1} \Delta_v \left(\frac{\widehat{m}_{\eta v} \phi_v}{v}\right) \sum_{i=1}^v i m_i + \frac{\widehat{m}_{\eta \eta} \phi_\eta}{\eta} \sum_{i=1}^{\eta} i m_i \\ &= \sum_{v=1}^{\eta-1} \Delta_v \left(\frac{\widehat{m}_{\eta v} \phi_v}{v}\right) (v+1) u_v + \frac{m_{\eta \eta} \phi_\eta}{\eta} (\eta+1) u_\eta \\ &= \sum_{v=1}^{\eta-1} \frac{1}{v} \widehat{m}_{\eta v} \phi_v u_v + \sum_{v=1}^{\eta-1} \Delta_v (\widehat{m}_{\eta v}) \phi_v u_v + \sum_{v=1}^{\eta-1} \widehat{m}_{\eta, v+1} \Delta \phi_v u_v \\ &\quad + \frac{\eta+1}{\eta} m_{\eta \eta} \phi_\eta u_\eta \\ &= W_{\eta,1} + W_{\eta,2} + W_{\eta,3} + W_{\eta,4}. \end{aligned}$$

It is sufficient to prove

$$\sum_{\eta=1}^{\infty} \left(\frac{p_\eta}{P_\eta}\right)^{\lambda(\mu\kappa+\kappa-1)} |W_{\eta,j}|^\kappa < \infty, \text{ for } j = 1, 2, 3, 4.$$

We first apply Hölder's inequality to obtain

$$\sum_{\eta=2}^{q+1} \left(\frac{p_\eta}{P_\eta}\right)^{\lambda(\mu\kappa+\kappa-1)} |W_{\eta,1}|^\kappa = \sum_{\eta=2}^{q+1} \left(\frac{p_\eta}{P_\eta}\right)^{\lambda(\mu\kappa+\kappa-1)} \left|\sum_{v=1}^{\eta-1} \frac{1}{v} \widehat{m}_{\eta v} \phi_v u_v\right|^\kappa$$

By using (17), (25), (16) and (26), we get

$$\begin{aligned} \sum_{\eta=2}^{q+1} \left(\frac{p_\eta}{P_\eta}\right)^{\lambda(\mu\kappa+\kappa-1)} |W_{\eta,1}|^\kappa &= O(1) \sum_{\eta=2}^{q+1} \left(\frac{p_\eta}{P_\eta}\right)^{\lambda(\mu\kappa+\kappa-1)} m_{\eta\eta}^{\kappa-1} \left(\sum_{v=1}^{\eta-1} \frac{1}{v^\kappa} u_v^\kappa m_{vv}^{1-\kappa} \widehat{m}_{\eta v} \phi_v^\kappa\right) \\ &= O(1) \sum_{\eta=2}^{q+1} \left(\frac{p_\eta}{P_\eta}\right)^{\lambda(\mu\kappa+\kappa-1)-\kappa+1} \left(\sum_{v=1}^{\eta-1} u_v^\kappa m_{vv} \widehat{m}_{\eta v} \phi_v^\kappa\right) \\ &= O(1) \sum_{v=1}^q m_{vv} u_v^\kappa \phi_v^\kappa \sum_{\eta=v+1}^{q+1} \left(\frac{p_\eta}{P_\eta}\right)^{\lambda(\mu\kappa+\kappa-1)-\kappa+1} \widehat{m}_{\eta v} \\ &= O(1) \sum_{v=1}^q m_{vv} u_v^\kappa \phi_v^\kappa \\ &= O(1) \sum_{v=1}^q \frac{1}{v} u_v^\kappa \phi_v \phi_v^{\kappa-1}. \end{aligned}$$

Using  $\phi_v^{\kappa-1} = O(1)$ , we have

$$\sum_{\eta=2}^{q+1} \left(\frac{p_\eta}{P_\eta}\right)^{\lambda(\mu\kappa+\kappa-1)} |W_{\eta,1}|^\kappa = O(1) \sum_{v=1}^q \frac{\phi_v}{v} u_v^\kappa.$$

Here, applying Abel's transformation, we have

$$\begin{aligned} \sum_{\eta=2}^{q+1} \left(\frac{p_\eta}{P_\eta}\right)^{\lambda(\mu\kappa+\kappa-1)} |W_{\eta,1}|^\kappa &= O(1) \sum_{v=1}^{q-1} \Delta\left(\frac{\phi_v}{v}\right) \sum_{i=1}^v u_i^\kappa + O(1) \frac{\phi_q}{q} \sum_{v=1}^q u_v^\kappa \\ &= O(1) \sum_{v=1}^{q-1} v \Delta\left(\frac{\phi_v}{v}\right) + O(1) \phi_q. \end{aligned}$$

Since

$$\begin{aligned} \Delta\left(\frac{\phi_v}{v}\right) &= \frac{\phi_v}{v} - \frac{\phi_{v+1}}{v+1} \\ &< \frac{\phi_v}{v^2} + \frac{\Delta \phi_v}{v+1}, \end{aligned}$$

we have

$$\begin{aligned} \sum_{\eta=2}^{q+1} \left(\frac{p_\eta}{P_\eta}\right)^{\lambda(\mu\kappa+\kappa-1)} |W_{\eta,1}|^\kappa &= O(1) \sum_{v=1}^{q-1} v \left(\frac{\phi_v}{v^2} + \frac{\Delta \phi_v}{v+1}\right) + O(1) \phi_q \\ &= O(1) \sum_{v=1}^{q-1} \frac{\phi_v}{v} + O(1) \sum_{v=1}^{q-1} \Delta \phi_v + O(1) \phi_q. \end{aligned}$$

In that case, we obtain

$$\sum_{\eta=2}^{q+1} \left(\frac{p_\eta}{\rho_\eta}\right)^{\lambda(\mu\kappa+\kappa-1)} |W_{\eta,1}|^\kappa = O(1) \sum_{v=1}^{q-1} \frac{\lambda_v X_v}{v} + O(1) \sum_{v=1}^{q-1} \Delta(\lambda_v X_v) + O(1) \lambda_q X_q = O(1) \sum_{\eta=2}^{q+1} \left(\frac{p_\eta}{\rho_\eta}\right)^{\lambda(\mu\kappa+\kappa-1)} \left(\sum_{v=1}^{\eta-1} u_v^\kappa m_{vv}^{1-\kappa} \widehat{m}_{\eta,v+1} (\Delta\phi_v)^\kappa\right) \left(\sum_{v=1}^{\eta-1} m_{vv} \widehat{m}_{\eta,v+1}\right)^{\kappa-1} = O(1) \text{ as } q \rightarrow \infty.$$

We now apply Hölder's inequality to obtain

$$\sum_{\eta=2}^{q+1} \left(\frac{p_\eta}{\rho_\eta}\right)^{\lambda(\mu\kappa+\kappa-1)} |W_{\eta,2}|^\kappa \leq \sum_{\eta=2}^{q+1} \left(\frac{p_\eta}{\rho_\eta}\right)^{\lambda(\mu\kappa+\kappa-1)} \left(\sum_{v=1}^{\eta-1} |\Delta_v(\widehat{m}_{\eta v})| \phi_v u_v\right)^\kappa \leq \sum_{\eta=2}^{q+1} \left(\frac{p_\eta}{\rho_\eta}\right)^{\lambda(\mu\kappa+\kappa-1)} \left(\sum_{v=1}^{\eta-1} |\Delta_v(\widehat{m}_{\eta v})| \phi_v u_v\right)^{\kappa-1} \left(\sum_{v=1}^{\eta-1} |\Delta_v(\widehat{m}_{\eta v})|\right).$$

By using (21) and (22), we get

$$\Delta_v(\widehat{m}_{\eta v}) = \widehat{m}_{\eta v} - \widehat{m}_{\eta, v+1} = \overline{m}_{\eta v} - \overline{m}_{\eta-1, v} - \overline{m}_{\eta, v+1} + \overline{m}_{\eta-1, v+1} = m_{\eta v} - m_{\eta-1, v}. \tag{29}$$

Thus using (21), (14), (15) and (29), we obtain

$$\sum_{v=1}^{\eta-1} |\Delta_v(\widehat{m}_{\eta v})| = \sum_{v=1}^{\eta-1} (m_{\eta-1, v} - m_{\eta v}) \leq m_{\eta \eta}. \tag{30}$$

Then, we get

$$\sum_{\eta=2}^{q+1} \left(\frac{p_\eta}{\rho_\eta}\right)^{\lambda(\mu\kappa+\kappa-1)} |W_{\eta,2}|^\kappa = O(1) \sum_{\eta=2}^{q+1} \left(\frac{p_\eta}{\rho_\eta}\right)^{\lambda(\mu\kappa+\kappa-1)} m_{\eta \eta}^{\kappa-1} \left(\sum_{v=1}^{\eta-1} |\Delta_v(\widehat{m}_{\eta v})| \phi_v u_v\right)$$

By using (25) and (27), we have

$$\begin{aligned} \sum_{\eta=2}^{q+1} \left(\frac{p_\eta}{\rho_\eta}\right)^{\lambda(\mu\kappa+\kappa-1)} |W_{\eta,2}|^\kappa &= O(1) \sum_{\eta=2}^{q+1} \left(\frac{p_\eta}{\rho_\eta}\right)^{\lambda(\mu\kappa+\kappa-1)-\kappa+1} \left(\sum_{v=1}^{\eta-1} |\Delta_v(\widehat{m}_{\eta v})| \phi_v u_v\right) \\ &= O(1) \sum_{v=1}^q \phi_v^\kappa u_v^\kappa \sum_{\eta=v+1}^{q+1} \left(\frac{p_\eta}{\rho_\eta}\right)^{\lambda(\mu\kappa+\kappa-1)-\kappa+1} |\Delta_v(\widehat{m}_{\eta v})| \\ &= O(1) \sum_{v=1}^q m_{vv} u_v^\kappa \phi_v^{\kappa-1} \phi_v \\ &= O(1) \text{ as } q \rightarrow \infty, \end{aligned}$$

as in  $W_{\eta,1}$ .

We now apply Hölder's inequality again to obtain

$$\sum_{\eta=2}^{q+1} \left(\frac{p_\eta}{\rho_\eta}\right)^{\lambda(\mu\kappa+\kappa-1)} |W_{\eta,3}|^\kappa = O(1) \sum_{\eta=2}^{q+1} \left(\frac{p_\eta}{\rho_\eta}\right)^{\lambda(\mu\kappa+\kappa-1)} \left(\sum_{v=1}^{\eta-1} \widehat{m}_{\eta, v+1} \Delta\phi_v u_v\right)^\kappa$$

Using (28), we have

$$\sum_{\eta=2}^{q+1} \left(\frac{p_\eta}{\rho_\eta}\right)^{\lambda(\mu\kappa+\kappa-1)} |W_{\eta,3}|^\kappa = O(1) \sum_{\eta=2}^{q+1} \left(\frac{p_\eta}{\rho_\eta}\right)^{\lambda(\mu\kappa+\kappa-1)} m_{\eta \eta}^{\kappa-1} \left(\sum_{v=1}^{\eta-1} u_v^\kappa m_{vv}^{1-\kappa} \widehat{m}_{\eta, v+1} (\Delta\phi_v)^\kappa\right)$$

By using (25), (26) and (16), we have

$$\sum_{\eta=2}^{q+1} \left(\frac{p_\eta}{\rho_\eta}\right)^{\lambda(\mu\kappa+\kappa-1)} |W_{\eta,3}|^\kappa = O(1) \sum_{\eta=2}^{q+1} \left(\frac{p_\eta}{\rho_\eta}\right)^{\lambda(\mu\kappa+\kappa-1)-\kappa+1} \left(\sum_{v=1}^{\eta-1} u_v^\kappa m_{vv}^{1-\kappa} \widehat{m}_{\eta, v+1} (\Delta\phi_v)^\kappa\right)$$

$$\begin{aligned} &= O(1) \sum_{v=1}^q u_v^\kappa m_{vv}^{1-\kappa} (\Delta\phi_v)^\kappa \sum_{\eta=v+1}^{q+1} \left(\frac{p_\eta}{\rho_\eta}\right)^{\lambda(\mu\kappa+\kappa-1)-\kappa+1} \widehat{m}_{\eta, v+1} \\ &= O(1) \sum_{v=1}^q u_v^\kappa v^{\kappa-1} (\Delta\phi_v)^\kappa. \end{aligned}$$

Here  $(v\Delta\phi_v)^{\kappa-1} = O(1)$ , then we have

$$\begin{aligned} \sum_{\eta=2}^{q+1} \left(\frac{p_\eta}{\rho_\eta}\right)^{\lambda(\mu\kappa+\kappa-1)} |W_{\eta,3}|^\kappa &= O(1) \sum_{v=1}^q u_v^\kappa \Delta\phi_v \\ &= O(1) \sum_{v=1}^q u_v^\kappa \Delta\lambda_v X_v + O(1) \sum_{v=1}^q u_v^\kappa \lambda_{v+1} \Delta X_v \\ &= Y_1 + Y_2. \end{aligned}$$

The condition (9) and Abel's transformation enable us to write

$$\begin{aligned} Y_1 &= O(1) \sum_{v=1}^q u_v^\kappa \frac{1}{v} \lambda_v X_v \\ &= O(1) \sum_{v=1}^{q-1} \Delta\left(\frac{\lambda_v X_v}{v}\right) \sum_{i=1}^v u_i^\kappa + O(1) \frac{\lambda_q X_q}{q} \sum_{v=1}^q u_v^\kappa. \end{aligned}$$

Then, we have

$$\begin{aligned} Y_1 &= O(1) \sum_{v=1}^{q-1} v \left(\frac{\lambda_v X_v}{v^2} + \frac{\Delta\lambda_v X_v}{v} + \frac{\lambda_{v+1} \Delta X_v}{v}\right) + O(1) \lambda_q X_q \\ &= O(1) \sum_{v=1}^{q-1} \frac{\lambda_v X_v}{v} + O(1) \sum_{v=1}^{q-1} \Delta\lambda_v X_v + O(1) \sum_{v=1}^{q-1} \lambda_v \Delta X_v + O(1) \lambda_q X_q \\ &= O(1) \text{ as } q \rightarrow \infty. \end{aligned}$$

By Abel's transformation and (9), (12), (13), (11), we get

$$\begin{aligned} Y_2 &= O(1) \sum_{v=1}^{q-1} \Delta(\lambda_v \Delta X_v) \sum_{i=1}^v u_i^\kappa + O(1) \lambda_q \Delta X_q \sum_{v=1}^q u_v^\kappa \\ &= O(1) \sum_{v=1}^{q-1} v \Delta(\lambda_v \Delta X_v) + O(1) q \lambda_q \Delta X_q \\ &= O(1) \sum_{v=1}^{q-1} v (\Delta\lambda_v \Delta X_v + \lambda_{v+1} \Delta^2 X_v) + O(1) q \lambda_q \Delta X_q \end{aligned}$$

$$\begin{aligned}
 &= O(1) \sum_{v=1}^{q-1} \lambda_v \Delta X_v + O(1) \sum_{v=1}^{q-1} v \lambda_v \Delta^2 X_v + O(1) q \lambda_q \Delta X_q \\
 &= O(1) \text{ as } q \rightarrow \infty .
 \end{aligned}$$

Since  $Y_1 = O(1)$  and  $Y_2 = O(1)$ , we get

$$\sum_{\eta=2}^{q+1} \left( \frac{p_\eta}{p_\eta} \right)^{\lambda(\mu\kappa+\kappa-1)} \left| W_{\eta,3} \right|^\kappa = O(1) \text{ as } q \rightarrow \infty .$$

Finally, using (25), (16) and Abel's transformation, we obtain

$$\begin{aligned}
 &\sum_{\eta=1}^q \left( \frac{p_\eta}{p_\eta} \right)^{\lambda(\mu\kappa+\kappa-1)} \left| W_{\eta,4} \right|^\kappa = O(1) \sum_{\eta=1}^q \left( \frac{p_\eta}{p_\eta} \right)^{\lambda(\mu\kappa+\kappa-1)} m_{\eta\eta}^{\kappa-1} m_{\eta\eta} \phi_\eta^\kappa u_\eta^\kappa \\
 &= O(1) \sum_{\eta=1}^q \left( \frac{p_\eta}{p_\eta} \right)^{\lambda(\mu\kappa+\kappa-1)-\kappa+1} m_{\eta\eta} \phi_\eta^{\kappa-1} \phi_\eta^\kappa u_\eta^\kappa \\
 &= O(1) \sum_{\eta=1}^q \left( \frac{p_\eta}{p_\eta} \right)^{\lambda(\mu\kappa+\kappa-1)-\kappa+1} \frac{\phi_\eta}{\eta} u_\eta^\kappa \\
 &= O(1) \sum_{\eta=1}^{q-1} \Delta \left( \frac{\phi_\eta}{\eta} \right) \sum_{v=1}^\eta \left( \frac{p_v}{p_v} \right)^{\lambda(\mu\kappa+\kappa-1)-\kappa+1} u_v^\kappa + O(1) \frac{\phi_q}{q} \sum_{\eta=1}^q \left( \frac{p_\eta}{p_\eta} \right)^{\lambda(\mu\kappa+\kappa-1)-\kappa+1} u_\eta^\kappa \\
 &= O(1) \sum_{\eta=1}^{q-1} \eta \Delta \left( \frac{\phi_\eta}{\eta} \right) + O(1) \phi_q .
 \end{aligned}$$

So, we have

$$\sum_{\eta=1}^q \left( \frac{p_\eta}{p_\eta} \right)^{\lambda(\mu\kappa+\kappa-1)} \left| W_{\eta,4} \right|^\kappa = O(1) \text{ as } q \rightarrow \infty ,$$

as in  $W_{\eta,1}$ .

Hence proof of the theorem is completed.

### Conclusion

If we choose  $\lambda = 1$ ,  $\mu = 0$  and  $p_\eta = 1$  for  $\forall \eta \in \mathbb{N}$ , then we obtain Theorem 1. In that case, (25) reduces to  $\eta m_{\eta\eta} = O(1)$  (first part of (16)). In addition, (26)-(28) are automatically satisfied.

### Conflicts of interest

The author state that did not have conflict of interests.

### References

[1] Cesàro E., Sur la Multiplication des Séries, *Bull. Sci. Math.*, 14 (1890) 114-120 (in French).

[2] Abel N.H., Untersuchungen über die Reihe:  $1 + \frac{m}{1}x + \frac{m(m-1)}{1.2}x^2 + \frac{m(m-1)(m-2)}{1.2.3}x^3 + \dots$ , *J. Reine Angew. Math.*, 1 (1826) 311-339 (in German).

[3] Nörlund N.E., Sur une Application des Fonctions Permutables, *Lunds Univ. Arssk.*, 16 (1919) 1-10 (in French).

[4] Riesz M., Sur L'equivalence de Certaines Méthodes de Sommmation, *Proc. London Math. Soc.*, 22 (1924) 412-419 (in French).

[5] Petersen G.M., Regular matrix transformations. New York: McGraw-Hill, (1966).

[6] Das G., Tauberian Theorems for Absolute Nörlund Summability, *Proc. London Math. Soc.*, 19 (1969) 357-384.

[7] Kishore N., Hotta G.C., On  $|\bar{N}, p_n|$  Summability Factors, *Acta Sci. Math. (Szeged)*, 31 (1970) 9-12.

[8] Tanović-Miller N., On Strong Summability, *Glas. Mat. Ser. III*, 14 (1979) 87-97.

[9] Bor H., On Two Summability Methods, *Math. Proc. Cambridge Philos. Soc.*, 97 (1985) 147-149.

[10] Bor H., On Local property of  $|\bar{N}, p_n; \delta|_k$  Summability of Factored Fourier Series, *J. Math. Anal. Appl.*, 179 (1993) 646-649.

[11] Özarlan H.S., Öğdük H.N., Generalizations of Two Theorems on Absolute Summability Methods, *Aust. J. Math. Anal. Appl.*, 1 (2004) Art.no.13.

[12] Özarlan H.S., Karakaş A., A New Study on Absolute Summability Factors of Infinite Series, *Maejo Int. J. Sci. Technol.*, 13 (2019) 257-265.

[13] Hardy G.H., Divergent series. Oxford: Oxford University Press, (1949).

[14] Sulaiman W.T., Inclusion Theorems for Absolute Matrix Summability Methods of an Infinite Series. IV, *Indian J. Pure Appl. Math.*, 34 (2003) 1547-1557.

[15] Sulaiman W.T., Some New Factor Theorem for Absolute Summability, *Demonstratio Math.*, 46 (2013) 149-156.

[16] Özarlan H.S., Öğdük H.N., On Absolute Matrix Summability Methods, *Math. Commun.*, 12 (2007) 213-220.

[17] Özarlan H.S., A Note on  $|A, p_n|_k$  Summability Factors, *Antarct. J. Math.*, 7 (2010) 23-30.

[18] Özarlan H.S., A New Application of Almost Increasing Sequences, *Miskolc Math. Notes*, 14 (2013) 201-208.

[19] Özarlan H.S., On Generalized Absolute Matrix Summability, *Asia Pacific J. Math.*, 1 (2014) 150-156.

[20] Özarlan H.S., Şakar M.Ö., A New Application of Absolute Matrix Summability, *Math. Sci. Appl. E-Notes*, 3 (2015) 36-43.

[21] Özarlan H.S., A New Application of Absolute Matrix Summability, *C. R. Acad. Bulgare Sci.*, 68 (2015) 967-972.

[22] Özarlan H.S., A New Study on Generalized Absolute Matrix Summability, *Commun. Math. Appl.*, 7 (2016) 303-309.

[23] Özarlan H.S., A New Application of Generalized Almost Increasing Sequences, *Bull. Math. Anal. Appl.*, 8 (2016) 9-15.

[24] Özarlan H.S., An Application of  $\delta$ -quasi Monotone Sequence, *Int. J. Anal. Appl.*, 14 (2017) 134-139.

[25] Karakaş A., On Absolute Matrix Summability Factors of Infinite Series, *J. Class. Anal.*, 13 (2018) 133-139.

[26] Özarlan H.S., Karakaş A., On Generalized Absolute Matrix Summability of Infinite Series, *Commun. Math. Appl.*, 10 (2019) 439-446.

[27] Özarlan H.S., An Application of Absolute Matrix Summability using Almost Increasing and  $\delta$ -quasi-monotone Sequences, *Kyungpook Math. J.*, 59 (2019) 233-240.

[28] Kartal B., On an Extension of Absolute Summability, *Konuralp J. Math.*, 7 (2019) 433-437.

[29] Özarlan H.S., A New Factor Theorem for Absolute Matrix Summability, *Quaest. Math.*, 42 (2019) 803-809.

## Solving the Generalized Rosenau-KdV Equation by the Meshless Kernel-Based Method of Lines

Murat Arı<sup>1,a</sup>, Bahar Karaman<sup>2,b,\*</sup>, Yılmaz Dereli<sup>2,c</sup>

<sup>1</sup> Department of Mathematics, Faculty of Science, Karamanoğlu Mehmetbey University, Karaman, Türkiye.

<sup>2</sup> Department of Mathematics, Faculty of Science, Eskişehir Technical University, 23119 Eskişehir, Türkiye.

\*Corresponding author

### Research Article

#### History

Received: 03/06/2021

Accepted: 20/06/2022

#### Copyright



©2022 Faculty of Science,  
Sivas Cumhuriyet University

### ABSTRACT

This current investigation consists of the numerical solutions of the Generalized Rosenau-KdV equation by using the meshless kernel-based method of lines, which is a truly meshless method. The governing equation is a nonlinear partial differential equation but the use of the method of lines leads to an ordinary differential equation. Thus, the partial differential equation is replaced by the ordinary differential equation. The numerical efficiency of the used technique is tested by different numerical examples. Numerical values of error norms and physical invariants are compared with known values in the literature. Moreover, Multiquadric, Gaussian, and Wendland's compactly supported functions are used in computations. It is seen that the used truly meshless method in computations is very effective with high accuracy and reliability.

**Keywords:** Generalized Rosenau-Kdv equation, Meshless Kernel-based method of lines, Radial basis function.

<sup>a</sup> [muratari@kmu.edu.tr](mailto:muratari@kmu.edu.tr)  
<sup>c</sup> [ydereli@eskisehir.edu.tr](mailto:ydereli@eskisehir.edu.tr)

<sup>ib</sup> <https://orcid.org/0000-0002-4039-5970>  
<sup>id</sup> <https://orcid.org/0000-0003-0149-0542>

<sup>b</sup> [bahar\\_korkmaz@eskisehir.edu.tr](mailto:bahar_korkmaz@eskisehir.edu.tr) <sup>id</sup> <https://orcid.org/0000-0001-6631-8562>

## Introduction

The nonlinear evolution equation is one of the most considerable scientific research areas. Many scientists improved various mathematical models to designate wave behavior during the past several decades. One of these models is called the KdV equation. In order to describe wave propagation and spread interaction, this equation can be used in [1 – 3]. The equation indicates the long-time evolution of wave phenomena, in which the effect of the nonlinear terms  $UU_x$  is counterbalanced by the dispersion  $U_{xxx}$ . There are a lot of works on this equation in the literature, see [4 – 9] and references therein.

In this paper, we consider the Generalized Rosenau-KdV equation which is a nonlinear partial differential equation. It is defined by the following form:

$$u_t + u_x + u_{xxx} + u_{xxxx} + \beta(u^p)_x = 0 \quad (1)$$

where  $\beta > 0$ ,  $p \geq 2$  is an integer. When  $p = 2$ , the Rosenau-KdV equation is obtained. Rosenau equation was proposed to describe the dynamics of dense discrete systems in [10, 11]. In the search, numerical outcomes will be conducted for different values of  $p$ . In calculations following initial and boundary conditions will be used:

$$u(a, t) = u(b, t) = 0, \quad 0 \leq t \leq T, \quad (2)$$

$$u(x, 0) = f(x) \quad (3)$$

The solitary solution and invariants for the generalized Rosenau-KdV equation are given in [12, 13]. There are a large number of theoretical and numerical studies for equation (1) which are seen in references [12 – 21].

The sech-ansätze method was used for the solitary solutions of the equation by Esfahani in [12]. Razborova et. al. [13] studied dynamics of dispersive shallow water wave of the Rosenau-KdV equation with power law nonlinearity. Solitary and periodic solutions were derived by Zuo in [14]. The solitary wave ansatz method is used to obtain topological 1-soliton solution of the generalized Rosenau-KdV equation in [15]. Conservative linear difference scheme was used to obtain numerical solutions of Rosenau-KdV and generalized Rosenau-KdV in [16]. Also, Zheng and Zhou [17] presented an average linear finite difference scheme for the numerical solution of the initial-boundary value problem of the generalized Rosenau-KdV equation. In the study [18], authors used a conservative Crank-Nicolson finite difference scheme for the initial-boundary value problem of the generalized Rosenau-KdV equation. It can be seen that the difference scheme shows a discrete analog of the main conservation laws associated to the equation in this paper. Karakoç et. al. [19] proposed the finite element method based on collocation. In the studies [20, 21], the authors solved the equation by using meshless method based on radial basis functions.

One of the important issues is a computation with high-dimensional data in many areas of science and engineering. As known, many traditional methods such as finite elements, finite differences, finite volumes, and boundary elements method require a regular domain mesh generation to solve problems. However, the meshless methods require neither domain nor surface discretization because they are independent of a mesh. So, instead of generating the mesh, they use scattered

nodes, which can be randomly distributed, through the computational domain. This is a great advantage since mesh generation is one of the most time-consuming parts of any mesh-based numerical simulation. Thus, meshfree methods provide an attractive alternative for solving certain problems. Up to now, the generalized Rosenau KdV equation has not been solved by using the meshless kernel-based method of lines. This method depends upon the meshless solution technique and so there is no need to an extra discretization. It is a way of approximating partial differential equations by ordinary differential equations. Therefore, the problem of correct time-stepping will be automatically solved by the ODE solver.

Our main intention in this present paper is to indicate that the method is appropriate and reliable to obtain a numerical solution to partial differential equations. That's why, in this paper, we construct the proposed method to obtain the numerical results for the generalized Rosenau KdV equation.

The design of this paper is as follows: In Sec. 2, we construct the implementation of the Meshless kernel-based method of lines. In Sec. 3, numerical outcomes are illustrated. End the study with a short conclusion given in Sec. 4.

### Governing of the Proposed Method to the Generalized Rosenau-KdV Equation

Our main intention of this investigation is to solve the mentioned equation by applying the meshless kernel-based method of lines. This method leads to a system of ordinary differential equations. The advantages of the present method are that there will no time discretization at all, and there will be no unnatural linearization of the differential equation as in diversified other articles. The problem of correct time-stepping will be automatically solved by the ODE solver we call.

Here, the approximate solution  $u$  is considered by a linear combination as follows [22] :

$$u(x, t) = \sum_{j=1}^N \alpha_j(t) v_j(x) \tag{4}$$

where  $\alpha_j(t)$  is an unknown term and  $v_j(x)$  is spatial term obtained by using different radial basis functions. The most commonly used RBFs are Gaussian (G), Multiquadric (MQ) and Wendland's compactly supported functions which are listed in the following, respectively:

1.  $\phi(r) = \exp(-r^2/\varepsilon^2)$ ,
2.  $\phi(r) = \sqrt{(\varepsilon r)^2 + 1}$ , where  $\varepsilon$  is a shape parameter (see the details in [23]).
3.  $\phi_{l,k}(r) = (1-r)_+^k h(r)$

Wendland's compactly supported functions ( $W$ ) (see the details in [24] ) which are defined as follows:

$$\begin{aligned} W_{4,2}(r) &= (1-r)_+^6(3+18r+35r^2), \\ W_{5,3}(r) &= (1-r)_+^8(1+8r+25r^2+32r^3), \\ W_{6,4}(r) &= (1-r)_+^{10}(5+50r+210r^2+450r^3+429r^4), \\ W_{7,5}(r) &= (1-r)_+^{12}(9+108r+566r^2+1644r^3+2697r^4+2048r^5) \end{aligned}$$

where  $r$  denotes the Euclidean distance between two collocation points. It is seen that these base functions depend on space variables. For ease notation in the rest of the paper,  $\phi_{l,k}$  will be used as  $W_{l,k}$ . Partial derivatives of  $u(x, t)$  easily evaluated as follows:

$$u_t(x, t) = \sum_{j=1}^N \alpha'_j(t) v_j(x) \tag{5}$$

$$u_x(x, t) = \sum_{j=1}^N \alpha_j(t) v'_j(x) \tag{6}$$

By writing necessary derivative terms in the equation (1) we get

$$\sum_{j=1}^N \alpha'_j(t) v_j(x) + \sum_{j=1}^N \alpha_j(t) v'_j(x) + \sum_{j=1}^N \alpha_j(t) v_j'''(x) + \sum_{j=1}^N \alpha'_j(t) v_j^{iv}(x) + \beta \left( \left( \sum_{j=1}^N \alpha_j(t) v_j(x) \right)^p \right)' = 0 \tag{7}$$

where the last term is a nonlinear term. After taking a derivative of nonlinear term the equation (7) can be written as follows:

$$\begin{aligned} \sum_{j=1}^N \left( v_j(x) + v_j^{iv}(x) \right) * \alpha'_j(t) &= - \sum_{j=1}^N \alpha_j(t) v'_j(x) - \sum_{j=1}^N \alpha_j(t) v_j'''(x) - \\ \beta p \left( \sum_{j=1}^N \alpha_j(t) v_j(x) \right)^{p-1} \sum_{j=1}^N \alpha_j(t) v'_j(x) & \end{aligned} \tag{8}$$

This equality is written in the following symbolic form

$$(V + V^{iv}) * \alpha'(t) = -(V' * \alpha(t)) - (V''' * \alpha(t)) - \beta p(V * \alpha(t))^{p-1} * (V' * \alpha(t)) \tag{9}$$

where V is an invertible matrix and its entries are base functions and  $\alpha(t)$  is a vector. Therefore, the equation (9) can be written as;

$$\alpha'(t) = -(V + V^{iv})^{-1} * [V' * \alpha(t) + V''' * \alpha(t) + \beta p(V * \alpha(t))^{p-1} * (V' * \alpha(t))] \tag{10}$$

Finally, the governing equation is converted to an ordinary differential equation. In our computations, the equation (10) is solved by using ode113 in MATLAB. The solver ode113 uses the Adams-Bashforth-Moulton predictor-corrector method.

### Numerical Results

This section illustrates some numerical results of the governing equation by using the method described above. Numerical values of error norms and invariants are prominent to test the accuracy of the method. Error norms are defined as follows:

$$L_2 = \sqrt{h \sum_{j=1}^N |u_j^{exact} - u_j^{num.}|^2} \tag{11}$$

$$L_\infty = \max_{1 \leq j \leq N} |u_j^{exact} - u_j^{num.}| \tag{12}$$

For a numerical comparison of invariants following mass and energy conservations are used [12]:

$$Q(t) = \int_a^b u(x, t) dx \text{ and} \tag{13}$$

$$E(t) = \|u\|^2 + \|u_{xx}\|^2 \tag{14}$$

In numerical treatments degree of a nonlinear term is taken as  $p = 2$ ,  $p = 3$ , and  $p = 5$ .

**Case 1:** When  $p = 2$  and  $\beta = 0.5$ , the solitary wave solution of the Rosenau-KdV equation is defined as follows [15]:

$$u(x, t) = \left(-\frac{35}{24} + \frac{35}{312}\sqrt{313}\right) \times \text{sech}^4 \frac{1}{24} \sqrt{-26 + 2\sqrt{313}} \left[x - \left(\frac{1}{2} + \frac{\sqrt{313}}{26}\right)t\right] \tag{15}$$

Solution domain is taken as  $-70 \leq x \leq 100$  with  $h = 1$  up to time  $T = 60$  with  $\Delta t = 0.1$ . Values of invariants are evaluated as  $Q = 5.498173$  and  $E = 1.9897829$  at time  $t = 0$ . Computed values of invariants are tabulated in Tables 1 and 2. As seen in the tables, the values of invariants are preserved. At the end of running time analytical value of amplitude is evaluated as 0.5258 at the location  $x = 71$ . For all numerical approximations same amplitude value and location data were evaluated. It is observed that solitary wave property is preserved by using different radial basis functions. Solitary wave simulations are plotted in Figure 1.

Table 1. Error norms and invariants for  $p = 2$  and  $T = 40$

Method	$L_2$	$L_\infty$	$Q$	$E$
$W_{7,5}$	5.195308e-6	1.024193e-6	5.4981736	1.9897829
$W_{6,4}$	5.049681e-6	1.736524e-6	5.4981736	1.9897828
G	8.541866e-4	3.372133e-4	5.4981736	1.9897971
MQ	2.025134e-4	4.563390e-5	5.4972047	1.9897816
[20]	1.152193e-3	4.02987e-4	5.49816	1.98978
[15]	5.297873e-3	1.878952e-3	5.49773	1.98470

Table 1. Error norms and invariants for  $p = 2$  and  $T = 40$

Method	$L_2$	$L_\infty$	$Q$	$E$
$W_{7,5}$	5.656446e-6	9.697467e-7	5.4981690	1.9897829
$W_{6,4}$	8.161006e-6	2.783771e-6	5.4981692	1.9897828
G	1.086041e-3	4.022695e-4	5.4981704	1.9897996
MQ	3.503223e-4	7.847234e-5	5.4960065	1.9897815
[19]	1.519562e-3	5.146861e-4	5.49815	1.98978

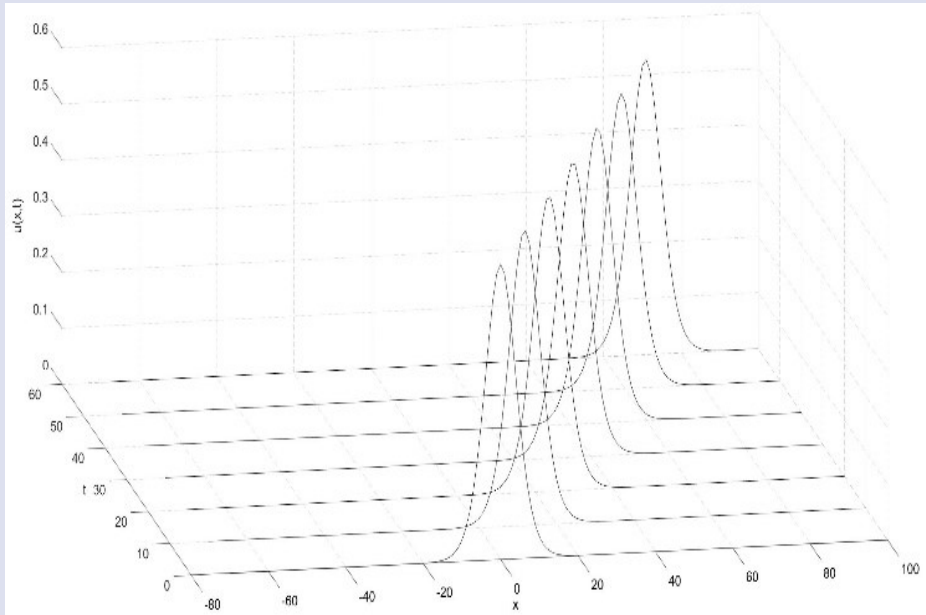


Figure 1. Solitary wave motion for  $p = 2$

**Case 2:** For  $p = 3$  and  $\beta = 1$ , the soliton solution is given as follows [12,13]:

$$u(x, t) = \frac{1}{4} \sqrt{-15 + 3\sqrt{41}} \times \operatorname{sech}^2 \frac{1}{4} \sqrt{\frac{-5 + \sqrt{41}}{2}} \left[ -\frac{1}{10} (+\sqrt{41})t \right] \quad (16)$$

Calculations are done in the domain  $-60 \leq x \leq 100$  with  $h = 1$  up to time  $T = 40$  for  $\Delta t = 0.1$  to make detailed comparisons with references. Comparison of evaluated numerical values is given in Table 3. It has been seen that very sensitive numerical values are computed. At the initial time, invariants are found as  $Q = 4.8989794$  and  $E = 1.6825477$ . Numerical values of invariants are almost the same as the initial values. Therefore, it is seen that the performance of the method is very high and reliable. The simulation of progressive waves keeping original forms are seen in Figure 2. In computations, it is seen that amplitude values are equal to the exact value 0.5096 at the position  $x = 46$  for all radial basis functions.

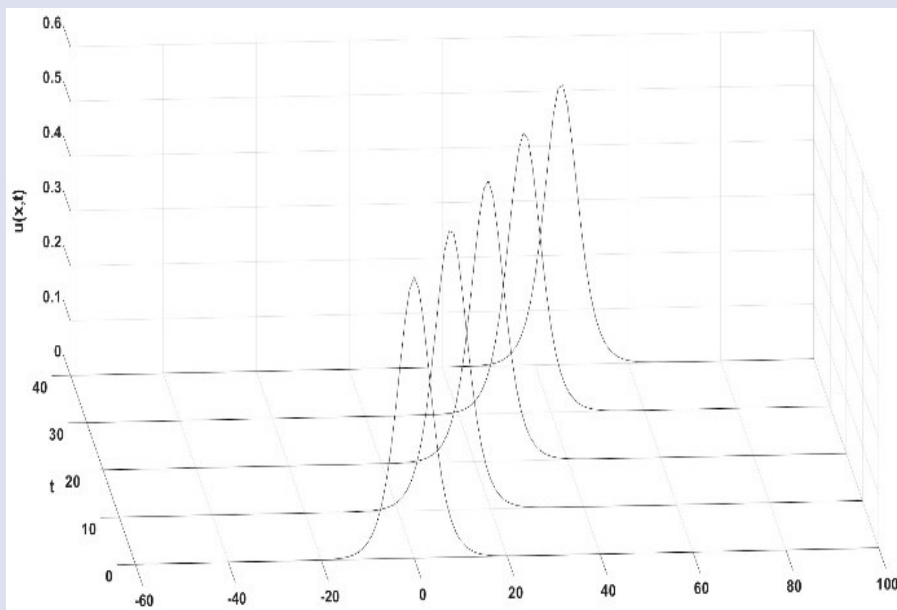


Figure 2. Solitary wave motion for  $p = 3$

Table 3. Error norms and invariants for  $p = 3$ .

Method	$L_2$	$L_\infty$	$Q$	$E$
$W_{7,5}$	1.0290e-06	3.0720e-07	4.8989794	1.6825477
$W_{6,4}$	6.1124e-06	2.3119e-06	4.8989795	1.6825477
G	1.8629e-06	5.7893e-07	4.8989797	1.6825477
MQ	3.0026e-04	6.4671e-05	4.8975866	1.6825450
[20]	1.7880e-03	6.3620e-04	4.8989794	1.682539
[15]	1.3498e-02			
[16]		7.5394e-03		1.6825466

Case 3: When  $p = 5$  and  $\beta = 1$  the soliton solution is defined as [16]:

$$u(x, t) = \sqrt[4]{\frac{4}{15}(-5 + \sqrt{34})} \times \operatorname{sech} \frac{1}{3} \sqrt{-5 + \sqrt{34}} \left[ x - \frac{1}{10} (5 + \sqrt{34}) t \right] \tag{17}$$

where the solution domain  $-60 \leq x \leq 100$  and time  $T = 40$ . In computations mesh step and the time step is taken as  $h = 1$  and  $\Delta t = 0.1$ . Comparison of numerical results with the results of some other papers is presented in Table 4. Numerical values of invariants at the beginning of the solitary wave are calculated as  $Q = 7.0936431$  and  $E = 3.1107123$ . The single solitary wave profile is illustrated in Figure 3. It can be observed that solitary wave keeps its original form during computing time. This situation implies that the energy is conservative. Solitary wave has amplitude= 0.6828 at  $x = 43$ . As seen is computed results, the present numerical method by using different radial basis functions is slightly better than other referenced works.

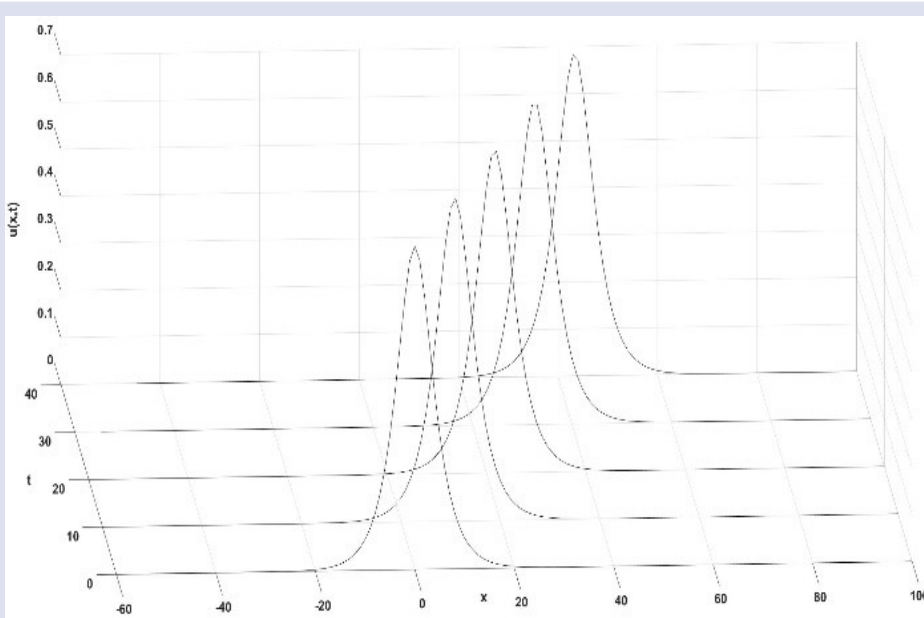


Figure 2. Solitary wave motion for  $p = 5$

Table 4. Error norms and invariants for  $p = 5$ .

Method	$L_2$	$L_\infty$	$Q$	$E$
$W_{7,5}$	2.2926e-06	8.1216e-07	7.0936430	3.1107122
$W_{6,4}$	1.6895e-05	6.0986e-06	7.0936431	3.1107119
G	3.8193e-05	2.2361e-05	7.0936631	3.1107123
MQ	4.8448e-04	1.2184e-04	7.0909712	3.1107111
[20]	3.3217e-03	1.1897e-03	7.0936431	3.205919
[16]	1.7998e-02			
[17]		1.2020e-02		3.1107099

### Conclusions

In this paper, the meshless kernel-based method of lines is applied successfully to get the numerical solution of the Generalized-Rosenau-KdV equation for different

nonlinear cases. In computations degree of the nonlinear term is used as 2,3 and 5. It is seen that the used proposed method is a very suitable technique solving for the given nonlinear partial differential equation and similar nonlinear equations. The method can be applied easily



because there is no need an extra linearization. Therefore, the governing equation is replaced by an ordinary differential equation and it is solved easily by using MATLAB ode-solver code. When we compare the studied in the literature with our numerical results, it can be seen that the results are obtained with high accuracy. It is said that the used meshless technique is a powerful solution method, and we believe that the current method can be applied to construct new solutions for these types of equations in future studies.

### Conflicts of interest

The authors state that there is no conflict of interest regarding the publication of this study.

### References

- [1] Korteweg D., Vries G. D., On the change in form of long waves advancing in rectangular canal and on a new type of longstationary waves, *Philos. Mag.*, 39 (1895) 422–443.
- [2] Cui Y., Mao D. K., Numerical method satisfying the first two conservation laws for the Korteweg-de Vries equation, *J. Comput. Phys.*, 227(1) (2007) 376–399.
- [3] Zhu S. and Zhao J., The alternating segment explicit-implicit scheme for the dispersive equation, *Appl. Math. Lett.*, 14(6) (2001) 57–662.
- [4] Kudryashov N.A., On new travelling wave solutions of the KdV and the KdV-Burgers equations, *Commun. Nonlinear Sci. Numer. Simul.*, 14 (2009) 1891-1900.
- [5] Wazzan L. A., Modified tanh-coth method for solving the KdV and the KdV-Burgers equations, *Commun. Nonlinear Sci Numer. Simul.*, 14 (2009) 443-450.
- [6] Biswas A., Solitary wave solution for KdV equation with power-law nonlinearity and time-dependent coefficients, *Nonlinear Dyn.*, 58 (2009) 345-348.
- [7] Wang G. W., Xu T. Z., Ebadi G., Johnson S., Strong A. J., A., Biswas A., Singular solitons, shock waves, and other solutions to potential KdV equation, *Nonlinear Dyn.*, 76 (2014) 1059-1068.
- [8] Dehghan M., Shokri A. A numerical method for KdV equation using collocation and radial basis functions, *Nonlinear Dynamics*, 50 (2007) 111-120.
- [9] Vaneeva O. O., Papanicolaou N. C., Christou M. A., Sophocleous C., Numerical solutions of boundary value problems for variable coefficient generalized KdV equations using Lie symmetries, *Commun. Nonlinear Sci. Numer. Simul.*, 19 (2014) 3074-3085.
- [10] Rosenau P. A quasi-continuous description of a nonlinear transmission line, *Phys. Scr.*, 34 (1986) 827-829.
- [11] Rosenau P., Dynamics of dense discrete systems, *Prog. Theor. Phys.*, 79 (1988) 1028-1042.
- [12] Esfahani A., Solitary wave solutions for generalized Rosenau-KdV equation, *Commun. Theor. Phys.*, 55(3) (2011) 396–398.
- [13] Razborova P., Triki H., Biswas A. Perturbation of dispersive shallow water waves, *Ocean Eng.*, 63 (2012) 1–7.
- [14] Zuo J. M., Solitons and periodic solutions for the Rosenau-KdV and Rosenau-Kawahara equations, *Appl. Math. Comput.*, 215(2) (2009) 835–840.
- [15] Saha A., Topological 1-soliton solutions for the Generalized Rosenau-Kdv equation, *Fundamental J. Math. Phys.*, 2(1) (2012) 19–23.
- [16] Hu J., Xu Y., Hu B., Conservative linear difference scheme for Rosenau-KdV equation, *Adv. Math. Phys.*, (2013) 423718.
- [17] Zheng M., Zhou J., An Average Linear Difference Scheme for the Generalized Rosenau-KdV Equation, *J. Appl. Math.*, (2014) 202793.
- [18] Luo Y., Xu Y., Feng M., Conservative Difference Scheme for Generalized Rosenau-KdV Equation, *Adv. Math. Phys.*, (2014) 986098 .
- [19] Ak T., Dhawan S., Karakoç S. B. G., Bhowmik S. K., Raslan K. R., Numerical Study of Rosenau-KdV Equation Using Finite Element Method Based on Collocation Approach, *Math. Model. Anal.*, 22(3) (2017) 373-388.
- [20] Korkmaz B., Dereli Y., Numerical solution of the Rosenau-KdV-RLW equation by using RBFs Collocation method, *Int. J. Mod. Phys. C*, 27(10) (2016) 1650117.
- [21] Karaman B., Dereli Y., Meshless Method Based on Radial Basis Functions for General Rosenau KdV-RLW Equation, *Anadolu University Journal of Science and Technology B-Theoretical Sciences*, 6(1) (2018) 45-54.
- [22] Schaback R., The Meshless Kernel-Based Method of Lines for Solving Nonlinear Evolution Equations, Preprint, Göttingen, (2008).
- [23] Rolland H.L. Multiquadric equations of topography and other irregular surfaces, *J. Geophys. Res.*, 176 (1971) 1905-1915.
- [24] Wendland H. Piecewise polynomial, positive definite and compactly supported radial functions of minimal degree, *Adv. Comp. Math.*, 4 (1995) 389-396.

## Variation of Pinning Force Density Throughout the TSMG Y123 Superconductor with Location

Bakiye Çakır<sup>1,a,\*</sup>

<sup>1</sup> Vocational School of Health Services, Artvin Çoruh University, Artvin, Türkiye.

\*Corresponding author

### Research Article

#### History

Received: 09/03/2022

Accepted: 05/05/2022

#### Copyright



©2022 Faculty of Science,  
Sivas Cumhuriyet University

### ABSTRACT

Top seeded melt growth (TSMG) Y123 sample with 35 mm diameter was produced by using Nd123 seed and its superconducting parameters such as transition temperature ( $T_c$ ), critical current density ( $J_c$ ) and pinning mechanism were locally examined by taking small specimens which are containing defects in different number, size and distribution from different locations throughout the sample. The  $T_c$  of the main sample was determined from the resistivity measurement as 93.4 K. It was observed that the  $J_c$  was higher in the region close to the seed, while the  $J_c$  decreased towards to the edge or the deeper regions of the sample. Effective pinning mechanisms at different temperatures were determined by plotting the curves of the pinning force density ( $f_p$ ) of the specimens versus reduced magnetic field ( $h = H_a/H_{max}$ ) and the locational variations of the  $f_p$  were examined. It was seen that below the value of  $h \approx 0.2$ , normal point pinning was dominant at 30 and 50 K, while surface pinning was dominant at 77 K, in the all specimens. In addition, a transition was observed between two different pinning mechanisms when the  $H_{max} > h > 0.2$ . The transition was took place between  $\Delta K$  and normal point pinning at 30 and 50 K while it was seen between  $\Delta K$  and surface pinning at 77 K.

**Keywords:** Pinning force density, Critical current density, Local variation of superconductivity, TSMG Y123.

[bcakir@artvin.edu.tr](mailto:bcakir@artvin.edu.tr)

<https://orcid.org/0000-0003-4339-1913>

## Introduction

Discovery of the high temperature superconductor (HTS) which offer a superconducting transition at the liquid nitrogen temperature have been lead to many studies on the usability of superconductors in both materials science and its engineering applications. It is essential to achieve high superconducting properties such as critical current density ( $J_c$ ), critical transition temperature ( $T_c$ ) and field trapping capabilities for the applications [1-3]. On the other hand the magnetic field penetrates in the form of vortices in the HTSs and vortices can move easily when the temperature approaches the  $T_c$  or when high fields are applied. At that case, the  $J_c$  value is suppressed by thermal fluctuations and the increasing applied magnetic field due to the vortex motion caused by the effect of the Lorentz force [4]. Therefore, the vortices are needed to pin into the crystals to improve the  $J_c$  by introducing effective pinning centers in the form of impurities and defects (such as oxygen vacancies, dislocations, aggregation defects, chemical additives and secondary phase particles) [5]. Additionally, the sizes of these defects must be in the nanometer range [6].

The HTSs are generally produced by annealing the samples, which are pressed in the selected composition with appropriate methods and heat treatments. The Y123 single crystals grow basically in a structure with non-superconducting green inclusions called the Y211 phase entrapped and distributed throughout the matrix. The obtained superconducting samples can be single or multi grained. For this reason it is important to determine the

optimum conditions for the fabrication of the sample in order to obtain a high current carrying capacity. It is possible to produce large single-grained samples aligned in the  $c$ -axis direction with the melting methods and especially top seed melt growth (TSMG) and infiltration growth (IG) methods are promising. Generally, seeds having a higher melting temperature and a similar crystal structure to the main sample are used in these methods [7-12].

On the other hand, since  $J_c$  in two-phase alloys is affected by the size and distribution of the second phase particles, the selected region cut from the sample affects the  $J_c$  value. Even  $J_c$  values can be change throughout the sample. If the small sections selected from multi-grain samples include in grain boundaries, micro cracks or different size and distribution of the pinning centers, it would be also effect the  $J_c$  value. So the superconducting properties of the melt growth bulk superconductor generally change with the position in the volume [13, 14]. In this study, the  $J_c$  values of the specimens taken from different parts of the TSMG Y123 sample were calculated and the regional variations of the pinning force densities and pinning mechanism were examined at different temperatures

## Material and Method

The powder mixture prepared in  $Y_2O_3$ :  $BaCO_3$ :  $CuO$  = 1:2:3 stoichiometric ratio was calcined in an alumina

crucible at 900°C for 30 hours with an intermediate grinding. The powder mixture was ground again after the calcination process and completely melted at 1450°C in a platinum crucible. The melted powder mixture poured onto a copper plate and cooled quickly by hitting with another copper plate. Thin plates obtained after the melting process was ground again and Y123 starting powder was prepared. 40 g of the starting powder was weighed and pressed into a 35 mm diameter pellet under 11 tons/cm<sup>2</sup> pressure. The Nd123 seed was placed in top surface center of the sample pressed into the pellet and the sample was placed on an alumina substrate with Y<sub>2</sub>O<sub>3</sub>

powder. The sample was growth by applying the heat treatment given in Figure 1. After all, the grown Y123 sample was annealed for 200 hours at 500°C in oxygen atmosphere.

Resistivity and magnetization measurements were made by taking small specimens from the Y123 sample obtained after crystal growth process. The location of the specimens (a, b, c and d) is schematically given in the Figure 2 and they were labeled as Y-a, Y-b, Y-c and Y-d. Y-a, Y-b and Y-c were used for magnetization measurements and Y-d was used resistivity measurement

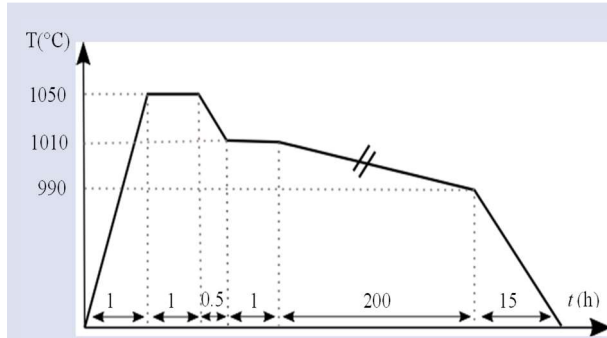


Figure 1. Thermal process of the crystal growth for TSMG Y123.

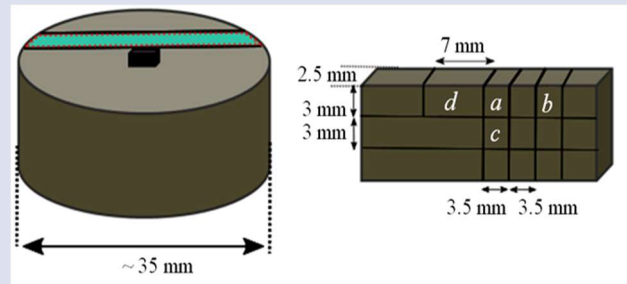


Figure 2. Schematic drawing of the specimen locations cut from the TSMG Y123 sample.

**Apparatus**

X-ray diffraction data were collected from the sample and small specimens cut from the main sample after the upper surfaces of the sample were cleaned by sanding and polished by using a Rikagu D/Max III C diffractometer, employing CuKα (λ = 1.5418 Å, 40 kV, 30 mA) radiation

Standard four probe resistivity measurement of the Y-d sample was performed at temperatures between 60 and 100 K at 0 T magnetic field using a PPMS. The magnetization measurements were operated by using VSM module of the PPMS system at constant temperatures 30, 50 and 77 K at a sweep speed of 100 Oe/s and by applying a magnetic field parallel to the c-axis between -5T and +5T. All the measurements were performed in zero-field cooling (ZFC) regime.

The critical current densities J<sub>c</sub> (A/cm<sup>2</sup>) of the specimens have been estimated from the magnetization measurements by using the extended Bean model as given the below equation.

$$J_c = 20\Delta M/a(1 - a/3b) \tag{1}$$

where ΔM is the width of the magnetization curve in emu·cm<sup>-3</sup>, a and b (a < b) are the dimensions of the rectangular cross section of the sample in cm.

Pinning mechanism was determined by using Dew-Hughes model [15]. The Dew-Hughes model of elementary pinning forces (F<sub>p</sub> = J<sub>c</sub> × B) is generally expressed with normalized pinning force density, f<sub>p</sub> = F<sub>p</sub>/F<sub>p,max</sub> and often scales with reduced field h = (H<sub>0</sub>/H<sub>irr</sub>) is the ratio between applied magnetic field external H<sub>0</sub> and

irreversibility field H<sub>irr</sub> (where F<sub>p</sub> = 0) which can be determined from magnetoresistivity, AC susceptibility and magnetization measurements. The scaling of f<sub>p</sub> - h for the HTS is often analyzed using the Equations (2-4) [16, 17].

$$f_p(b) = 3b^2(1 - 2b/3) \quad \Delta\kappa \text{ pinning} \tag{2}$$

$$f_p(b) = (9b/4)(1 - b/3)^2 \quad \text{Normal point pinning} \tag{3}$$

$$f_p(b) = (25\sqrt{b}/16)(1 - b/5)^2 \quad \text{Surface pinning} \tag{4}$$

Dislocations or needle-shaped precipitation are the point pinning centers and they can interact with only one flux line. Twin planes, grain boundaries and plane-like precipitation are the surface pinning centers. The large precipitation and thick-walls dislocations from cell-structures are the Δκ pinning (volume pinning) centers [18].

**Results and Discussion**

**Synthesis and Characterization**

X-ray diffraction patterns of the main Y123 sample and small specimens cut from the different position of the Y123 sample are shown in Figure 3. Main sample Y123 and the Y-a, Y-b and Y-c specimens have predominantly (00ℓ) orientation peaks and small amount of the non-superconducting Y211 inter phase formed by the heat treatment process was also observed in the structure. This indicates that the sample has almost single-crystal

structure and a preferential orientation in the c-axis direction. The preferred orientations of HTS result to higher  $J_c$  [19]. In addition, the presence of the he Y211 phases are known to function as pinning centers in Y123 samples produced by melting process. On the other hand, the specimens Y-b located near the corner and Y-c located near the bottom of the sample have also extra low intensity peak of Y211 phase different from the Y-a. This situation states that non superconducting residual phases increase with increasing distance from the seed.

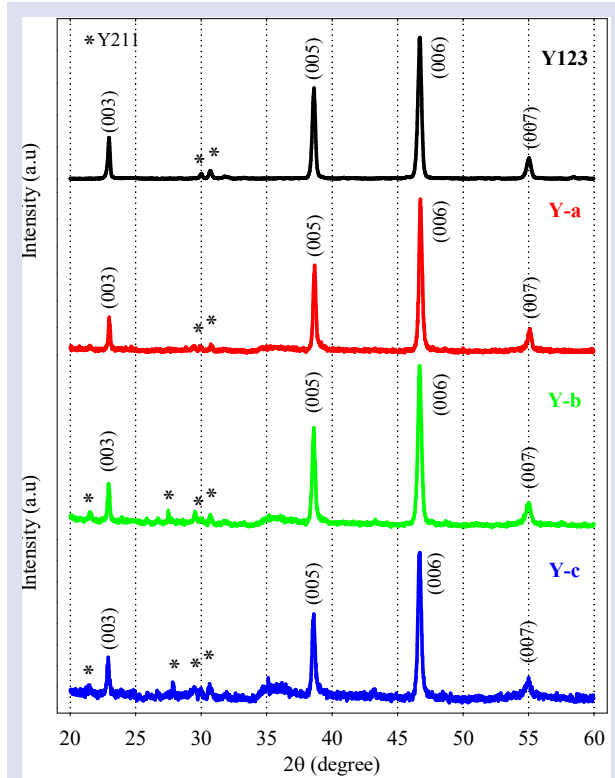


Figure 3. X-ray diffraction pattern of TSMG Y123 sample and Y-a, Y-b and Y-c specimens cut from the sample.

### Electrical Investigation

The resistivity-temperature curve of the Y-d specimen during heating at 0T magnetic field and the temperature change curve of  $dR/dT$  determined the  $T_c$  transition temperature at which the superconducting state starts are given in Figure 4. Transition temperature  $T_c$  was determined as 93.4 K from the maximum peak position of the  $dR/dT$  curve and the transition gap ( $\Delta T_c$ ) obtained full width half maximum of the curve was approximately 1 K. Shortness of the transition is due to the single grain property or strong inter-granular connection.

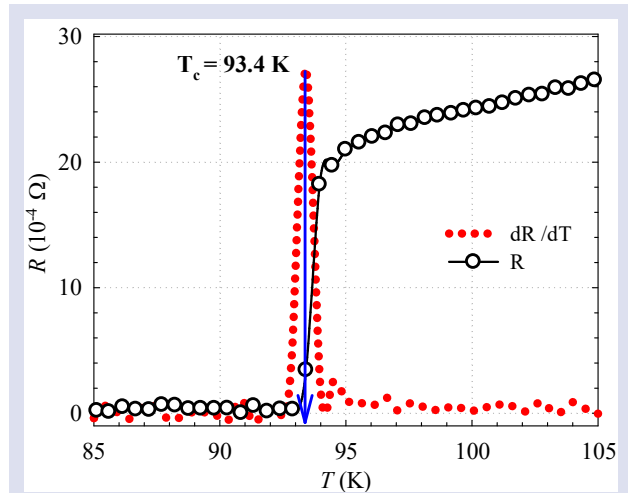


Figure 4. The resistivity-temperature curve of the Y-d specimen under 0 T magnetic field and the  $dR/dT$  curve determined the  $T_c$  value.

### Magnetic Investigation

Figure 5 shows the variation of  $J_c$  calculated from the Bean critical state model against the external magnetic field for Y-a, Y-b and Y-c specimens at 30, 50 and 77 K. In the low magnetic field and high temperature region,  $J_c$  decreases quickly with the temperature. It is clearly seen in Figure 5 that  $J_c$  changes slightly with the increasing field at 30 and 50 K. This variation shows that all specimens are resistant to the external magnetic field and this case observed in single crystal superconductors. In addition, there is no explicit difference between all the specimens, there are only small variations. The specimen Y-a cut from the near the seed at first layer had clearly higher  $J_c$  rather than the Y-b cut from far the seed at first layer and Y-c cut from the second layer. It is well known that the  $J_c$  decrease as the distance the seed location on the upper surface center of the sample increases [14]. The  $J_c$  decreases much more when the operated temperature approaches the  $T_c$  because of the flux pinning created by the linear correlated disorders such as interfaces between the Y211 particles and Y123 grains [20]. Even so, it is seen that the  $J_c$  value in 77 K does not decrease to zero even under 4T area. The high  $J_c$  value in 77 K shows the quality of the sample and it's preferred for technological applications. Homogeneity of the different phases and particles into the main matrix can be change with the position for the melt growth bulk superconductors and so the superconducting properties can be changed. It was thought that one of the reasons for this is that the distribution and the size of the 211 particles that acting as the pinning center in the structure. Because the applied magnetic field starts to penetrate into the structure at constant temperatures with the increasing field, the superconductivity weakens and  $J_c$  decreases due to mobility of the vortex [21]. The other reason is that the composition of the melt varies continuously during the melt process. The local microstructure and the local properties are defined from the melt composition [13].

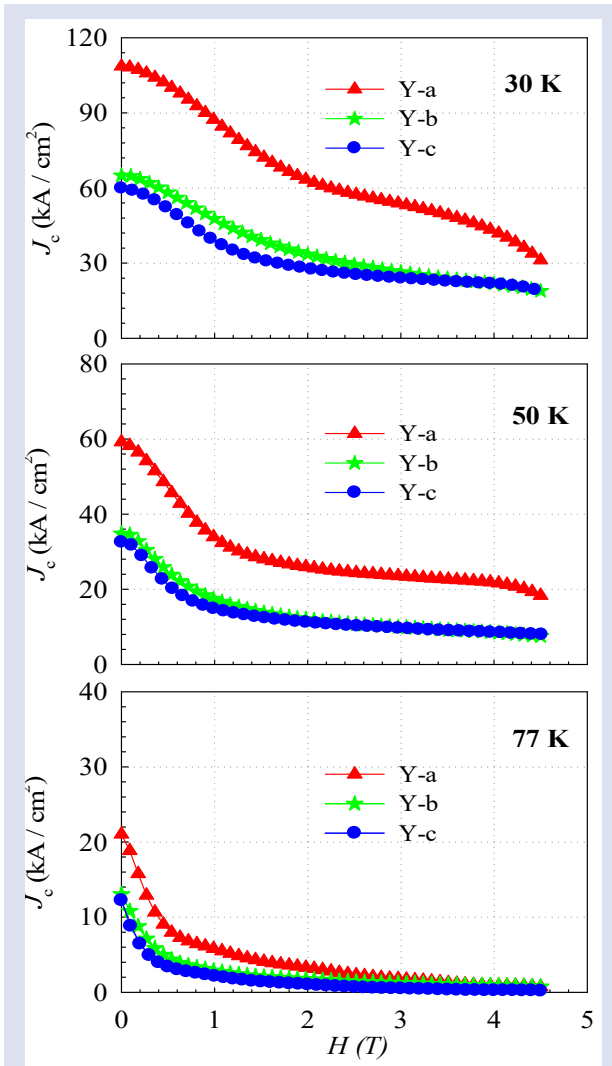


Figure 5. Critical current densities at 30, 50 and 77 K in the ZFC regime as a function of applied magnetic field for Y-a, Y-b and Y-c specimens.

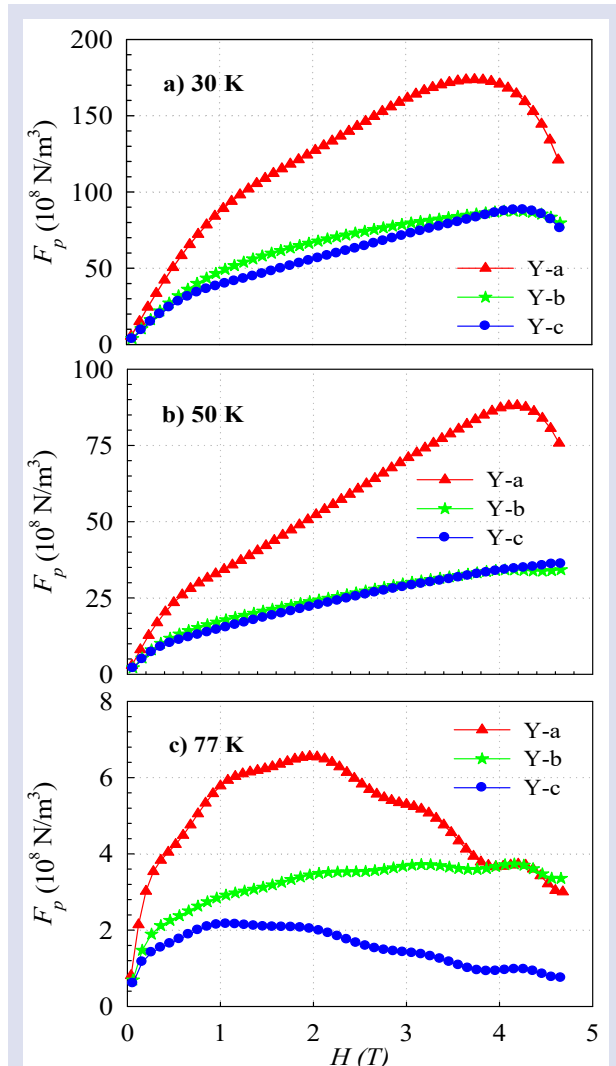


Figure 6. Plots of the volume pinning force ( $F_p$ ) as a function of applied magnetic field for the Y-a, Y-b and Y-c samples at a) 30 K, b) 50 K and c) 77 K.

In order to study the nature of the pinning mechanism, firstly the volume pinning force were calculated. The volume pinning forces,  $F_p$ , scaled in a function of the applied magnetic field for all the specimens at 30, 50 and 77 K and were given in Figure 6. In contrast to the  $J_c$ ,  $F_p$  always gives a maximum peak at  $H_{max}$ , before the  $F_p$  reaching zero at the irreversibility field ( $H_{irr}$ ). Since the  $F_p$  value does not drop to zero in the applied field, it is difficult to determine the  $H_{irr}$  value precisely for HTS. Therefore,  $H_{max}$  value was used instead of  $H_{irr}$  [17].  $H_{max}$  values were determined as 3.74, 4.15 and 4.22 T at 30 K, 4.16, 4.68 and 4.63 T at 50 K and 1.97, 4.16 and 1.08 T at 77 K for the Y-a, Y-b and Y-c, respectively.  $F_p(H)$  curves exhibit growing curvatures at low fields and low temperatures and the curve began to fall down after the peak value at high fields as 30 K and 50 K. On the other hand, the shape of the curvatures distorted at 77 K as the transition temperature is approached. Also, Y-a had a much greater pinning force than Y-b and Y-c as expected from the  $J_c$  results.

The normalized volume pinning force density  $f_p = F_p/F_{p,max}$  (where  $F_{p,max}$  is the maximum pinning force) are plotted versus the reduced magnetic field  $h = H_a/H_{max}$  in Figure 7. Equations (2)-(4) are also presented in the Figure 7. Dotted line represents that  $\Delta\kappa$  pinning, the dashed line represents normal ( $\Delta\ell$ ) point pinning and the solid line represents surface pinning. It is well known that HTSs have large  $\kappa$  values and core pinning is dominant rather than magnetic interaction in the superconductors. The core pinning leaves two different sources called  $\delta I$  and  $\Delta\kappa$  (or  $\delta T_c$ ) pinning [22].  $\delta I$  pinning centers are very effective at low fields and low temperatures and the centers behave like normal conducting particles embedded in the superconducting matrix. On the other hand,  $\Delta\kappa$  pinning centers are effective at the intermediate areas and temperatures, as they act as local oxygen deficient regions [23]. As shown in Figure 7, the specimens scaled in agreement below  $h \approx 0.2$  (low field region) with Equation (3), stating that the samples are predominantly affected by the normal point pinning at 30 and 50 K. The major defects in this category are the dislocation and needle

shape Y211 precipitations. When the magnetic fields increase a value between the  $h \approx 0.2$  and  $H_{max}$ , intermediate field region, the results are not scaled on a single theoretical curve. That is the plots are located between  $\Delta\kappa$  and normal point pinning. Because  $\Delta\kappa$  pinning centers consisting of the large precipitation, it is thought that the specimens have different sizes of the pinning centers in the samples. So, it can be said that large Y211 particles contribute to flux pinning.

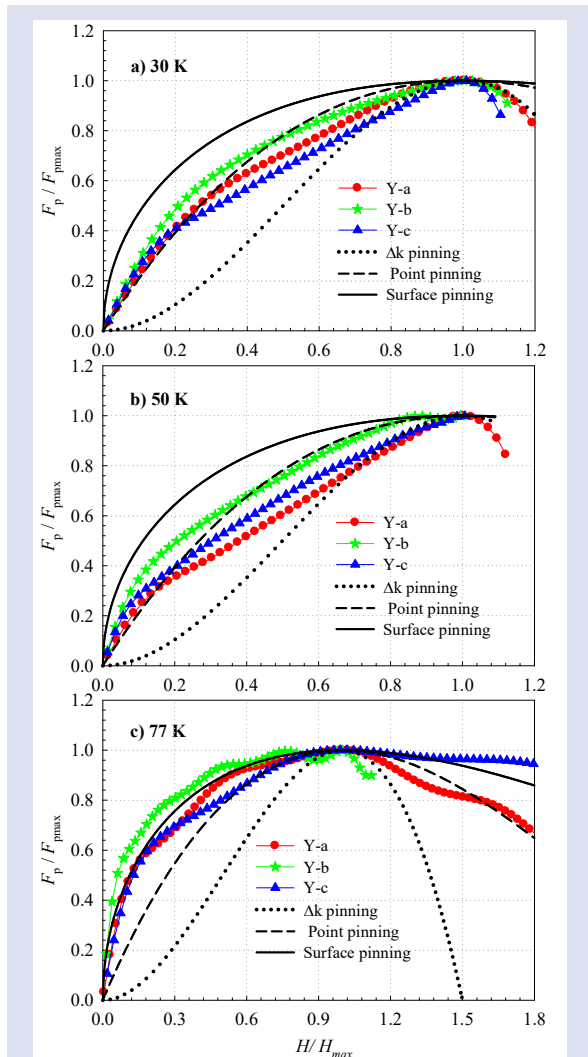


Figure 7. Plots of the normalized pinning force density ( $f_p$ ) versus reduced field  $b$  for the Y-a, Y-b and Y-c samples at a) 30 K, b) 50 K and c) 77 K. Dotted line is the fit curve of Equation (2) for  $\Delta\kappa$  pinning, dashed line is the fit curve of Equation (3) for normal point-pinning and solid line is the fit curve of Equation (4) for surface pinning.

## Conclusions

The pinning force scaling were analyzed for various specimens cut from the different location of the whole TSMG Y123 which is having different number, size and distribution of defects (Y211 inclusions, dislocation, stacking fault etc.). Observed (00 $\ell$ ) peaks indicate an

orientation in  $c$ -axis for all the specimens and states that single crystal behavior. The  $J_c$  value of the specimen cut from the close region to the seed of the top surface is higher than the specimens taken from the more extreme and lower regions of the sample. This difference in the  $J_c$  value change with depending on the number of 211 particles acting as the effective pinning center. The dominant pinning mechanism was normal point pinning (at 30 and 50 K) and surface pinning (at 77 K) below the low field region. The mechanism changed from  $\Delta\kappa$  to normal point pinning (at 30 and 50 K) and changed from  $\Delta\kappa$  to surface pinning (at 77 K) in  $H_{max} > h > 0.2$  field region. Dominant pinning mechanism changes with increasing the applied field and temperature due to the differences in the pinning centers. Observed transitions between the different pinning mechanisms as the applied field intensity increases originates from the different sizes and shapes of the Y211 particles presented into the structures of the samples. Therefore, the inhomogeneous distribution of different types and shapes of defects into the matrix causes the main superconducting properties such as  $J_c$  and flux pinning to vary locally. In this study, the defects that cause the superconducting properties to change are the Y211 particles trapped in the main matrix during the crystal growth process.

## Acknowledgment

This work was supported by the Scientific Research Support Fund of The Artvin Çoruh University, Artvin, Turkey, project number 2017.M80.02.02. The author would like to thank Prof. Dr. Alev AYDINER for valuable comments and useful discussions and Dr. Şeyda DUMAN for their help in experimental work.

## Conflicts of interest

The author states that did not have conflict of interests

## References

- [1] Yamachi N., Sakai N., Murakami M., Measurements of three-dimensional fields of bulk superconductors in varying external fields, *Supercond. Sci. Technol.*, 18 (2005) S67-S71.
- [2] Ikeda Y., Umakoshi S., Wongsatanawarid A., Seki H., Murakami M., Enhancement of mechanical strength in YBaCuO bulk superconductor through liquid binder addition, *Physica C*, 471 (2011) 846-849.
- [3] Lu Y., He D., Liu M., Magnetic force investigation of high- $T_c$  superconducting bulk over permanent magnet railway under different lateral offsets with experimental methods, *J. Mod. Phys.*, 4 (2013) 24-28.
- [4] Crisan A., Dang V.S., Mikheenko P, Nano-engineered pinning centres in YBCO superconducting films, *Physica C*, 533 (2017) 118-132.
- [5] Slimani Y., Almessiere M.A., Hannachi E., Baykal A., Manikandan A., Mumtaz M., Ben Azzouz F., Influence of  $WO_3$  nanowires on structural, morphological and flux pinning ability of  $YBa_2Cu_3O_y$  superconductor, *Ceramics International*, 45(2) (2019) 2621-2628.

- [6] Wang Y., Fundamental elements of applied superconductivity in electrical engineering. First. ed. Singapore: Science Press, John Wiley & Sons, (2013).
- [7] Ren H.T., Xiao L., Jiao Y.L., Zheng M.H., Processing and characterization of YBCO superconductors by top-seeded melt growth method in batch process, *Physica C*, 412–414 (2004) 597–601.
- [8] Hari Babu N., Jackson K.P., Dennis A.R., Shi Y.H., Mancini C., Durrell J.H., Cardwell D.A., Growth of large sized  $\text{YBa}_2\text{Cu}_3\text{O}_7$  single crystals using the top seeded melt growth process, *Supercond. Sci. Technol.*, 25 (2012) 075012.
- [9] Zhai W., Shi Y., Durrell J.H., Dennis A.R., Cardwell D.A., The influence of Y211 content on the growth rate and Y211 distribution in Y–Ba–Cu–O single grains fabricated by top seeded melt growth, *Cryst. Growth Des.*, 14 (2014) 6367–6375.
- [10] Volochova D., Kavcansky V., Antal V., Diko P., Yao X., Thermal stability of NdBCO/YBCO/MgO thin film seeds, *Supercond. Sci. Technol.*, 29 (2016) 044004.
- [11] Yang W.M., Yuan X.C., Guo Y.X., Influence of ZnO doping on the properties of single domain YBCO bulks fabricated by RE+011 TSIG process, *Int. J. Mod. Phys. B.*, 31(25) (2017) 1745018.
- [12] Namburi D.K., Shi Y., Dennis A.R., Durrell J.H., Cardwell D.A., A robust seeding technique for the growth of single grain (RE)BCO and (RE)BCO–Ag bulk superconductors, *Supercond. Sci. Technol.*, 31 (2018) 044003.
- [13] Xu Y., Izumi M., Tsuzuki K., Zhang Y., Xu C., Murakami M., Sakai N., Hirabayashi I., Flux pinning properties in a  $\text{GdBa}_2\text{Cu}_3\text{O}_{7-\delta}$  bulk superconductor with the addition of magnetic alloy particles, *J. Supercond. Nov. Magn.*, 22(9) (2009) 095009.
- [14] Aydinler A., Çakır B., Başoğlu M., Seki H., Wongsatanawarid A., Murakami M., Yanmaz E., Magnetic properties of YBCO single-crystal grown on Y2O3 layer by a cold top-seeding method, *J. Supercond. Nov. Magn.*, 25 (2012) 391–397.
- [15] Dew-Huges D., Flux pinning mechanism in type II superconductors, *Philosophical Magazine*, 30(2) (1974) 293–305.
- [16] Taylan Koparan E., Surdu A., Sidorenko A., Yanmaz E., Artificial pinning centers created by  $\text{Fe}_2\text{O}_3$  coating on  $\text{MgB}_2$  thin films, *Physica C*, 473 (2012) 1–5.
- [17] Li M., Chen L., You W-L., Ge J., Zhang J., Giant increase of critical current density and vortex pinning in Mn doped  $\text{K}_x\text{Fe}_{2-y}\text{Se}_2$  single crystals, *Appl. Phys. Lett.*, 105 (2014) 192602.
- [18] Çakır B., Taylan Koparan E., Savaşkan B., Relationship between pinning mechanism and excess conductivity analysis of x wt%  $\text{CaH}_6\text{O}_5$  (x= 0.0, 4.0 and 6.0) added bulk  $\text{MgB}_2$ , *J. Mater. Sci.: Mater. Electron.*, 32(15) (2021) 20317–20326.
- [19] Duman Ş., Çakır B., Aydinler A., Fluctuation-Induced Conductivity Analysis of  $\text{Y}_2\text{O}_3$ -Layered YBCO Single Crystal, *J. Supercond. Nov. Magn.*, 29 (2016) 2275–2280.
- [20] Feng Y., Wen J.G., Pradhan A.K., Koshizuka N., Zhou L., Chen S.K., Wang K.G., Wu X.Z., Preparation and properties of PMP YBCO bulk with submicrometre  $\text{Y}_2\text{BaCuO}_5$  particles, *Supercond. Sci. Technol.*, 13 (2000) 703–708.
- [21] Gupta S., Yadav R.S., Das B., Flux pinning by nano particles embedded in polycrystalline Y-123 superconductors, *arxiv.org*, (2011) 1107/1107.1116.
- [22] Crisan A., Dang V.S., Yearwood G., Mikheenko P., Huhtinen H., Paturi P., Investigation of the bulk pinning force in YBCO superconducting films with nano-engineered pinning centres, *Physica C*, 503 (2014) 89–93.
- [23] Kim G.C., Kim B.J., Cheon M.Y., Kim Y.C., Variation of pinning mechanism in  $\text{Bi}_{1.6}\text{Pb}_{0.4}\text{Sr}_2\text{CaCu}_2\text{O}_{8+\delta}$  single crystal, *Physica C*, 391 (2013) 305–308.

## Altering Electrical Features of LuFeO<sub>3</sub> Compound Via Ir Doping into Fe Sites

Özgür Polat<sup>1,2,a,\*</sup><sup>1</sup> CEITEC Brno University of Technology, Purkyňova 123, 612 00 Brno, Czech Republic<sup>2</sup> Institute of Physical Engineering, Brno University of Technology, Technická 2, 616 69 Brno, Czech Republic

\*Corresponding author

### Research Article

#### History

Received: 16/12/2021


Accepted: 09/05/2022

#### Copyright

©2022 Faculty of Science,  
Sivas Cumhuriyet University

### ABSTRACT

Three ceramic compounds, LuFeO<sub>3</sub>, LuFe<sub>0.95</sub>Ir<sub>0.05</sub>O<sub>3</sub>, and LuFe<sub>0.90</sub>Ir<sub>0.10</sub>O<sub>3</sub>, were synthesized via using solid-state reaction technique. Scanning electron microscopy (SEM) has been utilized to study surface morphology and the porous nature of the samples. The loss-tan( $\delta$ ) of Ir substituted compounds are less than the undoped sample at frequencies > 10<sup>5</sup> Hz. The impedance study has revealed the Ir substituted samples have higher impedance values. Z'' and M'' vs frequency plots unveiled the existence of a non-Debye relaxation with short-range migration of carriers in the examined compounds. It has been shown 5 mol % Ir substituted specimen holds the maximum resistivity at 100°C.

**Keywords:** Solid state reaction, The loss tangent, Complex impedance, Non-Debye relaxation, Resistivity. [ozgurpolat7@gmail.com](mailto:ozgurpolat7@gmail.com) <https://orcid.org/0000-0002-7410-1272>

### Introduction

It has been known that rare-earth orthoferrites having a formula of RFeO<sub>3</sub>, here R refers to rare earth element, crystallize in distorted orthorhombic structure because of the spatial position of rare-earth compound and Fe<sup>3+</sup> ions. It has been detailed that the optical, magnetic, and electrical characteristics of these materials can be altered by substitution into rare-earth and/or Fe compounds. Therefore, these materials have grabbed attention from the scientific community all over the globe [1,2]. Although these materials exhibit antiferromagnetic behavior having Neel temperature (T<sub>N</sub>) = 630 K – 750 K, they can have weak ferromagnetic feature, which is owing to the tilted spin moment of Fe<sup>3+</sup> ions. Furthermore, it has been shown these compounds display electric polarization [3] and hence, these materials are considered as multiferroic composites [4, 5]. In addition to magnetic features, it has been documented when the Fe sites are substituted with Os, Co, Ir dopants the optical features of rare-earth orthoferrites can be tuned [6-12]. LuFeO<sub>3</sub> (LFO), one of rare-earth compounds, illustrates significant distortion in the lattice due to Lu compound, which has ionic radius of 0.0861 for 3+ oxidation state, compared to the other earth compounds [13]. It is shown that LFO can have different crystalline structures depending upon fabrication method. For instance, it can hold hexagonal and orthorhombic structures [14,15]. LFO accommodates both magnetic and electrical features at the same time therefore it is considered as multiferroic material [16,17]. Due to low optical band gap of LFO, between ~ 2 eV for films and ~ 2.76 eV for ceramics [18,19], this compound has potential to be used in photocatalyst and solar cells [20]. Moreover, the magnetic and electrical properties of LFO are tuned by substitution of a wide range dopant elements into Lu and Fe sites such as Ni, Cr, Mn In, Sc, Bi and La [21-26]. The drives behind this investigation are as follows: 1) the first

time Ir dopant, having 0.2 nm metallic radius and 0.0625 nm ionic radius for 4+ oxidation level, is exploited to scrutinize a) loss-tan( $\delta$ ) versus frequency that quantifies how electromagnetic energy dissipates in the material, b) impedance versus frequency that i) inspects the influence of grains and grain boundaries on transport characteristics, ii) unveils the electrical response of various segments and the dynamic performance of confined and movable carriers in the bulk and interfacial areas, c) resistivity as function of frequency and temperature. Furthermore, Ir has been selected because it can have oxidation states from +1 to +9. As a result, its ionic radius varies depending on oxidation level. Such variations in both ionic radius and oxidation states influence optical, electrical, and magnetic properties of parent compound [27]. The previous investigations documented Ir dopant, inducing both charge imbalance and distortion in the lattice structure, tunes both optical and electrical characteristics of YbFeO<sub>3</sub>, which also belongs to rare-earth orthoferrite group [12, 13, 15].

In addition, a recent study has shown Ir substitution into Fe sites decreases the optical band gap of LFO from 2.19 eV to 2 eV [27]. It is known that the distortion taking place in the lattice structure influences characteristic features of materials. 2) Most of the investigations in the literature are related to the thin film of LFO with hexagonal structure. Hence, it is believed that this investigation helps to course more examinations for the ceramic form LFO in the literature. The LFO and Ir doped LFO samples have been obtained via using solid-state technique. SEM was exploited to analyze the surface structure of the samples. The electrical properties of the investigated samples have scrutinized by Broadband Dielectric/Impedance Spectrometer.



## Material and Method

### Powder Preparation and Measurements

The powders and pellets preparations for the present study have been detailed in reference [28]. Surface morphology of the prepared pellets has been investigated by using Ultraplus Zeiss scanning electron microscopy (SEM). Broadband Dielectric/Impedance Spectrometer (Novocontrol Concept 50) has been exploited to examine the electrical properties of the undoped and Ir doped LFO compounds. The operating temperature for the electrical measurements has been gradually varied from -100°C to 100°C with 20°C temperature steps. The frequency was changed from 1 Hz to 10<sup>7</sup> Hz.

## Results and Discussion

### SEM Analyses

The previous investigation has examined the crystalline nature of the samples via using X-ray powder diffraction (XRD) [28]. It has been realized that the examined samples hold orthorhombic structure and Ir substitution leads to growth in the lattice volume. In addition, the XRD studies have revealed the creation of minor phases in the samples such as Lu<sub>2</sub>O<sub>3</sub>, Fe<sub>5</sub>Lu<sub>3</sub>O<sub>12</sub>, Fe<sub>21.16</sub>O<sub>31.92</sub>, Fe<sub>3</sub>O<sub>4</sub> and Ir<sub>2</sub>Lu [28]. Furthermore, X-ray photoelectron spectroscopy (XPS) studies have laid down the valence states of Lu, Fe and Ir [28]. It has been unveiled that while Lu has 3+ state, Fe has mix of 2+ and 3+ valence states in the investigated samples. The oxidation state of Ir has been determined as 0 and 4+ in the Ir doped LFO samples. SEM examinations have shown the surface topography of the specimens and the obtained images are presented in Fig. 1. The initiation of agglomerations can be noticed in the samples. It should be bear in mind that such formation of agglomeration, caused by radical restructuring of particles at the initial phase of sintering, is common in the samples fabricated by solid-state reaction technique [6-12 17, 28]. The presence of voids can be also noticed in the images. Such void formations indicate that the samples have porous structure.

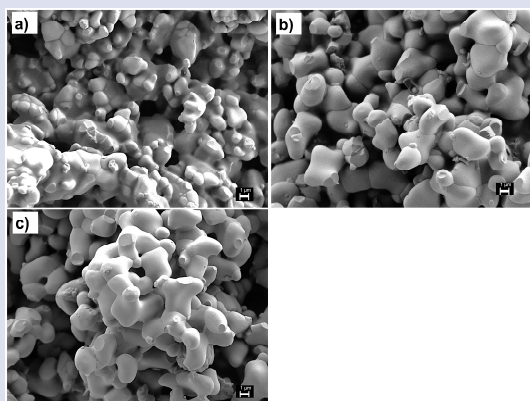


Figure 1. SEM images of studied samples a) LFO, b) 5% Ir and c) 10% Ir substituted LFO. Scale bar is 1 μm..

### Electrical Measurements

The loss-tan( $\delta$ ),  $\tan(\delta)=\epsilon''/\epsilon'$  where  $\epsilon''$  and  $\epsilon'$  denote the imaginary and real part of dielectric function, respectively, indicates how electromagnetic energy dissipates in the material under the applied frequencies. Fig. 2 (semi-log scale) displays the loss-tan( $\delta$ ) versus applied frequency, varying 1 Hz to 10<sup>7</sup> Hz, at temperature range of -100°C and 100 °C with  $\Delta T = 20^\circ\text{C}$  step for the investigated samples. Fig. 2 a) shows the loss-tan( $\delta$ ) versus frequency spectra for undoped LFO sample. It appears that the loss-tan( $\delta$ ) increases initially as the applied frequency raises and it makes a maximum peak (exhibiting relaxation process) then it decreases with further frequency at operating temperatures between -100°C and 0°C. While the maximum peak of loss-tan( $\delta$ ) vs. frequency takes place around 10<sup>2</sup> Hz at -100 °C, it moves toward around 10<sup>5</sup> Hz at 0°C. When the operating temperature  $\geq 20^\circ\text{C}$ , the company of two relaxation peaks, taking place at low and high frequencies, are noticeable. The first and second peaks appear around couple Hz and 2x10<sup>5</sup> Hz at 20 °C, respectively. As the temperature advances, these peaks move to higher frequencies. Such as the first peak is noted  $\sim 10^3$  Hz and second one is noticed  $\sim 5 \times 10^6$  Hz at 100°C. Such movements of relaxation peaks underscore that the relaxation process is influenced by temperature [29, 30]. Fig. 2 b) and c) represent the loss-tan( $\delta$ ) vs frequency for 5 mol and 10 mol % Ir doped LFO samples, respectively. It appears that the evolution of relaxation peaks is similar in both samples. Both samples have only one relaxation peak at all studied temperatures. The relaxation peak moves toward to higher frequencies as the temperature rises as observed in the undoped LFO sample. The comparison of the loss-tan( $\delta$ ) vs frequency at 100°C is given for all the studied samples. It is seen the Ir doped samples exhibit lower loss-tan( $\delta$ ) values than the undoped sample. Therefore, these materials with low loss-tan( $\delta$ ) values might considered a potential candidate for the applications of new generation electronic device, which require to operate at high frequencies. It should be state here that loss-tan( $\delta$ ) holds greater values at low frequencies that could be ascribed to 1) the presence of grain boundaries, which reduce/weaken the motion of charge carriers between ions and 2) the influence of interfacial loose. In addition, it is noticed that the loss-tan( $\delta$ ) has higher values at higher temperatures at the same operating frequencies. Such behavior of loss-tan( $\delta$ ) might be associated to the carrier exchange between Fe<sup>2+</sup> and Fe<sup>3+</sup> ions by resistive grain boundary.

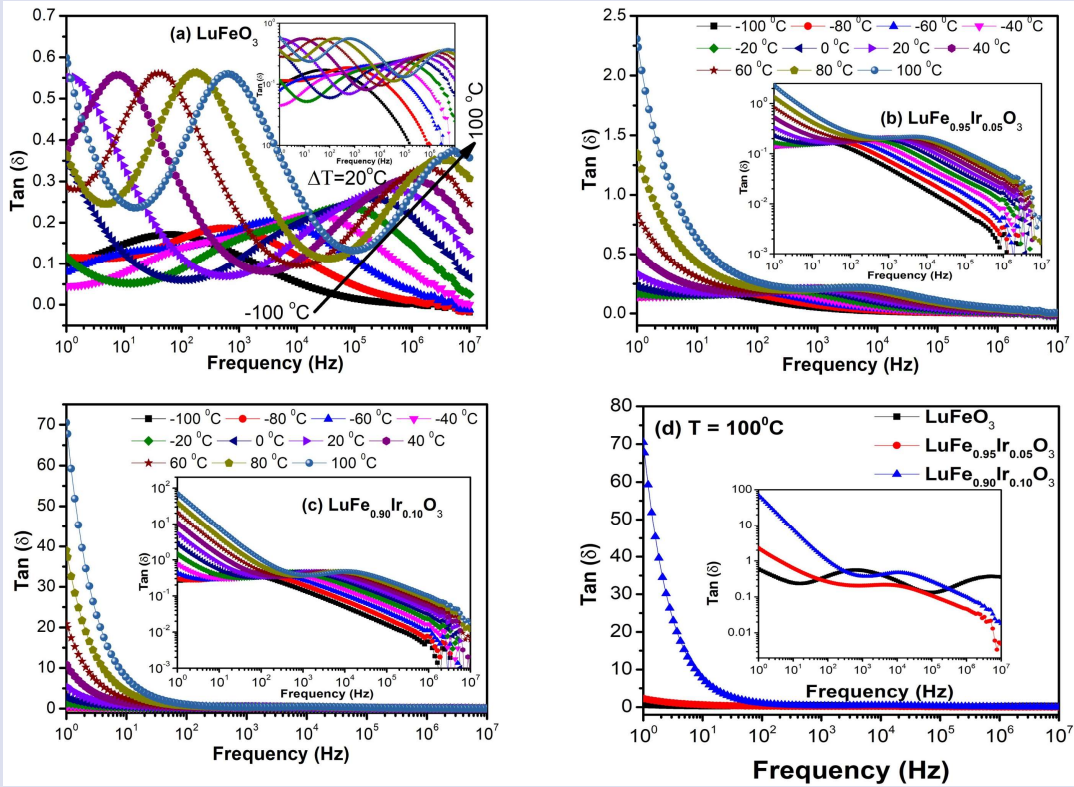


Figure 2. The  $\tan(\delta)$  for a) LFO, b) 5 mol % Ir and c) 10 mol % Ir doped LFO samples. d) represents the  $\tan(\delta)$  values of the studied samples at 100°C. Inset figures are in log-log scale.

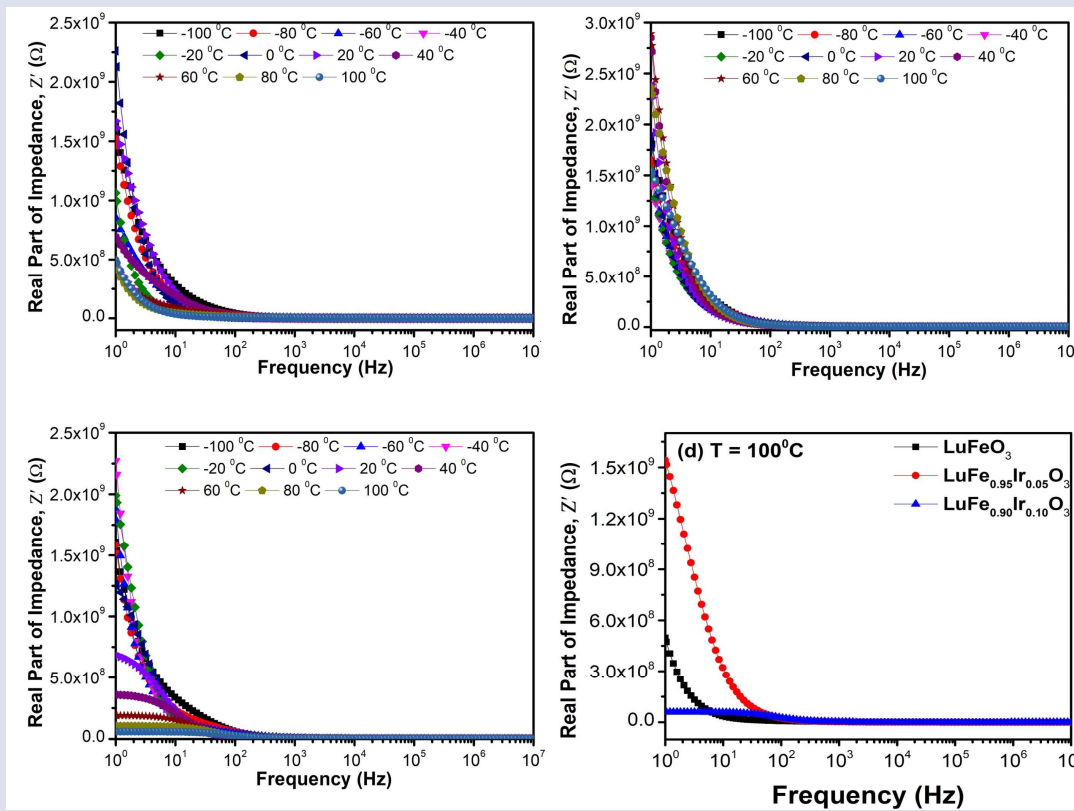


Figure 3. The  $\tan(\delta)$  for a) LFO, b) 5 mol % Ir and c) 10 mol % Ir doped LFO samples. d) represents the  $\tan(\delta)$  values of the studied samples at 100°C. Inset figures are in log-log scale.

The impact of grain boundary, grain, and electrode on the electrical characterizations of materials have been investigated via impedance measurements [31]. The complex impedance,  $Z^*$ , is given by the following relation [32];

$$Z^* = Z' - jZ'' = \frac{1}{j2\pi f \epsilon^* C_0} = \frac{\epsilon'' - j\epsilon'}{2\pi f C_0 [(\epsilon')^2 + (\epsilon'')^2]} \quad (1)$$

here  $Z'$  denotes the real part, the imaginary part of impedance is shown by  $Z''$ .  $f$ ,  $\epsilon^*$ , and  $C_0$  symbolize the frequency, complex dielectric function, and empty capacitance respectively. Fig. 3 (semi-log scale) exhibits the real part of impedance,  $Z'$ , of the samples under scrutiny. It is noted the  $Z'$  values of studied samples reduce with increasing the frequency up to  $\sim 10$  Hz and then the frequency free region is initiated at further applied frequencies due to reduction in energy barrier [33]. This plateau region is formed between 102 Hz- 107 Hz. It is also noted that frequency liberated area extends larger frequencies as the operating temperature surges. The comparison of  $Z'$  values of the inspected compounds is provided in Fig. 3 d) at 100°C. It is seen that 5 mol % Ir doped sample exhibits the maximum  $Z'$  values at 100°C until couple of hundred Hz then all the samples have the same  $Z'$  values at higher frequencies.

The imaginary part of impedance,  $Z''$ , for the studied specimens is given in Fig. 4 in semi-log scale. It is noted the undoped sample has sharp decrease in  $Z''$  values at low frequencies (between 0 and  $\sim 30$  Hz) and it forms plateau region, which is frequency independent area, at high frequencies, Fig. 4 a). Such behavior could be associated to the buildup of space charge carriers at high frequencies [34]. The undoped LFO sample does not exhibit relaxation peak at the investigated temperatures and frequencies in the instrument limit. Fig. 4 b) represents the  $Z''$  vs frequency for the 5 mol % Ir doped sample. Even though it exhibits similar frequency behavior at temperatures less than 80°C, the formation of relaxation peak, appearing around couple of Hz, can be noticed at 80°C and 100°C. Fig. 4 c) exhibits how  $Z''$  values vary with frequency and temperature in the case of 10 mol % Ir substitution. The initiation of relaxation peak becomes noticeable starting from -20°C at couple of Hz and the peak moves to  $\sim 10^2$  Hz at 100°C. Fig. 4 d) compares the  $Z''$  values for the explored samples at 100°C. It appears that 5 mol % Ir doped has the largest  $Z''$  values close to  $10^3$  Hz. As the frequency is further advanced, the  $Z''$  values start to overlap.

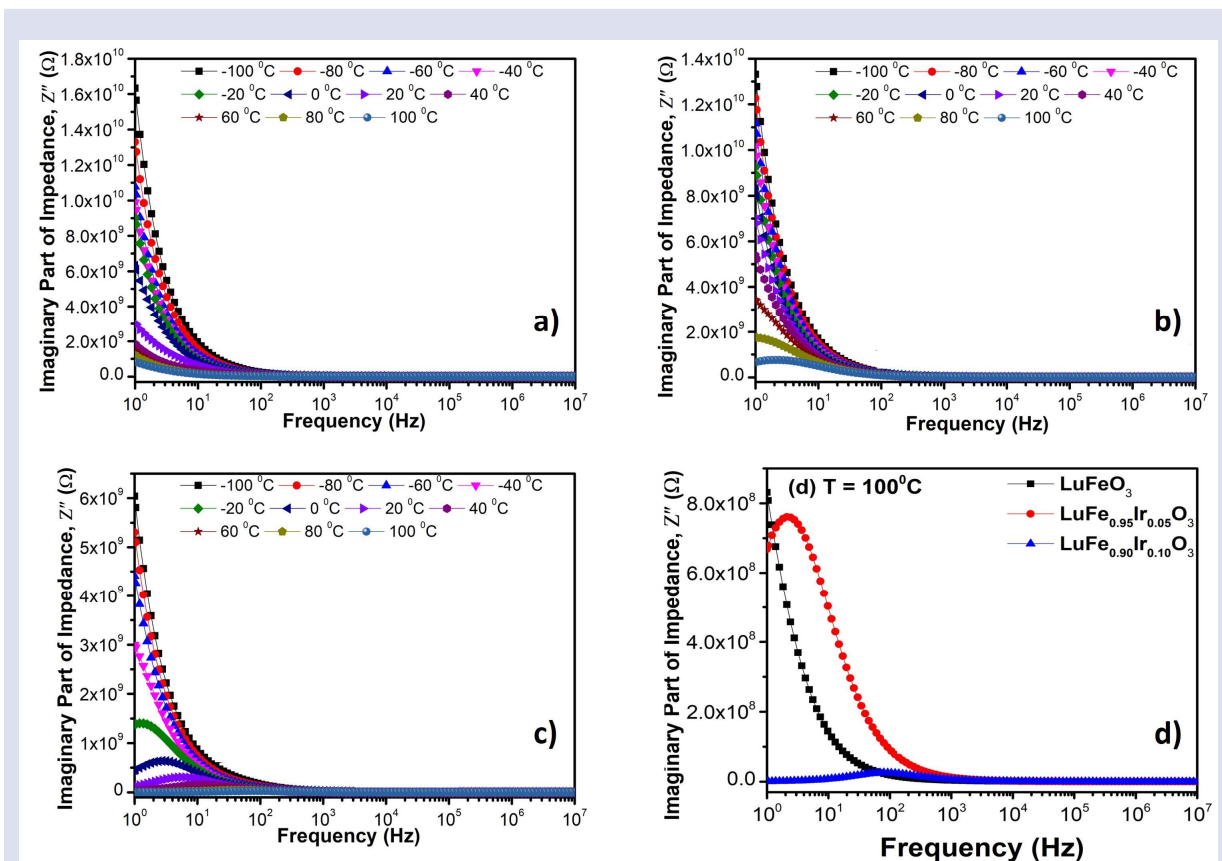


Figure 4. The imaginary part of impedance for a) LFO, b) 5 mol % Ir, c) 10 mol % Ir doped LFO composites. The comparison of imaginary part of impedances is given in d) at 100°C for all the samples.

Figure 5 exhibits  $Z''$  and  $M''$  vs. frequency spectra taken at two selected temperatures,  $-100^{\circ}\text{C}$  and  $100^{\circ}\text{C}$  for LFO and Ir doped LFO samples. It is noted that  $Z''$  vs. frequency plot does not exhibit the initiation of relaxation peak at both temperatures for the undoped LFO sample, Fig. 5 a), b). On the other hand,  $M''$  vs. frequency spectra demonstrate the formation of relaxation peak at  $-100^{\circ}\text{C}$  and  $100^{\circ}\text{C}$  for the same compound. The observed relaxation peaks are ascribed to grain at  $-100^{\circ}\text{C}$  and grain boundary at  $100^{\circ}\text{C}$ , Fig. 5 a), b) respectively. Fig. 5 c) and d) represents the  $Z''$  and  $M''$  vs. frequency at  $-100^{\circ}\text{C}$  and  $100^{\circ}\text{C}$  for the 5 mol % Ir substituted specimen, respectively. It is seen that  $Z''$  vs. frequency plot does not have any relaxation peak at  $-100^{\circ}\text{C}$ , Fig. 5 c) while it reveals the creation of a peak at very low frequencies at  $100^{\circ}\text{C}$ , Fig. 5 d). Nevertheless,  $M''$  vs. frequency plot of the same sample has one peak, associated to the grain, at  $-100^{\circ}\text{C}$ , Fig. 5 c). When the operating temperature reaches  $100^{\circ}\text{C}$ , the two peaks one at low frequency connected to the grain boundary and the second peak related to grain become eminent, Fig. 5 d). In the case of 10 mol % Ir doped LFO sample,  $Z''$  vs. frequency does not show any peak at  $-100^{\circ}\text{C}$ , Fig. 5 e). Yet, when the

operating temperature becomes  $100^{\circ}\text{C}$ , a relaxation peak is visible, which initiates around 200 Hz, Fig. 5 f).  $M''$  vs. frequency spectra for the sample reveals the presence of one relaxation peak connected to the grain at  $-100^{\circ}\text{C}$ , Fig. 5 e). As temperature is further advanced to  $100^{\circ}\text{C}$ , the existence of two relaxation peaks is noticed, Fig. 5 f). The first peak, which is attributed to the grain boundary, is visible around 10 Hz. The second peak is eminent around  $5 \times 10^4$  Hz and this peak is related to the grains in the material. The joint plots of  $Z''$  and  $M''$  vs frequency are utilized to distinguish the type of relaxation process, a short range or long-range motion of carriers [34]. In the case of shorth-range movement, the peaks of  $Z''$  and  $M''$  vs frequency take place at dissimilar frequencies yet for the long-range migration of carriers the peaks overlap at the same frequencies [35]. In this investigation, it can be noted the peaks of  $Z''$  and  $M''$  vs frequency do not coincide at the same frequencies that underscores the existence of shorth-range migration of carriers. Furthermore, it is noted that there is a non-Debye relaxation happens in the studied samples.

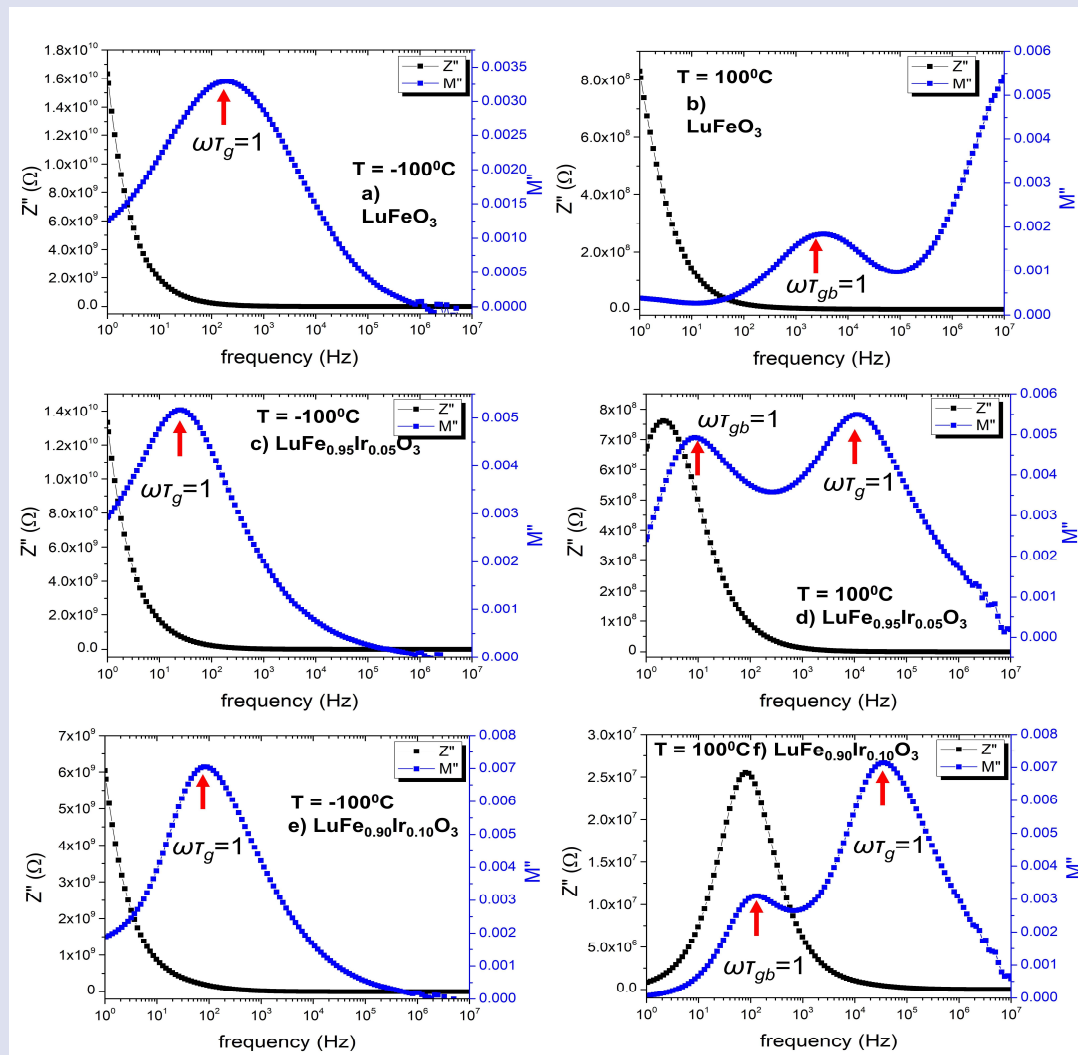


Figure 5.  $Z''$  and  $M''$  vs. frequency plots at (a)  $-100^{\circ}\text{C}$  and (b)  $100^{\circ}\text{C}$  for LFO and (c)  $-100^{\circ}\text{C}$  and (d)  $100^{\circ}\text{C}$  for 5 mol % Ir doped LFO sample, (e)  $-100^{\circ}\text{C}$  and (f)  $100^{\circ}\text{C}$  for 10 mol % Ir substituted LFO compound.

Table 1. displays the temperature dependent relaxation time, capacitance and resistance of grain and grain boundary regions. These parameters have deduced by using  $M''(\omega)$  vs. frequency spectra, shown in Fig. 5 in blue color, and following equations

$$M'' = \frac{C_0}{c} \left[ \frac{\omega RC}{1+(\omega RC)^2} \right], \quad \tau = RC, \quad \omega = 2\pi f, \quad \omega\tau = 1 \quad (2)$$

here  $C_0$ ,  $C$ ,  $\omega$ ,  $R$ ,  $\tau$  and  $f$  represent empty capacitance of the sample, capacitance, angular frequency, resistance, relaxation time and linear frequency, respectively. It is noted that the obtained values diminish with raising the operating temperature. In addition, it is seen that the resistance value of the grain boundary is much higher than that of the grain. Such behavior can be associated to the charge transfer phenomenon in the grain and grain

boundary areas. It is known that the carriers can migrate easier in the grain region compared to the grain boundary areas. That is why higher grain boundary resistance values are calculated. Furthermore, it is noticed that the resistance of both grain and grain boundary regions lowers with increasing the operating temperature, which is because of advancement in the carrier mobility pointing the semiconductor nature of the studied sample. The capacitance value of the grain and grain boundary drops with forwarding the temperature. This can be connected to the diminishing of charge accumulation near the grain boundary region. Because the thermal energy of carriers increases at high temperature and hence, they can move through the grain boundary region.

Table 1. The calculated resistance and other related parameters of undoped and Ir doped LFO compounds.

LuFeO3						
T (K)	$\tau_{gb}$ (s)	$\tau_g$ (s)	C <sub>gb</sub> (F) x10 <sup>-11</sup>	C <sub>g</sub> (F) x10 <sup>-11</sup>	R <sub>gb</sub> (Ω)	R <sub>g</sub> (Ω)
173		8.04x10 <sup>-4</sup>		1.84		4.36x10 <sup>7</sup>
193		9.43x10 <sup>-5</sup>		1.71		5.51x10 <sup>6</sup>
213		1.26x10 <sup>-5</sup>		1.59		7.89x10 <sup>5</sup>
233		2.81x10 <sup>-6</sup>		1.49		1.89x10 <sup>5</sup>
253		7.73x10 <sup>-7</sup>		1.40		5.51x10 <sup>4</sup>
273		2.50x10 <sup>-7</sup>		1.32		1.89x10 <sup>4</sup>
293	3.18x10 <sup>-2</sup>	1.07x10 <sup>-7</sup>	3.37	1.24	9.45x10 <sup>8</sup>	8.57x10 <sup>3</sup>
313	4.42x10 <sup>-3</sup>	5.17x10 <sup>-8</sup>	3.35	1.18	1.32x10 <sup>8</sup>	4.37x10 <sup>3</sup>
333	8.38x10 <sup>-4</sup>	3.04x10 <sup>-8</sup>	3.35	1.14		
353	1.88x10 <sup>-4</sup>	1.41x10 <sup>-8</sup>	3.33	1.12		
373	4.76x10 <sup>-5</sup>		3.33			

LuFe <sub>0.95</sub> Ir <sub>0.05</sub> O <sub>3</sub>						
T (K)	$\tau_{gb}$ (s)	$\tau_g$ (s)	C <sub>gb</sub> (F) x10 <sup>-11</sup>	C <sub>g</sub> (F) x10 <sup>-11</sup>	R <sub>gb</sub> (Ω)	R <sub>g</sub> (Ω)
173		7.96x10 <sup>-3</sup>		2.41		3.31x10 <sup>8</sup>
193		2.70x10 <sup>-3</sup>		2.39		1.13x10 <sup>8</sup>
213		1.21x10 <sup>-3</sup>		2.37		5.10x10 <sup>7</sup>
233		5.81x10 <sup>-4</sup>		2.33		2.50x10 <sup>7</sup>
253		2.94x10 <sup>-4</sup>		2.29		1.28x10 <sup>7</sup>
273		1.54x10 <sup>-4</sup>		2.26		6.79x10 <sup>6</sup>
293		8.73x10 <sup>-5</sup>		2.25		3.89x10 <sup>6</sup>
313		4.96x10 <sup>-5</sup>		2.25		2.21x10 <sup>6</sup>
333	9.37x10 <sup>-2</sup>	3.18x10 <sup>-5</sup>	2.67	2.25	3.50x10 <sup>9</sup>	1.41x10 <sup>6</sup>
353	3.98x10 <sup>-2</sup>	2.03x10 <sup>-5</sup>	2.62	2.25	1.52x10 <sup>9</sup>	9.02x10 <sup>5</sup>
373	1.77x10 <sup>-2</sup>	1.30x10 <sup>-5</sup>	2.52	2.25	7.02x10 <sup>8</sup>	5.78x10 <sup>5</sup>

LuFe <sub>0.90</sub> Ir <sub>0.10</sub> O <sub>3</sub>						
T (K)	$\tau_{gb}$ (s)	$\tau_g$ (s)	C <sub>gb</sub> (F) x10 <sup>-11</sup>	C <sub>g</sub> (F) x10 <sup>-11</sup>	R <sub>gb</sub> (Ω)	R <sub>g</sub> (Ω)
173		2.27x10 <sup>-3</sup>		1.42		1.60x10 <sup>8</sup>
193		8.17x10 <sup>-4</sup>		1.42		5.74x10 <sup>7</sup>
213		3.51x10 <sup>-4</sup>		1.42		2.47x10 <sup>7</sup>
233		1.67x10 <sup>-4</sup>		1.41		1.18x10 <sup>7</sup>
253	7.96x10 <sup>-2</sup>	8.78x10 <sup>-5</sup>	3.76	1.41	2.12x10 <sup>9</sup>	6.24x10 <sup>6</sup>
273	3.54x10 <sup>-2</sup>	4.59x10 <sup>-5</sup>	3.73	1.41	9.48x10 <sup>8</sup>	3.27x10 <sup>6</sup>
293	1.59x10 <sup>-2</sup>	2.66x10 <sup>-5</sup>	3.68	1.41	4.33x10 <sup>8</sup>	1.89x10 <sup>6</sup>
313	7.96x10 <sup>-3</sup>	1.54x10 <sup>-5</sup>	3.58	1.41	2.22x10 <sup>8</sup>	1.09x10 <sup>6</sup>
333	3.98x10 <sup>-3</sup>	9.85x10 <sup>-6</sup>	3.48	1.41	1.14x10 <sup>8</sup>	7.00x10 <sup>5</sup>
353	2.21x10 <sup>-3</sup>	6.61x10 <sup>-6</sup>	3.33	1.41	6.63x10 <sup>7</sup>	4.70x10 <sup>5</sup>
373	1.16x10 <sup>-3</sup>	4.47x10 <sup>-6</sup>	3.25	1.41	3.58x10 <sup>7</sup>	3.18x10 <sup>5</sup>

The resistivity of the studied samples is given semi-log scale in Fig. 6 and inset images are provided in log-log scale. It is seen that the resistivity decreases as the applied frequency increases and resistivity values at different temperatures overlaps. Furthermore, it is noticed that the undoped and 5 mol % Ir doped samples do not show the formation of dc resistivity, Fig. 6 a) and b), respectively. On the other hand, the existence of dc resistivity becomes visible at temperature  $T \geq 0^\circ\text{C}$  at  $\sim 5$  of Hz and it extends up to  $10^2$  Hz at  $100^\circ\text{C}$ , Fig. 6 c). The dc region is chased by ac resistivity, which decreases sharply with the applied frequency. Such decrement in resistivity with the frequency is associated to the exchanging of carriers between  $\text{Fe}^{2+}$  and  $\text{Fe}^{3+}$  ion sites [36]. Fig. 6 d) shows the comparison of the resistivities of examined samples at  $100^\circ\text{C}$ .

It is noted that 5 mol % sample has the highest resistivity. Such high resistivity of Ir substituted samples might be connected to lattice distortion created due to the Ir doping. The XPS analyses have unveiled that Ir has metallic and 4+ valence states in LFO structure. It needs to be cited that the radius of metallic Ir, which is 0.2 nm, is much larger than that of  $\text{Fe}^{2+}$  (0.078 nm) and  $\text{Fe}^{3+}$  (0.0645 nm) ions. Apparently, the lattice distortion is inevitable in LFO structure. Such lattice distortion can act carrier trap center and increase the resistivity of parent LFO compound [37]. A recent investigation about Os doping into Fe sites in LFO structure has also demonstrated similar trend [38]. Furthermore, it is known that conductivity or resistivity of rare-earth compounds is significantly influenced by carrier transfer between  $\text{Fe}^{2+}$  and  $\text{Fe}^{3+}$  ions in the system [36].

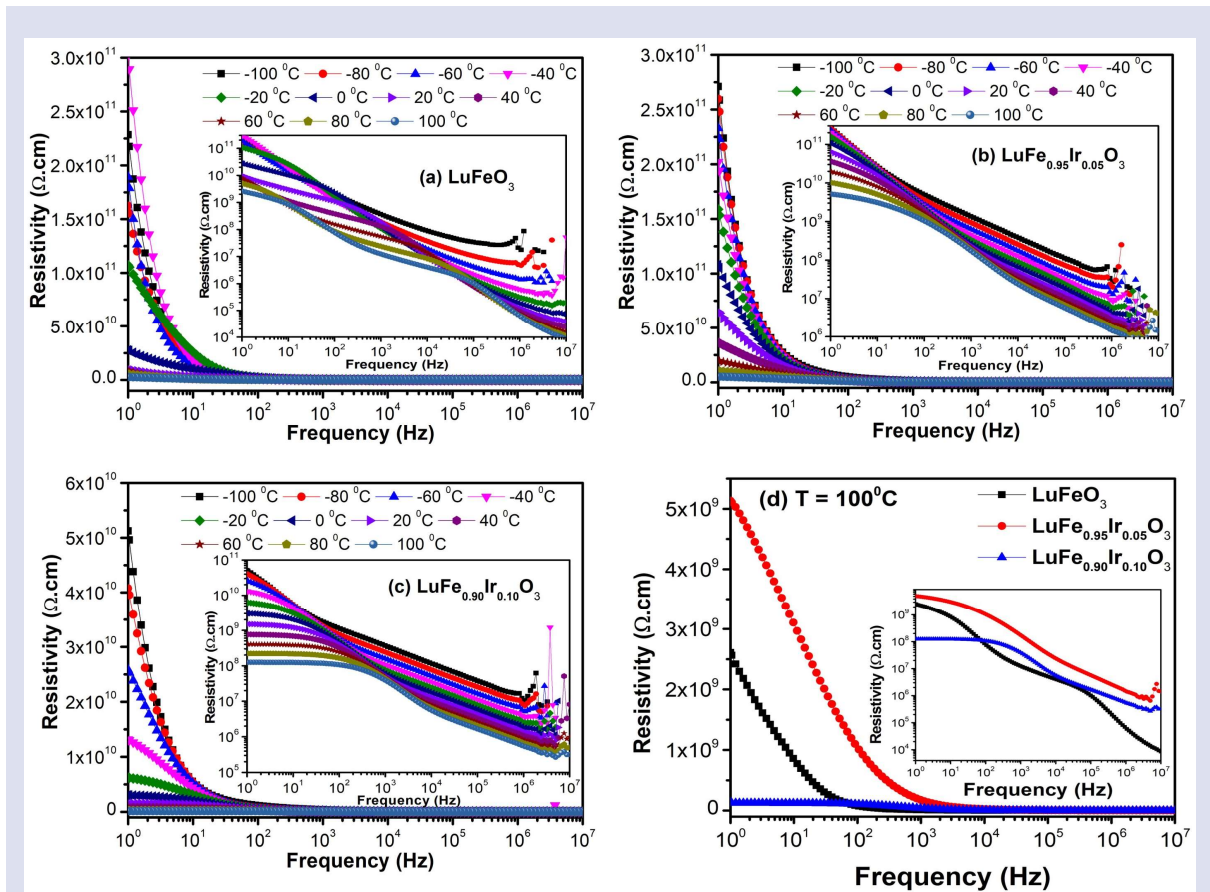


Figure 6. Resistivity of a) LFO, b) 5 mol %, c) 10 mol % Ir substituted LFO. d) Compares the resistivities at  $100^\circ\text{C}$ . The inset images represent the log-log scale resistivity versus frequency.

**Conclusions**

The porous nature of the LFO and Ir substituted LFO ceramics were revealed by SEM analyses. It has been shown that Ir doped samples have lower loss-  $\tan(\delta)$  values at high frequency and temperature than LFO sample. Impedance study has demonstrated that at low frequencies the 5 mol % Ir substituted sample has the

highest impedance values at  $100^\circ\text{C}$ .  $Z''$  and  $M''$  vs frequency plots revealed that the presence of a non-Debye relaxation with short-range movement of carriers in the investigated samples. The resistivity studies have underlined that Ir doped sample possess the highest resistivity than the undoped LFO. The augmentation in the resistance could be connected to the lattice distortion and reduction in the ratio of  $\text{Fe}^{2+}$  ions, which is known that

conductivity of rare-earth compounds is significantly influenced by carrier transfer/hopping between  $\text{Fe}^{2+}$  and  $\text{Fe}^{3+}$  ions in the system. Recently, LFO has seized attention from scientific community because of its electrical, magnetic, and optical features. Therefore, the present study has detailed that the electrical, optical, and magnetic characteristics of LFO can be adjusted with Ir substitution. This study could pave the way for doping other transition elements into not only Fe but also Lu sites in LFO structure.

### Acknowledgment

This work was supported by The Scientific and Technological Research Council of Turkey (TUBITAK) through Grant No: 116F025. The author would like to thank Prof. Dr. Abdulmecit Turut, Prof. Dr. Mujdat Caglar, Assoc. Prof. Mustafa Coskun, and Assoc. Prof. Zehra Durmus for their valuable comments.

### Conflicts of interest

The authors state that did not have conflict of interests.

### References

- [1] Luo S.J., Li S.Z., Zhang N., Wei T., Dong X.W., Wang K.F., Liu J.M., Preparation of epitaxial  $\text{DyFeO}_3$  thin films and magnetodielectric coupling, *Thin Solid Films*, 519 (2010) 240.
- [2] Pomiro F., Sanchez R.D., Cuello G., Maignan A., Martin C., Carbonio R. E., Spin reorientation, magnetization reversal, and negative thermal expansion observed in  $\text{RFe}_{0.5}\text{Cr}_{0.5}\text{O}_3$  perovskites (R=Lu,Yb,Tm), *Phys. Rev. B*, 94 (2016) 134402.
- [3] Mandal P., Bhadram V.S., Sundarayya Y., Narayana C., Sundaesan A., Rao C. N. R., Spin-reorientation, ferroelectricity, and magnetodielectric effect in  $\text{YFe}_{1-x}\text{Mn}_x\text{O}_3$  ( $0.1 \leq x \leq 0.40$ ), *Phys Rev. Lett.*, 107(13) (2011) 137202.
- [4] Yokota H., Nozue T., Nakamura S., Hojo H., Fukunaga M., Janolin P.-E., Kiat J.-M., Fuwa A., Ferroelectricity and weak ferromagnetism of hexagonal  $\text{ErFeO}_3$  thin films, *Phys. Rev. B*, 92(5) (2015) 054101.
- [5] Song Y.-Q., Zhou W.-P., Fang Y., Yang Y.-T., Wang L.-Y., Wang D.-H., Du Y.-W., Multiferroic properties in terbium orthoferrite, *Chin. Phys. B*, 23 (2014) 077505.
- [6] Polat O., Coskun M., Coskun F. M., Kurt B. Z., Durmus Z., Caglar Y., Caglar M., Turut A., Electrical characterization of Ir doped rare-earth orthoferrite  $\text{YbFeO}_3$ , *Journal of Alloys and Compounds*, 787 (2019) 1212-1224.
- [7] Coskun M., Polat O., Coskun F. M., Kurt B. Z., Durmus Z., Caglar M., Turut A., The Impact of Ir Doping on the Electrical Properties of  $\text{YbFe}_{1-x}\text{Ir}_x\text{O}_3$  Perovskite-Oxide Compounds, *J. Mater. Sci.: Mater. Electron.*, 31 (2020) 1731.
- [8] Polat O., M. Coskun, Kalousek R., Zlamal J., Kurt B. Z., Caglar Y., Caglar M., Turut A., Frequency and Temperature-Dependent Electric Modulus Spectroscopy of Os Doped  $\text{YbFeO}_{3-\delta}$  Structure, *J. Phys.: Condens. Matter.*, 32 (2020) 065701.
- [9] Polat O., Caglar M., Coskun F. M., Coskun M., Caglar Y., Turut A., An investigation of the optical properties of  $\text{YbFe}_{1-x}\text{Ir}_x\text{O}_{3-\delta}$  ( $x=0, 0.01$  and  $0.10$ ) orthoferrite films, *Vacuum*, 173 (2020) 109124.
- [10] Polat O., Caglar M., Coskun F. M., Coskun M., Caglar Y., Turut A., Examination of Optical Properties of  $\text{YbFeO}_3$  films via Doping Transition Element Osmium, *Optical Materials*, 105 (2020) 109911.
- [11] Polat O., Caglar M., Coskun F. M., Coskun M., Caglar Y., Turut A., An Experimental Investigation: The Impact of Cobalt Doping on Optical Properties of  $\text{YbFeO}_{3-\delta}$  Thin Film, *Mater. Res. Bull.*, 119 (2019) 110567.
- [12] Polat O., Coskun M., Coskun F. M., Zlamal J., Kurt B. Z., Durmus Z., Caglar M., Turut A., Co doped  $\text{YbFeO}_3$ : exploring the electrical properties via tuning the doping level, *Ionics*, 25 (2019) 4013-4029.
- [13] Liferovich R. P., Mitchell R. H., A structural study of ternary lanthanide orthoscarandate perovskites, *J. Solid. State. Chem.*, 177 (2004) 2188.
- [14] Magome E., Moriyoshi C., Kuroiwa Y., Masuno A., Inoue H., Noncentrosymmetric Structure of  $\text{LuFeO}_3$  in Metastable State, *Japan. J. Appl. Phys.*, 49 (2010) 09ME06.
- [15] Leelashree S., Srinath S., Investigation of Structural, Ferroelectric, and Magnetic Properties of La-Doped  $\text{LuFeO}_3$  Nanoparticles, *J. Supercond. Nov. Magn.*, 33 (2020) 1587-1591.
- [16] Wang W.B., Zhao J., Wang W.B., Gai Z., Balke N., Chi M.F., Lee H.N., Tian W., Zhu L., Cheng X.M., Keavney D.J., Yi J.Y., Ward T.Z., Snijders P.C., Christen H.M., Wu W.D., Shen J., Xu X.S., Room-temperature multiferroic hexagonal  $\text{LuFeO}_3$  films, *Phys. Rev. Lett.*, 110 (2013) 237601.
- [17] Coskun M., Synthesis, Characterization and Electrical Admittance Study of  $\text{LaCrO}_3$  Perovskite Compound, *Int. J. Adv. Eng. Pure Sci.* 1 (2019) 29-35.
- [18] Holinsworth B.S., Mazumdar D., Brooks C.M., Mundy J.A., Das H., Cherian J.G., McGill S.A., Fennie C.J., Schlom D.G., Musfeldt J.L., Direct band gaps in multiferroic h- $\text{LuFeO}_3$ , *Appl. Phys. Lett.*, 106 (2015) 082902.
- [19] Zhu L.P., Deng H.M., Sun L., Yang J., Yang P.X., Chu J.H., Optical properties of multiferroic  $\text{LuFeO}_3$  ceramics, *Ceram. Int.*, 40 (2014) 1171-1175.
- [20] Zhou M., Yang H., Xian T., Zhang C.R., A new photocatalyst of  $\text{LuFeO}_3$  for the dye degradation, *Phys. Scripta*, 90 (2015) 085808.
- [21] Suresh P., Laxmi K. V., Kumar P.S., Enhanced room temperature multiferroic characteristics in hexagonal  $\text{LuFe}_{1-x}\text{Ni}_x\text{O}_3$  ( $x = 0 - 0.3$ ) nanoparticles, *J. Magn. Magn. Mater.*, 448 (2018) 117-122.
- [22] Sarkar T., Manna K., Elizabeth S., Anil Kumar P.S., Investigation of multiferroicity, spin-phonon coupling, and unusual magnetic ordering close to room temperature in  $\text{LuMn}_{0.5}\text{Fe}_{0.5}\text{O}_3$ , *J. Appl. Phys.*, 121 (2017) 084102.
- [23] Lurgo F. E., Billoni O. V., Pomjakushin V., Bolletta J. P., Martin C., Maignan A., Carbonio R. E., Signs of superparamagnetic cluster formation in  $\text{LuFe}_{1-x}\text{Cr}_x\text{O}_3$  perovskites evidenced by magnetization reversal and Monte Carlo simulations, *Phys. Rev. B*, 103 (2021) 014447.
- [24] Lin L., Zhang H. M., Liu M. F., Shen S., Zhou S., Li D., Wang X., Yan Z. B., Zhang Z. D., Zhao J., Dong S., Liu J.M., Hexagonal phase stabilization and magnetic orders of multiferroic  $\text{Lu}_{1-x}\text{Sc}_x\text{FeO}_3$ , *Phys. Rev. B*, 93 (2016) 075146.
- [25] Liu J., Sun T.L., Liu X.Q., Tian H., Gao T.T., Chen X.M., A novel room-temperature multiferroic system of hexagonal  $\text{Lu}_{1-x}\text{In}_x\text{FeO}_3$ , *Adv. Funct. Mater.*, 28 (2018) 1706062.
- [26] Leelashree S., Srinath S., Investigation of structural, ferroelectric, and magnetic properties of La-doped  $\text{LuFeO}_3$  nanoparticles, *J. Supercond. Nov. Magnetism*, 33 (2019) 1587-1591.

- [27] Polat O., Altering magnetic and optical features of rare earth orthoferrite LuFeO<sub>3</sub> ceramics via substitution of Ir into Fe sites, *Journal of Solid State Chemistry*, 305 (2022) 122701.
- [28] Polat O., Coskun M., Roupcová P., Sobala D., Durmus Z., Caglar M., Sikola T., Turut A., Influence of iridium (Ir) doping on the structural, electrical, and dielectric properties of LuFeO<sub>3</sub> perovskite compound, *Journal of Alloys and Compounds*, 877 (2021) 160282.
- [29] Pattanayak S., Parida B.N., Das P. R., Choudhary R.N.P., Impedance spectroscopy of Gd-doped BiFeO<sub>3</sub> multiferroics. *Appl. Phys. A*, 112 (2013) 387
- [30] Jonscher A. K., The 'universal' dielectric response, *Nature*, 267 (1977) 673.
- [31] Petrovsky V., Manohar A., Dogan F., Dielectric constant of particles determined by impedance spectroscopy, *J. Appl. Phys.*, 100 (2006) 014102
- [32] Cheng P. F., Song J., Wang Q. P., Li S. T., Li J.Y., Wu K.N., Fine representation of dielectric properties by impedance spectroscopy, *Journal of Alloys and Compounds*, 740 (2018) 36-41.
- [33] Sekrafi H. E., Kharrata A. B. J., Wederni M.A., Khirouni K., Boudjadaa N. C., Boujelben W., Structural, electrical, dielectric properties and conduction mechanism of solgel prepared Pr<sub>0.75</sub>Bi<sub>0.05</sub>Sr<sub>0.1</sub>Ba<sub>0.1</sub>Mn<sub>0.98</sub>Ti<sub>0.02</sub>O<sub>3</sub> compound, *Mater. Res. Bull.*, 111 (2019) 329–337.
- [34] James A. R., Srinivas K., Low temperature fabrication and impedance spectroscopy of PMN-PT ceramics, *Mater. Res. Bull.*, 34 (1999) 1301.
- [35] Sinclair D.C., West A.R, Impedance and modulus spectroscopy of semiconducting BaTiO<sub>3</sub> showing positive temperature coefficient of resistance, *J. Appl. Phys.*, 66 (1989) 3850.
- [36] Auwal I.A., Erdemi H., Sözeri H., Güngüneş H., Baykal A., Magnetic and dielectric properties of Bi<sup>3+</sup> substituted SrFe<sub>12</sub>O<sub>19</sub> hexaferrite, *J. Magn. Magn. Mater.*, 412 (2016) 69-82.
- [37] Keelani A. O. A., Husain S., Khan W., Temperature dependent dielectric properties and ac conductivity of GdFe<sub>1-x</sub>Mn<sub>x</sub>O<sub>3</sub> (0 ≤ x ≤ 0.3) perovskites, *J. Mater. Sci.: Mater. Electron.*, 30 (2019) 20119–20131.
- [38] Polat O., Coskun M., Roupcová P., Sobala D., Durmus Z., Caglar M., Sikola T., Turut A., The Os substitution into Fe sites in LuFeO<sub>3</sub> multiferroic and its effects on the electrical and dielectric properties, *Journal of Alloys and Compounds* 911, (2022) 165035.



## Analysis of Magnetization Change with Temperature in an Artificial Spin Ice Network by Three Dimensional Finite Element Modeling

İbrahim Çınar <sup>1,a,\*</sup>

<sup>1</sup> Department of Medical Services and Techniques, Karamanoğlu Mehmetbey University, Karaman, Türkiye.

\*Corresponding author

### Research Article

#### History

Received: 09/03/2022

Accepted: 20/05/2022

#### Copyright





©2022 Faculty of Science,  
Sivas Cumhuriyet University

### ABSTRACT

A three dimensional finite element model calculation was constructed, which includes different submodels, all as a function of temperature, using an iterative approach, to investigate permalloy artificial spin ice network with square geometry on thermal annealing while applying a voltage pulse. Magnetization is also included into the simulation with an equation defining the change of the magnetization with temperature. The maximum temperature is obtained around the sharp corners due to current crowding, and therefore, minimum magnetization values are observed around the same place, even zero magnetization depending on the applied pulse magnitude and width, because of Curie temperature of permalloy. The aim of this study is to understand the dynamic behavior of the artificial spin ice network according to programming pulse and the importance of the device design to minimize the effect of joule heating.

**Keywords:** Artificial spin ice, Finite element modelling, Magnetization change,.

 [ibrahimcinar82@gmail.com](mailto:ibrahimcinar82@gmail.com)

 <https://orcid.org/0000-0002-0509-913X>

### Introduction

Magnetic configurations give scientists variety of the device designs for different purposes, such as, a sensor, oscillator or detector and so on. One of them is magnetic crystal, known as artificial spin ice (ASI) which is a new crystal arrangement to modify magnetic properties [1-5]. With advanced nanotechnology design, scientist can enable the generation of connected ferromagnetic nanowire networks such as magnetic metamaterials [6, 7]. Artificial spin ice is fabricated lithographically 2D ferromagnetic nanoscale islands to create an imitation of the complex magnetic order and collective behavior of magnetic islands [1, 5, 7, 8]. There are many areas of usage of ASI such as to study geometrical frustration and potential applications such as an information storage, signal propagation, and logic devices due to properties like ferromagnetic resonance (FMR) signal in the GHz-regime [9-18], although, there are few study about annealing the arrays to temperature near or above the Curie temperature of the ferromagnetic materials [19, 20]. Therefore, for these wide range studying area, the static and dynamic behaviors of the ASI structures should be studied in a systematic path in high temperature, while using a connected ASI network as a circuit element. For this purpose, the role of the current injection in a nanoscale ASI cell as a magnetic network should be studied to oversee temperature distribution without disturbing magnetic properties of magnetic network.

Heating profile is important for a device working parameters because temperature is a significant factor to effect the magnetic properties of the network. First, 3D finite element simulation was carried out in an ASI cell to understand the complex nature of the ASI network by

using COMSOL multiphysics. Simulation is consisted of electrical and thermal effects as a function of temperature, and also magnetization is added as an equation depending on the temperature. All of them are combined with iterative approach with coupled differential equations and also Seebeck coefficient was included to account for thermoelectric effect. The simulation results report that the heating profile is mainly due to isotropic/anisotropic heating depending on the geometry and amplitude of the current pulse. The model successfully predicts the temperature distribution and magnetization change during applied current pulse depending on the shape of the network.

A device design needs a clear explanation to understand not only the temperature, but also magnetization change according to applied voltage, especially, for magnetization which is an important parameter to design a magnetic device with spin ice frustration. Therefore, it is important to investigate with 3D finite element model for a network by using a square spin ice geometry

### Material and Method

#### Device Structure

Device geometry is illustrated in Figure 1. Patterned permalloy (NiFe) ASI cell structure is sandwiched between two 50 nm thick WTi metal electrodes. Au layer is also used for contact electrode and to isolate the device from the environment, Al<sub>2</sub>O<sub>3</sub> is used. Current pulse is applied from top contact to ASI. The thickness of permalloy is 10 nm.

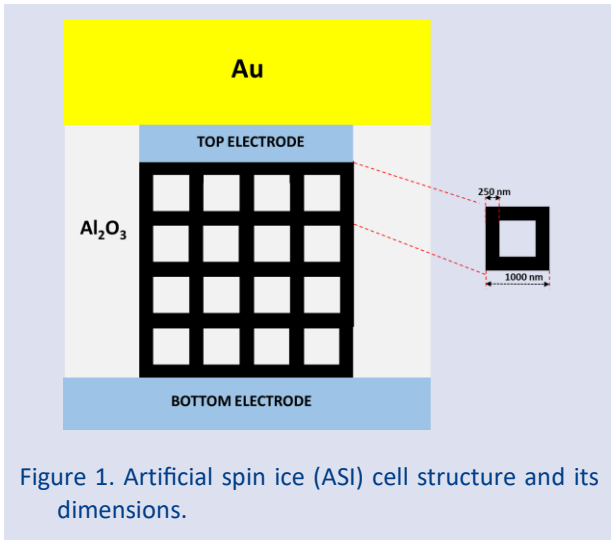


Figure 1. Artificial spin ice (ASI) cell structure and its dimensions.

### 3D Finite Element Model

It is crucial to know the momentary solution of equations in every point and every time in device during simulation. In the simulation, different equations (like Laplace equation, heat diffusion equation, magnetization change equation) are solved depending on the temperatures of the materials. Therefore, different sub models were constructed to solve the equations for each mesh element. In the electrical model, Laplace equation is solved iteratively (with 0.1ns time range) and to obtain the electrical potential distribution  $F(x,y,z)$ , thermal submodel is combined to electrical model.

$$\nabla \cdot [\sigma \cdot \nabla F] \tag{1}$$

Where  $\sigma$  is the electrical conductivity of the materials. At room temperature resistivity  $\rho$  is 202.4  $\mu\Omega \cdot \text{cm}$  [21]. It has to be note that  $\sigma$  ( $1/\rho$ ) electrical conductivity has temperature dependence, therefore, with temperature increase, Permalloy becomes highly conductive due to  $\sigma$  electrical conductivity.

In thermal model, due to electrical potential in device, there are two important parameters to contribute,

$$Q = (JA)^2 \cdot R \Delta t. \tag{2}$$

where  $A$  and  $\Delta t$  is the cross-sectional area and the simulation time step, respectively.  $J$  and  $R$  parameters are electrical current density and the resistance value of the material. Heat diffusion equation answers how the temperature is distributed in materials, therefore, the heat equation is solved iteratively to obtain temperature distribution  $T(x,y,z)$  in every point and time in device during simulation.

$$C \partial T / \partial t - \nabla \cdot [\kappa \nabla T] = Q + Q_{th} \tag{3}$$

Where  $C$  and  $\kappa$  is the heat capacity and the thermal conductivity, respectively. To account for the contribution of thermoelectric effect,  $Q_{th} = -T \nabla S$  is added to simulation. Where  $S$  temperature dependence Seebeck coefficient and the equation is following [22].

$$\nabla S = dS / dt \cdot \nabla T \tag{4}$$

For permalloy, room temperature thermal conductivity  $k$  value is 23 W/(m.K) [23] and Seebeck coefficient  $S$  value is 83.1  $\mu\text{V/K}$  [24]. For the magnetization of the Permalloy, I used an equation representing the change of magnetization according to temperature as following,

$$m(T) = m(0)(1 - T/T_c)^\beta \tag{5}$$

where  $\beta$  is coefficient from the obtained a 3D Heisenberg model [25] and  $T_c$  is the Curie temperature of permalloy.

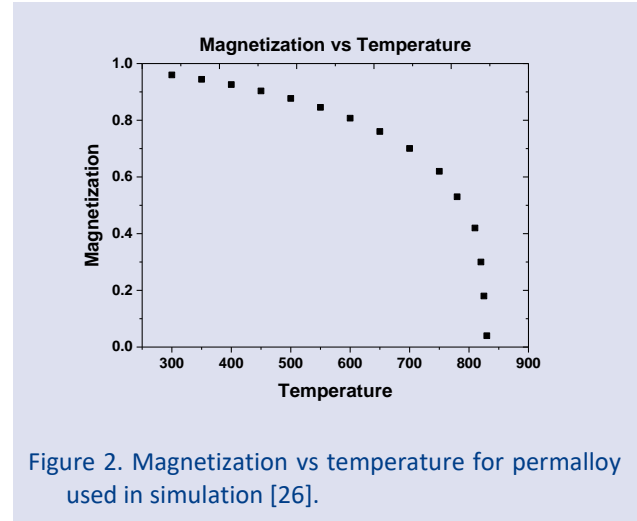


Figure 2. Magnetization vs temperature for permalloy used in simulation [26].

In a device structure, due to joule heating, change in the magnetization should be observed during simulation. The graph of equation of magnetization vs temperature for Permalloy used in simulation is given in Figure 2. The equation from the study, J Fassbender et al 2009 [26] was modified and used in the simulation.

### Simulation Results

During an applied voltage pulse 2V with 10 ns width and 2 ns trailing edge, the maximum temperature value is observed as 855.15 K at 9.7 ns and obtained magnetization change according to temperature is given in Figure 3. We can see the counter line for temperature and magnetization. Around the shape corner, counter line numbers are getting more and it is evidence to see maximum temperature and min magnetization value. As you can see here, because of current crowding, maximum temperature minimum magnetization is also obtained around the same corners. However, reaching Curie temperature of Permalloy, magnetization goes to zero because of being paramagnet and in the Figure 3b) blue color corresponds to zero magnetization from the color code for magnetization rate. Thermoelectric effect is small compare to Joule heating due to very short distance. The graph of temperature and magnetization change at point P with an applied voltage pulse are given in Figure 4. It is clear to see that, after applying 10 ns pulse but due to falling edge, maximum temperature is observed less than

10 ns and minimum magnetization due to the Curie temperature of permalloy was observed. Curie temperature of permalloy is around 833 K [26] and even we can see the results from the observed data

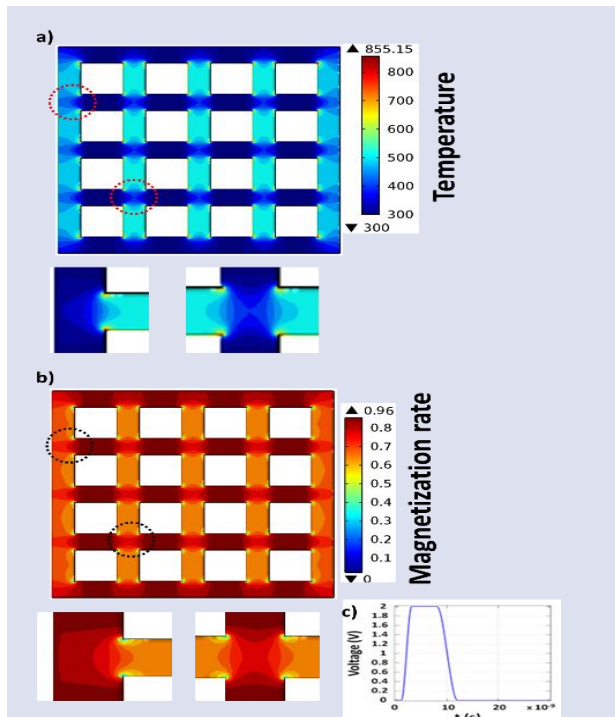


Figure 3. Magnetization vs a) Temperature and b) Magnetization change at 9.7 ns from the center slice and counter line to see the change when 10 ns width 2 V magnitude voltage pulse was applied c). Color codes correspond temperature in a) and magnetization rate in b).temperature for permalloy used in simulation [26].

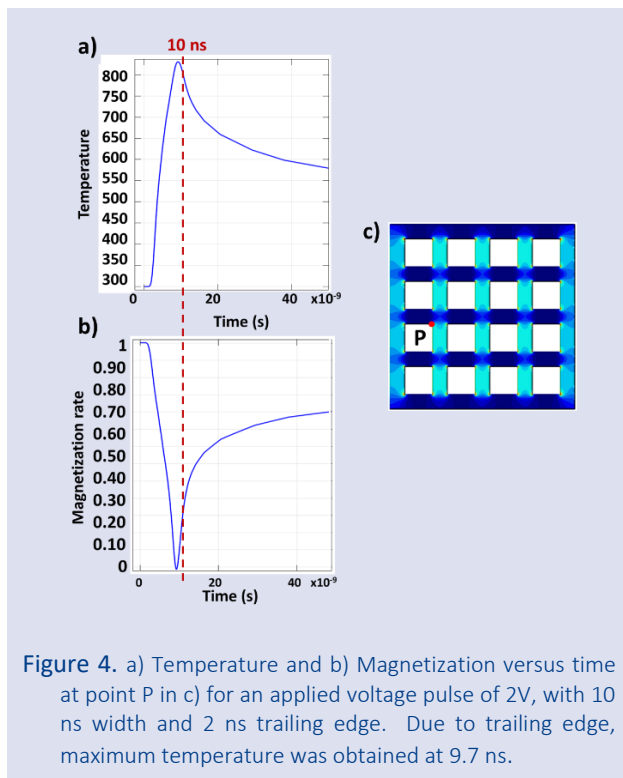


Figure 4. a) Temperature and b) Magnetization versus time at point P in c) for an applied voltage pulse of 2V, with 10 ns width and 2 ns trailing edge. Due to trailing edge, maximum temperature was obtained at 9.7 ns.

After 9.7ns, the magnetization increases with decreasing temperature, namely permalloy again demonstrates ferromagnetic behavior. However, this is very important to know while fabricating a magnetic device, especially estimating programming current to avoid losing magnetic properties of a ferromagnetic material. Therefore, for scientist, device design and material selection is crucial issues to fabricate new magnetic device without losing magnetic properties of the device.

## Discussion and Conclusion

In this study, the aim is to understand behavior of a magnetic network by using an electrical device while applying a voltage pulse and device design importance without losing magnetic properties. Due to joule heating, there is a temperature increase in the device and a possibility to lose magnetic properties. Temperature is a crucial factor for a magnetic material, especially around Curie temperature. Therefore, to avoid magnetization loss of device, applied programming pulse and device design to decrease the effect of joule heating are fundamental factor to fabricate a magnetic device to use for different purposes such as, sensor, detector or oscillator.

## Conflicts of interest

The authors state that did not have conflict of interests.

## References

- [1] Nisoli, C., Moessner R. Schiffer P., Artificial spin ice: Designing and imaging magnetic frustration. *Reviews of Modern Physics*, 85(4) (2013) 1473.
- [2] Qi, Y., T. Brintlinger, J. Cumings, Direct observation of the ice rule in an artificial kagome spin ice, *Physical Review B*, 77(9) (2008) 094418.
- [3] Elena Mengotti, Laura J. Heyderman, Arantxa Fraile Rodríguez, Frithjof Nolting, Remo V. Hügli Hans-Benjamin Braun, Real-space observation of emergent magnetic monopoles and associated Dirac strings in artificial kagome spin ice, *Nature Physics*, 7(1) (2011) 68-74.
- [4] Jason P. Morgan, Aaron Stein, Sean Langridge and Christopher H. Marrows, Thermal ground-state ordering and elementary excitations in artificial magnetic square ice, *Nature Physics*, 7(1) (2011) 75-79.
- [5] Heyderman, L.J. R.L. Stamps, Artificial ferroic systems: novel functionality from structure, interactions and Dynamics, *Journal of Physics: Condensed Matter*, 25(36) (2013) 363201.
- [6] Krawczyk, M. Grundler D., Review and prospects of magnonic crystals and devices with reprogrammable band structure, *Journal of Physics: Condensed Matter*, 26(12) (2014) 123202.
- [7] Wang R. F., Nisoli C, Freitas R. Si, Li J., McConville W., Cooley B. J., Lund M. S., Samarth N., Leighton C., Crespi V. H., Schiffer P., Artificial 'spin ice' in a geometrically frustrated lattice of nanoscale ferromagnetic islands, *Nature*, 439(7074) (2006) 303-306.
- [8] Gilbert, I., . Nisoli C, Schiffer P., Frustration by design, *Physics Today*, 69 (LA-UR-16-22359) (2016).
- [9] Sklenar J., Bhat V. S., DeLong L. E.,J. Ketterson B., Broadband ferromagnetic resonance studies on an artificial square spin-ice island array, *Journal of Applied Physics*, 113(17) (2013) 17B530.

- [10] Sebastian Gliga, Attila Ká'kay, Riccardo Hertel, and Olle G. Heinonen, Spectral analysis of topological defects in an artificial spin-ice lattice, *Physical Review Letters*, 110(11) (2013) 117205.
- [11] Jungfleisch M. B., Sklenar J., Ding J., Park J., Pearson J. E., Novosad V., Schiffer P., Hoffmann A., High-frequency dynamics modulated by collective magnetization reversal in artificial spin ice, *Physical Review Applied*, 8(6) (2017). 064026.
- [12] Jungfleisch M. B., Zhang W.S., Ding J., Jiang W., Sklenar J., Pearson J.E., Ketterson J.B., Hoffmann A., All-electrical detection of spin dynamics in magnetic antidot lattices by the inverse spin Hall effect, *Applied Physics Letters*, 108(5) (2016) 052403.
- [13] Wang Y. L., Xiao Z. L., Snezhko A., Xu J., Ocola L. E., Divan R., Pearson J. E., Crabtree G. W., Kwok W. K., Rewritable artificial magnetic charge ice, *Science*, 352(6288) (2016) 962-966.
- [14] Haldar, A., Kumar D., Adeyeye A.O., A recon Figureurable waveguide for energy-efficient transmission and local manipulation of information in a nanomagnetic device, *Nature Nanotechnology*, 11(5) (2016) 437-443.
- [15] Kim, S.K., Lee K.-S., Han D.-S., A gigahertz-range spin-wave filter composed of width-modulated nanostrip magnonic-crystal waveguides, *Applied Physics Letters*, 95(8) (2009) 082507.
- [16] Zhu, Y., Chi K., Tsai C., Magnonic crystals-based tunable microwave phase shifters, *Applied Physics Letters*, 105(2) (2014) 022411.
- [17] Podbielski, J., Giesen F., Grundler D., Spin-wave interference in microscopic rings, *Physical Review Letters*, 96(16) (2006) 167207.
- [18] Schneider T., A. Serga, Leven B., Hillebrands B., Stamps R. L., Kostylev M. P., Realization of spin-wave logic gate, *Applied Physics Letters*, 92(2) (2008) 022505.
- [19] Porro J M, Pinto A.B., A Berger and P Vavassori, Exploring thermally induced states in square artificial spin-ice arrays, *New Journal of Physics*, 15(5) (2013) 055012.
- [20] Zhang S., Gilbert I., Nisoli C., Chern G. W., Erickson M. J., O'Brien LK., Leighton C., Lammert P. E., Crespi V. H., Schiffer P., Crystallites of magnetic charges in artificial spin ice, *Nature*, 500(7464) (201) 553-557.
- [21] Council G., Devolder T., Kim J.-V., Crozat P., Chappert C., Zoll S., Fournel R., Temperature dependences of the resistivity and the ferromagnetic resonance linewidth in permalloy thin films, *IEEE transactions on Magnetics*, 42(10) (2006) 3323-3325.
- [22] Cinar I., Aslan O. B., Gokce A., Dincer O., Karakas V., Stipe B., Katine J. A., Aktas G., Ozatay O., Three dimensional finite element modeling and characterization of intermediate states in single active layer phase change memory devices, *Journal of Applied Physics*, 117(21) (2015) 214302.
- [23] Avery A. D., Mason S. J., Bassett D., Wesenberg D., Zink B. L., Thermal and electrical conductivity of approximately 100-nm permalloy, Ni, Co, Al, and Cu films and examination of the Wiedemann-Franz Law, *Physical Review B*, 92(21) (2015) 214410.
- [24] Holanda J., Santos O. A., Cunha R., O, Mendes J. B. S., Suárez R. L. R., A. Azevedo, and S. M. Rezende, Longitudinal spin Seebeck effect in permalloy separated from the anomalous Nernst effect: Theory and experiment, *Physical review B*, 95(21) (2017) 214421.
- [25] Le Guillou, J. Zinn J. J., Critical exponents for the n-vector model in three dimensions from field theory, *Physical Review Letters*, 39(2) (1977) 95.
- [26] Fassbender J., Strache T., Liedke M. O., Markó D., Wintz S., Lenz K., Keller A., Fácsko S., Mönch I., McCord J., Introducing artificial length scales to tailor magnetic properties, *New Journal of Physics*, 11(12) (2009) 125002.

## Influence of the Core Pillar Height on the Bandgap Characteristics of Piezoelectric Phononic Crystals with Ring-Shaped Grooves

Furkan Kuruoğlu<sup>1,a,\*</sup>

<sup>1</sup> Department of Physics, Faculty of Science, Istanbul University, Vezneciler 34134, Istanbul, Turkey.

\*Corresponding author

### Research Article

#### History

Received: 16/04/2022

Accepted: 16/06/2022

#### Copyright



©2022 Faculty of Science,  
Sivas Cumhuriyet University

### ABSTRACT

Dispersion profiles and surface acoustic wave attenuation characteristics of ring-shaped phononic crystals are investigated as a function of the core pillar height. Finite element method simulations are carried out for both band analyses and transmission spectra calculations. The results reveal that the increase at the core pillar height leads to a decrement in the local resonance band gap frequencies and the corresponding transmission peaks. The obtained dispersion profiles show that the phononic crystal bandgap also expands from 6 MHz to 11 MHz while the pillar height increases from 5  $\mu\text{m}$  to 7  $\mu\text{m}$ . Similar characteristics are also seen in the transmission spectra for the varying core pillar heights of the ring-shaped periodic grooves. In addition, surface acoustic wave attenuation competency depends on the core pillar height. The resonant frequency of the phononic crystals can be tuned by adjusting the core pillar height.

**Keywords:** Surface acoustic wave, Phononic crystal, Finite element method, Phononic bandgap.

 [furkan.kuruoglu@istanbul.edu.tr](mailto:furkan.kuruoglu@istanbul.edu.tr)  <https://orcid.org/0000-0002-5314-4441>

### Introduction

It has always been desired to sense and manipulate biological or inorganic objects by not only harmless but also contactless methods. Using light and acoustic waves [1] is the most practical way to reach this aim. Surface acoustic waves (SAWs) have been receiving extensive attention on various research and application areas related to delay lines [2], filters [3, 4], microfluidics [5–7], gas-detection [8, 9], mass detection [10] and bio-detection applications [11, 12]. Due to these wide ranges of research and application areas, SAW devices have drawn significant interest in recent decades.

By the proposition of the phononic crystals (PnCs)[13], which offer acoustic band gaps depending on the periodicity and geometry of the material, the guided SAWs have also been enabled, similar to photonic crystal slabs [14–16]. Recently, a periodic array of pillars emerged as the prominent phononic crystal geometry with a considerably broad range of application areas[17–19].

Piezoelectric phononic crystals (PPnCs), periodic elastic structures composed of either extrusions or grooves on a piezoelectric substrate, have also been drawing attention in terms of both physical properties and applications. Applications of PPnCs have emerged in different fields such as waveguiding [20–22], bio and mass sensing [23–25], energy harvesting [26] and microfluidics [27]. Fundamentally, the locally resonant and/or the Bragg bandgap of PPnCs paves the way for various types of applications and the bandgap characteristics are closely related to the geometric parameters of the PPnC.

Ash et al. showed that broader SAW band gaps could be achievable by using ring-shaped metamaterials as being piezoelectric phononic crystals [28]. Also, the

geometrical parameters like ring radii, pillar height and groove depth can tune the frequency range where the phononic crystal will be efficient. Because of these reasons, it is crucial to obtain the proper geometrical parameters and the effects on the acoustic bandgap for superior phononic device applications.

In this work, band profile of PPnC and SAW attenuation characteristics are simulated by means of the finite element method (FEM) for the ring-shaped groove model. Simulations are performed for various pillar heights, which differ from the groove height, while the inner and outer ring radii have fixed values.

### Material and Method

FEM simulations were performed to inspect the band structures of the ring-shaped PPnCs and SAW transmission spectra as a function of the PPnC pillar height. All simulations were carried out through COMSOL Multiphysics 5.3a by employing the piezoelectricity module, which couples the elastic wave equation and relevant Maxwell's equation (Gauss' law) to obtain stresses and electrical potential distributions over piezoelectric materials.

For ease of comparison to the work of Ash et al. [19], a two-dimensional (2D) PPnC in the square lattice is considered. As shown in Figure 1a), the square PPnCs are modeled by fixing the groove depth ( $h_{grv}$ ) to 6  $\mu\text{m}$ , groove top radius ( $r_o$ ) to 5  $\mu\text{m}$ , pillar bottom radius ( $r_i$ ) to 3  $\mu\text{m}$ , lattice constant ( $a$ ) to 12  $\mu\text{m}$ , while the pillar height ( $h_{pillar}$ ) is ranged from 5  $\mu\text{m}$  to 7  $\mu\text{m}$ . The wall inclination angle ( $\theta$ )

is set as  $10.2^\circ$ , which is experimentally reported for  $128^\circ$  Y-cut X-propagating (YX- $128^\circ$ ) lithium niobate ( $\text{LiNbO}_3$ ) [29]. This cut is defined in COMSOL through the Euler angles  $(\alpha, \beta, \gamma) = (0, 38^\circ, 0)$ . The definition of Euler angles is more convenient than the transformation of elasticity and coupling matrices of Z-cut  $\text{LiNbO}_3$ .

The eigenfrequencies are determined on the irreducible Brillouin zone (BZ) in the 1<sup>st</sup> BZ and the wavevector  $\mathbf{k}$  is swept on the boundaries along the  $\Gamma \rightarrow X \rightarrow M \rightarrow \Gamma$  path for the square array. Figure 1b represents the 3D schematic of the modeled PPnC unit cell. Bloch-Floquet periodic boundary condition (PBC) is defined for both opposing sides of the unit cell and the

bottom side of the unit cell was defined as a fixed constraint surface to avoid unwanted displacement effects. The piezoelectric slab height was chosen as  $h_{\text{slab}} = 200 \mu\text{m}$ , a value much higher than SAW penetration depth at the frequency range of interest (around 100 MHz). According to the geometric parameters of the PPnC unit cell given in Figure 1, there is a local resonance band gap (LRBG) resulting from the resonance vibrations of the core column, which is found to be below the expected Bragg band gap [19]. Here, it is shown that the characteristics, i.e., the LRBG edge frequencies and width can be tuned by varying  $h_{\text{pillar}}$ .

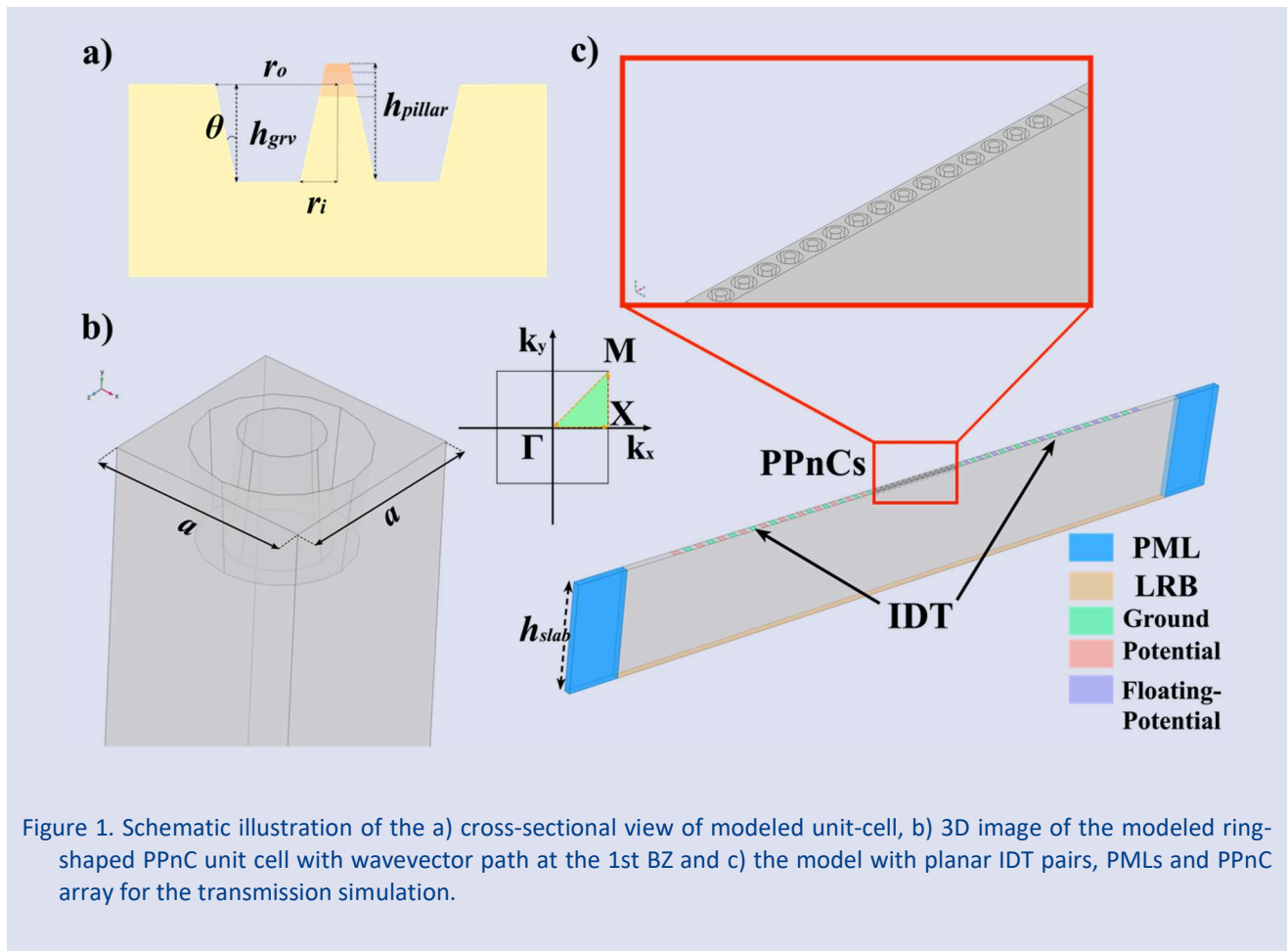


Figure 1. Schematic illustration of the a) cross-sectional view of modeled unit-cell, b) 3D image of the modeled ring-shaped PPnC unit cell with wavevector path at the 1st BZ and c) the model with planar IDT pairs, PMLs and PPnC array for the transmission simulation.

After the PPnC band structure is obtained for each  $h_{\text{pillar}}$  value, the corresponding transmission spectra are obtained through frequency domain FEM simulations. Here, Rayleigh-type SAWs are generated by interdigitated transducers (IDTs), which are the standard means of radio frequency (RF) SAW generation in such systems [30]. SAW transmission spectra are simulated for two facing identical IDTs and a PPnC array in between, as shown in Figure 1(c). To work in a broad frequency range, chirped IDTs [31] are modeled, where the finger width ranges from  $7.5 \mu\text{m}$  to  $12.5 \mu\text{m}$  with a step increase of  $\Delta\omega = 0.5 \mu\text{m}$  and the number of finger pairs in each IDT is  $N = 11$ . The PPnC array with 15 periodic units equally spaced from the IDT fingers lays along [10] direction. The IDT on the left in Figure 1(c) is

defined as the source to propagate SAW, while the right-side one is used to probe the transmitted signal through the floating potential ( $V_{\text{probe}}$ ). SAW transmittance ( $S_{21}$ ) is calculated from the  $S_{21} = 20 \times \log_{10}(V_{\text{probe}}/V_0)$  where  $V_0 = 50 \text{ V}$  is the RF amplitude. Perfectly matched layers (PML) [32] are placed at the edge of the model in the direction of the SAW propagation and the bottom side was defined as a low-reflecting boundary (LRB) to minimize the unwanted reflections. PBC is used on the sides parallel to the SAW propagation direction, that is only one row of the PPnC is modeled, while the infinitely-many rest images are replicates through the PBC.

## Results and Discussion

The band structure of the PPnC is plotted as a function of pillar height in Figure 2. The red dashed lines show the Rayleigh SAW modes of the unperturbed bulk and the other leaky SAW dispersion lines are not presented. The grey shaded areas denote the ranges of these leaky modes, which are ruled out. Below the SAW line in Figure 2, there appear several bands due to different vibration mechanisms. The lowermost two bands correspond to bending and expansion modes of the core pillar therefore flat they are [19]. The third band, on the other hand, comprises of anti-resonant modes of the outer grooves. The orange stripes lying between the second and third bands are the LRBGs, which appear between 105.2 - 111.2 MHz for the 5  $\mu\text{m}$  core pillar height and shift towards the frequencies between the 70.8-82.4 MHz while the core pillar height increases up to 7  $\mu\text{m}$ . Only one LRBG appears for each case, where the Bragg bandgap frequency is estimated to be around 200 MHz, from the condition  $\alpha/\lambda=1/2$ .

The two bands below the LRBG related to the pillar modes shift to lower frequencies by the increasing pillar height of the ring-shaped PPnC. Similar results were reported for the pillar type PPnC arrays, through both experimental and simulation results [17, 19, 33]. Besides, the gap between the dispersion lines corresponds to the localized modes of the pillar decreases with the increasing height.

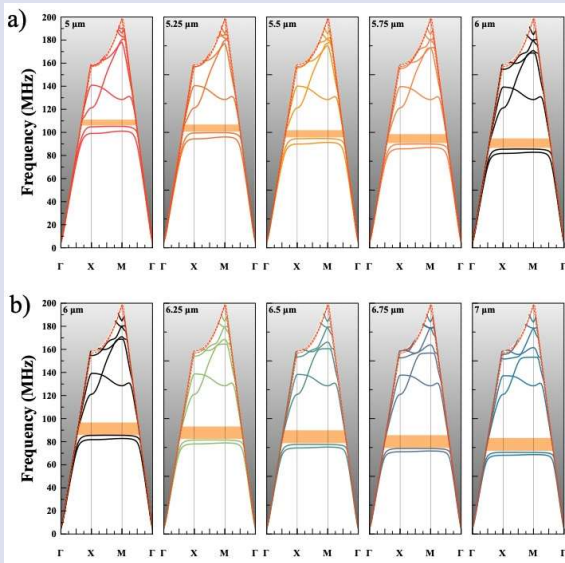


Figure 2. The band structures of the square array ring-shaped PPnCs with different pillar heights: a) 5  $\mu\text{m}$  to 6  $\mu\text{m}$  and b) 6  $\mu\text{m}$  to 7  $\mu\text{m}$ .

This pillar height dependence of the local resonant frequency also paves the way for the adjustment of the frequency, likewise the previous reports for the all-pillar type PPnCs, which is defined to be located above the surface of substrate [19]. Differently from the all-pillar PPnC arrays, for the ring-shaped PPnCs, the third band at the higher frequencies can be modulated by varying the pillar height of the ring-shaped PPnCs.

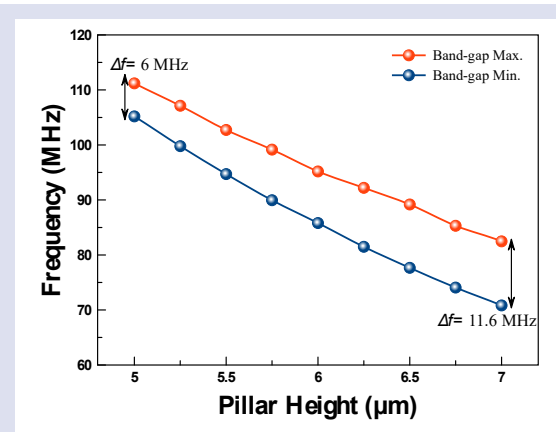


Figure 3. Variation of LRBG edge frequencies as a function of the PPnC pillar height.

Figure 3 shows the bandgap change as a function of the pillar height of the ring-shaped PPnCs. As seen in Figure 3, the LRBG location shifts towards lower frequency regions. At the same time, the bandgap expands nearly by a factor of 2 from the lowest (5  $\mu\text{m}$ ) to the highest (7  $\mu\text{m}$ ) pillar height. The monotonic behavior may be attributed to the added mass with increasing  $h_{\text{pillar}}$ , which results in elevated inertia of the core pillars.

The transmission spectra ( $S_{21}$ ) are obtained for a better understanding of PPnC and SAW interaction. Figure 4 shows the SAW transmission spectra ranged between 70 MHz and 130 MHz for each pillar heights from 5  $\mu\text{m}$  to 7  $\mu\text{m}$ . The red dashed line in Figure 4 represents the  $S_{21}$  spectrum of the bare chirped IDT pairs (i.e., without PPnC in between). Each transmission spectrum has two apparent peaks and the major one is located at nearly 100 MHz, while the minor one is around 80 MHz. As compared to the dispersion profiles, both  $S_{21}$  peaks shift towards lower frequencies until the pillar top is in line with the LiNbO<sub>3</sub> surface (i.e.,  $h_{\text{pillar}}=6 \mu\text{m}$ ). Just after the pillar reaches above the surface, the peak around the 100 MHz slightly shifts to higher frequencies, whereas the minor peak continues to shift towards lower frequencies. The characteristics of the minor peak can be attributed to pillar height dependency of the local resonant profile of the ring-shaped PPnC [18].

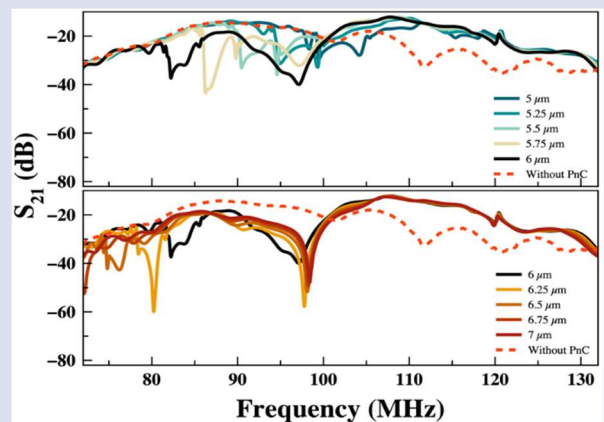


Figure 4. SAW transmission spectra of ring-shaped square PPnC array on the [10] orientation for different pillar heights

A drastic increment is also observed in the SAW attenuation (transmission loss) for  $h_{\text{pillar}} > h_{\text{grv}}$  in both major and minor peaks, as shown in Figure 5. For  $h_{\text{pillar}} \geq 6.25 \mu\text{m}$ , however, transmission loss shows a decreasing profile with the increment of the pillar height of the PPnC, Figure 5(b).

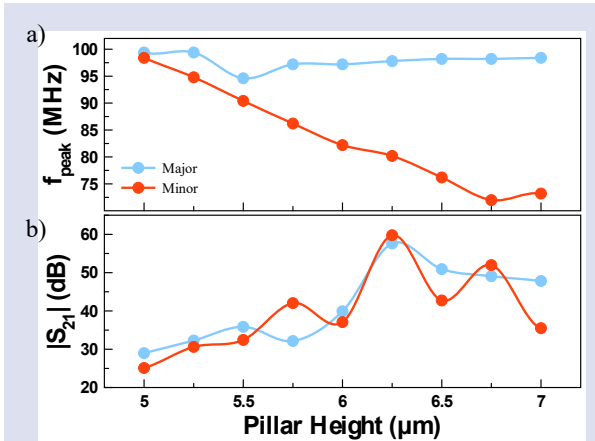


Figure 7. a) Major and minor peak frequencies in  $S_{21}$  spectra and, b) the attenuation intensity at the peak frequency for the various pillar height of the ring-shaped PPnC arrays.

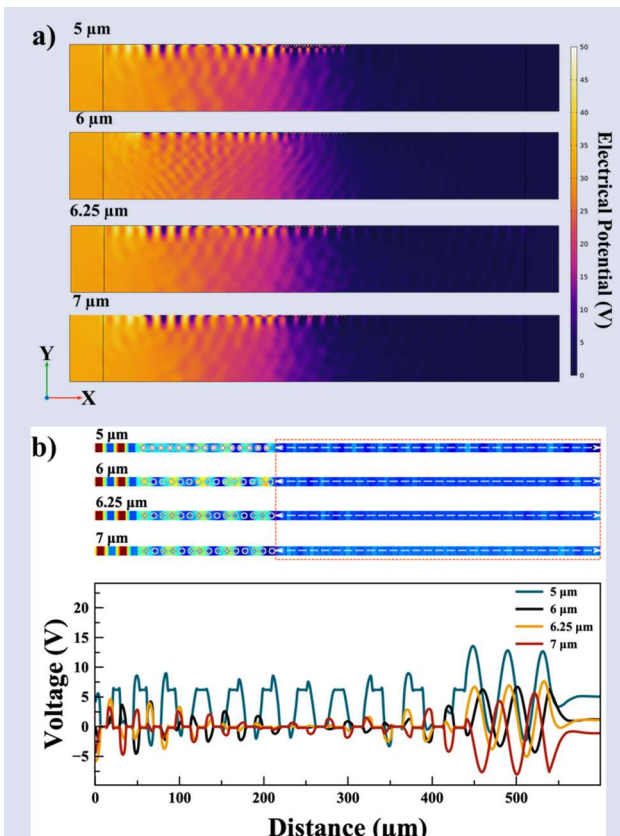


Figure 6. a) Cross-sectional view of the electrical potential distribution for different ring-shaped PPnC pillar heights calculated at the corresponding  $S_{21}$  major peak frequencies (99.4 MHz, 97.2 MHz, 97.8 MHz and 98.4 MHz, respectively). b) Electrical potential distribution on the slab surface and the line profile voltage distribution on the probe IDT for the various core pillar height.

Figure 6 visualizes the potential distribution over the simulated model at the major peak frequencies corresponding to different  $h_{\text{pillar}}$  values extracted from the SAW transmission spectra in Figure 4. It can be clearly seen in Figure 6 that PPnC arrays with lower height pillars ( $h_{\text{pillar}} < h_{\text{grv}}$ ) have no superior attenuation performance. In good agreement with the results in Figure 4, the PPnC arrays that have pillars with  $h_{\text{pillar}} \geq h_{\text{grv}}$ , exhibit better attenuation characteristics according to the more pronounced darker regions in Figure 6a and the voltage distributions in the Figure 6b.

## Conclusion

In summary, the band structures and the SAW transmission spectra of PPnCs with ring-shaped grooves are simulated as a function of core pillar height. It is observed that the increment in the pillar height of the ring-shaped PPnC leads to a decrease in the LRBG edge frequencies while the width of LRBG is increasing. Agreeing results are obtained from the SAW transmission peaks and the voltage distribution on the probe IDT, which tend to show decreasing attenuation profile with the increasing pillar height. The potential distributions also show the ring-shaped PPnCs with  $h_{\text{pillar}} \geq 6 \mu\text{m}$  have better attenuation performance.

Taking into account all of these findings from the simulations, the frequencies at which the ring-shaped PPnCs are functional can be utilized to tune surface acoustic wave attenuation by adjusting the pillar height of the model. Increasing pillar height is equivalent to adding extra load on the pillars. Thus, the investigated PPnC can be employed in sensing applications through the mass loading effect.

## Acknowledgment

I appreciate support from Prof. Dr. Ahmet Cicek and Prof. Dr. Ayse Erol for their valuable discussion on the results. The work is funded by The Scientific and Technological Research Council of Turkey (TUBITAK) (Project No: 120F337).

## Conflicts of interest

The author states that did not have a conflict of interests.

## References

- [1] Collins D.J., Devendran C., Ma Z., Ng, J.W., Neild A., Ai Y., Acoustic tweezers via sub-time-of-flight regime surface acoustic waves, *Sci. Adv.*, 2 (7) (2016) e1600089.
- [2] Topaltzikis D., Wielunski M., Hörner A.L., Küß M., Reiner A., Grünwald T., Schreck M., Wixforth A., Rühm W., Detection of x rays by a surface acoustic delay line in contact with a diamond crystal, *Appl. Phys. Lett.*, 118 (13) (2021) 133501.
- [3] Su R., Shen J., Lu Z., Xu H., Niu Q., Xu Z., Zeng F., Song C., Wang W., Fu S., Pan F., Wideband and Low-Loss Surface Acoustic Wave Filter Based on  $15^\circ$  YX-LiNbO<sub>3</sub>/SiO<sub>2</sub>/Si Structure, *IEEE Electr. Device L.*, 42 (3) (2021) 438-441.



- [4] Su R., Fu S., Shen J., Lu Z., Xu H., Yang M., Zeng F., Song C., Wang W., Pan F., Power Durability Enhancement and Failure Analysis of TC-SAW Filter With Ti/Cu/Ti/Cu/Ti Electrodes, *IEEE T. Device Mat. Re.*, 21 (3) (2021) 365-371.
- [5] Xie Y., Mao Z., Bachman H., Li P., Zhang P., Ren L., Wu M., Huang T.J., Acoustic Cell Separation Based On Biophysical Properties., *J. Biomechanical Eng.*, 142 (3) (2020) 031005-1-9
- [6] Qian J., Ren J., Liu Y., Lam R.H.W., Lee J.E.-Y., A two-chip acoustofluidic particle manipulation platform with a detachable and reusable surface acoustic wave device, *Analyst*, 145 (23) (2020) 7752-7758.
- [7] Agostini M., Greco G., Cecchini M., Full-SAW Microfluidics-Based Lab-on-a-Chip for Biosensing, *IEEE Access*, 7 (2019) 70901-70909.
- [8] Kumar A., Prajesh R., The Potential of Acoustic Wave Devices for Gas Sensing Applications, *Sens. Actuator A-Phys. Physical*, 339 (2022) 113498.
- [9] Hekiem N.L.L., Ralib A.A.M., Hattar M.A. bt M., Ahmad F., Nordin A.N., Rahim,R.A., Za'bah,N.F., Advanced vapour sensing materials, Existing and latent to acoustic wave sensors for VOCs detection as the potential exhaled breath biomarkers for lung cancer, *Sens. Actuator A-Phys.*, 329 (2021) 112792.
- [10] Wang Y., Wang., Liu, W., Chen D., Wu C., Xie J., An aerosol sensor for PM1 concentration detection based on 3D printed virtual impactor and SAW sensor, *Sens. Actuator A-Phys.*, 288 (2019) 67-74.
- [11] Zhang X.-F., Zhang Z.-W., He Y.-L., Liu Y.-X., L, S., Fang J.-Y., Zhang X.-A., Peng G., Sniffing lung cancer related biomarkers using an oxidized graphene SAW sensor *Frontiers of Physics*, 11 (2015) 2.
- [12] Kidakova A., Boroznjak R., Reut J., Öpik A., Saarma M., Syrtski V., Molecularly imprinted polymer-based SAW sensor for label-free detection of cerebral dopamine neurotrophic factor protein, *Sens. Actuator B-Chem.*, 308 (2020) 127708.
- [13] Kushwaha M.S., Halevi P., Martínez G., Dobrzynski L., Djafari-Rouhani, B., Theory of acoustic band structure of periodic elastic composites *Phys. Rev. B*, 49 (4) (1994) 2313-2322.
- [14] Sigalas M., Economou, E.N., Band structure of elastic waves in two dimensional systems, *Solid State Commun.*, 86 (3) (1993) 141-143.
- [15] Mead D.M., Wave Propagation In Continuous Periodic Structures, Research Contributions From Southampton, 1964–1995, *J.Sound Vibr.*, 190 (3) (1996) 495-524.
- [16] Kushwaha M.S., Halevi P., Dobrzynski L., Djafari-Rouhani B., Acoustic band structure of periodic elastic composites, *Phys.Rev. Lett.*, 71 (13) (1993) 2022-2025.
- [17] Achaoui Y., Khelif A., Benchabane S., Robert L., Laude V., Experimental observation of locally-resonant and Bragg band gaps for surface guided waves in a phononic crystal of pillars, *Phys. Rev. B*, 83 (10) (2011) 104201.
- [18] Achaoui Y., Laude V., Benchabane S., Khelif A., Local resonances in phononic crystals and in random arrangements of pillars on a surface, *J. Appl. Phys.* .114 (10) (2013) 104503.
- [19] Jin Y., Pennec Y., Bonello B., Honarvar H., Dobrzynski L., Djafari-Rouhani B., Hussein M.I., Physics of surface vibrational resonances, pillared phononic crystals, metamaterials, and metasurfaces, *Rep. Prog. Phys.*, 84 (8) (2021) 086502.
- [20] Vasseur J.O., Hladky-Hennion A.-C., Djafari-Rouhani B., Duval F., Dubus,B., Pennec Y., Deymier P.A., Waveguiding in two-dimensional piezoelectric phononic crystal plates, *J. Appl. Phys.*, 101 (11) (2007) 114904.
- [21] Oh J.H., Lee I.K., M, P.S., Kim Y.Y., Active wave-guiding of piezoelectric phononic crystals, *Appl. Phys. Lett.*, 99(8) (2011) 083505.
- [22] Zhang Z.-D., Liu F.-K., Yu S.-Y., Lu M.-H., Chen Y.-F., An integrable and configurable phononic beam splitter based on self-collimated surface acoustic waves, *Appl. Phys. Express*, 13 (4) (2020) 044002.
- [23] Schmidt M.-P., Oseev A., Lucklum R., Zubtsov M., Hirsch S., SAW based phononic crystal sensor, technological challenges and solutions, *Microsyst. Technol.*, 22 (7) (2016) 1593-1599.
- [24] Gharibi H., Khaligh A., Bahrami A., Ghavifekr H.B., A very high sensitive interferometric phononic crystal liquid sensor, *J. Mol. Liq.*, 296 (2019) 111878.
- [25] Gharibi H.,Mehaney A., Two-dimensional phononic crystal sensor for volumetric detection of hydrogen peroxide (H2O2) in liquids, *Phys. E Low-dimensional Syst. Nanostructures*, 126 (2021) 114429.
- [26] Cao D., Hu W., Gao Y., Guo X., Vibration and energy harvesting performance of a piezoelectric phononic crystal beam, *Smart Mater. Struct.*, 28 (8) (2019) 085014.
- [27] Bourquin Y., Wilson R., Zhang Y., Reboud J.,Cooper J.M., Phononic Crystals for Shaping Fluids, *Adv. Mater.*, 23 (12) (2011) 1458-1462.
- [28] Ash B.J., Worsfold S.R., Vukusic P.,Nash G.R., A highly attenuating and frequency tailorable annular hole phononic crystal for surface acoustic waves, *Nature Communications*, 8 (1) (2017) 174.
- [29] Ozgur Y., Birol O., Dong X., Srinivas S., Conicity and depth effects on the optical transmission of lithium niobate photonic crystals patterned by focused ion beam, *Opt. Mater. Express*, 1 (7) (2011) 1262-1271.
- [30] Levy M., Bass H., Stern R., Modern Acoustical Techniques for the Measurement of Mechanical Properties, *Elsevier Science*, (2001).
- [31] Laurell T., Lenshof A., Microscale Acoustofluidics, *Royal Society of Chemistry*, (2014).
- [32] Berenge, J.-P., Perfectly matched layer for the FDTD solution of wave-structure interaction problems, *IEEE T. Antenn. Propag.*, 44 (1) (1996) 110-117.
- [33] Pennec Y., Djafari-Rouhani B., Larabi H., Vasseur J.O., Hladky-Hennion A.C., Low-frequency gaps in a phononic crystal constituted of cylindrical dots deposited on a thin homogeneous plate, *Phys. Rev. B*, 78 (10) (2008) 104105.

## A New Extension Form for Continuous Probability Distributions: Uniform-X Distributions

Çiğdem Topçu Gülöksüz<sup>1,a,\*</sup>, Nuri Çelik<sup>2,b</sup>

<sup>1</sup> Department of Business Administration, Faculty of Economic and Administrative Sciences, OSTİM Technical University, Ankara, Türkiye

<sup>2</sup> Department of Mathematics, Faculty of Science, Gebze Technical University, Kocaeli, Türkiye

\*Corresponding author

### Research Article

#### History

Received: 17/12/2021

Accepted: 28/04/2022

#### Copyright



©2022 Faculty of Science,  
Sivas Cumhuriyet University

### ABSTRACT

In this paper, generating extension forms for continuous probability distribution functions is studied. The considered transformer function is applied to three well-known probability distributions- Normal, Kumaraswamy, Weibull- and new extensions of these distributions are obtained. The related functions of the new extensions are defined, random samples are generated from the new extensions and the results are presented. Parameter estimation procedures of the extensions are studied, and likelihood equations are obtained. To demonstrate the modeling performance of the extensions, three different data sets are considered, separately. Each data set is modeled by both the corresponding probability distribution and its extensions. The new extensions give the best fit to the corresponding data over the well-known probability distributions.

**Keywords:** Extensions of probability distributions, Transformer function, Quantile function, Maximum likelihood estimation, Skewness.

<sup>a</sup> [cigdem.guloksuz@ostimteknik.edu.tr](mailto:cigdem.guloksuz@ostimteknik.edu.tr) <sup>id</sup> <https://orcid.org/0000-0002-7433-1297>

<sup>b</sup> [nuricelik@gtu.edu.tr](mailto:nuricelik@gtu.edu.tr)

<sup>id</sup> <https://orcid.org/0000-0002-4234-2389>

## Introduction

Generalization of the well-known distributions have been widely used to get more flexible statistical models. For instance, the generalized gamma distribution for modeling the distribution of income rate is introduced in [1], proposed inverse Gaussian distribution is proposed in [2], the generalization of Pareto distributions are studied in [3-5] and, the generalized beta of the first and second kind as models for the size distribution of income is introduced in [6]. Beta distribution is used as a generator function by [7] and they propose a new class of distribution, which are called beta-generated (BG) distributions. This generalization proceeds as follows,  $F(x)$  is the cumulative distribution function (cdf) of any random variable  $X$ ,  $b(t)$  is the probability density function (pdf) of beta random variable then the cdf of beta-generated random variable  $G(x)$  is defined as

$$G(x) = \int_0^{F(x)} b(t) dt \quad (1.1)$$

(1.2) gives the pdf of beta-generated random variable.

$$g(x) = \frac{1}{B(\alpha, \beta)} f(x) [F(x)]^{\alpha-1} [1 - F(x)]^{\beta-1} \quad (1.2)$$

In literature, there are various types of studies including beta-generated distributions, see [8-13]. Kumaraswamy generalized distribution (KWG) by using Kumaraswamy distribution instead of beta distribution in (1.2) is introduced in [14]. Many researchers proposed some variations of KWG distributions, see [15-17].

Following the idea of generating BG distributions, a new technique to generate continuous probability distributions is proposed in [18]. This new approach is described as follows:

Let  $X$  be a random variable whose pdf is  $f(x)$  and cdf is  $F(x)$ . Let  $T$  be a continuous random variable with pdf  $h(t)$  defined on the interval  $[a, b]$ . The cdf of the new family of distribution is defined as

$$G(x) = \int_a^{W[F(x)]} h(t) dt \quad (1.3)$$

where  $W[F(x)]$  is differentiable and monotonically non-decreasing in  $x$ . It should be also noted that  $W[F(x)] \rightarrow a$  as  $x \rightarrow -\infty$  and  $W[F(x)] \rightarrow b$  as  $x \rightarrow \infty$ . The corresponding pdf of  $X$  can be written as

$$g(x) = \left\{ \frac{d}{dx} W[F(x)] \right\} h\{W[F(x)]\} \quad (1.4)$$

In this generalization procedure, the random variable  $T$  is called "transformed" into a new cdf  $G(x)$  through the function  $W[F(x)]$ , which is called "transformer". So,  $G(x)$  is called "Transformed-Transformer" or  $T - X$  distribution. Following the technique which is proposed and well defined in [18], we study with the transformer function  $W[F(x); \theta]$  which is introduced to generate a new life time distribution in [19]. This transformer function is also used to obtain a new extension of Generalized Extreme Value distribution which is proposed as a model for an earthquake data in [20].

In this paper, we study to obtain new extensions of the three probability distributions-Normal, Kumaraswamy, and Weibull by transforming uniform random variable through the transformer function  $W[F(x); \theta]$

The rest of the paper is organized as follows: In Section 2, a brief summary of the methodology is given. In Section 3 the methodology is applied to Normal, Kumaraswamy and Weibull distributions to get new extensions. The properties of new extensions distributions such as moments, quantiles functions and the maximum likelihood (ML) equations are obtained. Some simulations studies are conducted to present how the new extensions change according to the representative values of the parameter ( $\theta$ ) of the generator function,  $W[F(x); \theta]$ . In Section 4, real data examples are considered to present the performances of the new extensions of the studied probability distributions. Section 5 concludes the paper.

### Materials and Methods

The transformer function which is introduced by [19] is given and then recalling (1.3), the cdf of Uniform-X distributions is defined.

$$W[F(x); \theta] = \frac{\exp(-\theta F(x)) - 1}{\exp(-\theta) - 1} \tag{2.1}$$

where  $\theta \in R$ . Furthermore,  $W[F(x); \theta] \rightarrow 0$  as  $x \rightarrow -\infty$  and  $W[F(x); \theta] \rightarrow 1$  as  $x \rightarrow \infty$ .

**Definition 2.1** Let  $X$  be a random variable whose pdf is  $f(x)$ ;  $a < x < b$  and cdf is  $F(x)$ . Let  $T$  be a uniform random variable, whose pdf is  $h(t) = 1; 0 < t < 1$ . Then

$$G(x) = \int_0^{\frac{\exp(-\theta F(x))-1}{\exp(-\theta)-1}} dy = \frac{\exp(-\theta F(x)) - 1}{\exp(-\theta) - 1}, \quad a < x < b \tag{2.2}$$

is a cdf of the Uniform-X (Uni-X) distribution. The pdf of Uni-X distribution is in (2.3).

$$g(x) = \frac{\theta f(x) \exp(-\theta F(x))}{1 - \exp(-\theta)}, \quad a < x < b, \theta \in R \tag{2.3}$$

The properties of the Uni-X distribution are as follows:

1. For all bounded or unbounded intervals, this new extension of distributions inherits the properties of being a pdf
2. Extensions are defined on the same interval  $[a, b]$
3. If  $\theta$  goes to 0, the  $g(x)$  defined in (2.3) converges to the studied pdf distribution  $f(x)$

$$\lim_{\theta \rightarrow 0} \frac{\theta f(x) \exp(-\theta F(x))}{1 - \exp(-\theta)} \rightarrow f(x).$$

The moment generating function (mgf) of Uni-X distributions is defined as follows

$$M_X(t) = \int_a^b e^{tx} \frac{\theta f(x) \exp(-\theta F(x))}{1 - \exp(-\theta)} dx. \tag{2.4}$$

By substituting  $u = F(x)$ , Taylor series expansion of  $e^{tF^{-1}(u)} e^{-\theta u}$  can be considered to obtain the moments of the Uni-X distributions. However, the closed form of the moments of the studied Uni-X distributions in this study cannot be obtained.

The quantile function of Uni-X distributions in (2.5) is obtained by using the simple inverse cdf technique.

$$Q(p) = F^{-1} \left\{ -\frac{1}{\theta} \ln(p(\exp(-\theta) - 1) + 1) \right\} \tag{2.5}$$

The Uni-X distributions are extensions of the studied distributions firstly denoted by  $F(x)$  in (2.1). In this study, we study normal distribution (typical example of symmetric distributions), Weibull distribution (representative of the positively skewed distributions) and Kumaraswamy distribution (symmetric, positively skewed and negatively skewed form) as  $F(x)$  and introduce their extensions which are called Uni-Normal, Uni-Weibull, Uni-Kumaraswamy, respectively in the following three sub-sections.

#### Uniform-Normal Distribution

Consider a normal distribution with pdf  $\phi(z)$  and cdf  $\Phi(z)$  where  $z = \frac{x-\mu}{\sigma}$ ,  $\mu$  and  $\sigma$  are the location and the scale parameters, respectively. Recalling (2.2), the cdf of uniform-normal (Uni-Normal) distribution is defined as

$$G(x) = \frac{\exp(-\theta \Phi(z)) - 1}{\exp(-\theta) - 1}, \quad -\infty < x < \infty \tag{3.1}$$

The pdf of Uni-Normal distribution is defined as

$$g(x) = \frac{\theta \phi(z) \exp(-\theta \Phi(z))}{\sigma(1 - \exp(-\theta))}, \quad -\infty < x < \infty \tag{3.2}$$

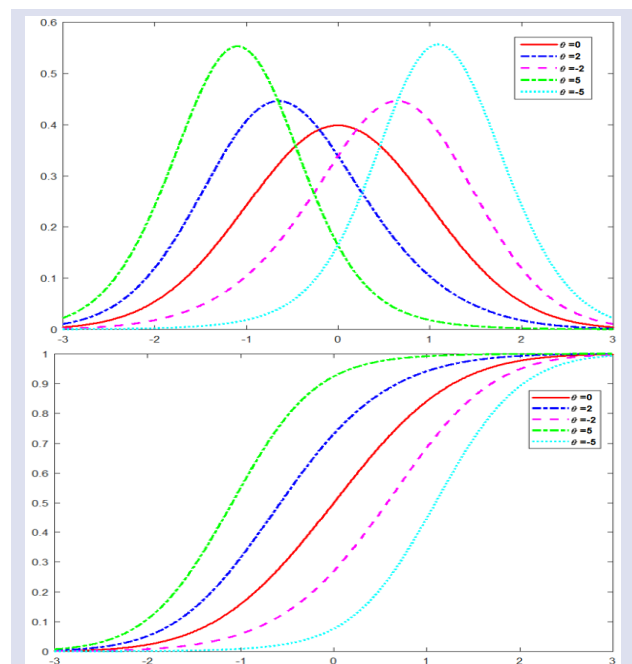


Figure 1. The pdfs and cdfs of Uni-Normal distribution,  $\mu = 0$  and  $\sigma = 1$

Figure 1 illustrates the pdfs and the cdfs of the Uni-Normal distribution for different  $\theta$  values. When  $\theta$  tends to 0, the pdf reduces to the well-known normal distribution, when  $\theta > 0$ , then the pdf becomes positively skewed and  $\theta < 0$  then the pdf becomes negatively skewed.

The quantile function  $Q(p)$ ,  $0 < p < 1$  and the median of the Uni-Normal distribution are defined as

$$Q(p) = \mu + \sigma \Phi^{-1} \left\{ -\frac{1}{\theta} \ln(1 - p(\exp(-\theta) - 1)) \right\} \quad (3.3)$$

Table 1. The simulation results for the Uni-Normal distribution,  $\mu = 0$  and  $\sigma = 1$

$\theta$	Mean	Variance	SV	KV
-5	1.082	0.767	-0.288	3.583
-2	0.534	0.938	-0.218	3.180
-0.001	0.001	0.997	-0.002	2.936
0	0.000	1.000	0	3.000
0.001	-0.001	0.997	0.001	2.938
2	-0.534	0.937	0.224	3.185
5	-1.081	0.767	0.289	3.534

Table 1 indicates that  $\theta$  tends to 0 the Uni-Normal distribution converges to the well-known normal distribution and  $\theta$  increases, the SV and the KV increase and the variance decreases.

Now, suppose  $Z_1, Z_2, \dots, Z_n$  are random variables from a Uni-Normal distribution defined in (3.1), then the likelihood function and the log-likelihood function are defined in (3.5) and (3.6), respectively.

$$L(\mu, \sigma, \theta) = \theta^n \sigma^{-n} (1 - \exp(-\theta))^{-n} \prod_{i=1}^n \phi(z_i) \prod_{i=1}^n \exp(-\theta \phi(z_i)) \quad (3.5)$$

$$l(\mu, \sigma, \theta) = n \ln \theta - n \ln \sigma - \ln(1 - \exp(-\theta)) + \sum_{i=1}^n \ln(\phi(z_i)) - \theta \sum_{i=1}^n \phi(z_i) \quad (3.6)$$

By differentiating the log-likelihood function with respect to the unknown parameters and equating them to zero, we obtain the following likelihood equations.

$$\begin{aligned} \frac{\partial \ln L}{\partial \mu} &= \sum_{i=1}^n z_i + \theta \sum_{i=1}^n \phi(z_i) = 0 \\ \frac{\partial \ln L}{\partial \sigma} &= -n + \sum_{i=1}^n z_i^2 + \theta \sum_{i=1}^n \phi(z_i) = 0 \\ \frac{\partial \ln L}{\partial \theta} &= \frac{n}{\theta} - \frac{n \exp(-\theta)}{1 - \exp(-\theta)} - \sum_{i=1}^n \phi(z_i) = 0 \end{aligned} \quad (3.7)$$

Solutions of (3.7) are called ML estimates. The equations need to be solved with numerical methods such as Newton Raphson or iteratively reweighting algorithm.

### Uniform-Kumaraswamy Distribution

Let  $f(x)$  and  $F(x)$  be the pdf and the cdf of Kumaraswamy distribution, respectively. Based on the Definition 2.1, the cdf of the Uniform-Kumaraswamy (Uni-Kums) distribution is obtained

$$Q\left(\frac{1}{2}\right) = \mu + \sigma \Phi^{-1} \left\{ -\frac{1}{\theta} \ln\left(1 - \frac{1}{2}(1 + \exp(-\theta))\right) \right\} \quad (3.4)$$

respectively.

Considering (3.3), a simulation study is conducted to present how to change sample mean, variance, skewness values (SV) and kurtosis values (KV) according to the different values of  $\theta$ . The random samples with size 100 are generated 100.000 times and the results are listed in Table 1.

$$K(x) = \frac{\exp(-\theta F(x)) - 1}{\exp(-\theta) - 1} = \frac{\exp(-\theta[1 - (1 - x^a)^b]) - 1}{\exp(-\theta) - 1} \quad (3.9)$$

$$k(x) = \frac{\theta f(x) \exp(-\theta F(x))}{1 - \exp(-\theta)} = \frac{\theta a b x^{a-1} (1 - x^a)^{b-1} \exp(-\theta[1 - (1 - x^a)^b])}{1 - \exp(-\theta)} \quad (3.10)$$

where  $0 < x < 1$ ,  $a, b > 0$

Figure 2 demonstrates the pdfs and the cdfs of Uni-Kums distribution for different values of  $\theta$ . The Uni-Kums distribution becomes more skewed (positively or negatively) according to the parameter  $\theta$  values.

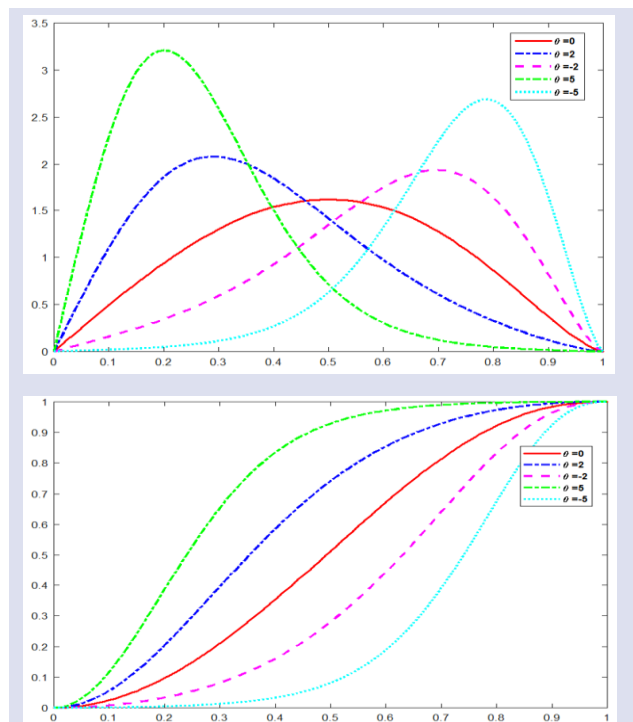


Figure 2. The pdfs and cdfs of Uni-Kums distribution,  $a = 2$  and  $b = 2.5$

The quantile function  $Q(p)$ ,  $0 < p < 1$  and the median of the Uni-Kums distribution are defined as respectively.

$$Q(p) = \left( 1 - \left[ 1 + \frac{\ln(1+p(\exp(-\theta)-1))}{\theta} \right]^{\frac{1}{b}} \right)^{\frac{1}{a}} \quad (3.11)$$

$$Q\left(\frac{1}{2}\right) = \left( 1 - \left[ 1 + \frac{\ln(1+0.5(\exp(-\theta)-1))}{\theta} \right]^{\frac{1}{b}} \right)^{\frac{1}{a}} \quad (3.12)$$

Considering (3.11), the simulation procedure in sub-section 3.1 is applied to Uni-Kums distribution with the parameters  $a = 2$  and  $b = 2$ . The results are listed in Table 2 indicate that  $\theta$  tends to 0, the Uni-Kums distribution converges to the well-known Kumaraswamy distribution and when  $\theta$  values increases the SV and the KV also increases.

Table 2. The simulation results for the Uni-Kums distribution, a=2, b=2

$\theta$	Mean	Variance	SV	KV
-5	0.766	0.143	-1.056	4.348
-2	0.652	0.199	-0.640	2.840
-0.001	0.533	0.221	-0.123	2.193
0	0.533	0.221	-0.123	2.193
0.001	0.533	0.221	-0.123	2.193
2	0.412	0.208	0.375	2.466
5	0.290	0.159	0.763	3.745

Suppose  $X_1, X_2, \dots, X_n$  are random variables from the Uni-Kums distribution defined in (3.9) and the likelihood function and the log-likelihood functions of this random sample are obtained as follows, respectively.

$$L = (a, b, \theta) = \left( 1 - \exp(-\theta) \right)^{-n} \theta^n a^n b^n \exp(-\theta \sum_{i=1}^n 1 - (1 - x_i^a)^b) \prod_{i=1}^n x_i^{a-1} \prod_{i=1}^n (1 - x_i^a)^{b-1} \quad (3.13)$$

$$l(a, b, \theta) = -n \ln(1 - \exp(-\theta)) + n \ln \theta + n \ln a + n \ln b + \sum_{i=1}^n (a-1) \ln x_i + \sum_{i=1}^n (b-1) \ln(1 - x_i^a) - \theta \sum_{i=1}^n [1 - (1 - x_i^a)^b] \quad (3.14)$$

By differentiating the log-likelihood function with respect to the unknown parameters and equating them to zero we obtain the following likelihood equations

$$\frac{\partial \ln L}{\partial a} = \frac{n}{a} + \sum_{i=1}^n \ln x_i - (b-1) \sum_{i=1}^n \frac{1}{1 - x_i^a} x_i^a \ln x_i + \theta \sum_{i=1}^n b(1 - x_i^a)^{b-1} x_i^a \ln x_i$$

$$\frac{\partial \ln L}{\partial b} = \frac{n}{b} + \sum_{i=1}^n \ln(1 - x_i^a) + \theta \sum_{i=1}^n (1 - x_i^a)^b \ln(1 - x_i^a) \quad (3.15)$$

$$\frac{\partial \ln L}{\partial \theta} = \frac{n}{\theta} - \frac{n \exp(-\theta)}{1 - \exp(-\theta)} - \sum_{i=1}^n [1 - (1 - x_i^a)^b]$$

Solutions of (3.16) are called ML estimates and which are obtained by solving the equations with numerical methods.

### Uniform-Weibull Distribution

In this sub-section, we consider  $h(x)$  and  $H(x)$  as the pdf and cdf of Weibull distribution, respectively. Considering the Definition 2.1, the cdf and pdf of the Uniform-Weibull (Uni-Weib) distribution are obtained as, respectively.

$$V(x) = \frac{\exp(-\theta H(x)) - 1}{\exp(-\theta) - 1} = \frac{e^{-\theta [1 - \exp(-(\frac{x}{\lambda})^k)]} - 1}{\exp(-\theta) - 1}, \quad x, \lambda, k > 0 \quad (3.16)$$

$$v(x) = \frac{\theta h(x) \exp(-\theta H(x))}{1 - \exp(-\theta)} = \frac{\theta \frac{k}{\lambda} (\frac{x}{\lambda})^{k-1} \exp(-(\frac{x}{\lambda})^k) \exp(-\theta [1 - \exp(-(\frac{x}{\lambda})^k)])}{\exp(-\theta) - 1}, \quad x, \lambda, k > 0 \quad (3.17)$$

The quantile function and the median of the Uni-Weib are defined, respectively.

$$Q(p) = \lambda \left[ -\ln \left( 1 + \frac{\ln(p(\exp(-\theta) - 1) + 1)}{\theta} \right) \right]^{\frac{1}{k}} \quad (3.18)$$

$$Q\left(\frac{1}{2}\right) = \lambda \left[ -\ln \left( 1 + \frac{\ln\left(\frac{1}{2}(\exp(-\theta) - 1) + 1\right)}{\theta} \right) \right]^{\frac{1}{k}} \quad (3.19)$$

Figure 3 illustrates the pdfs and the cdfs of the Uni-Weib distribution for some skewness parameter  $\theta$ .

Same simulation procedure in the previous sub-sections is applied to Uni-Weib distribution with parameters  $\lambda=1$  and  $k=1.5$ . The results for representative  $\theta$  values are listed in Table 3. When  $\theta$  tends to 0, the Uni-Weib distribution converges to the well-known Weibull distribution, as Figure 3 supports the results.

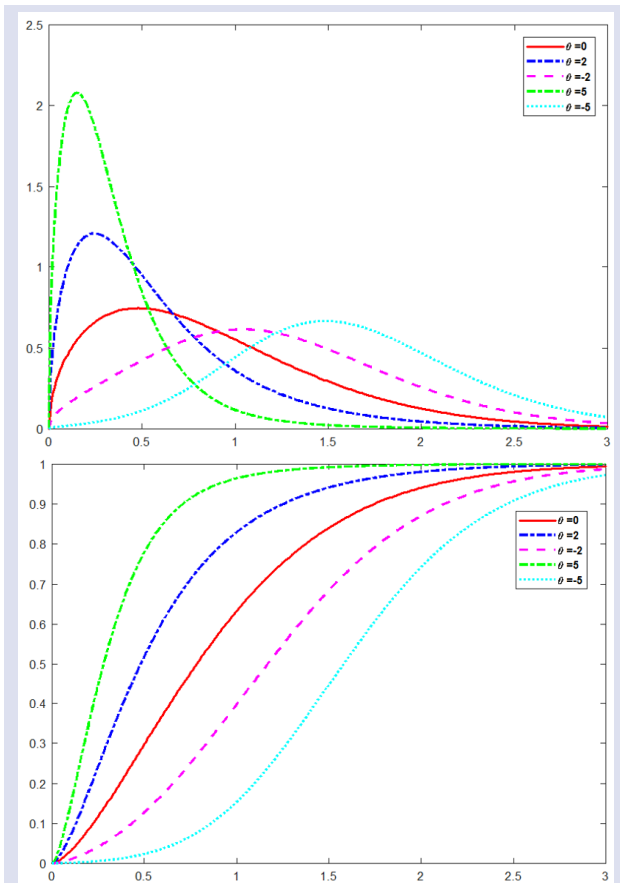


Figure 3. The pdfs and cdfs of Uni-Weib distribution,  $\lambda=1$  and  $k=1.5$

Same simulation procedure in the previous subsections is applied to Uni-Weib distribution with parameters  $\lambda=1$  and  $k=1.5$ . The results for representative  $\theta$  values are listed in Table 3. When  $\theta$  tends to 0, the Uni-Weib distribution converges to the well-known Weibull distribution, as Figure 3 supports the results.

Table 3. The simulation results for the Uni-Weib distribution,  $\lambda=1$  and  $k=1.5$

$\theta$	Mean	Variance	SV	KV
-5	1.631	0.636	0.486	3.438
-2	1.238	0.661	0.632	3.376
-0.001	0.903	0.610	1.003	4.044
0	0.904	0.610	1.003	4.036
0.001	0.904	0.610	1.006	4.052
2	0.606	0.484	1.512	5.953
5	0.352	0.291	1.862	8.406

Suppose  $X_1, X_2, \dots, X_n$  are random variables from the Uni-Weib distribution defined in (3.20). The likelihood and log-likelihood functions are given, respectively in (3.22) and (3.23).

$$L(k, \lambda, \theta) = (1 - \exp(-\theta))^{-n} \theta^n k^n \lambda^{-n} \exp(-\theta \sum_{i=1}^n [1 - \exp(-(\frac{x_i}{\lambda})^k)]) \prod_{i=1}^n (\frac{x_i}{\lambda})^{k-1} \exp(-\sum_{i=1}^n (\frac{x_i}{\lambda})^{k-1}) \quad (3.22)$$

$$l(k, \lambda, \theta) = -n \ln(1 - \exp(-\theta)) + n \ln \theta + n \ln k - n \ln \lambda + \sum_{i=1}^n (k-1) \ln(\frac{x_i}{\lambda}) - \sum_{i=1}^n (\frac{x_i}{\lambda})^k - \theta \sum_{i=1}^n [1 - \exp(-(\frac{x_i}{\lambda})^k)] \quad (3.23)$$

After differentiating the log-likelihood function with respect to the parameters and equating them to zero following likelihood equations are obtained.

$$\frac{\partial \ln L}{\partial k} = \frac{n}{k} + \sum_{i=1}^n (\frac{x_i}{\lambda}) - \sum_{i=1}^n (\frac{x_i}{\lambda})^k \ln(\frac{x_i}{\lambda}) + \theta \sum_{i=1}^n \exp(-(\frac{x_i}{\lambda})^k) (\frac{x_i}{\lambda}) \ln(\frac{x_i}{\lambda})$$

$$\frac{\partial \ln L}{\partial \lambda} = -n - \sum_{i=1}^n \frac{(k-1)}{x_i} + k \sum_{i=1}^n (\frac{x_i}{\lambda})^{k-1} + \theta k \sum_{i=1}^n \exp(-(\frac{x_i}{\lambda})^k) (\frac{x_i}{\lambda})^{k-1} \quad (3.24)$$

$$\frac{\partial \ln L}{\partial \theta} = -\frac{n}{\theta} - \frac{n \exp(-\theta)}{1 - \exp(-\theta)} - \sum_{i=1}^n (1 - \exp(-(\frac{x_i}{\lambda})^k))$$

### Results and Discussion

In this section, we compare the results which are obtained by fitting distributions to the real data sets. Each extension which are introduced in Section 3 and their original distributions are fitted to the data, separately. Akaike Information Criterion (AIC) and log-likelihood (loglik) values are calculated to compare fitting performances of the original distribution and their extensions.

#### FG Scores Data

The first data set refers the Ferriman–Gallwey (FG) scores which are studied by [21]. FG score is a method of evaluating and quantifying hirsutism in women. The data set consists of FG scores of the women living in different areas of Turkey. The data set is 28.774; 27.958; 39.751; 22.659; 31.232; 32.990; 34.408; 34.920; 35.822; 23.685; 41.101; 35.879; 9.811; 24.689; 13.217; 22.343; 28.273; 27.340; 25.214; 14.960; 39.724; 35.557; 37.173; 25.412; 46.286; 31.564; 13.321; 29.606; 25.112; 18.158; 33.057; 22.683; 36.380; 31.451; 37.919; 25.729. The descriptive statistics of the FG Scores data are listed in Table 4.

Table 4. Descriptive Statistics for FG Scores Data

Mean	Std. Dev.	Skewness	Kurtosis
29.004	8.509	-0.374	2.816

Maximum likelihood estimates of Normal and Uni-Normal distributions are listed in Table 5. The Uni-Normal distribution gives best fit over Normal distribution according to the calculated log-likelihood and AIC values (see Table 5). Figures 4 also illustrates this conclusion.

Table 5. The ML Estimates, Values of Loglik and AIC for Normal and Uni-Normal Distributions

	$\hat{\mu}$	$\hat{\sigma}$	$\hat{\theta}$	loglik	AIC
Normal	21.004	8.509	-	-127.66	259.32
Uni-Normal	28.941	11.866	0.581	-109.27	224.54

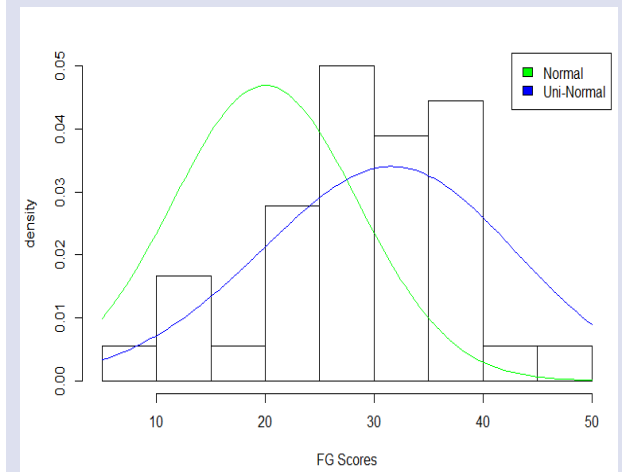


Figure 4. The histogram of FG Scores data with fitted pdfs

**Failure Times Data**

The second data refers the times of failure and running times for a sample of devices from a field-tracking study of a larger system. At a certain point in time, 30 units were installed in normal service conditions. Two causes of failure were observed for each unit that failed: the failure caused by an accumulation of randomly occurring damage from power-line voltage spikes during electric storms and failure caused by normal product wear. The data is studied by [222]. They proposed to fit Weibull distribution to the data. The times are 275, 13, 147, 23, 181, 30, 65, 10, 300, 173, 106, 300, 300, 212, 300, 300, 300, 2, 261, 293, 88, 247, 28, 143, 300, 23, 300, 80, 245, 266. The descriptive statistics of the Failure Times data are summarized in Table 6.

Table 6. Descriptive Statistics for Failure Times Data

Mean	Std. Dev.	Skewness	Kurtosis
178.142	112.971	-0.323	1.449

The ML estimates of Weibull and its extension Uni-Weibull are obtained, and values of log-likelihood and AIC are listed in Table 7.

Table 7. The ML Estimates, Values of Loglik and AIC for Weibull and Uni-Weib Distributions

	$\hat{\lambda}$	$\hat{k}$	$\hat{\theta}$	loglik	AIC
Weibull	188.041	1.265	-	-184.041	372.08
Uni-Weib	184.855	1.264	-0.5182	-165.835	337.67

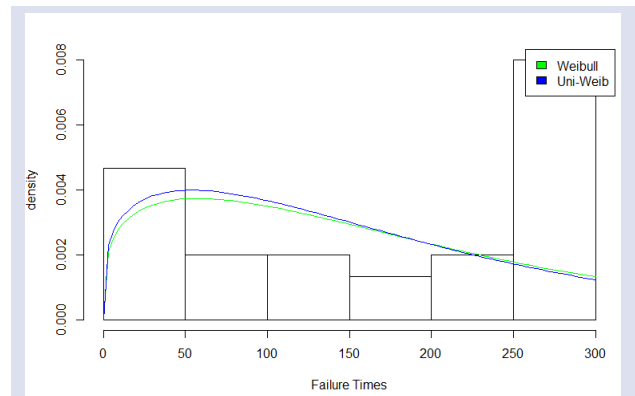


Figure 5. The histogram of Failure Times data with fitted pdfs

Table 7 and Figure 5 indicate that Uni-Weibull distribution gives best fit to the studied data over the well-known Weibull distribution.

**Petroleum Reservoir Data**

The last example has been studied by [23] and is about the shape measurements of 48 rock samples from a petroleum reservoir. The data set is: 0.09032, 0.14862, 0.18331, 0.11706, 0.12241, 0.16704, 0.18965, 0.16412, 0.20365, 0.16239, 0.15094, 0.14814, 0.22859, 0.23162, 0.17256, 0.15348, 0.20431, 0.26272, 0.20007, 0.14481, 0.11385, 0.29102, 0.24007, 0.16186, 0.28088, 0.17945, 0.19180, 0.13308, 0.22521, 0.34127, 0.31164, 0.27601, 0.19765, 0.32663, 0.15419, 0.27601, 0.17696, 0.43871, 0.16358, 0.25383, 0.32864, 0.23008, 0.46412, 0.42047, 0.20074, 0.26265, 0.18245, 0.20044.

Table 8 summarizes the descriptive statistics of the Petroleum Reservoir data.

Table 8. Descriptive Statistics for Petroleum Reservoir Data

Mean	Std. Dev.	Skewness	Kurtosis
0.218	0.083	1.208	4.372

Table 9. The ML Estimates, Values of Loglik and AIC for Kumaraswamy and Kums Distributions

	$\hat{a}$	$\hat{b}$	$\hat{\theta}$	loglik	AIC
Kumaraswamy	2.710	44.04	-	52.49	-100.98
Uni-Kums	2.729	24.701	-0.771	60.56	-115.13

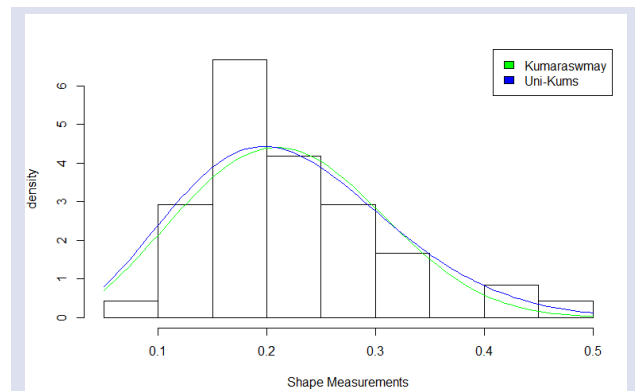


Figure 6. The histogram of Shape Measurements data with fitted pdfs

According to the results in Table 9 and the demonstration by Figure 6, the Uni-Kumaraswamy distribution can be proposed to model shape measurements data over the Kumaraswamy distribution.

## Discussion and Conclusion

In this paper, we proposed a general extension form of T - X family of distributions with an additional parameter. We consider -T- as Uniform distribution, then call the new extensions of distributions as Uniform-X distributions. Three examples of Uniform-X distributions which are Uniform-Normal (Uni-Normal), Uniform-Kumaraswamy (Uni-Kums) and Uniform-Weibull (Uni-Weib) distributions are introduced. The properties of these distributions such as the density functions, the medians and the quantile functions are examined. Simulation studies are conducted for demonstrating the sample behavior for the mean, the variance, the skewness and the kurtosis for new distributions. Simulation results show that if the additional parameter  $\theta$  tends to 0, the Uniform-X distributions converges to the original distributions. In the application section of the paper, the considered probability distributions and their extensions are compared in point of the fitting performances. For all the considered data sets, new extensions give better fit over the considered well-known probability distributions.

## Acknowledgment

The authors wish to place on record their appreciation to the chief editor of this journal and the anonymous reviewers for critically examining the paper, providing constructive comments and suggestions.

## Conflicts of Interest

The authors declared no conflict of interest.

## References

- [1] Amoroso L.R., Intorno Alla Curva dei Redditi, *Annali de Mathematica Series*, 4 (2) (1925) 123-159.
- [2] Good I.J. The Population Frequencies of the Species and the Estimation of Population Parameters, *Biometrika*, 40 (1953) 237-260.
- [3] Hoskings J.R.M., Wallis J.R. Parameter and Quantile Estimation for the Generalized Pareto Distribution, *Technometrics*, 29 (1987) 339-349.
- [4] Kinacı İ., Kuş C., Karakaya, K. and Akdoğan Y. APT-Pareto Distribution and its Properties, *Cumhuriyet Science Journal*, 40 (2) (2019) 378-387.
- [5] Ljubo M. Curves and Concentration Indices Generalized Pareto Distributions, *Statistical Review*, 15 (1965) 257-260.
- [6] McDonald J.B., Some Generalized Functions for the Size Distribution of Income, *Econometrica*, 52 (1984) 647-663.
- [7] Eugene E., Lee C., Famoye F., The beta-normal distribution and its application, *Commun.Stat, Theory Methods*, 31 (4) (2002) 497-512.
- [8] Akinsete A., Famoye F., Lee C. The beta-Pareto distribution, *Statistics*, 42 (2008) 457-563.
- [9] Alshawarbeh E., Famoye F., Lee C. The beta-Cauchy distribution: some properties and applications, *Journal of Statistical Theory and Applications*, 12 (4) (2013) 378-391.
- [10] Barreto-Souza W., Santos A.H.S., Corderio G.M., The beta generalized exponential distribution, *Journal of Statistical Computation and Simulation*, 80 (2) (2010) 159-172.
- [11] Famoye F., Lee C., Olumolade O., The beta-Weibull distribution, *J. Stat. Theory Appl.*, 4 (2) (2005) 121-136.
- [12] Nadarajah S., Kotz S., The beta Gumbel distribution, *Math. Probl. Eng.*, 4 (2004) 323-332.
- [13] Nadarajah S., Kotz S., The beta exponential distribution, *Reliab. Eng. Syst. Saf.*, 91 (6) (2005) 689-697.
- [14] Jones M.C., Kumaraswamy's distribution: a beta type distribution with tractability advantages, *Stat. Methodology*, 6 (2008) 70-81.
- [15] Cordeiro G.M., Ortega E.M.M., Nadarajah S., The Kumaraswamy Weibull distribution with application to failure data, *J. Franklin Inst.*, 347 (2010) 399-429.
- [16] Cordeiro G.M., Pescim R.R., Ortega E.M.M., The Kumaraswamy generalized half-normal distribution for skewed positive data, *J. Data Sci.*, 10 (2012) 195-224.
- [17] de Castro M.A.R., Ortega E.M.M., Cordeiro G.M., The Kumaraswamy generalized gamma distribution with application in survival analysis, *Stat. Methodol.*, 8 (5) (2011) 411-433.
- [18] Alzaatreh A., Lee C., Famoye F. A new method for generating families of continuous distributions, *Metron*, 71 (2013) 63-79.
- [19] Celik N., Guloksuz CT., A new lifetime distribution, *Ekspluatacija Niezawodnosc (Maintenance and Reliability)*, 19 (4) (2017) 634-639.
- [20] Guloksuz CT., Celik N., An Extension of Generalized Extreme Value Distribution: Uniform-GEV Distribution and Its Application to Earthquake Data, *Thailand Statistician*, 18 (4) (2020) 491-506.
- [21] Celik N., Robust Statistical Inference in ANOVA Models Using Skew Distributions and Applications", Phd Thesis, Ankara University, Graduate School of Natural and Applied Sciences, Turkey, 2012.
- [22] Meeker W.Q., Escobar L.A., Statistical methods for reliability data. USA: Wiley Series, (1998)
- [23] Javanshiri Z., Habibi Rad A., Arghami N.R. Exp-Kumaraswamy Distributions: Some Properties and Applications, *Journal of Sciences, Islamic Republic of Iran*, 26 (1) (2015) 57-69.



## **AUTHOR GUIDELINES**

Thank you for choosing to submit your paper to Cumhuriyet Science Journal. The following instructions will ensure we have everything required so your paper can move through pre-evaluating, peer review, production and publication smoothly. Please take the time to read and follow them as closely as possible, as doing so will ensure your paper matches the journal's requirements.

### **Submission**

*Cumhuriyet Science Journal* is an international, peer-reviewed, free of charge journal covering the full scope of both natural and engineering sciences. Manuscripts should be submitted by one of the authors of the manuscript as online submission after registration to the Cumhuriyet Sciences Journal. Microsoft Word (.doc, .docx, .rtf), files can be submitted. There is no page limit. If there is a problem while uploading the files of manuscript, please try to reduce their file size, especially manuscripts including embedded figures. Submissions by anyone other than one of the authors will not be accepted. The submitting author takes responsibility for the paper during submission and peer review. If for some technical reason submission through the online submission system is not possible, the author can contact [csj@cumhuriyet.edu.tr](mailto:csj@cumhuriyet.edu.tr) for support.

### **Submission or processing charges**

*Cumhuriyet Science Journal* does not charge any article submission, processing charges, and printing charge from the authors.

### **Terms of Submission**

Papers must be submitted on the understanding that they have not been published elsewhere (except in the form of an abstract or as part of a published lecture, review, or thesis) and are not currently under consideration by another journal. The submitting author is responsible for ensuring that the article's publication has been approved by all the other coauthors. It is also the authors' responsibility to ensure that the articles emanating from a particular institution are submitted with the approval of the necessary institution. Only an acknowledgment from the editorial office officially establishes the date of receipt. Further correspondence and proofs will be sent to the author(s) before publication unless otherwise indicated. It is a condition of submission of a paper that the corresponding author permit editing of the paper for readability. All enquiries concerning the publication of accepted papers should be addressed to [csj@cumhuriyet.edu.tr](mailto:csj@cumhuriyet.edu.tr). Please note that Cumhuriyet Science Journal uses iThenticate software to screen papers for unoriginal material. By submitting your paper to Cumhuriyet Science Journal are agreeing to any necessary originality checks your paper may have to undergo during the peer review and production processes. Upon receiving a new manuscript, the Editorial office conducts initial pre-refereeing checks to ensure the article is legible, complete, correctly formatted, original, within the scope of the journal in question, in the style of a scientific article and written in clear English. Any article that has problems with any of the journal criteria may be rejected at this stage.

### **Peer Review**

This journal operates a single blind review process. All contributions will be initially assessed by the editor for suitability for the journal. Papers deemed suitable are then typically sent to a minimum of two independent expert reviewer to assess the scientific quality of the paper. The author is required to upload the revised article to the system within 15 days by making the corrections suggested by the referee. The article will be rejected if there are no fixes in it. The Editor is responsible for the final decision regarding acceptance or rejection of articles. The Editor's decision is final

### **Title and Authorship Information**

The following information should be included

Paper title

Full author names

Full institutional mailing addresses

Corresponding address

Email address

### **Abstract**

The manuscript should contain an abstract. The researchers who are native speakers of Turkish have to add Turkish title and abstract as well. The abstract should be self-contained and citation-free and should be 250-300 words.

### **Keywords**

Keywords of the scientific articles should be selected from the web address of [www.bilimadresleri.com](http://www.bilimadresleri.com)

### **Introduction**

This section should be succinct, with no subheadings.

### **Materials and Methods**

This part should contain sufficient detail so that all procedures can be repeated. It can be divided into subsections if required.

### **Conflicts of interest**

Sample sentence if there is no conflict of interest: The authors stated that did not have conflict of interests.

### **Acknowledgements**

Sample sentences for acknowledgements: The work was supported by grants from CUBAP (T-1111). We would like to acknowledge Prof. Mehmet Sözer, MD, for his precious technical and editorial assistance. We would like to thank

### **References**

References to cited literature should be identified by number in the text in square brackets and grouped at the end of the paper in numerical order of appearance. Each reference must be cited in the text. Always give inclusive page numbers for references to journal articles and a page range or chapter number for books. References should be styled and punctuated according to the following examples

- [1] Karaca E., Ulusoy S., Morgül Ü., Ulusoy H.I., Development of Analytical Method for Sensitive Determination of Streptozotocin based on Solid Phase Extraction, Cumhuriyet Sci. J., 41 (4) (2020) 826-831. (sample reference for journals)
- [2] Keskin B., Ozkan A.S., Inverse Spectral Problems for Dirac Operator with Eigenvalue Dependent Boundary and Jump Conditions, Acta Math. Hungar., 130 (2011) 150-159(sample reference for journals)
- [3] Mazur M.T., Kurman R.J., Dysfunctional Uterine Bleeding. In: Mazur M.T., Kurman R.J., (Eds). Diagnosis of endometrial biopsies and curettings, A practical approach. 2nd ed. Berlin: Springer, (2005) 100-120. (sample reference for book chapters)
- [4] Mazur M.T., Kurman R.J.,Diagnosis of endometrial biopsies and curettings, A practical approach. 2nd ed. Berlin, (2005) 100-120. (sample reference for book)
- [5] National Cancer Institute, Surveillance Epidemiology and End Results. Cancer of the Corpus and Uterus, NOS. Available at: [http://seer.cancer.gov/statfacts/html/corp.html?statfacts\\_page=corp](http://seer.cancer.gov/statfacts/html/corp.html?statfacts_page=corp). Retrieved March 2, 2008. (sample reference for websites)
- [6] Surname N., Title of thesis, PD or master thesis, Name of university, name of institue, year. (sample reference for thesis)
- [7] Surname N., Title of fulltext conference paper, name of conference, city, year, pages. (sample reference for Abstratcs in conferences are not accepted as a valid reference except full text )

### **Preparation of Figures**

Each figure can be integrated in the paper body or separately uploaded and should be cited in a consecutive order. Figure widths can be 4-6 inch as 300 dpi. The labels of the figures should be clear and informative. The name and the subtitles of the figures must be 9-point font.

## **Preparation of Tables**

Tables should be cited consecutively in the text. Every table must have a descriptive title and if numerical measurements are given, the units should be included in the column heading. Tables should be simple with simple borders and text written as left text. The name and the subtitle of the tables must be 9-point font

## **Proofs**

Corrected proofs must be returned to the publisher within 2 weeks of receipt. The publisher will do everything possible to ensure prompt publication. It will therefore be appreciated if the manuscripts and figures conform from the outset to the style of the journal.

## **Copyright**

Open Access authors retain the copyrights of their papers, and all open access articles are distributed under the terms of the Creative Commons Attribution license, which permits unrestricted use, distribution and reproduction in any medium, provided that the original work is properly cited.

The use of general descriptive names, trade names, trademarks, and so forth in this publication, even if not specifically identified, does not imply that these names are not protected by the relevant laws and regulations.

While the advice and information in this journal are believed to be true and accurate on the date of its going to press, neither the authors, the editors, nor the publisher can accept any legal responsibility for any errors or omissions that may be made. The publisher makes no warranty, express or implied, with respect to the material contained herein.

## **Ethical Guidelines**

New methods and ethically relevant aspects must be described in detail, bearing in mind the following:

**Human Experiments.** All work must be conducted in accordance with the Declaration of Helsinki (1964). Papers describing experimental work on human subjects who carry a risk of harm must include:

A statement that the experiment was conducted with the understanding and the consent of the human subject.

A statement that the responsible Ethical Committee has approved the experiments.

**Animal Experiments.** Papers describing experiments on living animals should provide:

A full description of any anaesthetic and surgical procedure used.

Evidence that all possible steps were taken to avoid animal suffering at each stage of the experiment. Papers describing experiments on isolated tissues must indicate precisely how the donor tissues were obtained.

## **Submission Preparation Checklist**

As part of the submission process, authors are required to check off their submission's compliance with all of the following items, and submissions may be rejected that do not adhere to these guidelines.

The submission has not been previously published, nor is it before another journal for consideration (or an explanation has been provided in Comments to the Editor).

The submission file is in Microsoft Word document file (Times New Roman) format.

Where available, URLs for the references have been provided.

The text is single-spaced; uses a 11-point font; employs italics, rather than underlining (except with URL addresses); and all illustrations, figures, and tables are placed within the text at the appropriate points, rather than at the end.

The text adheres to the stylistic and bibliographic requirements outlined in the Author Guidelines, which is found in About the Journal.

If submitting to a peer-reviewed section of the journal, the instructions in Ensuring a Double-Blind Review have been followed.